Physics of the Solid State, Vol. 45, No. 9, 2003, pp. 1613–1616. Translated from Fizika Tverdogo Tela, Vol. 45, No. 9, 2003, pp. 1537–1540.

METALS AND SUPERCONDUCTORS

Effect of Electron–Plasmon and Plasmon–Phonon Interactions on Relaxation in Crystals of Bi and $Bi_{1-x}Sb_x$ Alloys

N. P. Stepanov* and V. M. Grabov**

** Transbaikalia State Pedagogical University, Chita, 672000 Russia*

e-mail: stepanov@academ.chita.ru

*** Russian State Pedagogical University, St. Petersburg, 191186 Russia*

Received December 27, 2002; in final form, March 7, 2003

Abstract—Upon introduction of a certain amount of tin acceptor impurities into crystals of Bi and $Bi_{1-x}Sb_x$ alloys, the energy of plasma oscillations becomes close in magnitude to the energies of interband transitions and optical phonons. This is accompanied by a substantial enhancement of the interaction between elementary excitations and a considerable change in the relaxation time of charge carriers, which is observed experimentally in the optical and electrical properties. © *2003 MAIK "Nauka/Interperiodica".*

1. INTRODUCTION

Optical investigations into the properties of crystalline bismuth and bismuth–antimony alloys with tin acceptor impurities have revealed interesting features in the behavior of their electron system, which are associated with the coincidence of the energies in the plasmon, phonon, and electron spectra [1, 2]. These features could be specific to the entire class of materials, namely, narrow-gap semiconductors and semimetals, which are widely used as thermoelectric materials [3]. The present paper reports on the results of our investigations, according to which the electron–plasmon and plasmon–phonon interactions affect the optical and electrical properties of crystalline bismuth and bismuth–antimony alloys.

2. EXPERIMENTAL TECHNIQUE

The polarized reflectivity spectra of crystalline bismuth and bismuth–antimony alloys were measured in the geometries $\mathbf{E} \perp C_3$ and $\mathbf{E} \parallel C_3$ (where $\mathbf{E}$ is the vector of the electric field of probe radiation and C_3 is the optic axis of the crystal) on a Bruker IFS-113V Fourier spectrometer in the range 50–800 cm^{-1} with a resolution of 2 cm^{-1} according to the procedure described in [1]. For the most part, the measurements were performed in polarized light. A degree of polarization of 98–99% over the entire spectral range covered was achieved by using polyethylene-based grating replicas. The angle of light incidence on the sample was no more than 8°. All the results presented in this work were obtained at a temperature of 80 K. We examined samples of undoped and tin-doped $Bi_{1-x}Sb_x$ single crystals (x = 0, 0.03, and 0.07) which were seed-grown by zone recrystallization [4]. The nonuniformity of the antimony distribution over the sample was checked using a Camebax x-ray microanalyzer and did not exceed 0.5%. For optical and galvanomagnetic measurements, the samples were obtained by spark cutting from the central part of the ingot. The concentration of free charge carriers and their type were determined from the measurements of the tensor components of the Hall effect and the resistivity at T = 80 K [4]. It should be noted that crystals of the bismuth type cannot be cleaved along the planes parallel to the C_3 axis. For this reason, in order to prepare samples suitable for our measurements, we used spark cutting and then removed the damaged layer by chemical or electrochemical polishing. The polishing quality was checked against the similarity of the reflectivity spectrum measured for the polished surface in the geometry $\mathbf{k} \perp C_3$ and $\mathbf{E} \perp C_3$ to the spectrum recorded for the natural mirror cleavage plane at $\mathbf{k} \parallel C_3$ and $\mathbf{E} \perp C_3$.

3. RESULTS AND DISCUSSION

In the context of our study, it is of interest to analyze the energy loss function of electromagnetic radiation interacting with a crystal:

$$-\mathrm{Im}(\varepsilon^{-1}) = \varepsilon_2/((\varepsilon_1)^2 - (\varepsilon_2)^2). \quad (1)$$

The energy loss function is directly related to the entropy production rate in the system [5]. Figure 1 shows the spectral dependences of the energy loss function, which were obtained with the use of the Kramers–Kronig relations from the reflectivity spectra of bismuth crystals with tin acceptor impurities [2]. The numbers of the spectra in Fig. 1 correspond to the sample numbers in the table. The table presents experimental values of the parameters obtained during electrical and optical measurements. The absolute maximum of the energy loss function corresponds to the frequency of plasma resonance. Indeed, if the imaginary part of the permittivity ε_2 is small, the energy loss function

1063-7834/03/4509-1613$24.00

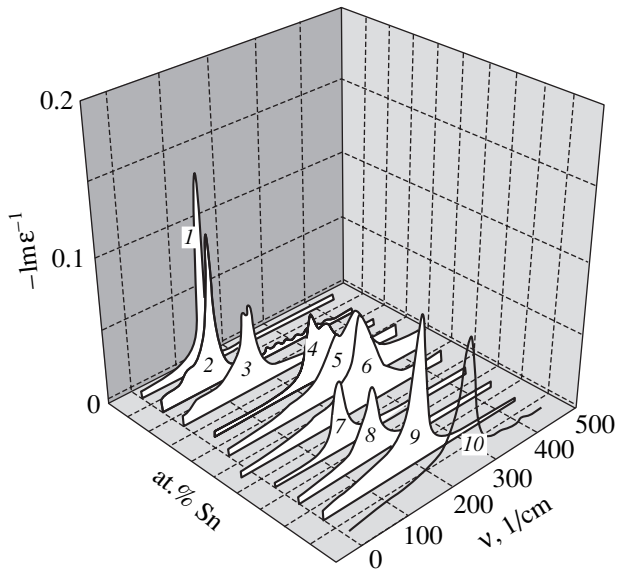

Fig. 1. Spectral dependences of the energy loss function $-\mathrm{Im}(\varepsilon^{-1})$ for bismuth single crystals with tin acceptor impurities. $\mathbf{E} \perp C_3$, $T = 80$ K. The numbers of the spectra correspond to the sample numbers in the table.

exhibits a maximum at the point where the real part ε_1 reduces to zero. When the refractive index $n = (\varepsilon_1)^{1/2}$ vanishes, according to the relationship $\lambda = 2\pi c/n\omega$, the wavelength becomes infinite. In this case, the electron system as a whole oscillates in phase [5], which is a condition of existence of collective plasma oscillations. At the plasma frequency, the radiation is intensively absorbed by the crystal, whereas the depth of radiation penetration into the crystal is minimum. Note also that the half-width of the energy loss line characterizes the decay time of plasma oscillations (plasmon relaxation).

The introduction of tin acceptor impurities (up to 0.05 at. %) into bismuth leads to a shift in the plasma frequency toward the low-energy range, which can be clearly seen from Fig. 1 and the table. This correlates well with the observed increase in the resistivity (see table). The shifts in the plasma minima, which are observed upon doping of Bi and $Bi_{1-x}Sb_x$ crystals with donor and acceptor impurities, agree with the concept of the band structure of the studied crystals [6]. The band structure is determined by the changes in the contributions of free charge carriers at the L_s, L_a, and T_{45} extrema of the valence band and the conduction band to the formation of the returned signal. For the band structure of bismuth crystals at $\omega_p\tau \gg 1$, the squares of the plasma frequencies can be expressed as follows:

$$\omega_{p\perp}^2 = \frac{e^2}{\varepsilon_{\infty\perp}}\frac{1}{2}\sum_i N_i\left[\frac{1}{(m_{11}^*)_i} + \frac{1}{(m_{22}^*)_i}\right];$$
$$\omega_{p\parallel}^2 = \frac{e^2}{\varepsilon_{\infty\parallel}}\sum_i N_i\left[\frac{1}{(m_{33}^*)_i}\right]. \quad (2)$$

where $\omega_{p\perp}$ and $\omega_{p\parallel}$ are the plasma frequencies corresponding to the orientations $\mathbf{E} \perp C_3$ and $\mathbf{E} \parallel C_3$, respectively; ε_∞ is the high-frequency permittivity; e is the elementary charge; N_i is the concentration of free charge carriers at the L_a, L_s, and T extrema; and $(m_{11}^*)_i$, $(m_{22}^*)_i$, and $(m_{33}^*)_i$ are the effective masses of charge carriers along the bisecting, binary, and trigonal axes of the crystal, respectively. The summation takes into account the multicomponent composition of the plasma.

As follows from expression (2) and the band structure of the $Bi_{1-x}Sb_x$ crystals (Fig. 2), the minima in the plasma frequency correlate with the minima in the concentration of light charge carriers at the L extrema. This situation arises when the chemical potential corresponds to an energy gap between the extrema of the valence band and the conduction band at the L point of the Brillouin zone, which occurs upon introduction of acceptor impurities. In this case, the energy of plasma oscillations $E_p \approx 10$ meV is determined primarily by the contribution of charge carriers at the strongly anisotro-

Experimental values of the resistivity tensor components ρ_{11} and ρ_{33} and plasma frequencies of bismuth single crystals at $T = 80$ K

Sn content in Bi crystals, at. %	ρ_{11}, 10^{-6} Ω m	ρ_{33}, 10^{-6} Ω m	$\omega_{p\perp}$, 10^{13} s^{-1} $\mathbf{E} \perp C_3$	$\omega_{p\parallel}$, 10^{13} s^{-1} $\mathbf{E} \parallel C_3$	Number of spectrum in Fig. 1
0			3.58	3.35	1
0.02	0.234	2.104	3.06	1.97	2
0.04	1.004	3.152	3.18	2.34	3
0.05(1)	1.134	3.351	3.07	2.42	4
0.05(2)	0.639	1.32	6.32	4.61	5
0.05(3)	0.660	–	5.47	3.61	6
0.06	1.116	3.541	3.72	1.71	7
0.08	0.942	2.673	3.99	1.89	8
0.15	0.708	1.592	5.76	3.87	9
0.2	0.726	1.464	7.72	6.59	10

pic extremum T_{45} (heavy holes). Therefore, the doping of crystalline bismuth and bismuth–antimony alloy with acceptor impurities leads to a decrease in the plasma frequencies (Fig. 1). As a result, the energy of plasma oscillations becomes close in magnitude to the energy of the longitudinal optical phonon at the Γ point of the Brillouin zone E_{ph} = 12.4 meV [7] and to the energy of interband transitions at the L point of the Brillouin zone [2]. In the framework of the two-band model, the energy of the interband transition can be calculated in terms of the Burstein–Moss shift: $E_T = E_{gL} + 2E_F$. In the case when the chemical potential corresponds to an energy gap at the L point of the Brillouin zone in bismuth crystals, we obtain the Fermi energy $E_F \approx 0$ and $E_T \approx E_{gL} \approx 15$ meV.

The energies of the aforementioned elementary excitations of the electron and phonon system become close to each other in magnitude, provided bismuth crystals are doped with tin acceptor impurities to a content of 0.04–0.05 at. %. For these crystals, the substantial changes observed in the spectra of optical functions, specifically in the spectra of the energy loss function (spectra *3*, *4*, *5* in Fig. 1), are accompanied by an increase in the rate of damping of plasma oscillations [8]. The observed changes in the optical functions suggest an intensive energy exchange between plasma oscillations and crystal lattice vibrations, which, in turn, affects the relaxation rate [1, 2, 8].

It should be noted that the energy of plasma oscillations $E_{p\perp}$ = 10 meV for bismuth crystals with 0.05 at. % Sn (for the $Bi_{0.93}Sb_{0.07}$ crystal, $E_{p\perp}$ = 8 meV at T = 80 K) is close to the energy k_BT = 6.8 meV at this temperature. Therefore, in semimetals and narrow-gap semiconductors, unlike metals, the plasma oscillations reach an energy $\hbar\omega_p \approx kT$ and can be excited thermally.

For $Bi_{1-x}Sb_x$ crystals ($0 \le x \le 0.22$), the energy of plasma oscillations E_p varies in the range 5–30 meV. Under these conditions, quasi-resonance interaction between excitations of the electron system and the crystal lattice becomes possible, which leads to changes in the excitation processes. For example, Bogdanov *et al.* [9] observed a sharp increase (by approximately one order of magnitude) in the lifetime of nonequilibrium charge carriers in the $Bi_{0.82}Sb_{0.18}$ crystal as compared to the $Bi_{0.9}Sb_{0.1}$ crystal (Fig. 3). It was also found that, in a magnetic field, the lifetime of charge carriers changes significantly in crystals containing less than 15 at. % Sb and remains unchanged in crystals with a higher Sb content [9].

Let us analyze these results together with data on the energy of plasma oscillations, the energy of interband transition at the L point of the Brillouin zone, and the energy of the longitudinal optical phonon. This analysis demonstrates that a decrease in the lifetime of nonequilibrium charge carriers in the $Bi_{0.9}Sb_{0.1}$ crystals is associated with the close values of the energies in the electron, plasmon, and phonon spectra, respectively. For

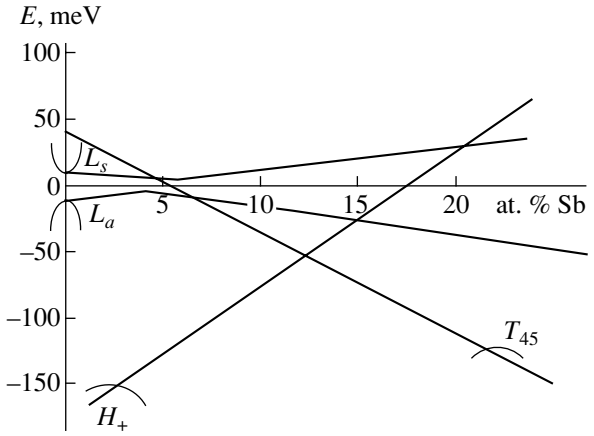

Fig. 2. Energy position of the band extrema as a function of the antimony content x in $Bi_{1-x}Sb_x$ crystals.

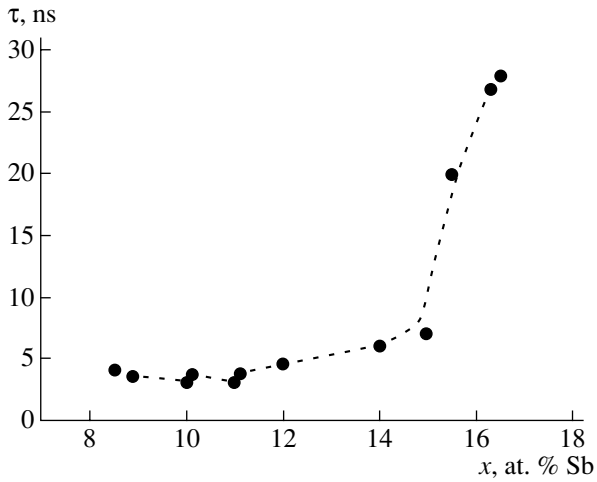

Fig. 3. Lifetime of nonequilibrium charge carriers as a function of the antimony content x in $Bi_{1-x}Sb_x$ crystals ($0.085 \le x \le 0.17$) at T = 4.2 K in the absence of a magnetic field [9].

example, according to Kulakovskiĭ and Egorov [10], the energy of plasma oscillations in the $Bi_{0.905}Sb_{0.095}$ crystal is equal to 9.6 meV. However, as was shown by Lifshits *et al.* [11], the band gap in the $Bi_{0.89}Sb_{0.11}$ crystal is 10.5 meV. A change in the antimony content in the studied crystals is accompanied by an increase in the difference between these energies. In particular, for the $Bi_{0.884}Sb_{0.116}$ crystal, the energy of plasma oscillations is equal to 7 meV [10], whereas the band gap is 12.5 meV [11]. For the $Bi_{0.84}Sb_{0.16}$ crystal, the band gap increases to 18 meV [11], whereas the plasma frequencies should reach minimum values, because the band gap in these crystals has a maximum value. Thus, an increase in the antimony content to 16 at. % causes an increase in the difference between the frequencies of the plasma resonance, the optical phonon, and the interband transition; consequently, the carrier lifetime

increases drastically (Fig. 3). Brandt *et al.* [6] observed a transition to a semimetal state in the $Bi_{0.78}Sb_{0.22}$ crystal. In this case, as the concentration of charge carriers increases, the plasma frequency again becomes close to the phonon frequency in magnitude. These features in relaxation processes are caused by electron–plasmon and plasmon–phonon interactions and may appear to be characteristic of other narrow-gap semiconductors, for example, $Cd_{1-x}Hg_xTe$ [12].

4. CONCLUSIONS

Thus, it was demonstrated that, upon changes in the energy position of the band extrema and in the concentration of free charge carriers in the crystals of semimetals and narrow-gap semiconductors due to variations in the composition, temperature, or doping, the energies of plasmons, phonons, and interband transitions become close in magnitude. This is attended by substantial variations in the relaxation processes, which should be taken into account in the design and prediction of the properties of semiconductor materials.

REFERENCES

1. N. P. Stepanov and V. M. Grabov, Opt. Spektrosk. **84**, 581 (1998) [Opt. Spectrosc. **84**, 515 (1998)].
2. N. P. Stepanov and V. M. Grabov, Opt. Spektrosk. **92**, 794 (2002) [Opt. Spektrosc. **92**, 710 (2002)].
3. I. V. Gasenkova, M. K. Zhitinskaya, S. A. Nemov, and L. D. Ivanova, Fiz. Tverd. Tela (St. Petersburg) **44**, 1766 (2002) [Phys. Solid State **44**, 1850 (2002)].
4. G. A. Ivanov and V. M. Grabov, Fiz. Tekh. Poluprovodn. (St. Petersburg) **29**, 1040 (1995) [Semiconductors **29**, 538 (1995)].
5. P. Grosse, *Freie Electronen in Festköpern* (Springer, Heidelberg, 1979; Mir, Moscow, 1982), Chap. 9.
6. N. B. Brandt, H. Dittman, and Ya. G. Ponomarev, Fiz. Tverd. Tela (Leningrad) **13**, 2860 (1971) [Sov. Phys. Solid State **13**, 2408 (1971)].
7. F. E. Macfarlane, J. Phys. Chem. Solids **1**, 989 (1971).
8. N. P. Stepanov and V. M. Grabov, Fiz. Tekh. Poluprovodn. (St. Petersburg) **36**, 1045 (2002) [Semiconductors **36**, 971 (2002)].
9. E. V. Bogdanov, N. B. Brandt, V. M. Manankov, and L. S. Fleĭshman, Fiz. Tekh. Poluprovodn. (Leningrad) **18**, 1263 (1984) [Sov. Phys. Semicond. **18**, 788 (1984)].
10. V. D. Kulakovskiĭ and V. D. Egorov, Fiz. Tverd. Tela (Leningrad) **15**, 2053 (1973) [Sov. Phys. Solid State **15**, 1507 (1973)].
11. T. M. Lifshits, A. B. Ormont, E. G. Chirkova, and A. Ya. Shul'man, Zh. Éksp. Teor. Fiz. **72**, 1130 (1977) [Sov. Phys. JETP **45**, 591 (1977)].
12. N. S. Baryshev, Fiz. Tekh. Poluprovodn. (Leningrad) **9**, 2023 (1975) [Sov. Phys. Semicond. **9**, 1324 (1975)].

Translated by N. Korovin

Physics of the Solid State, Vol. 45, No. 9, 2003, pp. 1617–1621. Translated from Fizika Tverdogo Tela, Vol. 45, No. 9, 2003, pp. 1541–1544.

METALS AND SUPERCONDUCTORS

Effect of Metal Vacancies on the Band Structure of Nb, Zr, and Y Diborides

I. R. Shein, N. I. Medvedeva, and A. L. Ivanovskiĭ

Institute of Solid-State Chemistry, Ural Division, Russian Academy of Sciences, Pervomaĭskaya ul. 91, Yekaterinburg, 620219 Russia

e-mail: shein@ihim.uran.ru

Received November 21, 2002

Abstract—The band structure of nonstoichiometric layered diborides $Me_{0.75}B_2$ (*Me* = Nb, Zr, or Y) is calculated for the first time in the framework of the self-consistent full-potential linearized muffin-tin orbital (FLMTO) method, and the energies of formation of *Me* vacancies are estimated numerically. It is established that metal vacancies affect the electronic properties and energy states of Group III–V metal diborides in radically different ways. The superconducting properties of these diborides are discussed with due regard for the results obtained. © *2003 MAIK "Nauka/Interperiodica".*

1. INTRODUCTION

The discovery of superconductivity in magnesium diboride MgB_2 (critical temperature $T_c \approx 39$ K) [1] and the preparation of superconducting MgB_2-based materials, such as porous and compact ceramics, thin (including nanostructured) films, wires, and tapes (see, for example, reviews [2–5]), have attracted considerable attention and lent impetus to intensive investigations into the properties of AlB_2-like hexagonal diborides of *d* transition metals that are isostructural to MgB_2. In the early stages of the research into the superconductivity phenomenon, no superconducting transition was found in the majority of *d* transition metal (Ti, Zr, Hf, V, Ta, Cr, Mo, Nb) diborides down to $T \approx 0.6$ K [6]. In more recent works [7–17], it has been demonstrated experimentally and theoretically that, for binary diborides of the general formula MeB_2, the superconducting transition at a critical temperature $T_c \geq 40$ K is impossible. The sole exception is provided by the MgB_2 compound, in which the critical temperature T_c reaches a high value owing to strong electron–phonon interactions with the participation of boron σ band states doped with holes.

According to recent publications [7–9], sufficiently high temperatures T_c are observed for ZrB_2 (5.5 K [7]), TaB_2 (9.5 K [8]), and NbB_2 (5.2 K [9]). However, Rosner *et al.* [10] did not reveal superconductivity in TaB_2 at temperatures above 1.5 K. Furthermore, as was shown by Gasparov *et al.* [7] and Kraczorwski *et al.* [8], the NbB_2 compound does not exhibit superconducting properties at temperatures above 2 K. Reasoning from the estimates of the electron–phonon interaction parameters for MeB_2 diborides, it was concluded that ZrB_2 does not possess superconducting properties [14] but TaB_2 and NbB_2 can undergo superconducting transitions at $T_c \approx 0.1$ K [13] and $T_c \approx 3$ K [12], respectively.

It should be particularly emphasized that, in all the aforementioned works [7–17], the compositions of the studied diborides were assumed to be strictly stoichiometric (B/*Me* = 2).

As is known, lattice vacancies are among the most commonly encountered crystal defects that substantially affect the properties of nonstoichiometric compounds in the homogeneity region. For example, cubic (*B*1 type) carbides, nitrides, and oxides of Group III–V *d* transition metals represent the class of so-called strongly nonstoichiometric phases with extremely extended regions of homogeneity (up to 30–55 at. %) [18].

Unlike the above compounds, diborides of Group III–V *d* transition metals under equilibrium conditions are characterized by very narrow regions of homogeneity [19]. Consequently, the nonstoichiometric effects, as a rule, are ignored in studies of the properties of these systems. To the best of our knowledge, no theoretical work has been done to date to investigate the influence of lattice vacancies on the properties of MeB_2 phases.

Recently, Yamamoto *et al.* [20] carried out the solid-phase synthesis of $Nb_{1-x}B_2$ and $Ta_{1-x}B_2$ nonstoichiometric diborides (AlB_2 structural type, $0 \leq x \leq 0.48$) at T = 900–1300°C and pressures ranging from 1 to 5 GPa. It was found that the $Nb_{1-x}B_2$ compounds transform into the superconducting state at $x > 0.04$. In this case, the critical temperature T_c increases with an increase in the content of Nb vacancies and reaches a maximum (≈9 K) for compositions with $x \approx 0.24$.

This paper reports on the results of the first investigations into the influence of *Me* vacancies on the electronic properties and energy states of *d* metal diborides.

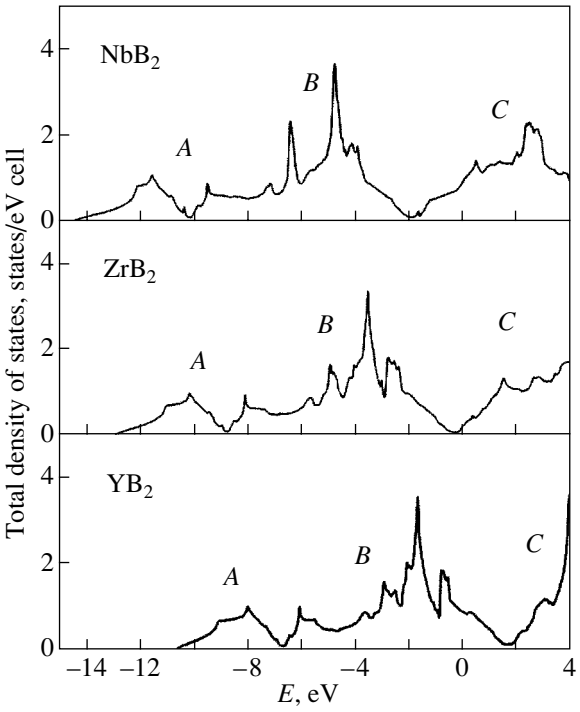

Fig. 1. Total densities of states of NbB_2, ZrB_2, and YB_2. $E_F = 0$.

2. MODEL AND CALCULATION TECHNIQUE

In our calculations, NbB_2, ZrB_2, and YB_2 hexagonal diborides containing 25% *Me* vacancies were used as models of nonstoichiometric diborides of *d* transition metals. This made it possible to elucidate the role played by metal vacancies in the evolution of the electronic properties of isostructural diborides for all possible types of occupation of the energy bands.

These phases have a hexagonal structure (space group *P*6/*mmm*) formed by layers consisting of metal trigonal prisms centered at boron atoms, which, in turn, form planar graphite-like networks. For modeling of $Me_{0.75}B_2$ nonstoichiometric phases, we used 12-atom supercells ($2 \times 2 \times 1$). The band structure calculations were performed using the scalar relativistic self-consistent full-potential linearized muffin-tin orbital (FLMTO) method with allowance made for the exchange–correlation effects in the framework of the generalized gradient approximation [21]. The lattice parameters of NbB_2, ZrB_2, and YB_2 stoichiometric diborides correspond to the data available in [22]. Since the experimental lattice parameters [20] of $Nb_{0.75}B_2$ ($a = 3.098$ Å, $c/a = 1.072$) differ from those for stoichiometric NbB_2 by no more than ≈0.3%, the parameters *a* and *c* for $Zr_{0.75}B_2$ and $Y_{0.75}B_2$ hypothetic defect structures are taken to be equal to those for the stoichiometric phases [22].

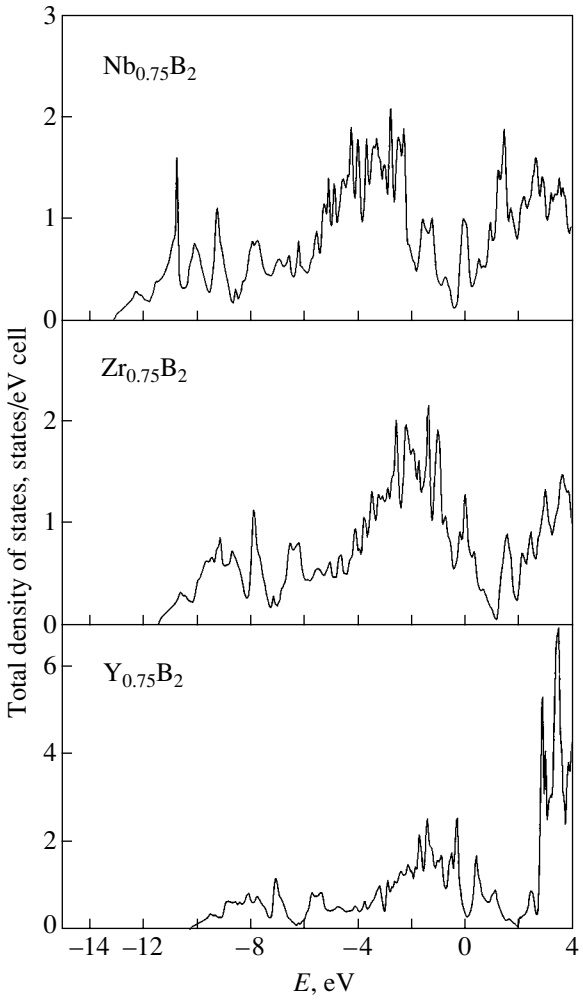

Fig. 2. Total densities of states of $Nb_{0.75}B_2$, $Zr_{0.75}B_2$, and $Y_{0.75}B_2$. $E_F = 0$.

3. RESULTS AND DISCUSSION

The total densities of states of stoichiometric (NbB_2, ZrB_2, YB_2) and defect-containing ($Nb_{0.75}B_2$, $Zr_{0.75}B_2$, $Y_{0.75}B_2$) phases are shown in Figs. 1 and 2, respectively. It can be seen that the valence band of AlB_2-like 4*d* metal diborides contains two groups of bands attributed to B 2*s* and B 2*p* bonding states (bands *A*, *B* in Fig. 1), which are separated from the band of antibonding states (band *C* in Fig. 1) by a pseudogap. Depending on the type of metal sublattice (or the number of valence electrons n_e), there exist three variants of occupation of the energy band in MeB_2. For the ZrB_2 diboride (n_e = 3.33 electrons/atom), the Fermi level is located in the pseudogap (at the lowest density of states). This suggests the highest chemical stability of ZrB_2 in the case when all the bonding states are completely occupied and the antibonding states are unoccupied (see also [23–25]). For the NbB_2 diboride (n_e = 3.66 electrons/atom), part of the antibonding states is occupied and the density of states at the Fermi level $N(E_F)$ increases (Table 1).

Table 1. Densities of states at the Fermi level (states/eV atomic formula) and electronic heat capacity coefficients γ (mJ mol^{-1} K^{-2}) for stoichiometric and nonstoichiometric diborides of Nb, Zr, and Y

	$N(E_F)$							γ	
	total	*Me s*	*Me p*	*Me d*	*Me f*	B *s*	B *p*		[24]
NbB_2	1.012	0.002	0.012	0.653	0.036	0.009	0.125	2.39	2.42
$Nb_{0.75}B_2$	0.993	0.009	0.021	0.544	0.022	0.010	0.146	2.34	–
ZrB_2	0.300	0.001	0.003	0.170	0.009	0.000	0.042	0.71	0.67
$Zr_{0.75}B_2$	1.220	0.005	0.027	0.426	0.019	0.018	0.331	2.87	–
YB_2	0.900	0.008	0.018	0.364	0.014	0.002	0.136	2.12	2.03
$Y_{0.75}B_2$	0.409	0.004	0.012	0.121	0.004	0.002	0.080	0.96	–

Contrastingly, for the YB_2 diboride (n_e = 3.0 electrons/atom), part of the bonding hybrid *d–p* states remains unoccupied. This is a simplified scheme that offers a qualitative explanation of the experimentally observed decrease in the cohesion characteristics of NbB_2 and YB_2 [19] (as compared to ZrB_2) and is confirmed by *ab initio* calculations of the band structures [23–25] (see also below).

Now, we consider the main effects induced upon introduction of *Me* vacancies and affecting the band structure of the diborides under investigation. In the case of the transition $MeB_2 \longrightarrow Me_{0.75}B_2$, these effects are associated with the following factors: (i) a decrease in the number of valence electrons n_e and (ii) local changes in the electron states of the atoms nearest to the vacancy.

The calculations demonstrate that the observed effects are different for diborides of Group III–V *d* transition metals. The presence of vacancies in the niobium sublattice of NbB_2 brings about considerable changes in the density of states in the near-Fermi region and gives rise to a new peak in the density of states (Fig. 2). Note that, in this case, vacancy states of the *s* type are located below the Fermi level E_F. A change in the charge density in $Nb_{0.75}B_2$ is clearly seen in Fig. 3: new Nb–Nb bonds passing through the vacancy center are not formed, and changes in the charge density contours indicate the vacancy growth along the Nb–Nb bonds in the vicinity of the defect. The density of states at the Fermi level $N(E_F)$ for $Nb_{0.75}B_2$ decreases insignificantly (by ≈ 1.9%) as compared to that for NbB_2.

It can be seen from Fig. 2 that, compared to NbB_2, the band structure of ZrB_2 undergoes a more radical transformation due to the presence of vacancies. The presence of Zr defects leads to the appearance of a new intense peak in the density of states in the vicinity of the pseudogap. As a result, the density of states at the Fermi level $N(E_F)$ for $Zr_{0.75}B_2$ increases drastically [from 0.30 (for ZrB_2) to 1.22 states/eV cell]. The opposite effect is observed for $Y_{0.75}B_2$, in which the Fermi level is located at a minimum in the density of states and the value of $N(E_F)$ decreases by a factor of more than two [from 0.900 (for YB_2) to 0.409 states/eV cell].

The presence of vacancies in the structure of the studied diborides has different effects on the distributions of partial densities of states of the metal and boron atoms (Table 1). For $Nb_{0.75}B_2$, the density of states at the Fermi level $N(E_F)$ decreases only slightly due to a decrease in the contribution $N^{Nb}(E_F)$ of the Nb 4*d* states, whereas the contribution $N^B(E_F)$ of the B 2 *p* states increases. Contrastingly, a drastic increase in the value of $N(E_F)$ for $Zr_{0.75}B_2$ is caused by a simultaneous increase in the contributions $N^{Zr}(E_F)$ and $N^B(E_F)$, whereas a decrease in the density of states at the Fermi level $N(E_F)$ for $Y_{0.75}B_2$ is associated with a decrease in the contributions $N^Y(E_F)$ and $N^B(E_F)$.

The above features in the transformation of the band structure of nonstoichiometric diborides should manifest themselves in the evolution of their properties,

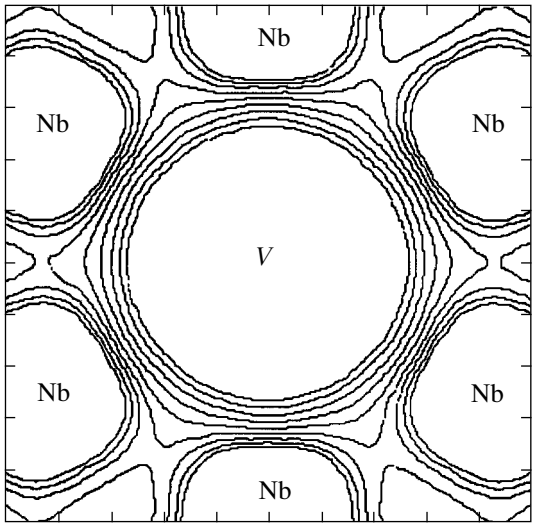

Fig. 3. Charge density map in the plane of a hexagonal niobium layer in $Nb_{0.75}B_2$.

Table 2. Energies of formation (ΔH), cohesion (E_{coh}), and formation of *Me* vacancies (E_{vf}) for stoichiometric and nonstoichiometric diborides of Nb, Zr, and Y (in eV/atomic formula)

	$E_{coh}^{MeB_2}$	ΔH^{MeB_2}	$E_{coh}^{Me_{0.75}B_2}$	$\Delta H^{Me_{0.75}B_2}$	E_{vf}
Nb–B	1.82	0.27	1.57	0.19	0.08
Zr–B	1.72	0.35	1.46	0.22	0.13
Y–B	1.42	0.26	1.23	0.16	0.10

which, in particular, depend on the density of states in the near-Fermi region. For the purposes of illustration, we estimated the low-temperature electronic heat capacity coefficients γ (Table 1) for stoichiometric MeB_2 and defect-containing $Me_{0.75}B_2$ diborides [in the free-electron approximation, $\gamma = (\pi^2/3)N(E_F)k_B^2$]. As can be seen from Table 1, the γ coefficients for the MeB_2 diborides decrease in the order $NbB_2 \longrightarrow YB_2 \longrightarrow ZrB_2$. For the $Me_{0.75}B_2$ nonstoichiometric phases, the γ coefficients decrease in a different order: $Zr_{0.75}B_2 \longrightarrow Nb_{0.75}B_2 \longrightarrow Y_{0.75}B_2$.

As was already noted, the effect of *Me* vacancies on the density of states at the Fermi level $N(E_F)$ most clearly manifests itself for ZrB_2. This suggests that the superconducting transition at the critical temperature $T_c \approx 5.5$ K for ZrB_2 [7] can be associated not only with the presence of impurities in ZrB_2 samples [17] but also with their nonstoichiometry in the zirconium sublattice. Our calculations did not reveal significant changes in the density of states at the Fermi level $N(E_F)$ for $Nb_{0.75}B_2$. It is quite possible that the evolution of the phonon spectrum of the $Nb_{1-x}B_2$ nonstoichiometric compounds with a decrease in their stability in the presence of lattice vacancies plays an important role in the observed increase in the critical temperature T_c [20]. As regards the $Y_{1-x}B_2$ compounds, the considerable decrease in $N(E_F)$ indicates that a superconducting transition in yttrium diboride is highly improbable in the region of its homogeneity.

Let us now analyze the changes in the stability of MeB_2 phases due to the presence of defects. For this purpose, we compare the results of numerical FLMTO calculations of the energies of cohesion (E_{coh}) and formation (ΔH) for MeB_2 and $Me_{0.75}B_2$ phases. The cohesion energies are determined from the relationships

$$E_{coh}^{MeB_2} = E_{tot}^{MeB_2} - (E_{at}^{Me} + 2E_{at}^{B}),$$

$$E_{coh}^{Me_{0.75}B_2} = E_{tot}^{Me_{0.75}B_2} - (0.75E_{at}^{Me} + 2E_{at}^{B}),$$

where E_{at}^{Me} and E_{at}^{B} are the total energies of *Me* and B free atoms, respectively, and $E_{tot}^{MeB_2}$ and $E_{tot}^{Me_{0.75}B_2}$ are the total energies (per formula unit) of MeB_2 and $Me_{0.75}B_2$ crystals, respectively. The energy of formation of the studied diborides are calculated from the expressions

$$\Delta H^{MeB_2} = (E_{tot}^{Me} + 2E_{tot}^{B}) - E_{tot}^{MeB_2},$$

$$\Delta H^{Me_{0.75}B_2} = (0.75E_{tot}^{Me} + 2E_{tot}^{B}) - E_{tot}^{Me_{0.75}B_2},$$

where E_{tot}^{Me} and E_{tot}^{B} are the total energies of the pure metal and α-boron crystals, respectively, which were obtained in the FLMTO calculations. As can be seen from Table 2, the energies of formation ΔH^{MeB_2} for the MeB_2 phases decrease in the order $ZrB_2 \longrightarrow NbB_2 \longrightarrow YB_2$, which is in complete agreement with available experimental data on the enthalpy of formation [19]. The cohesion energies (characterizing the energy effect of decomposition of the system into atoms) decrease in a different order: $E_{coh}^{NbB_2} > E_{coh}^{ZrB_2} > E_{coh}^{YB_2}$.

The presence of *Me* vacancies in the structure of the diborides under investigation leads to a substantial decrease in their stability (see the energies of formation ΔH in Table 2). An important energy parameter that characterizes the probability of generating vacancies is the energy of their formation:

$$E_{vf} = E_{tot}^{MeB_2} - E_{tot}^{Me_{0.75}B_2} - 0.25E_{tot}^{Me}.$$

Analysis of the results presented in Table 2 shows that the energy of formation E_{vf} of *Me* vacancies in NbB_2 is less than those in ZrB_2 and YB_2. Therefore, vacancies are more difficult to introduce into ZrB_2, which is the most stable phase among those studied in this work.

4. CONCLUSIONS

Thus, the calculations performed in this work made it possible for the first time to investigate the effect of lattice vacancies on the band structure of niobium, zirconium, and yttrium layered diborides and to elucidate the main features in the evolution of their electron states, which can differ radically depending on the type of metal sublattice (or the type of occupation of the energy bands). In particular, as the number of vacancies in $Me_{1-x}B_2$ increases, the density of states at the Fermi level $N(E_F)$ either decreases (YB_2), increases (ZrB_2), or remains nearly constant (NbB_2). The nonstoichiometric effects that manifest themselves in the metal sublattice are more specific to diborides of the Group III and V *d* transition metals in the Periodic Table.

ACKNOWLEDGMENTS

This work was supported by the Russian Foundation for Basic Research, project no. 02-03-32971.

REFERENCES

1. J. Nagamatsu, N. Nakagawa, T. Muranaka, *et al.*, Nature **410**, 63 (2001).
2. A. L. Ivanovskiĭ, Usp. Khim. **70** (9), 811 (2001).
3. C. Buzea and T. Yamashita, Supercond. Sci. Technol. **14**, R115 (2001).
4. A. L. Ivanovskiĭ, N. I. Medvedeva, I. G. Zubkov, and V. G. Bamburov, Zh. Neorg. Khim. **47** (4), 661 (2002).
5. P. C. Canfield and S. L. Bud'ko, Phys. World **15**, 29 (2002).
6. L. Leyarovsky and E. Leyarovski, J. Less-Common Met. **67**, 249 (1979).
7. V. A. Gasparov, N. S. Sidorov, I. I. Tsverkova, and M. P. Kulakov, Pis'ma Zh. Éksp. Teor. Fiz. **73** (10), 601 (2001) [JETP Lett. **73**, 532 (2001)].
8. D. Kraczorwski, A. J. Zaleski, O. J. Zogal, and J. Klamut, cond-mat/0103571 (2001).
9. N. Ogita, T. Kariya, H. Hiraoka, *et al.*, cond-mat/0106147 (2001).
10. H. Rosner, W. E. Pickett, S. Drechsler, *et al.*, Phys. Rev. B **64**, 144516 (2001).
11. N. I. Medvedeva, A. L. Ivanovskii, J. E. Medvedeva, and A. J. Freeman, Phys. Rev. B **64**, 20502 (2001).
12. P. P. Singh, cond-mat/0210091 (2002).
13. H. Rosner and W. E. Pickett, cond-mat/0106062 (2001).
14. H. Rosner, J. M. An, W. E. Pickett, and S. Drechsler, Phys. Rev. B **66**, 24521 (2002).
15. S. Elgazzar, P. M. Oppeneer, S. Drechsler, *et al.*, cond-mat/0201230 (2002).
16. I. R. Shein and A. L. Ivanovskii, cond-mat/0109445 (2001).
17. I. R. Shein, S. V. Okatov, N. I. Medvedeva, and A. L. Ivanovskii, cond-mat/0202015 (2002).
18. A. I. Gusev, A. A. Rempel, and A. J. Margel, *Disorder and Order in Strongly Non-Stoichiometric Compounds: Transition Metal Carbides, Nitrides, and Oxides* (Springer, Berlin, 2001).
19. G. V. Samsonov and I. M. Vinitskiĭ, *Handbook of Refractory Compounds* (Metallurgiya, Moscow, 1976; Plenum, New York, 1980).
20. A. Yamamoto, C. Takao, T. Masui, *et al.*, cond-mat/0208331 (2002).
21. M. Methfessel and M. Scheffler, Physica B (Amsterdam) **172**, 175 (1991).
22. P. Villars, *Pearson's Handbook: Crystallographic Data for Intermetallic Phases* (ASM International, Materials Park, Ohio, 1997).
23. A. L. Ivanovskiĭ, N. I. Medvedeva, and Yu. E. Medvedeva, Metallofiz. Noveishie Tekhnol. **21** (12), 19 (1999).
24. P. Vajeeston, P. Ravindran, C. Ravi, and R. Asokamani, Phys. Rev. B **63**, 045115 (2001).
25. T. Oguchi, J. Phys. Soc. Jpn. **71**, 1495 (2002).

Translated by O. Borovik-Romanova

Physics of the Solid State, Vol. 45, No. 9, 2003, pp. 1622–1628. Translated from Fizika Tverdogo Tela, Vol. 45, No. 9, 2003, pp. 1545–1550.

METALS AND SUPERCONDUCTORS

Influence of Disordering on the Critical Temperature of Superconductors with a Short Coherence Length

I. A. Semenikhin

Moscow Engineering Physics Institute, Kashirskoe sh. 31, Moscow, 115409 Russia

e-mail: isemenihin@mail.ru

Received January 23, 2003

Abstract—The influence of disordering on the critical temperature of *s*-wave superconductors with a short coherence length is studied by numerical simulation using the two-dimensional Hubbard model with attraction. The calculations are carried out within the Bogolyubov–De Gennes approach, which allows one to include the spatial inhomogeneity of the order parameter. The influence of the spatial inhomogeneity of physical quantities on the results obtained is studied. Disordering is shown to be able to cause a significant increase in the critical temperature. *© 2003 MAIK "Nauka/Interperiodica".*

1. INTRODUCTION

According to the Anderson theorem [1], nonmagnetic impurities affect the critical temperature T_c of ordinary low-temperature superconductors only slightly, which is confirmed by experimental data. The same conclusion follows from the Abrikosov–Gorkov theory [2] as applied to superconductors with isotropic *s*-wave pairing. This result is valid in the case of superconductors with a long coherence length ξ_0 when a variety of impurity configurations takes place within a distance scaling the range over which the order parameter $\Delta(\mathbf{r})$ varies. In this case, quantities averaged over impurity configurations can be used as is done when deriving Abrikosov–Gorkov equations for the critical temperature. A completely different situation arises in the case of superconductors with a short coherence length. Spatial variations of $\Delta(\mathbf{r})$ become significant in the presence of impurities, and the Anderson theorem is already inapplicable, possibly except for in some specific cases [3]. Currently, the behavior of the critical temperature and of the superconducting order parameter in superconductors with a short coherence length in the presence of disordering has not been studied in detail.

One of the reasons for this study was paper [4], where it was shown that the inclusion of spatial variations in $\Delta(\mathbf{r})$ weakens the influence of the depairing on the critical temperature. In this case, the correction to the results of the Abrikosov–Gorkov theory is of the order of T_c/E_f and becomes significant for superconductors with a short coherence length. In our opinion, the most interesting conclusion made in [4] is that, in the case of isotropic *s*-wave pairing, a minor amount of nonmagnetic impurities can increase the critical temperature in comparison with the impurity-free case. To verify this conclusion, we studied the influence of disordering on the critical temperature of a superconductor within the two-dimensional Hubbard model with attraction. Numerical calculations were carried out using the Bogolyubov–De Gennes method, which allows one to include the spatial inhomogeneity of the order parameter. The objective of this work was to ascertain the influence of the spatial inhomogeneity of physical quantities on the value of T_c of superconductors with a short coherence length. In our opinion, this is an important problem, since many theoretical approaches, including the Abrikosov–Gorkov theory, disregard this inhomogeneity. We show that the spatial inhomogeneity of $\Delta(\mathbf{r})$ in *s*-wave superconductors indeed results in an increase in T_c upon disordering in some specific cases.

2. MODEL

To simulate a disordered superconductor, we employ the two-dimensional Hubbard model with attraction and diagonal disorder:

$$H = -t\sum_{\langle i,j\rangle,\sigma} a_{i\sigma}^{+}a_{j\sigma} - \mu\sum_{i,\sigma} n_{i\sigma} + \sum_{i,\sigma}\varepsilon_i n_{i\sigma} + V_0\sum_i n_{i\uparrow}n_{i\downarrow}, \quad (1)$$

where $a_{i\sigma}^{+}$ and $a_{i\sigma}$ are the creation and annihilation operators, respectively, of an electron with spin projection σ at the *i*th site of the two-dimensional square lattice; $n_{i\sigma} = a_{i\sigma}^{+}a_{i\sigma}$; t is the hopping matrix element characterizing the kinetic energy; $\langle\ldots\rangle$ means summation over nearest neighbors; μ is the chemical potential; and V_0 is the matrix element of electron attraction at a site ($V_0 < 0$). The impurity potential ε_i is uniformly distrib-

1063-7834/03/4509-1622$24.00

uted over the interval (–*W*/2, *W*/2). The disorder characterized by the potential ε_i is an analog of nonmagnetic impurities and defects.

In terms of the Bogolyubov–De Gennes approach [5], problem (1) is reduced to solving the problem described by the effective Hamiltonian

$$H_{\text{eff}} = -t\sum_{\langle i,j\rangle,\sigma} a_{i\sigma}^{+}a_{j\sigma} - \mu\sum_{i,\sigma} n_{i\sigma} + \sum_{i,\sigma}\varepsilon_i n_{i\sigma} + \sum_{i,\sigma} U(\mathbf{r}_i)n_{i\sigma} + \sum_i [\Delta(\mathbf{r}_i)a_{i\uparrow}^{+}a_{i\downarrow}^{+} + \Delta^*(\mathbf{r}_i)a_{i\downarrow}a_{i\uparrow}], \quad (2)$$

where

$$\Delta(\mathbf{r}_i) = |V_0|\langle a_{i\uparrow}a_{i\downarrow}\rangle, \quad U(\mathbf{r}_i) = \frac{V_0}{2}\sum_\sigma \langle n_{i\sigma}\rangle \quad (3)$$

are the superconducting order parameter and the Hartree–Fock energy at the *i*th site, respectively. The Hamiltonian H_{eff} can be diagonalized using the Bogolyubov transform

$$a_{i\uparrow} = \sum_n u_n(\mathbf{r}_i)\gamma_{n\uparrow} - \nu_n^*(\mathbf{r}_i)\gamma_{n\downarrow}^{+},$$
$$a_{i\downarrow} = \sum_n u_n(\mathbf{r}_i)\gamma_{n\downarrow} + \nu_n^*(\mathbf{r}_i)\gamma_{n\uparrow}^{+}. \quad (4)$$

Here, γ_n^{+} and γ_n are new quasiparticle operators and the amplitudes $u_n(\mathbf{r}_i)$ and $\nu_n(\mathbf{r}_i)$ are determined from the equation

$$\begin{pmatrix} \hat{H}^N & \hat{\Delta} \\ \hat{\Delta}^* & -(\hat{H}^N)^* \end{pmatrix}\begin{pmatrix} u_n(\mathbf{r}_i) \\ \nu_n(\mathbf{r}_i) \end{pmatrix} = E_n\begin{pmatrix} u_n(\mathbf{r}_i) \\ \nu_n(\mathbf{r}_i) \end{pmatrix}, \quad (5)$$

where E_n is the energy of quasiparticle excitations, $\hat{H}^N u_n(\mathbf{r}_i) = -t\sum_\delta u_n(\mathbf{r}_i + \delta) + [\varepsilon_i - \mu + U(\mathbf{r}_i)]u_n(\mathbf{r}_i)$, $\hat{\delta} = (\pm\hat{x}, \pm\hat{y})$ are vectors corresponding to nearest neighbors, and $\hat{\Delta}u_n(\mathbf{r}_i) = \Delta(\mathbf{r}_i)u_n(\mathbf{r}_i)$. For $\nu_i(\mathbf{r}_i)$, the relations are similar. The potentials $\Delta(\mathbf{r}_i)$ and $U(\mathbf{r}_i)$ should satisfy the self-consistency conditions

$$\Delta(\mathbf{r}_i) = |V_0|\sum_n u_n(\mathbf{r}_i)\nu_n^*(\mathbf{r}_i)\tanh(E_n/2k_BT), \quad (6)$$

$$U(\mathbf{r}_i) = V_0\langle n_i\rangle/2 = V_0\sum_n |u_n(\mathbf{r}_i)|^2 f_n + |\nu_n(\mathbf{r}_i)|^2(1 - f_n), \quad (7)$$

where $f_n = 1/[1 + \exp(E_n/k_BT)]$ is the Fermi–Dirac distribution function and n_i is the average number of electrons at the *i*th site. The chemical potential is determined from the equation for the electron concentration

$$n_e = \sum_i \langle n_i\rangle/N. \quad (8)$$

The set of equations (5)–(7) on the $L \times L$ square lattice with periodic boundary conditions can be solved by iteration. For this purpose, a first approximation is chosen to $\Delta(\mathbf{r}_i)$ and $U(\mathbf{r}_i)$. Then $u(\mathbf{r}_i)$, $\nu(\mathbf{r}_i)$, and E_n are determined by exactly diagonalizing Eq. (5). Using Eqs. (6) and (7), the next approximation to $\Delta(\mathbf{r}_i)$ and $U(\mathbf{r}_i)$ is determined and so on, until the iterative process converges, i.e., until the differences between the preceding and current values of the potentials $\Delta(\mathbf{r}_i)$ and $U(\mathbf{r}_i)$ at each *i*th site become less than a preset value for several subsequent iteration cycles. Thereafter, the average concentration of electrons is determined from formula (8). If this concentration is larger than the preset value, the chemical potential is changed appropriately and Eqs. (5)–(7) are solved again until the average number of electrons in the system becomes equal to the preset value to within appropriate accuracy. In this way, the order parameter at a given temperature *T* is determined. As the temperature increases from $T = 0$, the order parameter $\Delta(\mathbf{r}_i)$ decreases in magnitude and, at a critical temperature $T = T_c$, becomes zero at all the sites $\mathbf{r}_i$. Unfortunately, when T_c is approached, the convergence of iteration of Eqs. (5)–(7) becomes considerably poorer, and this method becomes invalid near the critical temperature. Therefore, the value of *T* at which the order parameter is zero can be determined only by extrapolation. All these factors make this approach inefficient for determining T_c. An alternative method for determining the critical temperature was suggested in [6]. At $T \longrightarrow T_c$, we have $\Delta(\mathbf{r}_i) \longrightarrow 0$ and Eqs. (5) and (6) yield the following set of linear equations in $\Delta(\mathbf{r}_i)$:

$$\Delta(\mathbf{r}_i) = \frac{|V_0|}{2}\sum_j \Delta(\mathbf{r}_j)\sum_{n,m} u_n(\mathbf{r}_i)u_m(\mathbf{r}_i)u_n^*(\mathbf{r}_j)u_m^*(\mathbf{r}_j) \times \frac{\tanh(E_n/2k_BT) + \tanh(E_m/2k_BT)}{E_n + E_m}, \quad (9)$$

where $u(\mathbf{r}_i)$ and E_n are solutions to Eqs. (5), (7), and (8) for the system in the normal state, i.e., to the equations

$$\hat{H}^N u_n(\mathbf{r}_i) = E_n u_n(\mathbf{r}_i), \quad (10)$$

self-consistency equations

$$U(\mathbf{r}_i) = V_0\langle n_i\rangle/2 = V_0\sum_n |u_n(\mathbf{r}_i)|^2 f_n \quad (11)$$

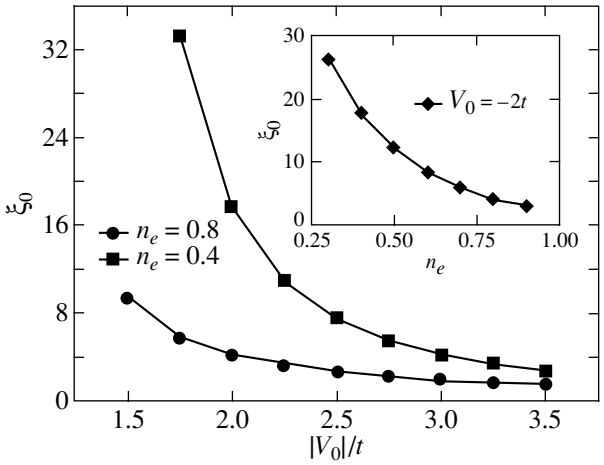

Fig. 1. Dependence of the coherence length ξ_0 in the absence of disorder on the electron–electron interaction energy V_0 at the electron concentration $n_e = 0.8$ and 0.4. The inset shows the dependence of ξ_0 on n_e at $V_0 = -2t$. The length ξ_0 is measured in units of the square lattice constant. The ξ_0 values were determined from the relation $\langle a(\mathbf{r}_i)a(\mathbf{r}_j)\rangle \sim |\mathbf{r}_i - \mathbf{r}_j|^{-1}\exp(|\mathbf{r}_i - \mathbf{r}_j|/\xi_0)$, which is valid at $|\mathbf{r}_i - \mathbf{r}_j| \gg \xi_0$ [8].

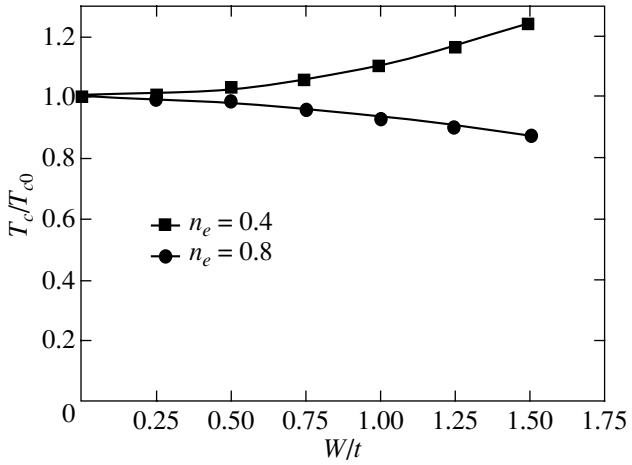

Fig. 2. Dependence of the relative critical temperature T_c/T_{c0} on W, where T_{c0} is the critical temperature in the absence of disorder. The calculation was carried out for a square lattice with $N = 32 \times 32$ sites and with the parameters $V_0 = -2t$ and $n_e = 0.8$ and 0.4; averaging was carried out over 20 various disorder configurations. The root-mean-square deviation is smaller than the symbol size.

and the corresponding equation of the chemical potential. If the temperature T is initially taken to be somewhat larger than T_c and then is decreased, the nonzero solution to the set of homogeneous equations (9) will arise only beginning from $T = T_c$. Thus, the critical temperature can be determined from the condition that the determinant of the set of equations (9) is zero. In this study, we mostly used this method for determining T_c, using the first method for checking in some cases. In calculations, the following parameters were used: V_0 was varied from $-1.5t$ to $-3.5t$, $n_e = 0.4$ and 0.8, and $L = 20$–50. The constraint on L is caused by a rapid increase in the required bulk of computation with increasing system size. When selecting V_0, we took into account the fact that the mean-field theory becomes invalid if the potential is large in magnitude [7]. At the same time, V_0 cannot be very small, since the size of the system under study has to be larger than the coherence length, which exponentially increases as V_0 decreases (Fig. 1). When selecting the average electron density n_e, we took into account that the mean-field theory yields incorrect results for a two-dimensional lattice near half-filling ($n_e = 1$) [7] and that the coherence length begins to increase rapidly at small values of n_e (see inset to Fig. 1). Since the results obtained within the mean-field theory become less reliable at high values of W [9], the maximum value of W was taken to be $W_{\max} = 1.5t$.

3. RESULTS AND DISCUSSION

Figure 2 shows the calculated dependence of the relative critical temperature T_c / T_{c0} on the parameter W, which determines the degree of disorder. We can see that, as disorder increases, the critical temperature decreases at the electron concentration $n_e = 0.8$ and increases for $n_e = 0.4$. Figure 3 shows the dependence of T_c/T_{c0} on the electron–electron interaction energy V_0 at $W = t$. We can see that, for $n_e = 0.4$, T_c/T_{c0} is always larger than unity and that disordering has the strongest effect on T_c at $|V_0| \approx 2.25t$. At $|V_0| < 1.5t$, the coherence length exceeds the system size; therefore, we cannot verify the Anderson theorem in the region of low values of T_c. The results suggest that T_c can increase due to disordering at certain values of the parameters.

It should be emphasized that while the critical temperature can be determined from the requirement of the order parameter vanishing in the absence of disorder, the situation in disordered superconductors is more ambiguous.[1] For example, simulations of the superconductor–insulator transition at zero temperature show that the order parameter retains a nonzero value even when a sample becomes an insulator [11]. During this transition, the sample is partitioned into a set of separate weakly bound regions with $\Delta(\mathbf{r}) \neq 0$ surrounded by regions with $\Delta(\mathbf{r}) \approx 0$. Although the average value of Δ is nonzero, the sample as a whole is no longer a superconductor. In other words, the condition $\Sigma_i\Delta(\mathbf{r}_i) \neq 0$ ceases to be the for the appearance criterion for the superconducting state. The superconducting transition

[1] In the selected range of values of the interaction potential V_0, the temperature of the formation of Cooper pairs, i.e., the temperature at which the order parameter takes on a nonzero value, almost coincides with the temperature of the Cooper pair condensation [10].

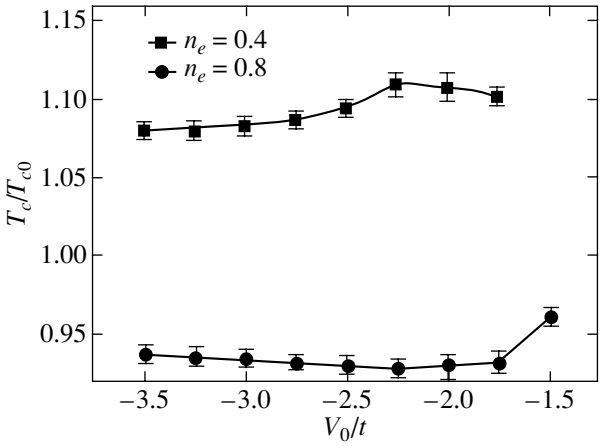

Fig. 3. Dependence of the relative critical temperature T_c/T_{c0} on the electron–electron interaction energy V_0 at $W = 1.0t$, where T_{c0} is the corresponding critical temperature in the absence of disorder. Since the coherence length shortens with increasing V_0, smaller lattices were taken to accelerate the calculations: for $n_e = 0.8$, $N = 40 \times 40$ ($V_0 = -1.5t$), 32×32 (V_0 was varied from $-1.75t$ to $-2.25t$), 24×24 ($V_0 = -2.5t$), and 20×20 ($V_0 = -2.75t$ to $-3.5t$); for $n_e = 0.4$, $N = 50 \times 50$ at $V_0 = -1.75t$ and the other lattice sizes are the same as in the case of $n_e = 0.8$. Averaging was carried out over 20 various disorder configurations for all cases.

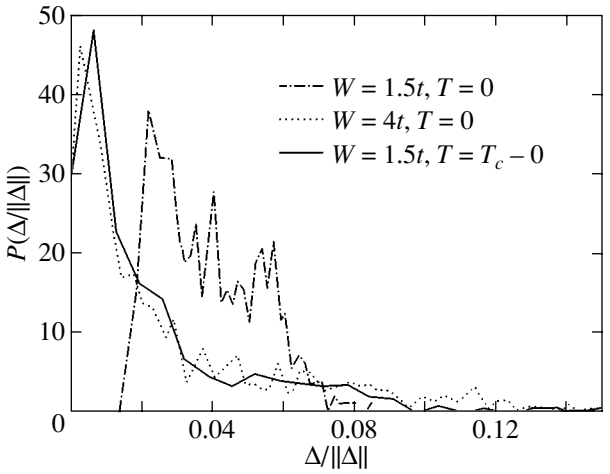

Fig. 4. Distribution function P of the normalized order parameter $\Delta(\mathbf{r}_i)/\|\Delta(\mathbf{r}_i)\|$ in the case of $T \longrightarrow T_c$ (the superconductor–metal transition) at $W = 1.5t$ (solid curve) and in the case of strong disorder with $W = 4t$ at $T = 0$ (dashed curve). For comparison, the distribution of $\Delta(\mathbf{r}_i)/\|\Delta(\mathbf{r}_i)\|$ is also given at $W = 1.5t$ and $T = 0$ (dash-dotted curve). The calculation was carried out for a square lattice with $N = 24 \times 24$ sites and with the parameters $V_0 = -2.5t$ and $n_e = 0.4$ for an arbitrarily chosen disorder configuration.

can be judged from the response to the applied magnetic field, namely, by the superfluid density ρ_s [12], which vanishes upon the superconducting transition. This property is a more reliable criterion for superconductivity, since it provides information about the sample state as a whole. At $T = T_c$, the superconductor–metal transition takes place, in contrast to the superconductor–insulator transition that occurs at $T = 0$. Figure 4 shows the similarity in the order parameter behavior during these transitions. We can see that $\Delta(\mathbf{r}_i)$ decreases irregularly in both cases. In the case of the superconductor–insulator transition, this irregular decrease in $\Delta(\mathbf{r}_i)$ can be an indication of the onset of the sample decomposition into superconducting and normal regions. Thus, in the case of the superconductor–metal transition, some doubts can arise with respect to the reliability of determining T_c as the temperature at which the order parameter becomes zero.

To clarify the situation, we calculated the critical temperature for several impurity configurations by using the system response to a magnetic field. The density ρ_s is conventionally calculated from a formula derived using the perturbation theory and by averaging over impurities [11, 13, 14]. In this study, we use a method which yields a similar result for a specific disorder configuration without averaging. As is known, exposure of a superconductor to a dc magnetic field causes electric currents that screen this field (the Meissner effect). In the case where the disordered system is in the normal state, persistent electric currents cannot arise. Therefore, in order to verify that the system is in the superconducting state, it is sufficient to show that a weak magnetic field applied normally to the plane of the quasi-two-dimensional sample induces an electric current. To carry out the corresponding calculation, it should be taken into account that, in the presence of a magnetic field described by the vector potential $\mathbf{A}(\mathbf{r})$, the matrix element $t_{l, l+\bar{x}}$ in Eq. (1) has the form [15]

$$t_{l, l+\bar{x}}(\mathbf{A}) = t\exp\left(\frac{ie}{\hbar c}\int\limits_{R_{l+\bar{x}}}^{R_l}\mathbf{A}(\mathbf{r})d\mathbf{r}\right), \qquad (12)$$

or, in the case where $\hbar$, c, and the lattice constant are taken equal to unity, $t_{l, l+\bar{x}}(\mathbf{A}) = t\exp[ieA_x(\mathbf{r}_l)]$, where $A_x(\mathbf{r}_l)$ is the projection of the vector potential $\mathbf{A}$ onto the x axis. The corresponding projection of the current density is

$$j_x(\mathbf{r}_l) = iet\sum_\sigma (e^{ieA_x(\mathbf{r}_l)}a^+_{l+\bar{x},\sigma}a_{l,\sigma} - e^{-ieA_x(\mathbf{r}_l)}a^+_{l,\sigma}a_{l+\bar{x},\sigma}). \qquad (13)$$

Let us write the vector potential as $\mathbf{A} = H_z(-y, 0, 0)$, where the z axis is perpendicular to the sample plane and the origin lies at the sample edge. Thus, the screening current will flow along the x axis. We impose periodic boundary conditions in x and take the boundary values on the y axis to be zero, so that the sample

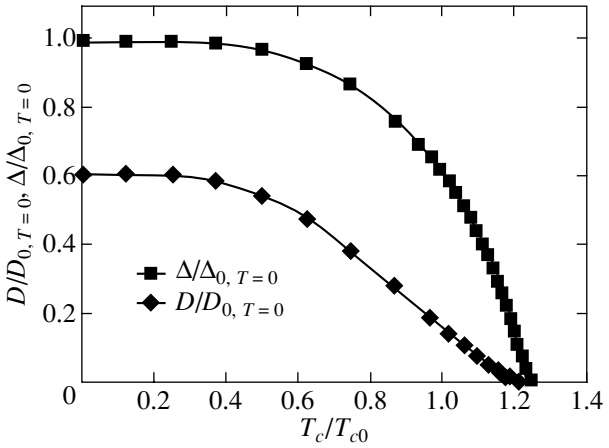

Fig. 5. Dependence of the parameters $D/D_{0,\,T=0}$ and $\Delta/\Delta_{0,\,T=0}$ on the relative temperature T/T_{c0}. $D_{0,\,T=0}$ and $\Delta_{0,\,T=0}$ are the values of the parameters D and Δ in the absence of disorder at $T = 0$. T_{c0} is the critical temperature in the absence of disorder. The calculation was carried out for a square lattice with $N = 24 \times 24$ sites and with the parameters $V_0 = -2.5t$, $W = 1.5t$, and $n_e = 0.4$ for an arbitrarily chosen disorder configuration.

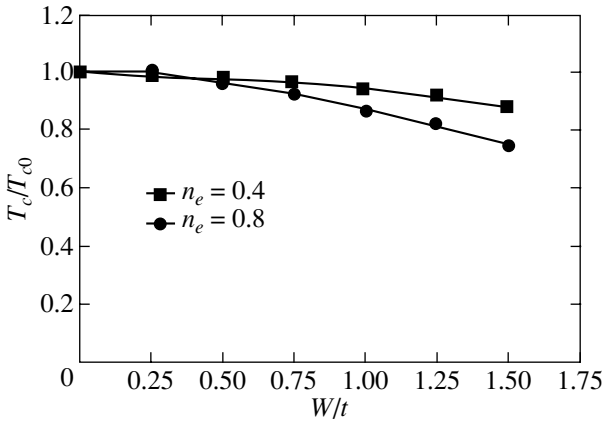

Fig. 6. Dependence of the relative critical temperature T/T_{c0} on W calculated without regard for the spatial inhomogeneity of $\Delta(\mathbf{r}_i)$ and (or) of the local density of states $g(\mathbf{r}_i, E)$. T_{c0} is the critical temperature in the absence of disorder. The calculation was carried out for a square lattice with $N = 32 \times 32$ sites and with the parameters $V_0 = -2t$ and $n_e = 0.8$ and 0.4; averaging was carried out over 20 various disorder configurations. The root-mean-square deviation is smaller than the symbol size.

becomes coiled.[2] Figure 5 shows the calculated temperature dependence of the ratio of the average current density $J_x = (1/N)\Sigma_l \langle j_x(\mathbf{r}_i)\rangle$ to the applied magnetic field H_z at $H_z \longrightarrow 0$. The calculation was carried out for an arbitrarily chosen disorder configuration at $W = 1.5t$. We can see from Fig. 5 that $D = \lim\limits_{H_z \to 0} (J_x/H_z)$ becomes zero simultaneously with the order parameter. Thus, both criteria for determining the critical temperature lead to identical results.

Thus, the critical temperature can indeed increase as a result of disordering. In this case, as is evident from Figs. 1 and 3 for $n_e = 0.4$, this tendency also persists at rather long coherence lengths. It should be noted that there are experimental data that show evidence of this behavior of T_c. For example, as transition-metal impurities are added to Ti, the critical temperature increases, which cannot be explained by a simple change in the carrier concentration [16]. We note that transition metals in Ti, as shown by Anderson [17], play the role of nonmagnetic impurities.

In the beginning of this paper, it was indicated that the spatial inhomogeneity of the physical quantities should be taken into account in the case of a superconductor with a short coherence length, and all the preceding calculations were carried out with allowance for such inhomogeneities. Let us consider how neglect of the inhomogeneities can change the results. To this end, we sum Eq. (9) over all the sites and divide the result by the number of sites N. This yields

$$\Delta = \frac{|V_0|}{2N}\int\limits_{-\infty}^{\infty} dE \sum_i g(\mathbf{r}_i, E)\Delta(\mathbf{r}_i)\frac{\tanh(E/2k_BT)}{E}, \quad (14)$$

where it was taken into account that the wave functions $u(\mathbf{r}_i)$ may be taken to be real in the absence of a magnetic field. Here, $\Delta = (1/N)\Sigma_i \Delta(\mathbf{r}_i)$ is the average order parameter and $g(\mathbf{r}_i, E) = (1/N)\Sigma_n u_n^2(\mathbf{r}_i)\delta(E - E_n)$ is the local density of states. Let us write Eq. (14) in the form

$$1 = \frac{|V_0|}{2}\int\limits_{-\infty}^{\infty} dE g(E)\frac{\tanh(E/2k_BT)}{E} + \frac{|V_0|}{2N}\int\limits_{-\infty}^{\infty} dE \sum_i \delta g(\mathbf{r}_i, E)\frac{\delta\Delta(\mathbf{r}_i)}{\Delta}\frac{\tanh(E/2k_BT)}{E}; \quad (15)$$

where $g(E) = (1/N)\Sigma_i g(\mathbf{r}_i, E)$, $\delta\Delta(\mathbf{r}_i) = \Delta(\mathbf{r}_i) - \Delta$, and $\delta g(\mathbf{r}_i, E) = g(\mathbf{r}_i, E) - g(E)$. When deriving Eq. (15), it was taken into account that $\Sigma_i \delta\Delta(\mathbf{r}_i) = 0$ and $\Sigma_i \delta g(\mathbf{r}_i, E) = 0$. If we disregard the spatial change in the order parameter or in the local density of states, the second term in the right-hand side disappears and we get the formula

$$1 \approx \frac{|V_0|}{2}\int\limits_{-\infty}^{\infty} dE g(E)\frac{\tanh(E/2k_BT_c)}{E}. \quad (16)$$

[2] The zero boundary values on the x axis are taken to exclude a jump in the vector potential $\mathbf{A}$ at the boundary $x = 0$.

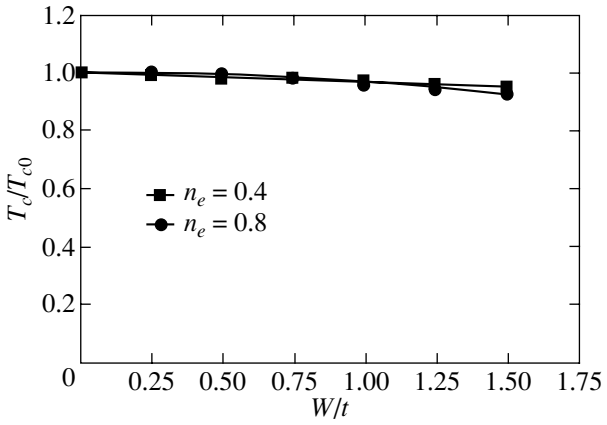

Fig. 7. Dependence of the relative critical temperature T/T_{c0} on the degree of disordering W calculated without regard for the spatial inhomogeneity of the order parameter $\Delta(\mathbf{r}_i)$ and of the Hartree–Fock energy $U(\mathbf{r}_i)$. T_{c0} is the critical temperature in the absence of disorder. The calculation was carried out for a square lattice with $N = 32 \times 32$ sites and with the parameters $V_0 = -2t$ and $n_e = 0.8$ and 0.4; averaging was carried out over 20 various disorder configurations. The root-mean-square deviation is smaller than the symbol size.

The critical temperature calculated for this case is shown in Fig. 6. We can see that the relative critical temperature in the case of $n_e = 0.4$ decreases with the impurity concentration. This result qualitatively differs from that obtained previously, which shows the importance of spatial variations in the order parameter and in the local density of states. We note that so far the spatial dependence of the Hartree–Fock energy $U(\mathbf{r}_i)$ was taken into account. If $U(\mathbf{r}_i)$ is constant, a somewhat different pattern arises (Fig. 7). We can see that T_c is almost not affected by disordering in this case. This is the same result as that obtained in the Abrikosov–Gorkov theory, where the spatial inhomogeneity of $\Delta(\mathbf{r}_i)$ and $U(\mathbf{r}_i)$ is also disregarded and the critical temperature is independent of the impurity concentration. A comparison of Figs. 6 and 7 shows that the critical temperature of a superconductor with impurities is sensitive to the spatial inhomogeneity of $U(\mathbf{r}_i)$. All the above-mentioned suggests that neglect of the spatial inhomogeneity can lead to incorrect results. In the case under consideration, this conclusion is well illustrated by the qualitative difference in the T_c behavior upon disordering in the case of $n_e = 0.4$.

In closing, we note that the calculated relative critical temperature in a disordered superconductor was always higher at $n_e = 0.4$ than at $n_e = 0.8$ (Figs. 6, 7). In our opinion, this is explained by the behavior of the density of states upon disordering. It can be shown that the major contribution to the integral in formula (16) is made by a region with a size of the order of $|V_0|$ near the Fermi energy, i.e., the region of low values of E (the energy is measured from the chemical potential, which is close to the Fermi energy in the case of very too high energies of the electron–electron interaction). In the case of the electron density $n_e = 0.8$, the Fermi energy is close to a density-of-states peak, which is smeared upon disordering and makes a smaller contribution to the integral. As a result, equality (16) is met at a lower value of T_c. At the same time, the energy range mainly contributing to the integral in formula (16) at $n_e = 0.4$ is far from this peak and the integral increases due to tails in the density of states that arise due to disordering. Hence, equality (16) in this case is met at a higher value of T_c. This consideration is valid for $|V_0|$ of the order of t. At large values of $|V_0|$, this dependence will be less pronounced, since the entire energy band will contribute to the integral. At small values of $|V_0|$, the critical temperature in formula (16) will depend almost exclusively on the density of states at the Fermi level; this case calls for detailed study of the $g(0)$ behavior. The change in the chemical potential upon disordering should also be taken into account, since the average number of electrons was fixed. We note that the mechanism described above is probably also valid in the case where the spatial variations in the order parameter and in the local density of states are not disregarded. However, this mechanism does not explain the increase in T_c upon disordering, because this increase is most likely a result of several factors and the most important role is played by the strong spatial inhomogeneity of $\Delta(\mathbf{r}_i)$ and $g(\mathbf{r}_i, E)$.

4. CONCLUSIONS

(i) The inhomogeneity of the superconducting order parameter in coordinate space should be taken into account in calculations of the physical characteristics of superconductors with a short coherence length.

(ii) The critical temperature of s-wave superconductors with a short coherence length can increase due to disordering.

ACKNOWLEDGMENTS

I would like to thank L.A. Openov for helpful discussions and remarks.

REFERENCES

1. P. W. Anderson, J. Phys. Chem. Solids **11**, 26 (1959).
2. A. A. Abrikosov and L. R. Gorkov, Zh. Éksp. Teor. Fiz. **35**, 1558 (1958) [Sov. Phys. JETP **8**, 1090 (1959)]; Zh. Éksp. Teor. Fiz. **36**, 319 (1959) [Sov. Phys. JETP **9**, 220 (1959)]; Zh. Éksp. Teor. Fiz. **39**, 1781 (1960) [Sov. Phys. JETP **12**, 1243 (1960)].
3. K. Tanaka and F. Marsiglio, Phys. Rev. B **62**, 5345 (2000).
4. M. E. Zhitomirsky and M. B. Walker, Phys. Rev. Lett. **80**, 5413 (1998).
5. P. G. de Gennes, *Superconductivity of Metals and Alloys* (Benjamin, New York, 1966; Mir, Moscow, 1968).

6. M. Mierzejewski and M. M. Maska, Phys. Rev. B **60**, 6300 (1999).
7. R. Micnas, J. Ranninger, and S. Robaszkiewicz, Rev. Mod. Phys. **62**, 113 (1990).
8. A. V. Svidzinskiĭ, *Spatially Irregular Problems of the Theory of Superconductivity* (Nauka, Moscow, 1982).
9. J. Lages and D. L. Shepelyansky, Phys. Rev. B **64**, 094502 (2001).
10. J. M. Singer, M. H. Pedersen, T. Schneider, *et al.*, Phys. Rev. B **54**, 1286 (1996).
11. A. Ghosal, M. Randeria, and N. Trivedi, Phys. Rev. B **65**, 014501 (2001).
12. D. J. Scalapino, S. R. White, and S. Zhang, Phys. Rev. B **47**, 7995 (1993).
13. T. Xiang and J. M. Wheatley, Phys. Rev. B **51**, 11721 (1995).
14. M. Franz, C. Kallin, A. J. Berlinsky, and M. I. Salkola, Phys. Rev. B **56**, 7882 (1997).
15. R. E. Peierls, Z. Phys. **80**, 763 (1933); J. M. Luttinger, Phys. Rev. **84**, 814 (1951).
16. B. T. Matthias, A. C. Compton, H. Suhl, and E. Corenzwit, Phys. Rev. **115**, 1597 (1959).
17. P. W. Anderson, Rev. Mod. Phys. **50**, 191 (1978).

Translated by A. Kazantsev

Physics of the Solid State, Vol. 45, No. 9, 2003, pp. 1629–1633. Translated from Fizika Tverdogo Tela, Vol. 45, No. 9, 2003, pp. 1551–1555.

METALS AND SUPERCONDUCTORS

Effect of Silver Content on the Mechanical and Electrical Properties of the YBaCuO/Ag Ceramic

L. K. Markov, T. S. Orlova, N. N. Peschanskaya, B. I. Smirnov, Yu. P. Stepanov, and V. V. Shpeizman

Ioffe Physicotechnical Institute, Russian Academy of Sciences, Politekhnicheskaya ul. 26, St. Petersburg, 194021 Russia

e-mail: shpeizm.v@mail.ioffe.ru

Received February 4, 2003

Abstract—Doping the YBaCuO superconducting ceramic with 3–5 wt % silver is shown to substantially increase its microplasticity and strength. Temperature spectra of microplastic strain rates for YBaCuO/Ag ceramics with 0, 1.6, 2.9, 4.2, and 7.6 wt % silver were obtained. The structure of the spectra and the relation of one of the peaks to the superconducting transition are discussed. The specific features of the *I–V* characteristics of samples cooled in a magnetic field are considered. It is shown that the position of the rising branch of a *I–V* characteristic depends on its origin; this observation can be used to fix two or more stable states of an HTSC-based memory cell. © *2003 MAIK "Nauka/Interperiodica".*

1. INTRODUCTION

A serious shortcoming plaguing high-temperature superconductors (HTSC) and limiting their application potential lies in their fairly poor mechanical properties, namely, the low strength and fracture toughness, the inability to undergo noticeable plastic deformation, and, as a consequence, the impossibility of mechanically processing blocks of HTSC materials and their tendency toward brittle fracture [1, 2]. This lends particular importance to attempts at developing and studying HTSC materials with improved mechanical characteristics. A major approach employed traditionally in this area is doping HTSCs with the aim of increasing the strength and plasticity while at the same time retaining (or improving) their electrical properties. Adding silver in the course of preparation of HTSC ceramics was one of the first techniques used, because silver enhances oxygen diffusion and, therefore, favors the retainment of superconductivity. Moreover, silver reduces the resistivity of HTSC materials in the normal state and also reduces their contact resistance. The strength and fracture toughness (the critical coefficient of fracture toughness K_{1c}) were observed to increase with Ag content in YBaCuO/Ag composites [3–5]. Silver doping was also found to reduce the effect of uniaxial compression on the *I–V* curves [6]. It was assumed that silver, as a soft metal, would be capable of lowering local strains at grain boundaries, which are weak links in HTSC ceramics, as well as favor the creation of internal long-range strain fields in a sample. A study was also made of the variation in the mechanical properties (strength, fracture toughness) with the way in which Ag is introduced (mixing YBaCuO with Ag metal powder or holding it in an $AgNO_3$ solution) [5].

Measurements of the critical superconducting transition temperature T_c and of the critical current density j_c were conducted on silver-doped HTSCs more than once, with sometimes contradictory results. For instance, T_c was reported to slightly increase (by 2–3 K) with increasing Ag content, to decrease subsequently at Ag concentrations of 8–10 wt % [5, 7, 8]. In [9], no changes in T_c were observed in YBaCuO with the addition of silver. After doping, the critical current at 77 K increased [5, 10], did not change [11], or varied nonmonotonically [6].

This communication focuses attention on the heretofore unexplored microplasticity of YBaCuO/Ag compounds; for this purpose, microplastic strain rate spectra of HTSC ceramic samples, with the Ag content varied from 0 to 15 wt %, were measured at temperatures ranging from 77 to 300 K. The measurements were conducted with a laser interferometer [12]. We also studied the strength of samples under compression, the *I–V* characteristics at 77 K, and hysteresis of the *I–V* curves of samples with a trapped magnetic flux, which was observed in [13, 14].

2. EXPERIMENTAL TECHNIQUE

Samples of YBaCuO and YBaCuO/Ag were prepared using the following technique. Powders of Y_2O_3, $BaCO_3$, and CuO were mixed in a ratio Y : Ba: Cu = 1 : 2 : 3, ground thoroughly, and pressed into $4 \times 4 \times$ 8-mm pellets. To obtain samples with silver, the YBaCuO pellets were again ground, with the addition of $AgNO_3$ powder. This mixture was subsequently pressed into YBaCuO/Ag pellets with different contents of Ag. All these pellets were twice calcined in

1063-7834/03/4509-1629$24.00

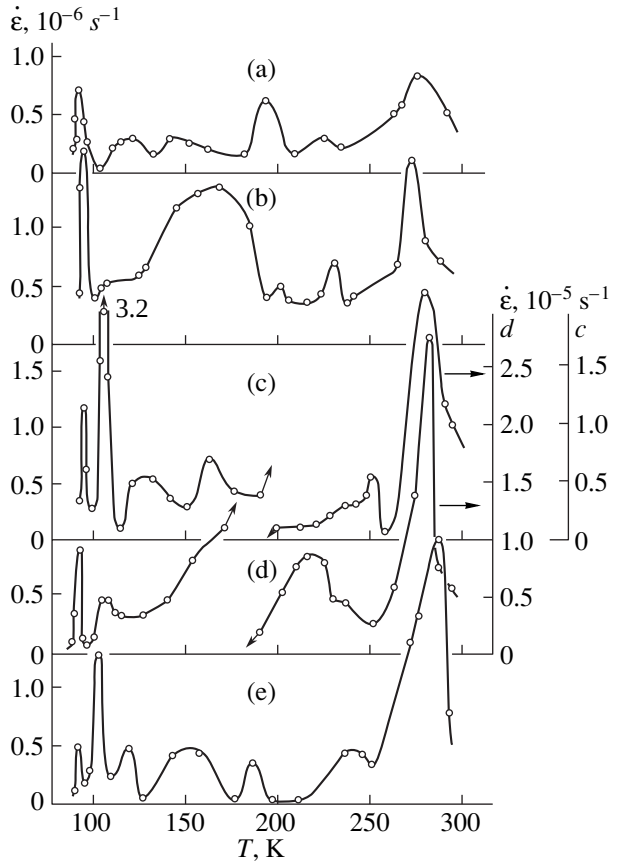

Fig. 1. Temperature spectra of microplastic strain rates for a YBaCuO/Ag ceramic with a silver content equal to (a) 0, (b) 1.6, (c) 2.9, (d) 4.2, and (e) 7.6 wt %.

oxygen at a temperature 1200 K for 6 h, with intermediate grinding and pressing. After this, the pellets were cut into samples measuring $2 \times 2 \times 4$ mm. Indium contacts were deposited lengthwise for electrical measurements. The *I–V* curves were measured with a P138 voltage-stabilized source, and the voltage was measured with a V7-21 microvoltmeter.

The compressive strength was measured on an Instron 1342 universal testing machine at room temperature. The rate of motion of the mobile grip was 0.2 mm/min.

In studying the microplasticity, the microplastic strain rate $\dot{\varepsilon}$ was recorded by the laser interferometer technique, which permits measurements at sample elongations $\Delta l \geq 0.15$ μm [12]. The interferogram consisted of the parts of a sine curve whose frequency was proportional to the strain rate and whose number of oscillation periods was proportional to the magnitude of the strain. As a rule, the sample was cooled to 77 K and loaded to a stress σ^* 10–20 times lower than the breakdown value. On passing the strain level necessary for determination of the strain rate, the sample was unloaded and heated to the next temperature, where the sample was again loaded to σ^*, $\dot{\varepsilon}$ was measured again, and so on. The strain rate was determined from the interferogram at each temperature under identical conditions after the length of the loaded sample has decreased by $\Delta l = 0.3$ μm. The use of the strain- rather than the time-based technique to measure the microstrain rate, as was done, for instance, in [15], is connected with the complex shape of the initial stage in the strain (creep) curve in the low-strain region (in particular, with the deformation delay in several cases) [12].

3. RESULTS AND DISCUSSION

3.1. Microplasticity and Strength

Figure 1 presents rate spectra of small inelastic strains of YBaCuO/Ag samples containing different amounts of silver. The spectra are seen to differ markedly in the magnitude of the strain rate (and of the strain). Because the times of holing under a load at different temperatures did not differ strongly, the strain was obviously larger, the higher the measured strain rate. The total strain suffered by a sample in the course of successive loading sessions made at different temperatures (disregarding the subsequent unloadings causing complete or partial recovery of the strain [15]) may be conveniently presented as the sum of measured strain rates multiplied by an average loading time. In the case of curves drawn through equal numbers of experimental points, the total strain can be numerically estimated from a comparison of the areas bounded by $\dot{\varepsilon}(T)$ curves obtained at different temperatures. The above relation (an increase of the strain rate and strain in magnitude with increasing Ag content) becomes evident upon inspection of Figs. 1a–1d, i.e., up to Ag concentrations ~5 wt %. For higher Ag concentrations, the measured strain rate decreases. This may be a consequence of a real decrease in the strain rate due to the material changing structurally with increasing Ag content. One could conceive, however, of another explanation, namely, that in the initial stage of loading the strain rate $\dot{\varepsilon}$ increased so much that at the time of its measurement we are already in the region of strain decay, i.e., close to the end of the microplasticity range [12]. As shown in [6], at low Ag concentrations, a compressive stress is observed to affect the *I–V* characteristics as well, whereas at higher concentrations this effect is not seen.

In the 77- to 300-K range, the microplastic strain rate spectrum in YBaCuO ceramic samples differing in structure and oxygen content was shown in [6, 12] to exhibit three main peaks, more specifically, one at the superconducting transition $T_c \approx 90$ K, one at 250–270 K, and one (sometimes two) peak in between with no fixed position. A similar situation (with some additional features) is observed in YBaCuO/Ag samples. The $\dot{\varepsilon}$ peak at T_c was found in all samples, but, in samples doped with Ag, this peak acquires a satellite at 100–105 K.

Also, while in the sample with 1.6 wt % Ag the second peak is barely discernible, in the samples with 2.9 and 7.6 wt % Ag, it considerably exceeds the peak at T_c in amplitude. As shown in [12, 15], the maximum in the $\dot{\varepsilon}(T)$ dependence signifies the appearance or disappearance of some mechanism of slowing down the deformation. For instance, the maximum at T_c is assigned to the acceleration of dislocation motion as a result of the electronic component of their retardation switching off at the transition to the superconducting state, an effect known to exist in metallic superconductors. As a result, the frequency factor in the expression for the rate of thermally activated dislocation depinning increases [16].

Anomalies near T_c were also observed to occur in studies of internal friction in YBaCuO samples and the temperature behavior of the elastic modulus, the linear expansion coefficient, and differential scanning calorimetry curves [8, 17–19]. The same studies also revealed the occasional appearance of a second peak at 115 K, which is particularly pronounced in Ag-doped samples [8]. It should, however, be noted that in some studies no features were observed in the temperature dependences of elastic characteristics near T_c [20].

The behavior of the peak at 250–270 K is similar to the behavior of the general level of strain rates described above; indeed, the peak amplitude grows with increasing Ag concentration up to ~5 wt %, after which it decreases. A sharp increase in the strain rate with temperature starts for YbaCuO with 2.9 or 4.2 wt % Ag from ~200 K. No features were revealed in the appearance of a peak (peaks) in the temperature interval between T_c and 250 K; the peak(s) can have a different amplitude, can be narrow or broad, and are unstable in temperature.

The increase in the rate and in the magnitude of microplastic strain with increasing Ag content also affects strength measurements. If we assume that an increase in temperature unfreezes some mobile structural elements in the region of the spectral peaks [15] (except the peak at T_c, which, by contrast, is associated with their freezing) and that the strength is determined by the integrated deformation (relaxation) ability of a material, then we come to the conclusion that the higher the strain rate for $T \le T^*$ (T^* is the strength measurement temperature), the higher the strength should be. As seen from Table 1, the room-temperature strength does indeed grow with Ag concentration, particularly at high Ag contents. The latter possibly argues for the above assumption that the spectrum obtained on the YBaCuO sample with 7.6 wt % Ag actually refers to strain measurement conditions at the end of the microplasticity range following a relatively large initial strain.

Table 1. Strength of YBaCuO/Ag samples with different Ag contents

Ag content, wt %	σ, MPa
0	146.3 ± 6.2
1.6	149.8
2.9	155.7
7.6	226.9

3.2. I–V Characteristics of YBaCuO/Ag Samples with Trapped Magnetic Flux

As shown earlier [13, 14], many HTSC ceramics with grain-trapped magnetic flux typically exhibit *I–V* hysteresis in the low-current region. This effect was assigned in [13, 14] to redistribution of the trapped flux and was observed, in particular, in silver-doped ceramic samples; it was sometimes pronounced to such an extent that as the current was increased after the initial *I–V* region the sample completely recovered its superconducting state, so that one actually could identify two values of the critical current I_c [14]. Figure 2 displays *I–V* curves of a sample with 10 wt % Ag. The arrows specify the sense of current variation, with the up-arrow indicating the increase and the down-arrow, the decrease. Curve *1* shows the initial increase in current through the superconductor. At a current I_f, the voltage drops from point *A* to point *B*, after which the voltage grows again with increasing *I* but now follows another curve, *BC*. The initial state is regained along smooth curve *2*. The loop closes at a point with the abscissa I_s, which is near the critical current I_c. An increase in the current above I_f does not change the lower branch of the hysteresis loop. If, however, one reduces the current

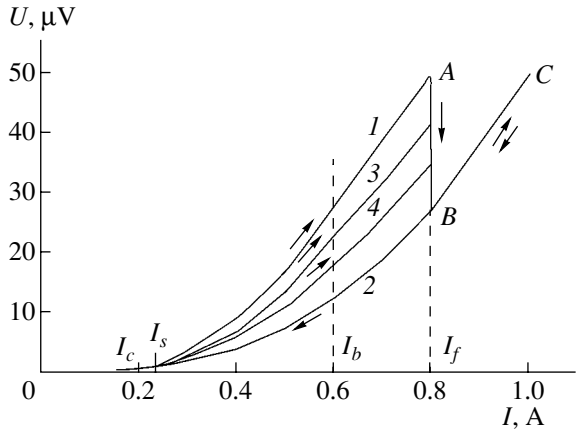

Fig. 2. *I–V* characteristics of a YBaCuO sample doped with 10 wt % Ag after its cooling in a magnetic field of 25 Oe. (*1–2*) Initial *I–V* curve; I_s is the starting point of the hysteresis loop, and I_f is the drop point. I_b is the chosen base position for recovering the starting (curve *1*) and obtaining intermediate rising curves (*3*, *4*) of the *I–V* hysteresis loop, which are determined by the pulses specified in Table 3.

below I_s to a level $I \le I_s$ and then starts to increase it again, the loop of the following cycle will be fully determined by the actual value of the current I. The loop becomes more narrow, the closer the point of the stop in current approaches I_s (curves *3*, *4* in Fig. 2). The current recovery after the drop always occurs along the fixed curve *2*. If, however, the current in an unclosed cycle is above I_s ($I > I_s$), the loop disappears and the *I–V* characteristic coincides with curve *2* in both directions. Note that this behavior of the *I–V* curves of samples with trapped magnetic flux can be used to advantage in extremely simple and convenient information storage devices.

There are reports of attempts to develop memory devices based on HTSC samples. For instance, in [21], it was proposed to employ the effect of critical current suppression in HTSCs, which appears when transport currents considerably in excess of the critical level are passed through a sample. However, this method requires high currents, which is undesirable, because thermal processes may play a significant role in this area. Rewriting of information is complicated in this case by the need to preliminarily delete the previous record, which can be achieved by heating the sample above the critical temperature, a certainly undesirable procedure.

The method proposed in [22] is based on the hysteresis of critical current observed to occur in HTSCs with weak links in cyclic magnetic fields. The observed behavior of the critical current is believed [22] to be caused by hysteresis of the intragrain magnetization of a superconductor. Because it is added to the external field at the weakly linked grain boundaries, the field originating from grain magnetization considerably affects the local critical current of the given Josephson junction. By varying the magnetic field amplitude properly, one can vary the grain magnetization and, hence, the critical current, which is used for information recording. To implement this method, a storage device is placed in a magnetic field, whose magnitude determines the superconductor grain magnetization. The information is contained in the value of the critical current, which is measured in a field lower than the recording field. The magnitude of the critical current substantially depends on the grain magnetization. While having certain merits (for instance, the possibility of writing a large number of values into a storage cell), this method is based on information recording by a magnetic field, which entails marked technological disadvantages. The implementation of this method is also complicated by the fact that the reading of stored information is effected by the measurement of the electrical characteristics.

At the same time, the existence of a hysteresis loop in the *I–V* curve of a superconductor with trapped magnetic flux permits one, by combining a base current I_b in the interval (I_s, I_f) with pulses ΔI that are variable in amplitude, to obtain various voltages across the HTSC sample which will correspond to the diverse stable states of the cell. To hold the cell at the given point on the *I–V* branch determined by the prehistory, a dc electrical current I_b is needed. Its value, as pointed out above, should lie within the hysteresis loop. A superconductor can be switched from one *I–V* branch to another by applying pulses to drive the superconductor beyond the *I–V* hysteresis region. The state of the cell (voltage U at a given current I_b) represents the actual information recorded. Weaker current pulses, which do not drive the HTSC beyond the hysteresis region, as well as variation in the base current to values $I_b > I_f$ or $I_b < I_s$, cannot be employed to record information.

To write information in the regime of two stable positions, it is necessary and sufficient to have two pulses, $\Delta I_1 > (I_f - I_b)$ and $\Delta I_2 = -I_b$. The amplitude of the first pulse is chosen such that the total current through the superconductor will exceed the drop current I_f, which will set the cell to a position on curve *2*. Similarly, the ΔI_2 pulse will set the cell to a stable position on curve *1*, because the total pulse current through the cell is zero. In this case, only the extreme branches of the superconductor *I–V* hysteresis loop are used. To record information in the regime of several (more than two) stable positions, two successive pulses, $\Delta I_1' = \Delta I_1$ and $\Delta I_2'$, are employed, with the amplitude of the second pulse satisfying the inequality $(-I_b) \le \Delta I_2' \le (I_s - I_b)$. In this case, the first pulse prepares the cell for recording by setting it to a position on curve *2*, whence it can fall on any of the available intermediate *I–V* branches. This preparation is necessary for unambiguous information recording. The recording itself is made by the second pulse $\Delta I_2'$, chosen such that the total current falls in the interval [0; I_s]; its amplitude identifies the specific *I–V* branch in the space between curves *1* and *2*. Hence, the pulse amplitude ΔI_2 will define the information recorded in the cell. The information recording process is seen to be extremely simple and convenient. The sample needs only to be preliminarily treated once by a magnetic field (cooling in it), the subsequent writing and reading being effected by electrical pulses only. Note that if the sample regains its superconducting state after the initial *I–V* region and the drop in voltage, which was frequently observed to occur in silver-doped samples [13], this cell may be particularly suitable for developing logic cells in which the zero voltage at the sample may be conveniently chosen to signify "0" and any nonzero voltage, to signify "1."

The present experiments were conducted on a YBaCuO/Ag ceramic with a low critical current to avoid the possible effect of contact heating. The sample measured $3 \times 3 \times 7$ mm. A magnetic field of 25 Oe was inserted into the sample by field cooling. Magnetic field trapping by the sample reduced its critical current from 0.76 to 0.22 A. The characteristic points on the hysteresis loop were $I_s = 0.25$ A and $I_f = 0.8$ A (Fig. 2). On

Table 2. Writing of information into the cell in the regime of two stable states, $\Delta I_1 > (I_f - I_b)$ and $\Delta I_2 = -I_b$

ΔI_1, A	ΔI_2, A	U, μV
0.4	–	12
–	−0.6	28

Table 3. Writing of information into the cell in the regime of four stable states, $\Delta I_1' > (I_f - I_b)$ and $-I_b \le \Delta I_2' \le (I_s - I_b)$

$\Delta I_1'$, A	$\Delta I_2'$, A	U, μV
0.4	−0.6	28
0.4	−0.5	23
0.4	−0.43	18
0.4	−0.35	12

these grounds, the value I_b = 0.6 A was chosen. The operation of the cell is illustrated in Tables 2 and 3, with the experimentally measured pulse amplitudes specified on the left and the cell voltage, on the right. Inspection of Tables 2 and 3 shows that the cell can occupy one of two extreme positions (Table 2) or any one in between, including the boundaries (Table 3).

4. CONCLUSION

Thus, silver-doped ceramic exhibits higher mechanical properties, such as the strength and microplastic strain rate, which is a technologically attractive point. The existence of *I–V* hysteresis in samples with trapped magnetic flux permits one to use them, in addition to the undoped material, for the development of storage cells with two or more stable positions.

REFERENCES

1. T. Shoji and Y. Tazava, Mater. Sci. Eng. A **143** (1/2), 241 (1991).
2. Q. Ni, A. Li, and Q. Kong, Chin. Phys. Lett. **6** (7), 321 (1989).
3. J. P. Singh, H. J. Leu, R. B. Poepell, *et al.*, J. Appl. Phys. **66** (7), 3154 (1989).
4. D. Lee and K. Salama, Jpn. J. Appl. Phys. **29** (11), L2017 (1990).
5. J. Joo, J.-G. Kim, and W. Nah, Supercond. Sci. Technol. **11**, 645 (1998).
6. T. S. Orlova, B. I. Smirnov, V. V. Shpeĭzman, *et al.*, Fiz. Tverd. Tela (Leningrad) **32** (4), 1031 (1990) [Sov. Phys. Solid State **32**, 606 (1990)].
7. Y. Nishi, S. Moriya, and Sh. Tokunaga, J. Mater. Sci. Lett. **7** (6), 596 (1988).
8. M. V. Galustashvili, D. G. Driyaev, I. A. Politov, *et al.*, in *Abstracts of 1st All-Union Meeting on High-Temperature Superconductivity* (Kharkov, 1988), Vol. 2, p. 140.
9. Y. Saito, T. Noji, A. Endo, *et al.*, Jpn. J. Appl. Phys. **26** (5), L832 (1987).
10. Z. Su, T. Zhao, S. Sun, *et al.*, Solid State Commun. **69** (11), 1067 (1989).
11. P. Singh, D. Shi, and D. W. Capone, Appl. Phys. Lett. **53** (3), 237 (1988).
12. N. N. Peschanskaya, B. I. Smirnov, V. V. Shpeĭzman, and P. N. Yakushev, Fiz. Tverd. Tela (Leningrad) **30** (11), 3503 (1988) [Sov. Phys. Solid State **30**, 2014 (1988)].
13. L. K. Markov and V. V. Shpeĭzman, Fiz. Tverd. Tela (Leningrad) **33** (11), 3308 (1991) [Sov. Phys. Solid State **33**, 1865 (1991)].
14. L. K. Markov and V. V. Shpeĭzman, Fiz. Tverd. Tela (St. Petersburg) **35** (11), 3008 (1993) [Phys. Solid State **35**, 1478 (1993)].
15. N. N. Peschanskaya, P. N. Yakushev, V. V. Shpeĭzman, *et al.*, Fiz. Tverd. Tela (St. Petersburg) **41** (5), 848 (1999) [Phys. Solid State **41**, 767 (1999)].
16. V. I. Startsev, V. Ya. Il'ichev, and V. V. Pustovalov, *Plasticity and Strength of Metals and Alloys at Low Temperatures* (Metallurgiya, Moscow, 1975).
17. A. I. Golovashkin, Usp. Fiz. Nauk **152** (4), 553 (1987) [Sov. Phys. Usp. **30**, 659 (1987)].
18. Yu. A. Burenkov, V. I. Ivanov, A. B. Lebedev, *et al.*, Fiz. Tverd. Tela (Leningrad) **30** (10), 3188 (1988) [Sov. Phys. Solid State **30**, 1837 (1988)].
19. Yu. F. Gorin, L. L. Nugaeva, L. Ya. Kobelev, *et al.*, Fiz. Met. Metalloved. **66** (1), 202 (1988).
20. M. Saint-Paul, J. L. Tholence, P. Monceau, *et al.*, Solid State Commun. **66** (6), 641 (1988).
21. P. P. Bezverkhiĭ, N. A. Bogolyubov, and V. G. Martynets, Sverkhprovodimost: Fiz., Khim., Tekh. **3** (3), 469 (1990).
22. K. Kwasnitza and Ch. Widmer, Cryogenics **29** (11), 1035 (1989).

Translated by G. Skrebtsov

Physics of the Solid State, Vol. 45, No. 9, 2003, pp. 1634–1637. Translated from Fizika Tverdogo Tela, Vol. 45, No. 9, 2003, pp. 1556–1559.

SEMICONDUCTORS AND DIELECTRICS

Photoluminescence of Bulk Eu-Doped GaN Crystals

V. V. Krivolapchuk, M. M. Mezdrogina, A. V. Nasonov, and S. N. Rodin

Ioffe Physicotechnical Institute, Russian Academy of Sciences,
Politekhnicheskaya ul. 26, St. Petersburg, 194021 Russia
e-mail: vlad.krivol@pop.ioffe.rssi.ru

Received January 30, 2003

Abstract—A study of the variation of photoluminescence spectra of bulk Eu-doped GaN samples revealed that the dopant can reside in the crystal in various charge states depending on the total defect concentration in the starting semiconductor host matrix. In crystals with the lowest concentration of shallow-level defects, the ion can exist only in one charge state, Eu^{3+}. At higher concentrations of such defects, Eu can be observed in two charge states, Eu^{2+} and Eu^{3+}. A rare-earth impurity was found to act as a getter of defects in the starting GaN matrix. © *2003 MAIK "Nauka/Interperiodica".*

1. INTRODUCTION

The development of light-emitting devices capable of operating at room temperature is a topical issue in present-day optoelectronics. Wide-band-gap GaN doped by rare-earth (RE) ions (GaN⟨RE⟩) is a promising material for this area. The interest in GaN⟨RE⟩ can be traced to the fact that the temperature quenching of photoluminescence (PL) characteristic of an intracenter transition in an RE ion is weaker, the wider the band gap of the semiconductor matrix doped by the RE ion [1–3]. Moreover, GaN⟨RE⟩ allows a considerable increase in the RE concentration as compared to crystalline Si (*c*-Si) and films of amorphous hydrogenated silicon (*a*-Si : H); therefore, the intracenter transition intensity can also be increased. As exemplified by the case of GaN⟨Er⟩, this distinction is a result of a change in the bonding type from ionic–covalent (Ga–N) to ionic (Er–N), in contrast to the Er–Si metallic bonding in *c*-Si⟨Er⟩ [4].

Despite considerable progress reached in the development of light-emitting devices based on gallium nitride, the decrease in the total defect concentration in crystals (by defects we understand here any lattice structure imperfections) remains an issue. One of the methods to reduce defect concentration in semiconductor materials consists in doping them with RE ions [5] to produce a gettering effect. Gettering methods are widely employed in semiconductor technology. For instance, gettering has been successfully employed to reduce the concentration of residual impurities and defects in crystalline silicon to 10^{11} cm^{-3}, which provided a favorable solution to the problem of obtaining a material for high-power and photoreceiving devices. This study explores europium (Eu) as a dopant. Eu was chosen for its ability to reside in the semiconductor matrix (GaN) in two different charge states, Eu^{2+} and Eu^{3+} [6]. There are grounds to believe that Eu^{2+} can act as an acceptor. This is important because an acceptor dopant provides compensation in *n*-type materials, to which bulk undoped GaN crystals usually belong.

The present communication reports on a study of photoluminescence spectra of bulk Eu-doped GaN crystals for a range of total defect concentrations in the starting semiconductor matrix.

2. EXPERIMENT

The starting bulk GaN crystals were prepared by chloride vapor phase epitaxy. X-ray structural analysis showed the halfwidth of the diffraction reflection curve to be the same not above 10′, in all the samples studied. The samples differed in surface morphology, with nonuniformities measuring from 1 to 10 μm. In the methods employed until recently, RE ions were incorporated into the GaN matrix either using molecular-beam epitaxy (MBE) during the growth [1, 2] or by implantation [3] with subsequent anneal. However, the effect of defect concentration in the starting semiconductor matrix on the PL spectra taken after doping was not considered. As in [6, 7], diffusion was used to dope Eu into GaN, because this technology of introducing a dopant provides a lower concentration of additional defects as compared to implantation involving a high-energy impact approach. In addition, the diffusion method, unlike in the introduction of Eu in the course of growth, brings about neither a change in the crystal growth kinetics nor the formation of residual segregates.

Luminescence was excited by a pulsed nitrogen laser (λ = 337.1 nm, spot diameter on a sample of 150 μm). The PL spectra were recorded using an SDL-2 diffraction spectrometer in the time-resolved photon counting mode. The spectral measurements were conducted at 77 K. To ensure adequate comparison of emission spectra of various samples, the controllable conditions of the experiment (temperature, excitation

density, spectral resolution, laser beam incidence angle) were maintained constant.

3. EXPERIMENTAL RESULTS AND DISCUSSION

The spectra of near-edge photoluminescence (NEPL) of the starting bulk GaN crystals (samples 1, 2) are displayed in Fig. 1. Inspection of the spectra of these samples reveals a large difference in the intensity and halfwidth (FWHM) and different positions of the line maximum. For sample 1, the energy of the maximum E = 3.463 eV (358.1 nm) and FWHM = 9 meV, while for sample 2, E = 3.451 eV (358.7 nm) and FWHM = 100 meV. The NEPL line intensity in sample 2 is an order of magnitude higher than that of sample 1. Our analysis of the PL spectra was focused primarily on the intensity of the NEPL line and its FWHM. This line is inhomogeneously broadened. The inhomogeneous broadening is due to the fact that the radiative recombination of carriers localized at various shallow centers occurs at slightly different wavelengths. The reason for this difference is the dispersion in the shallow-donor thermal activation energy E_{LT}. The dispersion in E_{LT} originates, in turn, from the different magnitude of the local potential V_{loc} at the location of the shallow impurities. This means that the various defects located close to shallow impurities change the crystal field and, thus, affect the radiation wavelength. Therefore, the large difference in the FWHM of the NEPL line between the starting samples is due to the various defects being present in them in different concentrations. The intensity and FWHM of the NEPL line depend on the concentration of the radiative and nonradiative states and the carrier transport to them. The carrier transport parameters are governed, in turn, by the density-of-states tails in the band gap and by the position of the percolation level [8–11]. Whence it follows that samples producing different PL intensities under identical experimental conditions differ primarily in the defect concentration. The defects create both deep levels (which substantially shorten the free-carrier lifetime) and fluctuations in the density of band states. In addition, in n-GaN crystals, the FWHM of the NEPL line at T = 77 K depends on carrier concentration [12] and, for the samples under study ($N_d - N_a > 10^{17}$ cm^{-3}), should be not less than 30 meV.

In sample 1, the emission line with energy E = 3.463 eV (358.1 nm) is due to the exciton bound to a shallow donor [13]. In view of the above factors favoring PL line broadening, the anomalously small value of FWHM for sample 1 appears remarkable. The small intensity and FWHM may be due to the shallow donors being located below the percolation level: so the number of donors involved in the formation of this emission line is small sample 2, has a lower defect concentration (compared to sample 1). It exhibits fairly strong NEPL and a band originating from donor–acceptor recombination (DAR PL). The presence of the DAR-PL band and the position of the NEPL line at E_{max} = 3.451 eV (which is assigned to the emission of a neutral-acceptor-bound exciton [14]) indicate the existence of shallow acceptor levels.

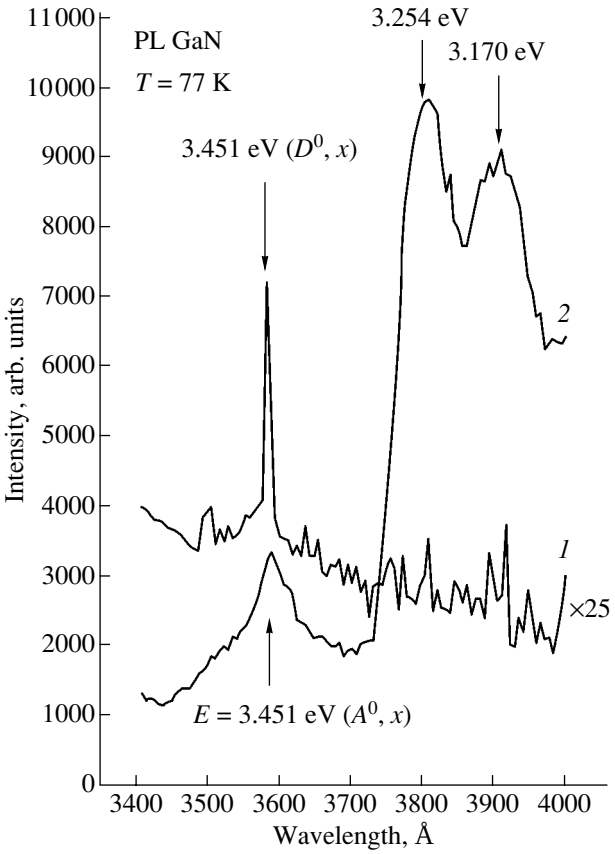

Fig. 1. Photoluminescence spectra of the starting GaN crystals: (*1*) sample 1 and (*2*) 2.

Figure 2 illustrates the spectra of the corresponding samples obtained after their doping with europium (curves *1*, *2*). Eu doping is seen to strongly affect the PL spectra (Fig. 2). Sample 1 exhibits an increase in both the intensity of the emission line at E_{max} = 3.451 eV (359.2 nm) (by five times) and the value of FWHM (by a factor 7.4) as compared to the undoped crystal; strong DAR-PL lines also appear at E = 3.254 eV (381 nm) and 3.17 eV (391 nm). Sample 2 reveals one line at E_{max} = 3.463 eV (358.0 nm), with its peak shifted shortward by 0.7 nm and FWHM = 9 meV. The intensity of this line decreased by nearly an order of magnitude as compared to the undoped sample, while the DAR PL line disappeared completely. It should be stressed that an increase in the DAR-PL intensity similar to that observed in sample 1 was found to occur in magnesium-doped GaN crystals grown by MBE on GaAs and sapphire substrates with an ionized acceptor concentration $n_a = 1.5 \times 10^{17}$ cm^{-3} [15]. It is presently believed that RE ions doped into III–V compounds create iso-

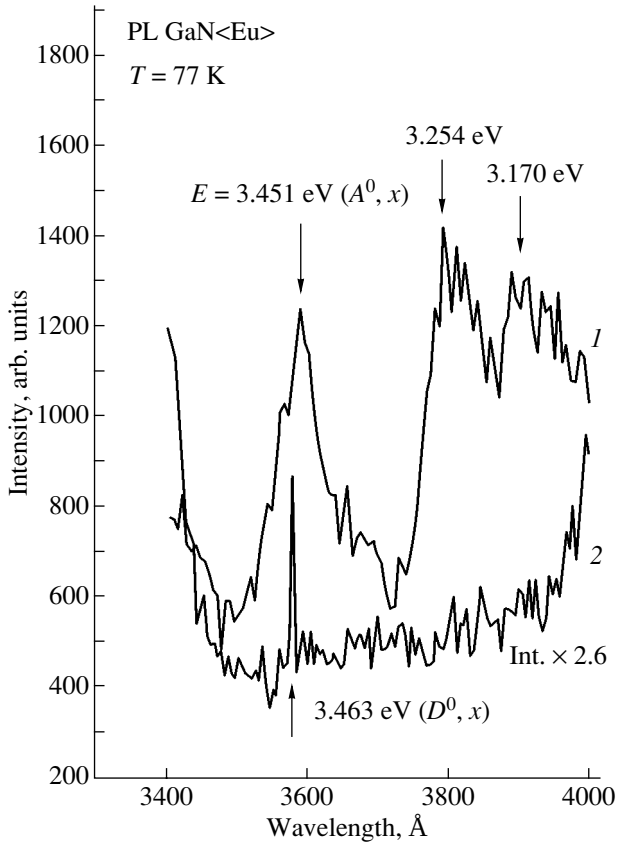

Fig. 2. Photoluminescence spectra of Eu-doped GaN crystals: (*1*) sample 1 and (*2*) 2.

electronic traps [16], but there are no experimental data indicating what part, donor or acceptor, they play in GaN. It is appropriate to note in this connection that the formation of a donor–acceptor recombination band in GaN⟨Eu⟩ suggests that, in this particular case, Eu^{2+} acts as an acceptor.

In addition, a long-wavelength emission is seen in Eu-doped samples. The spectrum of sample 1 features only one band, peaking at 660 nm, which is apparently due to the $^5D_1$–$^7F_3$ intracenter transition. The spectrum of sample 2 exhibits both a fairly broad band with a maximum at $E = 2.306$ eV (543 nm) and a band peaking at 660 nm.

The change in the shape of the PL spectra of Eu-doped samples should be analyzed with due account of the following points. As already mentioned, the starting samples differed in the host defect concentration and the scale of surface nonuniformities. Data obtained by Mössbauer and ESR spectroscopy [17] and measurements of the electrophysical properties of *a*-Si : H⟨Eu⟩ films suggest that the actual charge state of the Eu ion is determined by the host defect concentration (dangling and stressed Si–Si and Si–H bonds, deep and shallow levels). There are, therefore, grounds to expect that Eu ions present in GaN samples with different defect concentrations may also reside in different charge states (Eu^{2+}, Eu^{3+}). This property is known to result from the ionic radius of Eu^{3+} ($R_i \approx 0.95$ Å) being less than that of Eu^{2+} ($R_i \approx 1.1$ Å) [18]. The substantial decrease in the intensity and FWHM in sample 2 (by more than an order of magnitude) should be assigned to the fact that the Eu^{3+} ion acts here as a deep trapping level, thus complicating carrier transport to the radiating states accounting for the DAR-PL line intensity and FWHM. Note also that the donor–acceptor recombination band (associated with shallow impurities) disappears in crystal 2. This may mean the appearance of deep acceptors related to Eu^{2+} + nitrogen vacancy complexes. This assumption is supported by the presence of an emission at a wavelength of 430.4 nm (2.88 eV), which appears after Eu doping and is characteristic of a nitrogen vacancy [19]. The PL spectrum in the long-wavelength spectral region of this crystal is similar in shape to that of GaN⟨Eu⟩ reported in [20].

The only charge state that is realized preferentially after Eu doping in the starting (undoped with Eu) sample 1 with the lowest concentration of shallow defects but the highest concentration of deep defects is Eu^{3+}. This is indicated by the existence in the long-wavelength part of the spectrum of a band peaking at 660 nm, which is most likely due to Eu^{3+}. As is evident from the spectrum of sample 1 (Fig. 2), in this case, the DAR-PL line of GaN (3.451 eV) broadens. This broadening is caused by the formation of additional defects accompanying RE doping; these defects bring about an increase in the dispersion of shallow-state energies E_{LT} and an increase in the concentration of primarily shallow acceptors, which is indicated by the strong DAR-PL line appearing after doping with Eu. Thus, one may put forward the assumption that the gettering effect reduces to the decrease in the number of dangling or stressed Ga–N bonds [4].

Comparison of the PL spectra permits the conclusion that the incorporation of Eu in *n*-GaN crystals induces the gettering effect as a result of the formation of shallow acceptors originating from RE ions. The actual type of the acceptor (shallow or deep) is governed by the charge state of the Eu ion (3+ and 2+, respectively). The prevailing RE charge state will be determined by the defect concentration of the starting crystals. Gettering of defects by RE ions, in turn, occurs differently, depending on whether the crystal is doped primarily by the Eu^{3+} or Eu^{2+} ions. In the first case, deep levels transform predominantly into shallow ones. This gives rise to the appearance of a DAR PL line and an increase in the NEPL intensity and FWHM. In the second case (the presence of two charge states, Eu^{2+} and Eu^{3+}), conversely, shallow traps convert to deep levels, thus reducing both the FWHM and intensity of the NEPL. At the same time, when analyzing the factors responsible for the change in the FWHM of the 358.1-nm line (in the starting crystal), the longward shift of the maximum (359.2 nm), the increase in the NEPL intensity, and the appearance of the DAR-PL

band, one should bear in mind that intracenter emission of the Eu^{2+} and Eu^{3+} ions is known to occur in different spectral regions. In particular, within the 353- to 441-nm interval (depending on the host material), only the emission due to Eu^{2+} is observed. Therefore, the emergence of a narrow line at 359.2 nm should probably be assigned to the intracenter transition in the Eu^{2+} ion as well.

4. CONCLUSIONS

Thus, a study of the variation of PL spectra of bulk GaN⟨Eu⟩ crystals revealed an effect of defect gettering (which is most likely due to a decrease in the number of dangling bonds and a transformation of deep to shallow states and, conversely, of shallow to deep states) in the starting *n*-GaN matrix as a result of the creation of acceptor states. It was found that the different charge states of the Eu ion, Eu^{2+} and Eu^{3+} (or only Eu^{3+}), are realized depending on the defect concentration in the starting matrix. The lowest concentration of shallow levels and the highest deep-level concentration favor the prevalence of only one charge state of the impurity ion, Eu^{3+}, while in the opposite case, europium exists in two charge states, Eu^{3+} and Eu^{2+}. Therefore, the actual acceptor type (shallow or deep) is probably determined by the charge state of the RE ion.

ACKNOWLEDGMENTS

The authors are indebted to Yu.V. Zhilyaev and A.P. Skvortsov for useful discussions and valuable criticism.

REFERENCES

1. A. J. Steckl and B. Birkhahn, Appl. Phys. Lett. **73**, 1700 (1998).
2. A. J. Steckl, M. Garter, B. Birkhahn, and J. D. Scofield, Appl. Phys. Lett. **74**, 2161 (1999).
3. S. Kim, S. J. Rhee, and D. A. Turnbull, Appl. Phys. Lett. **71**, 2662 (1997).
4. P. H. Citrtn, P. A. Northrup, R. Birkhahn, and A. J. Steckl, Appl. Phys. Lett. **76**, 2865 (2000).
5. L. S. Vlasenko, A. T. Gorelenok, V. V. Emtsev, *et al.*, Fiz. Tekh. Poluprovodn. (St. Petersburg) **35** (2), 184 (2001) [Semiconductors **35**, 177 (2001)].
6. V. V. Krivolapchuk, M. M. Mezdrogina, S. D. Raevskiĭ, *et al.*, Pis'ma Zh. Tekh. Fiz. **28** (7), 19 (2002) [Tech. Phys. Lett. **28**, 270 (2002)].
7. Yu. V. Zhilyaev, A. S. Adrianov, M. M. Mezdrogina, *et al.*, in *Abstracts of II Russian Conference on Physics of Semiconductors, Novosibirsk* (1999), p. 56.
8. R. A. Street, Adv. Phys. **30**, 593 (1981).
9. S. Permogorov and A. Reznitsky, J. Lumin. **52**, 201 (1992).
10. E. Cohen and M. Sturge, Phys. Rev. B **25**, 3828 (1982).
11. A. Klochikhin, A. Reznitsky, S. Permogorov, *et al.*, Phys. Rev. B **59**, 12947 (1999).
12. E. Iliopoulos, D. Doppalapudi, H. M. Ng, and T. D. Moustakas, Appl. Phys. Lett. **73**, 375 (1998).
13. R. Dingle, D. D. Seil, S. E. Stakowsky, and M. Ilegems, Phys. Rev. B **4**, 1211 (1971).
14. V. Kiroilyuk, P. H. Hageman, and M. Zielenski, Appl. Phys. Lett. **79**, 4109 (1999).
15. V. Yu. Nekrasov, P. V. Belyakov, O. M. Sreseli, and N. N. Zinov'ev, Fiz. Tekh. Poluprovodn. (St. Petersburg) **33** (12), 1428 (1999) [Semiconductors **33**, 1284 (1999)].
16. H. I. Lozykowski, Phys. Rev. B **48**, 17758 (1993).
17. M. M. Mezdrogina, I. N. Trapeznikova, E. I. Terukov, *et al.*, Fiz. Tekh. Poluprovodn. (St. Petersburg) **36** (11), 1337 (2002) [Semiconductors **36**, 1252 (2002)].
18. S. V. Thiel, H. Cruguel, H. Wu, *et al.*, Phys. Rev. B **64**, 085107 (2001).
19. A. N. Georgobiani, A. N. Gruzintsev, M. O. Vorob'ev, *et al.*, Fiz. Tekh. Poluprovodn. (St. Petersburg) **35** (6), 725 (2001) [Semiconductors **35**, 695 (2001)].
20. J. Heikenfeld, M. Garter, D. S. Lee, *et al.*, Appl. Phys. Lett. **75**, 1189 (1999).

Translated by G. Skrebtsov

Physics of the Solid State, Vol. 45, No. 9, 2003, pp. 1638–1643. Translated from Fizika Tverdogo Tela, Vol. 45, No. 9, 2003, pp. 1560–1565.

SEMICONDUCTORS AND DIELECTRICS

Local Vibrational Mode in Zinc Telluride Associated with a Charged Nickel Impurity

V. I. Sokolov*, N. B. Gruzdev*, and I. A. Farina**

**Institute of Metal Physics, Ural Division, Russian Academy of Sciences, ul. S. Kovalevskoĭ 18, Yekaterinburg, 620219 Russia*

e-mail: visokolov@imp.uran.ru

***Institute of Physics, National Academy of Sciences of Ukraine, pr. Nauki 144, Kiev, 03039 Ukraine*

Received August 22, 2002; in final form, February 3, 2003

Abstract—Field exciton–vibration spectroscopy of the ZnTe : Ni semiconductor has revealed a local lattice vibrational mode due to the nickel impurity, which is negatively charged relative to the lattice. The electroabsorption spectrum of ZnTe : Ni contains equidistant vibrational replicas of the zero-phonon line of frequency 13 ± 1 THz, which exceeds the limiting phonon frequency in ZnTe by more than twofold. Possible reasons for the formation of the local mode in ZnTe : Ni are analyzed within the concept of ionic–covalent character of ZnTe bonding, and the large width of the local mode resulting from its anharmonicity is discussed. © *2003 MAIK "Nauka/Interperiodica".*

1. INTRODUCTION

3*d* transition-metal impurities in semiconductors exert a considerable effect on the electronic properties [1]. The influence of the 3*d* impurities on lattice vibrations of semiconductors have not attracted as much attention. The partially filled 3*d* shells of impurity atoms allow them to exist in a variety of charge states. Atoms of isoelectronic impurities are, as a rule, neutral relative to the lattice, because they donate as many electrons to the formation of a chemical bond as the atoms they substitute for. The changes in the mass and in the force constants resulting from the substitution of an impurity center for a lattice atom are small, and, therefore, the changes in the lattice vibrational modes induced by a 3*d* impurity are insignificant. A change may become manifest, for instance, in the appearance of additional weak peaks in the Raman spectra [2]. Transition metal impurities can, however, gain charge with respect to the lattice as a result of the change in the number of electrons in the *d* shell. The charge state of 3*d* impurities can change either through the formation of shallow impurity centers or in photoionization of the impurity by light. In this case, the Coulomb field of the charged impurity center displaces ions in the nearest environment, which strains the lattice in this region of the crystal and, thus, may affect its properties. This change may influence, for instance, the photorefractive effect, which is particularly noticeable for ZnTe and CdTe, which exhibit a large electrooptical effect [3, 4]. It thus appears of interest to study the properties of these semiconductors with 3*d* metal impurities charged relative to the lattice.

Such a study would also be of interest in connection with the reports an remarkable changes in the properties of wide-band-gap nickel-doped II–VI compounds (ZnS : Ni, ZnO : Ni, ZnSe : Ni, CdS : Ni) caused by the presence of a 3*d* charged impurity. The vibrational replicas of the impurity exciton zero-phonon line observed in the above compounds using field exciton-vibrational spectroscopy [5], as well as the abrupt drop in the phonon thermal conductivity of ZnSe : Ni detected recently in the 5- to 15-K interval [6], suggest that the charged nickel impurity induces local vibrations characterized by a strongly pronounced anharmonicity. An attempt was made in this work to detect and study the acceptor-like nickel exciton [d^9h] in ZnTe : Ni by field exciton-vibrational spectroscopy, because this state, on the one hand, is induced by a negatively charged nickel impurity and, on the other hand, interacts with the lattice vibrations initiated by a charged impurity center. The studies showed the photoinduced lattice vibrations of ZnTe : Ni to differ substantially from those of other II–VI Ni-doped compounds. The present communication deals with possible reasons for this difference.

2. EXPERIMENTAL

The absorption spectrum obtained at the edge of the photoionization band of a substitutional impurity consists of a zero-phonon line, due to an electronic transition to the impurity exciton state, and its vibrational replicas, reflecting the interaction of the impurity exciton with photoinduced lattice vibrations. The series of vibrational replicas becomes superposed on the absorption spectrum as a result of carrier transitions from the impurity to the allowed band; this process considerably complicates identification of this line from absorption spectra. Therefore, field-induced exciton–vibration spectroscopy (the method of electroabsorption) was

employed to detect the photoinduced vibrations. An ac electric field $F = F_M \cos\Omega t$ was applied to a sample through which light was passed. This field strongly affects the impurity exciton zero-phonon line and its vibrational replicas. A comprehensive description of the application of the electroabsorption method for investigating exciton states in semiconductors doped by 3*d* transition elements can be found in review [7].

We conducted measurements on ZnTe : Ni samples (nickel concentration 10^{18} cm^{-3}) within the spectral region 0.87–1.35 eV, with the electric field amplitude F_M varied from 20 to 40 kV/cm. At lower amplitudes, the field does not noticeably affect the impurity exciton lines, while higher fields are capable of initiating electrical breakdown of the sample. The electroabsorption spectra were measured on a setup with a MDR-3 monochromator that was employed earlier in studies of the acceptor-like nickel exciton in ZnS : Ni, ZnSe : Ni, ZnO : Ni, and CdS : Ni samples [5]. The edge of the nickel photoionization band in ZnTe : Ni falls in the infrared range; therefore, a PbS-based photoresistor, which is less sensitive than a PM tube, was used for signal detection. The resolution, ~3 meV, was substantially poorer than in measurements with a PM tube. The low sensitivity of the photoreceiver accounts for the fairly high noise level, which is particularly pronounced at the beginning of the spectrum (near the zero-phonon line) and at its end, where the dc and ac components of the signal decrease sharply because of the impurity absorption in the sample [8] (Fig. 1). The amplitude of the second electroabsorption harmonic α_2 was calculated from the relation $\alpha_2 = I_2/(dI_0)$, where d is the sample thickness in centimeters (it was 0.05 cm), I_2 is the ac photoreceiver signal component at the double frequency 2Ω, and I_0 is the dc component. The error in determining α_2 was 15–20% in the most unfavorable conditions. Despite the poorer photoreceiver sensitivity, we succeeded in obtaining new information on photoinduced vibrations in ZnTe : Ni, which is particularly interesting in comparison with the results quoted in [5].

The observed spectrum of the second electroabsorption harmonic amplitude α_2 (Fig. 1) consists of a zero-phonon line (ZPL) and a series of its vibrational replicas, which occupy approximately equidistant positions separated by 55 ± 4 meV (measurement error at a confidence level of 0.95). An electric field displaces the acceptor-like exciton lines toward lower energies, to form a structure with a positive and a negative peak of approximately the same amplitude, with the zero crossing point corresponding to the center of the absorption line [7].

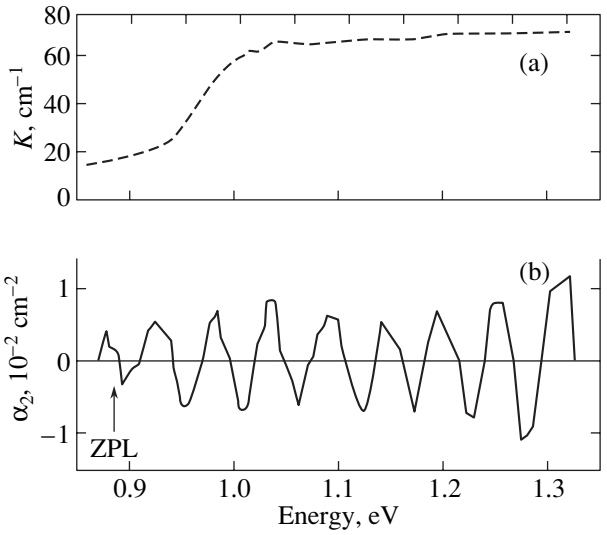

Fig. 1. (a) Absorption spectrum of ZnTe : Ni [8] (nickel concentration 10^{19} cm^{-3}, $T = 4.2$ K) and (b) electroabsorption spectrum of a ZnTe : Ni sample obtained in an electric field $F_M = 40$ kV/cm (nickel concentration 10^{18} cm^{-3}, $T = 4.2$ K).

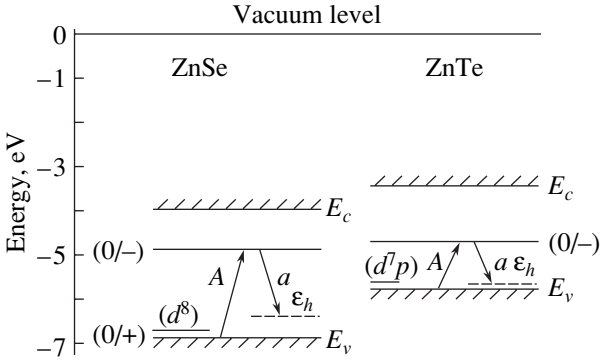

Fig. 2. Position of the ZnSe and ZnTe allowed band edges and of the nickel energy levels relative to the vacuum level [9–11]. (0/–) refers to acceptor levels, (0/+) refers to the donor level, and ε_h is the energy of a hydrogen-like carrier.

3. DISCUSSION OF RESULTS

3.1. Acceptor-Like Exciton

If the photon energy $\hbar\omega_A$ is equal to the distance from the nickel acceptor level (0/–) to the top of the valence band, an impurity absorption band produced by valence-band electrons transferring to the impurity center appears (transition *A* for ZnSe : Ni in Fig. 2):

$$d^8 + e_v + \hbar\omega_A \longrightarrow d^9 + h. \quad (1)$$

As a result of this transition, the impurity center, which was originally neutral with respect to the lattice, acquires a negative charge and a free hole is created in the valence band. The Coulomb field of the charged impurity center confines the hole to a hydrogen-like orbit to form an acceptor-like exciton (AE), which is actually the excited state of the impurity center (transition *a* for ZnSe : Ni in Fig. 2):

$$d^8 + e_v + \hbar\omega_a \longrightarrow [d^9 h]. \quad (2)$$

The brackets denote here Coulomb interaction.

It is to this transition that the zero-phonon line of the nickel acceptor-like exciton in ZnSe : Ni, ZnO : Ni, CdS : Ni, and ZnS : Ni was assigned in [5].

Relations (1) and (2) were written under the assumption that the nickel impurity creates states of the crystal field resonance (CFR) type in the lattice [12]. In other words, the energy needed to transfer an electron from a d^8 configuration state to the conduction band ($d^8 \longrightarrow d^7 + e$) is less than the band gap width E_g; i.e., the donor level (0/+) falls into the gap. For the ZnSe : Ni and ZnS : Ni compounds, this condition is satisfied, because donor levels have been experimentally detected for $\hbar\omega < E_g$ in studies of donorlike excitons [d^7e] [1, 7]. For ZnTe : Ni, the position of the donor level (0/+) reckoned from the vacuum level falls into the valence band [7, 9, 10] and there are grounds to believe that the states produced in the hybridization of *d* states of an impurity with *p* states of the valence band (i.e., of an anion) are expelled into the band gap. In this case, transitions (1), involving nickel photoionization, and transitions (2) to a state of an acceptor-type impurity exciton can be presented in the form

$$(d^7 p) + e_v + \hbar\omega_A \longrightarrow d^9 + h, \tag{3}$$

$$(d^7 p) + e_v + \hbar\omega_a \longrightarrow [d^9 h]. \tag{4}$$

Transitions (3) and (4) bring about rearrangement of the electronic density structure, with the *d* shell having now nine electrons. Note that the impurity, as in the case of transition (2), becomes negatively charged and its Coulomb field binds the hole formed in the valence band. This rearrangement is driven by the creation of a dangling bond hybrid (DBH)-type state [12], denoted here by (d^7p), in the ZnTe band gap by the Ni impurity. If, however, the impurity has an acceptor level (0/–) in the band gap and light of energy $\hbar\omega < E_g$ transfers an electron from the valence band to the impurity, then a d^9 configuration, i.e., a CFR-type state, forms. This interpretation is based on the observation in ZnTe : Ni of intracenter transitions of type $^2T_2 \longrightarrow {}^2E$ for the nickel d^9 configuration with an energy ~0.384 eV [13]. This figure agrees well with the energy of intracenter transitions of the nickel d^9 configuration in ZnSe : Ni (0.405 eV) and ZnS : Ni (0.438 eV) [13], where the presence of the d^9 configuration was reliably confirmed by EPR measurements during nickel photoionization, the reaction described by Eq. (1) [14, 15]. It is this situation that is illustrated in Fig. 2 for the ZnTe : Ni compound [9–11]. The position of the acceptor-like exciton line is determined by the energy separation between the valence band top and the (0/–) level minus the hydrogen-like carrier energy ε_h, as shown in Fig. 2. The hydrogen-like energy of a shallow acceptor in ZnTe is ~60 meV. Adding this energy to the energy of the acceptor-like exciton zero-phonon line (0.886 eV) yields 0.946 eV. It is approximately in this region of photon energies that absorption starts to grow rapidly with an increase in the energy of the photons (Fig. 1).

Note the very large width of the zero-phonon line compared to those in other II–VI Ni-doped compounds. Assuming the absorption line to have Lorentzian shape

$$\alpha(\hbar\omega) = \frac{A\Gamma}{(\hbar\omega - \hbar\omega_0)^2 + \Gamma^2/4}, \tag{5}$$

its width Γ can be estimated from the relation

$$\Gamma = \sqrt{3}(E_{\min} - E_{\max}), \tag{6}$$

where $E_{\min}$ and $E_{\max}$ are the energy positions of the minimum and maximum of the quantity $\alpha_2(\hbar\omega)$ [16]. In our case, $E_{\min} - E_{\max}$ = 13 meV; hence, Γ = 22.5 meV. This value exceeds the widths of the Ni [d^9h] AE lines for ZnS : Ni, ZnSe : Ni, ZnO : Ni, and CdS : Ni by a factor of two to three [5]. The short lifetime of the impurity exciton is due to the efficient nonradiative recombination, a process whose mechanism for the II–VI Ni-doped semiconductors is described in considerable detail in [17]. The efficiency of this mechanism derives from the excited intracenter states of the d^8 configuration, which lie below the zero-phonon line of the acceptor-like exciton in terms of energy. In ZnTe : Ni, however, the Ni AE undergoes annihilation [d^9h] $\longrightarrow$ (d^7p) through excited states of the (d^7p) configuration. Because these states differ substantially from the d^8 excited states in terms of number and structure, the nonradiative recombination

$$[d^9 h] \longrightarrow (d^7 p)^* \longrightarrow (d^7 p)$$

can be more efficient than [d^9h] $\longrightarrow$ (d^8)* $\longrightarrow$ (d^8). This accounts for the large width of the Ni AE line in ZnTe : Ni compared to other II–VI Ni-doped compounds.

In concluding the discussion of the acceptor-like exciton zero-phonon line, it is appropriate to note that, while the nickel acceptor-like exciton line [d^9h] observed by us in ZnTe : Ni is well within the bounds of the concept of the nickel excited states in II–VI compounds, the reason behind the large broadening of the acceptor-like exciton zero-phonon line requires further study.

3.2. Vibrational Replicas

The electroabsorption spectrum of ZnTe : Ni (Fig. 1) contains, besides the zero-phonon line, a series of its phonon replicas. Note the main features of this structure. First, only one peak is replicated after the zero-phonon line, which implies that the impurity exciton interacts solely with one vibrational mode, the repetition period $\Omega = 55 \pm 4$ meV yields the frequency of this mode. Second, the vibrational replicas have a very large width (Fig. 3). Third, the vibrational replicas vary insignificantly in intensity as their number *n* increases and, hence, do not obey the Poisson distribution

$$I_n = I_0 \frac{e^{-S} S^n}{n!}. \tag{7}$$

These features substantially discriminate the structure of vibrational replicas of the nickel AE [d^9h] zero-phonon line in ZnTe : Ni from the corresponding spectra observed in ZnSe : Ni, ZnO : Ni, CdS : Ni, and ZnS : Ni [5]. The spectra of the latter compounds exhibit, in the region of first-order processes, several vibrational replicas of the zero-phonon line separated by different energies. This means that the Ni [d^9h] impurity exciton interacts with several vibrational modes differing in frequency. In the region of higher order processes, these modes are coupled strongly to one another because of the anharmonicity. The coupling of the impurity exciton to lattice vibrations is determined by the ground-state symmetry of the nickel AE. The ZnSe, ZnS, and ZnTe compounds have the same symmetry group T_d; therefore, the nickel AEs in these compounds interact with the same set of vibrational states described by the irreducible representations Γ_1, Γ_3, and Γ_5 [7]. The presence of only one peak in the first-order region in ZnTe : Ni means that a change in the nickel charge state in the ZnTe : Ni lattice gives rise to only one local mode of the set with which the impurity exciton can interact. The frequency of this vibration mode is 13 ± 1 THz, which exceeds the limiting frequency of the lattice phonons of this compound by more than twofold (the LO and TO phonon frequencies at the Brillouin zone center are approximately 5.39 and 5.2 THz, respectively) [18].

Note also the absence of noticeable peaks in the electroabsorption spectrum that originate from interaction of the Ni [d^9h] AE with optical phonons in the region of first-order processes where the vibrational density-of-states spectrum (Fig. 3) exhibits two narrow strong peaks having a width larger than our spectral resolution (in Fig. 3, the region of first-order processes is bounded by a vertical dashed line shifted relative to the zero-phonon line by 55 meV, as in [5, Figs. 1–3]). The fact that the experimental spectra exhibit no vibrational replicas caused by interaction of the nickel acceptor-like exciton with phonons, whose density is very high compared to that of the local vibrations induced by the nickel impurity, suggests that the Ni [d^9h] AE interacts only weakly with the lattice phonons. This may be considered an argument against the possibility of strong interaction of acceptor- or donorlike excitons of 3d impurities with phonons of an ideal lattice; this view was put forward earlier [19, 20] but was subsequently changed on the basis of considerations of an indirect nature, which are presented in [5].

The very simple structure of the vibrational replicas of the Ni [d^9h] AE zero-phonon line implies that the charged nickel impurity in ZnTe : Ni induces local lattice vibrational modes different from those in other II–VI Ni-doped compounds. The high frequency of the vibrational mode indicates that the negatively charged impurity center forms a local mode in ZnTe : Ni. Local modes with a frequency in excess of that of the lattice vibrations appear when the impurity atom is considerably lighter than the replaced atom or when the force

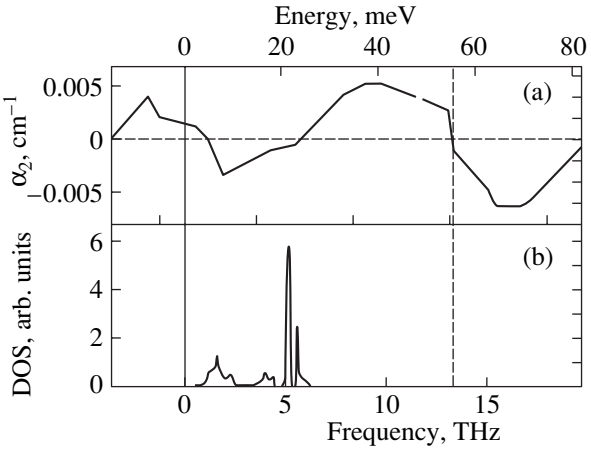

Fig. 3. (a) Zero-phonon line and its first replica in the electroabsorption spectrum of a ZnTe : Ni sample. The vertical solid line identifies the position of the zero-phonon line (ZPL) and the vertical dashed line is the boundary of the region of first-order processes. (b) Density of vibrational states of the ZnTe lattice [18].

constant of impurity interaction with the nearest environment atoms increases strongly. Because the mass of the nickel atom (58 a.m.u.) is only 10% less than that of the zinc atom (65 a.m.u.), it is the latter possibility that is apparently realized in our case as a result of a change in the impurity charge. The impurity atom begins to vibrate with a frequency higher than the phonon frequencies. This change should be expected to occur whenever the impurity center undergoes photoionization. There is no evidence, however, that a high-frequency local mode does form in the ZnSe : Ni, ZnO : Ni, CdS : Ni, and ZnS : Ni systems. At any rate, such a mode was not detected in the electroabsorption spectra of these materials. The frequencies of the strongest vibrational replicas in the region of first-order processes are either in resonance with the lattice vibrations or are very close to the upper edge of the lattice vibrational spectrum [5].

Let us discuss possible reasons for the increased interaction of a charged impurity center with ions of its nearest environment in ZnTe : Ni as compared to other II–VI materials, as well as what might cause the radical difference between the impurity vibrational states. One of these reasons lies in the different character of ionic–covalent bonding in ZnTe : Ni, ZnS : Ni, and ZnSe : Ni, as well as in the fact that the charge density in the materials of the given composition is distributed differently. The bond ionicity is characterized by the polarity of the ionic–covalent bonds, i.e., by the shift of the bound charge toward the anions. Polar contributions to electronic bonds directly affect the lattice dynamics. The bond polarity is characterized by the Phillips–Van-Vechten or Pauling scales [21]. For instance, for ZnSe, the polarity is 0.676 on the Phillips–Van-Vechten scale and 0.57 on the Pauling scale; for ZnTe, these polarities are 0.546 and 0.53, respectively. It appears, however,

practically impossible to analyze these quantities. The electronic density distribution among the ions of Groups II and VI is more revealing and analyzable. A calculation made in local density approximation (LDA) suggests that, as the mass ratio of atoms of Groups VI and II in the II–VI semiconductors decreases, bound charges are shifted toward the Group VI atoms [22]. The charge density distributions of valence band electrons in the (110) plane of ZnTe and ZnSe around the selenium and tellurium ions calculated within the LDA [22] were shown to differ substantially. The polarity of the Zn–Se chemical bonding is higher than that of the Zn–Te bond; hence, the character of bonding in ZnSe is more ionic than that in ZnTe. The position of the bound charge between ions of Groups II and VI is characterized by the distance of this charge to the ions. For ZnTe, the ratio r_{Zn}/r_{Te} is slightly above 2, and for ZnSe, $r_{Zn}/r_{Se} \approx 13:3$, which indicates ZnTe to be more covalent than ZnSe [21].

What is important for us, however, is the charge density distribution not only for the Zn–Te and Zn–Se atoms but also for the Ni–Se and Ni–Te pairs. Nickel donates probably as many electrons for the formation of chemical bonds as zinc does in the ZnTe : Ni and ZnSe : Ni compounds. The nickel 3*d* states, however, can hybridize with the *p* states of the anions, thus providing an additional possibility of electronic density redistribution for the Ni–Se and Ni–Te atoms. This is particularly important for ZnTe : Ni, because it is the *p–d* hybridization that determines the structure of nickel (d^7p) states in the ZnTe band gap. When the charge state of the nickel impurity is changed by interaction with light (i.e., when an electron transfers from the valence band to the impurity), the excess charge can also undergo redistribution through hybridization of the nickel-ion *d* states with the *p* states of the nearest neighbor ions. As a result, the nickel ion may have an effective negative charge smaller in magnitude than the electronic charge. The actual pattern of charge redistribution has yet to be calculated. We start, however, from the assumption that hybridization is stronger, the closer the nickel acceptor level (0/–) is to the valence band top. For ZnSe : Ni, this distance is 1.85 eV, and for ZnTe : Ni, it is 0.95 eV, i.e., approximately one half of the former. One can see now why the excess charge on an impurity center in ZnTe : Ni should be smaller than that in ZnSe : Ni. Because the ionicity of ZnTe is also smaller than that of ZnSe, the effective negative charge of nickel ions may turn out not large enough to displace tellurium and zinc ions located in two adjacent coordination shells. Thus, because the ionicity of ZnTe : Ni is less than that of other II–VI Ni-doped compounds, the lattice does not suffer noticeable deformation around the impurity center, as is the case with ZnSe : Ni and ZnS : Ni [5]. However, because the nickel ion nevertheless has an excess negative charge, the force constant of the Ni–Te interaction may be expected to increase noticeably, thus increasing the vibrational frequency of the nickel ions. In this way, a local mode forms whose frequency is higher than that of lattice vibrations. The amplitude of this vibration should decay rapidly with distance from the impurity center. The motion of the Ni^+ ion in the $NiTe_4Zn_{12}$ cluster is described by the Γ_5 irreducible representation. Therefore, the local vibration due primarily to Ni motion should have Γ_5 symmetry of group T_d.

There is another possible reason for the formation of a local mode in ZnTe : Ni. As already mentioned, in this compound, *p–d* hybridization can allow a transition to the impurity exciton state described by Eq. (4). This may also enhance the Ni–Te interaction and, hence, contribute to the formation of the local mode, as in the case of the appearance of a resonance vibration driven by soft local fluctuations of electronic density in a mixed-valence crystal [23].

One could expect the formation of local vibrations in ZnSe : Ni as well, because the charge of selenium ions and the excess charge of nickel ions are larger than those for ZnTe : Ni. However, the stronger interaction of the nickel ion with ions of its nearest environment in ZnSe : Ni brings about displacement of the latter ions to new equilibrium positions. As a result, the expansions of the potential energy of the nearest neighbor ions displaced from their equilibrium positions will contain, besides the harmonic force constant, anharmonic coefficients k_3 and k_4 of the third- and fourth-power terms:

$$U(x) = U_0 + k_x x^2 + k_3 x^3 + k_4 x^4. \qquad (8)$$

Due to the negative anharmonic constants k_3 and/or k_4, the vibration frequency of the ions displaced to new equilibrium positions can change to an extent where they may fall in resonance with lattice phonons. It is this situation that is apparently observed in the interaction of a nickel acceptor-like exciton with lattice vibrations in ZnSe : Ni, ZnO : Ni, CdS : Ni, and ZnS : Ni [5].

The local vibration in ZnTe : Ni has a large width, which is seen clearly from Fig. 3. The difference $E_{min} - E_{max}$ is 28 meV; following Eq. (6), the width of the corresponding line in the absorption spectrum should be 48 meV, which exceeds the zero-phonon line width by 16 meV. Note for comparison that broad vibrational replicas were observed for the Ni donorlike exciton in ZnS [24] and for combined vibrational replicas with a large *n* for the Ni AE in ZnO : Ni [25]. Several factors may cause additional broadening of local vibration lines. First, vibronic states can decay into a photoionization continuum. Second, the broadening can originate from the vibration anharmonicity. A local mode can decay into lattice phonons through the anharmonic third- or fourth-power terms in the expansion in host atom displacements [26]. Anharmonicity can also allow the local vibration to couple with phonons, thus giving rise to the appearance of its low- and high-frequency satellites in the absorption spectrum. This interaction with phonons may take place over a broad frequency range, thus broadening the absorption lines consider-

ably. In our case, at 4.2 K, the lattice anharmonicity is very small and we believe the broadening of the local vibration lines in the electroabsorption spectrum to originate from the anharmonicity of the vibration itself. This anharmonicity may cause the amplitudes of the vibrational replicas to deviate from the Poisson distribution (7). The peaks of the first replica exceed those of the zero-phonon line by a factor of 2.2. This means that the second vibrational replica, in accordance with Eq. (7), should be the strongest and all peaks with larger numbers n should decrease rapidly with increasing n. In a real spectrum, the peaks of all vibrational replicas are approximately equal in amplitude. A deviation from the Poisson distribution has also been observed for peaks of the combined vibrational replicas in ZnO : Ni [25], ZnSe : Ni and CdS : Ni [5], which was assigned to the anharmonicity of lattice vibrations induced by the charged nickel impurity. This feature of electroabsorption spectra requires further investigation.

4. CONCLUSIONS

Thus, a field exciton–vibration spectroscopy study revealed the line of the acceptor-like exciton Ni $[d^9h]$ and a series of its vibrational replicas at the edge of the impurity center photoionization band in nickel-doped zinc telluride. The Ni $[d^9h]$ AE line is at the expected position, but its large width requires further analysis. The vibrational replicas of the zero-phonon line are due to the impurity exciton interacting with an anharmonic local mode at 13 ± 1 THz. The formation of a local nickel mode in ZnTe : Ni can be assigned to ZnTe having a lower ionicity than the other wide-band-gap II–VI compound semiconductors and to the d states of nickel ions being strongly hybridized with the p state of the nearest neighbor anions. The local vibration in ZnTe : Ni differs strongly from the impurity-induced vibrations in ZnSe : Ni in that the local vibration originates from the motion of the impurity center under the conditions of increasing force constants, whereas the nickel-induced vibrational states in ZnSe : Ni are resonant and derive primarily from the motion of ions in the first two coordination shells around the impurity center. This suggests that the conditions under which the vibrations in ZnTe : Ni and other II–VI Ni-doped compounds occur are different. This finding may be considered indirect evidence of the lattice around the charged impurity Ni(d^9) in ZnSe : Ni, ZnO : Ni, CdS : Ni, and ZnS : Ni being strained.

ACKNOWLEDGMENTS

The authors are grateful to K.A. Kikoin for discussion of the possible reasons for the formation of a local mode in ZnTe : Ni.

REFERENCES

1. K. A. Kikoin and V. N. Fleurov, *Transition Metal Impurities in Semiconductors: Electronic Structure and Physical Properties* (World Sci., Singapore, 1994).
2. A. V. Krol', N. V. Levichev, A. L. Natadze, and A. I. Ryskin, Fiz. Tverd. Tela (Leningrad) **20** (1), 154 (1978) [Sov. Phys. Solid State **20**, 85 (1978)].
3. R. B. Bylsma, P. M. Bridenbaugh, D. H. Olson, and A. M. Glass, Appl. Phys. Lett. **51** (12), 889 (1987).
4. H. J. von Bardeleben, C. Miesner, J. Monge, *et al.*, Semicond. Sci. Technol. **11** (1), 58 (1996).
5. V. I. Sokolov, N. B. Gruzdev, E. A. Shirokov, and A. N. Kislov, Fiz. Tverd. Tela (St. Petersburg) **44** (1), 33 (2002) [Phys. Solid State **44**, 34 (2002)].
6. V. I. Sokolov and A. T. Lonchakov, Pis'ma Zh. Éksp. Teor. Fiz. **73** (11), 708 (2001) [JETP Lett. **73**, 626 (2001)].
7. V. I. Sokolov, Fiz. Tekh. Poluprovodn. (St. Petersburg) **28** (4), 545 (1994) [Semiconductors **28**, 329 (1994)].
8. Yu. P. Gnatenko and A. I. Zhmurko, Ukr. Fiz. Zh. **29** (8), 1182 (1984).
9. V. I. Sokolov and K. A. Kikoin, *Soviet Science Reviews: Physics*, Ed. by I. M. Khalatnikov (Harwood Academic, London, 1989), Vol. 12, p. 147.
10. V. I. Sokolov, Fiz. Tverd. Tela (Leningrad) **29** (6), 1848 (1987) [Sov. Phys. Solid State **29**, 1061 (1987)].
11. M. J. Caldas, A. Fassio, and A. Zunger, Appl. Phys. Lett. **45** (6), 671 (1984).
12. A. Zunger, Solid State Phys. **39**, 275 (1986).
13. U. Kaufmann, J. Windscheit, and G. Brunthaler, J. Phys. C: Solid State Phys. **17** (34), 6169 (1984).
14. B. Clerjaud, A. Geleneau, F. Gendron, *et al.*, J. Phys. C: Solid State Phys. **17** (21), 3837 (1984).
15. G. Roussos, J. Nagel, and H.-J. Schulz, J. Phys. B: Condens. Matter **53** (1), 95 (1983).
16. H. Lange and E. Gutsche, Phys. Status Solidi **32**, 293 (1969).
17. V. I. Sokolov and V. N. Starovoĭtova, Fiz. Tekh. Poluprovodn. (St. Petersburg) **35** (2), 143 (2001) [Semiconductors **35**, 138 (2001)].
18. Landolt–Börnstein, *Physics of II–VI Semiconductors*, Ed. by O. Madelung (Springer, Berlin, 1982).
19. S. G. Bishop, D. J. Robins, and P. J. Dean, Solid State Commun. **33**, 119 (1980).
20. R. Heitz, A. Hoffman, and I. Broser, Phys. Rev. B **48** (12), 8672 (1993).
21. M. Cohen, Usp. Fiz. Nauk **112**, 711 (1974).
22. V. Wagner, J. J. Liang, R. Kruse, *et al.*, Phys. Status Solidi B **215**, 87 (1999).
23. K. A. Kikoin and A. S. Mishchenko, Zh. Éksp. Teor. Fiz. **104** (5), 3810 (1993) [JETP **77**, 828 (1993)].
24. V. I. Sokolov, T. P. Surkova, M. P. Kulakov, and A. V. Fadeev, Solid State Cummun. **44**, 391 (1982).
25. V. I. Sokolov, E. A. Shirokov, A. N. Kislov, and V. G. Mazurenko, Phys. Status Solidi **221** (1), 553 (2000).
26. A. A. Maradudin, Solid State Phys. **18**, 273 (1966); *Defects and Vibrational Spectrum of Crystals* (Mir, Moscow, 1968), p. 432.

Translated by G. Skrebtsov

Physics of the Solid State, Vol. 45, No. 9, 2003, pp. 1644–1647. Translated from Fizika Tverdogo Tela, Vol. 45, No. 9, 2003, pp. 1566–1568.

SEMICONDUCTORS AND DIELECTRICS

Nonradiative Recombination and Kinetics of Optically Oriented Electrons at the GaAs/AlGaAs Interface

R. I. Dzhioev and K. V. Kavokin

Ioffe Physicotechnical Institute, Russian Academy of Sciences, Politekhnicheskaya ul. 26, St. Petersburg, 194021 Russia

Received February 25, 2003

Abstract—It is shown that optical orientation of electron spins in semiconductors can be used as a basis to develop a high-sensitivity method for measuring the dependence of the lifetime of carriers on their concentration. Experiments performed in a stationary regime on a GaAs/AlGaAs heterostructure at low excitation levels provided insight into the nonradiative recombination of electrons and holes separated by an electric field built into the interface. *© 2003 MAIK "Nauka/Interperiodica".*

1. The heterointerface region plays an important part in the operation of most devices based on semiconductor heterostructures. Note also that the interface is always an integral part of transmission semiconductor photocathodes and strained photocathode structures. The latter are promising for producing flows of photoelectrons with the highest possible spin polarization [1]. A study of polarized photoluminescence (PL) emitted from the region of the ferromagnetic heterointerface in an Ni/GaAs structure offered the possibility of detecting interaction between a thin, a few nanometers thick, ferromagnetic film and optically oriented electrons in a semiconductor [2]. In this connection, it appears of interest to investigate the behavior of spin-oriented electrons in the vicinity of a heterointerface.

Besides some specific information on spin transport [3, 4] essential for potential applications in spintronics, investigation of the electron spin dynamics near a heterointerface can provide valuable insight into the relaxation processes required to boost the efficiency of operation of conventional electronic and optoelectronic devices. This communication reports on our use of the optical orientation technique to study experimentally the effect of the GaAs/AlGaAs interface on the recombination kinetics and spin polarization of electrons. One of the main results obtained in this study is the detection of an efficient nonradiative recombination channel at the interface, which saturates at relatively low pumping levels.

Methods of time-resolved spectroscopy, which provide a unique possibility of measuring recombination rates directly, is widely used in studies of the kinetics of photoexcited carriers in semiconductor structures. On the other hand, illumination of samples with laser pulses of picosecond duration inevitably puts constraints on the potential of this method. The existence of saturating recombination centers should change the carrier lifetime as the luminescence decays. Therefore, the relation connecting the carrier lifetime with their concentration can be established only through extremely laborious calculations [5]. This feature lessens, to a certain extent, the revealing nature of this method and can bring about a loss in measurement accuracy. Second, the high ratio of the laser pulse repetition period to the pulse duration does not permit one to reduce the pulse amplitude to levels achievable in stationary excitation conditions.

Application of the optical orientation of electron spins to measurement of the effective lifetimes of carriers makes it possible to overcome the above limitations. These measurements are based on a comparison of the recombination times and spin relaxation of electrons with the precession period of their average spin in an external magnetic field applied to a sample in the direction perpendicular to that of the average spin. The experiments are conducted in stationary conditions; as a result, the measured lifetimes can be identified with fixed carrier concentrations.

This study deals with the specific features of electron kinetics in the *p*-GaAs layer of a GaAs/AlGaAs heterostructure caused by the presence of the interface. The optical orientation method permitted us to measure lifetimes at the lowest possible excitation levels. The observed dependence of the recombination rate on pumping intensity is accounted for by carrier trapping at deep centers close to the interface. The agreement between the experimental data and calculations based on the Shockley–Read–Hall model [6] allowed determination of the electron and hole recombination velocities at the heterointerface. The relative magnitude of the electron and hole trapping velocities for deep centers is evidence of band bending, which produces a barrier for holes.

1063-7834/03/4509-1644$24.00

2. The experiments were conducted at room temperature on a $GaAs/Al_{0.6}Ga_{0.4}As$ heterostructure. The samples studied were the $GaAs/Al_{0.6}Ga_{0.4}As$/glass inverse structures used in photocathode manufacture [7]. These samples have already been employed in measurements of the diffusion length and lifetime of electrons [8, 9]. This permitted us to determine the recombination rates in the bulk and at the interface separately.

The effective times were found by measuring the degree of polarization ρ of interband recombination radiation under stationary conditions of carrier generation by circularly polarized light. The GaAs layer was pumped through the wide-band AlGaAs window by a Kr^+ laser (λ_{ex} = 752.5 nm). The pump intensity was varied from 10 to 200 mW/cm^2. To improve the signal-to-noise ratio at low pump densities, the laser beam was focused by a cylindrical lens. A circular-polarization analyzer with a photoelastic modulator [10] was combined with a two-channel system to count the right- and left-polarized photons. The accuracy of measurement of the degree of polarization ρ was within 5×10^{-4}. To avoid the influence of electron diffusion from the exciting surface into the bulk of the crystal on ρ, the measurements were carried out in the long-wavelength wing of the photoluminescence line [8], where $\alpha L_e \ll 1$ (α is the absorption coefficient at the measurement wavelength).

If the surface recombination channel is operative, the effective electron lifetime τ_{eff} is given by

$$1/\tau_{eff} = 1/\tau_V + \eta_i/L_e, \quad (1)$$

where τ_V is the electron lifetime in the bulk of the crystal, η_i is the surface recombination velocity (in our case, at the interface), and L_e is the electron diffusion length. The values of τ_{eff} were calculated from the relation describing the PL polarization

$$\rho = 0.25 T_s/\tau_{eff}. \quad (2)$$

Here, $T_s = (\tau_s^{-1} + \tau_{eff}^{-1})^{-1}$ is the electron spin orientation lifetime (τ_s is the spin relaxation time). The time T_s was derived from the PL depolarization by a transverse magnetic field (the Hanle effect). Figure 1 presents normalized depolarization curves for two cases differing in the pump intensity. The curves are seen to coincide, which means that the electron spin orientation lifetime does not depend on the pump intensity ($T_s = 6.5 \times 10^{-1}$ s). This is also corroborated by the observation that the degree of PL polarization is fairly small ($\rho < 0.02$). Indeed, in this case, the times are related through $\tau_s \ll \tau_{eff}$; this means that the electron spin orientation lifetime T_s is dominated by the electron spin relaxation time τ_s, which is independent of pumping intensity. Thus, knowing the PL polarization, one can calculate the effective electron lifetime τ_{eff}.

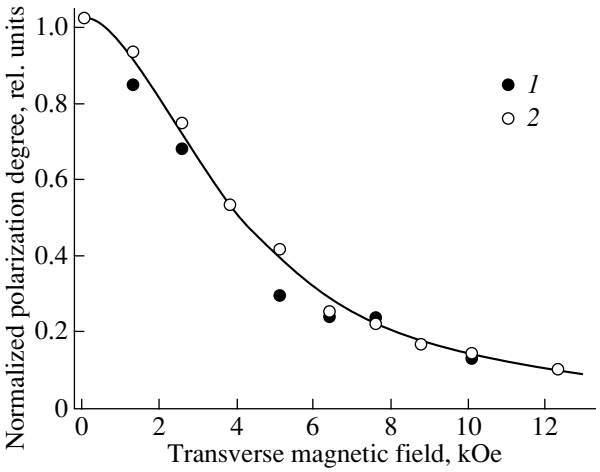

Fig. 1. Circular PL polarization plotted vs. transverse magnetic field (the Hanle effect). The experimental points (circles) were obtained for (*1*) a low pumping level (10 mW/cm^2) and (*2*) a high pumping level (200 mW/cm^2). The solid line is a Lorentzian.

To separate the recombination in the crystal bulk from that at the interface, we studied electron diffusion and the recombination radiation absorption in the crystal. We measured the dependence of ρ on the PL wavelength. The electron diffusion length $L = \sqrt{D\tau_V}$, where D is the electron diffusion coefficient, was determined by the method described in [8]. The experiment showed the value of L to be independent of the pumping intensity ($L \approx 4$ μm). The carrier lifetime in the region adjoining the interface likewise does not depend on the pumping intensity; indeed, it is longer than that in the bulk of the crystal because of the presence of a built-in electric field near the heterointerface. It is this time that should be understood as the parameter τ_V in the problem of nonradiative recombination saturation. Thus, we have $\tau_V = 3.6 \times 10^{-9}$ s [8].

The circles in Fig. 2 specify the experimentally measured pump intensity dependences of the ratio of the bulk carrier lifetime to the effective lifetime at the interface (Fig. 2a) and of the PL intensity (Fig. 2b).

3. Let us turn now to the development of a model describing the dependence of τ_{eff} on pumping intensity. The fluxes of electrons, $\eta_e n(0)$, and of holes, $\eta_h p(0)$, to the surface should be equal. Solving the continuity equation for electrons yields

$$n(z) = \frac{J\tau_{eff}}{L} e^{-z/L}, \quad (3)$$

where J is the pump intensity and z is the coordinate along the interface normal. It thus follows that

$$\eta_h p(0) = \frac{J\eta_e}{L(1/\tau_V + \eta_e/L)}, \quad (4)$$

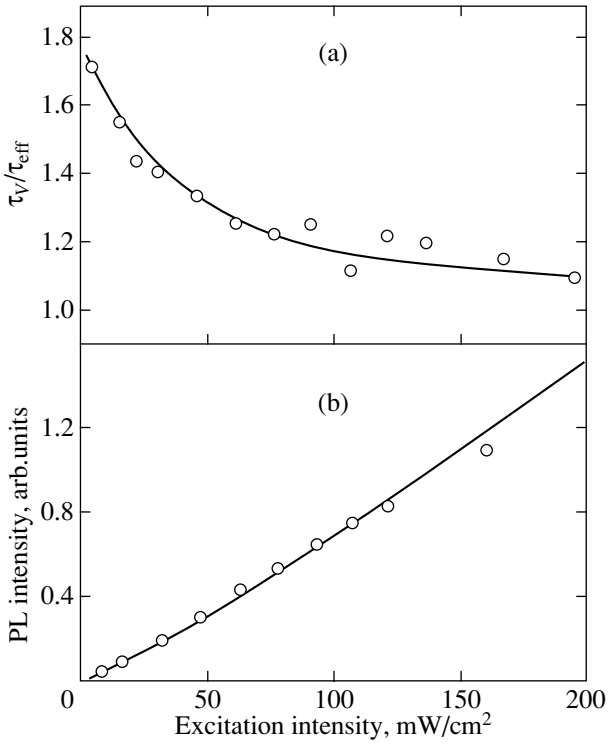

Fig. 2. Pump intensity dependences (a) of the bulk lifetime to effective lifetime ratio (τ_V/τ_{eff}) and (b) of the PL intensity. The solid lines are plots of Eqs. (6) and (3).

where $p(0)$ is the hole concentration at the interface.

To exclude uncertainty in solving Eq. (4), one has to introduce an additional relation connecting η_h and η_e. According to the Shockley–Read–Hall model used here, we have

$$\frac{\eta_h}{r_h} + \frac{\eta_e}{r_e} = 1, \quad (5)$$

where r_h and r_e are the hole and electron trapping velocities, respectively. Condition (5) means that an interface trapping center cannot hold more than one electron or hole simultaneously.

Solving the coupled equations (4) and (5) for τ_{eff}/τ_V yields

$$\tau_{eff}/\tau_V = \frac{1}{2j}[\sqrt{(1+a-j)^2+4aj} - (1+a-j)], \quad (6)$$

where $j = \dfrac{J}{p_0 r_h}$ and $a = \dfrac{L}{\tau_V r_e}$. Figure 2 shows τ_{eff} and the intensity calculated using Eq. (6) together with Eqs. (1)–(3) (solid curves). The best fit to experiment was obtained for the trapping velocities at the interface $r_e = 10^5$ and $r_h = 3 \times 10^{-2}$ cm/s.

Note the large difference between the trapping velocities of the electrons and holes. That the ratio r_e/r_h is six orders of magnitude larger than the figure observed for the GaAs/AlGaAs interface in [11] suggests the existence of a built-in electric field creating a barrier for the holes and a potential well for the electrons. Note that a built-in electric field in such structures was reported to exist in earlier publications as well. This is what accounted for the substantial difference between the relaxation times measured at the interface ($\tau_V = 3.6 \times 10^{-9}$ s, $T_s = 6 \times 10^{-11}$ s) and near a free GaAs surface ($\tau_V = 2.3 \times 10^{-9}$ s, $T_s = 4.4 \times 10^{-11}$ s [8]).

At doping levels of 10^{18} cm^{-3}, the built-in field is screened at distances from the interface much smaller than the diffusion length $L \approx 4$ μm. While Eq. (6) remains valid in these conditions, r_e and r_h have to be multiplied by the corresponding Boltzmann factors f_e and f_h. Disregarding size quantization of the carriers, we obtain

$$f_e/f_h = e^{u/k_B T}, \quad (7)$$

where u is the electrostatic potential at the interface. Thus, a band bending by a few hundred millielectronvolts at room temperature may account for the observed ratio r_e/r_h. No saturation of the nonradiative recombination channel was observed under pumping from the side of the free GaAs surface, because the recombination velocity at the surface is fairly high ($\eta = 7 \times 10^5$ cm/s) and the laser power density was not high enough to saturate the recombination centers. At 77 K, the effect is not observed even at the interface, because at such a temperature the nonradiative recombination centers are obviously occupied.

Thus, measurement of the dynamic parameters determining the nonuniform spin-density distribution of optically oriented electrons permitted us to follow the dependence of the lifetimes on the concentration of photoexcited carriers at the interface of the (Al,Ga)As heterostructure. Room-temperature optical-orientation experiments, conducted in stationary conditions and for low excitation levels, revealed nonradiative recombination of electrons and holes separated by a built-in electric field in the vicinity of the heterointerface.

ACKNOWLEDGMENTS

This study was supported by the Russian Foundation for Basic Research and by the Presidium of the Russian Academy of Sciences, program “Low-Dimensional Quantum-Well Structures.”

REFERENCES

1. H.-J. Drouhin, G. Lampel, Yu. A. Mamaev, *et al.*, in *Proceedings of 7th International Symposium on Physics and Technology, St. Petersburg* (1999), p. 291.
2. R. I. Dzhioev, B. P. Zakharchenya, and V. L. Korenev, Fiz. Tverd. Tela (St. Petersburg) **37** (11), 3510 (1995) [Phys. Solid State **37**, 1929 (1995)].

3. D. Z. Garbuzov, I. A. Merkulov, V. A. Novikov, and V. G. Fleĭsher, Fiz. Tekh. Poluprovodn. **10** (5), 934 (1976) [Sov. Phys. Semicond. **10**, 552 (1976)].

4. D. Hagele, M. Oestreich, W. W. Ruhle, *et al.*, Appl. Phys. Lett. **73** (11), 1580 (1998).

5. G. W.'t Hooft and C. van Opdorp, J. Appl. Phys. **60** (3), 1065 (1986).

6. R. N. Hall, Phys. Rev. **87**, 387 (1952).

7. J. P. Andre, P. Guittard, J. Hallais, and C. Piaget, J. Cryst. Growth **55**, 235 (1981).

8. R. I. Dzhioev, B. P. Zakharchenya, R. R. Ichkitidze, *et al.*, Fiz. Tverd. Tela (St. Petersburg) **35** (10), 2821 (1993) [Phys. Solid State **35**, 1396 (1993)].

9. R. I. Dzhioev and K. V. Kavokin, Fiz. Tverd. Tela (Leningrad) **33** (10), 2928 (1991) [Sov. Phys. Solid State **33**, 1654 (1991)].

10. S. N. Jasperson and S. E. Shnatterly, Rev. Sci. Instrum. **40**, 761 (1969).

11. R. K. Ahrenkiel, B. M. Keyes, and D. J. Dunlavy, J. Appl. Phys. **70**, 225 (1991).

Translated by G. Skrebtsov

Physics of the Solid State, Vol. 45, No. 9, 2003, pp. 1648–1654. Translated from Fizika Tverdogo Tela, Vol. 45, No. 9, 2003, pp. 1569–1575.

SEMICONDUCTORS AND DIELECTRICS

Electrical Properties of the $LaLi_{0.1}M_{0.1}Fe_{0.8}O_{3-\delta}$ Solid Solutions (M = Mn, Fe, Co, Ni)

S. I. Vecherskiĭ, N. N. Batalov, N. O. Esina, and G. Sh. Shekhtman

Institute of High-Temperature Electrochemistry, Ural Division, Russian Academy of Sciences, ul. S. Kovalevskoĭ 20, Yekaterinburg, 620219 Russia

e-mail: batalov@ihim.uran.ru

Received November 20, 2002; in final form, February 27, 2003

Abstract—The electrical conductivity (in the range 77–1073 K) and Seebeck coefficient (300–1073 K) of the $LaLi_{0.1}M_{0.1}Fe_{0.8}O_{3-\delta}$ solid solutions, where M = Mn, Fe, Co, and Ni and $\delta \geq 0$, were studied. It was established that these solid solutions are *p*-type semiconductors and that their electrical conductivity increases with increasing atomic number of the element M. The results obtained are interpreted in terms of the small-radius polaron hopping model. © *2003 MAIK "Nauka/Interperiodica".*

1. INTRODUCTION

Perovskite-like solid solutions and compounds with the general formula $La_{1-x}B_xM_{1-y}M'_yO_{3-\delta}$, where B stands for the alkaline-earth metal and M and M' stand for Mn, Fe, Co, or Ni, $\delta \geq 0$, have been attracting research interest because their structure, degree of oxidation of the transition metal ions, and the content of oxygen vacancies; as a consequence, the electrical and magnetic properties depend substantially on the species and concentration of the substituting atoms (B, M'), as well as on external factors (temperature, pressure, atmosphere) [1–8]. Particular interest is focused on the effect of giant magnetoresistance found to exist in partially substituted lanthanum manganites [1–3] and on the insulator (or semiconductor)–metal transitions in the $La_{1-x}B_xMO_3$ and $LaNi_xM_{1-x}O_3$ (M = Mn, Fe, Co) [3–8] systems. An increase in x in these systems brings about an increase in the conductivity and, eventually, a change in its type. This is accompanied, as a rule, by a change in the magnetic properties. Interestingly, metallic conduction sets in after a certain carrier concentration n (derived from Mott's relation $n^{1/3}a_H \approx 0.2$, where a_H is the Bohr radius) has been reached [3, 9].

In the above cases, the carrier concentration is increased either by substituting ions of alkaline-earth metals for La^{3+} or by replacing Mn, Fe, or Co ions by Ni ions. It is common knowledge, however, that a similar result can be attained in transition metal oxides by substituting lithium for the transition metal. $Li_xNi_{1-x}O$ with NaCl-type structure has been best studied in this respect [4, 9]. In addition to other oxides, the complex oxides of lanthanum with K_2NiF_4-type structure arouse particular interest [3, 4, 10, 11].

$LaFeO_3$-based perovskite-like oxides have been attracting considerably less attention (an exception is the report in [12] on the synthesis of stoichiometric $LaLi_{0.5}Fe_{0.5}O_3$ under a high oxygen pressure, 6×10^9 Pa; in this compound, iron ions exist in an extremely high oxidation state, Fe^{5+}). To partially fill this gap, we studied, as a first step, the region of existence and the electrical properties of the $LaLi_xFe_{1-x}O_{3-\delta}$ solid solution synthesized in air at normal pressure [13, 14]. It was established that its region of existence does not exceed $x = 0.1$. All single-phase samples are *p*-type semiconductors. As x is varied from 0 to 0.1, their electrical conductivity increases and the charge neutrality is maintained both through an increased degree of iron ion oxidation ($Fe^{3+} \longrightarrow Fe^{4+}$) and through oxygen vacancy formation ($\delta \geq 0$).

This communication continues the previous studies. It presents the results of an investigation of the electrical properties of $LaLi_{0.1}M_{0.1}Fe_{0.8}O_{3-\delta}$ samples, where M = Mn, Fe, Co, or Ni (samples 1–4, respectively). The purpose of the investigation was to establish the effect of the Mn, Co, and Ni impurity atoms on the electrical properties of the $LaLi_{0.1}Fe_{0.9}O_{3-\delta}$ boundary solid solution ($\delta \approx 0.08$ [13]) and to identify the possible conduction mechanisms operating in the samples prepared. The concentration of substituting atoms was chosen such that their contribution to electrical conductivity was noticeable but the properties of the Fe-containing matrix still could not be neglected. We studied the phase composition and the temperature dependences of the electrical conductivity σ and of the Seebeck coefficient α of the prepared samples.

2. EXPERIMENTAL

The samples were prepared from powders of carbonyl iron, Mn_2O_3, Co_3O_4, NiO, Li_2CO_3, and La_2O_3. The starting components were dissolved in a (1 : 1) water solution of HNO_3, evaporated, and subsequently slowly heated in air to 1023 K to decompose the nitrates

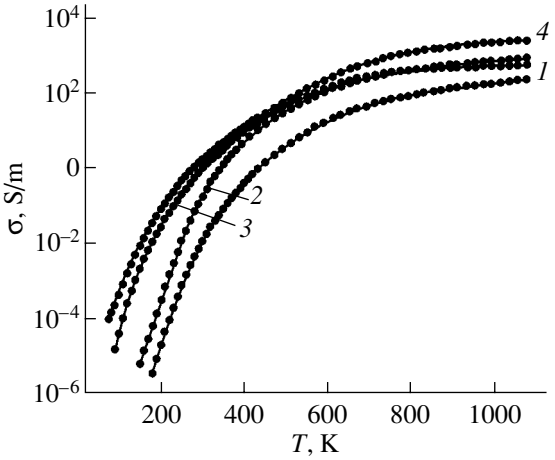

Fig. 1. Temperature dependences of the electrical conductivity of $LaLi_{0.1}M_{0.1}Fe_{0.8}O_{3-\delta}$ samples. M = (*1*) Mn, (*2*) Fe, (*3*) Co, and (*4*) Ni.

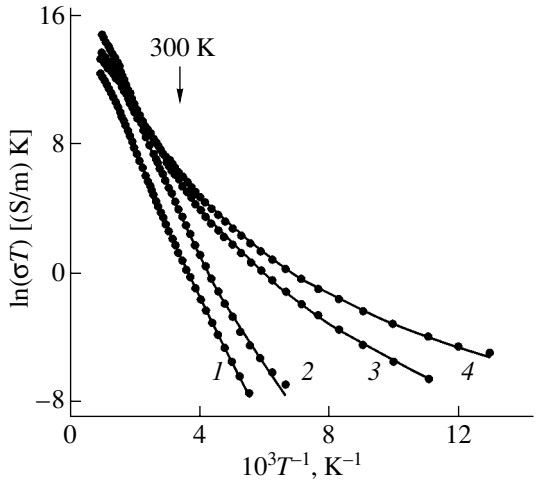

Fig. 2. Temperature dependences of the electrical conductivity of $LaLi_{0.1}M_{0.1}Fe_{0.8}O_{3-\delta}$ samples drawn on semilog paper. M = (*1*) Mn, (*2*) Fe, (*3*) Co, and (*4*) Ni.

formed. The mixtures thus obtained were pelletized and sintered at T = 1373 for 6 h. To reduce lithium losses through evaporation of Li_2O, the synthesis was conducted under a layer having the same composition as the samples being synthesized. To prepare samples for measurement of the electrical conductivity and thermopower, the pellets were ground in a ball mill and the powder thus obtained was pressed to produce parallelepiped-shaped samples, which were then fired over 6 h in the same conditions as in the synthesis.

The x-ray diffraction measurements were conducted on a DRON-3 diffractometer with CuK_α radiation. The porosity of the samples was estimated by comparing their density as determined from x-ray diffraction with the apparent values. Differential thermal (DTA) and thermogravimetric analysis (TGA) of the samples within the temperature range 290–1073 K was carried out in air on a Q-1500D derivatograph at a heating rate of 5 K/min.

The electrical conductivity in the range 77–1073 K was measured in air (by the dc four-probe technique). The correction coefficients to reduce the measured values of electrical conductivity of porous samples σ^{eff} to the conductivity of dense samples σ were calculated from the expression $\sigma = \sigma^{eff}q$. The method employed to calculate the coefficient q is described in [14]. For samples 1 and 2, the values of q were 1.3 and 1.2, respectively. The porosity q of samples 3 and 4 was found to be higher, 1.8 and 1.6, respectively.

The Seebeck coefficient was measured in the range 300–1073 K in air by the standard technique [15]. The temperature was monitored using chromel–alumel thermocouples.

3. EXPERIMENTAL RESULTS

As revealed by x-ray diffraction analysis, the synthesized samples were single-phase and had an orthorhombically distorted perovskite-like crystal lattice. The unit cell parameters of $LaLi_{0.1}Fe_{0.9}O_{3-\delta}$ (sample 2) were found to be a = 0.555, b = 0.557, and c = 0.787 nm. Partial replacement of the iron by Mn, Co, or Ni did not bring about any noticeable changes in them. DTA spectra of the synthesized samples did not exhibit any repeating features indicative of first-order phase transformations (for instance, a change in crystal structure). According to TGA, the relative change in sample weight caused by absorption or release of oxygen in the temperature range covered did not exceed ±0.06%. Samples 2 and 3 absorbed oxygen with increasing the temperature. Samples 1 and 4 released O_2. The corresponding change in δ in samples 1 and 4 was less than ±0.14%.

Figure 1 plots the temperature behavior of the electrical conductivity σ of samples 1–4. For T > 600 K, the electrical conductivity of sample 3 practically coincides with that of sample 2; at lower temperatures, the $\sigma(T)$ graphs diverge. Bearing in mind this comment, we can conclude that, on the whole, electrical conductivity increases with increasing atomic number of the chemical element M.

Figure 2 plots the same relations on semilog paper. Above room temperature, they can be approximated by straight lines, whose slope changes for T > 650 K. The same feature was found to exist in the $\ln(\sigma T)$ vs. T^{-1} relation for $LaFeO_3$ [14] when crossing the Néel temperature (T_N = 750 K [16]). In this case, however, the breaks are observed at lower temperatures. Below room temperature, the $\ln(\sigma T)$ plots for all samples, except sample 2, deviate from a straight-line behavior. For sample 2, the $\ln(\sigma T)$ relation scales as T^{-1} down to T =

Fitting parameters for the temperature dependences of the electrical conductivity and carrier mobility of $LaLi_{0.1}M_{0.1}Fe_{0.8}O_{3-\delta}$ samples (M = Mn, Fe, Co, Ni)

Sample	ΔT, K	E, eV	W, eV	E_0, eV	γ	$f_0 \times 10^{-13}$, Hz
$LaLi_{0.1}Mn_{0.1}Fe_{0.8}O_{3-\delta}$ (no. 1)	180–300	0.43	0.36	0.07	18	0.99
	300–650	0.43	0.36	0.07	–	–
	670–1073	0.34	0.23	0.12	–	–
$LaLi_{0.1}Fe_{0.9}O_{3-\delta}$ (no. 2)	150–200	0.37	0.22	0.15	8	1.3
	200–710	0.37	0.22	0.15	–	–
	770–1073	0.18	0.02	0.15	–	–
$LaLi_{0.1}Co_{0.1}Fe_{0.8}O_{3-\delta}$ (no. 3)	90–300	0.29	0.23	0.06	8	1.4
	300–610	0.29	0.23	0.06	–	–
	630–1073	0.25	0.04	0.18	–	–
$LaLi_{0.1}Ni_{0.1}Fe_{0.8}O_{3-\delta}$ (no. 4)	77–300	0.24	0.20	0.04	7	1.3
	300–430	0.24	0.20	0.04	–	–
	690–1073	0.31	0.19	0.12	–	–

Note: ΔT is a temperature interval.

200 K, with a deviation from the linear law setting in at lower temperatures.

We showed earlier [14] that the electrical conductivity of sample 2 for $T > 200$ K occurs by small-radius polaron (SRP) hopping and can be described, in the adiabatic approximation in various temperature intervals, by the relation [9]

$$\sigma = \frac{A_1}{T}\exp\left(-\frac{E}{kT}\right), \quad (1)$$

where A_1 is a constant coefficient and E is the activation energy for conduction. An analysis showed that, above room temperature, the $\sigma(T)$ relations of the other samples follow Eq. (1). The values of the activation energy E for samples 1–4 are listed in the table for the temperature regions covered.

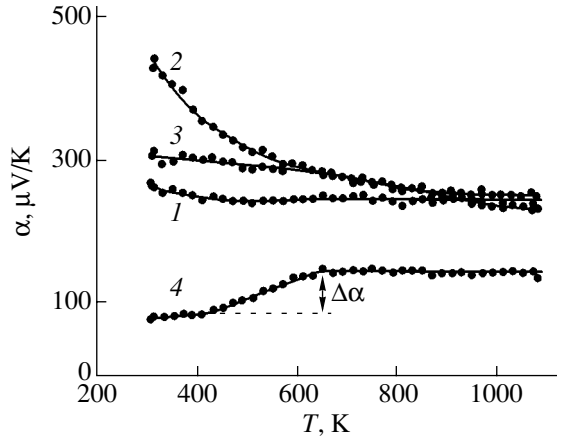

Fig. 3. Temperature dependences of the SC of $LaLi_{0.1}M_{0.1}Fe_{0.8}O_{3-\delta}$ samples. M = (*1*) Mn, (*2*) Fe, (*3*) Co, and (*4*) Ni.

Figure 3 demonstrates the temperature behavior of Seebeck coefficient (SC) for samples 1–4. For all samples, $\alpha > 0$. This indicates a predominance of p conduction. The SC of sample 1 decreases only weakly in the interval 300–500 K, to remain constant thereafter to the end of the interval. The SC of sample 2 falls off monotonically throughout the temperature region studied. The temperature behavior of the SC of sample 3 coincides, for $T > 550$ K, with $\alpha(T)$ of sample 2, while differing from it at lower temperatures. Note that the $\alpha(T)$ relations of samples 1–3 do not have features at higher temperatures, whereas the corresponding $\ln(\sigma T)$ vs. T^{-1} plots exhibit a break (Fig. 2).

The SC of sample 4 increases slowly as the temperature is increased from 300 to 430 K, but in the 430-to 650-K interval, $d\alpha/dT$ grows. For $T > 650$ K, α reaches a constant level one half that for the other samples (about 150 μV/K). The increment of SC $\Delta\alpha$ observed in the 400- to 650-K interval (Fig. 3) is about 60 μV/K. This change in SC is similar to that observed in $LaFeO_3$ near the Néel temperature [14], which we believe also to be due to the sample transferring from the magnetically ordered to paramagnetic state. More specifically, below 430 K, the sample is apparently in an ordered antiferromagnetic state, because it does not have a noticeable macroscopic magnetization characteristic of a ferromagnet. The transition region extends from 430 to 650 K.

In the temperature domain where conduction by SRP hopping can be realized, the SC can be written as [17]

$$\alpha = -\frac{k}{e}\ln\left(\frac{p}{N_V}\right) + C, \quad (2)$$

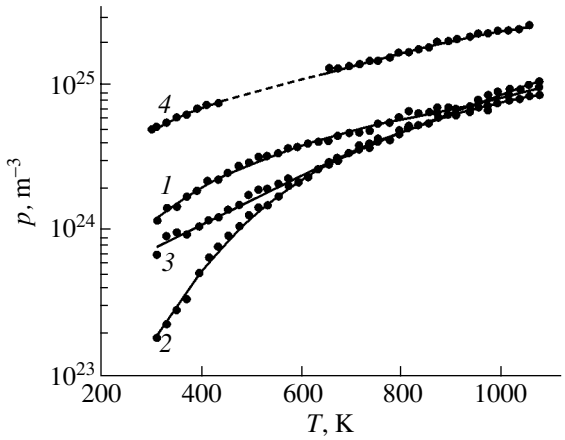

Fig. 4. Temperature dependences of small-radius polaron concentration in $LaLi_{0.1}M_{0.1}Fe_{0.8}O_{3-\delta}$ samples. M = (*1*) Mn, (*2*) Fe, (*3*) Co, and (*4*) Ni.

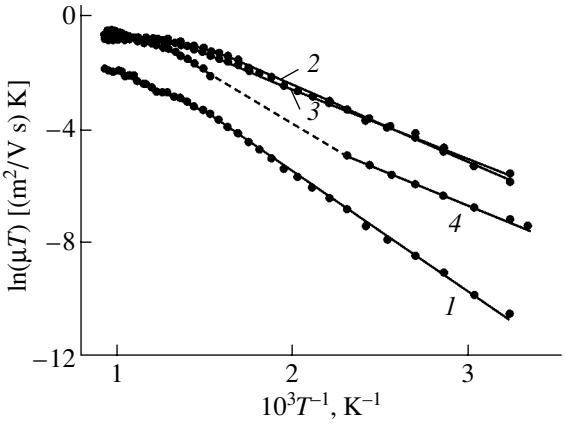

Fig. 5. Mobility of small-radius polarons in $LaLi_{0.1}M_{0.1}Fe_{0.8}O_{3-\delta}$ samples. M = (*1*) Mn, (*2*) Fe, (*3*) Co, and (*4*) Ni.

where $e > 0$ is the electronic charge and p is the concentration of mobile polarons. The constant $C < 10$ μV/K, and it may be neglected [17, 18]. If the SRP formation involves holes, then

$$N_V = 2\left(\frac{2\pi m_h^* kT}{h^2}\right)^{3/2}, \quad (3)$$

where h is the Planck constant and m_h^* is the effective hole mass in an unstrained lattice. By setting m_h^* equal to the free electron mass in Eq. (3) and using Eq. (2), one can estimate the polaron concentration $p = N_V \exp(-e\alpha/k)$.

It should be pointed out that Eq. (3) is valid in the absence of magnetic ordering, where all electronic states are doubly degenerate. Among the samples studied, this condition is satisfied for samples 1–3, whereas sample 4 becomes apparently antiferromagnetic below 650 K. The degeneracy factor was found in [18] to change in this case. In the antiferromagnetic state ($T < T_N$), all magnetic atoms (Fe) become distributed over two magnetic sublattices with oppositely oriented total magnetizations [19]. The atoms on each sublattice are in an effective magnetic field generated at their sites by atoms of the other sublattice. This field can be quite strong. For instance, in $LaFeO_3$ at room temperature, it is 52.2 T [13]. The effective magnetic field lifts the spin degeneracy; therefore, in calculating the carrier concentration in sample 4 below $T = 430$ K, one should replace the factor 2 outside the parentheses in Eq. (3) by unity. In the 430- to 650-K transition region, the effective degeneracy factor varies continuously from 1 to 2.

Figure 4 displays temperature dependences of the SRP concentration p in samples 1–4 measured above room temperature. The dashed line (sample 4) corresponds to the transition region where estimation of p was not performed. These relations can be approximated in various temperature intervals by an exponential,

$$p = p_0 \exp\left(-\frac{E_0}{kT}\right), \quad (4)$$

where p_0 is a constant and E_0 is the activation energy. The values of E_0 are listed in the table.

Because the electrical conductivity σ and the carrier mobility μ are related through [19]

$$\sigma = ep\mu, \quad (5)$$

after estimating the concentration of SRPs, one can calculate their mobility. The temperature dependences of SRP mobility in the 300- to 1073-K interval, which were calculated from the data on the electrical conductivity and Seebeck coefficient, are plotted in Fig. 5.

When conduction occurs by adiabatic SRP hopping, the carrier mobility can be described within a broad temperature range by [9, 17]

$$\mu = \frac{A_2}{T}\exp\left[-2\gamma\tanh\left(\frac{\hbar\omega_0}{4kT}\right)\right]. \quad (6)$$

Here, A_2 is a constant, $\hbar = h/2\pi$, $\gamma = 2W/\hbar\omega_0$ is the electron–phonon coupling constant, $W = (W_p + W_D)/2$ is the activation energy, W_p is the lattice strain energy associated with SRP formation, W_D is the disordering energy, and $\omega_0 = 2\pi f_0$, with f_0 being the optical phonon frequency. Retaining the first-order term in the expansion of tanh for the case of sufficiently high temperatures, we obtain $-W/kT$ for the expression inside the brackets [9]. We used this rough relation to find the activation energy for mobility W above room temperature (see table).

As pointed out earlier, the $\ln(\sigma T)$ vs. T^{-1} plots measured for samples 1–4 deviate from linearity below room temperature. Because σ and μ are related through

Eq. (5), we approximated the temperature dependence of SRP mobility by Eq. (6) and made an attempt at fitting $\sigma(T)$. We assumed that the SRP concentration p below room temperature is described by Eq. (4) and that the activation energies E_0 and W are constant and equal to their values immediately above room temperature. The activation energy for conduction is $E = W + E_0$. The results of the fitting are shown in Fig. 2 (solid lines). They fit the experimental values satisfactorily. The fitting parameters are listed in the table.

4. DISCUSSION OF RESULTS

Our analysis of the temperature dependences of the electrical conductivity and Seebeck coefficient showed that the experimental results obtained in the temperature interval covered can be interpreted in terms of SRP theory by assuming the charge transfer in the samples studied to occur through hole SRP hopping.

Note that mechanism (6), which we used to interpret the temperature behavior of the electrical conductivity of samples below room temperature, is not the only mechanism of conduction which can operate in perovskite-like oxides in the low-temperature domain. For instance, conduction in $La_{0.85}Sr_{0.15}MnO_3$ single crystals was found [20] to be dominated in the region 4.2–130 K by Mott's mechanism [9], namely, $\sigma(T) \sim \exp[-(T_0/T)^{1/4}]$, where T_0 is a characteristic temperature; i.e., conduction occurs by variable-range SRP hopping. The $\sigma(T)$ relations for samples 1–3 below room temperature can also be related to Mott's conduction mechanism, in which T_0 varies from 4×10^8 to 5×10^9 K for different samples. However, the temperature dependence of electrical conductivity of sample 4 plotted in the $\ln(\sigma T)$–$T^{-1/4}$ coordinates deviates from the Mott law below 140 K and σ does not vanish in the limit as $T \longrightarrow 0$. The same relation plotted in other coordinates (Fig. 2) does not exhibit an inflection point below 140 K, and mechanism (6) provides a good fit to the electrical conductivity of samples 1–4 within a broad temperature interval (Fig. 2).

Partial replacement of iron in $LaLi_{0.1}Fe_{0.9}O_{3-\delta}$ (sample 2) by other transition metals noticeably affects the electrical conductivity and Seebeck coefficient of the samples. By and large, this is associated with the variation of both the concentration of SRPs and their mobility (Figs. 4, 5). Above room temperature, the SRP mobility in samples 2 and 3 is practically the same (Fig. 5), but the SRP concentration in sample 3 is higher below 600 K (Fig. 4), as, accordingly, is the electrical conductivity (Fig. 1). For $T > 600$ K, the electrical conductivities of both samples differ very little from each other. In sample 1, the SRP concentration below 800 K is higher than that in the starting sample 2; because of the relatively low SRP mobility, however, σ of sample 1 is lower than that of sample 2 throughout the temperature region covered. We note that the electron–phonon coupling constants γ and the activation energies W in sample 1 are anomalously high as compared to those in the other samples (see table). This is possibly due to the disordering energy W_D increasing in the presence of the Mn^{3+} Jahn–Teller ions. While in sample 4 the SRP mobility below 700 K is lower than that in sample 2, this is compensated by the high SRP concentration. Therefore, the electrical conductivity of sample 4 is higher.

On the other hand, analysis of the data given in the table shows that only in sample 2 is the activation energy E_0 constant throughout the temperature interval studied. In the other samples, it grows substantially in the high-temperature domain. To understand the nature of the appearance of a nonzero activation energy E_0 and the reason for its change in the samples under study, we turn now to the spectrum of electronic states in $LaFeO_3$.

This spectrum was earlier believed to be similar to those of $LaCrO_3$ and $LaMnO_3$ [16, 21]. According to [21], a completely filled narrow band (π^* band) deriving from the hybridized t_{2g} orbitals of the transition metal and the $2p$ orbitals of oxygen lies in the gap between the valence and conduction bands of these oxides near the valence band top. Between the π^* band and the conduction band lie localized levels, which derive primarily from the d orbitals of the transition metal. In stoichiometric $LaFeO_3$, all $t_{2g\uparrow}^3$ and $e_{g\uparrow}^2$ levels (the arrow specifies the spin direction) are occupied at $T = 0$, while the $t_{2g\downarrow}^3$ and $e_{g\downarrow}^2$ levels are free, thus making this compound an insulator. At a high enough temperature, part of the electrons populating the upper occupied $e_{g\uparrow}^2$ level transfer to the nearest unoccupied localized $t_{2g\downarrow}^3$ levels. The activation energy $E_0 \approx E_g/2$, where E_g is the energy gap separating these levels. The appearance of a hole in the $e_{g\uparrow}^2$ level brings about deformation of the ion core and SRP formation. Charge transport occurs by SRP hopping between the nearest localized states.

Replacement of La or Fe by ions of lower valence states gives rise to the formation of Fe^{4+} ions [13, 22], which have the same electron configuration as Mn^{3+}, so that there are free $e_{g\uparrow}^2$ levels even at $T = 0$; their number grows with increasing temperature. Therefore, the electrical conductivity of partially substituted samples increases compared to that of $LaFeO_3$.

This model is capable of predicting the type of carriers and of explaining their transport mechanism. Later calculations made with due account of the Jahn–Teller effect [23] showed that this model indeed reproduces the energy spectrum of $LaMnO_3$ in its main details. It is invalid, however, for $LaFeO_3$. The fact is that, according to x-ray absorption measurements, the energy difference E_g between the occupied $e_{g\uparrow}^2$ levels and their

nearest neighbor free $t_{2g\downarrow}^3$ levels is 2.8–3.0 eV [24], which by far exceeds the values of $E_g \approx 2E_0$ calculated from the electrical characteristics of the samples. The same situation applies to $LaCoO_3$ in the semiconductor phase [25]. A new electronic density-of-states model for $LaCoO_3$ in this phase was proposed in [25]. It differs from the above model in that the fully occupied $t_{2g\uparrow}^3$ and $e_{g\uparrow}^2$ levels overlap the valence band and the singly occupied localized $t_{2g\downarrow}^3$ levels (the Co^{3+} ions in $LaCoO_3$ have $3d^6$ electronic configuration [25]) and the free $e_{g\downarrow}^2$ levels lie, as before, in the energy region separating the π^* from the conduction band. The lower lying $t_{2g\downarrow}^3$ levels are separated from the π^* band by a gap $E_g \approx 0.05$–0.08 eV [25]. According to this model, when electrons are excited into the $t_{2g\downarrow}^3$ levels, holes form in the narrow π^* band rather than in the $e_{g\uparrow}^2$ levels. The mechanism of charge transport is the same as described before.

Ab initio calculations of the density of states in $LaFeO_3$ can be found in [23]. They show the above model to be applicable to this oxide too. We used it to interpret the electrical conductivity data for $LaLi_xFe_{1-x}O_{3-\delta}$ samples [14]. It is apparently also valid for interpretation of the electrical conductivity of $LaLi_{0.1}M_{0.1}Fe_{0.8}O_{3-\delta}$.

This model clarifies the meaning of the quantity N_V defined by Eq. (3). This is the number of electronic states in the π^* band at a distance of kT from its top.

On the other hand, we believe that the energy E_0 = 0.15 eV found for sample 2 (see table), which remains constant throughout the temperature range covered, is the energy required to transfer electrons from the π^* band to its nearest neighbor unoccupied $t_{2g\downarrow}^3$ levels, i.e., the band gap $E_g \approx 0.3$ eV. In the other samples, E_0 varies. Partial replacement of iron ions in $LaLi_{0.1}Fe_{0.9}O_{3-\delta}$ by ions of other transition metals apparently brings about the formation of additional acceptor levels in the gap between the π^* band and the $t_{2g\downarrow}^3$ levels of the starting sample. As the temperature increases, the first to fill are the low-lying acceptor levels, with the $t_{2g\downarrow}^3$ states starting to fill only at higher temperatures.

This is one of the reasons for the appearance of the break in the temperature dependences of the electrical conductivity of samples 1–4 at high temperatures (Fig. 2). In this region, however, the mobility activation energy W also varies (see table). The Mössbauer study we performed earlier on sample 2 [13] showed that part of the Fe^{3+} ions in it reside at room temperature in the antiferromagnetic state, while the other part of Fe^{3+}, as well as the Fe^{4+} ions that formed in the partial substitution of lithium for iron, are in the paramagnetic state. Thus, sample 2 apparently contains both antiferromagnetic and paramagnetic regions and has a microdomain structure. Because the $\alpha(T)$ relation does not exhibit clearly pronounced features associated with antiferromagnetic ordering, it may be expected that at low temperatures charge transport occurs in it primarily over the paramagnetic regions containing the Fe^{3+} and Fe^{4+} ions. Nevertheless, the antiferromagnetic regions affect the electrical conductivity of the sample to a certain extent and the change in the activation energy W in the interval 710–770 K (see table) reflects their destruction.

It may be conjectured that the decrease in W in samples 1 and 3 is accounted for by the same factors. By contrast, the presence of nickel (sample 4) apparently favors the onset of magnetic order in the sample below T_N. This accounts for the features in the $\sigma(T)$ and $\alpha(T)$ relations observed in the 430- to 650-K interval (Figs. 2, 3).

ACKNOWLEDGMENTS

This study was supported by the Russian Foundation for Basic Research, project no. 01-03-96435.

REFERENCES

1. E. I. Nikulin, V. M. Egorov, Yu. M. Baĭkov, *et al.*, Fiz. Tverd. Tela (St. Petersburg) **44** (5), 881 (2002) [Phys. Solid State **44**, 920 (2002)].
2. E. S. Itskevich and V. F. Kraĭdenov, Fiz. Tverd. Tela (St. Petersburg) **43** (7), 1220 (2001) [Phys. Solid State **43**, 1267 (2001)].
3. C. N. R. Rao, J. Mater. Chem. **9**, 1 (1999).
4. C. N. R. Rao and J. Gopalakrishnan, *New Directions in Solid State Chemistry: Structure, Synthesis, Properties, Reactivity and Materials Design* (Cambridge Univ. Press, Cambridge, 1986; Nauka, Novosibirsk, 1990).
5. N. N. Loshkareva, A. V. Korolev, T. I. Arbuzova, *et al.*, Fiz. Tverd. Tela (St. Petersburg) **44** (10), 1827 (2002) [Phys. Solid State **44**, 1916 (2002)].
6. T. Maeder and J. G. Bednorz, J. Eur. Ceram. Soc. **19**, 1507 (1999).
7. L. A. Leonidov, V. L. Kozhevnikov, M. V. Patrakeev, *et al.*, Solid State Ionics **144**, 361 (2001).
8. A. N. Vlasov and O. O. Butorina, Fiz. Tverd. Tela (St. Petersburg) **34** (5), 1350 (1992) [Sov. Phys. Solid State **34**, 718 (1992)].
9. N. F. Mott and E. A. Davis, *Electron Processes in Non-Crystalline Materials* (Clarendon Press, Oxford, 1979; Mir, Moscow, 1982), Vol. 1.
10. Z. Hu, C. Grazioli, M. Knupfer, *et al.*, J. Alloys. Compd. **343**, 5 (2002).
11. G. Demazeau, M. Pouchard, N. Chevreau, *et al.*, Mater. Res. Bull. **16**, 689 (1981).
12. G. Demazeau, B. Buffat, M. Pouchard, and P. Hagenmuller, J. Solid State Chem. **45**, 88 (1982).
13. S. I. Vecherskiĭ, N. N. Batalov, V. A. Shabashov, and G. Sh. Shekhtman, Zh. Neorg. Khim. **44** (10), 1682 (1999).

14. S. I. Vecherskiĭ and N. N. Batalov, Zh. Neorg. Khim. **45** (9), 1525 (2000).
15. L. I. Anatychuk, *Thermal Converters and Thermoelectric Devices: Handbook* (Naukova Dumka, Kiev, 1979).
16. G. V. S. Rao, B. M. Wanklyn, and C. N. R. Rao, J. Phys. Chem. Solids **32** (2), 345 (1971).
17. D. Appel', in *Polarons*, Ed. by Yu. A. Firsov (Nauka, Moscow, 1975), p. 13.
18. S. R. Sehlin, H. U. Anderson, and D. M. Sparlin, Phys. Rev. B **52** (16), 11681 (1995).
19. J. M. Ziman, *Principles of the Theory of Solids*, 2nd ed. (Cambridge Univ. Press, Cambridge, 1972; Mir, Moscow, 1974).
20. É. A. Neĭfel'd, V. E. Arkhipov, N. A. Tumalevich, and Ya. M. Mukovskiĭ, Pis'ma Zh. Éksp. Teor. Fiz. **74** (11), 630 (2001) [JETP Lett. **74**, 556 (2001)].
21. J. B. Goodenough, J. Appl. Phys. **37** (3), 1415 (1966).
22. W. H. Jung and E. Iguchi, J. Phys.: Condens. Matter **7**, 1215 (1995).
23. P. Mahadevan, N. Shanthi, and D. D. Sarma, J. Phys.: Condens. Matter **9**, 3129 (1997).
24. M. Abbate, F. M. F. de Groot, J. C. Fuggle, *et al.*, Phys. Rev. B **46** (8), 4511 (1992).
25. M. A. Senaris-Rodríguez and J. B. Goodenough, J. Solid State Chem. **16**, 224 (1995).

Translated by G. Skrebtsov

Physics of the Solid State, Vol. 45, No. 9, 2003, pp. 1655–1657. Translated from Fizika Tverdogo Tela, Vol. 45, No. 9, 2003, pp. 1576–1578.

SEMICONDUCTORS AND DIELECTRICS

Profiles of Transmutation-Produced Isotopes in Proton- and Helium-Irradiated Germanium

V. A. Didik*, V. V. Kozlovskiĭ, R. Sh. Malkovich*, and E. A. Skoryatina***

**Ioffe Physicotechnical Institute, Russian Academy of Sciences, Politekhnicheskaya ul. 26, St. Petersburg, 194021 Russia*
e-mail: malkovich@mail.ioffe.ru
***St. Petersburg State Polytechnical University, Politekhnicheskaya ul. 25, St. Petersburg, 195251 Russia*
e-mail: kozlovski@tuexph.stu.neva.ru

Received February 27, 2003

Abstract—Profiles of radioactive isotopes produced in nuclear reactions in germanium irradiated by protons or ^{4}He nuclei were studied. The profiles were used to determine the energy dependence of the cross sections of nuclear reactions producing transmutation isotopes. *© 2003 MAIK "Nauka/Interperiodica".*

We report on a study of the profiles of isotopes produced in germanium under irradiation by protons or ^{4}He nuclei, as well as on an analysis of these profiles and their use for establishing the energy dependence of the nuclear-reaction cross sections.

Our earlier study [1] dealt with the profiles of isotopes produced under irradiation by protons, deuterons, and ^{3}He and ^{4}He nuclei in III–V compound semiconductor single crystals (GaAs, GaP, InAs) and $CuInSe_2$, in ceramic materials ($YBa_2Cu_3O_{7-x}$, $PbZr_{0.54}Ti_{0.46}O_3$), and in metallic zirconium.

The samples, shaped as 1-mm-thick plane-parallel plates with an area of ~2 cm^2, were pressed against a water-cooled brass plate and were bombarded by a cyclotron beam through a diaphragm 9 mm in diameter [2]. The incident protons had an energy of 10 MeV; the ^{4}He nuclei, 20 MeV. The beam was monochromatic to within 5%. The particle flux was 6×10^{11} cm^{-2} s^{-1} (current density 0.1 μA/cm^2), the irradiation time was 30 min, and the irradiation dose was ~1×10^{15} cm^{-2}. The profiles of the radioactive transmutation-produced isotopes were determined by successive removal of plane-parallel layers, followed by measurement of their γ-ray activity. Layers 1–5-μm thick when irradiated by ^{4}He nuclei and layers ~10-μm thick for proton bombardment were removed by grinding, and the layer activity was measured using a calibrated γ spectrometer with a Ge(Li) detector. The uniformity of the isotope distribution over the sample cross-sectional area was checked by autoradiography.

Proton bombardment produced a number of isotopes in the matrix; we were interested in the radioactive ^{67}Ga, ^{71}As, ^{72}As, ^{74}As, and ^{76}As isotopes (Fig. 1a) forming in the nuclear reactions ^{70}Ge(p, α)^{67}Ga, ^{70}Ge(p, γ)^{71}As, ^{72}Ge(p, n)^{72}As, ^{73}Ge(p, γ)^{74}As, ^{74}Ge(p, n)^{74}As, and ^{76}Ge(p, n)^{76}As [3]. The isotope concentration accumulated in the above irradiation conditions is ~1×10^{13} cm^{-3} for ^{72}As and ^{74}As and does not exceed 1.5×10^{11} cm^{-3} for the ^{71}As isotope (the concentration refers to the end of irradiation). The penetration depth varies from ~240 μm for ^{67}Ga to ~380 μm for the ^{71}As, ^{74}As, and ^{76}As isotopes. All the profiles follow a nonmonotonic pattern.

From the products of irradiation by ^{4}He nuclei, we studied the radioactive isotopes ^{73}As, ^{73}Se, and ^{75}Se (Fig. 1b) forming in the reactions ^{70}Ge(^{4}He, p)^{73}As, ^{70}Ge(^{4}He, n)^{73}Se, ^{72}Ge(^{4}He, p)^{75}Se, and ^{73}Ge(^{4}He, $2n$)^{75}Se. The concentration of the isotopes studied was as high as ~2×10^{12} cm^{-3}, and the profile depth did not exceed 100 μm.

The profile depth correlates with the particle range; indeed, the profile of the isotopes generated by protons forms at a considerably larger depth than that obtained under irradiation by the ^{4}He nuclei because the range of protons is much larger than that of the ^{4}He nuclei. At the same time, the depth of a profile increases as the threshold of the nuclear reaction producing the given isotope decreases. For instance, the depth is ~280 μm for the ^{72}As isotope for the 5.1-MeV reaction threshold and reaches ~380 μm for the ^{76}As isotope forming in the reaction with a threshold of 1.7 MeV [3].

The profiles of the transmutation-produced isotopes were used by us to establish the energy dependence of the nuclear-reaction cross sections σ(E) associated with the formation of the isotopes of interest [1]. This was done by determining the σ(x) function from the relation [1]

$$c(x) = N\Phi\sigma(x)\lambda^{-1}[1 - \exp(-\lambda\tau)]$$

[where N is the concentration of the stable matrix isotope, Φ is the particle flux, σ is the nuclear-reaction cross section, λ is the isotope decay constant, τ is the

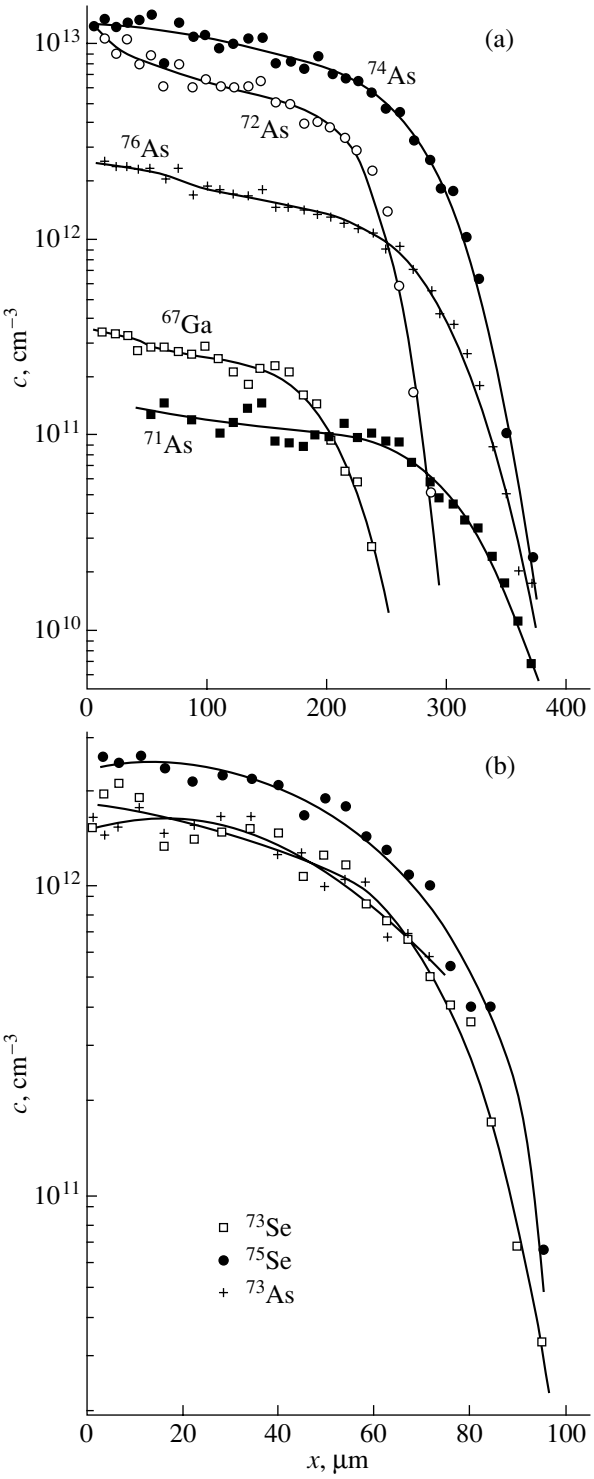

Fig. 1. Profiles of the isotopes forming in germanium under irradiation by (a) protons and (b) ^{4}He nuclei.

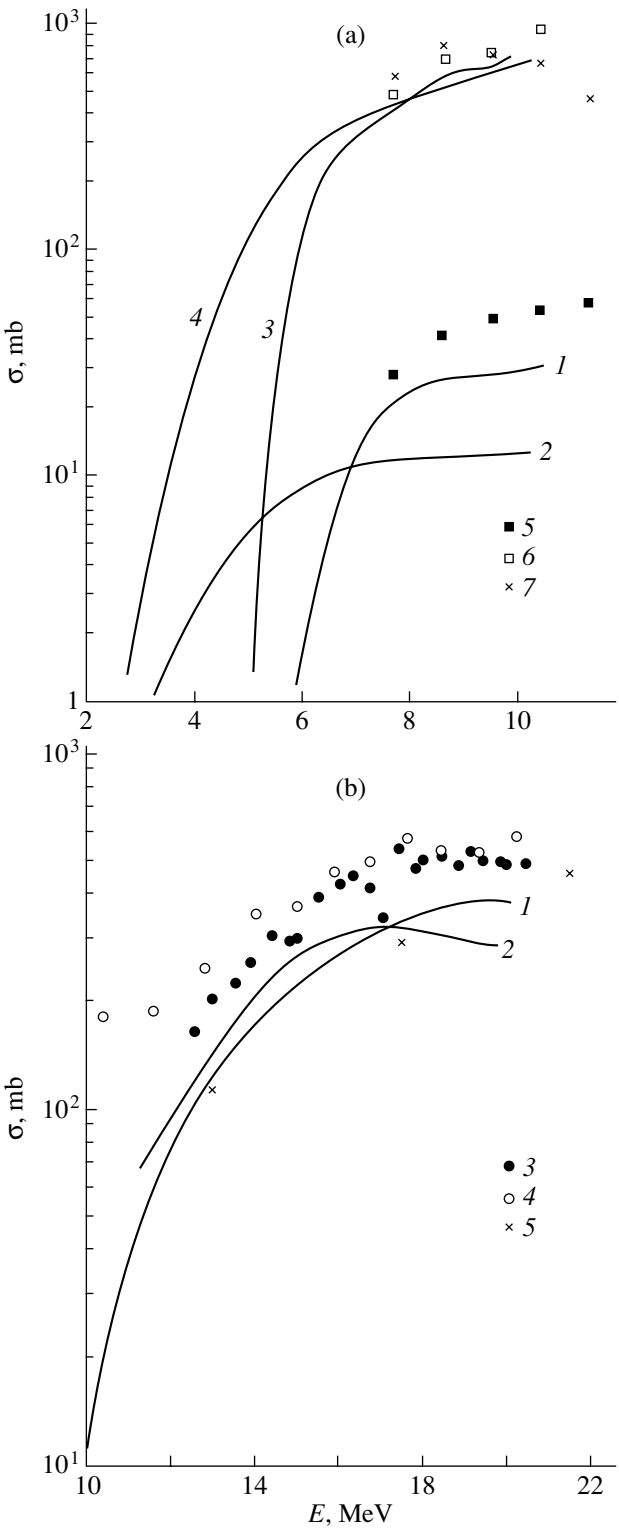

Fig. 2. Nuclear-reaction cross sections plotted vs. the energy of (a) protons and (b) ^{4}He nuclei. (a) (*1*, *5*) ^{70}Ge(*p*, α)^{67}Ga, (*2*) ^{70}Ge(*p*, γ)^{71}As, (*3*, *6*) ^{72}Ge(*p*, *n*)^{72}As, and (*4*, *7*) ^{76}Ge(*p*, *n*)^{76}As; (*1*–*4*) this study and (*5*–*7*) data from [6]. (b) (*1*, *3*–*5*) ^{70}Ge(^{4}He, *n*)^{73}Se and (*2*) ^{70}Ge(^{4}He, *p*)^{73}As; (*1*, *2*) this study, (*3*) [6], (*4*) [7], and (*5*) [8].

irradiation time, and x is the coordinate (distance from the sample surface)], after which the $E(x)$ dependence [4] was employed to find the $\sigma(E)$ relation we were looking for.

This paper reports on the determination of the cross sections of the nuclear reactions ^{70}Ge(p, α)^{67}Ga, ^{70}Ge(p, γ)^{71}As, ^{72}Ge(p, n)^{72}As, and ^{76}Ge(p, n)^{76}As (Fig. 2a), as well as of ^{70}Ge(^{4}He, p)^{73}As and ^{70}Ge(^{4}He, n)^{73}Se (Fig. 2b). Note that the reaction cross sections for the ^{74}As and ^{75}Se isotopes were not determined because these isotopes form simultaneously in two reaction channels, namely, in ^{73}Ge(p, γ)^{74}As and ^{74}Ge(p, n)^{74}As for the former isotope and in ^{72}Ge(^{4}He, p)^{75}Se and ^{73}Ge(^{4}He, 2n)^{75}Se for the latter.

Figure 2 also presents the available literature data on nuclear-reaction cross sections [5–8].

REFERENCES

1. V. A. Didik, R. Sh. Malkovich, E. A. Skoryatina, and V. V. Kozlovski, Nucl. Instrum. Methods Phys. Res. B **160**, 387 (2000).
2. B. P. Zabrodin, L. F. Zakharenkov, and V. V. Kozlovskiĭ, Vopr. At. Nauki Tekh., Ser.: Fiz. Radiats. Povrezhdenii Radiats. Materialoved. **3** (57), 87 (1991).
3. G. Maples, G. Goth, and J. Cerny, Nucl. Data, Sect. A **2**, 429 (1967).
4. O. F. Nemets and Yu. F. Gofman, *Handbook on Nuclear Physics* (Naukova Dumka, Kiev, 1975).
5. I. N. Boboshin, A. V. Varlamov, V. V. Varlamov, *et al.*, in *Proceedings of Second All-Russian Scientific Conference on Scientific Databases on Physics of Atomic Nuclei and Nuclear Reactions, Protvino, Russia* (2000), p. 39.
6. V. N. Levkovskiĭ, *Activation Cross Sections of Moderate-Mass Nuclides (A = 40–100) by Moderate-Energy Protons and Alpha Particles (E = 10–50 MeV)* (Inter-Vesy, Moscow, 1991).
7. A. Calboreanu, O. Salagean, C. Pencea, *et al.*, Rev. Roum. Phys. **32**, 725 (1987).
8. M. Guillaume, R. M. Lambrecht, and A. P. Wolf, Int. J. Appl. Radiat. Isot. **29**, 411 (1978).

Translated by G. Skrebtsov

Physics of the Solid State, Vol. 45, No. 9, 2003, pp. 1658–1668. Translated from Fizika Tverdogo Tela, Vol. 45, No. 9, 2003, pp. 1579–1589.

SEMICONDUCTORS AND DIELECTRICS

One-Phonon Raman Spectra of Carbon in Composite Films Prepared by Modification of Amorphous Hydrogenated Carbon by Copper and Cobalt

É. A. Smorgonskaya, T. K. Zvonareva, E. I. Ivanova, I. I. Novak, and V. I. Ivanov-Omskiĭ

Ioffe Physicotechnical Institute, Russian Academy of Sciences, Politekhnicheskaya ul. 26, St. Petersburg, 194021 Russia

Received December 11, 2002

Abstract—One-phonon visible-range Raman spectra of *a*-C : H⟨Cu⟩ and *a*-C : H⟨Co⟩ composite films with comparable metal and carbon contents were studied in the frequency region 1200–1700 cm^{-1} including the carbon sp^2-bond vibrations. Broad bands *G* and *D* characteristic of unmodified *a*-C : H films, as well as some additional features, are observed experimentally in the spectra. By unfolding the spectra into Gaussian components, it was possible to follow the variation of Raman shifts and of contributions of individual components to the spectrum as a function of metal content and thermal annealing. The data obtained, complemented by available information on carbon sp^2-coordinated systems, show that incorporation of Cu or Co favors growth and ordering of graphite-like nanoclusters in *a*-C : H, the effect being substantially stronger in the case of Co. It is shown that the process of metal-stimulated graphitization includes carbon bond breaking with the formation of short chainlike fragments and their linkage with the formation of aromatic-ring nanoclusters. A qualitatively similar sp^2-structure rearrangement takes place under thermal annealing. For the Cu and Co concentrations studied, the linear dimensions L_a of graphite-like clusters are estimated to vary from ~0.8 nm in unannealed *a*-C : H to ~1.0 and ~1.2 nm in annealed *a*-C : H⟨Cu⟩ and *a*-C : H⟨Co⟩, respectively. The number of aromatic rings in these clusters is approximately estimated to increase from 12 to 16 (for Cu) and 20 (for Co). © *2003 MAIK "Nauka/Interperiodica".*

1. INTRODUCTION

It is known that, by cosputtering graphite and a metal in a hydrogen environment, one can prepare composite films of amorphous hydrogenated carbon with different contents of the metal, *a*-C : H⟨*Me*⟩ (*Me* = Cu, Co, Mo, Ni) [1–3]. If the metal content is high enough, one may expect the production in such composites of a system of nanosized high-density metallic clusters embedded in a carbon–hydrogen medium *a*-C : H [4, 5]. In this case, *a*-C : H will play the part of a stabilizing matrix, without which a system of free isolated nanoclusters would be thermodynamically and chemically unstable. Such composites may prove promising as materials for nanoelectronics and, in particular, for the development of high-density information recording and storage devices. The potential of *a*-C : H as a matrix is based on the unique capability of carbon atoms to form valence bonds with differently hybridized outer shell electrons, from sp^1- to sp^2- and sp^3-type, and to form clusters of atoms with the same type of hybridization. As a result, *a*-C : H can support the coexistence of differently coordinated structural fragments, namely, chain-, planelike, and bent graphene- or diamond-like fragments [6, 7], while the incorporation of foreign inclusions provides the possibility of accommodating to them the surrounding carbon structures of short- and so-called medium-range order. This property makes it possible, for instance, to encapsulate metallic nanoclusters into a carbon shell using the arc discharge technology [8, 9].

To optimize the technology and to use to advantage composite *a*-C : H-based films with embedded metal nanoclusters, one has to know how the incorporation of a metal affects the structural organization of the carbon–hydrogen matrix. This communication reports on a study of this problem conducted on *a*-C : H⟨Cu⟩ and *a*-C : H⟨Co⟩ films using visible-range Raman spectroscopy in the region of one-phonon carbon bands. Because, unlike copper, cobalt easily reacts chemically with carbon to form the metastable carbide Co_2C, it appeared appropriate to compare the effect of these metals on the matrix structure at different concentrations, as well as for various heat treatments. The *a*-C : H⟨Co⟩ films are of particular interest in connection with the magnetic properties of the Co impurity.

Being a highly informative nondestructive method, Raman spectroscopy is widely used in studies of the structure of various carbon materials, including *a*-C : H amorphous films. Whereas one-phonon Raman spectra of perfect graphite single crystals exhibit only one, well-known narrow line *G* at 1581 cm^{-1}, *a*-C : H reveals, as a rule, two very broad, overlapping bands peaking in the regions 1540–1560 and 1340–1370 cm^{-1} (the so-called *G* and *D* bands [10–12]), which can be identified with the similar, but narrower, bands *G* and *D* in the spectrum of nanocrystalline graphite (*nc*-*G*) [13,

14]. In some cases, the *D* band in the spectra of amorphous films cannot be separated out from the background of the *G* band and appears as a low-frequency shoulder [11, 12]. Comprehensive studies [12] have shown that the positions of both Raman bands, *G* and *D*, in *a*-C : H depend on the exciting wavelength λ_{exc}, while for a given λ_{exc}, the positions of the maxima and the width and relative intensity of the bands depend on the actual technology of film preparation. Raman scattering in the visible region in *a*-C : H is dominated by sp^2-coordinated carbon clusters, because it is for these clusters rather than for the sp^3 fragments that the condition of resonance excitation in electronic transitions between the π and π^* states at the edges of the valence and conduction bands is satisfied [15] and the scattering cross section is maximal. The inhomogeneous broadening of the *G* and *D* bands is related primarily to the size distribution of sp^2 clusters, so that for a given λ_{exc} the maximum contribution to the *G* and *D* bands is due to those of the sp^2 fragments for which the gap between the π and π^* states is equal to the pump photon energy.

The Raman spectra of *a*-C : H⟨Cu⟩ and *a*-C : H⟨Co⟩ composite films with a high and fixed metal content were first reported recently in [16, 17]. Carbon IR absorption spectra of *a*-C : H⟨Cu⟩ and *a*-C : H⟨Co⟩ with different Cu and Co contents were used in [16, 17] to study the interaction of these metals with the *a*-C : H matrix. While earlier measurements [18] showed copper to activate the so-called quasi-Raman band *G* (in the IR spectrum), which is close in position to the *G* band in the Raman spectrum of *a*-C : H and is inactive in the IR spectrum of *a*-C : H, a higher frequency component *GG* close to the graphite *G* line was revealed in the *a*-C : H⟨Cu⟩ IR spectrum for a high Cu concentration in recent studies [16]. This warranted the conclusion that copper favors graphitization of the *a*-C : H matrix. Note that the effect of graphitization in *a*-C : H induced by the incorporation of small additions of molybdenum and nickel was revealed from Raman spectra in [2]. While cobalt was also shown [17] to activate the *G* band in IR absorption, the *GG* component was not isolated in the IR spectrum of *a*-C : H⟨Co⟩, and the pronounced enhancement of other components suggested that cobalt destroys graphite-like fragments in *a*-C : H. By analogy with the case of copper [19], the activation of the quasi-Raman band *G* by cobalt inclusions can be associated with a breaking of the selection rules for IR absorption in graphite-like clusters as they interact with metal atoms.

The present study follows, for a fixed wavelength λ_{exc} = 488 nm, the variations of the parameters of the *D* and *G* bands in carbon Raman spectra initiated by modification of *a*-C : H films by copper and cobalt (for comparable metal and carbon concentrations) as a function of metal content and as a result of thermal annealing of the modified films. A comparison of the results obtained with the available data for *a*-C : H permits certain conclusions on the metal-induced structural changes occurring in the sp^2 subsystem of the carbon–hydrogen matrix of *a*-C : H⟨Cu⟩ and *a*-C : H⟨Co⟩ composite films.

2. PREPARATION OF SAMPLES AND MEASUREMENTS

The *a*-C : H films were prepared by dc magnetron sputtering of a graphite target (cathode) in an argon–hydrogen plasma (80% Ar + 20% H_2). To incorporate copper or cobalt into *a*-C : H, copper or cobalt plates were fixed to the graphite cathode. The concentration of the metal to be inserted was varied by properly varying the area ratio between the metal and graphite target. The films were deposited on (100)-oriented substrates of KDB-20 single-crystal silicon heated to 200°C. The sputtering chamber was preliminarily evacuated to a base pressure of 10^{-6} Torr. The films were deposited in a flow of operating gas at a pressure of 10^{-2} Torr and an ion current density of 0.1 A/cm^2. The film growth rate was 2–7 nm/min. Some of the grown films were thermally annealed in vacuum for 1 h at a temperature T_a = 380°C.

The metal content in the *a*-C : H⟨Cu⟩ and *a*-C : H⟨Co⟩ films was characterized by the metal/carbon atom ratio ([Cu]/[C] and [Co]/[C]), which was derived from the Rutherford backscattering and instantaneous nuclear reaction methods, as in [20]. The measurements were conducted on *a*-C : H⟨Cu⟩ and *a*-C : H⟨Co⟩ samples whose atomic fraction of the metal with respect to carbon before annealing was [Cu]/[C] = 0.62 and 1.00 and [Co]/[C] = 0.35, 0.50, and 0.73.

The Raman scattering intensity from *a*-C : H⟨Cu⟩ and *a*-C : H⟨Co⟩ films, as well as from "pure" *a*-C : H, was measured with a SPEX Ramalog spectrometer under excitation by unpolarized argon-laser radiation at a wavelength λ_{exc} = 488 nm and intensity ~5 W/cm^2. The scattering was measured in the reflection geometry under normal pump-light incidence. All measurements were conducted at room temperature.

3. RESULTS OF MEASUREMENTS

3.1. Experimental Data

Figures 1 and 2 present experimental Raman spectra of modified *a*-C : H⟨Cu⟩ (Fig. 1) and *a*-C : H⟨Co⟩ (Fig. 2) films with different contents of Cu and Co, both before and after annealing. Also shown for comparison are spectra of an unmodified *a*-C : H film taken before and after the annealing. Note that incorporation of the metal substantially increases absorption in the films in the spectral region of interest, which gives rise to a marked decrease not only in the background luminescence level but also in the scattered signal intensity and the signal/noise ratio. Figures 1 and 2 display smoothed spectra after subtraction of the background luminescence intensity.

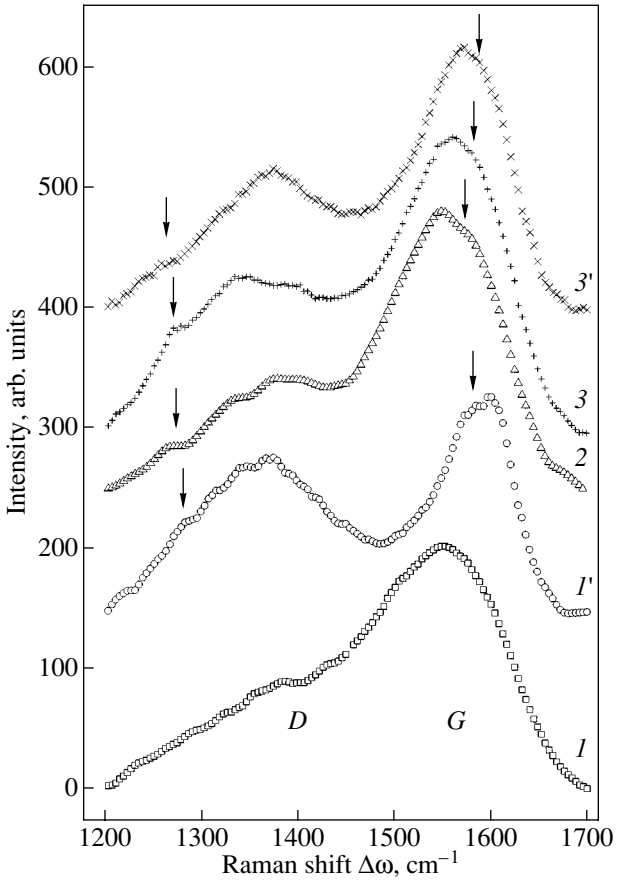

Fig. 1. Raman spectra of (*1*, *1*') *a*-C : H and (*2*, *3*, *3*') *a*-C : H⟨Cu⟩ films with different Cu contents (*1*–*3*) before and (*1*', *3*') after thermal annealing. [Cu]/[C]: (*1*, *1*') 0, (*2*) 0.62, and (*3*, *3*') 1.0.

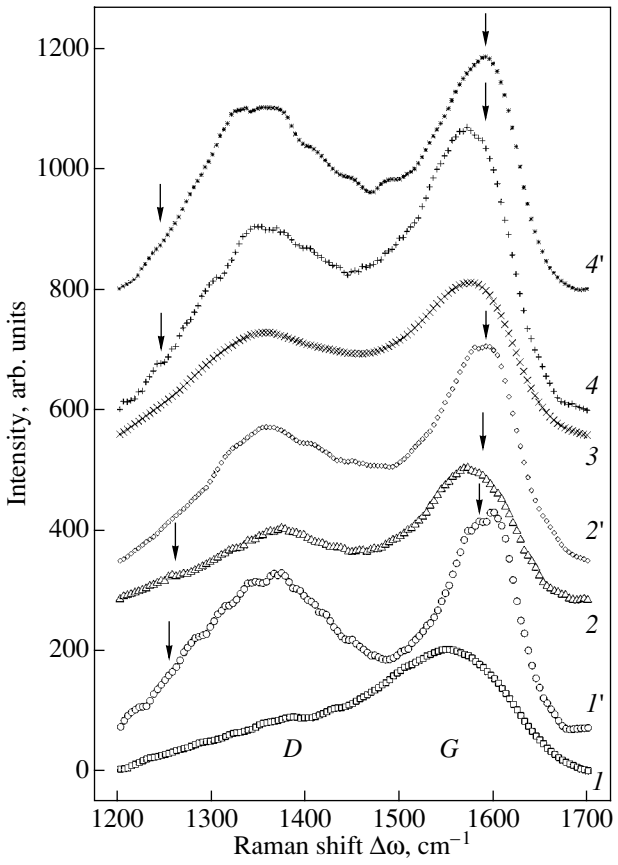

Fig. 2. Raman spectra of (*1*, *1*') *a*-C : H and (*2*, *2*', *3*, *4*, *4*') *a*-C : H⟨Co⟩ films with different Co contents (*1*–*4*) before and (*1*', *2*', *4*') after thermal annealing. [Co]/[C]: (*1*, *1*') 0, (*2*, *2*') 0.35, (*3*) 0.5, and (*4*, *4*') 0.73.

We readily see that incorporation of the metal initiates resolution of the *D* band in the Raman spectrum, with the absolute maximum of this band in unannealed films showing a tendency to shift toward lower frequencies with increasing metal content. The position of the absolute maximum of band *G* in the spectra of unannealed films turns out less sensitive to the metal content. In the case of copper, peak *G* for [Cu]/[C] = 0.62 lies near 1550 cm^{-1}, as in the unmodified *a*-C : H film, and shifts slightly toward higher frequencies (1560 cm^{-1}) only at a higher Cu content ([Cu]/[C] = 1.0). When cobalt is incorporated, peak *G* shifts noticeably toward higher frequencies at a lower Co content. Indeed, for [Co]/[C] = 0.35, the *G* maximum lies near 1570 cm^{-1}. The position of peak *G* in unannealed films, however, practically does not change with increasing Co content.

Annealing always results in a still more pronounced resolution of the *D* peak in the spectrum and a noticeable high-frequency shift of the absolute maximum of band *G*. This effect is observed, irrespective of the metal content, in the *a*-C : H⟨Cu⟩ and *a*-C : H⟨Co⟩ composite films and in pure *a*-C : H. In the latter case, as seen from Figs. 1 and 2, the shift is the largest, ~40 cm^{-1}. The annealing-induced shift of peak *G* in *a*-C : H⟨Co⟩ and *a*-C : H⟨Cu⟩ films is ~20 and ~13 cm^{-1}, respectively.

3.2. Unfolding of Experimental Spectra into Components

The experimental spectra were analyzed by unfolding them into Gaussian constituents. Using the Gaussian profile for individual components appears reasonable, because it describes the inhomogeneous broadening of spectral bands, which is characteristic of disordered structures. Indeed, frequencies contributing to a Raman spectrum of an amorphous structure can be shifted relative to their positions in the ordered counterpart, depending on the random stresses and local distortions of the structural unit involved in these vibrations. By following the behavior of the maximum and of the integrated intensity of a component with variation of the metal content or under annealing, one can establish the main relations governing structural rearrangement for the most representative local configurations. The

simplicity of unfolding into Gaussian profiles proves a valuable asset for revealing the presence of several spectral constituents in structurized spectra. This was demonstrated, in particular, when analyzing IR absorption spectra of *a*-C : H⟨Cu⟩ [16] and *a*-C : H⟨Co⟩ films [17].

The Raman spectra displayed in Figs. 1 and 2 reveal, in some cases, features against the background of the broad *G* and *D* bands; these features are, however, less pronounced than in the IR spectra [16, 17]. In view of the above-mentioned low signal level, only those features were processed that are reproduced in different spectra and, hence, are most likely not due to experimental errors (identified by arrows in Figs. 1, 2). Among such features is the shoulder on the high-frequency wing of band *G* in the spectra of *a*-C : H⟨Cu⟩ (curves *2*, *3*, *3*' in Fig. 1); this feature also manifests itself as a shoulder (curves *2*, *4* in Fig. 2) or as a maximum (curves *2*', *4*' in Fig. 2) in the spectra of *a*-C : H⟨Co⟩ films, as well as a shoulder on the low-frequency wing of band *G* in the spectrum of the annealed *a*-C : H sample not containing a metal (curve *1*'). A reproducible feature is the shoulder on the low-frequency wing of band *D*, which is observed in all *a*-C : H⟨Cu⟩ samples, annealed *a*-C : H (curves *1*', *2*, *3*, *3*' in Fig. 1), and is less pronounced in *a*-C : H⟨Co⟩ (curves *2*, *4*, *4*' in Fig. 2). Inclusion of the above features makes the spectral unfolding a more reliable procedure, although it cannot exclude completely a certain ambiguity in the results thus obtained. Figures 3a–3c illustrate the decomposition of Raman spectra for samples of various types.

The Raman shift $\Delta\omega$ (the position of the maximum) and the contribution of the Gaussian components to the total scattering intensity *s* in the spectral region of interest, which were found by unfolding the spectra of Figs. 1 and 2 with a computer for all *a*-C : H, *a*-C : H⟨Cu⟩, and *a*-C : H⟨Co⟩ samples, are listed in the table. The accuracy of $\Delta\omega$ determination was to within ± 5 cm^{-1}. The magnitude of *s* was found as the ratio of the integrated intensity of a given component to the total intensity of all components contributing to scattering in the frequency range considered. The table also lists the intensity ratios I_D/I_G of bands *D* and *G* calculated from the heights of the observed intensity peaks (absolute maxima), i.e., as $I_{D\max}/I_{G\max}$. If in estimating I_D/I_G we had used the integrated intensities of bands *G* and *D*, which consist of essentially overlapping components of different natures, the results would have been ambiguous. The values of $I_{D\max}$ and $I_{G\max}$ relate to the most probable structural configurations of sp^2-coordinated carbon atoms, and they can be conveniently employed to judge the evolution of such typical configurations under annealing or variation of the metal content.

As seen from the table, the spectra of all samples, except metal-free *a*-C : H, are fitted well by four to five components. For the unannealed *a*-C : H film, the corresponding components also apparently contribute to the spectrum, but the many-component Raman spectrum is made structureless by their strong overlap (curves *1* in Figs. 1, 2) and can be fitted well only by two very broad Gaussian profiles corresponding to bands *G* and *D*. Spectral decomposition in the region of band *G* for samples containing Cu or Co, as for the annealed *a*-C : H film, yields two or three Gaussians, namely, a low-frequency G_{low} (or G_{low1} and G_{low2}) and a high-frequency G_{high}, which accounts for the observed asymmetry of band *G*. Note that the maxima of G_{low} or G_{low1} and G_{low2} lie lower in frequency and the maximum of G_{high} lies higher than line *G* in the Raman spectrum of graphite. The spectra of the same samples exhibit, as a rule, a weak low-frequency component D_{low} superposed on the broad *D* band in the region 1250–1280 cm^{-1}. In the intermediate frequency region, between peaks *G* and *D*, one can see, as a rule, a component (called here *B*) peaking in the interval 1450–1480 cm^{-1}.

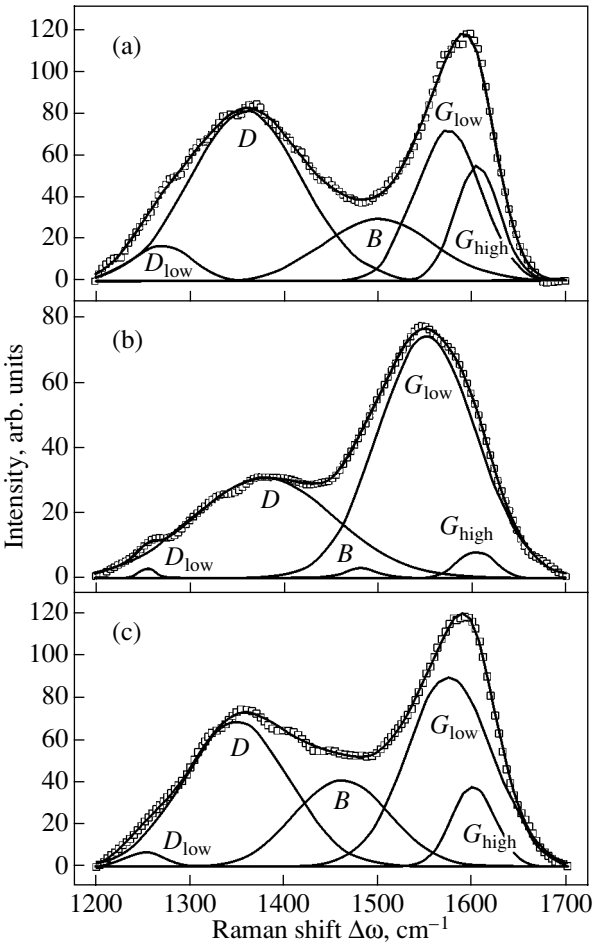

Fig. 3. Unfolding of Raman spectra into Gaussian constituents: (a) *a*-C : H (for curve *1*' from Figs. 1, 2); (b) *a*-C : H⟨Cu⟩ for [Cu]/[C] = 0.62 (for curve *2* from Fig. 1); and (c) *a*-C : H⟨Co⟩ for [Co]/[C] = 0.35 (for curve *2* from Fig. 2).

Parameters of Raman spectral components and size characteristics of graphite-like nanoclusters of *a*-C : H⟨Cu⟩, *a*-C : H⟨Co⟩, and *a*-C : H films before and after annealing

Film	[*Me*]/[C]*	Anne-aling	Raman shift Δω, cm^{-1}/Relative intensity *s*, %					I_D/I_G	L_a, Å	*M*
			G_{low}	G_{high}	*D*	D_{low}	*B*			
a-C : H	0	Before	1558/53		1406/47			0.39	8.4	12
		After	1577/23	1607/12	1361/44	1271/5	1502/16	0.71	11.4	21
a-C : H⟨Cu⟩	0.62	Before	1553/60	1605/2	1379/36	1255/1	1484/1	0.40	8.5	12
	1.0	Before	1560/36	1610/8	1331/28	1262/1	1466/27	0.52	9.7	16
		After	1570/45	1615/4	1374/44	1249/2	1492/5	0.54	9.9	16
a-C : H⟨Co⟩	0.35	Before	1532/32 1569/17	1612/11	1368/37	1256/3		0.54	9.9	16
		After	1575/37	1601/8	1348/35	1252/1	1461/19	0.62	10.6	19
	0.50	Before	1540/21	1594/24	1342/29	1263/4	1448/22	0.67	11.0	20
	0.73	Before	1539/23	1589/24	1346/29	1267/4	1447/20	0.65	10.9	20
		After	1573/25	1606/10	1341/35	1274/3	1466/27	0.78	11.9	23

* The values of the [*Me*]/[C] ratio for annealed films specify the initial metal content before annealing.

4. DISCUSSION OF RESULTS

4.1. General

Prior to making a detailed analysis of the behavior of the Raman components under modification of *a*-C : H by metals or thermal annealing of the films under study, let us briefly sum up the main available information on the nature of the one-phonon Raman bands in sp^2 coordinated carbon structures. The above-mentioned *G* line at 1581 cm^{-1} in the graphite spectrum derives from the E_{2g} sp^2-bond stretching vibration of six-membered rings on the graphene plane (at the Γ point in the Brillouin zone, for which the selection rule $\mathbf{q} = \mathbf{k} = 0$ for the phonon and photon wave vectors is satisfied in one-phonon Raman transitions). In nanocrystalline graphite, *nc*-*G*, size quantization of phonons in nanocrystals shifts the *G* line toward higher frequencies, up to 1590 and even 1600 cm^{-1}, for crystallites ~2.5 nm or less in size [14]. In addition, the *nc*-*G* spectrum exhibits a component *D*' at 1620 cm^{-1} (overlapping the *G* line) due to the peak in the phonon density of states (PDOS) with a wave vector $\mathbf{q} \neq 0$ (optical branch near the Γ point in the *T* direction between the Γ and *K* points); these phonons become Raman active as a result of breaking of the selection rule in size-quantized crystallites. A similar *D*' component was observed in neutron-irradiated pyrolytic graphite [21].

The Raman shift region 1500–1630 cm^{-1}, including the *G* graphite line, is characteristic of stretching vibrations of sp^2-coordinated conjugated C=C bonds in aromatic and chainlike molecules [22]. Therefore, the observation of the *G* band in disordered modifications of solid carbon cannot be considered unambiguous proof of the presence of graphene-like clusters in the structure; indeed, this band can be seen not only with plane regular carbon six-membered rings but with many other ring or chain sp^2-coordinated fragments. For the benzene molecule, for instance, the frequency of symmetric stretching vibrations of sp^2 bonds is 1588 cm^{-1}, which is higher than but still close enough to line *G* in graphite. Benzene rings also typically produce Raman bands at 1486 and 1311 cm^{-1} [23]. The first of them corresponds to semicircle benzene-ring vibrations in the plane of the benzene molecule, and the second, to asymmetric stretching vibrations of neighboring rings interacting with one another with variable force constants.

Disordering of ring structures, which involves variation of the bond lengths, valence angles, or number of atoms in a ring, softens the vibrations and shifts the *G* band toward low frequencies. Bending of graphene sheets produces a similar effect, and, as shown, for instance, for onionlike carbon structures [24], the larger the curvature, the larger this shift. By contrast, the vibrational frequencies of short chains with more strongly conjugated sp^2 bonds are typically in excess of 1600 cm^{-1}. Note, in particular, that the stretch vibration frequency of the C=C bond in the C_2H_4 ethylene molecule is 1630 cm^{-1}.

The selection rule $\mathbf{q} = 0$ not being rigorous accounts for such a fundamental feature of the Raman spectra of disordered carbon forms as the broad *D* band peaking at 1340–1370 cm^{-1}. In the spectrum of *nc*-*G*, the narrower peak *D* lies at 1355 cm^{-1} [14]. According to the concepts generalized in [25], band *D* originates from A_{1g}-type breathing modes of clusters of six-membered aromatic rings with conjugated sp^2 bonds. These modes are also resonantly excited in optical transitions of π electrons near the gap of the corresponding graphene clusters (close to the *K* point between the *K* and *M* points in the Brillouin zone of the crystalline counter-

part of these clusters, i.e., the graphite). The resonance condition can be written in the form of the so-called quasi-selection rule $q \approx 2k$, which was derived recently in the model of double resonance in Raman transitions in graphite with defects [26]. (The earlier accepted quasi-selection rule was $q \approx k$ [27].) The graphene-cluster breathing modes with $\mathbf{q} \neq 0$ become active in Raman scattering due to the finite size of these clusters in the ring plane, L_a, and this is what accounts for the conservation of momentum. Thus, it is band *D* rather than *G* that may serve as an indicator of the presence of clusters of sp^2-coordinated aromatic rings in the structure of disordered carbon.

Activation of Raman transitions with $\mathbf{q} \neq 0$ makes possible the appearance of bands corresponding to more or less diffuse PDOS peaks in disordered graphite-like structures. Besides the above-mentioned band *D*', the feature at ~1250 cm^{-1} [28], also reported in [14], is assigned to a PDOS peak. Calculations suggest the presence of a fairly strong density-of-states peak near 1470 cm^{-1} as well [29].

4.2. Unannealed Films

4.2.1. Band *G*. The very broad band *G* with a peak near 1558 cm^{-1} shifted to lower frequencies relative to the *G* line in graphite, combined with the strongly broadened *D* band, suggests that the unmodified *a*-C : H structure includes a system of strongly disordered sp^2-coordinated ring clusters and, possibly, fairly long chains with sp^2 bonds. The slight high-frequency *G* band shift observed in samples with copper is actually associated with the manifestation of a weak (s = 2–8%) high-frequency component G_{high} peaking at 1605–1610 cm^{-1} (see Fig. 3a, table). Note that the maximum of the low-frequency component G_{low} at 1553–1560 cm^{-1} practically coincides in frequency with the *G* maximum in *a*-C : H. It thus follows that incorporation of Cu does not involve a dramatic rearrangement of the disordered carbon structure. At the same time, the enhancement of the high-frequency component G_{high} with increasing copper content (increase in [Cu]/[C]) implies that the incorporation of Cu atoms brings about the breaking of some rings or chains, which results in the formation of short chains with stronger C=C bonds. The slight shift of G_{high} toward higher frequencies with increasing [Cu]/[C] at a practically unchanging (within experimental error) position of G_{low} cannot be assigned to an increase in the contribution of the 1620-cm^{-1} component characteristic of graphite nanocrystallites (see Section 4.1). As we shall see below, the increase in the intensity ratio I_D/I_G of bands *D* and *G* and the shift of band *D* toward lower energies compared to *a*-C : H may indicate the linking of disordered rings responsible for the G_{low} component into larger clusters and, possibly, the closure of some chains (which also contribute to G_{low}) with the formation of rings. However, the absence of noticeable changes in the position of G_{low} with increasing [Cu]/[C] implies that these clusters, at least up to [Cu]/[C] = 1, remain disordered to about the same extent as in *a*-C : H. Copper can apparently favor ordering of the sp^2 matrix in *a*-C : H only at fairly high concentrations, which is suggested by the activation of the *GG* component, close to the *G* line, in the IR spectrum of *a*-C : H⟨Cu⟩ at [Cu]/[C] = 1.3 [16].

Insertion of cobalt produces stronger changes in the structure of the carbon matrix (see table). The high-frequency component G_{high} turns out to be substantially more intense (s = 11%), and its maximum lies at a higher frequency of 1612 cm^{-1} at Co contents lower than those of copper, [Co]/[C] = 0.35 (Fig. 3b). This means that, in the case of cobalt incorporation, the formation of short chains with conjugated C=C bonds through the breakup of rings and chains proceeds more efficiently and the chain fragments themselves are shorter than in the case of copper incorporation. Note also that the low-frequency component G_{low} consists, in turn, of two components, G_{low1} (~1532 cm^{-1}) and G_{low2} (~1569 cm^{-1}), whose inclusion results in the best fitting of the observed spectrum. The maxima of G_{low1} and G_{low2} are shifted relative to peak *G* in the spectrum of unmodified *a*-C : H toward lower and higher frequencies, respectively. The existence of these components indicates that insertion of cobalt into the carbon matrix initiates, besides the breaking of sp^2 rings and/or chains (G_{high}), two more processes, which act in opposition; namely, on the one hand, the surrounding local structure becomes increasingly more disordered (G_{low1}), while on the other, the graphene-like clusters undergo the reverse process of ordering (graphitization) (G_{low2}). The ordering in clusters may bring about an enhancement of the G_{high} component and its shift toward higher frequencies due to the contribution of band *D*' (1620 cm^{-1}), which was mentioned in Section 4.1 and is associated with possible ordering-induced enhancement of the corresponding peak in the phonon density of states. Note that insertion of an even larger amount of copper ([Cu]/[C] = 1.0) results in a somewhat smaller shift (1610 cm^{-1}) and enhancement (s = 8%) than in the case of cobalt incorporation, which suggests that both the destructive and ordering effects of copper on the *a*-C : H matrix are noticeably weaker.

In *a*-C : H⟨Co⟩ films with a higher atomic fraction of Co ([Co]/[C] = 0.5), band *G* is fitted well by two components, G_{high} and G_{low}. Compared to the sample with a lower relative Co content, the high-frequency component G_{high} turns out to be markedly enhanced (s = 24%) and shifted toward lower frequencies to ~1594 cm^{-1}, while the low-frequency component G_{low} near 1540 cm^{-1} occupies an intermediate position between G_{low1} and G_{low2} and corresponds to a more ordered ring cluster state than does G_{low1}. The tendency of the G_{high} frequency to decrease persists with a further increase in

[Co]/[C] to 0.73. By contrast, the position of G_{low} practically does not change (see table) and corresponds to a lower frequency, ~1540 cm^{-1}, than is the case with the samples with copper or the unmodified *a*-C : H.

The high relative intensity of the G_{high} component and its energy position, 1594 and 1589 cm^{-1} in samples with [Co]/[C] = 0.5 and 0.73, respectively, may be considered to be caused by the evolution of the two bands, G_{high} and G_{low2}, revealed at [Co]/[C] = 0.35 with increasing Co content. In view of the data reported on *nc*-*G* [14] (Section 4.1), as well as of the dispersion of band *G* in amorphous carbon [12], one may conceive of the following scenario: growth of an *a*-C : H⟨Co⟩ film with a high enough Co content is accompanied by both breaking of rings and chains and their linkage, with the formation of small, fairly well-ordered graphene-like clusters, and the latter process dominates; i.e., most of the fragments become linked. Because the stretching vibration frequency of sp^2 bonds in such clusters is lower than that in chain fragments, the frequency of the G_{high} peak should decrease with linkage of the fragments. The low-frequency shift of the G_{high} component with increasing [Co]/[C] observed to occur in the presence of hydrogen may also be associated with the formation of benzene rings from chain fragments, a process that should enhance the contribution of the 1588 cm^{-1} mode to G_{high}. Thus, the growth in intensity and the shift of G_{high} induced by the insertion of cobalt indicate a breakdown of disordered clusters and chains, which is accompanied by graphitization of the forming small clusters. At the same time, a noticeable fraction of ring clusters and sp^2-coordinated chains remains disordered even at a relatively high Co content, which is indicated by the G_{low} component near 1540 cm^{-1} with s = 21–23%. The evolution of band *D* and of the I_D/I_G ratio with increasing Co content in *a*-C : H⟨Co⟩ films also suggests that cobalt initiates the formation of small ordered graphene-like clusters in the matrix (see Section 4.2.2). Because cobalt stimulates graphitization of the matrix, it may be conjectured that small graphene-like clusters form primarily in the immediate vicinity of Co atoms or, at higher Co contents [5], near nuclei of cobalt nanoclusters.

4.2.2. Band *D*. As is evident from the table, insertion of a metal is conducive to a relative intensity enhancement of band *D*; indeed, the ratio I_D/I_G for films with Cu or Co is higher than that for *a*-C : H and shows a distinct tendency to grow with increasing metal content. This effect is stronger in the case of cobalt and becomes manifest at lower concentrations than in the case of copper, which suggests a stronger interaction of cobalt with the *a*-C : H matrix and supports the conclusion made above in the analysis of the behavior of the band *G* components. For [Co]/[C] $\gtrsim$ 0.5, the enhancement of the *D* band apparently stops.

The spectral position of the *D* component itself is sensitive to metal insertion, the effect being stronger for cobalt than for copper. When Cu or Co is incorporated, the maximum of *D* shifts noticeably from its position in *a*-C : H toward lower frequencies, to occupy a similar position in the spectra of films with a content of Cu higher than that of Co.

Because, as mentioned in Section 4.1, it is aromatic ring clusters that are responsible for the *D* band, one may assume that, in the *a*-C : H matrix unmodified by metals, for which the *D* band becomes manifest only as a shoulder in the *G* band, the concentration of such clusters is low; the clusters are small, strongly distorted by bond and valence angle strains, and contain rings of more or less than six atoms; etc. Generally speaking, the growth of the I_D/I_G ratio observed to occur under metal insertion may indicate an increase in the number of aromatic rings, growth of the ring clusters in size (ring coalescence), and internal ordering. When copper is incorporated in the concentrations used here, however, the latter of the above processes is hardly discernible, because, as already pointed out, the high-frequency shift of the G_{low} component with increasing Cu content, which could indicate ordering in graphene-like clusters, is insignificant. Unlike copper, when a comparatively small amount of cobalt is inserted ([Co]/[C] = 0.35), the ordering in ring clusters proceeds more efficiently and it primarily involves the formation of new small clusters through linkage of chain fragments, a point mentioned in Section 4.2.1 when discussing the behavior of the *G* band components. When the Co content is increased still further, however ([Co]/[C] $\gtrsim$ 0.5), practically no further ordering of the ring cluster structure is seen, even though, judging from the still continuing low-frequency shift of the G_{high} component, new aromatic clusters show a tendency to form but, at the same time, disordering is enhanced (the G_{low} component increases).

The metal-induced increase of aromatic clusters in size is supported by the low-frequency shift of the maximum of the *D* component. Indeed, because the minimum of the optical phonon branch responsible for the breathing modes of graphene clusters lies at the *K* point [30], the larger the cluster, the narrower its optical gap and the closer its breathing mode excited at resonance to the *K* point, and, hence, the lower its frequency. Interestingly, ring clusterization with increasing metal content leaves the disorder in the forming graphite-like fragments unchanged. This is indicated not only by the lower G_{low} frequency with respect to line *G* in graphite (see Section 4.2.1) but also by the lower frequency position of the *D* maximum in the spectra of *a*-C : H⟨Cu⟩ and *a*-C : H⟨Co⟩ compared to *nc*-*G* for fairly high Cu or Co contents (see table). Indeed, for [Cu]/[C] = 1.0, the *D* component peaks near 1332 cm^{-1} and, for [Co]/[C] = 0.73, near 1346 cm^{-1}, which is considerably lower than 1355 cm^{-1} in *nc*-*G*. Such a softening of the A_{1g}-type breathing mode can be assigned to strong disorder in the structure of graphite-like clusters. The lower energy position of component *D* for the higher energy position

of G_{low} in the *a*-C : H⟨Cu⟩ sample compared to the *a*-C : H⟨Co⟩ sample and for the above-mentioned contents of Cu and Co should most likely be attributed to the fact that in the former sample the fraction of larger and more ordered ring clusters responsible for G_{low} is larger (s = 36%) than in the latter (s = 23%). The total number of ordered aromatic rings and, hence, the ratio I_D/I_G for *a*-C : H⟨Co⟩ are, however, larger than those for C : H⟨Cu⟩ (see table).

The conclusion on the cobalt-stimulated formation of fairly well-ordered small clusters of aromatic rings correlates well with the observed relatively smaller dip between the *D* and *G* bands or, in other words, with the larger broadening of band *D* toward higher frequencies at larger values of [Co]/[C] (curves *2–4* in Fig. 2). Indeed, in view of the position and relative intensity of component *B* (see Section 4.2.3 below) remaining constant with increasing [Co]/[C], for instance, from 0.50 to 0.73 (see table), this behavior may indicate an increase in the fraction of clusters with higher frequency breathing modes, i.e., of fairly small clusters.

The linear dimensions of the graphite-like clusters, L_a, along the graphene layers in our samples can be roughly estimated using the following relation, which remains valid as one passes from a very strongly disordered to a more ordered state of *a*-C : H for $L_a < 20$ Å (γ is a coefficient of proportionality) [25]:

$$I_D/I_G = \gamma L_a^2. \quad (1)$$

We assume that for $L_a > 20$ Å one can use the following well-known empirical relation established for *nc*-*G* under excitation at a wavelength λ_{exc} = 515.5 nm [13], which is close to the one employed in our experiments:

$$I_D/I_G = 44/L_a. \quad (2)$$

We also assume that, for L_a = 20 Å, relations (1) and (2) yield the same ratio I_D/I_G = 2.2 [25]. Then, one can find the coefficient γ and estimate the linear dimensions of graphene-like clusters, L_a, from experimental values of I_D/I_G for all the samples studied. The values of L_a thus obtained are listed in the table. We readily see that graphene clusters are fairly small in all samples ($L_a \sim$ 1 nm), with the increase in L_a induced by inserting the metal in the concentrations used not being large. For instance, in *a*-C : H⟨Co⟩ films with [Co]/[C] = 0.73, where the relative increase $\Delta L_a/L_a$ is larger than that for *a*-C : H, $\Delta L_a/L_a$ only slightly exceeds 30%. Based on the interatomic distance of 0.142 nm in a six-membered graphite ring, one can roughly estimate the number *M* of rings in separate clusters. The values of *M* vary from 10 to 20 (see table). The estimates obtained show that cobalt stimulates growth of the graphite-like ordered regions in an sp^2-coordinated structure more than copper does.

The small size of the aromatic clusters as estimated from Raman spectra is in reasonable agreement with the direct measurements made with an electron microscope on *a*-C : H in [31], as well as with data available for the optical gap in *a*-C : H [7, 32]. These estimates appear more reliable than those derived earlier from IR absorption spectra of *a*-C : H⟨Cu⟩ films [16], which do not agree with [7, 32]. Relation (2) used in [16] is obviously inapplicable for such strongly disordered structures as the amorphous films under study here, for which the widths of bands *G* and *D* are in substantial excess of 50 cm^{-1} [11, 25].

4.2.3. Other components (D_{low}, *B*). The low-frequency component of band *D*, D_{low}, peaking in the region 1250–1280 cm^{-1} (see table) receives apparently a contribution from a disorder-induced component near 1250 cm^{-1}, which can be identified with a diffuse PDOS peak [28]. In addition, as seen from the table, the contribution of D_{low} to the spectrum slightly increases and the maximum shifts toward higher energies with increasing metal content in the composite films. Both these trends can be associated with the increasing contribution to D_{low} from vibrations of interacting benzene molecules at a frequency of 1311 cm^{-1} [23], which was mentioned in Section 4.1. The table reveals a correlation between the enhancement of D_{low} and that of the high-frequency *G* component, G_{high}, and this may indicate that the breaking of disordered clusters or chains in the *a*-C : H matrix induced by metal incorporation is accompanied by the formation, in particular, of benzene rings. This effect is more clearly pronounced in *a*-C : H⟨Co⟩ rather than in *a*-C : H⟨Cu⟩ films, thus supporting the stronger destructive action of cobalt in the *a*-C : H matrix. As pointed out in Section 4.2.1, as the Co content increases, the G_{high} component approaches the benzene ring vibration line at 1588 cm^{-1}, which also lends support to the conclusion that cobalt-induced formation of benzene rings takes place. A similar conclusion has been reached in an IR spectroscopic study of *a*-C : H⟨Co⟩ films with variable Co content [17].

The *B* component is also most likely a superposition of inhomogeneously broadened components of various natures. First, this component can be contributed by the softened and disorder-broadened graphite PDOS peak near 1470 cm^{-1} [29]. A fairly high PDOS in this frequency region has recently been established in phonon spectrum calculations made for a single graphene layer [30]. Second, benzene ring vibrations at the frequency 1486 cm^{-1} may likewise contribute to the *B* component (Section 4.1). If, however, we limit ourselves to these contributions only, it will be unclear why component *B* shifts toward lower energies with increasing metal content. We note, in this connection, that the IR spectra of various types of *a*-C : H [33], as well as of composite *a*-C : H⟨Co⟩ films [17], exhibit an absorption band near 1450 cm^{-1}, which was tentatively assigned to the deformation modes of sp^2-coordinated CH groups, as well as of tetrahedrally coordinated CH_3 or CH_2 sp^3 groups. These modes were not resolved in Raman spectra of the same *a*-C : H types even under UV excitation [12]. As

for their indirect contribution, it was probably overlooked, because, in their unfolding of the Raman spectra, the above authors approximated the *G* band with an asymmetric Breit–Wigner–Fano profile whose low-frequency wing tailed into the frequency region of interest. Gaussian approximation of the bands in composite films usually reveals the *B* component (see table). (It cannot be separated from the G_{low1} component only in the case of *a*-C : H⟨Co⟩ with [Co]/[C] = 0.35.) It may be conjectured, for instance, that, because insertion of a metal (primarily, of cobalt) favors the formation of aromatic clusters, this also increases the concentration of the sp^2-coordinated CH groups, which results in an enhancement of the contribution due to the corresponding mode to the Raman spectrum near 1450 cm^{-1} and, as a consequence, in the shift of component *B* to lower frequencies. When copper is incorporated, the enhancement of the component near 1450 cm^{-1} and the low-frequency shift of the *B* component are less pronounced, which may be considered another argument for the absence of chemical interaction between copper and the matrix carbon.

4.3. Effect of Annealing

As follows from the observed Raman spectra (Figs. 1, 2) and their unfolding into components (see table), annealing results in rearrangement of the carbon sp^2 structure in samples of all types. The main changes occurring in the matrices of composite *a*-C : H⟨Cu⟩ and *a*-C : H⟨Co⟩ films and in a pure *a*-C : H film are qualitatively similar. In all cases, the spectra exhibit a well-pronounced high-frequency component G_{high} (1601–1615 cm^{-1}). Interestingly, annealing noticeably shifts the low-frequency component G_{low} toward higher frequencies. After annealing, the maximum of G_{low} falls into the region 1573–1577 cm^{-1} and approaches the graphite *G* line while remaining lower in energy. The ratio I_D/I_G also increases. As a rule, the maximum of component *D* exhibits a tendency, except in the *a*-C : H⟨Cu⟩ case, to a low-frequency shift under annealing. All these data indicate that annealing brings about structural ordering of the sp^2-coordinated atomic rings and an increase of the graphene-like clusters in size, which agrees with the earlier findings obtained for amorphous carbon [34].

The existence of the G_{high} component suggests that the formation of such clusters includes a stage of thermally activated breaking of the carbon–carbon bonds. Part of them also remain unclosed in fragments of chainlike structures after annealing (G_{high}), but the larger fraction (G_{low} is higher in intensity than G_{high}) closes in rings in the course of annealing to form more ordered graphene-like clusters (G_{low}, increase in I_D/I_G). In this case, the *D*' mode, characteristic of the Raman spectrum of *nc*-*G* (see Sections 4.1, 4.2), may also contribute to the G_{high} component.

The qualitative similarity in behavior between films, either containing Cu or Co or free of them, under annealing is easy to understand. Due to the thermally activated diffusion of metal atoms originally bound to carbon by weak polarization (Cu) or, at least, partially bound by strong chemical interaction (Co) with the formation of Co–C bonds, the metal–carbon interaction in the matrix weakens and the growth of metal clusters intensifies (see, e.g., [5]). In these conditions, it becomes possible for the matrix to transfer to an energetically preferable state, i.e., to undergo graphitization, as in the absence of the metal. At the same time, the smaller relative changes in the values of I_D/I_G, L_a, and *M* obtained under annealing of a composite as compared to those for unmodified *a*-C : H films (see table) show that the presence of a metal somewhat hampers the growth of graphite-like clusters while favoring, at the same time, their internal ordering. Indeed, annealing practically does not affect the size of such clusters in *a*-C : H⟨Cu⟩ with [Cu]/[C] = 0.62, so that after the annealing they turn out to be smaller in size and, judging from the position of G_{low}, less ordered than in the copper-free annealed *a*-C : H.

Thermally activated growth of graphite-like clusters in *a*-C : H⟨Co⟩ films under annealing is much more clearly pronounced (see table). From changes in the IR absorption spectra of *a*-C : H⟨Co⟩ films, it was also found that the cobalt–carbon interaction weakens under annealing [17]. Note that T_a = 380°C corresponds to the temperature of Co–C bond rupture in the Co_2C cobalt carbide [35]. One may therefore conjecture that the Co–C bond rupture at T_a in the *a*-C : H⟨Co⟩ structure, where before the annealing most of the Co atoms were chemically bound to carbon, produces a considerable "excess" concentration of carbon dangling bonds, which creates favorable conditions for the formation and ordering of aromatic ring clusters. If the Co content before the annealing was high enough ([Co]/[C] = 0.73), the graphite-like clusters in an annealed *a*-C : H⟨Co⟩ film turned out to be even larger than in the annealed *a*-C : H (see table). By contrast, *a*-C : H⟨Cu⟩ films do not have Cu–C valence bonds, so annealing does not produce such excess dangling bonds and no efficient growth of graphite-like clusters occurs.

This suggestion is also argued for by the very small contribution *s* of the *B* and D_{low} components to the spectrum of the annealed *a*-C : H⟨Cu⟩ film. Indeed, because *B* and D_{low} are determined, in particular, by the PDOS peaks of graphite in size-quantized clusters (Section 4.1), the corresponding values of *s* should correlate with the degree of ordering of such clusters. In the case of annealed *a*-C : H⟨Co⟩ films, the contribution of *B* and D_{low} to the spectrum is substantially larger than that of *a*-C : H⟨Cu⟩, which is determined, most likely, both by the higher ordering of graphite-like clusters and by the higher content of benzene rings embedded in the matrix structure.

Although it is difficult to quantitatively compare analogous parameters of Raman components in samples of different types, one can see that the G_{low} component in annealed *a*-C : H⟨Cu⟩ and *a*-C : H⟨Co⟩ samples is always slightly lower in energy and higher in the relative contribution to the spectrum than that in annealed *a*-C : H (see table). One may assume, in this connection, that, on the average, G_{low} originates to a considerable extent from more bent graphene-like fragments, which form in the immediate vicinity of metal clusters. In other words, it may be conjectured that annealing stimulates encapsulation of metal clusters in a graphite-like shell. Some indications in support of this idea come from a study of the structure of *a*-C : H⟨Co⟩ films with a high-resolution electron microscope [5].

The spectral position of *D* is governed by many factors, such as the cluster size, the extent of deviation from resonance in the excitation of scattering in clusters differing in size, and the degree of disorder in clusters of a given size. As already mentioned (Section 4.2.2), the low-frequency shift of component *D* reveals a general trend toward graphitization of the carbon–hydrogen matrix. This is what occurs in the annealing of *a*-C : H⟨Co⟩ films with [Co]/[C] = 0.35. For larger values of [Co]/[C], the shift of *D* is smaller in magnitude, which suggests ordering inside graphite-like clusters (a noticeable increase in I_D/I_G) rather than their growth. Annealing of an *a*-C : H⟨Cu⟩ film shifts the *D* component in the opposite direction, which, in view of only a weak increase in I_D/I_G, suggests a certain ordering, primarily in smaller clusters.

5. CONCLUSIONS

Thus, a study of one-phonon Raman spectra conducted in the frequency interval 1200–1700 cm^{-1} corresponding to carbon–carbon sp^2-bond vibrations has revealed the main trends in the variation of the *a*-C : H carbon matrix structure in the course of formation of *a*-C : H⟨Cu⟩ and *a*-C : H⟨Co⟩ composite films with a high metal content. It is shown that metal insertion stimulates two parallel processes in the matrix, namely, breaking of sp^2 bonds and fragmentation of disordered ring- or chainlike fragments, on the one hand, and subsequent linkage of a large part of dangling bonds with the formation of aromatic ring clusters (graphite-like clusters) having large ordered regions, on the other. The evolution of the components of the *a*-C : H⟨Co⟩ Raman spectra with increasing Co content indicates that the destructive action of cobalt in *a*-C : H is much stronger than that of copper, exactly what should be expected for a carbide-forming metal. This property, however, also accounts for the higher efficiency of clusterization of the graphite-like phase. Estimates show that graphite-like clusters in *a*-C : H⟨Co⟩ films reach about the same size for Co contents approximately three times lower than the Cu content in *a*-C : H⟨Cu⟩.

The effect of metals on the structure of the *a*-C : H carbon matrix is qualitatively similar to that of thermal annealing. Annealing is also conducive to graphitization, which includes both the breaking and linking of sp^2 bonds. While both these processes occur under annealing in both composite and metal-free films, the presence of a metal hampers, to some extent, the growth of ordered regions. On the other hand, in *a*-C : H⟨Co⟩ composite films, the annealing-induced graphitization of the matrix is facilitated by the Co–C bond breaking, which favors the formation and growth in size of ring structures. This mechanism of structural rearrangement does not operate in *a*-C : H⟨Cu⟩. The information obtained on the variations in the Raman spectra of composite films suggests that annealing may produce encapsulation of metal nanoclusters in a bent graphite-like shell, but this point requires further study.

ACKNOWLEDGMENTS

This study was supported by the Russian Foundation for Basic Research, project no. 00-02-17004-a.

REFERENCES

1. V. I. Ivanov-Omskiĭ and G. S. Frolova, Zh. Tekh. Fiz. **65** (9), 186 (1995) [Tech. Phys. **40**, 966 (1995)].
2. Q. F. Huang, S. F. Yoon, Rusli, *et al.*, J. Appl. Phys. **90** (9), 4520 (2001).
3. J. L. Flottard, J. Akinnifesi, E. Cambril, and B. Despax, J. Appl. Phys. **70**, 798 (1991).
4. V. I. Ivanov-Omskii, NATO ASI Ser., Ser. 3 **38**, 171 (1997).
5. A. V. Kolobov, J. Tominaga, T. K. Zvonareva, *et al.*, J. Appl. Phys. **92**, 6195 (2002).
6. J. Robertson, Prog. Solid State Chem. **21**, 199 (1991).
7. S. G. Yastrebov, V. I. Ivanov-Omskii, V. I. Siklitskii, and A. A. Sitnikova, J. Non-Cryst. Solids **227–230**, 622 (1998).
8. Jun Jiao and Supapan Seraphin, J. Appl. Phys. **83** (5), 2442 (1998).
9. T. Cabioc'h, A. Naudon, M. Jaouen, *et al.*, Philos. Mag. **79** (3), 501 (1999).
10. M. Tamor and W. Vassel, J. Appl. Phys. **76**, 3823 (1994).
11. J. Schwan, S. Ulrich, V. Batolly, *et al.*, J. Appl. Phys. **80** (1), 440 (1996).
12. A. C. Ferrari and J. Robertson, Phys. Rev. B **64**, 075414 (2001).
13. F. Tuinstra and J. L. Koening, J. Chem. Phys. **53** (3), 1126 (1970).
14. R. J. Nemanich and S. A. Solin, Phys. Rev. B **20** (2), 392 (1979).
15. J. Robertson and E. P. O'Reilly, Phys. Rev. B **35**, 2946 (1987).
16. V. I. Ivanov-Omskiĭ, T. K. Zvonareva, and G. S. Frolova, Fiz. Tekh. Poluprovodn. (St. Petersburg) **34** (12), 1450 (2000) [Semiconductors **34**, 1391 (2000)].

17. T. K. Zvonareva, E. I. Ivanova, G. S. Frolova, *et al.*, Fiz. Tekh. Poluprovodn. (St. Petersburg) **36** (6), 734 (2002) [Semiconductors **36**, 695 (2002)].
18. V. I. Ivanov-Omskiĭ and G. S. Frolova, Zh. Tekh. Fiz. **65** (9), 186 (1995) [Tech. Phys. **40**, 966 (1995)].
19. V. I. Ivanov-Omskiĭ and É. A. Smorgonskaya, Fiz. Tverd. Tela (St. Petersburg) **41** (5), 868 (1999) [Phys. Solid State **41**, 786 (1999)].
20. T. K. Zvonareva, V. M. Lebedev, T. A. Polyanskaya, *et al.*, Fiz. Tekh. Poluprovodn. (St. Petersburg) **34** (9), 135 (2000) [Semiconductors **34**, 1094 (2000)].
21. H. Maeta and Y. Sato, Solid State Commun. **23**, 23 (1977).
22. D. Lin-Vien, N. B. Coltharp, W. G. Fateley, and J. G. Graselli, *The Handbook of Infrared and Raman Characteristic Frequencies of Organic Molecules* (Academic, New York, 1991).
23. N. Colthup, L. Daly, and S. Wiberley, *Introduction in Infrared and Raman Spectroscopy* (Academic, New York, 1975).
24. E. D. Obratsova, M. Fujii, S. Hayashi, *et al.*, Carbon **35** (5–6), 821 (1998).
25. A. C. Ferrari and J. Robertson, Phys. Rev. B **61** (20), 14095 (2000).
26. C. Thomsen and S. Reich, Phys. Rev. Lett. **85** (24), 5214 (2000).
27. I. Pocsik, M. Hundhausen, M. Koosh, and L. Ley, J. Non-Cryst. Solids **227–230**, 1083 (1998).
28. M. S. Dresselhaus, M. A. Pimenta, A. Marucci, *et al.*, in *Proceedings of International Symposium of Carbon* (Tokyo, 1998), p. 94.
29. R. Nicklow, N. Wakabayashi, and H. G. Smith, Phys. Rev. B **5**, 4951 (1972).
30. C. Mapelli, C. Castiglioni, G. Zebri, and K. Mullen, Phys. Rev. B **60**, 12710 (1999).
31. V. I. Ivanov-Omskii, A. B. Lodygin, A. A. Sitnikova, *et al.*, in *Diamond and Diamond-like Film Applications: Proceedings of 3rd International Symposium on Diamond Films, St. Petersburg, 1996*, Ed. by P. Gielisse, V. I. Ivanov-Omskii, G. Popovichi, and M. Prelas (Technomic, Lancaster, 1998), p. 486.
32. V. I. Ivanov-Omskii, V. I. Siklitskii, A. A. Sitnikova, *et al.*, Philos. Mag. B **76** (6), 973 (1997).
33. J. Ristein, R. T. Stief, L. Ley, and W. Bayer, J. Appl. Phys. **84** (7), 3836 (1998).
34. V. I. Ivanov-Omskiĭ, A. V. Tolmachev, and S. G. Yastrebov, Fiz. Tekh. Poluprovodn. (St. Petersburg) **35** (2), 227 (2001) [Semiconductors **35**, 220 (2001)].
35. J. J. Delaunay, T. Hayashi, M. Tomita, and S. Hurono, J. Appl. Phys. **82** (5), 2200 (1997).

Translated by G. Skrebtsov

Physics of the Solid State, Vol. 45, No. 9, 2003, pp. 1669–1671. Translated from Fizika Tverdogo Tela, Vol. 45, No. 9, 2003, pp. 1590–1592.

SEMICONDUCTORS AND DIELECTRICS

Regularities of the Formation of Polytype Structures in Layered Metal Dichalcogenides

G. B. Dubrovskiĭ

Ioffe Physicotechnical Institute, Russian Academy of Sciences, Politekhnicheskaya ul. 26, St. Petersburg, 194021 Russia

e-mail: Genrich.Dubrovsky@mail.ioffe.ru

Received January 24, 2003

Abstract—Possible sequences of alternating triple layers *X–M–X* in MX_2 dichalcogenides (where *M* is a metal and *X* is a chalcogen) that are consistent with the close packing conditions are considered, and the structure and symmetry of the unit cells of the main polytypic modifications of these compounds are determined. Reasoning from the molecular structure of the crystals and the fact that their smallest structural unit is an MX_2 molecule, the notation of each triple layer can be represented in a reduced form in which only the position of the central metal atom and the orientation of the molecule are specified. In the proposed notation, allowances are made for two types of coordination of the metal atom in the molecule, namely, the octahedral coordination, in which the nearest *X* layers occupy different positions and form close packing, and the trigonal prismatic coordination, in which both *X* layers occupy identical positions. The use of the reduced (molecular) form of the notation significantly simplifies the analysis of the polytype structures and makes it possible to distinguish several structural groups differing in structure and symmetry among the crystals with unit cells including two, three, and four layers. © *2003 MAIK "Nauka/Interperiodica".*

The structure of layered metal dichalcogenides of the general formula MX_2 (where *M* is a metal and *X* is a chalcogen) consists of close-packed monomolecular triple layers *X–M–X* with a planar hexagonal coordination in each of their constituent chalcogen and metal layers. In these compounds, the atoms located within each triple layer are involved in strong ion–covalent bonding, whereas the adjacent triple layers are linked through weak van der Waals forces. This gives grounds to assert that MX_2 crystals belong to a special class of crystal structures, namely, quasi-one-dimensional molecular crystals [1].

For MX_2 layers, there exist two types of coordination: the octahedral coordination, in which chalcogen atoms of the upper and lower layers occupy positions corresponding to close packing (Fig. 1), and the trigonal prismatic coordination, in which the chalcogen layers occupy identical positions (Fig. 2). In both cases, the boundary chalcogen layers of the adjacent triple layers always occupy positions in close packing [2]. As in all close packings, all atoms of MX_2 crystals are located along three triad axes that are perpendicular to the layer plane and pass through the lateral edges and the center of the hexagonal prism. These axes are usually designated as *A*, *B*, and *C* (for metal atoms, these are the α, β, and γ axes, respectively). For example, the sequences of *X* and *M* alternating layers in the configurations drawn in Figs. 1 and 2 can be written as *AγB* and *AγA*, respectively.

Comprehensive information on the atomic arrangement in a triple layer can be obtained by specifying the positions of the metal atoms. For this purpose, it is necessary to introduce additional indices that characterize the arrangement of the chalcogen atoms surrounding the metal atom. For example, the octahedral coordination can be represented by both the direct sequence *AγB*, which is designated by γ, and the possible mirror sequence $B\bar{\gamma}A$, which is denoted by a bar over the symbol, i.e., $\bar{\gamma}$. For a trigonal prismatic coordination, it is sufficient to specify the arrangement of two chalco-

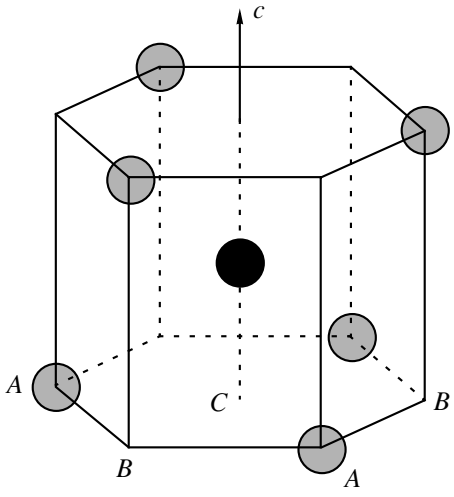

Fig. 1. Octahedral coordination of the metal in the *X–M–X* triple layer. Hatched circles indicate the chalcogen atoms, and the closed circle represents the metal atom.

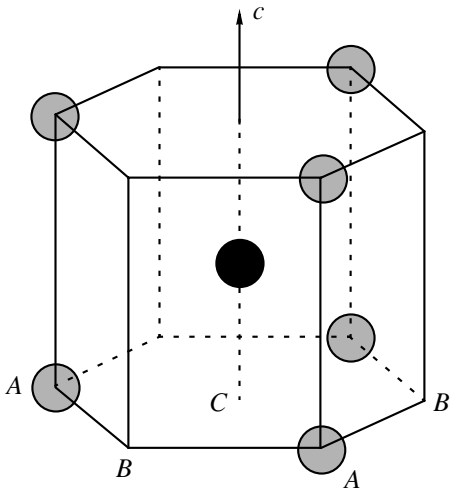

Fig. 2. Trigonal prismatic coordination of the metal in the *X–M–X* triple layer. Designations of the atoms are the same as in Fig. 1.

gen layers, for example, $\gamma_A(A\gamma A)$ or $\gamma_B(B\gamma B)$. The notational system proposed above reduces the notation of the sequence of alternating layers along the *c* axis in the unit cell of the crystal by a factor of three. This is particularly important when molecular close packing, like atomic packing, is considered to possess polytypism, owing to which the unit cell length in the crystals can reach hundreds of atomic layers.

In order to describe the structure of an MX_2 crystal through the sequences of alternating triple layers, it is necessary to determine the sequences consistent with the close packing rules.

(A) Crystals with an Octahedral Coordination of Atoms in Triple Layers

There are six variants of the atomic arrangement in triple layers: $\alpha(B\alpha C)$, $\bar{\alpha}(C\bar{\alpha}B)$, $\beta(C\beta A)$, $\bar{\beta}(A\bar{\beta}C)$, $\gamma(A\gamma B)$, and $\bar{\gamma}(B\bar{\gamma}A)$. All these layers are equivalent to one another in the sense that the choice of any one of them as the first layer is simply the choice of the origin. The stacking of the subsequent layers leads to variants of layer packing that result in the formation of different structures in the crystal. Therefore, we will restrict our consideration to the case where any of the above layers can be chosen as the first layer. However, when constructing the crystal, it will be necessary to take into account all the allowed extensions of each subsequent layer. Without violating the close packing rules, each of these layers can be combined with only four different layers:

$$\alpha\colon\ \alpha,\ \bar{\beta},\ \gamma,\ \bar{\gamma};\quad \bar{\alpha}\colon\ \bar{\alpha},\ \beta,\ \bar{\beta},\ \gamma;$$

$$\beta\colon\ \alpha,\ \bar{\alpha},\ \beta,\ \bar{\gamma};\quad \bar{\beta}\colon\ \alpha,\ \bar{\beta},\ \gamma,\ \bar{\gamma};\qquad \text{(A.1)}$$

$$\gamma\colon\ \bar{\alpha},\ \beta,\ \bar{\beta},\ \gamma;\quad \bar{\gamma}\colon\ \alpha,\ \bar{\alpha},\ \beta,\ \bar{\gamma}.$$

Let us consider the possible sequences of layer packing starting, for example, from the α layer. Upon superposition of the second layer on the α layer, according to list (A.1), we obtain the following four cases.

(1) αα. If all the layers of the structure occupy the α position, the symmetric unit cell is one layer in height and contains one molecule. This is the simplest modification of the MX_2 crystal with D_{6h} hexagonal symmetry, which can be denoted by the molecular symbol 1*H*.

(2) $\alpha\bar{\beta}$. This sequence can be repeated in the crystal: it corresponds to a hexagonal unit cell with a height equal to two molecular layers and is designated as 2*H*.

(3) αγ. This combination represents an incomplete unit cell, because, according to list (A.1), α cannot follow γ; i.e., this combination is not repetitive.

(4) $\alpha\bar{\gamma}$. This combination corresponds to a 2*H* hexagonal unit cell identical to $\alpha\bar{\beta}$.

After superposition of the third layer, it is possible to obtain 16 variants, of which 6 correspond to unit cells with the Zhdanov symbol (2211) (for chalcogen atoms) and the molecular symbol $(2_0\bar{1})$. In the latter symbol, the numerals indicate the number of molecular layers along the *c* axis, the bar over the numeral signifies mirror symmetry of the layer, and the zero means repetition of identical layers. These variants of layer packing have a $3T_a$ structure. Three variants with the respective symbols (33) and $(11\bar{1})$ characterize a $3T_b$ structure. Five variants correspond to incomplete unit cells or, upon a further extension, can represent 1/3 of the unit cell of the 9*R* rhombohedral crystal with the Zhdanov symbol $(51)_3$ and the molecular symbol $(12_0)_3$, as, for example, in the case (**3**–**4**) [the case **3** and the 4th layer of the extension allowed by list (A.1)]: αγγβαγγββ. The case (**3**–**2**), or the αγβ packing, is of special interest. This structure is a molecular analog of the *ABCABC* structure in atomic close packings. The symmetric unit cell of this structure contains one molecule and is also characterized by the Zhdanov symbol ∞. However, compared to the face-centered cubic cell of β-SiC, the former cell is significantly elongated along the *c* axis. This structure is denoted by the symbol 1*T*. The Brillouin zone of the MX_2 crystal with the 1*T* structure is shown in Fig. 3. As the number of layers in the sequence increases, the number of possible variants of their combination increases in a geometric progression. For example, upon superposition of the fourth layer, it is possible to obtain 64 variants. They correspond to several groups of 4*H* four-layer hexagonal structures. Each of these groups involves identical structures. This description of the crystal structure includes all possible structures that are consistent with the close packing rule. However, it is probable that not

all of them can be formed during the growth and remain stable. In our opinion, the simplest structures with the Zhdanov symbols (44) and (17) and the molecular symbols $(2\bar{2})$ and $(3\bar{1})$ are the most promising from this point of view, including those described by the sequences $\alpha\gamma\bar{\beta}\bar{\gamma}$ and $\alpha\gamma\beta\bar{\gamma}$.

(B) Crystals with the Trigonal Prismatic Atomic Coordination in Triple Layers

For a trigonal prismatic coordination, there also exist six variants of the atomic arrangement in the layers: α_B, α_C, β_A, β_C, γ_A, and γ_B. Each of these layers can be combined with only four different layers:

$$\begin{aligned}&\alpha_B\colon\ \alpha_C, \beta_A, \beta_C, \gamma_A;\quad \beta_C\colon\ \alpha_B, \beta_A, \gamma_A, \gamma_B;\\ &\alpha_C\colon\ \alpha_B, \beta_A, \gamma_A, \gamma_B;\quad \gamma_A\colon\ \alpha_B, \alpha_C, \beta_C, \gamma_B;\\ &\beta_A\colon\ \alpha_B, \alpha_C, \beta_C, \gamma_B;\quad \gamma_B\colon\ \alpha_C, \beta_A, \beta_C, \gamma_A.\end{aligned} \qquad \text{(B.1)}$$

Note that, here, the choice of the initial layer is of no significance, as is the case in crystals with an octahedral coordination of atoms in the layers. If the α_B layer is taken as the initial layer, the following four sequences become possible in accordance with list (B.1): (1) $\alpha_B\alpha_C$, (2) $\alpha_B\beta_A$, (3) $\alpha_B\beta_C$, and (4) $\alpha_B\gamma_A$. From these combinations, it follows that the 1*H* monolayer unit cells are impossible in this case, because the sequence of identical layers contradicts the close packing conditions. All the sequences listed above correspond to 2*H* bilayer hexagonal unit cells. The first two sequences differ in structure but have D_{6h} symmetry. The 3rd and 4th sequences are identical in structure and have D_{3h} symmetry.

The construction of three-layer and four-layer packings in crystals with a trigonal prismatic coordination of atoms in the layers is similar to that in crystals with an octahedral coordination; therefore, we need not describe it completely here. Both trigonal and octahedral packings, which are obtained according to the rules of molecular close packing (B.1), can form several structural groups that differ in structure and symmetry. Special mention should be made of one of the three-layer packings, namely, $\alpha_B\gamma_A\beta_C$, which is similar to the $\alpha\beta\gamma$ structure with an octahedral coordination. The symmetric cell of this packing contains one molecule and is characterized by the Zhdanov symbol (∞). In this case, the Brillouin zone is similar to that presented in Fig. 3. This structure is also described by the molecular symbol 1*T*.

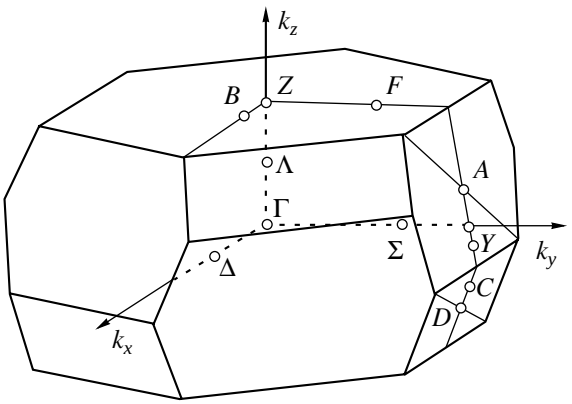

Fig. 3. Brillouin zone of the MX_2 crystal with the 1*T* structure.

ACKNOWLEDGMENTS

This work was supported by the Russian Foundation for Basic Research, project no. 00-02-16890.

REFERENCES

1. G. B. Dubrovskiĭ, Fiz. Tverd. Tela (St. Petersburg) **40** (9), 1712 (1998) [Phys. Solid State **40**, 1557 (1998)].
2. J. A. Wilson and A. D. Yoffe, Adv. Phys. **18**, 193 (1969).

Translated by N. Korovin

Physics of the Solid State, Vol. 45, No. 9, 2003, pp. 1672–1675. Translated from Fizika Tverdogo Tela, Vol. 45, No. 9, 2003, pp. 1593–1596.

SEMICONDUCTORS AND DIELECTRICS

Effect of Substitutional Order on the Relaxation of Aluminum Nuclei in $Y_{3-x}Lu_xAl_5O_{12}$ Mixed Garnets

E. V. Charnaya*, C. Tien, T. Y. Her**, S. N. Ivanov***, and E. N. Khazanov*****

**Fok Institute of Physics, St. Petersburg State University, ul. Pervogo Maya 100, Petrodvorets, St. Petersburg, 198504 Russia*

e-mail: charnaya@paloma.spbu.ru

***Department of Physics, National Cheng Kung University, 701 Tainan, Taiwan*

****Institute of Radio Engineering and Electronics, Russian Academy of Sciences, Mokhovaya ul. 11, Moscow, 101999 Russia*

Received February 20, 2003

Abstract—The spin–lattice relaxation time of ^{27}Al nuclei residing in the octahedral and tetrahedral oxygen environment in $Y_{3-x}Lu_xAl_5O_{12}$ mixed aluminum–yttrium garnets was measured by the NMR method for $0 \le x \le 3$. A maximum in the concentration dependence of the relaxation time was observed for both crystallographic positions at $x = 0.75$; this maximum correlates with the minimum in the NMR linewidth, indicating the ordering obtained as the yttrium and lutetium ions occupy the dodecahedral positions in the garnet lattice.

1. INTRODUCTION

Establishing the occupation of various lattice positions by ions of different species and the effect exerted by this substitutional order on the properties of solid solutions is one of the most complex issues in the physics of mixed crystals and is of importance from the standpoint of applications [1, 2]. Depending on the interaction energies of the ions of the solid-solution constituents and on their radii, ions of different species can either be distributed in a random manner over the lattice or mutually ordered. The short-range order in the latter case can be identified either with clusterization of the solid solution or with a regular alternation of ions of the various constituents, which, in the case of strong correlations, gives rise to the onset of long-range order, in particular, to the formation of a superlattice at certain concentrations. It is known that substitutional order substantially affects many physical properties of mixed crystals and accounts, for instance, for the features observed in the concentration dependences of the electrical conductivity of alloys [2, 3], bond lengths (see [4] and references therein), and luminescence [5], as well as in the electrical conductivity and ultrasound damping in dielectric and semiconducting solid solutions [6].

Revealing order in mixed crystals is a fairly complex problem. X-ray and neutron scattering studies provide unambiguous information primarily on the superlattice formation, although methods involving diffuse neutron scattering are also useful in the case of partially ordered solid solutions [1]. On the other hand, because the main NMR parameters, such as the line shape, chemical shift, and relaxation times, are very sensitive to local changes in crystal structure, the NMR method may be expected to provide useful information on the pattern of mutual ion arrangement in mixed crystals, particularly in the case of incomplete ordering. Indeed, NMR has been employed to study substitutional order in a number of mixed garnets and aluminates [7, 8], as well as in binary and ternary semiconductor solid solutions [9, 10]. The above studies analyzed the NMR line shape and chemical shift to establish the pattern of site occupation by ions. The effect of ordering in dielectric mixed crystals on nuclear-relaxation processes, in particular, on the nuclear spin–lattice relaxation, has not been considered thus far.

This communication reports on a study of the spin–lattice relaxation of ^{27}Al nuclei in mixed crystals of aluminum–yttrium–lutetium garnets $Y_{3-x}Lu_xAl_5O_{12}$ for $0 \le x \le 3$ and analyzes the relation of the spin–lattice relaxation time of aluminum nuclei with substitutional order in these solid solutions.

Although the aluminum–yttrium and aluminum–lutetium garnets, $Y_3Al_5O_{12}$ and $Lu_3Al_5O_{12}$, corresponding to the extreme concentrations $x = 0$ and 3, are well studied in connection with the broad scope of their applications [11], the same cannot be said of their solid solutions. The possibility of partial ordering in the $Y_{3-x}Lu_xAl_5O_{12}$ mixed crystals was first suggested by a study conducted in [7] of the concentration dependence of the thermal phonon relaxation time, ultrasound damping coefficient, and NMR linewidth. A later multiquantum NMR study, conducted under rotation about the magic angle, revealed ordering in the occupation of lattice sites by Y and Lu ions at concentrations x close to 0.75.

1063-7834/03/4509-1672$24.00

2. EXPERIMENT

Single crystals of $Y_{3-x}Lu_xAl_5O_{12}$ mixed garnets with $x = 0$, 0.2, 0.6, 0.75, 1, 2, and 3 were grown by the Czochralski technique. X-ray diffraction measurements showed the mixed garnets to have the same structure as the pure aluminum–yttrium and aluminum–lutetium compositions, namely, cubic symmetry and space group $Ia3d(O_h^{10})$. The lattice constant varies from 12.008 Å for $Y_3Al_5O_{12}$ to 11.914 Å for $Lu_3Al_5O_{12}$ (see table). The garnet lattice unit cell contains 40 aluminum nuclei, which occupy two different crystallographic positions corresponding to the octahedral (16 nuclei) and tetrahedral (24 nuclei) oxygen environment [13]. The oxygen octahedra and tetrahedra are distorted such that the crystal field at aluminum nucleus sites has axial symmetry and is oriented along the unit cell diagonals for the octahedral position and along the cubic axes for the tetrahedral position. In accordance with the garnet lattice, the static NMR spectrum of ^{27}Al (spin $I = 5/2$) for an arbitrarily oriented external quantizing magnetic field consists of 25 lines in single-crystal samples. When a sample is rotated about the magic angle, the spectrum consists of two sets of lines, corresponding to the octahedral and tetrahedral crystallographic positions, whose energy and shape are governed by the chemical shift and quadrupole coupling with the asymmetry parameter η_Q equal to zero [14].

Measurements of the NMR spectra and spin–lattice relaxation times of ^{27}Al nuclei in this study were conducted on an Avance 400 pulsed spectrometer (Bruker) under rotation about the magic angle with a frequency of 12 kHz at room temperature. The Larmor precession frequency was 104.3 MHz. The spectral line position was determined relative to the NMR signal from a 1-mol $Al(NO_3)_3$ water solution. The spin–lattice relaxation times were derived from the recovery of the central lines corresponding to the octahedral and tetrahedral positions after application of a 180° inverting pulse.

3. RESULTS AND DISCUSSION

The central part of the ^{27}Al NMR spectrum obtained under rotation about the magic angle consists, for all the samples studied, of a narrow line corresponding to the octahedral aluminum position and a broadened line due to the tetrahedral position. The central part of the spectrum is shown in Fig. 1 for the $x = 2$ composition. This pattern of the spectrum is in agreement with reported data on both pure and mixed garnets [12, 14]. The difference in width between the lines corresponding to the two aluminum positions originates from an order-of-magnitude difference in the quadrupole coupling constants. The values of the quadrupole coupling constants found from the shape of the central line for the tetrahedral position and from the shape of the total spectrum for the octahedral position are listed in the table for all the mixed crystals studied. In addition, the results of spectral measurements were used to determine the widths of the central NMR lines corresponding to the octahedral position. Figure 2 plots the dependence of the linewidth on garnet composition.

Lattice constant a and quadrupole coupling constants for ^{27}Al nuclei in the octahedral, $(e^2qQ/h)_{oct}$, and tetrahedral environment, $(e^2qQ/h)_{tetr}$, for the mixed garnets under study

x	α, Å	$(e^2qQ/h)_{oct}$, MHz	$(e^2qQ/h)_{tetr}$, MHz
0	12.008	0.65 ± 0.01	6.05 ± 0.01
0.2	12.002	0.82 ± 0.03	6.07 ± 0.03
0.6	11.989	0.91 ± 0.03	6.09 ± 0.03
0.75	11.984	0.92 ± 0.02	5.98 ± 0.03
1	11.976	1.04 ± 0.03	6.07 ± 0.04
2	11.945	1.16 ± 0.03	6.17 ± 0.05
3	11.914	1.20 ± 0.02	6.24 ± 0.02

The spin–lattice relaxation times for both crystallographic positions are also displayed in Fig. 2 as functions of garnet composition. For all garnet compositions, the relaxation time of the nuclei occupying the tetrahedral position was longer than that for the octahedral one. A maximum is seen to appear in the concentration dependence of the relaxation times near $x \sim 0.75$. This maximum correlates with the minimum in the linewidth of aluminum nuclei in the octahedral position. Studies carried out in [7, 12] by the heat pulse technique, acoustic measurements, stationary and, particularly, pulsed multiquantum NMR showed that the

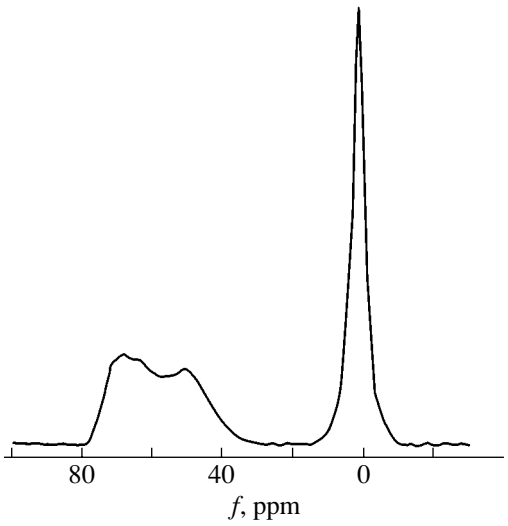

Fig. 1. Central part of the ^{27}Al NMR spectrum obtained under rotation about the magic angle for the $x = 2$ composition. The broad and the narrow line are due to aluminum nuclei in the tetrahedral and octahedral oxygen environment, respectively.

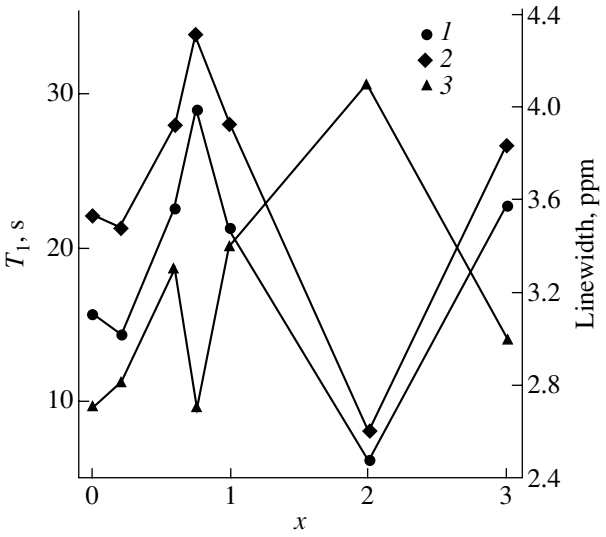

Fig. 2. Spin–lattice relaxation times of ^{27}Al nuclei in (*1*) the octahedral and (*2*) tetrahedral positions and (*3*) the NMR linewidth for the octahedral position plotted vs. mixed-garnet composition. The solid lines, connecting the experimental points, are drawn to guide the eye.

structure of mixed aluminum–yttrium–lutetium garnets exhibits, near the concentration $x = 0.75$, fairly good ordering of the yttrium and lutetium nuclei over lattice sites, which accounts, in particular, for the NMR lines of this composition being narrower than those of the other mixed garnets. The observed correlation between the ^{27}Al NMR linewidth and the spin–lattice relaxation times suggests that substitutional order affects the nuclear relaxation rate as well.

Spin–lattice relaxation of nuclei possessing a quadrupole moment in dielectric crystals occurs primarily through the interaction of nuclear quadrupoles with the dynamic gradients of the electric fields generated under thermal vibrations of the crystal lattice [15]. At temperatures above a fraction of one Kelvin, the main contribution to relaxation comes from two-phonon Raman processes. Within the Debye approximation for the thermal vibration spectrum, the spin–lattice relaxation time is given by

$$T_1^{-1} = A_2 I_6 / \rho^2 v^5, \qquad (1)$$

where I_6 is the Debye integral, ρ is the density, v is the sound velocity, and the factor A_2 is proportional to the squared quadrupole coupling constant [15]. Thus, the concentration dependence of the spin–lattice relaxation time is dominated by the variations in the quadrupole coupling constant and in the phonon spectrum.

The aluminum ions residing in the lattice of pure yttrium garnets in the both octahedral and tetrahedral oxygen environment have six neighboring yttrium ions occupying dodecahedral positions [11]. In mixed garnets, the yttrium and lutetium ions are distributed over dodecahedral positions such that the aluminum resides in an environment determined by the actual substitutional pattern. The probability $P(n, x)$ of an aluminum ion in a disordered solid solution with concentration x having n Y ions and $6 - n$ Lu ions in its environment is given by the binomial distribution

$$P(n, x) = \left\{\frac{6!}{n!(6-n)!}\right\}\left(\frac{x}{3}\right)\left(1 - \frac{x}{3}\right)^{6-n}. \qquad (2)$$

In partially ordered solid solutions, the distribution of ions varies, producing a higher probability for some values of n.

Variations in the aluminum environment may affect the distribution of crystal electric fields and the magnitude of the antiscreening constant and, hence, make the dynamic gradients of electric fields dependent on substitutional order. As follows, however, from the experimental data listed in the table, the effect of ordering on the quadrupole coupling constant weakly manifests itself in a deviation from the monotonic dependence on concentration only for aluminum in the tetrahedral positions and cannot account for the observed marked increase in the relaxation time in the region of ordering in mixed garnets. One should thus assume that the substitutional pattern in solid solutions gives rise to a considerable change in the thermal lattice vibration spectrum with reference to the phonon spectrum of disordered mixed crystals. While such changes should affect the Debye temperature, data on the Debye temperature in mixed garnets are presently lacking.

4. CONCLUSIONS

Thus, we have reported on a first study of the spin–lattice relaxation rate for aluminum nuclei over the total aluminum–yttrium–lutetium mixed garnet series and revealed a correlation between the relaxation time and the NMR linewidth for ions occupying the octahedral positions. It was shown that the maximum in the concentration dependence of T_1 lies at the $x = 0.75$ composition, which multiquantum NMR measurements (made under rotation about the magic angle) reveal to be associated with the maximum substitutional order. The effect of ordering on spin–lattice relaxation in mixed garnets was interpreted assuming that the thermal lattice vibration spectrum undergoes variations. The results obtained in this study demonstrate the possibility of using nuclear spin–lattice relaxation times to derive information on substitutional order in mixed dielectric crystals.

ACKNOWLEDGMENTS

This study was supported by the program “Integration” (project no. A0147) and the State Committee on Science of Taiwan (project no. 91-2112-M-006-017).

REFERENCES

1. J. M. Ziman, *Models of Disorder: The Theoretical Physics of Homogeneously Disordered Systems* (Cambridge Univ. Press, Cambridge, 1979; Mir, Moscow, 1982).
2. A. I. Kitaĭgorodskiĭ, *Mixed Crystals* (Nauka, Moscow, 1983; Springer, Berlin, 1984).
3. S. V. Kozyrev and A. Yu. Maslov, Fiz. Tekh. Poluprovodn. (Leningrad) **22**, 433 (1988) [Sov. Phys. Semicond. **22**, 265 (1988)].
4. H. M. Vieth, S. Vega, N. Yellin, and D. Zamir, J. Phys. Chem. **95**, 1420 (1991).
5. L. G. Grigor'eva, D. K. Millers, A. V. Nomoev, *et al.*, Izv. Akad. Nauk Latv. SSR **3**, 46 (1988).
6. Yu. P. Efitsenko and E. V. Charnaya, Fiz. Tverd. Tela (Leningrad) **32**, 2436 (1990) [Sov. Phys. Solid State **32**, 1413 (1990)].
7. P. Y. Efitsenko, E. N. Khazanov, S. N. Ivanov, *et al.*, Phys. Lett. A **147**, 135 (1990).
8. E. V. Charnaya, N. A. Grigorieva, S. N. Ivanov, *et al.*, Phys. Status Solidi B **213**, 433 (1999).
9. K. Beshah, D. Zamir, P. Becla, *et al.*, Phys. Rev. B **36**, 6420 (1987).
10. L. Frydman and J. S. Harwood, J. Am. Chem. Soc. **117**, 5367 (1995).
11. A. A. Kaminskiĭ, L. K. Aminov, V. L. Ermolaev, *et al.*, in *Physics and Spectroscopy of Laser Crystals*, Ed. by A. A. Kaminskiĭ (Nauka, Moscow, 1986).
12. E. V. Charnaya, C. Tien, J. J. Lu, *et al.*, J. Phys.: Condens. Matter **13**, 8775 (2001).
13. R. Z. Menzer, Z. Kristallogr. **69**, 300 (1929).
14. N. Gautier, M. Gervais, C. Landron, *et al.*, Phys. Status Solidi A **165**, 329 (1998).
15. A. R. Kessel', *Nuclear Acoustical Resonance* (Nauka, Moscow, 1969).

Translated by G. Skrebtsov

Physics of the Solid State, Vol. 45, No. 9, 2003, pp. 1676–1678. Translated from Fizika Tverdogo Tela, Vol. 45, No. 9, 2003, pp. 1597–1559.

SEMICONDUCTORS AND DIELECTRICS

Study of ESR Spectra of Ce^{3+} Ions in Polycrystalline $Sr_2B_5O_9Br$

A. V. Sidorenko*, P. A. Rodnyĭ*, O. Guillot-Noel, D. Gourier**, and C. W. E. van Eijk*****

**St. Petersburg State Polytechnical University, Politekhnicheskaya ul. 25, St. Petersburg, 195251 Russia*
e-mail: sidorenkoa@mail.ru
***Laboratoire de Chimie Appliquée de l'Etat Solide, CNRS-UMR 7574 ENSCP, 75231 Paris Cedex 05, France*
****Interfaculty Reactor Institute, Delft University of Technology, Mekelweg 15, 2629 JB Delft, The Netherlands*
Received February 14, 2003; in final form, March 3, 2003

Abstract—ESR spectra of Ce^{3+} ions in polycrystalline $Sr_2B_5O_9Br$ were studied, and the two crystallographic positions of the Ce^{3+} ion in this compound were identified on the basis of the data obtained. The ESR spectrum of Ce^{3+} ions with local charge compensation contains a broad line indicating the existence of several types of charge compensation. ESR spectra of Ce^{3+} ions in samples activated additionally by K^+ ions are similar to those of the regular Ce^{3+} centers, which indicates that the effect of the univalent cation on Ce^{3+} is negligible. *© 2003 MAIK "Nauka/Interperiodica".*

1. INTRODUCTION

Haloborates activated by Ce^{3+} ions have been recently shown to be a promising material for detecting thermal neutrons [1]. The spectroscopic properties and thermoluminescent characteristics of $Sr_2B_5O_9Br : Ce^{3+}$ are presented in [2]. $Sr_2B_5O_9Br : Ce^{3+}$ revealed cerium centers of two types. One of them is produced by direct substitution of strontium ions without any local charge compensation. The second center is an associate of the cerium ion Ce(III) with a charge-compensating defect. Only one type of Ce^{3+} emission center was revealed in samples of the haloborates codoped by Na^+ or K^+ ions. Charge compensation centers were established to influence the intensity of photostimulated luminescence. This communication reports on a continuation of the study of the properties of $Sr_2B_5O_9Br : Ce^{3+}$ by ESR spectroscopy.

While information on the crystallographic structure of $Sr_2B_5O_9Br$ are lacking, structural data on $Eu_2B_5O_9Br$ do exist [3]. Europium can occupy two crystallographic positions in the matrix, in each of which it is surrounded by seven oxygen atoms of the borate groups and two halogen atoms. Because the ionic radii of Eu^{2+} and Sr^{2+} are close in magnitude [4], we assumed the europium- and strontium-based haloborates to have similar crystallographic parameters. The two strontium atoms in $Sr_2B_5O_9Br$, which occupy different crystallographic positions, have a very similar environment, but with a slightly different arrangement of the nearest neighbor oxygen ions (Fig. 1).

The ground state of the Ce^{3+} ion is $^2F_{5/2}$, i.e., $L = 3$, $S = 1/2$, and $J = 5/2$. The excited state $^2F_{7/2}$ lies approximately 2000 cm^{-1} above $^2F_{5/2}$. The low-symmetry crystal field splits the $^2F_{5/2}$ ground state into three Kramers doublets with M_J equal to ±5/2, ±3/2, and ±1/2. The spacing between the doublets varies from 50 to 100 cm^{-1} depending on the actual crystal field.

2. EXPERIMENTAL

Solid solutions of the haloborates were prepared by the solid-solution method as described in [5]. The Ce^{3+} concentration in $Sr_2B_5O_9Br$ was varied from 0.05 to 1.0 mol %. We also studied samples codoped by K^+ and Na^+ ions to a concentration of 0.1 mol %. The ESR spectra were studied on a Bruker EPS300a ESR spectrometer in the *X* range (~9.5 GHz). The frequencies in the microwave range were measured with a Systron Donner meter.

3. RESULTS AND DISCUSSION

Figure 2 displays ESR spectra of $Sr_2B_5O_9Br : Ce^{3+}$, K^+ taken at 9 and 20 K. Both spectra exhibit a resonance at magnetic field B = 1578 G, which can be assigned to the presence of Fe^{3+} ions [6]. The narrow lines at B = 2035 and 2180 G, as well as the broad band at $B \approx 4380$ G, are clearly seen at 9 K but are absent at 20 K. It is known that Ce^{3+} ions are usually difficult to detect at temperatures above 30 K because of the strong spin–orbit coupling and the short relaxation time of the lower $4f^1$ state [7]. This gives us grounds to attribute these ESR lines to the Ce^{3+} centers.

The falloff in the 20-K ESR spectrum observed for $B > 2200$ G (Fig. 2) is due to the Ce^{3+} resonance being broadened as a result of spin–lattice relaxation. The nuclear spin of all stable Ce isotopes is zero, and, there-

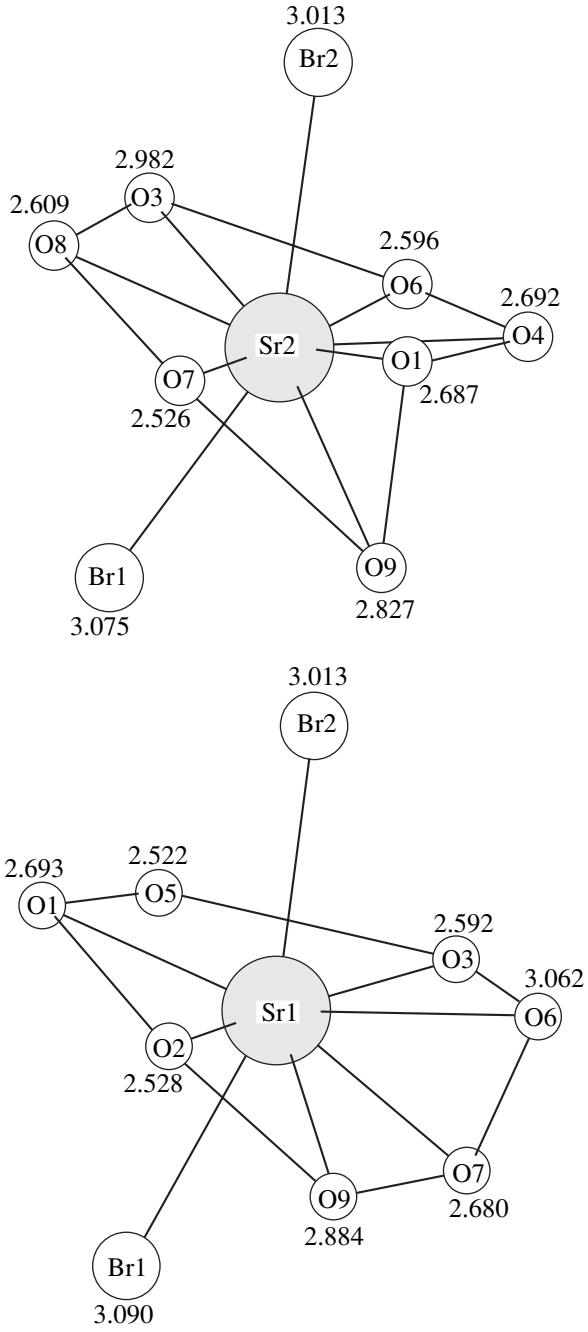

Fig. 1. Polyhedra of substituted strontium ions in two crystallographic positions. The number of surrounding oxygen and halogen ions in both cases is the same.

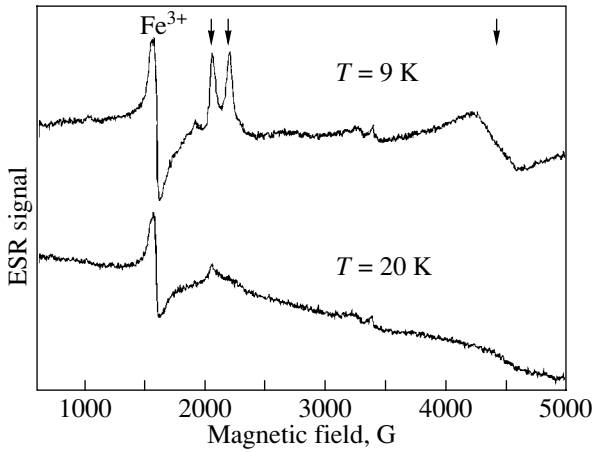

Fig. 2. ESR spectra of an $Sr_2B_5O_9Br$: (0.1 mol % Ce^{3+}, 0.1 mol % K^+) sample measured at 9 and 20 K. The arrows identify lines corresponding to Ce^{3+} centers.

fore, there is no hyperfine structure. The **g**-tensor components corresponding to the Ce^{3+} ions occupying low-symmetry crystallographic positions have been obtained earlier for $YAlO_3$ (3.162, 0.402, 0.395) [8], barium–strontium niobate (3.55, 0.89, 0.54) [9], and $LaCl_3$ (4.037, 0.23, 0.23) [10], i.e., for crystals where Ce^{3+} ions sit at sites with C_{3h} symmetry. For all these systems, the first component of the **g** tensor is considerably larger than the others. Because some components of the **g** tensor can be very small, the corresponding ESR lines may not fit within the span on the abscissa axis in Fig. 2. This suggests that the two narrow ESR lines in Fig. 2 are related to the first **g**-tensor components (with g_1 = 3.32, 3.16) of Ce^{3+} centers in the two different crystallographic positions shown in Fig. 1. The ESR lines corresponding to the second **g**-tensor component are indistinguishable for the different Ce^{3+} positions, and this accounts for the broad band with $g_2 \approx 1.54$.

The effect of cerium ion concentration on the ESR spectra of $Sr_2B_5O_9Br$: Ce^{3+} is illustrated in Fig. 3. The signals due to Ce^{3+} ions are seen to have approximately the same intensity for all the samples studied. An increase in Ce^{3+} content in the samples is accompanied by a corresponding increase in the ESR line intensity with g_1 of 3.32 and 3.16. This relation supports the conclusion that it is the Ce^{3+} ions that are responsible for these resonances. At the same time, a broad resonance line with $g \approx 3.6$ appears in the ESR spectra of samples with a high Ce^{3+} concentration at 9 K. This resonance is not observed at 20 K. As shown in [2], an increase in Ce^{3+} concentration brings about an increase in the contribution to the total intensity of luminescence due to Ce^{3+} centers with local charge compensation. At a low Ce^{3+} center concentration (0.05 mol %), there is no band with $g \approx 3.6$, which may indicate the presence of single Ce^{3+} centers only. The latter conjecture correlates with the results reported in [2]. Because the intensity of the ESR line with $g \approx 3.6$ grows with increasing Ce^{3+} center concentration, we can assign this line to the first **g**-tensor component with local Ce^{3+} charge compensation. As for the narrow ESR line in $Sr_2B_5O_9Br$: 1 mol % Ce^{3+} with $g \approx 3.94$, it can likewise be related to the Ce^{3+} centers.

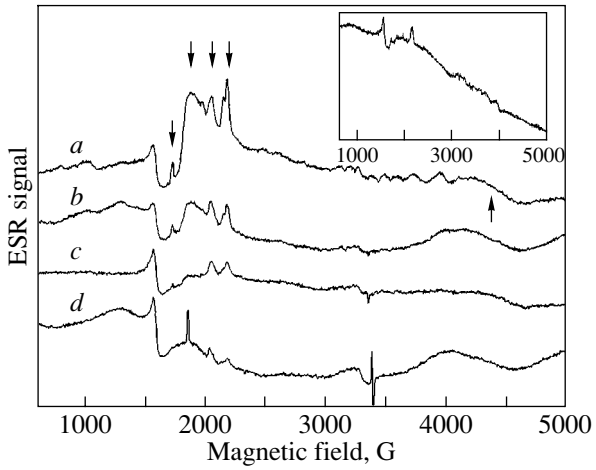

Fig. 3. ESR spectrum of $Sr_2B_5O_9Br$ samples with different impurity Ce^{3+} ion concentrations: (a) 1, (b) 0.5, (c) 0.2, and (d) 0.05 mol %. The spectra were measured at 9 K. The arrows identify lines corresponding to Ce^{3+} centers. The inset shows an ESR spectrum of an $Sr_2B_5O_9Br$: 1 mol % Ce^{3+} sample obtained at 30 K.

The formation of (Ce_{Sr}–K_{Sr}) complexes in the course of codoping $Sr_2B_5O_9Br$ by K^+ ions was considered in [5]. Adding a univalent cation enhances the solubility of Ce^{3+} ions in the matrix and does not require additional charge compensation. This is why the ESR spectrum of $Sr_2B_5O_9Br$: (Ce^{3+},K^+) consists only of the lines corresponding to the two Ce^{3+} crystallographic positions. The luminescence spectra of these Ce^{3+} centers are practically identical to those of single Ce^{3+} ions present in samples not subjected to codoping [2]. The values of the first **g**-tensor components of Ce^{3+} in these two cases are also similar. The small effect of the codopant (the K^+ ion) should be attributed either to the two neighboring Sr^{2+} ions being separated by B_2O_9 bridges or to the K^+ ions occupying the site adjacent to the Sr^{2+} position.

The ESR band with $g_1 \approx 3.6$ seen in samples that were not codoped is related to the Ce^{3+} centers whose charge is compensated by neighboring defects. This resonance is broader than that observed in the case of single Ce^{3+} centers. Our optical measurements did not succeed in resolving the 5*d* excitation level structure of the Ce^{3+} centers with compensated charge into individual components at 12 K. This implies that charge compensation may occur through more than one mechanism. Thus, the ESR band with $g_1 \approx 3.6$ and the long-wavelength optical emission band reported in [2] are actually superpositions of contributions due to several Ce^{3+} centers with different kinds of local charge compensation.

REFERENCES

1. A. V. Sidorenko, A. J. J. Bos, P. Dorenbos, *et al.*, Nucl. Instrum. Methods Phys. Res. A **486**, 160 (2002).
2. A. V. Sidorenko, A. J. J. Bos, P. Dorenbos, *et al.*, J. Phys.: Condens. Matter (in press).
3. K. Machida, T. Ishino, G. Adachi, and J. Shiokawa, J. Mater. Res. Bull. **14** (12), 1529 (1979).
4. R. D. Shanon, Acta Crystallogr. A **32**, 751 (1976).
5. V. P. Dotsenko, I. V. Berezovskaya, N. P. Efryushina, *et al.*, J. Lumin. **93** (2), 137 (2001).
6. A. Bishay, C. Quadros, and A. Piccini, Phys. Chem. Sol. **15**, 4 (1974).
7. A. Abragam and B. Bleaney, *Electron Paramagnetic Resonance of Transition Ions* (Clarendon, Oxford, 1970; Mir, Moscow, 1972).
8. H. R. Asatryan, J. Rosa, and J. A. Mares, Solid State Commun. **104** (1), 5 (1997).
9. J. Wingbermv̈hle, M. Meuer, O. F. Schirmer, *et al.*, J. Phys.: Condens. Matter **12**, 4277 (2000).
10. R. J. Birgeneau and M. T. Hutchings, Phys. Rev. **175** (3), 1116 (1968).

Translated by G. Skrebtsov

Physics of the Solid State, Vol. 45, No. 9, 2003, pp. 1679–1682. Translated from Fizika Tverdogo Tela, Vol. 45, No. 9, 2003, pp. 1600–1602.

DEFECTS, DISLOCATIONS, AND PHYSICS OF STRENGTH

Kinetics of Point Defects and Amorphization in Thin Films under Irradiation

I. A. Ovid'ko and A. B. Reĭzis

Institute of Problems in Machine Science, Russian Academy of Sciences, Vasil'evskiĭ ostrov, Bol'shoĭ pr. 61, St. Petersburg, 199178 Russia

e-mail: ovidko@def.ipme.ru

Received February 11, 2003

Abstract—A theoretical model is proposed for describing the evolution of an ensemble of point defects (vacancies and interstitial atoms) and its effect on the solid-phase amorphization in crystalline thin films under irradiation. Kinetic equations are derived for point defects in irradiated thin films in the absence of ion implantation. The temperature dependence of the radiation dose required for the onset of solid-phase amorphization is calculated using numerical solutions of the kinetic equations. The results obtained are compared with available experimental data. © *2003 MAIK "Nauka/Interperiodica".*

1. INTRODUCTION

Structural and phase transformations in solids under irradiation have been a subject of intensive investigation. Special interest has been expressed by researchers in radiation-induced amorphization (the crystal–glass phase transition) in initially crystalline solids [1–11], because this effect is of great technological importance. The radiation-induced amorphization is a multiparameter process, which, in particular, depends on the radiation dose, the nature and energy of incident particles, and the microstructure and chemical composition of irradiated solids. In this respect, the elucidation of the behavior of point defects that usually play a crucial role in radiation-induced amorphization is of particular interest for revealing the basic regularities in the amorphization.

The main objective of the present work was to construct a theoretical model describing the kinetics of an ensemble of point defects (vacancies and interstitial atoms) and its effect on the solid-phase amorphization in thin films under irradiation. Within the proposed model, we calculated the temperature dependence of the "dose of the onset of amorphization" (the radiation dose required for the onset of solid-phase amorphization) in irradiated films. The results obtained were compared with available experimental data [1] on the irradiation of an Al_2O_3 single-crystal film by Kr and Xe ions.

2. KINETICS OF AN ENSEMBLE OF VACANCIES AND INTERSTITIAL ATOMS IN IRRADIATED CRYSTALLINE FILMS

Let us consider a thin film exposed to irradiation by high-energy ions. In most cases, high-energy ions penetrate through thin films, which results in only a small number of implanted (under irradiation) ions [1]. Consequently, in this situation, the processes of amorphization in irradiated thin films substantially depend on the evolution of point defects, namely, vacancies and interstitial atoms, which are formed intensively under irradiation. Therefore, as a first approximation, we can restrict our consideration to the case of the evolution of the scalar densities of vacancies (ϕ) and interstitial atoms (ψ) in irradiated crystalline thin films.

Now, we analyze the behavior of point defects in irradiated films in terms of the kinetic theory of defects (see, for example, [12, 13]). According to the proposed model, the kinetics of an ensemble of point defects can be described by the following equations:

$$d\phi/dt = A - B\phi - C\phi\psi, \quad (1)$$

$$d\psi/dt = F - G\psi - C\phi\psi, \quad (2)$$

where t is the irradiation time and A, B, C, F, and G are positive time-independent parameters. The first term on the right-hand side of the kinetic equation (1) characterizes the generation of point defects under irradiation. The parameter A is defined as the rate (or intensity) of generation of point defects and is measured in units of dpa/s ("inelastic displacements per atom per second"), and the parameter $F = \alpha A$, where the coefficient $\alpha = 0.7$ accounts for the decrease in the density of just knocked-on interstitial atoms due to their sputtering (knocking out of the film).

The second term on the right-hand side of kinetic equation (1) accounts for the decrease in the density ϕ of migrating vacancies due to their escape from the bulk to the free surface of the film. In this case, the model parameter B is determined to be $B \approx 1/\tau_v^*$, where τ_v^* is the mean lifetime of a vacancy in the model situation where migrating vacancies are eliminated exclu-

1063-7834/03/4509-1679$24.00

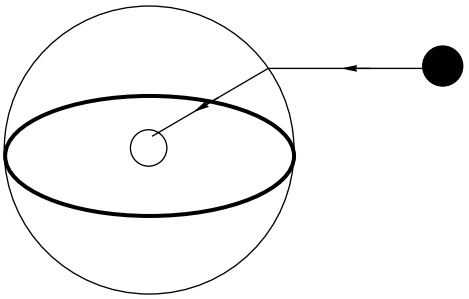

Fig. 1. A migrating interstitial atom (closed circle) and a vacancy (open circle) with the capture region (sphere of radius r).

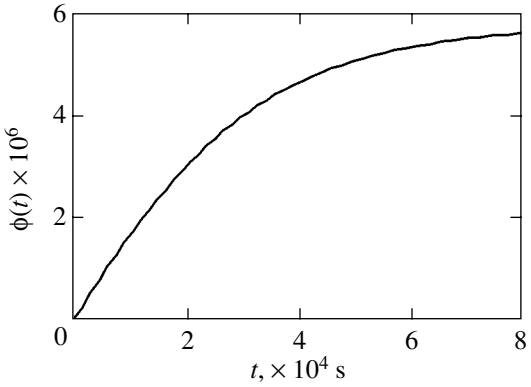

Fig. 2. Dependence $\phi(t)$.

sively through their escape from the bulk to the free surface. Similarly, the term $-G\psi$ in kinetic equation (2) characterizes the decrease in the density ψ of migrating interstitial atoms. In this equation, the model parameter G is estimated as $G \approx 1/\tau_i^*$, where τ_i^* is the mean lifetime of an interstitial atom. In the general case, we have the mean lifetime of the vacancy $\tau_v^* \approx l^*/\langle V_v \rangle$ and the mean lifetime of the interstitial atom $\tau_i^* \approx l^*/\langle V_i \rangle$, where l^* is the mean free path of the point defect and $\langle V_v \rangle$ and $\langle V_i \rangle$ are the mean velocities of migration of vacancies and interstitial atoms in the model situation, respectively. According to Vladimirov [14], the mean velocities of migration of point defects and the temperature T are related by the expressions

$$V_v = \tilde{V}\exp(-\varepsilon_{mv}/kT) \quad (3)$$

and

$$V_i = \tilde{V}\exp(-\varepsilon_{mi}/kT). \quad (4)$$

Here, $\tilde{V}$ is the velocity of migration of point defects at $T = 0$ K; ε_{mv} and ε_{mi} are the migration activation energies of the vacancy and the interstitial atom, respectively; and k is the Boltzmann constant. The mean free path l^* is assumed to be identical for the vacancies and interstitial atoms and, in the case of a single-crystal film is approximately equal to $3/2h$, where h is the film thickness.

The third term on the right-hand side of kinetic equations (1) and (2) describes the annihilation of the vacancies and interstitial atoms. In order to determine the dependence of the parameter C on the structural characteristics of the irradiated thin film, we consider a model situation in which point defects are eliminated exclusively due to their annihilation. Since the mean velocity of migration V_v of vacancies in this case is substantially less than the mean velocity of migration V_i of interstitial atoms (see, for example, [14]), it is assumed that the interstitial atoms are mobile point defects which collide with immobile vacancies when migrating over the crystal. Each collision leads to the annihilation of the vacancy and the interstitial atom. Within this approach, each vacancy is characterized by the so-called capture region, i.e., a spherical region of radius r (with the center at the vacancy position) where a migrating interstitial atom is attracted to the vacancy due to elastic interaction (Fig. 1), which is accompanied by their annihilation.

In the model situation under consideration, each annihilation event results in the elimination of a single vacancy and a single interstitial atom. Therefore, in each of the kinetic equations (1) and (2), the term characterizing the decrease in the density of point defects due to the annihilation can be represented as $-(\psi/\tau)$, where ψ is the density of interstitial atoms and τ is the mean lifetime of an interstitial atom. In turn, the mean lifetime of an interstitial atom is determined to be $\tau \approx l/V_i$, where l is the mean free path of the interstitial atom and V_i is the mean velocity of the interstitial atom. According to the concept of capture regions near the vacancies (Fig. 1), the mean free path of a migrating interstitial atom can be estimated as $l \approx 1/\pi r^2\phi$, where πr^2 is the capture area of a single vacancy and ϕ is the density of vacancies (and, consequently, capture regions) in the ensemble. On this basis, the model parameter C can be represented by the expression

$$C \approx \tilde{V}\pi r^2 \exp(-\varepsilon_{mi}/kT). \quad (5)$$

Let us return to the analysis of the kinetic equations (1) and (2). The solutions to these equations can be obtained only numerically. In this case, we use the initial conditions [15]:

$$\phi_0 \approx \rho\exp(-27T_m/T), \quad (6)$$

$$\psi_0 \approx \rho\exp(-9T_m/T), \quad (7)$$

where ρ is the density of atoms in the crystal and T_m is the melting temperature. Figure 2 depicts a typical curve $\phi(t)$, which was obtained from formulas (1)–(7) for the following parameters: $\varepsilon_{mi} \approx 4kT_m$, $\varepsilon_{mv} \approx 8kT_m$,

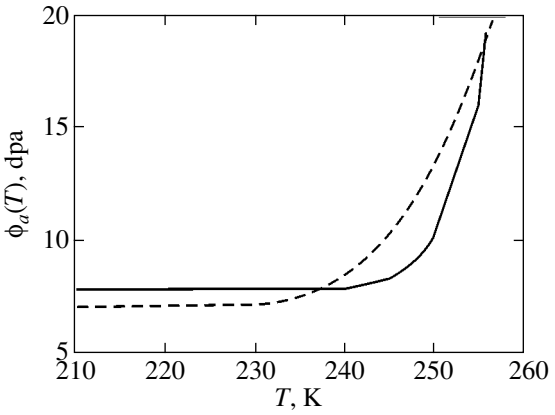

Fig. 3. Theoretical (solid line) and experimental (dashed line) temperature dependences of the dose of the onset of amorphization $\phi_a(T)$.

$r \approx 3a$ ($a = 3 \times 10^{-10}$ m), $\tilde{V} \approx n_k \omega_0 a \approx 3 \times 10^3$ ($n_k = 10$, $\omega_0 = 10^{12}$ s^{-1}) [14], $\rho = 1.17 \times 10^{29}$, $T \approx 0.2T_m$, $A = 0.0017$ dpa/s [1], and the film thickness (corresponding to the experiment performed in [1]) $h \approx 100$ nm.

3. TEMPERATURE DEPENDENCE OF THE DOSE OF THE ONSET OF AMORPHIZATION

Now, we elucidate the role played by point defects in radiation-induced amorphization. The accumulation of point defects in the irradiated crystal is accompanied by an increase in the density of the free energy (or another relevant thermodynamic potential) of the crystal phase. According to [9, 16–19], the nucleation of the amorphous phase (the crystal–glass phase transition) under irradiation and other actions takes place when the free energy density of the crystal phase with defects is comparable to the difference ε_{a-c} between the energy densities of the amorphous phase and defect-free crystal phase. In our case, the onset of the amorphization in the irradiated film with point defects is determined by the condition

$$\phi\varepsilon_v + \psi\varepsilon_i = \varepsilon_{a-c}. \quad (8)$$

According to Friedel [20], we can write $\varepsilon_v = Ga^3/2$ and $\varepsilon_i = 3Ga^3$, where G is the shear modulus. In the case when the initial density of point defects is not very high, we obtain $\varepsilon_{a-c} \approx G/83 - G/63$ [21].

Within the proposed model, we calculated the temperature dependence of the dose required for the onset of the amorphization, i.e., the quantity frequently measured in experiments on radiation-induced amorphization (see, for example, [1]). In our interpretation, the dose required for the onset of the amorphization is determined as the density $\phi_a = At_a$ of vacancies nucleated in the crystalline film under irradiation during the period of irradiation $[0, t_a]$, where t_a is the instant of the onset of amorphization. Note that t_a can be approximately determined from condition (8) at $t = t_a$.

Figure 3 shows the temperature dependence of the dose of the onset of amorphization $\phi(T)$, which was numerically calculated according to formulas (1)–(8) for an Al_2O_3 single-crystal film irradiated with Kr and Xe ions at energies of 600 and 900 keV, respectively. In the experiment, the film thickness was equal to 100 nm, the ion flux was 10^{18} m^{-2} s^{-1}, and the irradiation temperature ranged from 90 to 300 K. The dependences $\phi(T)$ calculated in the framework of the theoretical model are in reasonable quantitative agreement with the experimental dependence $\phi_a(T)$ obtained in [1] for an Al_2O_3 film exposed to irradiation (Fig. 3).

4. CONCLUSIONS

Thus, we obtained a theoretical description of the influence of three basic processes (generation of point defects under irradiation, annihilation of point defects, and escape of point defects from the bulk to the free surface of the film) on the evolution of an ensemble of point defects, namely, vacancies and interstitial atoms, and on the solid-phase amorphization in irradiated thin films. The solution to kinetic equations (1) and (2), which account for the aforementioned processes, provides the basis for the calculation of the dose necessary for the onset of the amorphization (a quantity measured in the experiments). The temperature dependence of the dose of the onset of amorphization, which was calculated in the framework of the model proposed in this work, is in satisfactory quantitative agreement with the experimental data [1] obtained for Al_2O_3 films under irradiation.

ACKNOWLEDGMENTS

This work was supported in part by the Russian Foundation for Basic Research (project no. 01-02-16853) and by the Russian Federal Program “Integration” (project no. B0026).

REFERENCES

1. H. Abe, Sh. Yamamoto, and H. Naramoto, Nucl. Instrum. Methods Phys. Res. B **127/128**, 170 (1997).
2. V. A. Skuratov, A. E. Efimov, and D. L. Zagorskiĭ, Fiz. Tverd. Tela (St. Petersburg) **44** (1), 165 (2002) [Phys. Solid State **44**, 171 (2002)].
3. V. R. Galakhov, D. A. Zatsepin, L. V. Elokhina, *et al.*, Fiz. Tverd. Tela (St. Petersburg) **44** (7), 1318 (2002) [Phys. Solid State **44**, 1380 (2002)].
4. F. Banhart, Fiz. Tverd. Tela (St. Petersburg) **44** (3), 388 (2002) [Phys. Solid State **44**, 399 (2002)].
5. D. Pacifici, E. C. Moriera, G. Franzo, *et al.*, Phys. Rev. B **65** (14), 144109 (2002).
6. J. Yamasaki, Seiji Takeda, and K. Tsuda, Phys. Rev. B **65** (11), 115213 (2002).

7. S. X. Wang, L. M. Wang, and R. C. Ewing, Phys. Rev. B **63**, 024105 (2001).
8. A. Meldrum, L. A. Boatner, and R. C. Ewing, Phys. Rev. Lett. **88** (2), 025503 (2002).
9. D. F. Pedraza, J. Less-Common Met. **140**, 219 (1988).
10. M. Rose, G. Gorzawski, G. Miehe, *et al.*, Nanostruct. Mater. **6**, 731 (1995).
11. M. Rose, A. G. Balogh, and H. Hahn, Nucl. Instrum. Methods Phys. Res., Sect. B **127/128**, 119 (1997).
12. G. A. Malygin, Usp. Fiz. Nauk **169** (9), 979 (1999) [Phys. Usp. **42**, 887 (1999)].
13. G. A. Malygin, Fiz. Tverd. Tela (St. Petersburg) **44** (11), 1979 (2002) [Phys. Solid State **44**, 2072 (2002)].
14. V. I. Vladimirov, *Physical Theory of Plasticity and Strength*, Part 2: *Point Defects: Hardening and Recovery* (Leningr. Politekh. Inst., Leningrad, 1975).
15. Yu. V. Trushin, *Physical Fundamentals of Radiative Materials Science* (St. Petersburg Gos. Tekh. Univ., St. Petersburg, 1998).
16. I. A. Ovid'ko and A. B. Reĭzis, Neorg. Mater. **35** (6), 766 (1999).
17. I. A. Ovid'ko and A. B. Reizis, J. Phys. D **32** (22), 2833 (1999).
18. M. Yu. Gutkin and I. A. Ovid'ko, *Defects and Mechanisms of Plasticity in Nanocrystalline and Non-Crystalline Materials* (Yanus, St. Petersburg, 2001).
19. M. Yu. Gutkin and I. A. Ovid'ko, Phys. Rev. B **63** (6), 064515 (2001).
20. J. Friedel, *Dislocations* (Pergamon, Oxford, 1964; Mir, Moscow, 1967).
21. R. G. Morris, J. Appl. Phys. **50** (10), 3250 (1979).

Translated by O. Moskalev

Physics of the Solid State, Vol. 45, No. 9, 2003, pp. 1683–1687. Translated from Fizika Tverdogo Tela, Vol. 45, No. 9, 2003, pp. 1603–1607.

DEFECTS, DISLOCATIONS, AND PHYSICS OF STRENGTH

Electrically Stimulated Motion of Dislocations in a Constant Magnetic Field

A. A. Skvortsov, L. I. Gonchar, and A. M. Orlov

Ul'yanovsk State University, Ul'yanovsk, 432970 Russia

e-mail: scvor@sv.uven.ru

Received October 18, 2002; in final form, January 9, 2003

Abstract—This paper reports on the results of investigations into the dislocation mobility in *n*-Si single crystals ($N_d = 5 \times 10^{24}$ m^{-3}) upon simultaneous exposure to electric ($j = 3 \times 10^5$ A/m^2) and magnetic ($B \le 1$ T) fields. It is found that the introduction of dislocations ($\approx 10^9$ m^{-2}) into dislocation-free silicon doped with phosphorus leads to the appearance of the paramagnetic component of the magnetic susceptibility. The paramagnetic component increases with an increase in the dopant concentration. Similar transformations in silicon account for the formation of magnetically sensitive impurity stoppers that respond to external magnetic perturbations. An analysis of the behavior of dislocations in electric and magnetic fields has revealed a parabolic dependence of the dislocation path length on the magnetic induction *B*. The effective charges and mobilities of dislocations are numerically calculated from the results obtained. A model is proposed according to which the observed increase in the dislocation mobility is associated with the decrease in the retarding power of magnetically sensitive stoppers due to a local change in the magnetic characteristics of the material and the spin-dependent reactions stimulated by a magnetic field. © *2003 MAIK "Nauka/Interperiodica".*

1. INTRODUCTION

It is known that dislocations in a semiconductor crystal are electrically active and can lead to substantial changes in the electrical parameters of the crystal [1, 2]. The interaction of dislocations with impurity atoms of doped semiconductors results in the formation of impurity atmospheres in the vicinity of dislocation cores [3, 4]. These regions affect the behavior of structural defects exposed to different disturbing fields. In this respect, it is of particular interest to investigate the influence of magnetic fields on the electric field–stimulated motion of dislocations. This problem, as applied to ionic crystals, has been intensively studied in recent years [5–10]. However, information on the magnetically stimulated behavior of linear defects in elemental semiconductors with impurity atoms is lacking.

2. EXPERIMENTAL TECHNIQUE

The experimental investigation of the above problem was performed using phosphorus-doped dislocation-free single-crystal silicon samples with the [111] orientation ($N_d = 5 \times 10^{24}$ m^{-3}). Dislocations were introduced through plastic deformation of the silicon sample ($4 \times 10^{-2} \times 1 \times 10^{-2} \times 4 \times 10^{-4}$ m) according to the three-support bending method with a bending deflection of 1 mm at a temperature of 1273 K for 25 min. Dislocations were revealed from etch pits formed after the treatment of deformed samples in the etching solution $HNO_3 : HF : CH_3COOH$ (glacial) = 5 : 3 : 3 (in volume) for 35 s. The mean density ρ of introduced dislocations was equal to 10^9 m^{-2}. As was shown in our previous work [11], a similar bending initiates primarily edge dislocations.

In the experiments, a direct current ($j = 3 \times 10^5$ A/m^2) was passed through each sample along the [110] direction with simultaneous exposure to a dc magnetic field (up to 1 T), which was accompanied by heating of the sample to 323 K. In this case, the magnetic induction vector was aligned parallel to the sample plane and perpendicular to the direction of the electric current. The mobility of dislocations in the samples exposed to electric and magnetic fields simultaneously was evaluated by measuring their path lengths according to the standard technique of double chemical etching. The positions of etch pits prior to and after the experiment were determined using an MII-4 microscope (magnification, ×450).

From the results of measurements, we constructed the histograms of dislocation path lengths $n/N(l)$, where n is the number of dislocations traversing a distance l and N is the total number of detected defects (Figs. 1, 2). The dependence of the mean-statistic path length l on the magnetic induction B was processed using regression analysis. The results obtained demonstrated that the least variance can be achieved for the relationship $l \sim f(\sqrt{B})$. It was found that the treatment in a magnetic field at $B = 1$ T brings about an approximately 40-fold increase in the velocity of moving dislocations in silicon in an electric field at a current density of 3×10^5 A/m^2 (Fig. 3). This effect can be explained by a change in the retarding power of impu-

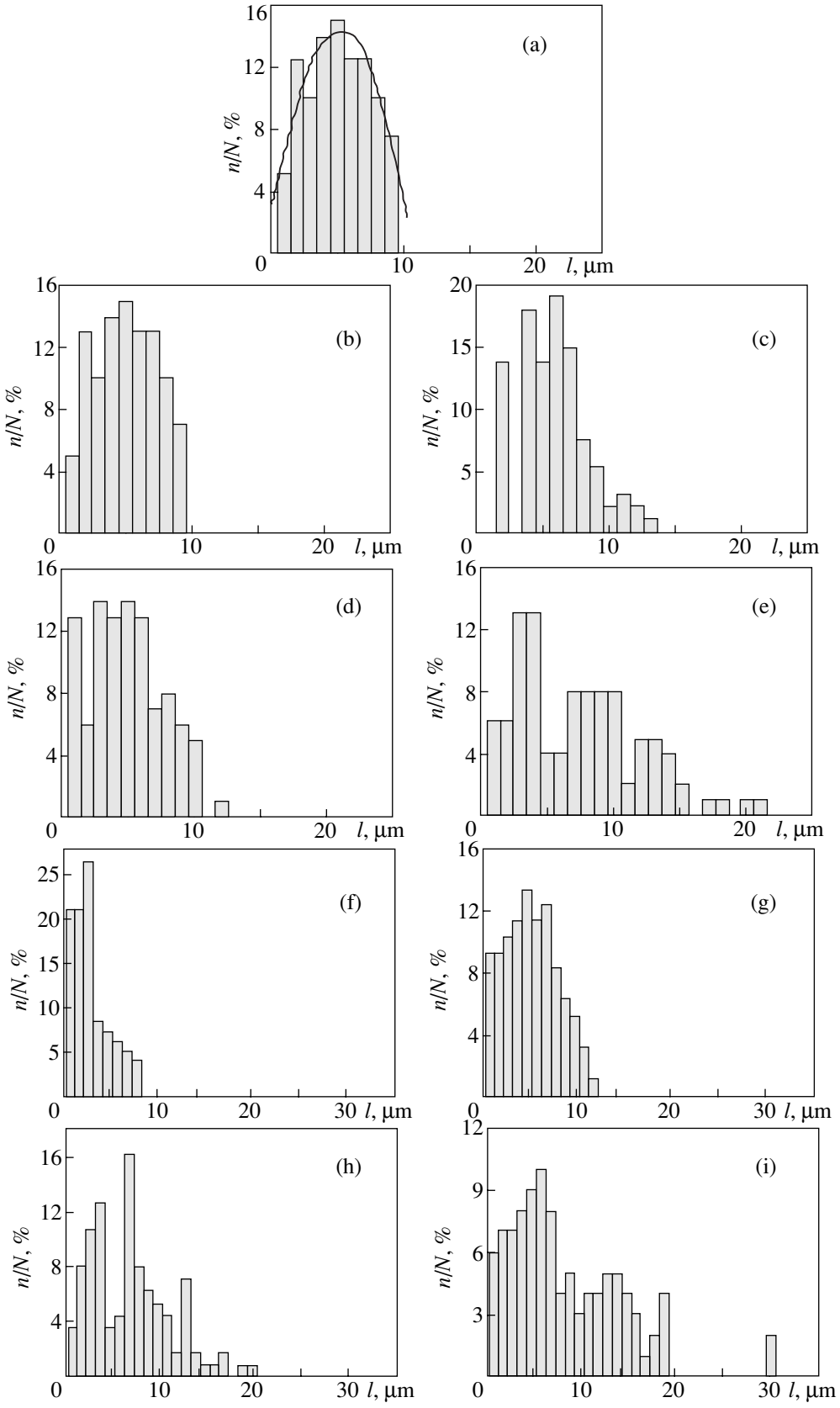

Fig. 1. Histograms of the distribution of dislocations over path lengths after electric treatment ($j = 3 \times 10^5$ A/m^2, $T = 380$ K) of *n*-Si single crystals (0.01 Ω cm): (a) 48-h electric treatment without a magnetic field (the solid line indicates the normal distribution of dislocation path lengths), (b–e) 60-min electric treatment in a magnetic field, and (f–i) 120-min electric treatment in a magnetic field at B = (b, f) 0.3, (c, g) 0.5, (d, h) 0.8, and (e, i) 1 T.

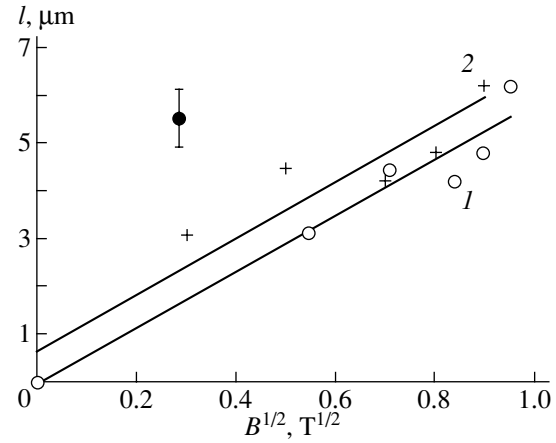

Fig. 2. Field dependences of the dislocation path length in *n*-Si for electrically stimulated motion of dislocations ($j = 3 \times 10^5$ A/m^2, $T = 380$ K) in a magnetic field. Electric treatment time: (*1*) 60 and (*2*) 120 min.

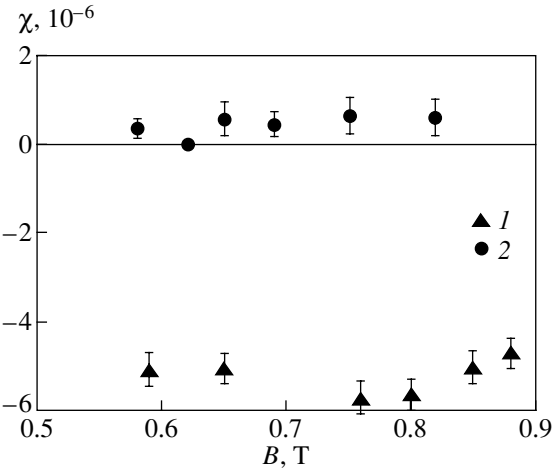

Fig. 3. Field dependences of the magnetic susceptibility of *n*-Si ($N_d = 6 \times 10^{24}$ m^{-3}) at ρ = (*1*) 0 and (*2*) 10^9 m^{-2}.

rity stoppers that hold dislocations in an equilibrium state. In actual fact, the electrical and magnetic properties of defect regions in the vicinity of the dislocation core differ significantly from those of undisturbed regions of the crystal. This is confirmed by the data available in the literature [12] and the results of our measurements of the magnetic susceptibility χ prior to and after the introduction of dislocations.

The magnetic susceptibility was measured by the force *F* acting on the sample in a magnetic field according to the Gouy method [13]. The magnetic susceptibility of the sample studied was calculated from the expression

$$\chi = 2F\mu_0/[s(B_2^2 - B_1^2)],$$

where B_1 and B_2 are the magnetic inductions at the end points of the sample and *s* is the area of the sample face.

Under the condition $B_1 \ll B_2$ and by ignoring the effect of the geomagnetic field, the magnetic susceptibility can be determined, to sufficient accuracy, from the relationship

$$\chi = 2F\mu_0/[sB^2].$$

3. RESULTS AND DISCUSSION

An analysis of the experimental results demonstrated that the introduction of a large amount of dislocations (≈10^9 m^{-2}) into the sample substantially affects its magnetic characteristics and the observed change in the magnetic susceptibility $\Delta\chi = 5.5 \times 10^{-6}$ is of paramagnetic nature (Fig. 4).

It is obvious that the magnetic susceptibility of doped silicon is determined by the following main susceptibility components:

$$\chi = \chi_{Si} + \chi_p + \chi_e + \chi_{def},$$

where χ_{Si} and χ_p are the atomic susceptibilities of pure silicon and an impurity, respectively, and χ_e and χ_{def} are the electronic and structural components [12] of the magnetic susceptibility, respectively.

The introduction of dislocations leads to a redistribution of impurities in the crystal. A region with strongly disturbed ordering is formed around the dislocation core. As a result, charge carriers are redistributed among the conduction band, the donor level, and the dislocation level. The degree of this redistribution can be determined from the factor of filling of dangling bonds of dislocations with electrons [14]; that is,

$$f = \frac{a\varepsilon_0\varepsilon E_t}{3e^2}\ln^{-1}\left(\frac{0.163\varepsilon_0\varepsilon E_t}{e^2 N_d^{1/3}}\right) = 0.12,$$

where *a* is the lattice parameter (*m*), ε_0 is the permittivity of free space (F/m), ε is the permittivity of the material, $E_t = 0.4$ eV is the energy at the dislocation level in the band gap, and *e* is the elementary charge (C).

For the densities of dislocations used, their filling with electrons cannot be considered the dominant mechanism responsible for the change in the magnetic susceptibility. Apparently, the increased magnetic susceptibility of the material in the bulk of a dislocation pipe is associated with closely spaced magnetic impurity centers that are coupled through a strong exchange interaction. In turn, this interaction can lead to the formation of new clusters with large magnetic moments. The region in the vicinity of the dislocation core can be treated as a system in which clusters consisting of 10^6–10^9 atoms, rather than individual paramagnetic ions,

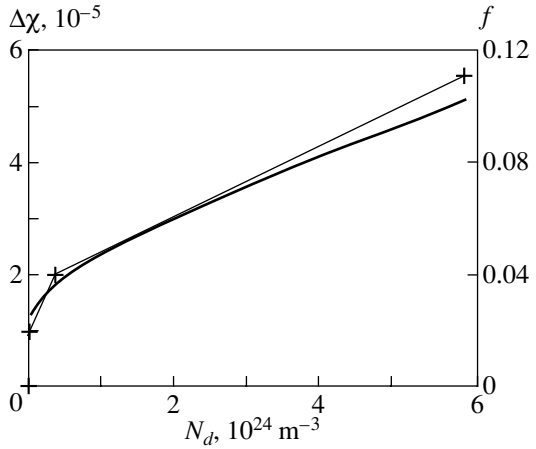

Fig. 4. Concentration dependence of the change in the magnetic susceptibility (thin line) and the factor f of filling of dangling bonds of dislocations with electrons (thick line) for n-Si. The mean density of dislocations in the samples is 10^9 m^{-2}.

play the role of elementary units responsible for the magnetic properties. These clusters behave like paramagnetic inclusions dissolved in the diamagnetic matrix [14].

The change in the magnetic susceptibility due to the introduction of dislocations is more pronounced in the samples with a higher impurity concentration. For example, the magnetic susceptibility remains unchanged at a phosphorus concentration of 3×10^{21} m^{-3}. As the dopant concentration increases, the paramagnetic contribution of dislocation regions increases and becomes equal to 1.9×10^{-5} at a dopant concentration of 6×10^{24} m^{-3} (Fig. 4).

One more reason for the large paramagnetic contribution can be associated with the uncompensated electron spins localized at dangling bonds within each unit cell of the dislocation core. These spin moments are oriented in an external magnetic field. As a consequence, there arises magnetization aligned antiparallel to the field. An increase in N_d leads to a decrease in the number of unpaired electrons at dangling bonds. This results in an increase in the paramagnetic contribution to the susceptibility of the deformed sample. In weak magnetic fields, the above magnetization can be determined as

$$J = \chi H = \chi \frac{B}{\mu_0} = 4.38B.$$

It is characteristic that the magnetic susceptibility χ within a disordered region of the dislocation core can substantially exceed the volume-averaged susceptibility [15, 16]. An increased local magnetization of the material can lead to a change in the energy in the region of the dislocation core. At $B = 1$ T, the density of the magnetic field energy is determined to be $\omega = 4 \times 10^5$ J/m^3. Taking into account that the dislocation length is approximately equal to 0.01 m and the dislocation pipe radius is of the order of 2 nm, we obtain the energy of the magnetic field localized in the region of the dislocation core $W = \omega\pi r^2 L = 5 \times 10^{-14}$ J and the energy of the magnetic field localized in the region of one dangling bond $W = 5 \times 10^{-21}$ J. It is clear that the energy W is too low to reduce the Peierls barrier but can appear to be sufficient for initiating the previously forbidden transitions in a dislocation core–stopper system. The probability of breaking the structural bond pinning the dislocation depends on the multiplicity of the electron pair forming this bond, i.e., on the polarization of the "dislocation core–stopper" spin chain. The magnetic field stimulates the evolution of the spin state in the paramagnetic center–dislocation system, which is completed by removing the forbiddenness from a particular electron transition. As a result, the configuration of covalent bonds in the region of the dislocation core undergoes a transformation, which leads to an increase in the probability of depinning the dislocation from the stopper and its motion in the field of internal stresses of the crystal. In this case, the total energy of the system remains virtually unchanged. Similar effects are caused by the spin selectivity of the transitions under investigation and reactions of structural defects.

The effect of the magnetic field on the ability of a dislocation to be displaced from an equilibrium position in response to the current passing through the sample was quantitatively evaluated from the effective dislocation charge eZ_{eff}. This quantity characterizes the electrostatic interaction forces and the drag of dislocations by charge carriers.

The resultant force that determines the velocity v of a moving linear defect can be described by the relationship [17]

$$F = Z_{\text{eff}} N_{\text{at}} E - \frac{\pi c_0 \gamma L}{2 D_d kT} v \ln \frac{v r_0}{D_d}. \quad (1)$$

Here, L is the dislocation length, D_d is the diffusion coefficient of atoms in the Cottrell cloud, c_0 is the equilibrium impurity concentration in the defect-free region of the crystal, γ is the dimensional constant, v is the dislocation velocity, N_{at} is the number of atoms lying along the dislocation line, eZ_{eff} is the effective dislocation charge, r_0 is the characteristic size of the impurity atmosphere, and E is the electric field strength in the sample.

The velocity of a moving dislocation under the action of the constant force F can represented by the standard equation

$$v = \frac{D_d}{kT} F. \quad (2)$$

By using relationships (1) and (2) and the experimental values of $D_d = 3.2 \times 10^{-18}$ m^2/s, $r_0 = 2 \times 10^{-9}$ m [12], $L = 0.01$ m, $\gamma = 10^{-63}$ (J m)^2, and $N_d = 10^{24}$ m^{-3}, we calculated the effective charges Z_{eff} and the electric field–

Velocities of moving dislocations in a dc electric field and their effective charges in different magnetic fields (motion toward the anode)

B, T	V, m/s	Z_{eff}, 1/atom	μ_e, cm^2/(V s)
0	5×10^{-11}	0.002	2.1×10^{-13}
0.3	6.4×10^{-11}	0.015	2.7×10^{-12}
0.5	9.8×10^{-10}	0.019	4.1×10^{-12}
0.8	1.3×10^{-9}	0.02	5.1×10^{-12}
1.0	1.5×10^{-9}	0.021	6.3×10^{-12}

stimulated mobilities of dislocations at different values of the magnetic induction (see table).

The passage of electric current through the crystal is attended by displacement of the dislocation or its segment from an equilibrium position to the adjacent metastable position with diffusion drag of impurity atoms to new positions toward the positive electrode. The diffusion of impurity atoms is the controlled stage of motion of the impurity cloud–dislocation system [17]. Note that the distribution of dislocations over path lengths is described by a Gaussian function [17].

The electrically stimulated motion of dislocations in a dc magnetic field leads to a change in the distribution of dislocations over path lengths and the appearance of a clearly defined tail (Fig. 1). Moreover, it can be seen from the histograms that, with an increase in the magnetic induction B, the path lengths of a number of dislocations (≈2%) become larger than those of the main bulk of dislocations. This indicates that dislocations of different types (for example, dislocations with edge and screw components predominating) are involved in the electrically stimulated motion and that the dc magnetic field has an anisotropic effect on these dislocations.

4. CONCLUSIONS

Thus, we investigated the electrically stimulated motion of dislocations in silicon in a dc magnetic field at room temperature. It was found that the mobility of linear defects substantially increases upon electric treatment (at $j = 3 \times 10^5$ A/m^2) of the samples in a dc magnetic field (at $B = 1$ T). The magnetic susceptibility was measured in dislocation-containing and dislocation-free samples. It was shown that regions with disturbed ordering strongly affect the magnetic properties of the crystal.

REFERENCES

1. T. Suzuki, H. Yosinaga, and S. Takeucti, *Dislocation Dynamics and Plasticity* (Syokabo, Tokyo, 1986; Mir, Moscow, 1989).
2. V. B. Shikin and Yu. V. Shikina, Usp. Fiz. Nauk **165** (8), 887 (1995) [Phys. Usp. **38**, 845 (1995)].
3. J. P. Hirth and J. Lothe, *Theory of Dislocations* (McGraw-Hill, New York, 1967; Atomizdat, Moscow, 1972).
4. N. K. Nechvolod, *Creep of Crystalline Materials at Low Temperatures* (Vysshaya Shkola, Kiev, 1980).
5. Yu. I. Golovin and R. B. Morgunov, Zh. Éksp. Teor. Fiz. **115** (2), 605 (1999) [JETP **88**, 332 (1999)].
6. V. I. Al'shits, E. V. Darinskaya, and O. L. Kazakova, Zh. Éksp. Teor. Fiz. **111** (2), 615 (1997) [JETP **84**, 338 (1997)].
7. Yu. I. Golovin and R. B. Morgunov, Fiz. Tverd. Tela (St. Petersburg) **40** (11), 2065 (1998) [Phys. Solid State **40**, 1870 (1998)].
8. Yu. I. Golovin and R. B. Morgunov, Fiz. Tverd. Tela (St. Petersburg) **39** (4), 630 (1997) [Phys. Solid State **39**, 550 (1997)].
9. Yu. I. Golovin and R. B. Morgunov, Pis'ma Zh. Éksp. Teor. Fiz. **58** (3), 189 (1993) [JETP Lett. **58**, 191 (1993)].
10. A. A. Urusovskaya, V. I. Al'shits, and N. N. Bekkauér, Fiz. Tverd. Tela (St. Petersburg) **42** (2), 267 (2000) [Phys. Solid State **42**, 274 (2000)].
11. A. A. Skvortsov, A. M. Orlov, and A. A. Solov'ev, Fiz. Tverd. Tela (St. Petersburg) **43** (4), 616 (2001) [Phys. Solid State **43**, 640 (2001)].
12. S. V. Vonsovskiĭ, *Magnetism* (Nauka, Moscow, 1971; Wiley, New York, 1974).
13. V. G. Antonov, L. M. Petrov, and A. P. Shchelkin, *Instruments for Measurement of Magnetic Parameters of Materials* (Énergoatomizdat, Leningrad, 1986).
14. I. V. Aleksandrov, *Theory of Magnetic Relaxation* (Nauka, Moscow, 1975).
15. V. I. Al'shits, E. V. Darinskaya, and T. M. Perekalina, Fiz. Tverd. Tela (Leningrad) **29** (2), 467 (1987) [Sov. Phys. Solid State **29**, 265 (1987)].
16. P. C. Tripathy and T. N. Sahu, Semicond. Sci. Technol. **10** (4), 447 (1995).
17. A. A. Skvortsov, A. M. Orlov, V. A. Frolov, and A. A. Solov'ev, Fiz. Tverd. Tela (St. Petersburg) **42** (11), 1998 (2000) [Phys. Solid State **42**, 2054 (2000)].

Translated by O. Borovik-Romanova

Physics of the Solid State, Vol. 45, No. 9, 2003, pp. 1688–1693. Translated from Fizika Tverdogo Tela, Vol. 45, No. 9, 2003, pp. 1608–1613.

DEFECTS, DISLOCATIONS, AND PHYSICS OF STRENGTH

Effect of the Electric Fields of Immobile Dislocations on Photoluminescence and EPR in Deformed ZnS Crystals

S. A. Omel'chenko, M. F. Bulanyĭ, and O. V. Khmelenko

Dnepropetrovsk National University, pr. Gagarina 72, Dnepropetrovsk, 49050 Ukraine

e-mail: bulanyi@mail.dsu.dp.ua

Received August 22, 2002; in final form, February 7, 2003

Abstract—The influence of the electric fields of immobile growth dislocations on the luminescence properties of deformed zinc sulfide crystals is considered. Variations in the photoluminescence and EPR spectra with plastic deformation of ZnS crystals are shown to be caused by an increase in the radius of Read cylinders during the breakaway of growth dislocations from Cottrell atmospheres. *© 2003 MAIK "Nauka/Interperiodica".*

1. INTRODUCTION

Since plastic deformation of crystals is accompanied by many processes, the mechanisms of its effect on the electrical and optical properties of crystals can be diverse. Therefore, it is difficult to reveal the nature of the deformation-induced changes in the luminescence properties of ZnS crystals described in this work. Apart from the factors common to all materials, we have to take into account factors peculiar to zinc sulfide. For example, the initial structure of microtwins and polytypes in ZnS crystals is known to transform into the sphalerite structure as a result of the motion of partial dislocations during plastic deformation [1, 2]. Of course, it is important to take into account this factor when analyzing changes in all structure-sensitive properties. Moreover, dislocations moving upon plastic deformation in ZnS crystals were shown to have a negative electric charge; therefore, there is a strong interaction between the dislocation and electronic subsystems [3–5]. Immobile dislocations in zinc sulfide crystals were also found to generate electric fields that can ionize impurity centers [6]. However, the effect of these fields on recombination processes has not been taken into account.

To reveal the main causes of changes in the luminescence properties of ZnS : Mn and ZnS : Fe crystals that are produced by plastic deformation and recorded after the completion of deformation, we used electron paramagnetic resonance (EPR) alongside optical measurements. The choice of the impurities is obviously optimum, since they are convenient paramagnetic probes for EPR studies and, in addition, well-known centers of intracenter (manganese) and recombination luminescence (iron).

2. EXPERIMENTAL

We studied ZnS single crystals grown from melt by using the Bridgman technique at an inert-gas pressure of 150 atm. Manganese (5×10^{-1} at. %) and iron (10^{-2} at. %) impurities were introduced in the crystals in the course of their growth.

Specimens $2 \times 2 \times 4$ mm in size were cut from the single crystals, and their surfaces were polished with a diamond polishing paste. The $(111)_s$ slip plane that was active during deformation was at an angle of 45° to the deforming stress. Deformation was carried out at a constant rate of $\sim 2 \times 10^{-5}$ m/s and a temperature of 400 K. For this geometry and under these loading conditions, partial dislocations are known to move in the basal plane of ZnS crystals [1, 2]. EPR and photoluminescence (PL) spectra were recorded after each deformation act, and the conditions of deformation were identical for all experiments.

EPR spectra were recorded on an SE/X-2543 RADIOPAN spectrometer in the *X* range. Photoluminescence in the specimens was excited with the radiation of a DRSh-500 mercury lamp (wavelength λ = 365 nm). Luminescence spectra were recorded by a standard procedure using a computer-assisted device and data processing. Measurements were performed at 300 and 77 K.

3. EXPERIMENTAL RESULTS

The stress–strain curves of the specimens under study indicate that, for the deformation mode used, the initial stress of plastic flow for the ZnS : Fe crystals is higher than that for the ZnS : Mn crystals by a factor of ~7–12. Note also that the ZnS : Mn specimens were easily deformed to $\varepsilon \approx 20$–25%, whereas the maximum deformation for the ZnS : Fe crystals was $\varepsilon \approx 7$–9% (after which they failed).

3.1. Luminescence

The PL spectra of the ZnS : Fe crystals consist of two bands (Fig. 1, curve *a*). One of them is in the red

1063-7834/03/4509-1688$24.00

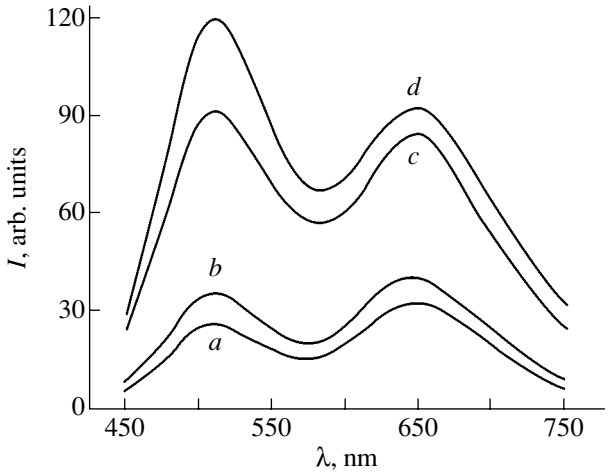

Fig. 1. PL spectra of deformed ZnS : Fe crystals for (*a*) ε = 0, (*b*) 3.27, (*c*) 5.78, and (*d*) 10.43%.

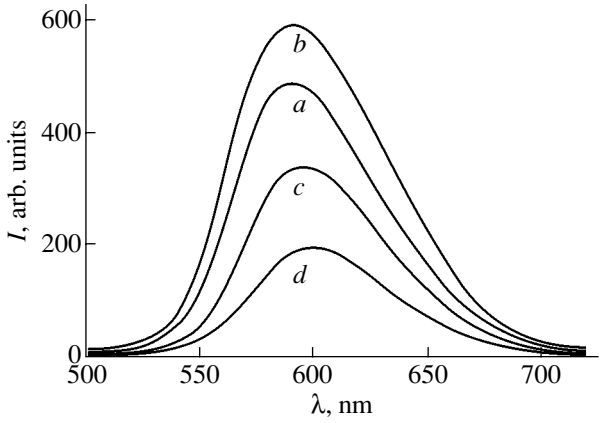

Fig. 2. PL spectra of the Mn^{2+} centers in deformed ZnS : Mn crystals for (*a*) ε = 0, (*b*) 2, (*c*) 7.8, and (*d*) 14.2%.

spectral range, has a maximum at λ = 640 nm, and is caused by Fe^{3+} centers [7]. The maximum of the other band is located in the green–blue range at λ = 510 nm. Luminescence in this spectral region is characteristic of zinc sulfide and is often observed even in undoped samples [8].

The ZnS : Mn crystals exhibit only one PL band of Mn^{2+} centers in the orange spectral range, with a maximum at λ = 580 nm (Fig. 2, curve *a*) [9].

After plastic deformation, virtually all parameters of the PL spectra of the specimens under study are changed (Figs. 1, 2). In the ZnS : Fe crystals, the luminescence intensities in both bands monotonically increase with the degree of deformation (Figs. 1, 3). The maximum of the red band shifts toward longer wavelengths (Δλ = 8 nm at ε = 7%), and the maximum of the green–blue band is virtually independent of the deformation. The PL band maximum of the manganese centers in the ZnS : Mn crystals also shifts toward longer wavelengths (Δλ = 5–7 nm at ε = 10–12%), and its intensity first increases in the initial deformation stage (for strains of up to ε ≈ 2–3%; Fig. 2, curve *b*) and then decreases to below the initial values with increasing deformation (Fig. 2, curves *c*, *d*; Fig. 4).

3.2. EPR

The EPR spectrum measured at 77 K on undeformed ZnS : Fe specimens irradiated with ultraviolet light with λ = 365 nm is shown in Fig. 5a. This spectrum contains five lines from the fine structure of the Fe^{3+} EPR spectrum, the central-transition line of the Cr^{+} EPR spectrum, and the characteristic hyperfine-structure sextet of the EPR spectrum of an uncontrolled impurity of bivalent manganese ions. The analogous spectra taken after plastic deformation are shown in Figs. 5b and 5c. It is seen that the side-transition lines, corresponding to the fine-structure levels with *M* = 5/2, 3/2, –1/2, and –3/2 (where *M* is the quantum number), in the EPR spectrum of Fe^{3+} ions broaden and their shapes approach Gaussian shape. At deformations ε ≈ 5–6%, these lines are almost invisible as a result of their strong broadening. The intensities of the central (*M* = 1/2) transitions in the EPR spectra of Fe^{3+} and Cr^{+} increase with deformation. Since the widths and shapes of these lines in the spectra of the initial specimens and of the specimens in the final stage of deformation coincide, we conclude that this increase unambiguously reflects the character of deformation-induced changes in the concentration of photosensitive Fe^{3+} and Cr^{+} paramagnetic centers.

Detailed studies of the EPR spectra of Mn^{2+} ions in plastically deformed ZnS : Mn crystals were carried out earlier in [2, 10]. Those studies supported x-ray diffrac-

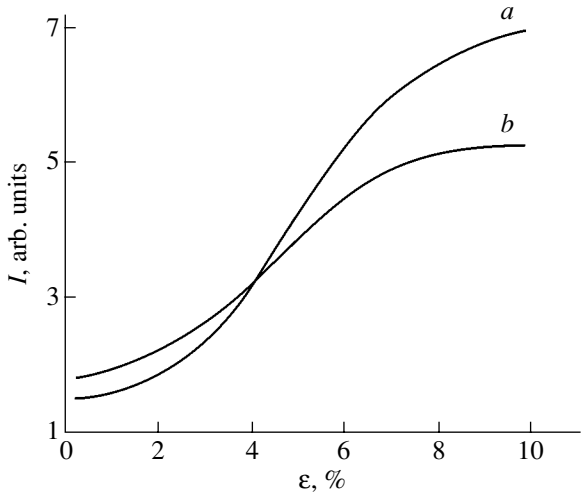

Fig. 3. Variation in the maximum intensities of the PL bands of ZnS : Fe crystals with deformation: (*a*) the green–blue band and (*b*) the PL of the Fe^{3+} centers.

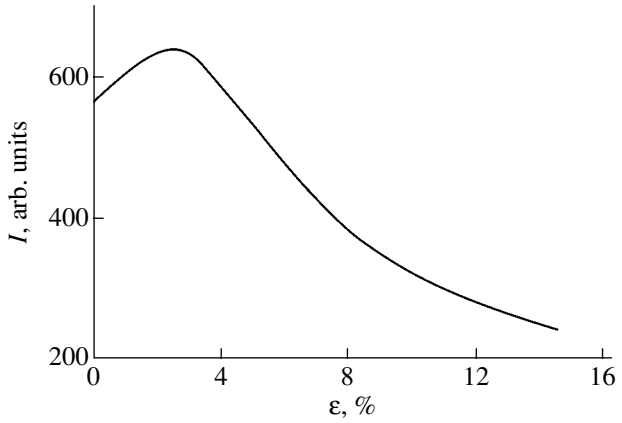

Fig. 4. Variation in the PL maximum intensity of Mn^{2+} ions in ZnS : Mn crystals with deformation.

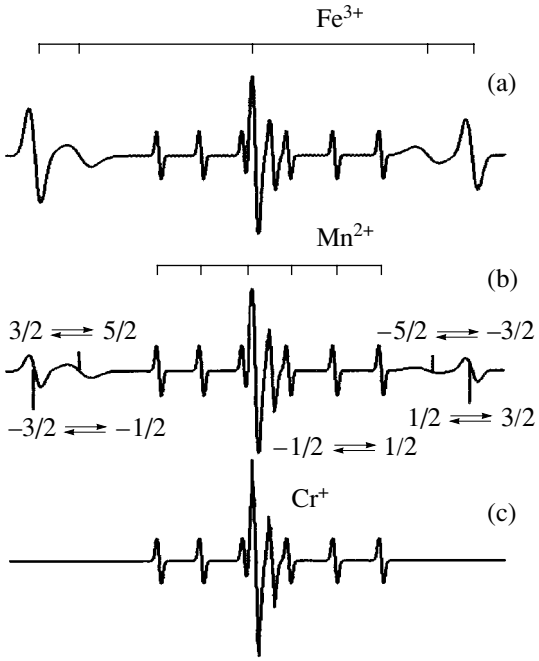

Fig. 5. Variation in the EPR spectra of Mn^{2+}, Fe^{3+}, and Cr^{+} ions in ZnS : Fe crystals with deformation: (a) ε = 0, (b) 3.27, and (c) 5.78%.

tion data showing that ZnS crystals are deformed via partial-dislocation motion [1] and established the kinetics of the deformation-induced reorientation of the crystal lattice of microtwins and polytypes into a sphalerite structure having only one orientation. Information on the effect of deformation on the width and shape of resonance lines is of greatest interest for us. It was found that the EPR lines of Mn^{2+} ions in the starting crystals have intermediate shapes between Lorentzian and Gaussian and that after 2–3% deformation the EPR lines broaden and acquire predominantly Gaussian shape. After further deformation, the shapes and widths of the EPR lines become identical to those for the initial samples. It should be noted that, in the initial stage of deformation, the changes in the shapes and widths of the EPR lines of Fe^{3+} ions in the ZnS : Fe crystals are qualitatively similar to those in the EPR lines of Mn^{2+} ions in the ZnS : Mn crystals.

4. DISCUSSION OF THE RESULTS

Virtually all deformation dependences obtained in our work exhibit specific features at low degrees of deformation (from 0 to 5–6%). After these deformations, for example, the rates of increase in the PL intensity and concentration of the Fe^{3+} and Cr^{+} centers are maximum, the fine structure of the EPR spectra of Fe^{3+} ions disappears, and the PL intensity of the Mn^{2+} centers becomes maximum. These features also manifest themselves in the behavior of the widths and shapes of the fine-structure lines of the EPR spectra of Mn^{2+} ions [10], the electrical conductivity [11], and the deformation dependence of the linear density of the dislocation electric charge [12].

When compared, these facts (which do not exhaust all possible the cases) indicate that they are consequences of processes that are related to dislocation motion and proceed in the initial stage of deformation. We believe that these processes are (1) the breakaway of dislocations from Cottrell atmospheres and (2) changes in the electrical properties of dislocations, which are caused by the first process. Moreover, if, apart from these processes, we take into account a deformation-induced increase in the density of dislocations, virtually all experimental results obtained in this work can be explained (including those at small deformations).

Growth dislocations form in ZnS crystals at high temperatures, i.e., under the conditions of a high concentration of point defects and high efficiency of the diffusion processes. Impurities and other defects migrate to dislocations and form Cottrell atmospheres. These atmospheres can pin dislocations, in other words, strengthen the crystals. This situation is likely to take place upon doping ZnS crystals with an Fe impurity, which is indicated not only by the data given above but also by our results from an experimental study on changes in the structure of ZnS : Fe crystals during their quenching from temperatures above the temperature of the wurtzite–sphalerite phase transformation (1297 K). According to [1, 2], the transformation of the high-temperature modification of zinc sulfide into the low-temperature one occurs as a result of partial-dislocation motion. When the crystals are grown from the melt, the phase transformation is incomplete; and the crystals grown are always sphalerite microtwins. However, after quenching from $T > 1297$ K, the ZnS : (Fe, Mn) crystals simultaneously exhibit the Mn^{2+} EPR spectra characteristic of both sphalerite [13] and wurtzite [14]

microtwins. This indicates that the phase transformation in this case is incomplete and that regions with a "frozen" high-temperature hexagonal structure are always retained in the quenched samples. Note that a similar effect is also observed upon quenching of ZnS crystals doped with aluminum and is absent in ZnS crystals with manganese impurity alone.

Thus, we believe that the iron concentration in Cottrell atmospheres is significantly higher than in crystal regions far from growth dislocations; that is, unlike the manganese impurity [2, 5], the iron impurity is nonuniformly distributed over the volume of the ZnS crystals.

It should also be noted that dislocations that move during plastic deformation of zinc sulfide crystals have a negative electric charge [12, 15]. The electric field of charged dislocations ionize defects located near them, which results in the shielding of cylindrical regions with a positive spatial charge (Read cylinders). The radii of the cylinders are specified by the dislocation charge and impurity concentration. Atoms in impurity atmospheres can move only via diffusion, which is hindered at the deformation temperatures used. Therefore, when dislocations start to move, they partially break away from the compensating clouds of impurities and vacancies. As a result, the radii of the Read cylinders increase, which is equivalent to growth in their "geometric charge." We believe that their actual charges can also change under these conditions, since the increases in the radii of the Read cylinders and in the distances between dislocation cores and the centers of Cottrell atmospheres cause qualitative and quantitative changes in the impurity environment of the dislocations and since the total dislocation charge depends not only on the ionic component but also on the population of the dislocation electronic level [12, 16].

Thus, in the range of small deformations (during the breakaway of dislocations from Cottrell atmospheres), the radii of the Read cylinders and, hence, their charges (at least, the geometric charges) increase. Upon further deformation, when dislocations have come from impurity atmospheres to regions with a uniform impurity distribution, their charges remain virtually unchanged. The character of the variation in dislocation charge with plastic deformation is the same both during deformation (see [12, Fig. 4]) and after its termination (for immobile dislocations).

As noted above, the PL spectrum of the undeformed ZnS : Fe crystals consists of two bands: a red band with λ_{max} = 640 nm and a green–blue band with λ_{max} = 510 nm. As for the nature of luminescence centers in the green–blue spectral range, different opinions exist [8, 17]; these centers are most often related to intrinsic defects in crystals. We believe, as in [17], that PL in the band with λ_{max} = 510 nm appears because of the radiative transitions of photoelectrons to doubly charged sulfur vacancies, whose energy levels ($E_v = 1.05 \pm 0.1$ eV) correspond to acceptor centers. PL centers in the red spectral range are Fe^{3+} ions. Iron atoms in ZnS : Fe crystals are known to isoelectronically substitute for zinc and have the charge state Fe^{2+} (electronic configuration $3d^6$; EPR spectra are not detected). The Fe^{2+} centers in zinc sulfide are acceptors whose occupied levels are located 1.1 eV above the valence band top [7]. When the crystals are irradiated by UV light with an energy close to their fundamental absorption band edge, electron–hole pairs are generated; then, holes are entrapped by the Fe^{2+} centers to form Fe^{3+} centers (electronic configuration $3d^5$; EPR spectra are detected and shown in Fig. 5). The red luminescence with λ_{max} = 640 nm appears as a result of the radiative transitions of electrons from shallow levels to the Fe^{3+} center levels ($Fe^{3+} + e \longrightarrow Fe^{2+}$). Thus, at a given level of UV excitation, a certain steady-state concentration of Fe^{3+} ions is reached; their PL and EPR spectra are given in Figs. 1 and 5, respectively.

As noted above, the charges of immobile dislocations and the radii of their Read cylinders increase after the initial deformation. As a result, part of the volume in the deformed specimens is under the efficient action of electric fields of negatively charged dislocations. Bending of energy bands in such regions does not lead to changes in the probability of formation of electron–hole pairs and recombination processes but affects the concentration of charge carriers. The PL intensity in the red range is specified by two competing processes: a decrease in the concentration of electrons (repulsed by the electric fields of dislocations) and the related increase in the concentration of Fe^{3+} centers. It is easy to understand that these two processes compensate each other to some extent; hence, the PL intensity of the Fe^{3+} centers located inside the Read cylinders should be virtually constant. On the contrary, in regions far from dislocations, the process of radiative recombination becomes more intense due to the addition of nonequilibrium electrons rejected from the Read cylinders. As a result, the integrated intensity of the red PL band should increase after the deformation of zinc sulfide crystals. In the range of small deformations, when dislocations have not left Cottrell atmospheres, electrons are repulsed to iron-rich regions and the effect of increasing the PL intensity of the Fe^{3+} centers is more pronounced. Exactly this trend of the variation of the intensity of the red PL band is experimentally observed in the ZnS : Fe specimens (Fig. 3, curve *b*). The fact that the iron centers that enter into impurity atmospheres significantly contribute to the increase in the PL intensity is indicated by the shift of the luminescence maximum in the red band. Indeed, dislocations coming into the iron-rich regions bring about an increase in internal mechanical stresses, which change the interatomic distances and, hence, the band gap. Since the red band shifts toward the long-wavelength region, we conclude that radiative Fe^{3+} centers are located in dilatation regions. The absence of a deformation-induced shift in the position of the luminescence maximum of the green–blue band may mean that the luminescence cen-

ters are either located beyond the coverage of the mechanical stress fields of dislocations or, quite the contrary, are bound to them, namely, are constantly localized near dislocations. The latter does not conflict with the model of green–blue luminescence centers accepted by us, since dislocation motion in II–VI compounds is known to occur with the formation of double kinks [16], which is inevitably accompanied by the formation of vacancies [18].

The results of EPR studies confirm the key statements of the proposed scheme of the processes. The electron concentration in regions far from dislocations increases after deformation, which is unambiguously indicated by an increase in the intensity of the EPR spectrum of Cr^+ centers (Fig. 5). An increase in the intensity of the line of the $M = 1/2$ transition in the EPR spectra of Fe^{3+} ions (Fig. 5) reflects the corresponding change in the total concentration of these ions. The main thing is that the EPR data corroborate the basic point of our model about an increase in the radii of the Read cylinders after dislocations have started to move. This conclusion follows from an analysis of the deformation-induced changes in the shapes and widths of the side lines in the fine structure of the EPR spectra of Fe^{3+} ions. The changes observed indicate that they are caused by the effect of nonuniform electric fields on paramagnetic centers [19]. It is natural to assume that, in our case, the sources of such fields are dislocations, whose negative electric charges increase in magnitude during their breakaway from impurity atmospheres. It should also be taken into account that, when dislocations move with respect to centers of positively charged impurity clouds that remain behind, long-lived dipoles form; the nonuniform electric fields of the dipoles operate most efficiently at low degrees of deformation. In all these cases, we expect that the effect of the EPR line-broadening factors indicated above becomes weaker as dislocations exit impurity atmospheres to regions with a low iron concentration. This behavior is not observed in the ZnS : Fe specimens, since growth dislocations are strongly pinned and, therefore, cannot completely leave Cottrell atmospheres. As a result, the deformation of such crystals proceeds mainly via the motion of dislocations that are not associated with the crystal growth and have no impurity atmospheres around them. These dislocations are most likely to be perfect dislocations, since the generation of partial dislocations in sphalerite should be accompanied by the formation of hexagonal close-packed layers, which is energetically unfavorable at the temperatures of our experiments. Since perfect dislocations do not have sufficient mobility at these temperatures [16], the ZnS : Fe specimens cannot be deformed to a degree higher than 7–9%. However, as noted above, the widths and shapes of the EPR lines of the ZnS : Mn crystals, where impurities cannot pin growth dislocations, become equal to those of the initial samples as the degree of deformation increases.

Now, we discuss the deformation-induced PL changes in the ZnS : Mn crystals. In order to explain their specific features at low deformations, it is necessary to take into account that, according to modern concepts, manganese luminescence centers are excited in zinc sulfide crystals via resonance energy transfer from sensitization centers (intrinsic lattice defects or their associates with atoms of certain uncontrollable impurities) [20]. It is natural to assume that the concentration of such sensitization centers is higher in the regions around growth dislocations. Therefore, the manganese centers, which are also located near dislocations, should be excited most efficiently. The deformation of the specimens leads to the displacement of growth dislocations from their initial positions, which causes an increase in the dislocation electric charge; as a result, strong (on the order of 10^7 V/cm) electric fields of dislocations begin to affect the sensitizer–manganese center resonance systems. The effect of the fields can increase the efficiency of the resonance channel of energy transfer and, thus, increase the luminescence intensity of the Mn centers. As growth dislocations move away from their Cottrell atmospheres, the situation should return to its initial position; therefore, the PL intensity is recovered. It should be noted, however, that the higher concentration of intrinsic defects (sensitization centers) in Cottrell atmospheres is due to mechanical stresses caused by dislocations. Obviously, after dislocations have left a certain place, equilibrium is recovered there and the PL intensity decreases. Exactly this character of the deformation-induced PL changes was experimentally observed in the ZnS : Mn crystals (Fig. 4). The fact that dislocations actually have left the luminescence centers emitting the PL of the undeformed crystals is also indicated by the deformation-induced shift in the position of the maximum of the Mn luminescence band toward long wavelengths. Thus, we can state that only before the beginning of deformation were the luminescence centers and sensitizers located in places where the crystal lattice was distorted by the mechanical stress fields of dislocations.

Now, we discuss the effect of the electric fields of immobile dislocations on the luminescence properties of the crystals. Let us estimate the number of luminescence centers that can be within the Read cylinders.

The total volume of the spatial charge around dislocations is

$$\Omega = \pi R^2 N_d V, \tag{1}$$

where V is the specimen volume, N_d is the dislocation density, and R is the radius of a Read cylinder. Using the etch pitting technique, we found that $N_d \sim 10^5$–10^6 cm^{-2} in the undeformed crystals. For dislocations surrounded by impurity atmospheres, we have $R \sim 10^{-6}$ cm. Therefore, $\Omega/V \sim 10^{-7}$–10^{-6}, which means that the fraction of an undeformed specimen occupied by the Read cylinders is very low. However, if the luminescence centers decorate dislocations, their local concen-

tration can be rather high (~10^{20}–10^{21} cm^{-3}). In this case, the regions where the dislocation electric fields are significant in a specimen $2 \times 2 \times 4$ mm in size contain ~10^{10}–10^{12} centers. After deformation, the dislocation density and the radius of their Read cylinders increase; at the same time, the dislocations become located in regions with a significantly lower concentration of impurities. After a 4–5% deformation, the dislocation density is $N_d \sim 3 \times 10^6$–10^7 cm^{-2} and $R \sim 10^{-5}$ cm [16]. In this case, we have $\Omega/V \sim 10^{-3}$. However, the concentration of impurity centers is ~10^{18}–10^{19} cm^{-3}; therefore, ~10^{13}–10^{14} luminescence centers are subject to the electric fields of dislocations. A further deformation can increase the number of luminescence centers due to dislocation multiplication.

Thus, at least ~10^{12}–10^{14} luminescence centers are located in the regions where the electric fields of immobile dislocations are significant in the zinc sulfide crystals under study. Obviously, these centers can affect the luminescence properties of the crystals and their variation during plastic deformation in the case of sufficiently efficient excitation and a high quantum yield of luminescence.

REFERENCES

1. B. A. Abdikamalov, S. I. Bredikhin, M. P. Kulakov, *et al.*, Fiz. Tverd. Tela (Leningrad) **18** (8), 2468 (1976) [Sov. Phys. Solid State **18**, 1442 (1976)].
2. S. A. Omel'chenko, S. I. Bredikhin, P. A. Berlov, *et al.*, Fiz. Tverd. Tela (Leningrad) **24** (9), 2803 (1982) [Sov. Phys. Solid State **24**, 1586 (1982)].
3. A. V. Zaretskiĭ, Yu. A. Osip'yan, V. F. Petrenko, and G. K. Strukova, Fiz. Tverd. Tela (Leningrad) **19** (2), 418 (1977) [Sov. Phys. Solid State **19**, 240 (1977)].
4. Yu. A. Osip'yan and V. F. Petrenko, Zh. Éksp. Teor. Fiz. **75** (1), 296 (1978) [Sov. Phys. JETP **48**, 147 (1978)].
5. S. I. Bredikhin and S. Z. Shmurak, Zh. Éksp. Teor. Fiz. **76** (3), 1028 (1979) [Sov. Phys. JETP **49**, 520 (1979)].
6. S. I. Bredikhin, S. A. Omel'chenko, and S. Z. Shmurak, Zh. Éksp. Teor. Fiz. **90** (1), 209 (1986) [Sov. Phys. JETP **63**, 120 (1986)].
7. P. Jasrczyn-Kopec and B. Lambert, J. Lumin. **10** (4), 243 (1975).
8. N. K. Morozova and V. A. Kuznetsov, *Zinc Sulfide. Production and Optical Properties* (Nauka, Moscow, 1987).
9. N. D. Borisenko, M. F. Bulanyĭ, F. F. Kodzhespirov, and B. A. Polezhaev, Zh. Prikl. Spektrosk. **55** (3), 452 (1991).
10. S. I. Bredikhin, S. A. Omel'chenko, S. Z. Shmurak, and N. A. Yakunina, Fiz. Tverd. Tela (Leningrad) **23** (3), 903 (1981) [Sov. Phys. Solid State **23**, 521 (1981)].
11. S. A. Omelchenko, O. V. Khmelenko, Yu. A. Gulevski, and M. F. Bulanyi, in *Proceedings of the 21st International Conference on Defects in Semiconductors, Giessen* (2001), p. 317.
12. S. I. Bredikhin and S. Z. Shmurak, Zh. Éksp. Teor. Fiz. **73** (4), 1460 (1977) [Sov. Phys. JETP **46**, 768 (1977)].
13. P. A. Berlov, M. F. Bulanyĭ, and S. A. Omel'chenko, Kristallografiya **43** (3), 496 (1998) [Crystallogr. Rep. **43**, 457 (1998)].
14. S. P. Keller, I. I. Gelles, and W. V. Smith, Phys. Rev. **110** (4), 850 (1958).
15. L. G. Kirichenko, V. F. Petrenko, and G. V. Uĭmin, Zh. Éksp. Teor. Fiz. **74** (2), 742 (1978) [Sov. Phys. JETP **47**, 389 (1978)].
16. *Electronic Properties of Dislocations in Semiconductors*, Ed. by Yu. A. Osip'yan (Éditorial URSS, Moscow, 2000).
17. A. N. Georgobiani, M. B. Kotlyarevskiĭ, and V. N. Mikhalenko, Tr. Fiz. Inst. im. P.N. Lebedeva, Akad. Nauk SSSR **138**, 79 (1983).
18. J. P. Hirth and J. Lothe, *Theory of Dislocations* (McGraw-Hill, New York, 1967; Atomizdat, Moscow, 1972).
19. *Electrical Effects in Radiospectroscopy*, Ed. by M. F. Deĭgen (Nauka, Moscow, 1981).
20. N. D. Borisenko, M. F. Bulanyĭ, B. A. Polezhaev, *et al.*, Neorg. Mater. **29** (9), 1219 (1993).

Translated by K. Shakhlevich

Physics of the Solid State, Vol. 45, No. 9, 2003, pp. 1694–1700. Translated from Fizika Tverdogo Tela, Vol. 45, No. 9, 2003, pp. 1614–1620.

DEFECTS, DISLOCATIONS, AND PHYSICS OF STRENGTH

Elastic Fields of a Screw Superdislocation with a Hollow Core (Pipe) Perpendicular to the Free Crystal Surface

A. G. Sheĭnerman and M. Yu. Gutkin

Institute of Problems of Mechanical Engineering, Russian Academy of Sciences, Vasil'evskiĭ ostrov, Bol'shoĭ pr. 61, St. Petersburg, 199178 Russia

e-mail: gutkin@def.ipme.ru

Received February 12, 2003; in final form, February 21, 2003

Abstract—Screw superdislocations with hollow cores (pipes) which arise during growth of semiconductor crystals such as silicon carbide and gallium nitride are considered. Exact analytical expressions are first derived for the displacements, strains, and stresses associated with a pipe oriented perpendicular to the free planar surface of an elastically isotropic half-space. It is shown that the stress field of the dislocation present in the pipe is heavily affected when the exact boundary conditions at the free cylindrical surface of the pipe are taken into account. The influence is the strongest in the region around the pipe at distances of the order of the pipe radius from the surface of the pipe. In this region, the elastic strains can be as large as a few tenths of one percent. The results obtained can be useful in analyzing the interaction of pipes with one another and with other defects, as well as in simulating the behavior of pipes during crystal growth. © *2003 MAIK "Nauka/Interperiodica".*

1. INTRODUCTION

The fact that screw superdislocations with hollow cores form in the course of growth of certain crystals has been known for more than half a century [1]. Such dislocations have been detected in crystals of silicon carbide, which is one of the materials that show the greatest promise for use in high-power electronics. In silicon carbide, superdislocations have the form of nearly rectilinear cylindrical voids (micropipes) up to tens of micrometers in diameter; they are oriented along the crystal growth direction and propagate through the crystal. The density of these dislocations in commercial crystals can be as high as 10 to 100 cm^{-2}, depending on the size and quality (cost) of a sample [2]. In the mid 1990s, screw dislocations with hollow cores (nanopipes) were first reported to be observed in gallium nitride [3, 4]. This material has currently received considerable attention as a wide-band-gap semiconductor holding much promise for optoelectronics. In this material, nanopipes range in diameter from 3.5 to 50 nm and their density can be as high as 10^5–10^7 cm^{-2} [3–5]. Although micro- and nanopipes differ significantly in size and density, their general geometry and dislocation nature allow one to analyze these objects on a unified basis. In what follows, we refer to them as pipes, implying that they contain screw (super)dislocations.

There is a considerable amount of evidence that such pipes adversely affect the performance characteristics of devices based on silicon carbide crystals [2, 6–9]. The adverse effect can be so strong that the pipes are sometimes called killing defects of devices [2, 10] and their density is considered an important indicator of the quality of grown crystals. The effect of pipes on the performance of devices based on gallium nitride has also been intensively studied [11–14]. Pipes were the subject of experimental studies in [3–11, 13–30].

The first theoretical model of pipe formation was proposed by Frank [31], who pointed out that hollow cores of dislocations with large Burgers vectors arise in the regions of high elastic stresses around the dislocation lines, thereby decreasing the energy of these defects. Thus, pipes form in crystals where there are superdislocations. Theoretically, pipes can contain screw, edge, and mixed dislocations; however, in most cases, pipes with only screw dislocations are observed, and we will consider only such pipes in what follows. Superdislocations bringing about the formation of micropipes can arise near impurities [17–19], inclusions of another phase [21, 22], voids [5, 21, 26], and surface steps [21, 27]. Pipes can also form at low-angle boundaries [19, 29] separating different polytypes, i.e., regions with different types of crystal lattice [8].

Since pipes contain (super)dislocations, which produce long-range elastic stresses in the crystal, the evolution of the pipes (their motion [15, 29], splitting [7, 24, 25, 28, 30], or combining [29]) in the course of crystal growth and subsequent annealing is determined chiefly by the elastic interaction of dislocations with one another and with other defects or strained regions of the crystal. For instance, splitting and merging of pipes (which can result in their healing [7, 24, 25, 29] and the formation of macrocavities [29], respectively) are consequence of the dissociation and combining of dislocations contained in the pipes. Therefore, there are many processes in which the interaction of pipes with one another and with other defects is of importance.

1063-7834/03/4509-1694$24.00 © 2003 MAIK "Nauka/Interperiodica"

In the previous theoretical papers dedicated to studying the interaction of pipes with screw dislocations [32, 33] and with one another [33] and to analyzing the conditions under which pipe splitting occurs [30], pipes were assumed to be in an infinite medium. However, the motion of pipes and the processes of their combining and splitting take place, for the most part, at the front of crystal growth. Therefore, the free surface of a growing crystal has a determining effect on the evolution of an array of pipes. The objective of this paper is to theoretically analyze the "elastic component" of this effect, i.e., to investigate the screening effect of the free surfaces of the crystal and of the pipe on the elastic fields of the dislocation contained in the pipe. Therefore, we should exactly solve the boundary-value problem of the elasticity theory for a pipe perpendicular to the free crystal surface. The elastic displacement and stress fields calculated for a pipe containing a screw dislocation can be further used, in particular, to determine the energy and interaction forces for an array of pipes and to analyze the conditions of their combining or splitting.

2. STRESS FIELD

We consider an elastically isotropic half-space $z \geq 0$ with a cylindrical cavity of radius R_0 containing a screw dislocation with a Burgers vector $\mathbf{b} = b\mathbf{e}_z$ (Fig. 1). In a cylindrical system of coordinates (r, φ, z) with the origin placed on the axis of the cylindrical cavity, the stresses σ_{ij} produced by the dislocation must satisfy the boundary conditions $\sigma_{iz}|_{z=0} = 0$ and $\sigma_{ir}|_{r=R_0} = 0$, where i is r, φ, or z. To solve this boundary-value problem, we employ the method of virtual surface defects [34]. In this method, the stress field σ_{ij} is represented in the form

$$\sigma_{ij} = \sigma_{ij}^d + \sigma_{ij}^v, \tag{1}$$

where σ_{ij}^d is the stress field produced by the dislocation in the absence of the cavity and σ_{ij}^v is an additional stress field, which is chosen so as to satisfy the boundary conditions at the surface of the cavity $r = R_0$.

The stress field σ_{ij}^d is calculated from the formulas [34, 35]

$$\sigma_{r\varphi}^d = -\frac{Gb}{2\pi R_0}\frac{\tilde{r}^2}{\tilde{R}(\tilde{R}+\tilde{z})^2}, \tag{2}$$

$$\sigma_{z\varphi}^d = \frac{Gb}{2\pi R_0}\frac{\tilde{z}}{\tilde{r}\tilde{R}}, \tag{3}$$

$$\sigma_{rr}^d = \sigma_{\varphi\varphi}^d = \sigma_{zz}^d = \sigma_{zr}^d = 0, \tag{4}$$

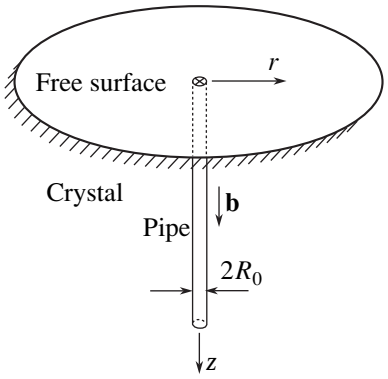

Fig. 1. Pipe with a screw (super)dislocation perpendicular to the free planar crystal surface.

where $\tilde{r} = r/R_0$, $\tilde{z} = z/R_0$, $\tilde{R} = \sqrt{\tilde{r}^2 + \tilde{z}^2}$, and G is the shear modulus. The stress field σ_{ij}^d satisfies the boundary conditions $\sigma_{iz} = 0$ $(i = r, \varphi, z)$ at the surface $z = 0$.

The stress field σ_{ij}^v can be expressed in terms of the stress fields of virtual twist disclination loops $\sigma_{ij}^l(\tilde{r}, \tilde{z}, \tilde{z}')$ in the half-space $z \geq 0$. These loops are assumed to be circles of radius R_0, with their centers located on the z axis; the coordinate of the center of a loop is designated as z'. The planes of the virtual loops are parallel to the free planar surface $z = 0$ and the loops are continuously distributed over the surface of the cylinder. In this case, the total stress field of the loops is

$$\sigma_{ij}^v(\tilde{r}, \tilde{z}) = \int_0^\infty \rho(\tilde{z}')\sigma_{ij}^l(\tilde{r}, \tilde{z}, \tilde{z}')d\tilde{z}', \quad \tilde{z} \geq 0, \quad \tilde{r} > 1, \tag{5}$$

where $\rho(\tilde{z}')$ is the density of virtual disclination loops. The stress field σ_{ij}^l produced by an individual loop in the half-space can be written as [36]

$$\sigma_{ij}^l(\tilde{r}, \tilde{z}, \tilde{z}') = \sigma_{ij}^\infty(\tilde{r}, \tilde{z} - \tilde{z}') - \sigma_{ij}^\infty(\tilde{r}, \tilde{z} + \tilde{z}'), \tag{6}$$

where $\sigma_{ij}^\infty(\tilde{r}, \tilde{z} - \tilde{z}')$ is the stress field of a twist disclination loop situated in an infinite medium. The loop line is specified by the coordinates $\tilde{r} = 1$ and $\tilde{z} = \tilde{z}'$.

At any point beyond the loop, the stress field $\sigma_{ij}^\infty(\tilde{r}, \tilde{z})$ is given by [36]

$$\sigma_{r\varphi}^\infty = -\frac{G\omega}{2}\operatorname{sgn}\tilde{z}J(2, 2; 1), \tag{7}$$

$$\sigma_{z\varphi}^\infty = -\frac{G\omega}{2}J(2, 1; 1), \tag{8}$$

$$\sigma_{rr}^\infty = \sigma_{\varphi\varphi}^\infty = \sigma_{zz}^\infty = \sigma_{rz}^\infty = 0, \tag{9}$$

where ω is the strength of the disclination loop (the magnitude of the Frank vector) and $J(m, n; p)$ is a Lipschitz–Hankel integral [37, 38], defined as $J(m, n; p) = \int_0^\infty J_m(\kappa) J_n(\kappa\tilde{r}) e^{-\kappa|\tilde{z}|} \kappa^p d\kappa$. Here, $J_l(t)$ is a Bessel function of the first kind.

By substituting the total field of virtual loops (5) and Eqs. (6)–(9) into the boundary condition at the free surface of the cavity, $\sigma^v_{r\varphi}(\tilde{r} = 1, \tilde{z}) = -\sigma^d_{r\varphi}(\tilde{r} = 1, \tilde{z})$, where $\sigma^v_{ij}(\tilde{r} = 1, \tilde{z}) = \lim_{\substack{\tilde{r} \to 1 \\ \tilde{r} > 1}} \sigma^v_{ij}(\tilde{r}, \tilde{z})$, we obtain an integral equation for the density of virtual loops $\rho(\tilde{z}')$. In order to solve this equation, we extend the function $\rho(\tilde{z}')$ (defined in the region $z \geq 0$) into the region $z < 0$ by using the relation $\rho(-\tilde{z}') = -\rho(\tilde{z}')$. In this case, Eq. (5), in combination with Eq. (6), can be written as

$$\sigma^v_{ij}(\tilde{r}, \tilde{z}) = \int_{-\infty}^{\infty} \rho(\tilde{z}') \sigma^\infty_{ij}(\tilde{r}, \tilde{z} - \tilde{z}') d\tilde{z}', \quad (10)$$

and the boundary condition $\sigma^v_{r\varphi}(\tilde{r} = 1, \tilde{z}) = -\sigma^d_{r\varphi}(\tilde{r} = 1, \tilde{z})$ reduces to a Cauchy-type integral equation

$$\int_{-\infty}^{\infty} \rho(\tilde{z}') \sigma^\infty_{r\varphi}(\tilde{r} = 1, \tilde{z} - \tilde{z}') d\tilde{z}' = -\sigma^d_{r\varphi}(\tilde{r} = 1, \tilde{z}). \quad (11)$$

Taking the Fourier transform $\hat{f}(k) = \int_{-\infty}^{\infty} f(\tilde{z}) e^{-ik\tilde{z}} d\tilde{z}$ of Eq. (11), we obtain

$$\hat{\rho}(k) \hat{\sigma}^\infty_{r\varphi}(\tilde{r} = 1, k) = -\hat{\sigma}^d_{r\varphi}(\tilde{r} = 1, k). \quad (12)$$

The quantities $\rho(\tilde{z})$ and $\sigma^\infty_{r\varphi}(\tilde{r} = 1, \tilde{z})$ are odd functions of $\tilde{z}$. Therefore, $\hat{\rho}(k)$ and $\hat{\sigma}^\infty_{r\varphi}(\tilde{r} = 1, k)$ are odd functions of k, $\hat{\sigma}^d_{r\varphi}(\tilde{r} = 1, k)$ is an even function of k, and $\sigma^d_{r\varphi}(\tilde{r} = 1, \tilde{z})$ is an even function of $\tilde{z}$. For this reason, we define $\sigma^d_{r\varphi}$ in the region $z < 0$ using the relation $\sigma^d_{r\varphi}(\tilde{r} = 1, \tilde{z}) = \sigma^d_{r\varphi}(\tilde{r} = 1, -\tilde{z})$.

By substituting Eqs. (2) and (7) into Eq. (12) and calculating the relevant integrals, we find the Fourier transform of the distribution function of virtual disclination loops located on the surface of the cavity:

$$\hat{\rho}(k) = \frac{b}{i\pi\omega R_0} \frac{-K_2(|k|) + 2/k^2}{kI_2(|k|)K_2(|k|)}, \quad (13)$$

where i is the imaginary unit and $I_2(|k|)$ and $K_2(|k|)$ are the modified second-order Bessel functions of the second kind.

In order to calculate σ^v_{ij} we take the Fourier transform of Eq. (10):

$$\hat{\sigma}^v_{ij}(\tilde{r}, k) = \hat{\rho}(k) \hat{\sigma}^\infty_{ij}(\tilde{r}, k). \quad (14)$$

The quantity $\sigma^\infty_{r\varphi}(\tilde{r}, \tilde{z})$ is an odd function of $\tilde{z}$; therefore, $\hat{\sigma}^\infty_{r\varphi}(\tilde{r}, k)$ is an odd function of k and $\hat{\sigma}^v_{r\varphi}(\tilde{r}, k)$ is an even function of k. Similarly, since $\sigma^\infty_{z\varphi}(\tilde{r}, \tilde{z})$ is an even function of $\tilde{z}$, $\hat{\sigma}^v_{z\varphi}(\tilde{r}, k)$ is an odd function of k. The stresses σ^v_{ij} are obtained from Eq. (14) by taking the inverse Fourier transform:

$$\sigma^v_{ij}(\tilde{r}, \tilde{z}) = \frac{1}{2\pi} \int_{-\infty}^{\infty} \hat{\rho}(k) \hat{\sigma}^\infty_{ij}(\tilde{r}, k) e^{ik\tilde{z}} dk. \quad (15)$$

By substituting Eqs. (7)–(9) and (13) into Eq. (15) and evaluating the integrals, we obtain

$$\sigma^v_{r\varphi} = \frac{Gb}{\pi^2 R_0} \int_0^\infty \frac{[-K_2(k) + 2/k^2] K_2(\tilde{r}, k)}{K_2(k)} \cos k\tilde{z} dk, \quad (16)$$

$$\sigma^v_{z\varphi} = \frac{2Gb}{\pi^2 R_0} \left[-\frac{\pi}{4} \frac{\tilde{z}}{\tilde{r}\sqrt{\tilde{r}^2 + \tilde{z}^2}} + \int_0^\infty \frac{K_1(\tilde{r}k)}{k^2 K_2(k)} \sin k\tilde{z} dk \right], \quad (17)$$

$$\sigma^v_{rr} = \sigma^v_{\varphi\varphi} = \sigma^v_{zz} = \sigma^v_{rz} = 0, \quad \tilde{z} \geq 0, \quad \tilde{r} > 1. \quad (18)$$

In deriving Eq. (17), we used the equality $\int_0^\infty J_2(\kappa) J_1(\kappa\tilde{r}) d\kappa = 0$ for $\tilde{r} > 1$. Due to this equality, expressions (16)–(18) for σ^v_{ij} are continuous at $\tilde{r} = 1$; namely, $\lim_{\substack{\tilde{r} \to 1 \\ \tilde{r} > 1}} \sigma^v_{ij}(\tilde{r}, \tilde{z}) = \sigma^v_{ij}(1, \tilde{z})$.

Thus, the stress field σ_{ij} of the pipe perpendicular to the free crystal surface $z = 0$ is the sum of the stress fields σ^d_{ij} given by Eqs. (2)–(4) and σ^v_{ij} given by Eqs. (16)–(18). By using the relation

$$\frac{\pi}{2} \frac{\tilde{r}^2}{\tilde{R}(\tilde{R} + \tilde{z})^2} = \int_0^\infty \left[-K_2(\tilde{r}k) + \frac{2}{(\tilde{r}k)^2} \right] \cos k\tilde{z} dk, \quad (19)$$

we represent the sought-for stress field of the pipe σ_{ij} in a compact form:

$$\sigma_{r\varphi} = \frac{2Gb}{\pi^2 R_0} \int_0^\infty \left(\frac{K_2(\tilde{r}k)}{K_2(k)} - \frac{1}{\tilde{r}^2} \right) \frac{\cos k\tilde{z}}{k^2} dk, \quad (20)$$

$$\sigma_{z\varphi} = \frac{2Gb}{\pi^2 R_0} \int_0^\infty \frac{K_1(\tilde{r}k)}{k^2 K_2(k)} \sin k\tilde{z} dk, \quad (21)$$

$$\sigma_{rr} = \sigma_{\varphi\varphi} = \sigma_{zz} = \sigma_{rz} = 0. \quad (22)$$

It is easy to verify that this solution satisfies the boundary conditions at the free planar crystal surface $\sigma_{z\varphi}|_{\tilde{z}=0} = 0$ and at the free cylindrical surface of the pipe $\sigma_{r\varphi}|_{\tilde{r}=1} = 0$.

Equations (20)–(22) are convenient for numerical computations of the elastic stresses and strains $\varepsilon_{i\varphi} = \sigma_{i\varphi}/(2G)$ produced by the pipe near the crystal surface. The calculated $\sigma_{z\varphi}(\tilde{z})$, $\sigma_{z\varphi}(\tilde{r})$, and $\sigma_{r\varphi}(\tilde{z})$ dependences are shown in Fig. 2 by solid curves (the stresses are given in units of $Gb/(2\pi R_0)$. The dashed curves represent the corresponding stresses $\sigma^d_{z\varphi}$ and $\sigma^d_{r\varphi}$ produced by a screw dislocation with a full core. It can be seen from Fig. 2 that, near the free surface of the pipe ($\tilde{r} = 1$), both its nonzero stress field components, given by Eqs. (20) and (21), differ significantly from the respective stress field components of the dislocation with a full core, given by Eqs. (2) and (3). Contrarily, at distances larger than $2R_0$ from the dislocation line (located at $\tilde{r} = 0$), both solutions are close to each other. In this region, Eqs. (20)–(22) for the stress field of the pipe can be approximated by the simpler solution for the stress field of the screw dislocation with a full core, which is given by Eqs. (2)–(4).

Let us estimate the elastic strains produced by a pipe near the free crystal surface. As an example, we take the well-studied 6*H*-SiC crystal, for which the Frank relation [31] $R_0 = Gb^2/8\pi^2\gamma$ has been established to be valid (γ is the surface energy density of the free pipe surface). Using this relation, the elastic strains can be written as $\varepsilon_{i\varphi}(\tilde{r}, \tilde{z}) = \sigma_{i\varphi}(\tilde{r}, \tilde{z})/2G = (2\pi\gamma/Gb)\Phi_{i\varphi}(\tilde{r}, \tilde{z})$, where the functions $\Phi_{i\varphi}(\tilde{r}, \tilde{z})$ stand for the integrals in Eqs. (20) and (21) multiplied by $4/\pi$ (it is the functions $\Phi_{i\varphi}(\tilde{r}, \tilde{z})$ that are plotted in Fig. 2). From the experimental data for 6*H*-SiC crystals, the value of γ/G was estimated in [39] to be $(1.1–1.6) \times 10^{-3}$ nm. The magnitude of the Burgers vector is assumed to lie in the range from $2c$ to $7c$ [39], where c is the lattice parameter along the crystal growth direction [0001] ($c \approx 1.5$ nm [32]). In this case, we have $2\pi\gamma/Gb \approx (0.7–3.4) \times 10^{-3}$. For the values of $\Phi_{i\varphi}(\tilde{r}, \tilde{z})$ corresponding to the solid curves in Fig. 2, we find that the shear strain component $\varepsilon_{z\varphi}$ (Figs. 2a, 2b) varies from zero to approximately $(0.7–3.4) \times 10^{-3}$ and the component $\varepsilon_{r\varphi}$ (Fig. 2c) varies from approximately $-(0.3–1.4) \times 10^{-3}$ to zero. Thus, the elastic strains can be as large as several tenths of a percent near the free surfaces of the pipe and the crystal.

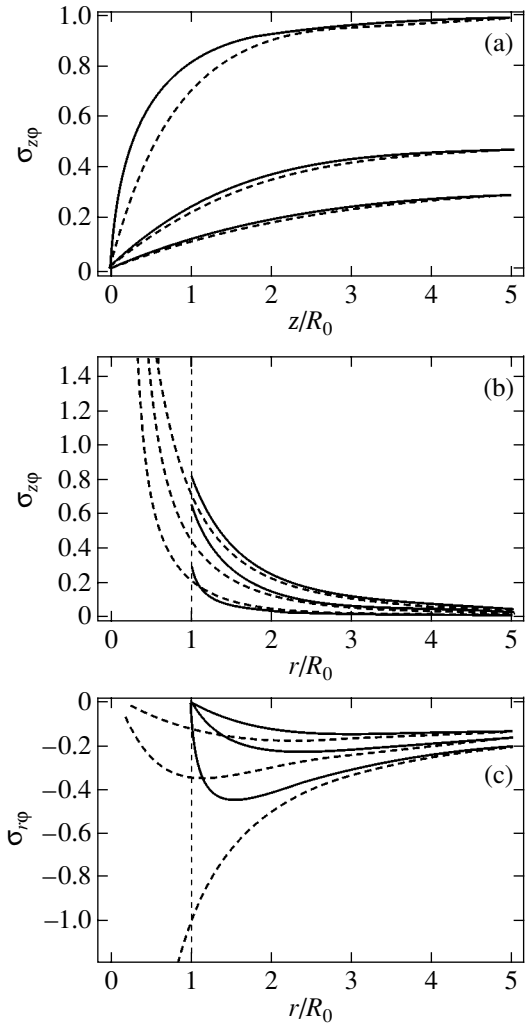

Fig. 2. Stresses $\sigma_{z\varphi}$ and $\sigma_{r\varphi}$ (solid curves) and stresses $\sigma^d_{z\varphi}$ and $\sigma^d_{r\varphi}$ (dashed curves) produced by a pipe and a screw dislocation with a full core, respectively, positioned perpendicular to the free crystal surface; (a) $\sigma_{z\varphi}(z/R_0)$ and $\sigma^d_{z\varphi}(z/R_0)$ for $r/R_0 = 1, 2, 3$ (from top to bottom, respectively); (b) $\sigma_{z\varphi}(r/R_0)$ and $\sigma^d_{z\varphi}(r/R_0)$ for $z/R_0 = 0.2, 0.5, 1.0$ (from top to bottom); and (c) $\sigma_{r\varphi}(r/R_0)$ and $\sigma^d_{r\varphi}(r/R_0)$ for $z/R_0 = 0.2, 0.5, 1.0$ (from bottom to top). Stresses are given in units of $Gb/2\pi R_0$.

3. DISPLACEMENT FIELD

The exact solution for the displacement field of the pipe perpendicular to the free crystal surface may also be of interest for practical applications (e.g., for analysis of electron-microscopic images of pipes and high-resolution x-ray topography [20]). The displacement field u_i can also be calculated as the sum of the displacement field u^d_i of the screw dislocation with a full core [35],

$$u^d_\varphi = \frac{b}{2\pi}\frac{\tilde{r}}{\tilde{R}+\tilde{z}}, \tag{23}$$

$$u^d_z = \frac{b}{2\pi}\varphi, \tag{24}$$

$$u^d_r = 0, \tag{25}$$

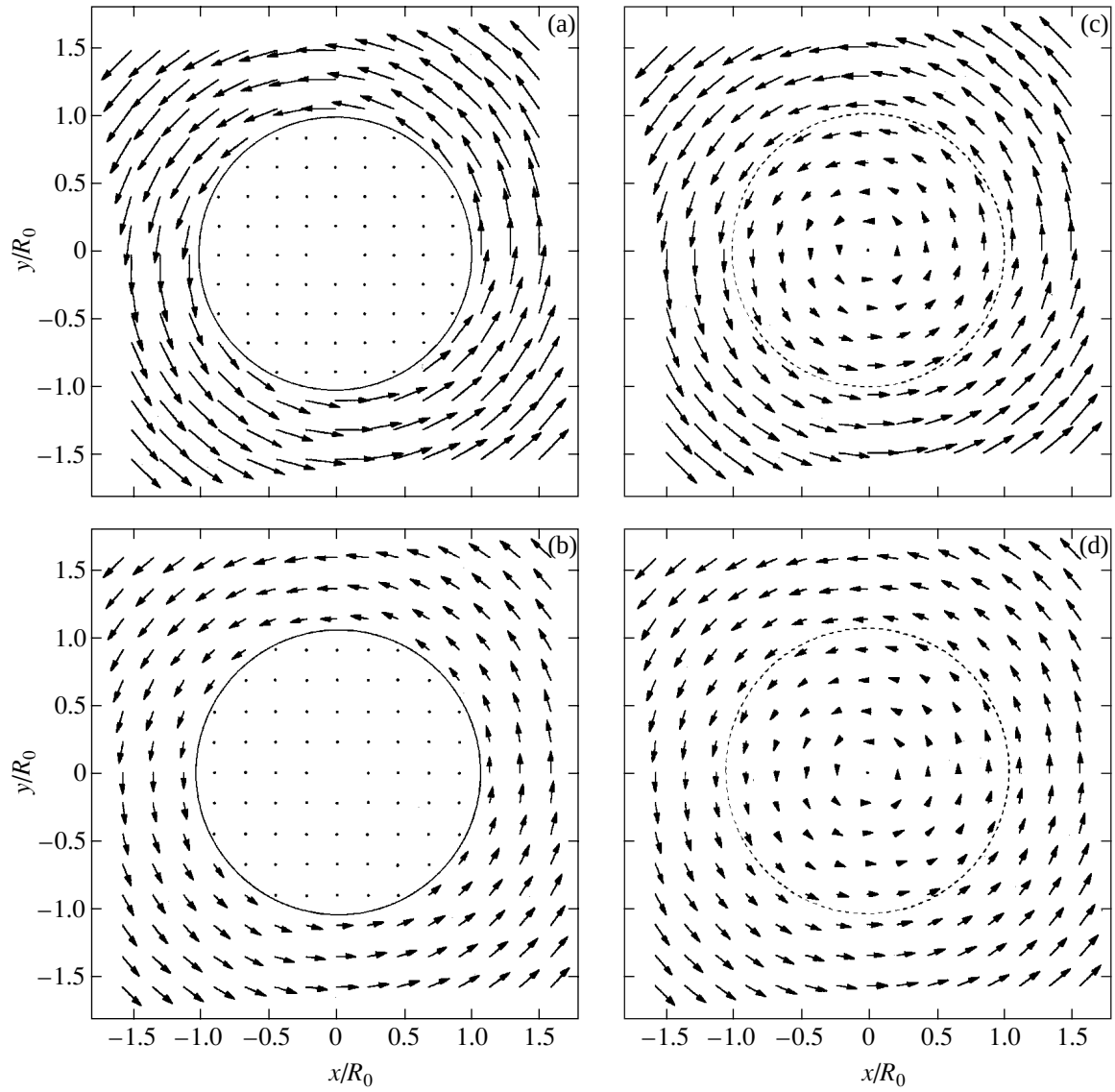

Fig. 3. Displacements produced (a, b) by a pipe and (c, d) by a screw dislocation with a full core in the planes (a, c) $z = 0$ and (b, d) $z = R_0$, which are parallel to the free crystal surface. Displacements (a, b) u_φ and (c, d) u_φ^d are proportional to the lengths of the corresponding arrows, which can be determined using the scales in the coordinate axes; the coefficient of proportionality is $b/2$. The circles $r = R_0$ (a, b) indicate the pipe surface or (c, d) are drawn for convenience of comparison of displacements produced by a pipe and a screw dislocation with a full core.

and the additional displacement field u_i^v of virtual twist disclination loops distributed over the cylindrical surface of the pipe,

$$u_i^v(\tilde{r}, \tilde{z}) = \int_{-\infty}^{\infty} \rho(\tilde{z}')u_i^\infty(\tilde{r}, \tilde{z} - \tilde{z}')d\tilde{z}', \quad (26)$$

where $u_i^\infty(\tilde{r}, \tilde{z} - \tilde{z}')$ is the displacement field of a twist disclination loop located in an infinite medium and specified by the coordinates $\tilde{r} = 1$ and $\tilde{z} = \tilde{z}'$. The field $u_i^\infty(\tilde{r}, \tilde{z})$ has the form [36]

$$u_\varphi^\infty = \frac{\omega R_0}{2}\operatorname{sgn}\tilde{z}J(2, 1; 0), \quad (27)$$

$$u_r^\infty = u_z^\infty = 0. \quad (28)$$

Using Eqs. (13) and (26)–(28), the displacement field u_i^v is calculated in the same way as the stress field σ_{ij}^v. As a result, we obtain

$$u_\varphi^v = -\frac{b}{\pi^2}\int_0^\infty \frac{[-K_2(k) + 2/k^2]K_1(\tilde{r}k)}{kK_2(k)}\cos k\tilde{z}dk, \quad (29)$$

$$u_r^v = u_z^v = 0. \quad (30)$$

Thus, the sought-for displacement field u_i is equal to the sum of the field u_i^d given by Eqs. (23)–(25) and the field u_i^v given by Eqs. (29) and (30). It follows from Eq. (30) that the free surface of the pipe has no effect on the displacement components u_r and u_z but significantly affects the displacement component u_φ. Figure 3 shows the displacements u_φ produced by the pipe in two parallel planes, namely, the free surface $z = 0$ (Fig. 3a) and the plane $z = R_0$ (Fig. 3b). For comparison, Figs. 3c and 3d show the displacements u_φ^d produced in these planes by the screw dislocation with a full core. The displacements u_φ and u_φ^d are proportional to the lengths of the corresponding arrows, which can be determined using the scales in the coordinate axes. The coefficient of proportionality is $b/2$. For example, in Fig. 3a, the length of the arrows near the surface of the pipe is approximately 0.25; therefore, $u_\varphi \approx b/8$. The displacements u_φ and u_φ^d characterize the magnitude of twisting of the material near the free surface. It can be seen from Fig. 3 that near the free surface of the pipe the displacements u_φ are significantly larger than the displacements u_φ^d produced in the same regions by the screw dislocation with a full core. Therefore, the presence of the free surface of the pipe is favorable for twisting of the crystal near the free planar surface $z = 0$ and the free cylindrical surface $r = R_0$. This conclusion is in accordance with Fig. 2a, which shows that the stress component $\sigma_{z\varphi}$ (and, hence, the strain $\varepsilon_{z\varphi}$) produced by the screw dislocation near the free crystal surface increases when the core of the dislocation becomes hollow. It is seen from Fig. 3 that the displacements u_φ produced by the pipe, as well as the displacements u_φ^d produced by the screw dislocation with a full core, decreases with increasing distance from the free surface $z = 0$.

It should be noted that knowledge of the displacement field produced by pipes near the free surface of a crystal is essential for correct determination of the diffraction contrast of the pipes. Indeed, high-resolution x-ray diffractometry allows one to determine the Burgers vectors of pipes in a sample with a low density of pipes. In the case of small-angle reflections of x rays from crystallographic planes near the crystal surface, both nonzero components, u_z and u_φ, of the displacement field of a pipe contribute to the diffraction contrast. Because of the absence of exact calculations of these components, the expressions for the displacement field of a pipe in an infinite medium and for the displacement field produced by a screw dislocation with a full core near the free crystal surface were used in [20] to calculate the diffraction contrast of pipes near the surface of a crystal. When the expressions for the displacement field of a pipe in an infinite medium were used, the agreement between the calculations and the experimental data was poor. With the expressions for the displacement field produced by a screw dislocation near the free crystal surface, the agreement became better but was far from complete. The exactly calculated displacement field of a pipe given by Eqs. (29) and (30) can be used to settle the remaining discrepancies.

4. CONCLUSION

In this paper, exact expressions have been derived for the first time for the stresses, strains, and displacements produced by a pipe that is perpendicular to the free crystal surface and contains a screw dislocation. It has been shown that the free surface of the pipe significantly affects the elastic fields produced by the dislocation associated with the pipe at distances from its surface of the order of the pipe radius. The expressions obtained for the elastic fields of a straight pipe were employed by the present authors to calculate the elastic fields of analogous pipes with steps, which arise during motion of the near-surface segments of the pipes, and the forces acting on these segments. The calculated stress field of a pipe can also be used to analyze the conditions under which pipes split and eventually disappear as a crystal grows. For example, a screw dislocation with a full core can split off from the original pipe when the dislocation acquires a kink in a near-surface layer, which is accompanied by splitting of the surface step associated with the screw dislocation [28]. If a dislocation segment that split off from the pipe has a sufficiently large Burgers vector, this segment can transform into a new pipe. In this way, branching of micropipes occurs [30]. A detailed analysis of this process will be the aim of our further investigations.

ACKNOWLEDGMENTS

This study was supported by the Ministry of Industry of the Russian Federation (program “Physics of Solid Nanostructures”) and the program “Integration” (project no. B0026).

REFERENCES

1. A. R. Verma, *Crystal Growth and Dislocations* (Butterworths, London, 1953; Inostrannaya Literatura, Moscow, 1958).
2. J. Newey, Compd. Semicond., July (2002) (http:/www.compoundsemiconductor.net/magazine/article/8/7/2/1).
3. W. Qian, M. Skowronski, K. Doverspike, *et al.*, J. Cryst. Growth **151**, 396 (1995).
4. W. Qian, G. S. Rohrer, M. Skowronski, *et al.*, Appl. Phys. Lett. **67** (16), 2284 (1995).
5. E. Valcheva, T. Paskova, P. O. Å. Persson, and B. Monemar, Phys. Status Solidi A **194** (2), 532 (2002).

6. Q. Wahab, A. Ellison, C. Hallin, *et al.*, Mater. Sci. Forum **338–342**, 1175 (2000).
7. I. Kamata, H. Tsuchida, T. Jikimoto, and K. Izumi, Jpn. J. Appl. Phys., Part 2 **40**, L1012 (2001).
8. N. Ohtani, T. Fujimoto, M. Katsuno, *et al.*, in *Technical Digest of International Conference on SiC and Related Materials (ICSCRM 2001), Tsukuba, Japan* (2001), p. 192.
9. L. Scaltrito, F. Giorgis, C. F. Pirri, *et al.*, J. Phys.: Condens. Matter **14**, 13397 (2002).
10. N. Ohtani, T. Fujimoto, M. Katsuno, *et al.*, J. Cryst. Growth **237–239**, 1180 (2002).
11. C.-Y. Hwang, M. J. Schurman, W. E. Mayo, *et al.*, J. Electron. Mater. **26** (3), 243 (1997).
12. J. Elsner, R. Jones, P. K. Sitch, *et al.*, Phys. Rev. Lett. **79** (19), 3672 (1997).
13. D. Cherns, J. Phys.: Condens. Matter **12** (49), 10205 (2000).
14. Z. Liliental-Weber, J. Electron. Mater. **49**, 339 (2000).
15. D. D. Avrov, A. S. Bakin, and S. I. Dorozhkin, in *Proceedings of the 6th International Conference on Silicon Carbide and Related Materials (ICSCRM'95), Kyoto, Japan* (1995), Inst. Phys. Conf. Ser., No. 142, Chap. 1, p. 73.
16. Yu. A. Vodakov, A. D. Roenkov, M. G. Ramm, *et al.*, Phys. Status Solidi B **202** (1), 177 (1997).
17. Z. Liliental-Weber, Y. Chen, S. Ruvimov, *et al.*, Mater. Res. Soc. Symp. Proc. **449**, 417 (1997).
18. J. Heindl, H. P. Strunk, V. D. Heydemann, and G. Pensl, Phys. Status Solidi A **162** (1), 251 (1997).
19. G. Augustine, H. McD. Hobgood, V. Balakrishna, *et al.*, Phys. Status Solidi B **202** (1), 137 (1997).
20. X. R. Huang, M. Dudley, W. M. Vetter, *et al.*, Appl. Phys. Lett. **74** (3), 353 (1999).
21. M. Dudley, X. R. Huang, W. Huang, *et al.*, Appl. Phys. Lett. **75** (6), 784 (1999).
22. D. Hofmann, M. Bickermann, R. Eckstein, *et al.*, J. Cryst. Growth **198–199**, 1005 (1999).
23. L. M. Sorokin, A. S. Tregubova, M. P. Shcheglov, *et al.*, Fiz. Tverd. Tela (St. Petersburg) **42** (8), 1384 (2000) [Phys. Solid State **42**, 1422 (2000)].
24. B. M. Epelbaum, D. Hofmann, U. Hecht, and A. Winnacker, in *Abstracts of 3rd European Conference on SiC and Related Materials (ECSRM), KlosterBanz, Germany* (2000), p. 49.
25. I. Kamata, H. Tsuchida, T. Jikimoto, and K. Izumi, Jpn. J. Appl. Phys., Part 1 **39** (12A), 6496 (2000).
26. T. A. Kuhr, E. K. Sanchez, M. Skowronski, *et al.*, J. Appl. Phys. **89** (8), 4625 (2001).
27. N. Ohtani, M. Katsuno, T. Fujimoto, *et al.*, J. Cryst. Growth **226** (2/3), 254 (2001).
28. B. M. Epelbaum and D. Hofmann, J. Cryst. Growth **225** (1), 1 (2001).
29. T. S. Argunova, M. Yu. Gutkin, J. H. Je, *et al.*, J. Mater. Res. **17** (10), 2705 (2002).
30. M. Yu. Gutkin, A. G. Sheinerman, T. S. Argunova, *et al.*, J. Appl. Phys. **92** (2), 889 (2002).
31. F. C. Frank, Acta Crystallogr. **4**, 497 (1951).
32. P. Pirouz, Philos. Mag. A **78** (3), 727 (1998).
33. M. Yu. Gutkin and A. G. Sheinerman, Phys. Status Solidi B **231** (2), 356 (2002).
34. A. L. Kolesnikova and A. E. Romanov, Preprint No. 1019, FTI AN SSSR (Physicotechnical Inst., USSR Academy of Sciences, Leningrad, 1986).
35. S. J. Shaibani and P. M. Hazzledine, Philos. Mag. A **44** (3), 657 (1981).
36. T.-W. Chou, J. Appl. Phys. **42** (12), 4931 (1971).
37. G. Eason, B. Noble, and I. N. Sneddon, Philos. Trans. R. Soc. London **247** (935), 529 (1955).
38. V. A. Likhachev and R. Yu. Khaĭrov, *Introduction to the Theory of Disclinations* (Leningr. Gos. Univ., Leningrad, 1975).
39. W. Si, M. Dudley, R. Glass, *et al.*, J. Electron. Mater. **26** (3), 128 (1997).

Translated by Yu. Epifanov

Physics of the Solid State, Vol. 45, No. 9, 2003, pp. 1701–1705. Translated from Fizika Tverdogo Tela, Vol. 45, No. 9, 2003, pp. 1621–1625.

DEFECTS, DISLOCATIONS, AND PHYSICS OF STRENGTH

Investigation of the Local Mechanical Properties of Potassium Chloride Single Crystals by Atomic Force Microscopy

Ya. M. Soĭfer* and A. Verdyan**

** Institute of Solid State Physics, Russian Academy of Sciences, Chernogolovka, Moscow oblast, 142432 Russia*
e-mail: soifer@hait.ac.il
*** Holon Academic Institute of Technology, Holon, 59512 Israel*

Received February 21, 2003

Abstract—Using an atomic force microscope (AFM), the of hardness H and Young's modulus E are measured in near-surface layers of KCl single crystals to a depth of 300 nm at loads of 5–100 μN. The values of H and E are estimated indirectly by analyzing $P(h)$ curves (load vs. indentation depth curves). The value of H is also estimated directly by measuring the area of an indentation with the help of an AFM with a nanoscale resolution. The effect of structural features of the surface around an indentation on the accuracy of the H and E estimates is revealed. The sharp dependence of H on the load (the nanoscale effect) is revealed. The experimental results agree qualitatively with the predictions of the geometrically necessary dislocation model developed by Nix and Gao. However, in order to quantitatively estimate mass transfer from a nanoindenter, a structural analysis is required with allowance for plastic deformation in crystals. © *2003 MAIK "Nauka/Interperiodica".*

1. INTRODUCTION

Nanoindentation of materials has been widely applied over the past 15 years to study the mechanical properties of thin films and the surface layers of bulk materials. The progress in the development and application of the nanoindentation technique is mainly due to the development of micro- and nanotechnologies in modern analytical engineering. The following two aspects of the problem of nanoindentation should be considered: first, improving the technique and obtaining information required for predicting the mechanical behavior of materials used in micro- and nanodevices, and, second, establishing the physical nature of mechanisms responsible for the strength and plasticity of small volumes in materials. At present, both aspects of this problem are being intensively studied by various scientific groups.

Nanoindentation is based on monitoring the penetration of a nanoindenter into a material and finding quantitative relations between the parameters of the load vs. indentation depth ($P(h)$) curve and the mechanical properties (such as the hardness H and Young's modulus E) of the material. Conventional nanoindenters allow one to use loads from micronewtons to millinewtons and to measure indentation depths from nanometers to micrometers. The hardness and Young's modulus are estimated from the relations

$$H = \frac{P}{A}, \tag{1}$$

$$E_{\text{eff}} = \frac{E}{1-\nu^2} = \frac{\sqrt{\pi}}{2}\frac{S}{\sqrt{A}}, \quad \frac{1}{E_{\text{eff}}} = \frac{1-\nu^2}{E_{\text{ind}}} + \frac{1-\nu^2}{E}, \tag{2}$$

where P is the maximum load, A is the contact area, E_{eff} is the effective modulus specified by the Young moduli and Poisson ratios of the material under study and of the indenter material, and S is the contact stiffness of the material. The conventional procedure of estimating S from a $P(h)$ dependence is described in [1]. Thus, analysis of a $P(h)$ curve allows estimation of such important mechanical properties as the hardness and elasticity of a material for extremely small loads and, hence, small indentation depths, i.e., estimation of the local mechanical properties of small volumes in the material. However, as shown by Randall [2], this procedure does not take into account the pile-up and sink-in effects during nanoindentation, which can substantially change the contact area A measured experimentally. Since both the hardness and Young's modulus calculated from Eqs. (1) and (2) depend on A, they can be determined with high error if the value of A is not controlled by another independent method. Such a control is possible in methods that combine nanoindentation of materials with a topographic study of their surfaces by atomic force microscopy (AFM). In this case, nanoindentation is performed with a diamond nanoindenter, which can simultaneously be used as a sharp tip for scanning a surface to obtain its topographic (two- or three-dimensional) image in the AFM contact or tapping mode. The surface relief is recorded with a nanoscale spatial resolution. The combination of AFM and nanoindentation makes it possible to visually choose a place for a nanotest 0.5–1 μm^2 in size and to obtain a three-dimensional image of an indentation and of the surface around it with a resolution of 0.5 nm. Indentation images can be used to calculate the contact area and compare it with the value calculated from a $P(h)$

1063-7834/03/4509-1701$24.00 © 2003 MAIK "Nauka/Interperiodica"

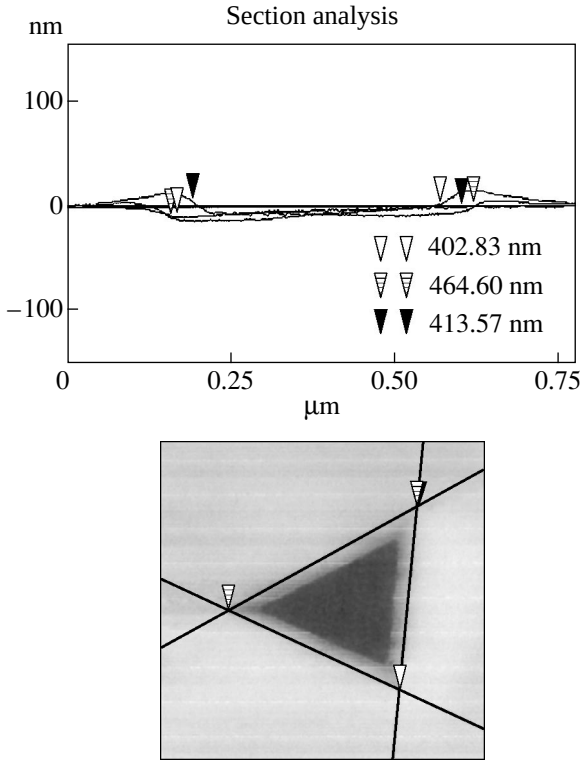

Fig. 1. An example of measuring the contact area. The distances between the marks in the upper part of the figure correspond to the sides of the triangle (indentation) in the lower part of the figure.

curve. Thus, it becomes possible to substantially improve the reliability of estimating the hardness and elasticity of small volumes in materials, to visualize structural features of the surface around an indentation with a nanoscale spatial resolution, and to experimentally check the physical models describing deformation in small volumes [3–5].

In this work, we study the local mechanical properties of KCl single crystals by using AFM. Defect structures and their relation to the bulk mechanical properties of KCl crystals are well known [6]; therefore, these crystals are often used as a model material to establish mechanisms responsible for the plasticity of crystals. For AFM, KCl single crystals are convenient, since it is easy to prepare samples with almost atomically smooth surfaces of crystal blocks from these crystals through simple cleavage along cleavage planes.

2. EXPERIMENTAL

We investigated KCl Czochralski-grown single crystals having high plasticity and a microhardness of 0.1 GPa. This means that indentations are rather large even at small loads and measurement at extremely small loads of nanoindentation causes high errors due to both the indenter shape and the determination of the loading force parameters. To enhance their hardness, the KCl single crystals were irradiated by γ rays from a Co^{60} source to a dose of about 5×10^6 rad and then cleaved along the (100) cleavage planes to prepare specimens for indentation. Nanoindentation was carried out only on as-cleaved cleavage surfaces.

For measurements, we used a Di Dimension 3100 atomic force microscope with a diamond indenter serving as a tip mounted at the end of a steel cantilever. The spring constant of the cantilever was 297 N/m, and its resonance frequency was ~78 kHz. The indenter was a trihedral 90° pyramid with a radius of curvature of about 25 nm. This structure of the indenter allowed us to perform nanoindentation and to measure a surface relief with a high spatial resolution without changing the cantilever. Indentation was carried out at various loading rates (loading times varied from 10 to 0.01 s) and various loads (from 5 to 400 μN). The bending flexure of the cantilever served as a measure of the load applied. To calculate the force applied to a specimen during indentation, we preliminary calibrated the cantilever sensitivity using very hard materials. To this end, we used sapphire with a hardness of 25 GPa and a Young's modulus of 470 GPa. Indentation was performed by pressing the indenter into the surface of a specimen to reach the required bending of the specimen. Then, the indenter was raised to its initial position above the specimen surface. For each indentation, we recorded the dependence of the cantilever load on the cantilever displacement in the vertical direction. Based on this dependence and taking into account the cantilever sensitivity, we plotted the $P(h)$ curve and analyzed it using the procedure described at the beginning of this article to estimate the hardness H and Young's modulus of the specimen. As a reference specimen, we used fused silica with a Young's modulus of 72 GPa and a hardness of 9 GPa. Moreover, we directly estimated the hardness using Eq. (1); the indentation area was measured by scanning the indented surface. This area can be measured by various techniques; most often, we measured the lengths of indent sides (Fig. 1). This technique was used according to the following considerations. As shown by many investigators [7, 8], the shape of an indentation changes during microindentation and, especially, nanoindentation due to the elastic aftereffect during unloading. In rather plastic materials, the vertices of indents do not change their position; that is, the distances between the vertices remain the same during recovery. The procedure of measurement was the following. Specimens were $10 \times 10 \times 5$ mm in size. An optical microscope was used to choose a place convenient for indentation, and the cantilever with the indenter of the atomic force microscope was lowered to this place. The topography of a surface was recorded across a 80×80-μm^2 area in the tapping mode to find a proper place at a microscopic level, and then an indentation was made at a given load and loading rate in an area of 1 μm^2. Once an indentation was made, the surface was scanned in the tapping mode to obtain the topography of the indent and of the surface around it.

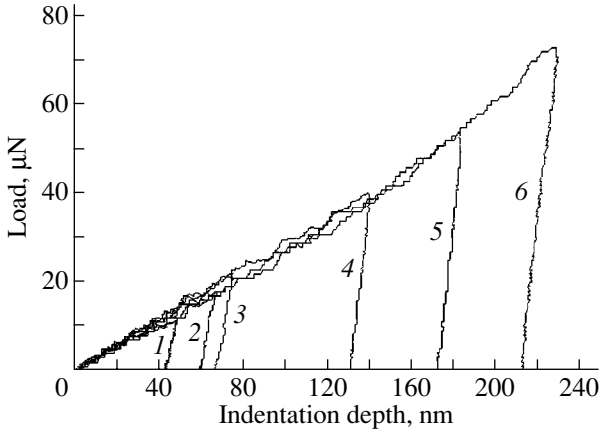

Fig. 2. $P(h)$ dependences at various loads of indentation: (*1*) P = 10, (*2*) 15, (*3*) 20, (*4*) 40, (*5*) 53, and (*6*) 73 μN.

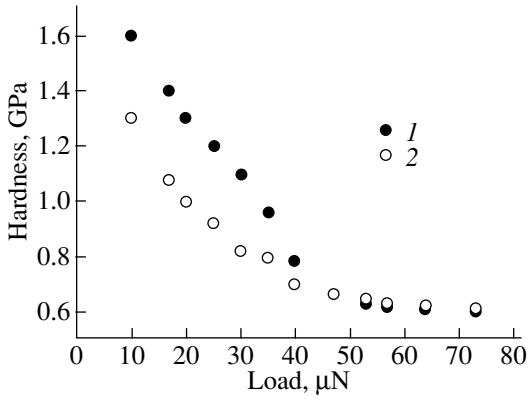

Fig. 3. Dependence of the hardness H on the load of indentation P: (*1*) the hardness H as estimated from the $P(h)$ dependences and (*2*) the hardness H determined from direct measurements of the contact area.

This technique allowed us to make series of indents at the same load or at loads increasing with a given step. In this case, surface images were taken after the completion of a series. Before and after the experiments, we calibrated the equipment on standard materials: fused silica and sapphire.

3. RESULTS AND DISCUSSION

The dependences of the load on the indentation depth are shown in Fig. 2. For illustration, six dependences, recorded at different maximum indenter loads (from 10 to 75 μN), are given here. The loading and unloading times in all cases were 0.5 s. This means that the loading rates varied from 20 to 150 μN/s. The variation of the loading rate is seen to exert no effect on the shape of the $P(h)$ curve. The $P(h)$ curve was analyzed according to the procedure described in [1]; that is, h_C corresponding to the contact depth was first determined from the curve and then the contact area A was calculated from the relation $A = 2.56h_C^2$ (coefficient 2.56 corresponds to a 90° pyramid). Using Eqs. (1) and (2), we calculated the hardness and Young's modulus E_{eff}, respectively. The latter is approximately equal to Young's modulus E of a specimen, since the Young's modulus of diamond is much higher than the modulus E, which means that the term $(1 - \nu^2)/E_{\text{ind}}$ in Eq. (2) can be neglected. Young's moduli of the KCl specimens estimated from the $P(h)$ curves by the procedure described above differ by almost two times, depending on $P_{\max}$ (the Young's modulus is 11.2 GPa at an indenter load of 73 μN and is 21 GPa at 10 μN), whereas the Young's modulus of KCl determined from acoustic measurements on its bulk sample is higher than or equal to 23.4 GPa [9]. The fact that the Young's modulus calculated from acoustic measurements can be higher is not surprising, since acoustic measurements are carried out at very low amplitudes and, hence, purely elastic deformations. Therefore, the elastic constants, whose combination is Young's modulus, can be determined with a high accuracy from these measurements. The Young's modulus that is estimated from the load vs. indentation depth curve corresponds to rather high stresses, and it is impossible to exclude the effect of anelastic processes (unloading is not a purely elastic process), which decrease Young's modulus, especially in plastic materials. The scatter of the E values depending on the maximum load can be due to at least two causes: errors in estimating the material stiffness S and an increase in the effect on anelastic processes on the unloading curve with increasing maximum load. The latter indicates that the modulus is underestimated at higher loads; therefore, the value of E obtained at lower stresses should be used.

The fact that Young's moduli calculated from the $P(h)$ curves at small loads are greater than those determined from acoustic measurements is most likely due both to an increase in the fraction of the elastic component and to an increase in the error of estimating the quantities entering into Eq. (2). Nevertheless, the difference between the estimates of Young's modulus obtained from the $P(h)$ curves and the acoustic values is not large, which is extremely important, since traditional acoustic techniques are inapplicable to measurement in such small volumes of a material as are used in nanoindentation. Thus, nanoindentation is currently the only method of measuring the elastic properties of small volumes in a material.

Figure 3 shows the variation of the hardness H with the applied load and the results of the direct estimation of hardness at the same loads (in the same experiment) obtained by division of the load by the contact area determined from an indent image. As is seen, the character of the load dependence is identical to that in the former case, although the absolute values are somewhat lower. One of the possible causes of this discrepancy is the formation of pileups around indents (Fig. 4), which,

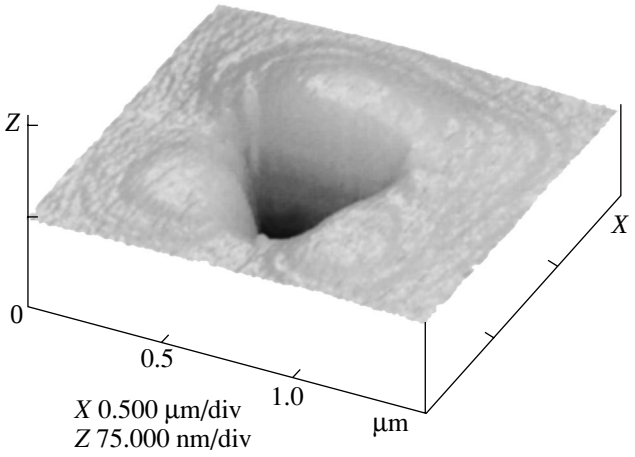

Fig. 4. Three-dimensional image of an indent made at a load of 53 μN.

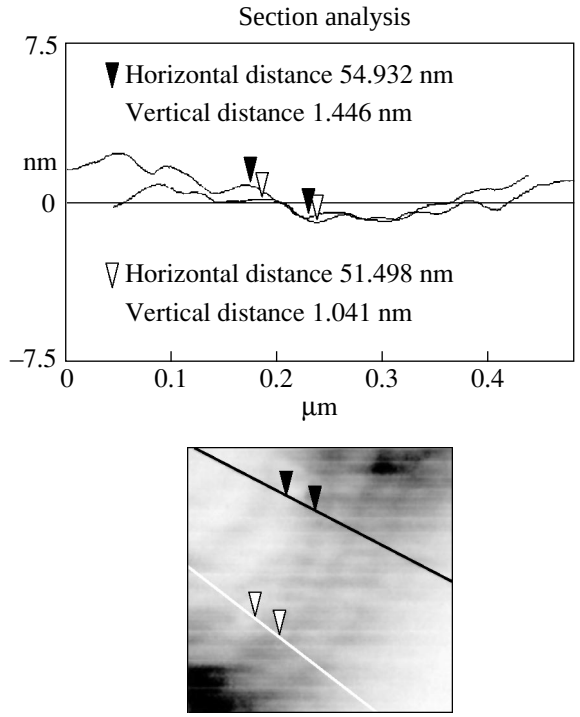

Fig. 5. Relief of the surface (pileup) around the indent shown in Fig. 4. The distances between the marks in the upper panel correspond to the height and width of the pileup steps shown in the lower panel.

as shown above, can result in overestimated H values when calculated from the $P(h)$ curve. Although the KCl crystal was irradiated and, hence, was more rigid than the nonirradiated one, it was rather plastic and pileups were small. An interesting feature of the surface relief around an indentation is that pileups have a terrace structure. The terrace height is about 1.5 nm, and its width is 50 nm (see Fig. 5, which is a magnified two-dimensional image of the descending part of a pileup). At smaller loads, the terrace height can be even smaller (0.9 nm). Although studying the terrace structure of the pileups can be of great interest for determining the mechanism of indentation, we restrict our investigation in this work to ascertaining a discrete structure of the pileups, leaving its detailed experimental investigation to the near future (including the study of other single crystals with the use of indenters of various shapes).

The values of the hardness calculated from both the $P(h)$ curve and the measured indentation area using a topographic pattern decrease with increasing load, thus demonstrating the well-known nanoscale effect. Although this effect has been extensively studied, it has not been unambiguously interpreted. At present, one of the most known models that quantitatively describes this effect is the geometrically necessary dislocation model developed in [5]. In this model, the dependence of hardness on the indentation depth is represented as

$$H^2 = 27a^2b^2\mu^2\rho_s + (40.5ba^2\mu^2\tan^2\Theta)\frac{1}{h}, \qquad (3)$$

where H is the hardness at the given indentation depth h, a is a constant equal to 1/3, μ is the shear modulus, b is the Burgers vector, ρ is the density of statistically stored dislocations, and Θ is the indenter apex angle. The first term here represents hardening due to stored dislocations, and the second is caused by geometrically necessary dislocations generated during nanoindentation. However, the results of the experimental check of this model are contradictory. On the one hand, some authors assert that experimental data processing in the context of the geometrically necessary dislocation model exhibits good agreement with experiment [5, 10]; on the other hand, other authors who studied the same metallic materials did not confirm this conclusion [11, 12]. Liu and Ngan [12] note that the $H(P)$ curve depends strongly on the state of the sample surface (on its roughness and methods of polishing the sample, i.e., factors that are not taken into account in the model). In this connection, the nanoindentation of KCl crystals is convenient to check this model, since the crystals are rather plastic and their cleavage surfaces are atomically smooth. Figure 6 shows the $H(P)$ dependence plotted as H^2 versus $1/h$. The $H^2(1/h)$ dependence is seen to be virtually linear for the directly estimated H, which allows us to experimentally determine the quantities entering into Eq. (3). Taking $a = 1/3$, $\tan\Theta = 1.1$ (90° pyramid), and the Burgers vector $b = 0.44$ nm [6], we can estimate the shear modulus from the parameters of the straight line; the result is 6.32 GPa. The acoustically determined shear modulus of bulk KCl is $\mu = 10.9$ GPa, which agrees with the above value if we taking into account the simplifications made upon deriving Eq. (3). However, the calculated dislocation density $\rho \sim 2 \times 10^{11}$ cm^{-2} seems to be strongly overestimated. We think that the model inadequately describes the results, since it is rather simple and does not take into account crystallographic slip and the mechanism of dislocation harden-

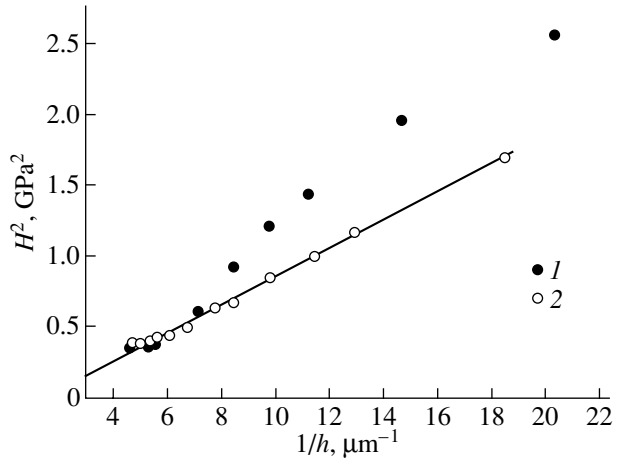

Fig. 6. Data from Fig. 3 plotted as H^2 versus $1/h$: (*1*) the hardness H as estimated from the $P(h)$ dependence and (*2*) the hardness H as determined from direct measurements of the contact area.

ing of ionic crystals. Moreover, it is likely that the dislocation mechanism is not the only mechanism responsible for deformation in nanovolumes. Apparently, other mass-transfer mechanisms, involving rapid diffusion in a stress field and a high concentration of point defects, can operate during nanoindentation. As for the $H^2(1/h)$ dependence constructed using the $P(h)$ curves, it differs from the results of direct measurements only at small loads. This disagreement is likely due to the pile-up effect, whose relative contribution to the values of H estimated from the $P(h)$ curves increases with decreasing load.

REFERENCES

1. W. C. Oliver and G. M. Pharr, J. Mater. Res. **7**, 1564 (1992).
2. N. X. Randall, Philos. Mag. A **82** (10), 1883 (2002).
3. N. A. Fleck, G. M. Muller, M. F. Ashby, and J. W. Hutchinson, Acta Metall. Mater. **42**, 475 (1994).
4. W. J. Poole, M. F. Ashby, and N. A. Fleck, Scr. Mater. **34**, 559 (1996).
5. W. D. Nix and H. Gao, J. Mech. Solids **46** (4), 411 (1998).
6. B. I. Smirnov, *Dislocation Structure and Hardening of Crystals* (Nauka, Leningrad, 1981).
7. N. A. Stelmashenko, M. G. Walls, L. M. Brown, and Y. V. Milman, Acta Metall. Mater. **41**, 2855 (1993).
8. J. V. Pethica, R. Hutchings, and W. C. Oliver, Philos. Mag. A **48**, 593 (1983).
9. O. L. Anderson, in *Physical Acoustics: Principles and Methods*, Ed. by W. P. Mason (Academic, New York, 1965; Mir, Moscow, 1968), Vol. 3, Part B, p. 77.
10. Q. Ma and D. R. Clarke, J. Mater. Res. **10**, 853 (1995).
11. Y. Y. Lim and M. M. Chaudri, Philos. Mag. A **79**, 2979 (1999).
12. Y. Liu and A. H. W. Ngan, Scr. Mater. **44**, 237 (2001).

Translated by K. Shakhlevich

Physics of the Solid State, Vol. 45, No. 9, 2003, pp. 1706–1718. Translated from Fizika Tverdogo Tela, Vol. 45, No. 9, 2003, pp. 1626–1636.

DEFECTS, DISLOCATIONS, AND PHYSICS OF STRENGTH

Dislocation and Disclination Loops in the Virtual-Defect Method

A. L. Kolesnikova* and A. E. Romanov**

**Institute of Problems of Mechanical Engineering, Russian Academy of Sciences, Vasil'evskiĭ ostrov, Bol'shoĭ pr. 61, St. Petersburg, 199178 Russia*

***Ioffe Physicotechnical Institute, Russian Academy of Sciences, Politekhnicheskaya ul. 26, St. Petersburg, 194021 Russia*

e-mail: aer@mail.ioffe.ru

Received February 27, 2003

Abstract—A method of virtual circular defect loops is developed for determining the elastic fields produced by defects in a bounded medium in the case of an axially symmetric geometry. In this method, continuously distributed virtual circular Volterra and Somigliana dislocation loops are adjusted in such a way as to satisfy the boundary conditions imposed at free surfaces and interfaces. Original calculations of the elastic fields of circular defect loops of different types are carried out. The elastic fields are found for the case of straight dislocations and disclinations in a plate that are perpendicular to the plate plane and for the case of circular disclination loops parallel to the plate plane or to an interface.© *2003 MAIK "Nauka/Interperiodica".*

1. INTRODUCTION

Defects in a solid, e.g., dislocations [1] and disclinations [2], usually produce elastic fields characterized by a certain energy. Real solids possess exterior boundaries and can also have interfaces, which cause a redistribution of the elastic fields produced by defects. In order to take this effect into account correctly within various physical models describing the behavior of dislocations and disclinations, efficient methods are required for solving the corresponding boundary-value problems in the theory of defects.

Several comprehensive reviews devoted to the methods for solving the boundary-value problems in the theory of dislocations and to the relevant results obtained are available in the literature [3–5]. There are also original papers devoted to calculations of the elastic fields and energies of dislocations situated near boundaries; some of those papers are important both fundamentally and for practical applications (e.g., the calculation of the electron-microscopic contrast carried out in [6]) or for model treatments (e.g., the analysis of the stability of dislocations in nanocrystals performed in [7]). Solutions of boundary problems for disclinations are presented in monograph [2]; more recent results can be found in original papers [8–10].

One of the efficient methods for solving the boundary problems of the theory of dislocations and disclinations is the virtual-defect method. This method was mainly developed by Louat [11] and then successfully employed by many authors to solve various boundary problems in the theory of defects (see, e.g., [5, 8, 12–15]). In this paper, we use this method to solve axially symmetric boundary problems in the theory of dislocations and disclinations, with circular defect loops taken as virtual defects.

This paper is organized as follows. In Section 2, we briefly describe the virtual-defect method. Section 3 is devoted to calculations of the elastic fields of defect loops of different types from their given plastic distortions. Finally, in Section 4, we present exact analytical solutions to the boundary problems for dislocations and disclinations in a plate that are perpendicular to the plate plane and for circular disclination loops parallel to the plate plane or to an interface.

2. VIRTUAL-DEFECT METHOD

The merits of the virtual-defect method are its simplicity and clearness, which allow one to solve boundary problems for different fields (e.g., elastic and magnetic ones) produced by defects, as well as for fields not associated with defects, on a unified basis. Originally, this method used only surface dislocations [11–13], but later it was extended to the case of surface disclinations [2] and surface distributions of fluxoids (vortex lines) in type-II superconductors [16].

Essentially, the method is as follows. The field produced by a defect (or a field not associated with a defect) in a medium with interior or exterior boundaries is written as the sum of the field produced by the defect in an infinite medium and an additional field generated by continuous distributions of surface defects. The surface defects are chosen such that their field contains components involved in the boundary conditions. Therefore, the additional field automatically satisfies the equations of the medium (e.g., the equilibrium and compatibility equations in the elasticity theory or the

London equations in the theory of type-II superconductors) and the boundary conditions take the form of integral equations for the distribution functions of the virtual surface defects. We note that the virtual defects are located outside the medium in which their field is searched for. However, these defects may be located at the free surface of the medium. (For this reason, the continuously distributed virtual defects are called surface defects, in contrast to image defects.) Thus, virtual defects are different from real ones, which possess cores of a finite size in crystals. The core of any virtual defect can be taken to be infinitely small, and, therefore, the virtual defect itself will be a singular source of an elastic or magnetic field in this case.

The method in question has been used to advantage, in cases where the role of surface defects was played by infinite straight defect lines, to calculate the fields of straight defect lines parallel to an interface [8, 13, 16, 17] and to solve certain special boundary problems for straight dislocations that end at the surface or cross an interface [5, 14]. In [5, 14], distributions of surface dislocation segments were used.

In this paper, virtual surface defects are taken to be circular loops of dislocations and disclinations and axially symmetric boundary problems are solved. For example, we consider (i) a straight defect line perpendicular to the planar free crystal surfaces or to an interface, (ii) a circular defect loop parallel to the planar free crystal surfaces or to an interface, and (iii) a circular loop and a circular cylinder (including a multilayered one) having a common axis. It will be shown that making use of virtual defect loops simplifies solution of the problem in many cases, because the difficulties associated with the point at which the real linear defect terminates at the surface of the solid are obviated.

3. ELASTIC FIELDS PRODUCED BY CIRCULAR DEFECT LOOPS

In order to solve boundary-value problems by using the method of virtual circular defect loops, one has to calculate the fields of total displacements and elastic stresses for a fairly wide range of defects, because the continuity conditions are imposed on these fields at an interface. Below, we demonstrate how the elastic fields of circular loops can be calculated using a universal method [18] and present calculated fields of the total displacements and of the elastic stresses for loops of prismatic and glide dislocations, loops of wedge and twist disclinations, and Somigliana dislocation loops (radial-disclination and radial-dislocation loops).

A dislocation–disclination loop (Volterra dislocation) is characterized by its plastic distortion β_{ij}^*, which is written in the form [18]

$$\beta_{ij}^* = \delta_i(S)[-b_j - e_{jpq}\omega_p(x_q - x_q^0)], \qquad (1)$$

where $\delta_i(S) = \int_{S_i} \delta(\mathbf{r} - \mathbf{r}')dS_i'$ is the three-dimensional $\delta(\mathbf{r} - \mathbf{r}')$ function, S_i is the surface of a cut made along the loop plane with a normal vector $\mathbf{n}_i$, b_j is the Burgers vector of the dislocation, ω_p is the Frank vector of the disclination, x_q^0 is the coordinate of the rotation axis, and e_{jpq} is the Levi–Civita tensor. The expression in square brackets is the jump in displacement $[u_j]$ in the surface of the cut S_i. This jump is the result of the following procedure: cutting along the surface S_i and displacing the upper edge of the cut S_i^+ relative to the lower edge S_i^- by the amount $[u_j]$.[1] Upon adding (or removing) the material to eliminate the discontinuities (or overlaps) thus produced and gluing the edges of the cut, we obtain a defect with distortion β_{ij}^*. In general, the plastic distortion β_{ij}^* is a function of an arbitrary jump $[u_j]$ at the surface S.

The plastic distortion β_{ij}^* determines the total displacements u_m in the elastic body [18]:

$$u_m(r') = -i\int_{-\infty}^{\infty}\int\int \xi_l C_{jikl} L_{mk} \bar{\beta}_{ij}^* \exp(i\boldsymbol{\xi}\cdot\mathbf{r})d\xi_x d\xi_y d\xi_z, \qquad (2)$$

where C_{jikl} are the elastic constants; L_{mk} and $\bar{\beta}_{ij}^*$ are the Fourier transforms of the Green's function for the elastic medium and of the plastic distortion, respectively; and $\boldsymbol{\xi}\cdot\mathbf{r} = \xi_x x + \xi_y y + \xi_z z$. For an isotropic medium, we have [18]

$$C_{jikl} = \frac{2G\nu}{1-2\nu}\delta_{ji}\delta_{kl} + G(\delta_{ik}\delta_{jl} + \delta_{il}\delta_{jk}),$$
$$L_{mk} = \frac{1}{(2\pi)^{3/2}}\frac{2(1-\nu)\xi^2\delta_{mk} - \xi_m\xi_k}{2(1-\nu)G\xi^4}, \qquad (3)$$

where G is the shear modulus, ν is the Poisson ratio, δ_{mk} is the Kronecker symbol, and $\xi^2 = \xi_x^2 + \xi_y^2 + \xi_z^2$. Equations (2) and (3) can be used to calculate the elastic fields of Volterra and Somigliana dislocations of any configuration, in particular, in the form of circular loops.

Now, we consider different types of circular loops, whose plastic distortions are linearly independent in a Cartesian or a cylindrical coordinate system and are the zeroth or first terms of the Fourier series. For circular

[1] Here and in another of our publications [9], the choice of the edges of the cut and of the jump in displacement is opposite to that made in [18]. However, the defects obtained in both cases are identical.

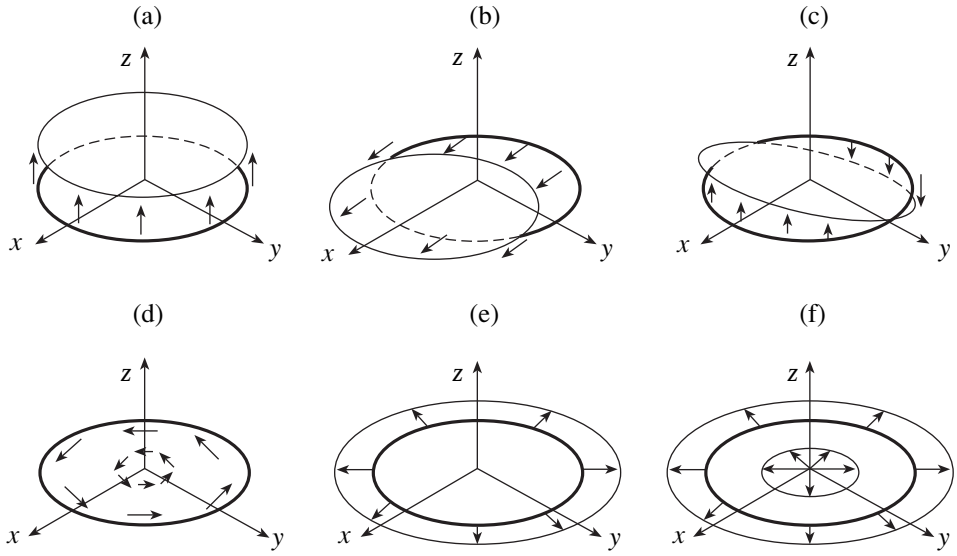

Fig. 1. Various types of defects that can be used as virtual defect loops in solving boundary-value problems: (a) prismatic dislocation loop, (b) glide dislocation loop, (c) wedge disclination loop, (d) twist disclination loop, (e) radial disclination loop (Somigliana dislocation), and (f) radial dislocation loop (Somigliana dislocation). Arrows indicate the displacements of the upper edge of the cut that should be made to form a defect loop with a given plastic distortion.

loops lying in the *xy* plane and centered at the origin, the distortions are

$$\beta_{zj}^* = A_0 + A_1\cos\varphi + B_1\sin\varphi,$$

$$A_0 = A_1 = B_1 = (b + \omega r)H\left(1 - \frac{r}{a}\right)\delta(z), \qquad (4)$$

$$j = x, y, z \quad \text{or} \quad j = r, \varphi, z.$$

Here, $H\left(1 - \frac{r}{a}\right)$ is a Heaviside function, $\delta(z)$ is a one-dimensional δ function, and a is the radius of a loop. The distortions of loops are linear functions of $\cos\varphi$ and $\sin\varphi$ and are linearly independent only in a Cartesian or a cylindrical coordinate system. The possible defect loops are considered in more detail in [9].

Below, we present the plastic distortions, total displacements, and elastic stresses for different types of defect loops lying in the *xy* plane and centered at the origin, with the defect line directed counterclockwise.

3.1. Prismatic Dislocation Loop with Burgers Vector $\mathbf{b} = -b\mathbf{e}_z$ *(Fig. 1a)*

The plastic distortion of this loop is $\beta_{zz}^* = bH\left(1 - \frac{r}{a}\right)\delta(z)$. The total displacements are

$$u_r = \frac{b}{4(1-\nu)}\left[(2\nu - 1)J(1, 1; 0) + \frac{|z|}{a}J(1, 1; 1)\right],$$

$$u_\varphi = 0, \qquad (5)$$

$$u_z = \frac{b\,\mathrm{sgn}(z)}{4(1-\nu)}\left[2(1-\nu)J(1, 0; 0) + \frac{|z|}{a}J(1, 0; 1)\right].$$

Here and henceforth, $\mathrm{sgn}(z)$ is equal to –1 for $z < 0$ and +1 for $z > 0$ and $J(m, n; p)$ are Lipschitz–Hankel integrals [19] defined as $J(m, n; p) = \int_0^\infty J_m(\kappa)J_n(\kappa r/a)\exp(-\kappa|z|/a)\kappa^p d\kappa$, with $J_m(\kappa)$ being Bessel functions.

By calculating the elastic strains from Eqs. (5) and using the Hooke law, the elastic stresses can be found to be

$$\sigma_{rr} = \frac{Gb}{2(1-\nu)}\left[\frac{1-2\nu}{r}J(1, 1; 0) + \frac{|z|}{a^2}J(1, 0; 2)\right.$$

$$\left. - \frac{1}{a}J(1, 0; 1) - \frac{|z|}{ar}J(1, 1; 1)\right],$$

$$\sigma_{\varphi\varphi} = \frac{Gb}{2(1-\nu)}\left[\frac{2\nu - 1}{r}J(1, 1; 0)\right.$$

$$\left. - \frac{2\nu}{a}J(1, 0; 1) + \frac{|z|}{ar}J(1, 1; 1)\right], \qquad (6)$$

$$\sigma_{zz} = -\frac{Gb}{2(1-\nu)}\left[\frac{1}{a}J(1, 0; 1) + \frac{|z|}{a^2}J(1, 0; 2)\right],$$

$$\sigma_{rz} = -\frac{Gb}{2(1-\nu)}\frac{z}{a^2}J(1, 1; 2),$$

$$\sigma_{z\varphi} = \sigma_{r\varphi} = 0.$$

The fields given by Eqs. (5) and (6) can also be found as a particular case of the well-known solution for a prismatic dislocation loop in a two-phase material [20].

3.2. Glide Dislocation Loop with Burgers Vector $\mathbf{b} = -b\mathbf{e}_x$ *(Fig. 1b)*

The plastic distortion is $\beta^*_{zx} = bH\left(1-\frac{r}{a}\right)\delta(z)$ The total displacements are

$$u_r = \frac{b\,\mathrm{sgn}(z)\cos\varphi}{4(1-\nu)}\left[2(1-\nu)J(1,0;0) - \frac{|z|}{a}J(1,0;1) + \frac{|z|}{r}J(1,1;0)\right],$$
$$u_\varphi = \frac{b\,\mathrm{sgn}(z)\sin\varphi}{4(1-\nu)}\left[2(\nu-1)J(1,0;0) + \frac{|z|}{r}J(1,1;0)\right], \quad (7)$$
$$u_z = \frac{b\cos\varphi}{4(1-\nu)}\left[(1-2\nu)J(1,1;0) + \frac{|z|}{a}J(1,1;1)\right].$$

The elastic stresses are

$$\sigma_{rr} = \frac{Gb\,\mathrm{sgn}(z)\cos\varphi}{2(1-\nu)}\left[-\frac{2}{a}J(1,1;1) + \frac{|z|}{a^2}J(1,1;2) - \frac{|z|}{ar}J(1,2;1)\right],$$
$$\sigma_{\varphi\varphi} = \frac{Gb\,\mathrm{sgn}(z)\cos\varphi}{2(1-\nu)}\left[\frac{|z|}{ar}J(1,2;1) - \frac{2\nu}{a}J(1,1;1)\right],$$
$$\sigma_{zz} = -\frac{Gb\cos\varphi}{2(1-\nu)}\frac{z}{a^2}J(1,1;2),$$
$$\sigma_{z\varphi} = \frac{Gb\sin\varphi}{2(1-\nu)}\left[\frac{1-\nu}{a}J(1,0;1) + \frac{\nu}{r}J(1,1;0) - \frac{|z|}{ar}J(1,1;1)\right], \quad (8)$$
$$\sigma_{rz} = \frac{Gb\cos\varphi}{2(1-\nu)}\left[-\frac{1}{a}J(1,0;1) + \frac{|z|}{a^2}J(1,0;2) - \frac{|z|}{ar}J(1,1;1) + \frac{\nu}{r}J(1,1;0)\right],$$
$$\sigma_{r\varphi} = \frac{Gb\,\mathrm{sgn}(z)\sin\varphi}{2(1-\nu)} \times \left[-\frac{|z|}{ar}J(1,2;1) + \frac{1-\nu}{a}J(1,1;1)\right].$$

These fields agree with the solutions presented in [21].

3.3. Wedge Disclination Loop with Frank Vector $\boldsymbol{\omega} = -\omega\mathbf{e}_y$ *(Fig. 1c)*

The plastic distortion is $\beta^*_{zz} = \omega r\cos\varphi H\left(1-\frac{r}{a}\right)\delta(z)$. The total displacements are

$$u_r = \frac{\omega a\cos\varphi}{8(1-\nu)}\left[(1-2\nu)J(2,0;0) + (2\nu-1)J(2,2;0) - \frac{|z|}{a}J(2,0;1) + \frac{|z|}{a}J(2,2;1)\right],$$
$$u_\varphi = \frac{\omega a\sin\varphi}{4(1-\nu)} \times \left[(2\nu-1)\frac{a}{r}J(2,1;-1) + \frac{|z|}{r}J(2,1;0)\right], \quad (9)$$
$$u_z = \frac{\omega a\,\mathrm{sgn}(z)\cos\varphi}{4(1-\nu)} \times \left[2(1-\nu)J(2,1;0) + \frac{|z|}{a}J(2,1;1)\right].$$

The elastic stresses are

$$\sigma_{rr} = \frac{G\omega\cos\varphi}{2(1-\nu)}\left[(1-2\nu)\frac{a}{r}J(2,2;0) - J(2,1;1) + \frac{|z|}{a}J(2,1;2) - \frac{|z|}{r}J(2,2;1)\right],$$
$$\sigma_{\varphi\varphi} = \frac{G\omega\cos\varphi}{2(1-\nu)}\left[(2\nu-1)\frac{a}{r}J(2,2;0) - 2\nu J(2,1;1) + \frac{|z|}{r}J(2,2;1)\right],$$
$$\sigma_{zz} = -\frac{G\omega\cos\varphi}{2(1-\nu)}\left[J(2,1;1) + \frac{|z|}{a}J(2,1;2)\right], \quad (10)$$
$$\sigma_{z\varphi} = -\frac{G\omega\sin\varphi z}{2(1-\nu)r}J(2,1;1),$$
$$\sigma_{rz} = \frac{G\omega\cos\varphi}{2(1-\nu)}\left[\frac{z}{a}J(2,0;2) - \frac{z}{r}J(2,1;1)\right],$$
$$\sigma_{r\varphi} = \frac{G\omega\sin\varphi}{2(1-\nu)}\left[(1-2\nu)\frac{a}{r}J(2,2;0) - \frac{|z|}{r}J(2,2;1)\right].$$

Equations (9) and (10) for the elastic fields differ from the corresponding (incorrect) expressions presented in [22], which, for example, do not satisfy the equilibrium condition $\sigma_{ij,j} = 0$, in contrast to Eq. (10).

3.4. Twist Disclination Loop with Frank Vector $\boldsymbol{\omega} = -\omega\mathbf{e}_z$ *(Fig. 1d)*

The plastic distortion is $\beta^*_{z\varphi} = \omega r H\left(1 - \frac{r}{a}\right)\delta(z)$. The total displacements are

$$u_\varphi = \frac{\omega a}{2}\mathrm{sgn}(z)J(2, 1; 0), \qquad u_r = u_z = 0. \tag{11}$$

The elastic stresses are

$$\sigma_{r\varphi} = -\frac{G\omega}{2}\mathrm{sgn}(z)J(2, 2; 1), \quad \sigma_{z\varphi} = -\frac{G\omega}{2}J(2, 1; 1), \quad \sigma_{rr} = \sigma_{\varphi\varphi} = \sigma_{zz} = \sigma_{rz} = 0. \tag{12}$$

Equations (11) and (12) complement the results presented in [23]; there is discordance between the expressions for the stress component $\sigma_{r\varphi}$ (see [23, Eq. (8)]). Furthermore, in [23], the sign of the plastic distortion is inconsistent with the sign of the disclination. Equations (11) and (12) satisfy the equilibrium condition, which is indicative of their correctness.

3.5. Radial Disclination Loop (Somigliana Dislocation) with Displacement Jump $[u_r] = \omega r$ *(Fig. 1e)*

The plastic distortion is $\beta^*_{zr} = \omega r H\left(1 - \frac{r}{a}\right)\delta(z)$. The total displacements are

$$u_r = \frac{\omega a\,\mathrm{sgn}(z)}{4(1-\nu)}\left[2(1-\nu)J(2, 1; 0) - \frac{|z|}{a}J(2, 1; 1)\right], \quad u_\varphi = 0, \quad u_z = \frac{\omega a}{4(1-\nu)}\left[(2\nu-1)J(2, 0; 0) - \frac{|z|}{a}J(2, 0; 1)\right]. \tag{13}$$

The elastic stresses are

$$\sigma_{rr} = \frac{G\omega\,\mathrm{sgn}(z)}{2(1-\nu)}\left[2(\nu-1)\frac{a}{r}J(2, 1; 0) - \frac{|z|}{a}J(2, 0; 2) + 2J(2, 0; 1) + \frac{|z|}{r}J(2, 1; 1)\right],$$

$$\sigma_{\varphi\varphi} = \frac{G\omega\,\mathrm{sgn}(z)}{2(1-\nu)}\left[2(1-\nu)\frac{a}{r}J(2, 1; 0) - \frac{|z|}{r}J(2, 1; 1) + 2\nu J(2, 0; 1)\right], \tag{14}$$

$$\sigma_{zz} = \frac{G\omega}{2(1-\nu)}\frac{z}{a}J(2, 0; 2),$$

$$\sigma_{rz} = \frac{G\omega}{2(1-\nu)}\left[\frac{|z|}{a}J(2, 1; 2) - J(2, 1; 1)\right],$$

$$\sigma_{r\varphi} = \sigma_{z\varphi} = 0.$$

3.6. Radial Dislocation Loop (Somigliana Dislocation) with Displacement Jump $[u_r] = b$ *(Fig. 1f)*

The plastic distortion is $\beta^*_{zr} = bH\left(1 - \frac{r}{a}\right)\delta(z)$. The elastic fields of this loop can be obtained from Eqs. (13) and (14) for the radial disclination loop by replacing ω with $b/2a$ and, in addition, replacing the Lipschitz–Hankel integrals $J(2, n; p)$ by integrals of the form $\int_0^\infty [J_1(\kappa)\mathbf{H}_0(\kappa) - J_0(\kappa)\mathbf{H}_1(\kappa)]J_n(\kappa r/a)\exp(-\kappa|z|/a)\kappa^p d\kappa$, where $\mathbf{H}_i(\kappa)$ is a Struve function [24].

Details of the calculations and expressions for the elastic strain fields and energies of the defect loops can be found in [9].

4. SOLUTION OF BOUNDARY-VALUE PROBLEMS IN THE THEORY OF DEFECTS USING CONTINUOUS DISTRIBUTIONS OF VIRTUAL CIRCULAR LOOPS

We solve axially symmetric boundary problems using some of the defects loops considered above, namely, prismatic dislocation loops (Fig. 1a), twist disclination loops (Fig. 1c), and radial disclination loops (Somigliana dislocations, Fig. 1e). With continuous distributions of virtual circular loops, the boundary conditions, namely, the continuity of the elastic-stress components normal to an interface and the continuity of all components of total displacements (the latter condition is not imposed at a free surface), reduce to integral equations for the unknown loop distribution functions. The angular dependence of the field components of virtual loops must be consistent with that of the real defect for which the boundary problem is to be solved. There are also some restrictions on the indices of the Lipschitz–Hankel integrals and on the dependence of the field of virtual loops on coordinate *r*. However, those restrictions are not of fundamental importance, because they are imposed in order to simplify solution of the integral equations. For boundary problems with planar boundaries (such problems are considered below), the loop distribution functions depend on the loop radii. Since the kernels of the integral equations

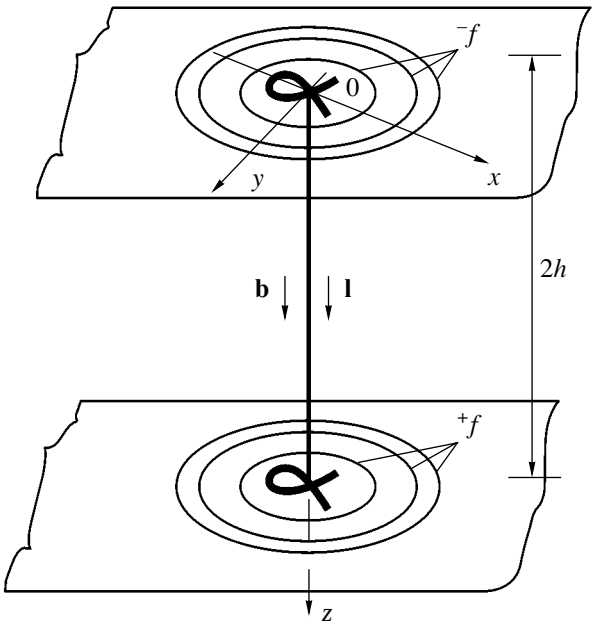

Fig. 2. Screw dislocation in a plate of finite thickness. In the plate surface, virtual twist disclination loops are shown, which are introduced to satisfy the boundary conditions.

contain Bessel functions, it is convenient to employ the Hankel–Bessel transformation [25]

$$H_\nu(\lambda) = \int_0^\infty f(r) J_\nu(\lambda r) r dr, \qquad (15)$$

$$f(r) = \int_0^\infty H_\nu(\lambda) J_\nu(\lambda r) \lambda d\lambda, \qquad (16)$$

where $H_\nu(\lambda)$ is the Hankel transform of the function $f(r)$ and the index ν indicates the order of the Bessel function involved in the transformation. Integral transformations (15) and (16) are convenient, because the elastic fields of circular loops are represented in the form of Lipschitz–Hankel integrals, which allows one to perform mathematical manipulations, such as changing the integration variables and interchanging the orders of integration in double integrals.

We illustrate these methods by solving the simple problem of a screw dislocation perpendicular to the free surface of a plate or of a half-space (Fig. 2). For other boundary-value problems, such as a disclination dipole or an edge dislocation in a plate (Fig. 3) and a twist disclination loop in a plate, a half-space, or a two-phase material (Fig. 4), we present only the final expressions for the total displacements and elastic stresses.

We note that, in problems for a cylinder (e.g., a circular loop in a cylinder sharing a common axis with the loop), the virtual-loop distribution functions depend on the coordinate along the cylinder axis. In such problems, it is convenient to use the Fourier transformation.

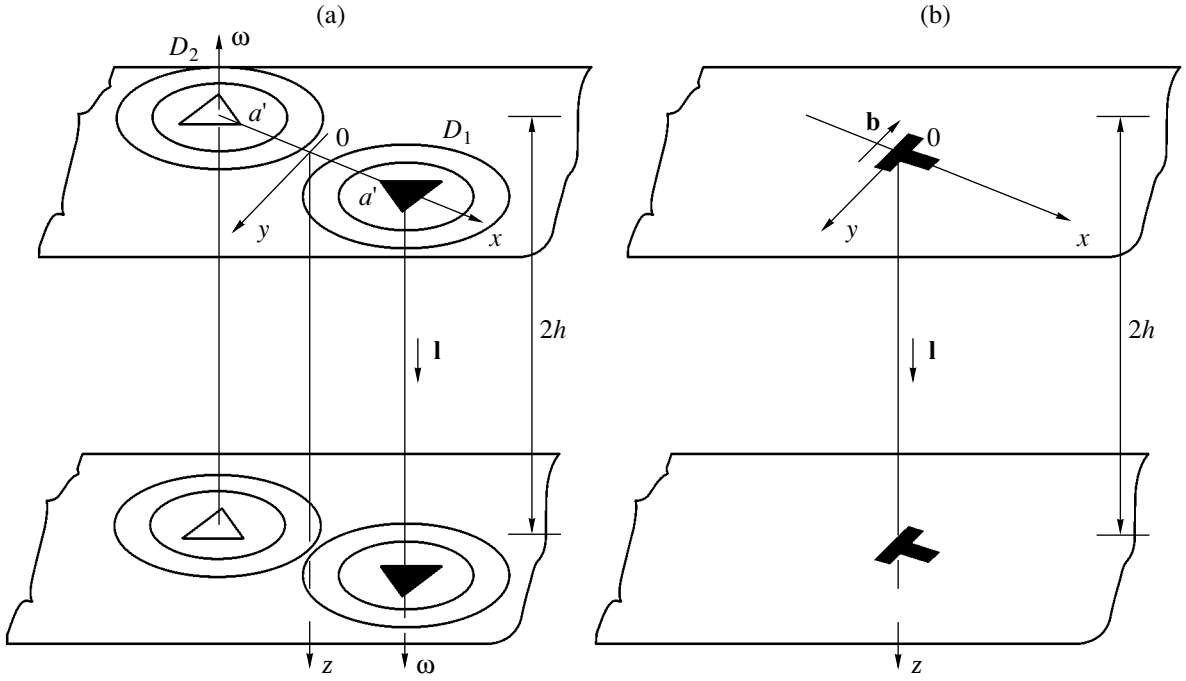

Fig. 3. Wedge disclination dipole and an edge dislocation in a plate of finite thickness. (a) For the disclination dipole, virtual prismatic dislocation loops and radial disclination loops are shown, which enclose the disclination end points at the surface and allow the boundary conditions to be satisfied. (b) Edge dislocation perpendicular to the plate surfaces that results from the disclination dipole in the limiting case indicated in the text.

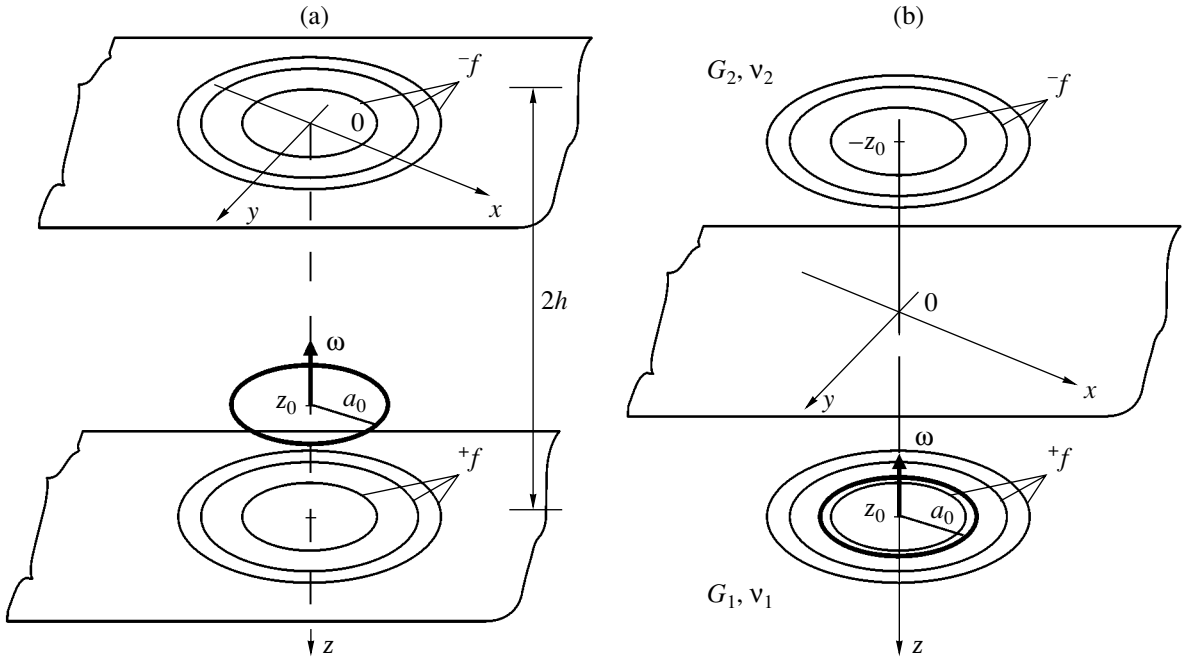

Fig. 4. Boundary-value problems for the twist disclination loop: (a) the loop in a plate and (b) the loop near a planar interface. Thin lines show virtual twist disclination loops, which are introduced to satisfy the boundary conditions.

4.1. Screw Dislocation in a Plate and in a Half-Space

A dislocation with Burgers vector $\mathbf{b} = b\mathbf{e}_z$ (the line vector $\mathbf{l} = \mathbf{e}_z$) is perpendicular to the plane of the plate $2h$ thick with the elastic moduli G and ν (Fig. 2). In this geometry, the stress field of the screw dislocation in an infinite medium ($^{\infty}\sigma_{ij}$) has a single nonzero component [25],

$$^{\infty}\sigma_{z\varphi} = \frac{Gb}{2\pi r}. \tag{17}$$

At the free surfaces of the plate, the boundary conditions are

$$\sigma_{z\varphi}\Big|_{\left\{\begin{array}{l} z = 0 \\ z = 2h \end{array}\right\}} = 0. \tag{18}$$

Within the virtual-loop method, boundary conditions (18) are satisfied by representing the field of the dislocation in the plate σ_{ij} as the sum of the field of the dislocation in an infinite medium $^{\infty}\sigma_{ij}$ and an additional field $^{i}\sigma_{ij}$ produced by a continuous set of circular twist disclination loops located at the upper and lower surfaces of the plate (Fig. 2). The stress field of a twist disclination loop (12), as well as the stress field of the dislocation (17), has a single component $\sigma_{z\varphi}$ that is involved in the continuity conditions imposed on the stress components normal to the free plate surface. By substituting the stress field expressed in terms of surface distributions of twist disclination loops into Eq. (18), we obtain integral equations for the unknown loop radius distribution functions $^{-}f(a)$ and $^{+}f(a)$ at the upper and lower plate surfaces, respectively:

$$\frac{Gb}{2\pi r} + \int_0^{\infty} {}^{-}f(a)\,{}^{-}\sigma_{z\varphi}(r, z, a)\Big|_{\left\{\begin{array}{l} z = 0 \\ z = 2h \end{array}\right\}} da + \int_0^{\infty} {}^{+}f(a)\,{}^{+}\sigma_{z\varphi}(r, z, a)\Big|_{\left\{\begin{array}{l} z = 0 \\ z = 2h \end{array}\right\}} da = 0, \tag{19}$$

where $^{\pm}\sigma_{z\varphi}|_{z = 0}$ and $^{\pm}\sigma_{z\varphi}|_{z = 2h}$ are the elastic stresses produced by both (+ and –) virtual-loop distributions at the $z = 0$ and $z = 2h$ surfaces, respectively.

Using Eq. (12), we rewrite Eqs. (19) in the form

$$\begin{aligned} &\frac{G\omega}{2}\int_0^{\infty} {}^{-}f(a)da\int_0^{\infty} J_2(\kappa)J_1\left(\kappa\frac{r}{a}\right)\kappa d\kappa \\ &+ \frac{G\omega}{2}\int_0^{\infty} {}^{+}f(a)da\int_0^{\infty} J_2(\kappa)J_1\left(\kappa\frac{r}{a}\right)\exp\left(-\kappa\frac{2h}{a}\right)\kappa d\kappa = \frac{Gb}{2\pi r}, \\ &\frac{G\omega}{2}\int_0^{\infty} {}^{-}f(a)da\int_0^{\infty} J_2(\kappa)J_1\left(\kappa\frac{r}{a}\right)\exp\left(-\kappa\frac{2h}{a}\right)\kappa d\kappa \\ &+ \frac{G\omega}{2}\int_0^{\infty} {}^{+}f(a)da\int_0^{\infty} J_2(\kappa)J_1\left(\kappa\frac{r}{a}\right)\kappa d\kappa = \frac{Gb}{2\pi r}. \end{aligned} \tag{20}$$

Upon introducing a new variable $\beta = \frac{\kappa}{a}$, interchanging orders of integration in the double integrals, and using the Hankel–Bessel transformation (15) with the kernel $J_1(\beta r)$, we obtain a set of linear algebraic equations for the Hankel transforms ${}^{\pm}H_2(\beta) = \int_0^\infty [{}^{\pm}f(a)a]J_2(a\beta)ada$ of the functions ${}^{\pm}f(a)a$, from which we find

$$ {}^{-}H_2 = {}^{+}H_2 = \frac{b}{2\pi\omega}\frac{\exp(h\beta)}{\beta\cosh(h\beta)}. \quad (21)$$

Taking the Hankel–Bessel transform (16), we obtain the distribution functions ${}^{\pm}f(a)$ of virtual twist disclination loops in their radius:

$$ {}^{+}f = {}^{-}f = \frac{b}{2\pi\omega a}\int_0^\infty J_2(a\beta)\frac{\exp(h\beta)}{\cosh(h\beta)}d\beta. \quad (22)$$

We note that the equality of the distribution functions at the upper and lower surfaces of the plate, ${}^{+}f = {}^{-}f$, is a direct consequence of the symmetry of the problem and can be used from the outset. However, we did not use this property, because our aim was to demonstrate the general calculational procedure.

Given the loop radius distribution functions (22) and the elastic fields of a single virtual twist disclination loop (11) and (12), we can calculate the additional fields of displacements ${}^{i}u_j$ and elastic stresses ${}^{i}\sigma_{jk}$ (elastic strains ${}^{i}\varepsilon_{jk}$) produced by the screw dislocation in the plate. Furthermore, in order to calculate these fields, it will suffice to know the Hankel transforms ${}^{\pm}H_2$ given by Eq. (21). Using Eqs. (11) and (12) and the displacement field of the dislocation in an infinite medium ${}^{\infty}u_z$ [1, 26], we find the field of total displacements for the screw dislocation in the plate:

$$ u_r = {}^{\infty}u_r = 0,$$
$$ u_\varphi = {}^{i}u_\varphi = \frac{b}{2\pi}\int_0^\infty J_1(r\beta)\frac{\sinh[(h-z)\beta]}{\beta\cosh(h\beta)}d\beta, \quad (23)$$
$$ u_z = {}^{\infty}u_z = \frac{b\varphi}{2\pi}, \quad 0 \le z \le 2h.$$

The stress field is calculated from Eqs. (12), (17), and (21) to be

$$ \sigma_{z\varphi} = \frac{Gb}{2\pi}\left[\frac{1}{r} - \int_0^\infty J_1(r\beta)\frac{\cosh[(z-h)\beta]}{\cosh(h\beta)}d\beta\right],$$
$$ \sigma_{r\varphi} = \frac{Gb}{2\pi}\int_0^\infty J_2(r\beta)\frac{\sinh[(z-h)\beta]}{\cosh(h\beta)}d\beta, \quad (24)$$
$$ \sigma_{rr} = \sigma_{\varphi\varphi} = \sigma_{zz} = \sigma_{rz} = 0, \quad 0 \le z \le 2h.$$

The stresses found are expressed in terms of integrals rather than in the form of series of cylindrical functions as in [27]. Our result is identical to the solution found in [28] for a screw dislocation in a plate by using another method. The stresses given by Eqs. (24) can be shown to satisfy the equilibrium equations and the boundary conditions.

If the plate is infinitely thick ($2h \longrightarrow \infty$), Eqs. (23) and (24) give the fields produced by the screw dislocation in a half-space

$$ u_r = 0,$$
$$ u_\varphi = \frac{b}{2\pi}\frac{r}{R+z}, \quad (25)$$
$$ u_z = {}^{\infty}u_z = \frac{b\varphi}{2\pi}, \quad 0 \le z,$$

$$ \sigma_{z\varphi} = \frac{Gb}{2\pi}\left[\frac{1}{r} - \frac{r}{R(R+z)}\right],$$
$$ \sigma_{r\varphi} = -\frac{Gb}{2\pi}\frac{r^2}{R(R+z)^2}, \quad (26)$$
$$ \sigma_{rr} = \sigma_{\varphi\varphi} = \sigma_{zz} = \sigma_{rz} = 0, \quad 0 \le z,$$

where $R^2 = r^2 + z^2$.

A comparison of Eq. (26) with the results obtained in [3, 29] shows that the formulas derived using the method of virtual circular loops are correct.

4.2. Wedge Disclination Dipole in a Plate and in a Half-Space

The dipole D_1D_2 shown in Fig. 3a consists of wedge disclinations perpendicular to the free surfaces of the plate. The Frank vectors of disclinations D_1 and D_2 are $\boldsymbol{\omega}_1 = \omega\mathbf{e}_z$ and $\boldsymbol{\omega}_2 = -\omega\mathbf{e}_z$, respectively. The distance between the disclinations is $2a'$. Taking, as virtual circular loops, distributions of prismatic dislocation loops and of radial disclination loops, we find the field of total displacements and the field of elastic stresses (strains) produced by the disclination dipole in the plate. The results are as follows. The total-displacement field is

$$ u_{\begin{Bmatrix} r \\ \varphi \end{Bmatrix}} = {}^{\infty}u_{\begin{Bmatrix} r \\ \varphi \end{Bmatrix}} - \frac{\omega\nu}{4\pi(1-\nu)}\sum_{i=1}^{2}(-1)^{i-1}\begin{Bmatrix} \cos(\varphi-\varphi_i) \\ -\sin(\varphi-\varphi_i) \end{Bmatrix}$$
$$ \times \int_0^\infty J_1(r_i\beta)(S_2H_1 + S_4H_2)d\beta,$$
$$ u_z = \frac{\omega\nu}{4\pi(1-\nu)}\sum_{i=1}^{2}(-1)^{i-1}\int_0^\infty J_0(r_i\beta)(W_1H_1 + W_2H_2)d\beta, \quad (27)$$
$$ 0 \le z \le 2h.$$

Here, ${}^{\infty}u_i$ is the displacement field of dipole D_1D_2 in an infinite medium [26]:

$$
{}^{\infty}u_{\begin{Bmatrix} r \\ \varphi \end{Bmatrix}} = \frac{\omega}{4\pi(1-\nu)}\sum_{i=1}^{2}(-1)^{i-1}
$$

$$
\times\left[(1-2\nu)r_i(\ln r_i - 1)\begin{Bmatrix} \cos(\varphi-\varphi_i) \\ -\sin(\varphi-\varphi_i) \end{Bmatrix}\right. \qquad (28)
$$

$$
\left. + 2(1-\nu)r_i\varphi_i\begin{Bmatrix} \sin(\varphi-\varphi_i) \\ \cos(\varphi-\varphi_i) \end{Bmatrix}\right].
$$

The stress field of the disclination dipole in the plate is given by

$$
\sigma_{\begin{Bmatrix} rr \\ \varphi\varphi \end{Bmatrix}} = {}^{\infty}\sigma_{\begin{Bmatrix} rr \\ \varphi\varphi \end{Bmatrix}} + \frac{G\omega\nu}{4\pi(1-\nu)}
$$

$$
\times\sum_{i=1}^{2}(-1)^{i-1}\left[\{\pm\}\cos(2(\varphi-\varphi_i))\right.
$$

$$
\times\int_0^{\infty}J_2(r_i\beta)(S_2H_1 + S_4H_2)\beta d\beta
$$

$$
\left. + \int_0^{\infty}J_0(r_i\beta)((2S_1+S_2)H_1 + (2S_3+S_4)H_2)\beta d\beta\right],
$$

$$
\sigma_{zz} = {}^{\infty}\sigma_{zz} + \frac{G\omega\nu}{2\pi(1-\nu)}
$$

$$
\times\sum_{i=1}^{2}(-1)^{i-1}\int_0^{\infty}J_0(r_i\beta)(T_1H_1 + T_2H_2)\beta d\beta, \qquad (29)
$$

$$
\sigma_{r\varphi} = {}^{\infty}\sigma_{r\varphi} - \frac{G\omega\nu}{4\pi(1-\nu)}\sum_{i=1}^{2}(-1)^{i-1}\sin(2(\varphi-\varphi_i))
$$

$$
\times\int_0^{\infty}J_2(r_i\beta)(S_2H_1 + S_4H_2)\beta d\beta,
$$

$$
\sigma_{\begin{Bmatrix} z\varphi \\ zr \end{Bmatrix}} = \frac{G\omega\nu}{2\pi(1-\nu)}\sum_{i=1}^{2}(-1)^{i-1}\begin{Bmatrix} -\sin(\varphi-\varphi_i) \\ \cos(\varphi-\varphi_i) \end{Bmatrix}
$$

$$
\times\int_0^{\infty}J_1(r_i\beta)(Q_1H_1 + Q_2H_2)\beta d\beta,
$$

$$
0 \le z \le 2h.
$$

Here, ${}^{\infty}\sigma_{ji}$ is the stress field of dipole D_1D_2 in an infinite medium [26]:

$$
{}^{\infty}\sigma_{\begin{Bmatrix} rr \\ \varphi\varphi \end{Bmatrix}} = \frac{G\omega}{2\pi(1-\nu)}
$$

$$
\times\sum_{i=1}^{2}(-1)^{i-1}\left[\ln r_i + \begin{Bmatrix} \sin^2(\varphi-\varphi_i) \\ \cos^2(\varphi-\varphi_i) \end{Bmatrix}\right],
$$

$$
{}^{\infty}\sigma_{zz} = \frac{G\omega\nu}{\pi(1-\nu)}\ln\frac{r_1}{r_2}, \qquad (30)
$$

$$
{}^{\infty}\sigma_{r\varphi} = \frac{G\omega}{4\pi(1-\nu)}\sum_{i=1}^{2}(-1)^{i-1}\sin[2(\varphi-\varphi_i)],
$$

$$
{}^{\infty}\sigma_{zr} = {}^{\infty}\sigma_{z\varphi} = 0.
$$

In Eqs. (27)–(30), we introduced the following notation:

$$
r_1^2 = r^2 - 2ra'\cos\varphi + a'^2,
$$

$$
r_2^2 = r^2 + 2ra'\cos\varphi + a'^2,
$$

$$
\cos(\varphi-\varphi_1) = \frac{(r - a'\cos\varphi)}{r_1},
$$

$$
\cos(\varphi-\varphi_2) = \frac{(r + a'\cos\varphi)}{r_2},
$$

$$
\sin(\varphi-\varphi_1) = \frac{-a'\sin\varphi}{r_1},
$$

$$
\sin(\varphi-\varphi_2) = \frac{a'\sin\varphi}{r_2},
$$

$$
H_1 = \frac{2}{\beta^2}\frac{(1-2h\beta)\exp(-2h\beta)-1}{1+[4h\beta-\exp(-2h\beta)]\exp(-2h\beta)},
$$

$$
H_2 = -\frac{4}{\beta}\frac{h\exp(-2h\beta)}{1+[4h\beta-\exp(-2h\beta)]\exp(-2h\beta)},
$$

$$
S_1 = z\beta E_1 - E_1 - E_2 - (z-2h)\beta E_2,
$$

$$
S_2 = (1-2\nu)(E_1+E_2) - z\beta E_1 + (z-2h)\beta E_2,
$$

$$
S_3 = 2(E_1+E_2) - z\beta E_1 + (z-2h)\beta E_2,
$$

$$
S_4 = z\beta E_1 - 2(1-\nu)(E_1+E_2) - (z-2h)\beta E_2,
$$

$$
T_1 = -E_1 - E_2 - z\beta E_1 + (z-2h)\beta E_2,
$$

$$
T_2 = z\beta E_1 - (z-2h)\beta E_2,
$$

$$
Q_1 = -z\beta E_1 - (z-2h)\beta E_2,
$$

$$
Q_2 = E_2 - E_1 + z\beta E_1 + (z-2h)\beta E_2,
$$

$$W_1 = 2(1-\nu)(E_1 - E_2) + z\beta E_1 + (z-2h)\beta E_2,$$

$$W_2 = (1-2\nu)(E_2 - E_1) - z\beta E_1 - (z-2h)\beta E_2,$$

$$E_1 = \exp(-z\beta), \quad E_2 = \exp[(z-2h)\beta].$$

If the plate is infinitely thick ($2h \longrightarrow \infty$), Eqs. (27)–(30) give the fields produced by a dipole consisting of wedge disclinations perpendicular to the free surface of a half-space. In this case, the stress field is given by

$$\sigma_{\begin{Bmatrix} rr \\ \varphi\varphi \end{Bmatrix}} = {}^{\infty}\sigma_{\begin{Bmatrix} rr \\ \varphi\varphi \end{Bmatrix}} - \frac{G\omega\nu}{2\pi(1-\nu)}\sum_{i=1}^{2}(-1)^{i-1}$$

$$\times\left\{(1+2\nu)\ln(R_i+z) + \frac{z}{R_i}\right.$$

$$+\{\pm\}\left[(1-2\nu)\frac{r_i^2\cos(2(\varphi-\varphi_i))}{2(R_i+z)^2}\right.$$

$$\left.\left.-\frac{zr_i^2\cos(2(\varphi-\varphi_i))}{R_i(R_i+z)^2}\right]\right\},$$

$$\sigma_{zz} = {}^{\infty}\sigma_{zz} + \frac{G\omega\nu}{\pi(1-\nu)}\sum_{i=1}^{2}(-1)^{i-1}\left[\frac{z}{R_i} - \ln(R_i+z)\right], \quad (31)$$

$$\sigma_{r\varphi} = {}^{\infty}\sigma_{r\varphi} + \frac{G\omega\nu}{4\pi(1-\nu)}\sum_{i=1}^{2}(-1)^{i-1}\left[(1-2\nu) - \frac{2z}{R_i}\right]$$

$$\times\frac{r_i^2\sin(2(\varphi-\varphi_i))}{(R_i+z)^2},$$

$$\sigma_{\begin{Bmatrix} z\varphi \\ zr \end{Bmatrix}} = \frac{G\omega\nu}{\pi(1-\nu)}\sum_{i=1}^{2}(-1)^{i-1}\begin{Bmatrix} -\sin(\varphi-\varphi_i) \\ \cos(\varphi-\varphi_i) \end{Bmatrix}\frac{zr_i}{R_i(R_i+z)},$$

$$z \geq 0,$$

where $R_i^2 = r_i^2 + z^2$, with $i = 1, 2$.

The field obtained in this limit is identical to the corresponding field calculated by a different method and presented in [30].

The disclination dipole transforms into an edge dislocation with Burgers vector $\mathbf{b} = -b\mathbf{e}_y$ in the limit $2a' \longrightarrow 0$ and $\omega \longrightarrow \frac{b}{2a'}$ ($2a'$ is the distance between the disclinations, ω is the disclination force; Fig. 3b). The calculated total displacements and elastic stresses of an edge dislocation perpendicular to the plate plane can be found in [9, 31]. It is shown in [9] that, when the plate thickness tends to zero, the solution reduces to that for an edge dislocation in an infinitely thin disk. In the case of an infinitely thick plate, we obtain the solution for an edge dislocation perpendicular to the free surface of a half-space.

4.3. Twist Disclination Loop in a Plate and in a Half-Space

Now, we consider a twist disclination loop with Frank vector $\boldsymbol{\omega} = -\omega\mathbf{e}_z$ and radius a_0 positioned in an isotropic plate $2h$ thick at a distance z_0 from the surface of the plate and parallel to the plate surface (Fig. 4a). The stress field ${}^{\infty}\sigma_{ij}$ of the loop is given by Eq. (12). The additional field is assumed to be produced by a continuous set of virtual twist disclination loops. Using the method described above, the fields of the twist disclination loop in the plate are found to be

$$u_\varphi = {}^{\infty}u_\varphi - \frac{\omega a_0}{2}\int_0^{\infty} J_2(\kappa)J_1(\bar{r}\kappa)\frac{1}{\sinh(2\bar{h}\kappa)}$$

$$\times[\sinh((2\bar{h}-\bar{z}_0)\kappa)\exp(-\bar{z}\kappa)$$

$$-\sinh(\bar{z}_0\kappa)\exp(-(2\bar{h}-\bar{z})\kappa)]d\kappa, \quad (32)$$

$$u_r = u_z = 0, \quad 0 \leq \bar{z} \leq 2\bar{h}, \quad 0 \leq \bar{z}_0 \leq 2\bar{h},$$

where $\bar{r} = \frac{r}{a_0}$, $\bar{z} = \frac{z}{a_0}$, and the displacement field ${}^{\infty}u_i$ in an infinite medium is given by Eqs. (11) with $z - z_0$ in place of z;

$$\sigma_{r\varphi} = {}^{\infty}\sigma_{r\varphi} + \frac{G\omega}{2}\int_0^{\infty} J_2(\kappa)J_2(\bar{r}\kappa)\frac{1}{\sinh(2\bar{h}\kappa)}$$

$$\times[\sinh((2\bar{h}-\bar{z}_0)\kappa)\exp(-\bar{z}\kappa)$$

$$-\sinh(\bar{z}_0\kappa)\exp(-(2\bar{h}-\bar{z})\kappa)]\kappa d\kappa,$$

$$\sigma_{z\varphi} = {}^{\infty}\sigma_{z\varphi} + \frac{G\omega}{2}\int_0^{\infty} J_2(\kappa)J_1(\bar{r}\kappa)\frac{1}{\sinh(2\bar{h}\kappa)} \quad (33)$$

$$\times[\sinh((2\bar{h}-\bar{z}_0)\kappa)\exp(-\bar{z}\kappa)$$

$$+\sinh(\bar{z}_0\kappa)\exp(-(2\bar{h}-\bar{z})\kappa)]\kappa d\kappa,$$

$$\sigma_{rr} = \sigma_{\varphi\varphi} = \sigma_{zz} = \sigma_{rz} = 0,$$

$$0 \leq \bar{z} \leq 2\bar{h}, \quad 0 \leq \bar{z}_0 \leq 2\bar{h},$$

where ${}^{\infty}\sigma_{ij}$ is given by Eqs. (12) with $z - z_0$ in place of z.

In [32, 33], the elastic fields of a twist disclination loop in a plate were calculated using image loops and the result was represented in the form of infinite series.

It can be verified that Eqs. (32) and (33) derived in this paper can be transformed into the expressions presented in [32, 33].

The fields of a twist disclination loop in a half-space are obtained from Eqs. (32) and (33) by going to the limit $2h \longrightarrow \infty$. In this case, the displacement field is

$$u_\varphi = {}^\infty u_\varphi - \frac{\omega a_0}{2} J^\cdot(2, 1; 0), \qquad u_r = u_z = 0, \tag{34}$$

and the elastic field is

$$\sigma_{r\varphi} = {}^\infty\sigma_{r\varphi} + \frac{G\omega}{2} J^\cdot(2, 2; 1),$$

$$\sigma_{z\varphi} = {}^\infty\sigma_{z\varphi} + \frac{G\omega}{2} J^\cdot(2, 1; 1), \tag{35}$$

$$\sigma_{rr} = \sigma_{\varphi\varphi} = \sigma_{zz} = \sigma_{rz} = 0, \quad 0 \le \bar{z}, \quad 0 \le \bar{z}_0,$$

where the fields ${}^\infty u_i$ and ${}^\infty\sigma_{ij}$ are given by Eqs. (11) and (12) with $z - z_0$ replacing z and $J^\cdot(m, n; p)$ is equal to $J(m, n; p)$ with $z + z_0$ in place of z.

It follows from Eqs. (34) and (35) that the elastic field of the twist disclination loop in a half-space is the sum of the field of this loop in an infinite medium and the field of the image loop. This fact was first pointed out in [34]. The energy of the disclination loop in a plate and in a half-space was calculated in [9].

4.4. Twist Disclination Loop in a Two-Phase Medium

The twist disclination loop with Frank vector $\boldsymbol{\omega} = -\omega\mathbf{e}_z$ and radius a_0 is positioned in a medium with the elastic moduli G_1 and ν_1 (Fig. 4b); the interface is taken to be the xy plane. At the interface, the total displacements ${}^\alpha u_j$ and the elastic-stress components normal to the interface ${}^\alpha\sigma_{zj}$ ($\alpha = 1, 2$ specifies the media) must satisfy the continuity conditions

$${}^1u_j\big|_{z=0} = {}^2u_j\big|_{z=0}, \qquad {}^1\sigma_{zj}\big|_{z=0} = {}^2\sigma_{zj}\big|_{z=0}, \quad j = x, y, z. \tag{36}$$

Conditions (36) can be satisfied if the field in medium 1 is represented as the sum of the field of the real loop and the field of a continuous set of virtual twist disclination loops located in medium 2; the field in medium 2 is produced by a continuous set of virtual twist disclination loops situated in medium 1.

By solving the corresponding integral equations, the displacement field and the stress field are found to be

$${}^1u_\varphi = \frac{\omega a_0}{2}\operatorname{sgn}(z - z_0)\,{}^1J(2, 1; 0) + \frac{\omega a_0}{2}\frac{G_2 - G_1}{G_2 + G_1}J(2, 1; 0),$$

$${}^1u_r = {}^1u_z = 0, \quad z \ge 0, \quad z_0 > 0,$$

$${}^2u_\varphi = -\omega a_0\frac{G_1}{G_2 + G_1}\,{}^1J(2, 1; 0),$$

$${}^2u_r = {}^2u_z = 0, \quad z \le 0, \quad z_0 > 0, \tag{37}$$

$${}^1\sigma_{r\varphi} = -\frac{G_1\omega}{2}\operatorname{sgn}(z - z_0)\,{}^1J(2, 2; 1) - \frac{G_1\omega}{2}\frac{G_2 - G_1}{G_2 + G_1}J(2, 2; 1),$$

$${}^1\sigma_{z\varphi} = -\frac{G_1\omega}{2}\,{}^1J(2, 1; 1) - \frac{G_1\omega}{2}\frac{G_2 - G_1}{G_2 + G_1}J(2, 1; 1),$$

$${}^1\sigma_{rr} = {}^1\sigma_{\varphi\varphi} = {}^1\sigma_{zz} = {}^1\sigma_{rz} = 0, \quad z \ge 0, \quad z_0 > 0, \tag{38}$$

$${}^2\sigma_{r\varphi} = G_2\omega\frac{G_1}{G_2 + G_1}\,{}^1J(2, 2; 1),$$

$${}^2\sigma_{z\varphi} = -G_2\omega\frac{G_1}{G_2 + G_1}\,{}^1J(2, 1; 1),$$

$${}^2\sigma_{rr} = {}^2\sigma_{\varphi\varphi} = {}^2\sigma_{zz} = {}^2\sigma_{rz} = 0, \quad z \le 0, \quad z_0 > 0,$$

where ${}^1J(m, n; p)$ is equal to $J(m, n; p)$ with $z - z_0$ in place of z and ${}^2J(m, n; p)$ is equal to $J(m, n; p)$ with $z + z_0$ in place of z. The energy of the loop in a two-phase medium was calculated in [9].

5. CONCLUSIONS

The general method of virtual circular surface loops developed by us can be used to advantage for solving a wide class of axially symmetric boundary-value problems in the theory of defects. In this method, planar sets of circular defect loops are introduced in order to satisfy the boundary conditions at interfaces. The unknown distribution functions of circular loops in their radius (for problems with planar boundaries) or in their center coordinate along the cylindrical axis (e.g., for the problem of a loop in a cylinder sharing a com-

mon axis with the loop) are found by solving the corresponding integral equations.

We have classified defect loops and calculated the displacement fields and the elastic stress fields for six types of defect loops. The results obtained for the prismatic and glide dislocation loops and for the wedge and twist disclination loops have been compared with the published data. The fields of the radial disclination loop and the radial dislocation loop (Somigliana dislocations) were calculated for the first time. The elastic fields and the energies of circular dislocation loops can be used, e.g., in analyzing the relaxation processes occurring in the regions near nanoclusters in semiconductors [35, 36].

Using the general method, we have found the elastic fields of linear defects perpendicular to the plane of an isotropic plate. The elastic fields of the screw dislocation were represented in a new, integral form. The solution found for the dipole consisting of wedge disclinations perpendicular to the plate plane is published in a scientific journal for the first time (earlier, this solution was available only from a FTI preprint [9]). From the solution for the disclination dipole, by going to the corresponding limit, one can find the elastic fields of the edge dislocation in a plate [31], knowledge of which is required to correctly analyze the electron-microscopic dislocation contrast in thin films. The solution for disclinations can also be used to analyze electron-microscopic images of partial disclinations arising in highly deformed metals [10, 37].

The method developed for calculating the elastic fields of the twist disclination loop parallel to a boundary has allowed us to find solutions (in a compact form) for the loop in a plate and the loop positioned near an interface. By using the method of virtual circular defect loops, we have verified or, in some instances, corrected the formulas obtained earlier for the elastic fields of twist disclination loops in the geometry indicated above.

Thus, the method of surface circular loops of dislocations and disclinations can be used to advantage for solving axially symmetric boundary-value problems. This method is clear and allows one to calculate, on a unified basis, the elastic fields of various defects in media with boundaries.

ACKNOWLEDGMENTS

This study was supported by the Ministry of Industry of the Russian Federation (program "Physics of Solid Nanostructures") and the Volkswagen Foundation (grant no. I/74645).

REFERENCES

1. J. P. Hirth and J. Lothe, *Theory of Dislocations* (McGraw-Hill, New York, 1967; Atomizdat, Moscow, 1972).
2. V. I. Vladimirov and A. E. Romanov, *Disclinations in Crystals* (Nauka, Leningrad, 1986).
3. J. D. Eshelby, in *Dislocations in Solids*, Ed. by F. R. N. Nabarro (North-Holland, Amsterdam, 1997), Vol. 1, p. 167.
4. J. Lothe, in *Elastic Strain Fields and Dislocation Mobility*, Ed. by V. L. Indenbom and J. Lothe (North-Holland, Amsterdam, 1992), p. 329.
5. A. Yu. Belov, in *Elastic Strain Fields and Dislocation Mobility*, Ed. by V. L. Indenbom and J. Lothe (North-Holland, Amsterdam, 1992), p. 391.
6. S. K. Maksimov, G. N. Gaĭdukov, and A. P. Filippov, Poverkhnost, No. 10, 95 (1984).
7. V. G. Gryaznov, I. A. Polonsky, A. E. Romanov, and L. I. Trusov, Phys. Rev. B **44** (1), 42 (1991).
8. V. I. Vladimirov, A. L. Kolesnikova, and A. E. Romanov, Fiz. Met. Metalloved. **60** (6), 1106 (1985).
9. A. L. Kolesnikova and A. E. Romanov, Preprint No. 1019, FTI AN SSSR (Physicotechnical Inst., USSR Academy of Sciences, Leningrad, 1986).
10. A. L. Kolesnikova, V. Klemm, P. Klimanek, and A. E. Romanov, Phys. Status Solidi A **191** (2), 467 (2002).
11. N. Louat, Nature **196** (4859), 1081 (1962).
12. M. J. Marcinkowski, Phys. Status Solidi A **63** (1), 401 (1983).
13. K. Jagannadham and M. J. Marcinkowski, J. Mater. Sci. **15** (2), 709 (1980).
14. A. J. Belov, V. A. Chamrov, V. L. Indenbom, and J. Lothe, Phys. Status Solidi B **119** (2), 565 (1983).
15. N. Louat and K. Sadananda, Philos. Mag. A **64** (31), 213 (1991).
16. V. I. Vladimirov, A. E. Romanov, and A. L. Kolesnikova, in *Physics and Technology of Metal Surface Processing* (Fiz. Tekh. Inst. Akad. Nauk SSSR, Leningrad, 1984), p. 33.
17. M. Yu. Gutkin and A. E. Romanov, Phys. Status Solidi A **125** (1), 107 (1991).
18. T. Mura, *Micromechanics of Defects in Solids* (Martinus Nijhoff, Boston, 1987).
19. G. Eason, B. Noble, and I. N. Sneddon, Philos. Trans. R. Soc. London **247** (935), 529 (1955).
20. J. Dundurs and N. J. Salamon, Phys. Status Solidi B **50** (1), 125 (1972).
21. N. J. Salamon and J. Dundurs, J. Phys. C **10** (4), 497 (1977).
22. H. H. Kuo and T. Mura, J. Appl. Phys. **43** (4), 1454 (1972).
23. H. H. Kuo, T. Mura, and J. Dundurs, Int. Eng. Sci. **11** (1), 193 (1973).
24. A. P. Prudnikov, Yu. A. Brychkov, and O. I. Marichev, *Integrals and Series. Special Functions* (Nauka, Moscow, 1983; Gordon and Breach, New York, 1986).
25. Ya. S. Uflyand, *Integral Transformations in Problems of the Theory of Elasticity* (Nauka, Leningrad, 1967).

26. R. de Wit, *Continuum Disclination Theory*, Ed. by A. A. Vakulenko (Mir, Moscow, 1977).
27. J. D. Eshelby and A. N. Strogh, Philos. Mag. **42** (335), 1401 (1951).
28. K. Saito, R. O. Bozkurt, and T. Mura, J. Appl. Phys. **43** (1), 182 (1972).
29. S. J. Shaibani and P. M. Hazzledine, Philos. Mag. A **44** (3), 657 (1981).
30. A. E. Romanov, Poverkhnost, No. 12, 121 (1982).
31. A. L. Kolesnikova and A. E. Romanov, Pis'ma Zh. Tekh. Fiz. **13** (6), 656 (1987) [Sov. Tech. Phys. Lett. **13**, 272 (1987)].
32. T.-W. Chou, J. Appl. Phys. **42** (10), 4092 (1972).
33. H. H. Kuo and T. Mura, J. Appl. Phys. **43** (10), 3926 (1972).
34. T.-W. Chou, J. Appl. Phys. **42** (12), 4931 (1971).
35. V. V. Chaldyshev, N. A. Bert, A. E. Romanov, *et al.*, Appl. Phys. Lett. **80** (3), 377 (2002).
36. N. A. Bert, A. L. Kolesnikova, A. E. Romanov, and V. V. Chaldyshev, Fiz. Tverd. Tela (St. Petersburg) **44** (12), 2139 (2002) [Phys. Solid State **44**, 2240 (2002)].
37. V. Klemm, P. Klimanek, A. L. Kolesnikova, *et al.*, Ann. Chim. Sci. Mater. **27** (3), 25 (2002).

Translated by Yu. Epifanov

Physics of the Solid State, Vol. 45, No. 9, 2003, pp. 1719–1722. Translated from Fizika Tverdogo Tela, Vol. 45, No. 9, 2003, pp. 1637–1640.

DEFECTS, DISLOCATIONS, AND PHYSICS OF STRENGTH

Stress Rate Dependence of the Strength of the Polycrystalline Ferroelectric PZT-22

L. V. Zhoga*, A. V. Shil'nikov*, V. V. Shpeĭzman, and A. T. Bulgakov***

** Volgograd State Architecture and Building Academy, Akademicheskaya ul. 1, Volgograd, 400074 Russia*

*** Ioffe Physicotechnical Institute, Russian Academy of Sciences, Politekhnicheskaya ul. 26, St. Petersburg, 194021 Russia*

e-mail: shpeizm.v@mail.ioffe.ru

Received January 29, 2003

Abstract—The bending strength of a polycrystalline $Pb_{0.95}Sr_{0.05}(Zr_{0.46}Ti_{0.54})O_3$ + 0.78 wt % Cr_2O_3 (PZT-22) ferroelectric is measured at loading rates of 5×10^{-2}–10 MPa/s and temperatures of 293–873 K (including the Curie temperature T_C = 593 K). The results are interpreted within the framework of the relaxation model of brittle fracture. The dependences of the strength on the loading rate at various temperatures are used to determine the effective activation volume of fracture. Changes in the activation characteristics in the range of the phase transformation are discussed. © *2003 MAIK "Nauka/Interperiodica".*

1. INTRODUCTION

When solids fail under stationary conditions, an increase in the loading rate results in an increase in the breaking stresses. This conclusion follows from the kinetic-fracture concept and is corroborated by direct experiments conducted on many materials [1]. It is also known, however, that the loading-rate dependences of flow stresses and of breaking stresses can be nonmonotonic, decreasing with increasing rate, or independent of the loading rate, which conflicts with the kinetic concepts of fracture [2]. A decrease in the breaking stress with an increase in the loading rate or its independence from loading rate for brittle solids (and for solids whose plasticity drops in a certain rate range due to, e.g., aging) can be qualitatively explained if the brittle fracture kinetics is assumed to be caused by two processes, fracture and the relatively slow relaxation of local stresses. The latter decreases the overstress coefficient and thereby slows down the fracture process. The effect of relaxation becomes more pronounced with decreasing test rate (i.e., with increasing test time) and, therefore, can lead to higher average stresses in a solid, i.e., to its higher strength.

For linearly increasing stresses σ ($\sigma = \omega t$, t is time, ω is the stress rise rate), Kozachuk *et al.* [2] obtained the following dependence of the breaking stress σ_f on the loading rate:

$$\sigma_f = \frac{kT}{V_{\text{eff}}} \ln\left[1 + \frac{\tau_0\left(\exp\frac{U_0}{kT}\right)\omega V_{\text{eff}}}{kT}\right]. \qquad (1)$$

Here, k is the Boltzmann constant, τ_0 and U_0 are the material constants, and τ_0 is the preexponential factor in the formula $\tau = \tau_0 \exp(U_0 - V_{\text{eff}}\sigma/kT)$ for the time to fracture τ at a constant stress σ, where $V_{\text{eff}} = nV$, V is the real activation volume, $n = \sigma_l/\sigma$ is the overstress coefficient, σ_l is the local stress in a fracture nucleus, σ is the average stress, and T is the test temperature.

Under the conditions of rapid relaxation (lowering) of local stresses, we have $n = n_S$, where n_S is the overstress coefficient for a stationary loading level. For slow relaxation, we have $n = n_0 - \dfrac{\alpha}{\omega t_0}$, where t_0 and α are the stress relaxation constants and n_0 is the overstress coefficient at $t = 0$.

Therefore, the effect of stress relaxation is reduced to a change in the overstress coefficient, which is $\alpha/(\omega t_0)$ behind a certain initial coefficient n_0 under the conditions of slow relaxation.

Generalizing these considerations, we conclude that, depending on the parameters of local stress relaxation, the breaking stress can either increase or decrease with increasing loading rate.

In this work, the relaxation fracture model is applied to analyze the stress rate dependence of the strength of the ferroelectric ceramic PZT-22.

2. EXPERIMENTAL

Nonpolarized $Pb_{0.95}Sr_{0.05}(Zr_{0.46}Ti_{0.54})O_3$ + 0.78 wt % Cr_2O_3 (PZT-22) ferroelectric samples in the form of disks of thickness h = 0.96 mm with silver electrodes were studied. The disks were subjected to axisymmetric bending at a constant loading rate in the range from 0.05 to 12 MPa/s.

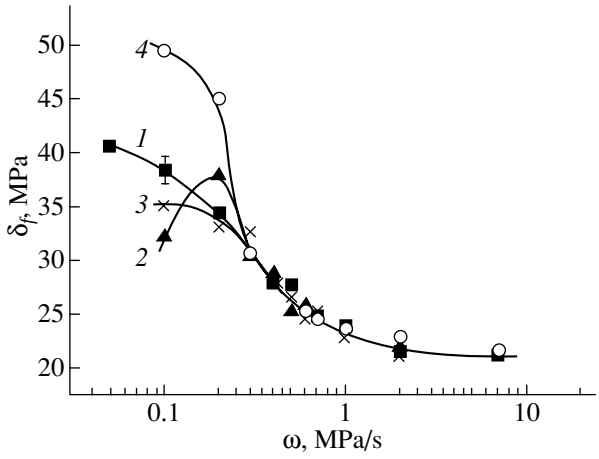

Fig. 1. Dependence of the strength of the polycrystalline ferroelectric PZT-22 on the loading rate at (*1*) T = 293, (*2*) 473, (*3*) 673, and (*4*) 873 K.

The stresses were calculated from the formula for the axisymmetric bending of disks with a low bending flexure [3]:

$$\sigma = \frac{3}{2}\frac{1+\nu}{\pi h^2}\left(\ln\frac{b}{a} + \frac{1-\nu}{1+\nu}\frac{b^2-a^2}{2c^2}\right)P, \qquad (2)$$

where $2b$ = 13 mm and $2a$ = 7 mm are the diameters of the ring support and loading punch, respectively; $2c$ = 20 mm is the sample diameter; and P is the load.

Tests were carried out in the temperature range from room temperature to 873 K, which included the Curie temperature (T_C = 593 K). Before the tests, we measured the capacitance and dielectric loss tangent to reject samples with defects [4]. The temperature was maintained with an accuracy of ±1 K.

3. RESULTS AND DISCUSSION

Figure 1 shows the dependences of the breaking stress σ_f on the loading rate for the ferroelectric ceramic PZT-22 at various temperatures. Each point is a result of averaging over five to ten tests. The root-mean-square error for the average strength is shown in the curve corresponding to room temperature.

The form of the $\sigma_f(\omega)$ dependences allows the following conclusions. Over the whole loading-rate range (covering two orders of magnitude) and at all test temperatures, the strength decreases with increasing loading rate (except at the temperature 473 K, where there is a small segment of increasing σ_f). At loading rates above 1 MPa/s, however, the strength is virtually constant.

The decrease in breaking stress with increasing loading rate means that processes of local deformation occur even in such a brittle material as PZT-22 and even at room temperature and short loading times (2–7 s). Otherwise, the breaking stress would have increased linearly with the logarithm of the loading rate, with the coefficient of proportionality determined by the initial value of $n = n_0$.

This result conflicts with the conception of brittle fracture as a critical process, since in this case the strength should be independent of rate. The lack of the loading-rate dependence of the strength in a certain rate range makes the generality of the kinetic concept of fracture doubtful; therefore, we will redress this issue in what follows. The kinetic nature of fracture, namely, the fact that fracture develops in time and is not a critical event, is also confirmed by the appearance of time effects in other experiments, for example, by data on the fatigue of ferroelectric ceramics, which has been detected upon cyclic variation of both mechanical [5] and electrical [6] loads.

The independence of the strength from the loading rate and temperature at relatively high loading rates can indicate the critical character of fracture or, at least, its approaching the critical point. However, in the context of the relaxation fracture model [2], this independence can be connected with either an increase in the fracture activation energy or an increase in τ_0 to 10^{-6}–10^{-9} s. An increase in τ_0 means a decrease in the preexponential factor V_0 in the formula for the fracture rate, $V_0 \sim 1/\tau_0$, which corresponds to a decrease in the attempt frequency for overcoming the potential barrier due to a more pronounced cooperative character of fracture (to the transition from a monatomic elementary act to a multiatomic one [7, 8]). Both these causes (increasing τ_0 and U_0), which can proceed simultaneously lead to weakening of both the temperature and loading-rate dependences of the strength [see Eq. (1)], which is observed experimentally (Fig. 1).

As follows from Fig. 1, the strength is temperature-independent at loading rates above 0.3 MPa/s (loading times below 100 s). Hence, if we take the creation and relaxation of overstresses to be due to domain-wall motion, these processes cannot proceed in such a short time even at high temperatures (up to 573 K). At high rates, the number of domain walls taking part in the process decreases (only 20% of domain walls are known to take part in the process of impact fracture; their number increases to 80% as the loading rate decreases [9]), which further weakens the effect of domain mechanisms.

Thus, the analysis of the rate dependence of the breaking stress shows that this dependence characterizes a nonsteady state with a variable overstress coefficient in a fracture nucleus. In the case of a variable overstress coefficient, we can calculate the effective activation volume V_{eff} by solving Eq. (1) numerically. In our case, we used the numerical values $U_0 = 2.88 \times 10^{-19}$ J and $\tau_0 = 10^{-12}$ s taken from the data of static tests [10]; the results of calculations are represented as a $V_{\text{eff}} = f(\log\omega)$ plot (Fig. 2, curves *1, 2*). For these parameters, Eq. (1) has a solution only in the low-temperature range

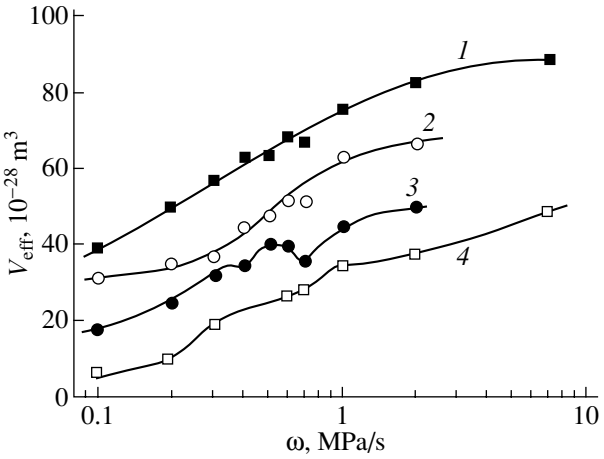

Fig. 2. Dependence of the effective activation volume of the polycrystalline ferroelectric PZT-22 on the loading rate at (*1*) T = 293, (*2*) 473, (*3*) 673, and (*4*) 873 K.

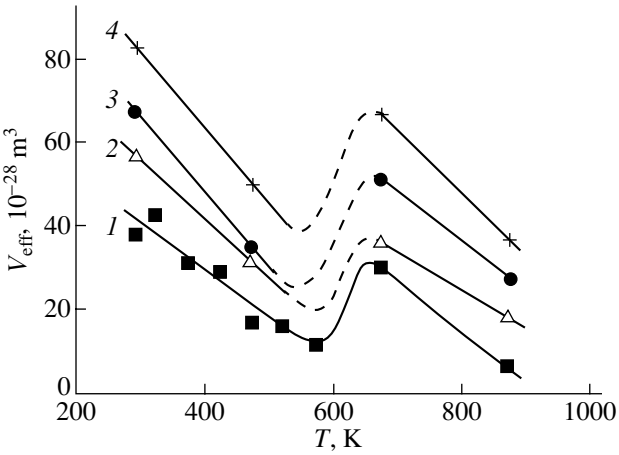

Fig. 3. Dependence of the effective activation volume of fracture for the polycrystalline ferroelectric PZT-22 on the temperature at a loading rate of (*1*) 0.1 (*2*) 0.3, (*3*) 0.7, and (*4*) 2 MPa/s.

(293–473 K). When the values of U_0 and τ_0 indicated above are substituted at higher temperatures (673, 873 K), Eq. (1) has no solution. However, if we increase U_0 to 4.5×10^{-19} J or τ_0 to 10^{-7} s, which is physically grounded (as noted above), then solutions exist and are similar to those for lower temperatures (Fig. 2, curves *3*, *4*). The authors of [11, 12] proposed that the fracture energy U_0 could increase at high temperatures due to a change in the character of the interatomic bond upon reconstructing the lattice. The cooperative character of the process can become more pronounced because of different competing relaxation mechanisms: domain and dislocation rearrangement at 293 and 473 K and dislocation mechanisms alone at 673 and 873 K.

Note that an increase in the effective activation volume with the loading rate is determined from the formula $V_{eff} = V(n_0 - \alpha/\omega t_0)$, which follows from the relaxation fracture model [1].

Figure 3 shows the variation of the effective activation volume with temperature. To refine this dependence in the ferroelectric phase at a loading rate $\omega = 0.1$ MPa/s, we determined the strength at intermediate temperatures (323, 373, 423, 523, 573 K). These data are given in the table, and the V_{eff} values, in Fig. 3 (curve *1*). It is significant that the effective activation volume decreases as the temperature is increased from room temperature to approximately the Curie temperature (i.e., in the ferroelectric phase). This fact can be due to possible stress relaxation in the ferroelectric phase via the motion of domain walls and grain boundaries, whose mobility and interaction with dislocations rise with temperature. In the expression for V_{eff}, this behavior formally corresponds to an increase in the relaxation rate, which is specified by the variation of the coefficient α with increasing temperature. Above the temperature of the phase transformation, V_{eff} changes jumpwise, which is obviously due to the relaxation becoming less efficient, as noted above. Finally, in the paraelectric phase ($T > T_C$), the effective activation volume decreases at all loading rates, because the relaxation rate increases with temperature; in this case, the relaxation is caused by only dislocation mechanisms, which are operative in the paraelectric phase. It should be noted that grain boundaries can also play an important role near T_C, since the phase transformation is diffuse.

4. CONCLUSIONS

Thus, we have experimentally found the variation of the strength of the polycrystalline ferroelectric PZT-22 with the loading rate ranging over two orders of magnitude and with the temperature ranging from 293 to 873 K. The decrease in the strength with increasing loading rate is explained by the relaxation of local stresses that proceeds during loading. At loading rates above 0.3 MPa/s, the strength is virtually temperature-independent.

Strength of the polycrystalline ferroelectric PZT-22 at various temperatures

T, K	293	323	373	423	473	523	573	673	873
σ_f, MPa	43.5	35.9	42.0	37.6	48.3	37.8	31.2	35.0	49.4

Note: The loading rate is $\omega = 0.1$ MPa/s.

Based on the relaxation fracture model, we have calculated the effective activation volumes of fracture at various temperatures and loading rates. The effective activation volume increases with the loading rate and decreases with increasing temperature in both the ferroelectric phase and paraelectric phase. The activation characteristics of fracture vary jumpwise near the phase transformation because of changes in both the fracture mechanism and the mechanisms of local stress relaxation.

ACKNOWLEDGMENTS

This work was supported by the Russian Foundation for Basic Research, project no. 02-02-016232.

REFERENCES

1. V. R. Regel', A. I. Slutsker, and É. E. Tomashevskiĭ, *Kinetic Nature of the Strength of Solids* (Nauka, Moscow, 1974).
2. A. I. Kozachuk, I. Yu. Solntseva, V. A. Stepanov, and V. V. Shpeĭzman, Fiz. Tverd. Tela (Leningrad) **25** (7), 1945 (1983) [Sov. Phys. Solid State **25**, 1122 (1983)].
3. F. F. Vitman, Ya. S. Uflyand, and B. S. Ioffe, Prikl. Mekh. **6** (5), 122 (1970).
4. B. Jaffe, W. R. Cook, and H. Jaffe, *Piezoelectric Ceramics* (Academic, New York, 1971; Mir, Moscow, 1974).
5. J. M. Moreno, F. Guiu, M. Meredith, *et al.*, J. Eur. Ceram. Soc. **19** (6–7), 1321 (1999).
6. H. Weitzing, G. A. Schneider, G. Steffens, *et al.*, Eur. Ceram. Soc. **19** (6–7), 1333 (1999).
7. A. I. Slutsker, in *Problems of Strength and Plasticity of Solids* (Nauka, Leningrad, 1979), p. 179.
8. V. A. Stepanov, N. N. Peschanskaya, and V. V. Shpeĭzman, *Strength and Relaxation Phenomena in Solids* (Nauka, Leningrad, 1984).
9. S. O. Kramarov and Yu. V. Dashko, Probl. Prochn., No. 10, 52 (1987).
10. L. V. Zhoga, V. I. Dorogin, E. G. Shatalova, and V. V. Shpeĭzman, Available from VNIIS, Gosstroĭ SSSR, No. 8032 (1988).
11. I. S. Zheludev, *Physics of Crystalline Dielectrics* (Nauka, Moscow, 1968; Plenum, New York, 1971), Vols. 1 and 2.
12. R. L. Coble and N. M. Parikh, in *Fracture*, Vol. 7: *Fracture of Nonmetals and Composites*, Ed. by H. Liebowitz (Academic, New York, 1972; Mir, Moscow, 1976), Part 1.

Translated by K. Shakhlevich

Physics of the Solid State, Vol. 45, No. 9, 2003, pp. 1723–1726. Translated from Fizika Tverdogo Tela, Vol. 45, No. 9, 2003, pp. 1641–1644.

DEFECTS, DISLOCATIONS, AND PHYSICS OF STRENGTH

Effect of the Composition of the Solid Solution on the High-Temperature Microhardness of SiGe Heteroepitaxial Layers Grown on Ge and Si Substrates

M. V. Mezhennyĭ*, M. G. Mil'vidskii, and T. G. Yugova*

** Giredmet Federal State Unitary Enterprise, Bol'shoĭ Tolmachevskiĭ per. 5, Moscow, 109017 Russia*

*** Institute for Chemical Problems of Microelectronics, Bol'shoĭ Tolmachevskiĭ per. 5, Moscow, 109017 Russia*

e-mail: icpm@mail.girmet.ru

Received February 4, 2003

Abstract—The effect of the composition of epitaxial layers (ELs) of the Si_xGe_{1-x} solid solution grown on Ge and Si substrates on their microhardness and the length of dislocation rosettes forming around indentations is studied at a homologous temperature $0.5T_{melt}$ for each composition. For the Si_xGe_{1-x}/Ge ($0 \le x < 0.15$) and Si_xGe_{1-x}/Si ($0.85 < x \le 1$) ELs, the dependences of the microhardness and the length of dislocation rosettes on the solid-solution composition are nonmonotonic. The nonmonotonic change in the plasticity of the ELs is most likely caused by hardening of the solid solutions in a certain composition range due to their spinodal decomposition with the formation of clusters and disperse precipitates. © *2003 MAIK "Nauka/Interperiodica".*

1. INTRODUCTION

The dislocation structure of an epitaxial heterostructure depends on the plasticity ratio of the layer and its substrate, as well as on the character of motion of individual dislocations and their interaction in the materials forming the heteropair [1]. One of the most informative methods for studying the mechanical properties of epitaxial layers over a wide temperature range is based on measurement of their microhardness. This method allows one to study the properties of a material in the ranges of both its brittle fracture and plasticity. In the latter case, the investigation of rosettes of dislocations forming around an indentation makes it possible to determine the dislocation mobility in an epitaxial layer. In spite of obvious advantages, the microhardness of epitaxial layers of Si_xGe_{1-x} solid solutions has been measured only in a few studies and only at room temperature [2, 3].

In this work, we study the "hot" microhardness and structure of dislocation rosettes that form in heteroepitaxial layers of the Si_xGe_{1-x} solid solutions during testing.

2. EXPERIMENTAL

Epitaxial layers (ELs) of the Si_xGe_{1-x} ($0 \le x < 0.15$) solid solutions were grown on Ge(111) substrates through hydride epitaxy, and ELs of the Si_xGe_{1-x} ($0.85 < x \le 1$) solid solutions were grown on Si(100) substrates through molecular beam epitaxy with on Si plate and gaseous GeH_4 used as the source. The dislocation density in the Ge substrates was lower than 1×10^3 cm^{-2}, and the Si substrates were dislocation-free. The EL thickness was 1.0–2.0 μm.

The microhardness was measured on an automatic Toyoseike (Japan) microhardness tester with a diamond Vickers pyramid. The microhardness of samples of each group was measured at the same homologous temperature (averaged over all solid solutions of the corresponding composition range), $0.5T_{melt}$ (T_{melt} is the melting temperature). The measurement temperature was 330°C for the Si_xGe_{1-x}/Ge ($0 \le x < 0.15$) solid solutions, and 570°C for the Si_xGe_{1-x}/Si ($0.85 < x \le 1$) solid solutions. The samples were heated with an attachment placed directly on the stage of the microhardness tester. The temperature of a sample was controlled with a chromel–alumel thermocouple. Once a given temperature was reached, a sample was held at this temperature for 15 min and then indented ten times at a load of 5 pN. The load was chosen such that the indentation depth in an epitaxial layer did not exceed 30% of its thickness. As shown in [4], the effect of the substrate/layer interface and of the substrate on the results of measurements can be neglected in this case. The pyramid was in contact with a sample for 30 s. The microhardness measurement error was 5%.

Dislocation rosettes around indentations were revealed by etching the Si_xGe_{1-x} ($0 \le x < 0.15$) ELs in an etchant based on $K_3Fe(CN)_6$ and KOH for 2 min and the Si_xGe_{1-x} ($0.85 < x \le 1$) ELs in the etchant HF : 0.5M CrO_3 : H_2O = 4 : 1 : 1.5 for 15 s. The indentation diagonals coincided with the [110] and $[1\bar{1}0]$ directions. The length of a rosette ray was taken to be half the distance between the centers of its limiting dislocation

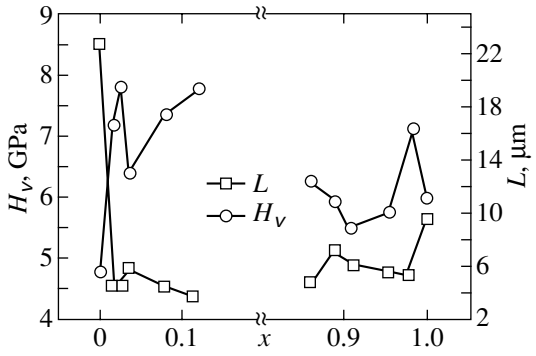

Fig. 1. Concentration dependences of the microhardness H_V and of the ray length L of dislocation rosettes forming around indentations in Si_xGe_{1-x}/Ge and Si_xGe_{1-x}/Si epitaxial layers.

etch pits. For each indentation, the value averaged over two rays in two directions was chosen. A measurement series consisted of five indentations, and the average length was determined for each series.

3. EXPERIMENTAL RESULTS

All Si_xGe_{1-x} ($0 \le x < 0.15$) solid solutions studied exhibited "diagonal" microcracks around indentations. Cracking in this case can be due to both relatively high brittleness of these solid solutions and tensile strains induced in the ELs on Ge substrates. The Si_xGe_{1-x} ($0.85 < x \le 1$) solid solutions, as a rule, were not subjected to cracking.

Figure 1 shows the concentration dependences of the microhardness of the solid solutions. The variation in the microhardness is seen to be nonmonotonic and similar for the two composition ranges. As the content of the solute in the solid solutions increases (Si in the Si_xGe_{1-x}/Ge solid solution and Ge in the Si_xGe_{1-x}/Si solid solution), the microhardness first increases, then drops, and then again increases slowly at $x > 0.035$ and $x < 0.91$, respectively. The microhardness is maximum at $x = 0.025$ and 0.978, respectively.

Typical dislocation rosettes forming around indentations in the Si_xGe_{1-x}/Ge and Si_xGe_{1-x}/Si layers are shown in Figs. 2 and 3. A dislocation rosette consists of a central region and rays along the ⟨110⟩ direction. The character of dislocation rosettes is obviously different for various compositions of the solid solutions. The lengths of rosette rays in solid-solution layers are significantly shorter than in substrates made of the corresponding pure components, all other things being equal. The dislocation rays are wide in the Si_xGe_{1-x}/Si solid solutions and are narrow in the Si_xGe_{1-x}/Ge solid solutions.

The dependence of the ray length of dislocation rosettes on the solid-solution composition is shown in Fig. 1. The concentration dependence of dislocation

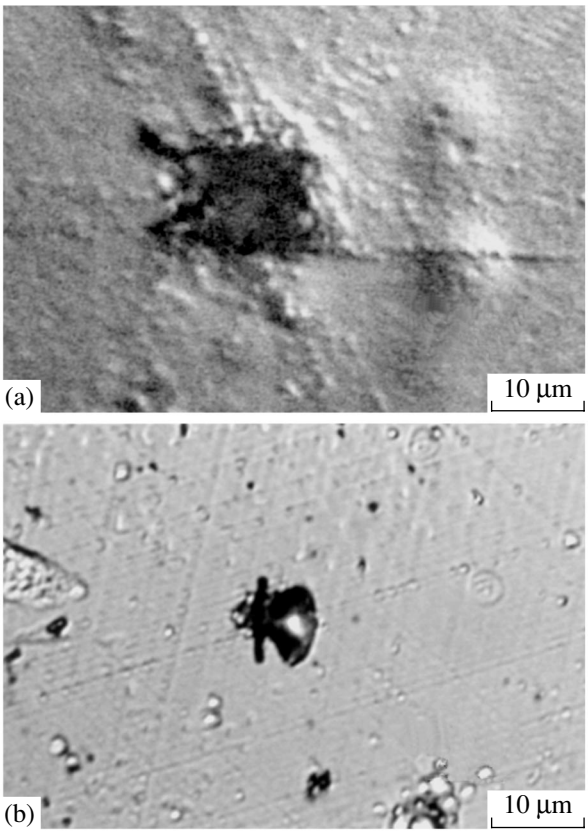

Fig. 2. Typical dislocation rosette forming around an indentation in Si_xGe_{1-x}/Ge epitaxial layers at 330°C: (a) Ge and (b) Si_xGe_{1-x} ($x = 0.35$).

rosette ray length, of microhardness, is nonmonotonic. As the solute content in the solid solutions increases, the ray length first drops, then insignificantly increases, and then gradually decreases at $x > 0.035$ and $x < 0.91$, respectively. Thus, pronounced minima at $x = 0.025$ and 0.978 exist in the concentration dependence of the ray length of dislocation rosettes induced by indentation. The positions of these minima correlate well with the positions of the maxima in the concentration dependence of microhardness.

4. DISCUSSION OF THE RESULTS

The investigation of microhardness provides information on some fundamental characteristics of a material, such as the character and strength of interatomic bonds [5]. It has been shown that the microhardness of Si and Ge at room temperature approaches the theoretical shear strength [6]. The shear moduli for Si and Ge at room temperature are ~80 and ~70 GPa and their microhardness are 8 and 11 GPa, respectively [7]. Since the theoretical shear strength is 10–15% of the shear modulus, we can conclude that plastic deformation at room temperature is strongly hindered in these materials.

The microhardness of Si_xGe_{1-x} polycrystalline ingots and epitaxial solid solutions was studied over a wide composition range at room temperature in [2, 3]. Unfortunately, the authors of [2, 3] did not study the solid solutions with a low solute content (<0.1 atomic fraction). They observed monotonic dependences of microhardness on the composition in both cases. The observed variation of the microhardness of the solid solutions with their composition was related in [4] to changes in the interatomic interaction between the components making up the solid solutions. It should be noted that these results were obtained at room temperature, where the contribution of plastic deformation to the microhardness can be neglected.

The situation is radically changed when the microhardness is measured at high temperatures. As the temperature increases, the plasticity of the materials under study significantly rises and plastic deformation with the formation of dislocations begins to play an increasingly important part in the processes that occur during indentation. This conclusion is supported by the formation of characteristic dislocation rosettes around indentations. The ray length of the dislocation rosettes is an objective characteristic of the mobility of dislocations forming upon indentation.

The temperature at which the contribution of plastic deformation to the mechanical properties of a material becomes substantial is different for different materials and depends on the melting temperature. To compare the results obtained on the microhardness and ray lengths of dislocation rosettes for solid solutions of different compositions, it is necessary to perform investigations at certain homologous temperatures that are fractions of T_{melt}. In our case, the test temperature was $0.5T_{melt}$. According to the data from [8], Ge and Si are rather plastic at these temperatures.

The data presented in Fig. 1 show that the microhardness of the Si_xGe_{1-x}/Ge ($0 < x \le 0.15$) ELs is higher and the ray lengths of dislocation rosettes in term are smaller than those for Ge. For the Si_xGe_{1-x}/Si ($0.85 \le x < 1$) ELs, the situation is more complex. The ray lengths of dislocation rosettes in these solid solutions are smaller than in Si, whereas the microhardness has a more complex concentration dependence. In the range $0.87 < x < 0.96$, the microhardness of these solid solutions is lower than that of Si. Shorter rays of dislocation rosettes indicate that the dislocation mobility in the solid solutions is significantly lower than in the pure components. Moreover, the wide dislocation rays forming in Si_xGe_{1-x}/Si ELs likely indicate that dislocation cross slip plays a significant role in plastic deformation in this case.

Our results show that, in ELs of the SiGe solid solutions, comparatively low solute contents cause nonmonotonic changes in both the microhardness and the ray lengths of dislocation rosettes forming around indentations. Extremum values of these parameters are observed at $x = 0.025$ for the Si_xGe_{1-x}/Ge heterostructures and at $x = 0.978$ for the Si_xGe_{1-x}/Si heterostructures. The maximum values of microhardness correspond to the shortest ray lengths of dislocation rosettes. These results correlate well with the results of our earlier investigation of the dislocation structure in ELs of these heterostructures [9, 10], according to which the concentration dependences of the densities of tilt dislocations and misfit dislocations in these ELs are nonmonotonic and these densities are minimum at the same solid-solution compositions as in this work.

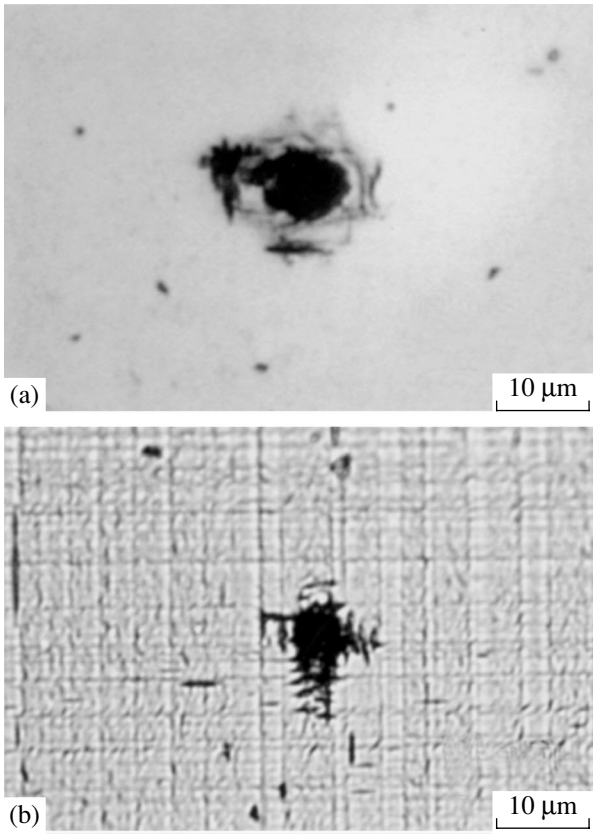

Fig. 3. Typical dislocation rosette forming around an indentation in Si_xGe_{1-x}/Si epitaxial layers at 570°C: (a) Si and (b) Si_xGe_{1-x} ($x = 0.89$).

On the whole, all these data allow the conclusion that the plasticity of the solid solutions studied varies nonmonotonically. In certain composition ranges ($0 \le x < 0.025$ for the Si_xGe_{1-x}/Ge heterostructures and $0.978 < x \le 1$ for the Si_xGe_{1-x}/Si heterostructures), the introduction of the solute is accompanied by hardening of the ELs. This effect is most likely caused by spinodal decomposition of the Si_xGe_{1-x} solid solution. At relatively low solute contents, the spinodal decomposition proceeds via the formation of clusters or disperse precipitates in ELs of the solid solution, which are efficient barriers for the motion of dislocations forming upon microindentation. As a result, the microhardness of the ELs substantially increases and the rays of dislocation rosettes shorten. As the solute content in the solid solu-

tion increases, progressively coarser precipitates form in the ELs during the spinodal decomposition. Such precipitates cease to be efficient barriers for dislocation motion and to harden the material, which leads to a decrease in the microhardness of the ELs and to an increase in the ray length of dislocation rosettes.

The more complex concentration dependences of these parameters studied in the Si_xGe_{1-x}/Si ELs at $x < 0.95$ is not completely understood. Such dependences may be assumed to be caused by the difference in the sign of misfit stresses (tension in the Si_xGe_{1-x}/Ge layers and compression in the Si_xGe_{1-x}/Si layers) operating in the ELs and by a possible asymmetry in the positions of the boundaries of the solid-solution stability regions in the composition axis for this binary system. Note that no reliable data on the GeSi solid-solution stability regions are available in the literature.

5. CONCLUSION

Thus, we have studied the high-temperature microhardness of the Si_xGe_{1-x}/Ge ($0 \le x < 0.15$) and Si_xGe_{1-x}/Si ($0.85 < x \le 1$) heterostructures. In the composition ranges studied, the concentration dependences of the microhardness and of the ray length of dislocation rosettes forming around indentations were found to be nonmonotonic. The nonmonotonic changes in the EL plasticity are most likely caused by hardening of the solid solutions in a certain composition range due to their spinodal decomposition with the formation of clusters and disperse precipitates.

REFERENCES

1. M. G. Mil'vidskiĭ and V. B. Osvenskiĭ, *Defects of the Structure in Epitaxial Layers of Semiconductor Materials* (Metallurgiya, Moscow, 1985).
2. I. Yonenaga, Physica B (Amsterdam) **273–274**, 612 (1999).
3. B. Roos, H. Richter, and J. Wollweber, Solid State Phenom. **47–48**, 509 (1996).
4. D. Y. Watts and A. F. W. Willoughby, Mater. Lett. **2**, 355 (1984).
5. V. M. Glazov and V. N. Vigdorovich, *Microhardness of Metals and Semiconductors*, 2nd ed. (Mir, Moscow, 1971).
6. V. R. Regel', A. I. Slutsker, and É. E. Tomashevskiĭ, *Kinetic Nature of the Strength of Solids* (Nauka, Moscow, 1974).
7. L. Garbato and A. Rucci, Philos. Mag. **35** (6), 1681 (1977).
8. S. S. Gorelik, Yu. M. Litvinov, and M. G. Lozinskiĭ, Élektron. Tekh., Ser. 6: Materialy **6**, 54 (1975).
9. V. I. Vdovin, M. G. Mil'vidskii, T. G. Yugova, *et al.*, J. Cryst. Growth **141**, 109 (1994).
10. T. G. Yugova, V. I. Vdovin, M. G. Mil'vidskii, *et al.*, Thin Solid Films **336**, 112 (1998).

Translated by K. Shakhlevich

Physics of the Solid State, Vol. 45, No. 9, 2003, pp. 1727–1734. Translated from Fizika Tverdogo Tela, Vol. 45, No. 9, 2003, pp. 1645–1652.

MAGNETISM AND FERROELECTRICITY

Bubble-Domain Lattices in the Vicinity of the Compensation Point

Yu. A. Mamaluĭ, Yu. A. Siryuk, and A. V. Bezus

Donetsk State University, Universitetskaya ul. 24, Donetsk, 83055 Ukraine

e-mail: coyote@skif.net

Received December 10, 2002

Abstract—The behavior of a hexagonal lattice of bubble domains in thin uniaxial films of garnet ferrites is studied in the temperature range from the compensation point to the Néel temperature. Two types of first-order phase transitions (preserving and not preserving the total number of domains in the bubble-domain lattice) occurring with variation of the temperature were studied. It is shown that the type of a phase transition is determined by the temperature dependence of the characteristic length of the film. The existence of two types of phase transitions is explained in terms of magnetostatic pressure existing in a bubble-domain lattice. © *2003 MAIK "Nauka/Interperiodica".*

1. INTRODUCTION

In this paper, we present the results of an experimental study on hexagonal lattices of bubble domains (BDs) in thin uniaxial films with the easy-magnetization axis normal to the film surface. The experiments were performed in a temperature range in the vicinity of the compensation point T_c. The domain structure (DS) of a thin magnetic film in the vicinity of T_c was studied theoretically in [1–3]. In [1], it was shown that, in a zero bias magnetic field, there is always a temperature range near T_c in which the thin magnetic film is in a single-domain state. The following sequence of various DSs existing near T_c was suggested. In a certain temperature range close to T_c, there exists a nonuniform state; with receding from this temperature range, BDs are formed, and with a further increase in the magnitude of the interval $T - T_c$ on both sides of T_c, the BDs transform into stripe domains.

The effect of an applied magnetic field on the parameters of the stripe DS in a uniaxial magnetic film in a temperature range including T_c was studied theoretically in [2] (see also review [3]). In [2], the DS period and the field under which the transition into a uniform state occurs were found as a function of temperature; analytical expressions describing the stability of individual BDs and of BD lattices in the vicinity of T_c were derived, and an expression (consistent with the experimental data from [4, 5]) was obtained for the temperature interval in which the single-domain state exists near T_c. In most experimental studies, the emphasis was on the stripe and labyrinth DSs and on the structure of domain walls in the vicinity of T_c [6–10]. In [10], field-induced phase transitions were shown to occur near T_c. It was found that the application of a magnetic field in the immediate vicinity of T_c brings about the development of metastable DS states: domains with magnetization directed upwards and/or downwards along the normal to the film surface and regions with spin-flop states having much larger magnetization (which results in enhancement of the Faraday effect). The transformation of up- and down-polarization domains into the spin-flop state occurs abruptly and is accompanied by a temperature and field hysteresis. The difference between the results obtained in [10] and [4] lies in this.

Phase transitions of BD lattices in thin garnet-ferrite films in the vicinity of T_c in zero field were studied in [11].

An analysis of the results obtained in the studies cited above shows that the behavior of BD lattices in the vicinity of T_c has not been adequately investigated. Little attention has been given to the occurrence of various types of phase transitions in BD lattices upon cooling and heating of films and to the deciding role of the procedure used to produce an equilibrium BD lattice in a thin magnetic film at a given temperature. These problems are studied in this article.

2. EXPERIMENTAL RESULTS

We studied uniaxial single-crystal garnet-ferrite films differing in composition, thickness, quality factor $Q \gg 1$, and compensation point. The films were grown through liquid-phase epitaxy on substrates of Gd–Ga garnet with the (111) orientation. The easy-magnetization axis was directed normal to the film surface. The parameters of the films are listed in Table 1.

Domains were observed using the Faraday effect. The magneto-optical setup provided the possibility of varying the temperature of a film in the temperature range from 90 K to T_N and for applying a unipolar pulsed magnetic field H_p directed perpendicular to the

1063-7834/03/4509-1727$24.00

Table 1. Film characteristics at room temperature

Film	Composition	h, μm	T_N, K	p, μm	d, μm	a, μm	H_c, Oe	l, μm	$4\pi M_S$, G	σ, erg/cm^2
1	$(TmBi)_3(FeGa)_5O_{12}$	8.4	437	13.5	12.5	16.9	100	0.67	175	0.16
2	$(YGdTm)_3(FeGa)_5O_{12}$	3.3	443	3.7	3.3	4.4	270	0.14	400	0.16
3	$(GdTm)_3(FeGa)_5O_{12}$	2.3	528	7.5	6.6	8.9	100	0.42	270	0.22
4	$(YBi)_3(FeGa)_5O_{12}$	2.8	483	17.5	15.5	21	30	1.12	146	0.19

Note: h is the film thickness, T_N is the Néel temperature, p is the stripe-structure period, d is the BD diameter, a is the BD lattice parameter, H_c is the BD collapse field, l is the characteristic length of a film, M_S is the saturation magnetization, and σ is the energy density of a domain wall.

film surface. A BD lattice was formed in a pulsed magnetic field of a certain frequency and amplitude with subsequent removal of the field.

There are two ways of studying BD lattice parameters. In the first method, a BD lattice is formed at different temperatures and the parameters $a(T)$ and $d(T)$ are determined, which are continuous functions of temperature [11]. Such lattices are equilibrium at the temperature of their formation; i.e., their parameters correspond to the energy minimum for the given $l(T)$ and $M_S(T)$ dependences [12]. The parameter $y = \frac{d}{a} = 0.74$ remains constant in the entire temperature range of existence of the equilibrium BD lattice [13]. Another type of $a(T)$ and $d(T)$ dependences is observed if the BD lattice is formed at a certain fixed temperature (e.g., at room temperature) and then the temperature of the film is varied. In this case, the lattice persists in a certain temperature range and then a spontaneous phase transition occurs into a new BD lattice with other equilibrium parameters corresponding to the new temperature [14]. This method was used in the present study. Let us consider a phase transition in a BD lattice caused by film cooling. As can be seen from Fig. 1, the lattice formed in film 1 at room temperature persists as the film is cooled to 215 K, since the parameter a remains constant upon cooling to this temperature (the image of this lattice is shown in Fig. 2a). Then, a phase transition to a new lattice with larger parameters a and d occurs. From Fig. 2b, it can be seen that some BDs contract and disappear, while others expand and absorb the neighboring domains. The application of a pulsed magnetic field transforms this lattice into an equilibrium hexagonal lattice with larger parameters and a smaller number of BDs covering the entire surface of the film (Fig. 2c). This lattice is stable at temperatures down to 175 K (Fig. 1), at which a phase transition again occurs with increased values of a and d and a decreased number of BDs (Fig. 2d). A new BD lattice produced by applying the field H_p (Fig. 2e) persists as the film is cooled to 170 K. With a further decrease in temperature, low-temperature collapse of the lattice occurs; individual BDs disappear. As a rule, it is the central domains that disappear first and then the BD lattice is destroyed (Fig. 2f). This situation is similar to the collapse of a BD lattice that takes place in a thin film at a constant temperature under the action of a bias field close in strength to the BD collapse field. At $T \le 160$ K, isolated BDs of a very large size are observed (Fig. 2g); they look unstable, move randomly, and chaotically change shape (Fig. 2h). At $T = 150$ K, the film transforms into a single-domain state.

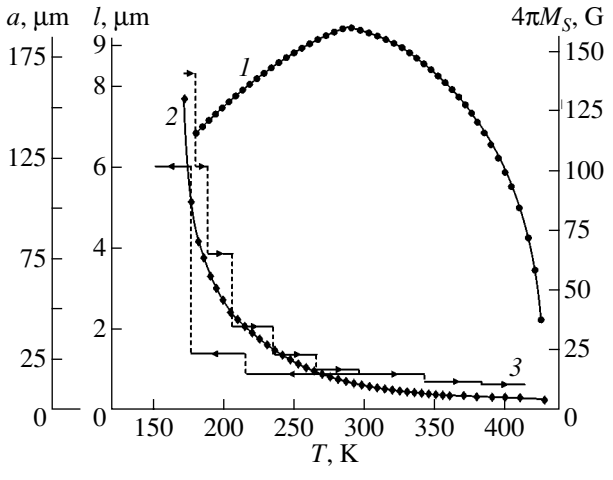

Fig. 1. Temperature dependences of (*1*) saturation magnetization $4\pi M_S$, (*2*) characteristic length l, and (*3*) BD lattice parameter a for film 1.

In order to investigate the evolution of DSs receding from T_c, the film was heated starting from low temperatures. When the temperature reaches 160 K, a stripe DS arises (Figs. 1, 3a), followed by isolated BDs (Fig. 3b), which immediately transform into stripe domains. The action of the pulsed field H_p for a short time results in the formation of a hexagonal BD lattice at 170 K (Fig. 3c), which persists up to 180 K. Then, a phase transition occurs and the lattice spontaneously decomposes into blocks of a new lattice separated by stripes. The parameters a and d of the new lattice inside blocks are smaller and correspond to the parameters of the equilibrium lattice at the given temperature (Figs. 1, 3d). The total number of domains n in the course of such processes remains constant. The application of the

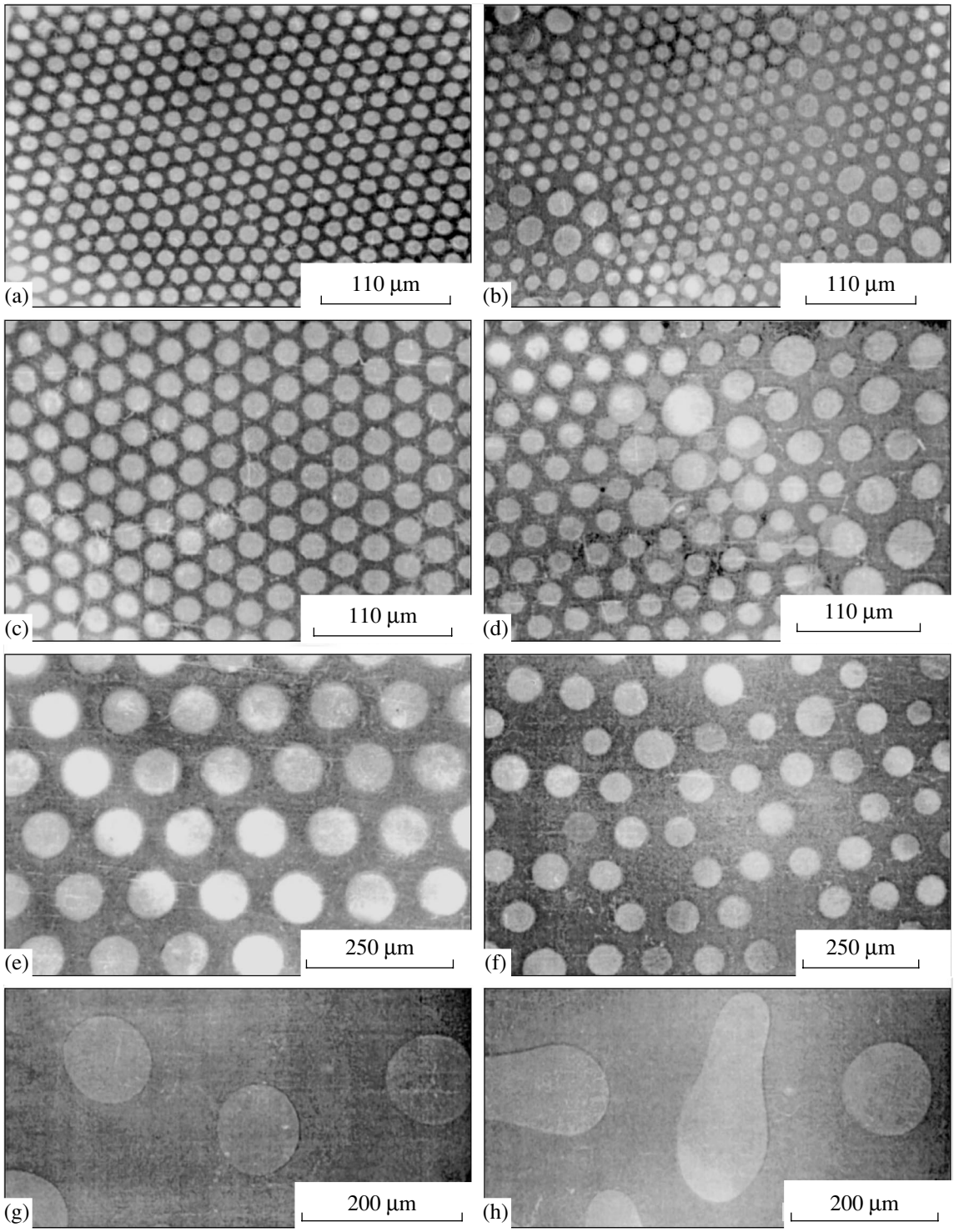

Fig. 2. Domain structure observed in film 1 upon cooling: (a) BD lattice at 300 K, (b) phase transition in BD lattice at 215 K, (c) BD lattice at 215 K, (d) phase transition in BD lattice at 175 K, (e) BD lattice at 175 K, (f) low-temperature collapse of BD lattice at 170 K, (g) isolated domains at 160 K, and (f) unstable domains at 158 K.

pulsed field H_p creates a bulk BD lattice with parameters corresponding to those in blocks. The lattice persists as the film is heated to 205 K, and then a new phase transition occurs to a two-phase structure consisting of stripes and lattice blocks with smaller parameters. As can be seen from Fig. 1, several phase transitions of this type occur during the film heating (Fig. 3). The number of phase transitions and the temperature intervals of BD

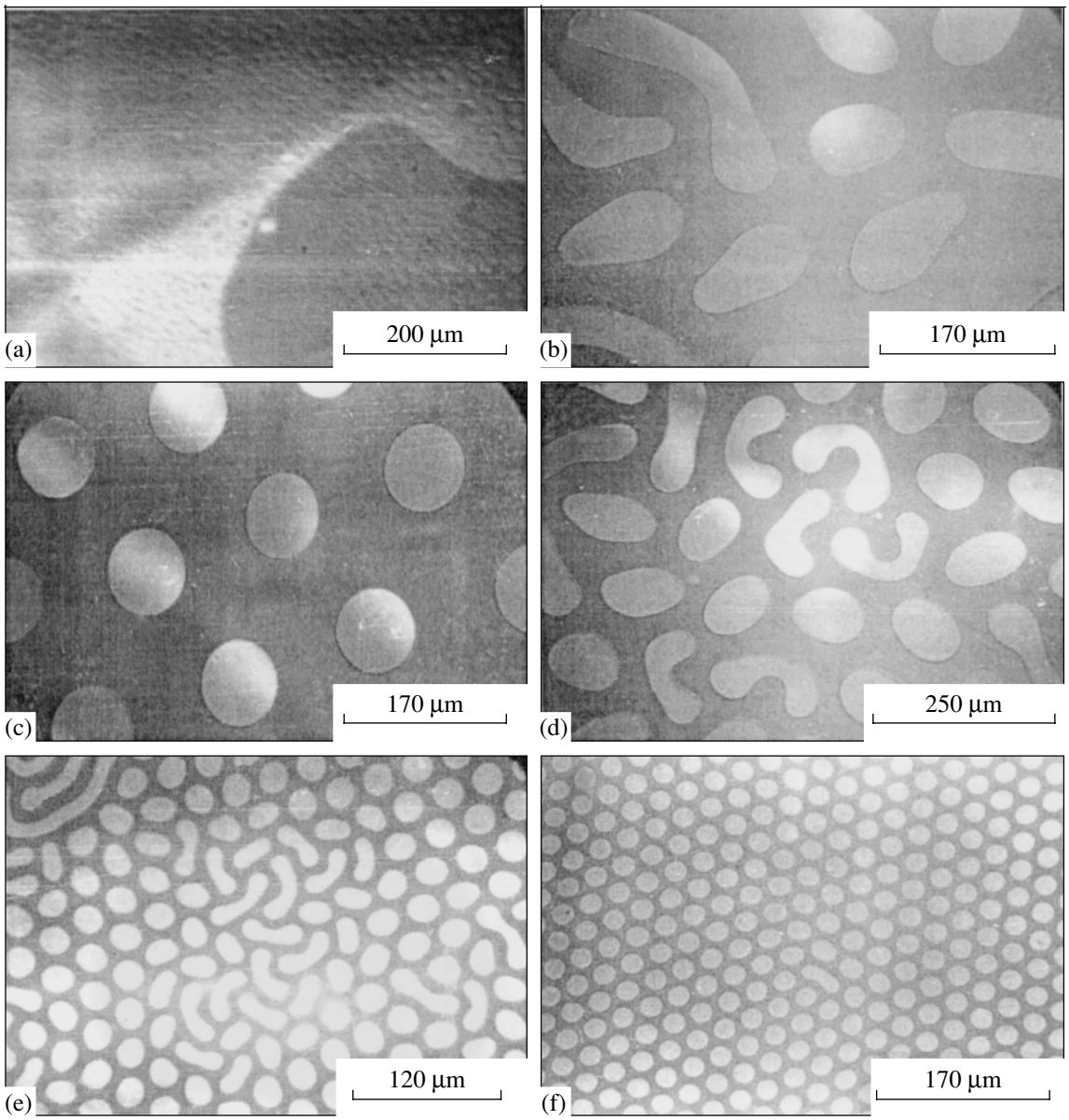

Fig. 3. Domain structure observed in film 1 upon heating: (a) stripes at 160 K, (b) isolated domains at 170 K, (c) BD lattice at 170 K, (d) phase transition in BD lattice at 180 K, (e) phase transition in BD lattice at 232 K, and (f) BD lattice at 232 K.

lattice stability upon heating of the film differ from those observed upon film cooling; i.e., a hysteresis is observed. It is also worth noting that phase transitions occurring upon both cooling and heating are initiated by defects in the BD lattice (Figs. 2, 3) and proceed spontaneously (abruptly).

A similar temperature behavior of phase transitions in the BD lattice is observed in film 2 (Fig. 4). Film 3 is of particular interest because, in contrast to films 1 and 2, this film allows one to study the temperature dependence of the DS on both sides of T_c (Fig. 5). As the temperature approaches T_c from either side, the DS parameters increase and reach their threshold values at which domains disappear. In the immediate vicinity of T_c, a single-domain region exists, where the net magnetization of a sample becomes so small that the formation of "Weiss domains" due to demagnetizing fields becomes unfavorable from the energy standpoint and the film transforms into a uniformly magnetized state. As seen from Fig. 5, the single-domain region in the vicinity of T_c covers the interval 150–230 K.

When the temperature approaches T_c from the higher temperature side, the DS behavior is the same as in films 1 and 2; namely, several phase transitions take place in the BD lattice (Fig. 5). Each transition is accompanied by an increase in the values of the lattice parameters and a decrease in the number of BDs. Further cooling results in low-temperature collapse of the

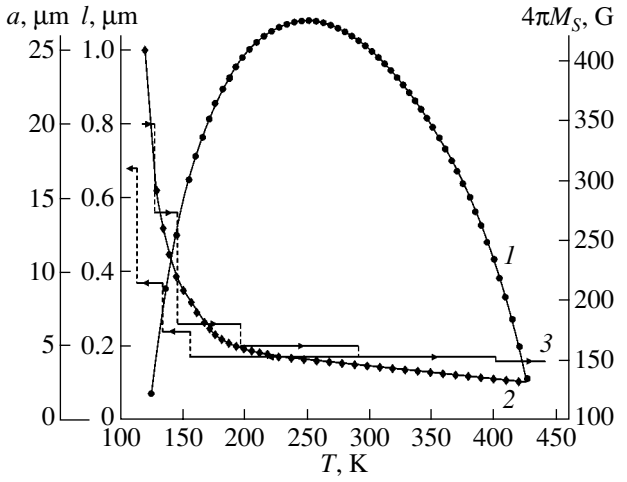

Fig. 4. Temperature dependences of (*1*) saturation magnetization $4\pi M_S$, (*2*) characteristic length *l*, and (*3*) BD lattice parameter *a* for film 2.

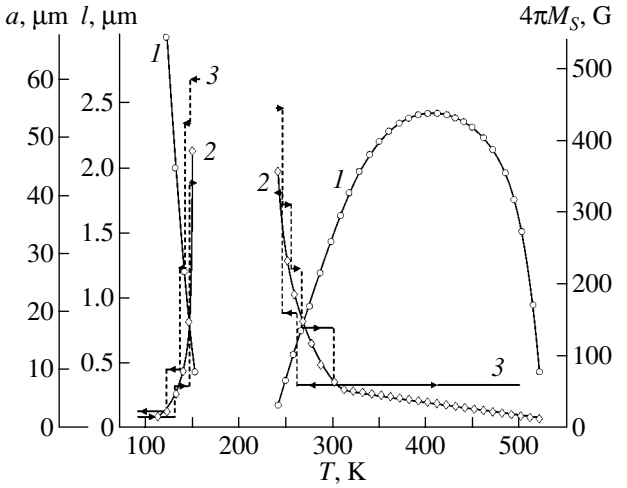

Fig. 5. Temperature dependences of (*1*) saturation magnetization $4\pi M_S$, (*2*) characteristic length *l*, and (*3*) BD lattice parameter *a* for film 3.

lattice, isolated BDs appear, and, finally, the single-domain state forms. As one moves away from T_c (upon heating), a stripe domain is formed and subsequently solitary bubbles appear. The application of H_p causes these solitary bubbles to form a hexagonal BD lattice. A further increase in temperature leads to a phase transition to a two-phase state in which the total number of domains remains unchanged.

With cooling from T_c (Fig. 5), after the formation of the single-domain state, a stripe domain appears and then individual bubbles are formed. The application of H_p results in the formation of a BD lattice. With receding from T_c, the lattice decomposes into blocks of a new lattice with smaller parameters; the blocks are separated by stripes; i.e., a phase transition to a two-phase structure occurs.

From the results presented above, it follows that the character of the phase transitions that occur in the BD lattice as one goes away from T_c is the same in the regions above and below T_c. As T_c is approached, several phase transitions occur in the BD lattice, which are accompanied by an increase in the lattice parameters and a decrease in the number of BDs. Next, collapse of the BD lattice occurs with the formation of solitary BDs, and then a single-domain state is formed.

Thus, the measurements on film 3 made it possible to study the behavior of the DS at both $T < T_c$ and $T > T_c$ and to conclude that this behavior is independent of whether we approach T_c from the lower temperature or the higher temperature side. The same can be said about the behavior of the BD lattice as one goes away from T_c.

Film 4 differs from the other films in that its compensation point is close to T_N (Fig. 6). As the temperature is increased from room temperature to T_c, several phase transitions are observed in the BD lattice, which are accompanied by an increase in the lattice parameter *a* and a decrease in the number of BDs (Fig. 6). However, in contrast to the phase transitions occurring in the other films as one approaches T_c, the increase in the BD diameter *d* due to a phase transition in film 4 is much larger, such that the bubbles almost contact with each other and the DS consists of blocks with intimately contacting bubbles. The situation is similar to the case of a phase transition occurring in a honeycomb structure with increasing bias field at constant temperature [13]. The temperature intervals of lattice stability are very narrow (Fig. 6); the single-domain state is reached at 320 K. Upon film cooling from T_c, stripes are formed. The application of H_p produces a BD lattice, which persists upon cooling in a certain temperature range. Then, a phase transition occurs and the lattice transforms into a two-phase structure consisting of lattice blocks with

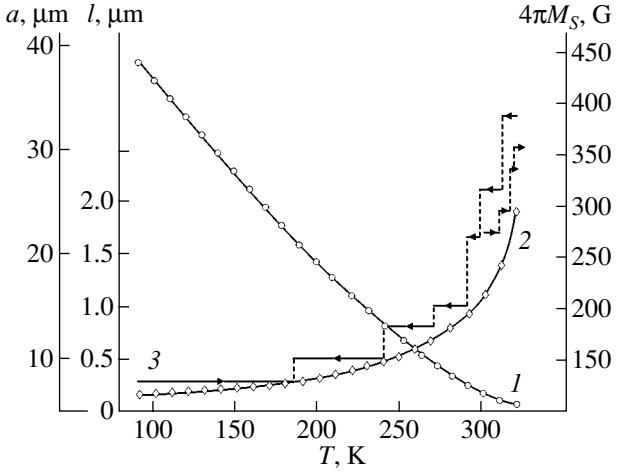

Fig. 6. Temperature dependences of (*1*) saturation magnetization $4\pi M_S$, (*2*) characteristic length *l*, and (*3*) BD lattice parameter *a* for film 4.

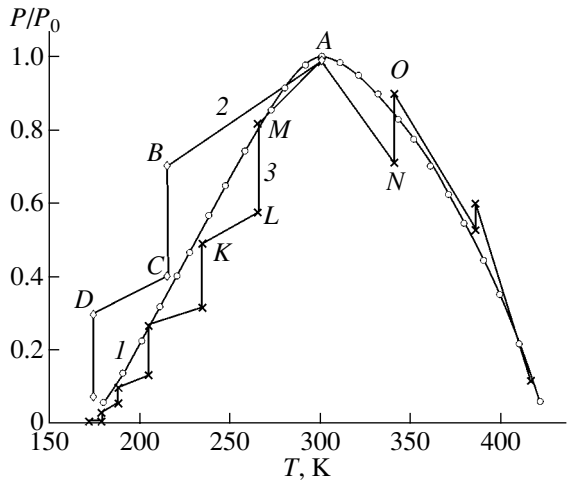

Fig. 7. Temperature dependences of P/P_0 for BD lattices in film 1: (*1*) equilibrium BD lattices and (*2*, *3*) BD lattices stable in a certain temperature range as one (*2*) approaches and (*3*) goes away from the magnetic compensation point T_c.

smaller parameters separated by stripes. After the application of H_p, the lattice with smaller parameters extends over the entire surface of the film. As can be seen from Fig. 6, the lattice parameters decrease with decreasing temperature at each phase transition, while the stability interval increases.

3. CONCLUDING DISCUSSION

Based on the results of our experiments, one can make the following conclusions.

The equilibrium BD lattice formed at a certain temperature remains stable in a certain temperature range. In [12], it is shown that the interval of thermostability of a BD lattice depends on the slope of the temperature dependence of the characteristic length $l(T)$.

As one of the limits of the stability range is reached, a spontaneous transition from the BD lattice to a two-phase structure occurs. The latter consists of blocks of the new BD lattice and the regions of stripe domains, with the total number of domains being unchanged. This kind of spontaneous transition in a BD lattice induced by a change in the temperature of the film is observed if the temperature recedes from T_c. At the other limit of the thermostability range, a transition to an equilibrium BD lattice with larger parameters occurs and is accompanied by the collapse of part of domains. The remaining domains abruptly increase in diameter and form a BD lattice with a period that is at equilibrium at the given temperature. This kind of spontaneous transition in a lattice is observed on approaching the magnetic compensation point.

Since they have qualitative distinctions, both kinds of transitions in a BD lattice share a common feature; namely, they proceed spontaneously (abruptly) when the temperature changes by two to three degrees and exhibit thermal hysteresis, which indicates that these phase transitions are of the first order.

Our experiments have shown that, in the vicinity of T_c, there exists a hexagonal BD lattice with parameters considerably larger than the film thickness. On approaching T_c, a low-temperature collapse of the BD lattice occurs and the film contains only solitary BDs.

The behavior of the DS is the same at $T < T_c$ and $T > T_c$ as T_c is approached. The same can be said about the behavior of the DS when the film is cooled or heated from T_c, but the character of the phase transitions in this case is quite different.

It has been found that, in the vicinity of T_c, as follows from theory [1], a sample is in a single-domain state, because the sample magnetization is decreased.

Our studies of various films have shown that the behavior of the DS is independent of the position of T_c on the temperature scale.

Previously, the thermostability region for a BD lattice upon heating [12] and cooling [15] of a film was analyzed using the chemical potential of the BD lattice and of stripe domains.

To explain the features of a BD lattice, we employ the idea of the magnetostatic pressure P defined in [16] as the pressure acting on a length unit of a contour bounding the area of the BD lattice. As follows from [17, 18], the pressure in a BD lattice is given by

$$P = BM_S^2 h\frac{d^4}{a^5} = BM_S^2 h\frac{y^4}{a}, \qquad (1)$$

where B is a constant. For the equilibrium BD lattice, we have $y = \text{const} = 0.74$ and Eq. (1) can be rewritten as

$$P = C\frac{M_S^2}{a}, \qquad (2)$$

where $C = Bhy^4 = \text{const}$. Using the experimental data and Eqs. (1) and (2), one can calculate the pressure of equilibrium and nonequilibrium BD lattices for films studied at various temperatures.

Figure 7 shows the $\frac{P}{P_0}(T)$ curves for equilibrium BD lattices and for BD lattices that are stable in a certain temperature range (film 1). The calculated pressure versus temperature curves for other films are similar and allow one to determine how the DS pressure varies as a phase transition occurs.

Let us consider a phase transition which occurs in a lattice as the temperature approaches T_c (Figs. 1, 7). The lattice formed at 300 K is an equilibrium lattice and corresponds to the condition $\frac{P}{P_0} = 1$ (point *A* in Fig. 7). Upon cooling, this BD lattice persists in the temperature range 300–215 K, with its pressure decreasing (segment *AB* in Fig. 7). Nevertheless, the pressure of

the lattice at point B is much higher than the pressure of the equilibrium lattice at $T = 215$ K. The lattice with the initial parameters becomes energetically unfavorable. Since the characteristic length l of the film grows as the temperature approaches T_c and since y = const for the equilibrium lattice, the parameters a and d should also increase, which is possible only if the number n of domains decreases. This means that a high magnetostatic pressure favors the collapse of part of the domains (segment BC in Fig. 7) and a phase transition occurs to an equilibrium BD lattice with larger parameters. In the same way, it is possible to describe the lattice that is stable in the temperature range 215–175 K and the phase transition at 175 K to an equilibrium BD lattice. However, at 170 K, as seen from Fig. 7, the pressure of the equilibrium lattice tends to zero. The lattice can no longer exist; its low-temperature collapse occurs, and solitary BDs are formed.

As one goes away from T_c, the phase transition in a BD lattice behaves differently, as follows from the experimental data. Two situations are possible. The first situation is realized when magnetization M_S increases and l decreases as one goes away from T_c. An equilibrium lattice formed, say, at 232 K persists within the temperature range 232–265 K. Its pressure increases (segment KL in Fig. 7), but at 265 K the pressure of this lattice is much lower than the pressure of the equilibrium lattice at the same temperature. For the equilibrium lattice, $M_S(T)$ increases together with $P(T)$. Since y = const at equilibrium, a decrease in l causes a decrease in both the lattice period and BD diameter; therefore, the number of domains n should increase. However, the formation of new domains requires additional energy, which can be provided, e.g., by an external pulsed magnetic field. Therefore, the number of domains is conserved and blocks of a BD lattice with smaller values of a and d at y = const are formed. The area between the blocks is occupied by stripe domains that form from the BDs not incorporated into blocks (the lattice pressure favors the formation of stripes). The pressure of such a DS is lower than that of an equilibrium BD lattice at the same temperature (point L in Fig. 7). When a pulsed field creates an additional quantity of BDs from stripes, the lattice becomes equilibrium (point M in Fig. 7).

The second situation is realized when the saturation magnetization and the characteristic length decrease with increasing temperature. As an illustration, let us consider the case where the temperature is increased from 300 K. An equilibrium lattice formed at 300 K persists upon heating of the film in the temperature range 300–342 K. As seen from Fig. 7, the heating reduces the pressure P (segment AN in Fig. 7). Since the equilibrium corresponds to y = const and a decrease in l is accompanied by a decrease in parameters a and d, the number of BDs should increase. The lattice with the initial parameters becomes unstable at 342 K. As in the previous situation, a phase transition occurs in the lattice to a two-phase structure consisting of lattice blocks with smaller parameters and of stripe-domain regions, with the total number of domains remaining unchanged. By applying H_p, an additional number of BDs is formed from stripes and the pressure of the DS increases (segment NO in Fig. 7), with the consequence that an equilibrium lattice with new parameters covers the entire observable area of the film. In the same manner, we can explain the behavior of the DS and the character of phase transitions occurring in the BD lattice with variation of the temperature in the other films studied.

Table 2. Phase transitions in a BD lattice

Variation of film characteristics with temperature	Phase arising upon phase transition
$M_S\downarrow, P\downarrow, l\uparrow \longrightarrow a\uparrow, d\uparrow, n\downarrow$	Equilibrium BD lattice
$M_S\uparrow, P\uparrow, l\downarrow \longrightarrow a\downarrow, d\downarrow, n$ = const $M_S\downarrow, P\downarrow, l\downarrow \longrightarrow a\downarrow, d\downarrow, n$ = const	Two-phase system consisting of BD lattice blocks and stripes

A diagram that sums up the transformations taking place in a BD lattice at phase transitions for the case y = const is shown in Table 2.

It can be seen that the character of the phase transitions does not depend on the change in M_S with temperature but is determined only by the sign of the change in the characteristic length with temperature. At $\Delta l > 0$, a phase transition to an equilibrium BD lattice with new parameters occurs with a decreased number n (collapse) of domains, while at $\Delta l < 0$, a phase transition occurs to a two-phase structure consisting of blocks of a new BD lattice with smaller parameters and of stripe-domain regions, with the total number of domains n remaining unchanged. Magnetostatic pressure P in the first case is higher than the equilibrium pressure, which results in the contraction and disappearance of part of the domains. This process continues until the pressure becomes equal to its equilibrium value. In the second case, the magnetostatic pressure is smaller than the equilibrium value; therefore, part of the BDs enlarge and transform into stripes. In the course of such transformation, the pressure of the remainder of the BD lattice increases to the equilibrium level. As shown in [17, 18], the coexisting BD and stripe-domain phases are in equilibrium provided their magnetostatic pressures at the transition point are equal. It follows that the character of a phase transition in a BD lattice is determined both by the magnetostatic pressure of the BD lattice and by the sign of the change in the characteristic length of the film. The phase transition temperature, as shown in [12, 15], depends on the slope of the $l(T)$ dependence.

REFERENCES

1. V. G. Bar'yakhtar and Yu. I. Gorobets, Fiz. Tverd. Tela (Leningrad) **18** (8), 2376 (1976) [Sov. Phys. Solid State **18**, 1386 (1976)].
2. A. N. Bogdanov and D. A. Yablonskiĭ, Fiz. Tverd. Tela (Leningrad) **22** (3), 680 (1980) [Sov. Phys. Solid State **22**, 399 (1980)].
3. V. G. Bar'yakhtar, A. N. Bogdanov, and D. A. Yablonskiĭ, Usp. Fiz. Nauk **156** (1), 47 (1988) [Sov. Phys. Usp. **31**, 810 (1988)].
4. F. V. Lisovskiĭ, E. G. Mansvetova, and V. I. Shapovalov, Zh. Éksp. Teor. Fiz. **71** (4), 1443 (1976) [Sov. Phys. JETP **44**, 755 (1976)].
5. G. S. Kandaurova, L. A. Pamyatnykh, N. P. Kochneva, and A. G. Titova, Fiz. Tverd. Tela (Leningrad) **21** (2), 612 (1979) [Sov. Phys. Solid State **21**, 363 (1979)].
6. A. I. Belyaeva, V. P. Yur'ev, and V. A. Potakova, Zh. Éksp. Teor. Fiz. **83** (9), 1104 (1982) [Sov. Phys. JETP **56**, 626 (1982)].
7. G. S. Kandaurova and L. A. Pamyatnykh, Fiz. Tverd. Tela (Leningrad) **31** (8), 132 (1989) [Sov. Phys. Solid State **31**, 1351 (1989)].
8. V. V. Randoshkin, A. F. Martynov, and A. Ya. Chervonenkis, Fiz. Tverd. Tela (St. Petersburg) **38** (5), 1592 (1996) [Phys. Solid State **38**, 875 (1996)].
9. G. Vertesy, I. Tomas, and L. Pust, J. Magn. Magn. Mater. **149** (3), 260 (1995).
10. P. Molho and M. P. de Albuquerque, J. Magn. Magn. Mater. **226–230**, 1388 (2001).
11. E. F. Khodosov, A. O. Khrebtov, and Yu. A. Siryuk, Pis'ma Zh. Tekh. Fiz. **8** (6), 363 (1982) [Sov. Tech. Phys. Lett. **8**, 157 (1982)].
12. E. A. Zavadskii and V. A. Zablotskii, Phys. Status Solidi A **112**, 145 (1989).
13. V. A. Zablotskiĭ, Yu. A. Mamaluĭ, and Yu. A. Siryuk, Ukr. Fiz. Zh. **33** (3), 403 (1988).
14. V. G. Bar'yakhtar, É. A. Zavadskiĭ, Yu. A. Mamaluĭ, and Yu. A. Siryuk, Fiz. Tverd. Tela (Leningrad) **26** (8), 2381 (1984) [Sov. Phys. Solid State **26**, 1443 (1984)].
15. V. A. Zablotskii, Ju. A. Mamalui, and Ju. A. Siryuk, J. Phys.: Condens. Matter **3** (4), 2623 (1992).
16. V. G. Bar'yakhtar and Yu. I. Gorobets, *Cylindrical Magnetic Domains and Their Lattices* (Naukova Dumka, Kiev, 1988).
17. V. A. Zablotskii and Ju. A. Mamalui, Mod. Phys. Lett. **9** (2), 1353 (1995).
18. V. A. Zablotskiĭ, K. V. Lamonova, Yu. A. Mamaluĭ, and Yu. A. Siryuk, Fiz. Tekh. Vys. Davlenii **6** (2), 34 (1996).

Translated by A. Zalesskiĭ

Physics of the Solid State, Vol. 45, No. 9, 2003, pp. 1735–1741. Translated from Fizika Tverdogo Tela, Vol. 45, No. 9, 2003, pp. 1653–1659.

MAGNETISM AND FERROELECTRICITY

Magnetic Structure of Er_5Ge_3 at 4.2 K

A. P. Vokhmyanin and Yu. A. Dorofeev

Institute of Metal Physics, Ural Division, Russian Academy of Sciences, ul. S. Kovalevskoĭ 18, Yekaterinburg, 620219 Russia
e-mail: avokhm@imp.uran.ru

Received September 6, 2002; in final form, January 17, 2003

Abstract—A symmetry analysis of the possible magnetic structures of Er_5Ge_3 in the ground state is performed using the results of measurements of elastic magnetic neutron scattering at 4.2 K. It is shown that the minimum discrepancy factor $R_m \approx 9.5\%$ corresponds to a modulated collinear magnetic structure in which the magnetic moments of erbium atoms are oriented along the $\mathbf{a}_3$ axis of the unit cell of the crystal structure and induce an antiferromagnetic longitudinal spin wave (AFLSW). The magnetic structure is characterized by the wave vector $\mathbf{k} = 2\pi(0, 0, \mu/a_3)$ (where $\mu \approx 0.293$) and the modulation period $\lambda \approx 3.413a_3$. The magnetic ordering temperature $T_N \approx 38$ K is determined from the temperature dependence of the intensity of magnetic reflections. © *2003 MAIK "Nauka/Interperiodica".*

1. INTRODUCTION

There are a number of works [1–9] concerned with the investigation of the magnetic structure of intermetallic compounds with the general formula R_5M_3[where R is a rare-earth element (Tb, Nd, Ho, Dy, Er) and M is Ge, Sb, Si, or Sn], namely, Tb_5Ge_3 [1], Nd_5Ge_3 [2], Tb_5Sb_3 [3], Tb_5Si_3 [4], Ho_5Sb_3 [5], Dy_5Sb_3 [6], Nd_5Sn_3 [7], Er_5Si_3 [8], and Tb_5Sn_3 [9]. The crystal structure of these compounds is described by the space group D_{6h}^3 ($P6_3/mcm$). In the structure, rare-earth atoms are located at the 4(d) and 6(g) positions, whereas Ge, Sb, Si, and Sn atoms occupy the 6(g) positions. The magnetic structure with the wave vector $\mathbf{k} = 2\pi(0, 0, \mu/a_3)$ is observed in Tb_5Ge_3 [1], Tb_5Si_3 [4], and Dy_5Sb_3 [6] at low temperatures; Tb_5Sb_3 [3] in the temperature range $80 \le T \le 150$ K; and Tb_5Sn_3 [9] at $T = 55$ K. The magnetic structure with the wave vector $\mathbf{k} = 2\pi(\mu/a_1, 0, 0)$ is revealed in Nd_5Ge_3 [2], Ho_5Sb_3 [5], Nd_5Sn_3 [7], and Er_5Si_3 [8] at low temperatures. According to [10], the parameters $\mathbf{a}_1$ and $\mathbf{a}_3$ are introduced as the fundamental periods of the direct lattice (the parameters $\mathbf{a}_1$, $\mathbf{a}_2$, and $\mathbf{a}_3$ correspond to the universally accepted parameters **a**, **b**, and **c**). The values of μ determined in each specific case are given in [1–9].

In our opinion, the main disadvantage of the aforementioned works [1–9] is that a systematic symmetry analysis of the magnetic structures studied was not carried out in any of them. The present paper reports on the results of neutron diffraction studies of the magnetic structure of intermetallic Er_5Ge_3, which is a crystal analog of the above compounds. Particular attention is given to the results obtained in the symmetry analysis of the possible magnetic structures of intermetallic compounds of this type.

The Er_5Ge_3 intermetallic compound (like the compounds studied in [1–9]) is a convenient object for use in neutron diffraction investigations and symmetry analyses of the possible magnetic structures owing to its simple crystal structure and small number of magnetically active atoms involved in the unit cell. Some difficulties encountered in such studies are associated with the fact that magnetically active atoms occupy positions of two types. However, this circumstance, though slightly complicating the problem under consideration, is of little consequence. The results obtained in the symmetry analysis can be extended to all intermetallic compounds with magnetically active atoms located at the 4(d) and 6(g) positions, provided these compounds have a crystal structure with space group D_{6h}^3 ($P6_3/mcm$) and a magnetic structure with the corresponding wave vector.

2. EXPERIMENTAL TECHNIQUE

In our neutron diffraction investigations, we used the polycrystalline sample Er_5Ge_3 supplied by researchers at the Department of General Physics of the Ural State Technical University (Yekaterinburg). Neutron diffraction measurements were performed on two diffractometers ($\lambda \approx 1.805$ and 2.4232 Å) installed in horizontal channels of an IVV-2M reactor at temperatures of 293, 80, and 4.2 K. The powder sample was placed in a vanadium cell 8 mm in diameter and 60 mm in height. The neutron diffraction patterns measured at 293 and 80 K differ insignificantly. Figures 1 and 2 show the neutron diffraction patterns measured on a diffractometer at $\lambda \approx 2.4232$ Å with a higher resolution at the liquid-nitrogen and liquid-helium temperatures, respectively. The neutron diffraction patterns were processed with the Fullprof program, which, at present, is commonly used in analyzing diffractometric data. In

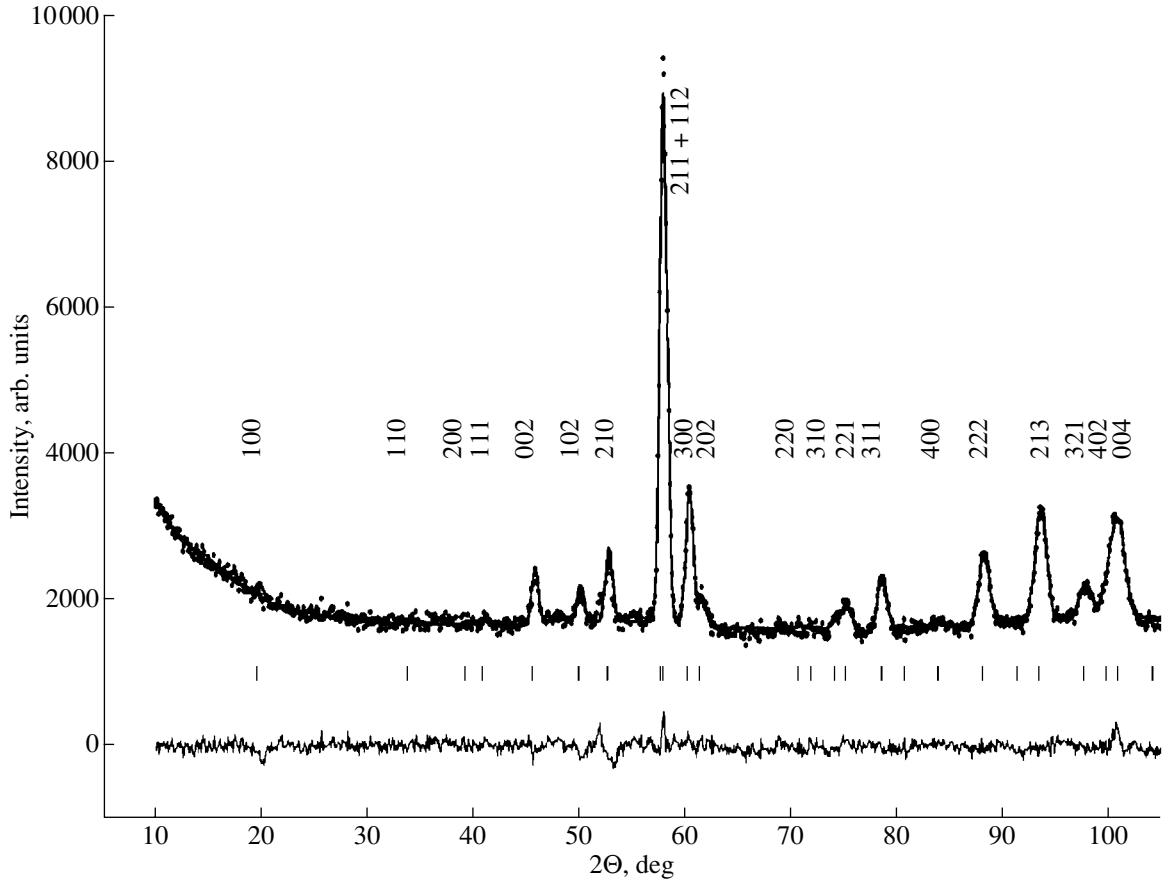

Fig. 1. Neutron diffraction pattern of Er_5Ge_3 at 80 K.

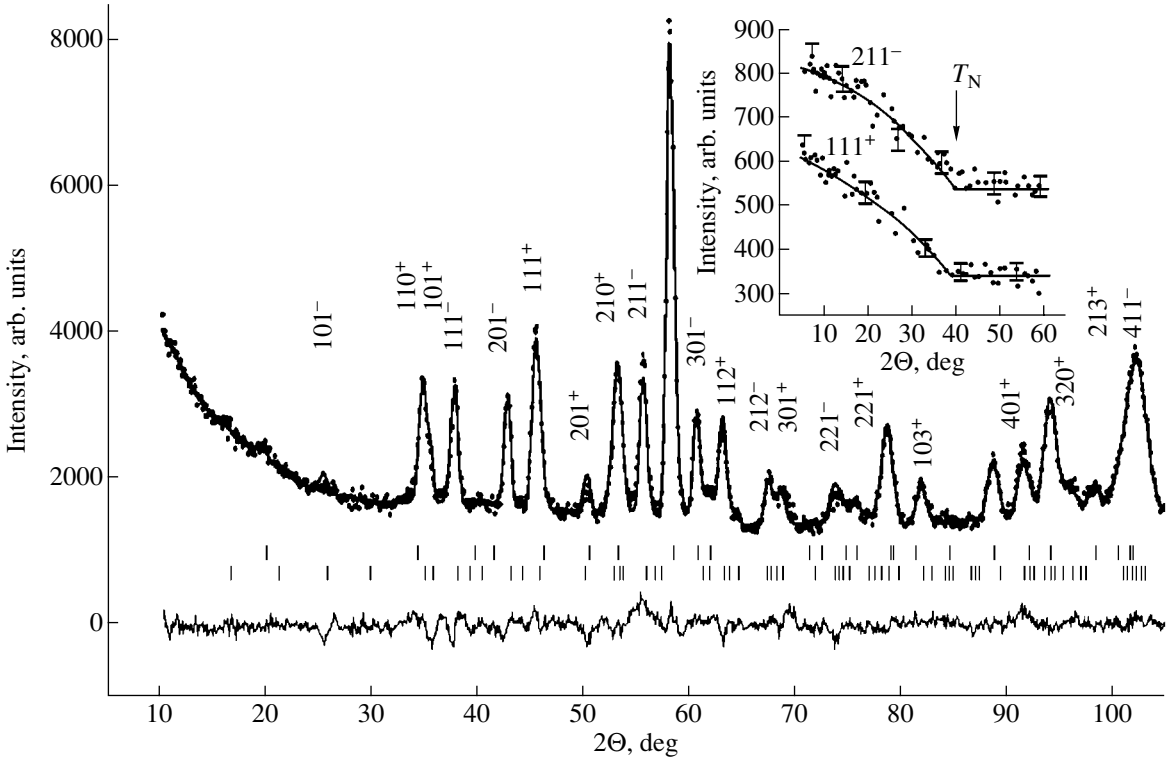

Fig. 2. Neutron diffraction pattern of Er_5Ge_3 at 4.2 K. The inset shows the temperature dependences of the intensity of the $(111)^+$ and $(211)^-$ reflections.

the range of small scattering angles ($2\Theta = 2°–10°$), no reflections were observed in the neutron diffraction patterns measured with prolonged exposure. For this reason, the small-angle portions of the neutron diffraction patterns are not shown in Figs. 1 and 2.

The starting models of the magnetic structure were constructed from the basis functions of the irreducible representations of the space group D_{6h}^3 ($P6_3/mcm$). These representations are involved in the magnetic representation with a wave vector determined by indexing the neutron diffraction patterns measured at a low temperature. The technique of calculating the basis functions is described in detail in [11]. When describing this technique, we will follow the notation used in [11].

3. CRYSTAL STRUCTURE

An analysis of the neutron diffraction patterns recorded at 80 and 4.2 K (Figs. 1, 2) demonstrates that, at these temperatures, the Er_5Ge_3 compound has a crystal structure with space group D_{6h}^3 ($P6_3/mcm$). According to [12], the Er(I) atoms are located at the 4(d) positions with the coordinates 1(1/3, 2/3, 0), 2(1/3, 2/3, 1/2), 3(2/3, 1/3, 0), and 4(2/3, 1/3, 1/2) and the Er(II) atoms occupy the 6(g) positions with the coordinates 1(x, 0, 0.25), 2(0, x, 0.25), 3($\bar{x}$, $\bar{x}$, 0.25), 4($\bar{x}$, 0, 0.75), 5(0, $\bar{x}$, 0.75), and 6(x, x, 0.75), where $x \approx 0.240$. The Ge atoms occupy the 6(g) positions with $x \approx 0.605$. Therefore, the unit cell contains 16 atoms, i.e., two formula units. The results of the calculations are as follows: $a_1 = a_2 \approx (8.414 \pm 0.003)$ Å, $a_3 \approx (6.306 \pm 0.002)$ Å, $x_{Er}(6(g)) \approx 0.244$, $x_{Ge} \approx 0.606$, $R_B \approx 7.41\%$, and $R_f \approx 10.4\%$ at $T \approx 80$ K and $a_1 = a_2 \approx (8.390 \pm 0.002)$ Å, $a_3 \approx (6.279 \pm 0.002)$ Å, $x_{Er}(6(g)) \approx 0.240$, $x_{Ge} \approx 0.605$, $R_B \approx 4.22\%$, and $R_f \approx 5.66\%$ at $T \approx 4.2$ K.

4. MAGNETIC STRUCTURE

4.1. Wave Vector of the Magnetic Structure

Compounds with a crystal structure described by the space group D_{6h}^3 ($P6_3/mcm$) belong to the hexagonal crystal system. The list of vectors—representatives of stars of wave vectors permissible in the hexagonal crystal system—is presented in [10]. These stars of wave vectors following the star notation used in [11] are given below:

$$\{\mathbf{k}_1\} = \mu\mathbf{b}_1 + \nu\mathbf{b}_2; \quad \{\mathbf{k}_2\} = \mu\mathbf{b}_1 + \nu\mathbf{b}_2 + \mathbf{b}_3/2;$$

$$\{\mathbf{k}_3\} = \mu\mathbf{b}_1 + \nu\mathbf{b}_3; \quad \{\mathbf{k}_4\} = \mu(\mathbf{b}_1 + \mathbf{b}_2) + \nu\mathbf{b}_3;$$

$$\{\mathbf{k}_5\} = \mu\mathbf{b}_1; \quad \{\mathbf{k}_6\} = \mu(\mathbf{b}_1 + \mathbf{b}_2);$$

$$\{\mathbf{k}_7\} = \mu\mathbf{b}_1 + \mathbf{b}_3/2; \quad \{\mathbf{k}_8\} = \mu(\mathbf{b}_1 + \mathbf{b}_2) + \mathbf{b}_3/2;$$

$$\{\mathbf{k}_9\} = \mathbf{b}_1/2 + \mu\mathbf{b}_3; \quad \{\mathbf{k}_{10}\} = (\mathbf{b}_1 + \mathbf{b}_2)/3 + \mu\mathbf{b}_3;$$

$$\{\mathbf{k}_{11}\} = \mu\mathbf{b}_3; \quad \{\mathbf{k}_{12}\} = \mathbf{b}_1/2;$$

$$\{\mathbf{k}_{13}\} = (\mathbf{b}_1 + \mathbf{b}_2)/3; \quad \{\mathbf{k}_{14}\} = (\mathbf{b}_1 + \mathbf{b}_3)/2;$$

$$\{\mathbf{k}_{15}\} = (\mathbf{b}_1 + \mathbf{b}_2)/3 + \mathbf{b}_3/2; \quad \{\mathbf{k}_{16}\} = 0;$$

$$\{\mathbf{k}_{17}\} = \mathbf{b}_3/2.$$

Here, $\mathbf{b}_1$, $\mathbf{b}_2$, and $\mathbf{b}_3$ are the designations used in [10] for the primitive vectors of the reciprocal lattice that correspond to the universally accepted vectors **a***, **b***, and **c***.

A comparison of the neutron diffraction patterns of the Er_5Ge_3 compound at 4.2 and 80 K shows that the neutron diffraction pattern measured at a lower temperature contains purely magnetic reflections to which the integral Miller indices (hkl) cannot be assigned on the basis of the unit cell.

Judging from the angular positions of the magnetic reflections (in our case, satellites) in the neutron diffraction pattern of Er_5Ge_3 at 4.2 K, the Er_5Ge_3 compound at this temperature has a magnetic structure characterized by the wave vector $\mathbf{k} = \mu\mathbf{b}_3 = 2\pi(0, 0, \mu/a_3)$, where $\mu \approx 0.293$. Magnetic structures with wave vectors of this type are referred to as incommensurate or modulated structures [11, 13, 14].

4.2. Symmetry Analysis of the Possible Magnetic Structures in Compounds with Space Group D_{6h}^3 ($P6_3/mcm$) and with Star of the Wave Vector $\{\mathbf{k}_{11}\} = \mu\mathbf{b}_3$

In this section, by using the Er_5Ge_3 compound as an example, we will briefly describe the symmetry analysis of the magnetic structure of compounds that have a crystal structure with space group D_{6h}^3 ($P6_3/mcm$) and atoms located at the 4(d) and 6(g) positions. Particular attention is focused on the description of this technique, because the symmetry analysis is rarely used in practice, even though the methods of symmetry analysis, as applied to neutron diffractometry of magnets, can provide useful information.

The wave vector $\mathbf{k} = \mu\mathbf{b}_3 = 2\pi(0, 0, \mu/a_3)$ is one of the prongs of the two-pronged star $\{\mathbf{k}_{11}\} = \mu\mathbf{b}_3$ [10]. The notion of the star of a wave vector and the prong of a star are given in [11].

The loaded irreducible representations taken from [10] for the star $\{\mathbf{k}_{11}\} = \mu\mathbf{b}_3 = 2\pi(0, 0, \mu/a_3)$ are tabulated prior to calculations. The table obtained contains four one-dimensional (τ_1–τ_4) and two two-dimensional (τ_5, τ_6) representations. The irreducible representations τ_5 and τ_6 with the complex quantities

$$\omega = \exp(i\pi/3) = (1 + i\sqrt{3})/2,$$

$$\omega^2 = \exp(2i\pi/3) = (-1 + i\sqrt{3})/2,$$

$$\omega^4 = \exp(4i\pi/3) = (-1 - i\sqrt{3})/2,$$

and

$$\omega^5 = \exp(5i\pi/3) = (1 - i\sqrt{3})/2,$$

can be transformed into the real form with the use of the unitary matrix

$$u = \frac{1}{\sqrt{2}}\begin{pmatrix} 1 & -i \\ -i & 1 \end{pmatrix} \quad \text{and} \quad u^{-1} = \frac{1}{\sqrt{2}}\begin{pmatrix} 1 & i \\ i & 1 \end{pmatrix}.$$

The irreducible-representation matrices transformed into the real form will be used in the further analysis. According to [10], for space group D_{6h}^3 ($P6_3/mcm$), the symmetry elements H_1, H_3, H_5, H_{20}, H_{22}, and H_{24} have the accompanying translation $\boldsymbol{\tau}_h = 0$ and the symmetry elements H_2, H_4, H_6, H_{19}, H_{21}, and H_{23} possess the accompanying translation $\tau = (0, 0, \mathbf{a}_3/2)$. These symmetry elements form the group of the wave vector $\mathbf{k} = 2\pi(0, 0, \mu/a_3)$. By multiplying the projective (i.e., loaded irreducible) representations into $\exp(-i\mathbf{k}\boldsymbol{\tau}_h)$, we obtain the minor representations (see [11]). In what follows, we will use quantities that are complex conjugate to the minor representations.

Next, in the 4(d) and 6(g) positions, it is expedient to change over from the coordinate system I used in [12] to the coordinate system K used in [10]. The relation between these coordinate systems for the space group D_{6h}^3 ($P6_3/mcm$) [$(XYZ)K = (XYZ)I - (0, 0, 0.25)$] is described in [10]. The permutations of atoms due to the elements of the wave vector group are tabulated for each of the positions 4(d) and 6(g).

The multiplicity of occurrence of the irreducible magnetic representation in the reducible representation is determined from the formula

$$n_\nu = \frac{1}{n(G_k^0)}\sum_{h \in G_k^0} \chi_M^k(g)\chi^{*k\nu}(g),$$

where $n(G_k^0)$ is the number of elements of the point group of the wave vector G_k^0,

$$\chi_M^k(g) = \delta_h Sp R^h \sum_j \exp[-i\mathbf{k}\mathbf{a}_p(g, j)]\delta_{j, gj}$$

is the magnetic-representation character,

$$\sum_j \exp[-i\mathbf{k}\mathbf{a}_p(g, j)]\delta_{j, gj} = \chi_p^k$$

is the permutation-representation character, $\delta_h = 1$ (if h is the rotation) or $\delta_h = -1$ (if h is the inversion rotation), R^h is the matrix of rotational transformation, $\mathbf{a}_p$ is the reciprocal translation, $\delta_{j, gi}$ is the Kronecker delta symbol, and $\chi^{k\nu}$ is the character of the irreducible representation $d^{k\nu}$.

After the calculations, we obtain the following magnetic representation for the 4(d) and 6(g) positions:

$$d_M^{k_{11}}(4(d)) = \tau_1 + \tau_2 + \tau_3 + \tau_4 + 2(\tau_5 + \tau_6),$$

$$d_M^{k_{11}}(6(g)) = \tau_1 + 2(\tau_2 + \tau_3) + \tau_4 + 3(\tau_5 + \tau_6).$$

From the formula [11]

$$S\begin{pmatrix} k\nu \\ \lambda \end{pmatrix} i \Bigg) = \sum_{h \in G_k^0} d_{\lambda[\mu]}^{*k\nu}(g)\exp[-i\mathbf{k}\mathbf{a}_p(g, j)]\delta_{i, g[j]}\begin{pmatrix} R_{x[\beta]}^h \\ R_{y[\beta]}^h \\ R_{z[\beta]}^h \end{pmatrix},$$

we determine the basis functions of the irreducible representations of the space group D_{6h}^3 ($P6_3/mcm$), which enter into the magnetic representation with the star $\{\mathbf{k}_{11}\} = \mu\mathbf{b}_3 = 2\pi(0, 0, \mu/a_3)$ (for the prong $\mathbf{k}_1 = \mu\mathbf{b}_3$) for the 4($d$) and 6($g$) positions. These functions are complex quantities.

Since the magnetic moments inducing the magnetic structure are real quantities, the basis functions of the irreducible representations should also be derived in the form of real quantities. For this purpose, it is recommended [11] to find the basis functions for the prong $\mathbf{k}_2 = -\mathbf{k}_1$ from the relationship

$$S\begin{pmatrix} k_L\nu \\ \lambda \end{pmatrix} i' \Bigg) = \exp[-i\mathbf{k}_L\mathbf{a}_p(g_L, i)]\delta_{h_L} R^{h_L} S\begin{pmatrix} k\nu \\ \lambda \end{pmatrix} i \Bigg)$$

and to set up a linear combination (to accomplish the prong mixing) of the basis functions of the irreducible representations determined for the prongs $\mathbf{k}_1$ and $\mathbf{k}_2 = -\mathbf{k}_1$ with a mixing coefficient that determine the real magnetic moment of each atom in all positions for each irreducible representation. In order to change over from the prong $\mathbf{k}_1$ to the prong $\mathbf{k}_2$, the elements $\{H_{13}|0\}$ and $\{H_7|0\}$ are used for the 4(d) and 6(g) positions, respectively. For the zeroth (initial) unit cell of the crystal, the real quantities can be obtained as follows:

$$S_{0i}(4(d)) = [S_{0i}^{k_1}(4(d)) + \varepsilon S_{0i}^{k_2}(4(d))]/2,$$

where $\varepsilon = \exp(-i\pi\mu)$,

$$S_{0i}(6(g)) = [S_{0i}^{k_1}(6(g)) + S_{0i}^{k_2}(6(g))]/2.$$

Here, we used the designations in compact form. The simplicity of the expression for $S_{0i}(6(g))$ can be explained by the fact that the quantities $S_{0i}^{k_1}(6(g))$ and

$S_{0i}^{k_2}(6(g))$ appear to be complex conjugates; consequently, the mixing coefficients for these quantities turn out to be identical and equal to 1/2. At the final stage of calculations, we return to the coordinate system used in [12].

A preliminary analysis of the results of calculations demonstrates that it is impossible to obtain equal magnetic moments of the atoms located at all sites with different coordinates z for each type [4(d) or 6(g)] of position for the space group D_{6h}^3 ($P6_3/mcm$). Therefore, the magnetic moments can induce several variants of magnetic structures of the spin wave type. These structures are as follows: (i) the longitudinal spin wave, when the magnetic moments are parallel to the $\mathbf{a}_3$ axis and the wave vector $\mathbf{k}$ of the magnetic structure; (ii) the transverse spin wave, when the magnetic moments are perpendicular to the same axis and the same vector (if the concept of one irreducible representation [11] is true); and (iii) their vector sum, when it is necessary to use the basis functions that determine projections of the magnetic moment onto both the basal plane and the $\mathbf{a}_3$ axis of the unit cell.

4.3. Magnetic Structure

The calculations performed with the Fullprof program allow us to make the following inferences. The magnetic structure in the 4(d) and 6(g) positions is formed in accordance with the irreducible representations τ_3 and τ_3', respectively. This variant leads to the minimum discrepancy factor for the crystal and magnetic structures, which is treated as the criterion of reliability for the results obtained.

For atoms located at the 4(d) positions, we have

$$S\left(\begin{array}{c} k_{11}\tau_3 \\ \lambda \end{array}\middle| 1\right) = S\left(\begin{array}{c} k_{11}\tau_3 \\ \lambda \end{array}\middle| 3\right) = S(0, 0, 1),$$

$$S\left(\begin{array}{c} k_{11}\tau_3 \\ \lambda \end{array}\middle| 2\right) = S\left(\begin{array}{c} k_{11}\tau_3 \\ \lambda \end{array}\middle| 4\right) = S(0, 0, \bar{1})\mathrm{Re}\,\varepsilon$$

and $-\mathrm{Re}\,\varepsilon = -\cos\pi\mu = \cos(\pi + \pi\mu)$. Here, the quantities $S(0, 0, 1)$ and $S(0, 0, \bar{1})$ correspond to the cases where the atomic magnetic moment is aligned with the $\mathbf{a}_3$ axis and in the opposite direction, respectively. Hence, it follows that the magnetic moments $\boldsymbol{\mu}_1$, $\boldsymbol{\mu}_2$, $\boldsymbol{\mu}_3$, and $\boldsymbol{\mu}_4$ induce a longitudinal spin wave. Note that the phase $\varphi = 0$ can be assigned to the moments $\boldsymbol{\mu}_1$ and $\boldsymbol{\mu}_3$ and the phase $\pi + \pi\mu$ can be attributed to the moments $\boldsymbol{\mu}_2$ and $\boldsymbol{\mu}_4$. This implies that the moments $\boldsymbol{\mu}_2$ and $\boldsymbol{\mu}_4$ are antiparallel to the moments $\boldsymbol{\mu}_1$ and $\boldsymbol{\mu}_3$ and have a smaller magnitude due to the factor $\mathrm{Re}\,\varepsilon = \cos\pi\mu$.

Similar results are obtained for the atoms located at the 6(g) positions; that is,

$$S\left(\begin{array}{c} k_{11}\tau_3' \\ \lambda \end{array}\middle| 1\right) = S\left(\begin{array}{c} k_{11}\tau_3' \\ \lambda \end{array}\middle| 2\right)$$

$$= S\left(\begin{array}{c} k_{11}\tau_3' \\ \lambda \end{array}\middle| 3\right) = S(0, 0, 1),$$

$$S\left(\begin{array}{c} k_{11}\tau_3' \\ \lambda \end{array}\middle| 4\right) = S\left(\begin{array}{c} k_{11}\tau_3' \\ \lambda \end{array}\middle| 5\right) = S\left(\begin{array}{c} k_{11}\tau_3' \\ \lambda \end{array}\middle| 6\right)$$

$$= S(0, 0, \bar{1})\cos\pi\mu = S(0, 0, 1)\cos(\pi + \pi\mu).$$

This model of the magnetic structure can be referred to as the antiferromagnetic longitudinal spin wave (AFLSW).

Moreover, in order to obtain the minimum discrepancy factor for the magnetic structure in calculations with the Fullprof program, an additional phase shift with respect to the magnetic moments of atoms at the 4(d) positions needs to be assigned to all the magnetic moments of atoms at the 6(g) positions. This phase shift was calculated to be $\Delta\varphi \approx (-0.508 \pm 0.022)\pi$. However, in our opinion, there are no physical grounds to consider that the phase shift differs from $-\pi/2$.

Knowing the wave vector $\mathbf{k}$, we can determine the period of the longitudinal spin wave; that is,

$$\lambda = 2\pi/|\mathbf{k}| \approx 3.413a_3.$$

Figure 3 illustrates the proposed model of the magnetic structure within four unit cells arranged in series along the $\mathbf{a}_3$ axis in an interval equal to the length of the longitudinal spin wave. The atoms located at the 4(d) positions within the set of unit cells placed along the $\mathbf{a}_3$ axis of the crystal form two equivalent chains with the coordinates ($x_1 = 1/3$, $y_1 = 2/3$) and ($x_2 = 2/3$, $y_2 = 1/3$) (one of these chains is shown in Fig. 3), in which the distance between the nearest neighbor atoms along the $\mathbf{a}_3$ axis is equal to $a_3/2$. The atoms located at the 6(g) positions form six equivalent chains with the coordinates (x, 0), (0, x), ($\bar{x}$, $\bar{x}$), ($\bar{x}$, 0), (0, $\bar{x}$), and (x, x), in which the distance between the nearest neighbor atoms is equal to a_3. The magnitude and direction of the magnetic moments of the atoms in the two types of positions do not depend on the coordinates (x, y) but depend on the coordinate z. For clarity, Fig. 3 shows the dependences of $\cos(\varphi_0 + \Delta\varphi)$ on the coordinate z for the cases $\varphi_0 = 0$, π, $-\pi/2$, and $\pi/2$ (where φ_0 is the initial phase and $\Delta\varphi = 2\pi\mu z$ is the phase resulting from the modulation of the magnetic structure). The arrow length corresponds to the quantity $\mu_{a3} = \mu_0\cos(\varphi_0 + \Delta\varphi)$. Here, the notation μ_{a3} indicates that the magnetic moment is oriented along the $\mathbf{a}_3$ axis and $\mu_0(4(d)) \approx (9.54 \pm 0.10)\mu_B$ and $\mu_0(6(g)) \approx (6.12 \pm 0.07)\mu_B$ are the maximum magni-

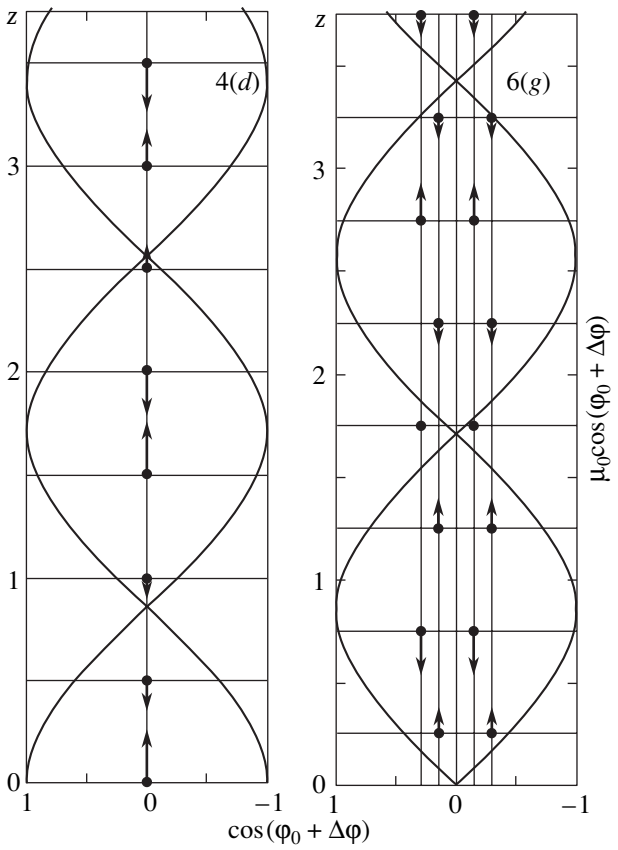

Fig. 3. Model of the magnetic structure of Er_5Ge_3 at 4.2 K (for more details, see text).

tudes of the magnetic moments of erbium atoms in the 4(*d*) and 6(*g*) positions, respectively. The portion of each cosine curve located to the left of the value $\cos(\varphi_0 + \Delta\varphi) = 0$ corresponds to the positive projection of the magnetic moment of the atom (situated at the given height) onto the *z* axis, whereas the other portion of this curve corresponds to the negative projection of the magnetic moment. These curves clearly illustrate the dependences of the magnitude and direction of the magnetic moments of each atom on its own position in the crystal lattice. The magnitudes of the magnetic moments and the error in their calculation were determined with the Fullprof program ($R_m \approx 9.55\%$).

It should be noted that the magnetic moment $\mu_0(4(d)) \approx (9.54 \pm 0.10)\mu_B$ coincides (within the accuracy of the measurement and calculation) with the commonly accepted value

$$\mu_J = g\sqrt{J(J+1)} \approx 9.58\mu_B.$$

Here,

$$g = 1 + \frac{J(J+1) + S(S+1) - L(L+1)}{2J(J+1)} = 1.2$$

is the Landé factor, $S = 3/2$ is the total spin quantum number, $L = 6$ is the total orbital quantum number, and $J = S + L = 15/2$ is the total angular momentum of the Er^{3+} cation (see, for example, [15]). Since $\lambda/a_3 \approx 3.413$ is a quantity of the order of unity, the longitudinal spin wave obtained should be considered a short-period wave.

An analysis of the temperature dependences of the intensity of the reflections $(111)^+$ at $2\Theta \approx 44.8°$ and $(211)^-$ at $2\Theta \approx 55.02°$ in the neutron diffraction pattern of Er_5Ge_3 in the temperature range from 4.2 to 80 K (see inset to Fig. 2) shows that, as the temperature increases, the magnetic contribution to the reflections decreases monotonically and becomes zero at $T \approx 38$ K. The latter circumstance can be associated with magnetic disordering in the Er_5Ge_3 compound at this temperature. The temperature $T \approx 38$ K can be treated as the Néel temperature of the intermetallic compound under investigation.

5. RESULTS AND DISCUSSION

Yakinthos *et al.* [3] noted that, in the temperature range $80 \le T \le 150$ K, the Tb_5Sb_3 compound has a magnetic structure of the conical-spiral type (the cone axes form an angle of 51.5° with the $\mathbf{a}_3$ axis, and the angular half-opening of the cone is 28.5°). Semitelou *et al.* [4] argued that, in the Tb_5Si_3 compound at 4.2 K, the terbium atoms occupying the 4(*d*) positions form a simple spiral, whereas the terbium atoms located at the 6(*g*) positions make up a conical spiral in which the cone axis is aligned parallel to the $\mathbf{a}_3$ axis and the angle between the magnetic moment and the $\mathbf{a}_3$ axis is equal to 76°.

However, the above models of the magnetic structures cannot be constructed from the basis functions of the irreducible representations derived in the present work. It is our opinion that these models are in contradiction with the results of the symmetry analysis. In this respect, they need revision and further refinement.

Our attempts to improve the model proposed in this work for the magnetic structure of Er_5Ge_3 (by adding the basis functions of other irreducible representations to those already used) were not successful. The AFLSW model is quite adequate and fairly simple. We believe that, at this stage, the AFLSW model has no need for refinement. Moreover, the results of earlier investigations of the crystal-field effects have demonstrated that the higher order components of the crystal field should be favorable for the orientation of the magnetic moments of erbium atoms along the $\mathbf{a}_3$ axis (see, for example, [16]). This fact also counts in support of the inferences drawn in the present study regarding the magnetic structure of Er_5Ge_3.

The results of neutron diffraction investigations of the magnetic structure of the Er_5Si_3 intermetallic compound at $T = 20$ K (at this temperature, we also revealed an antiferromagnetic longitudinal spin wave) will be presented in future papers.

ACKNOWLEDGMENTS

We would like to thank V.E. Naĭsh, S.B. Petrov, and Yu.N. Skryabin for their participation in discussions of the results and helpful remarks. We are also grateful to V.I. Bobrovskiĭ and V.A. Kazantsev for their assistance in preparing the manuscript.

This work was supported by the Ministry of Industry, Science, and Technology of the Russian Federation (State Contract no. 40.012.1.1.1150).

REFERENCES

1. P. Schobinger-Paramantellos, J. Magn. Magn. Mater. **28** (1–2), 97 (1982).
2. P. Schobinger-Paramantellos and K. H. J. Buschow, J. Magn. Magn. Mater. **49** (3), 349 (1985).
3. J. K. Yakinthos, I. P. Semitelou, and E. Roudaut, Solid State Commun. **59** (4), 227 (1986).
4. I. P. Semitelou, Hel. Konguetsof, J. K. Yakinthos, and E. Roudaut, J. Magn. Magn. Mater. **79** (1), 131 (1989).
5. I. P. Semitelou, Hel. Konguetsof, and J. K. Yakinthos, J. Magn. Magn. Mater. **82** (2–3), 223 (1989).
6. I. P. Semitelou, P. Kotsanidis, J. K. Yakinthos, and E. Roudaut, J. Magn. Magn. Mater. **116** (1–2), 103 (1992).
7. I. P. Semitelou, J. K. Yakinthos, and E. Roudaut, J. Magn. Magn. Mater. **128** (1–2), 79 (1993).
8. I. P. Semitelou, J. K. Yakinthos, and E. Roudaut, J. Phys. Chem. Solids **56** (7), 891 (1995).
9. I. P. Semitelou and J. K. Yakinthos, J. Magn. Magn. Mater. **186** (1–2), 107 (1998).
10. O. V. Kovalev, *Representations of the Crystallographic Space Groups: Irreducible Representations, Induced Representations, and Corepresentations* (Nauka, Moscow, 1986; Gordon and Breach, Yverdon, Switzerland, 1993).
11. Yu. A. Izyumov, V. E. Naĭsh, and R. P. Ozerov, *Neutron Diffraction of Magnetic Materials* (Atomizdat, Moscow, 1981; Consultants Bureau, New York, 1991).
12. *International Tables for X-ray Crystallography* (Kynoch Press, Birmingham, 1952), Vol. 1.
13. Yu. A. Izyumov and R. P. Ozerov, *Magnetic Neutron Diffraction* (Nauka, Moscow, 1966; Plenum, New York, 1979).
14. Yu. A. Izyumov, *Diffraction of Neutrons on Long-Period Structures* (Énergoatomizdat, Moscow, 1987).
15. S. V. Vonsovskiĭ, *Magnetism* (Nauka, Moscow, 1971; Wiley, New York, 1974), Vols. 1 and 2.
16. K. N. R. Taylor and M. I. Darby, *Physics of Rare Earth Solids* (Chapman and Hall, London, 1972; Mir, Moscow, 1974).

Translated by O. Borovik-Romanova

Physics of the Solid State, Vol. 45, No. 9, 2003, pp. 1742–1745. Translated from Fizika Tverdogo Tela, Vol. 45, No. 9, 2003, pp. 1660–1663.

MAGNETISM AND FERROELECTRICITY

Giant Nonlinear Absorption in the NiO Antiferromagnet

S. I. Shablaev and R. V. Pisarev

Ioffe Physicotechnical Institute, Russian Academy of Sciences, Politekhnicheskaya ul. 26, St. Petersburg, 194021 Russia

Received January 30, 2003

Abstract—A study of the spectrum of nonlinear two-photon and two-step absorption in NiO single crystals, carried out in the energy region $\hbar\omega_1 + \hbar\omega_2 = 2.45$–$4.575$ eV, showed it to have a complex shape and consist of very strong peaks (from 0.05 to 2.7 cm/MW). Within the energy interval 2.45–3.3 eV, the spectrum is due to *d*–*d* transitions in the Ni^{2+} ion. The band gap width was determined to be $E_g = 3.466$ eV. The spectral features seen above this energy originate from interband transitions from three valence subbands to the conduction band bottom. © *2003 MAIK "Nauka/Interperiodica".*

1. INTRODUCTION

The character of local and valence- and conduction-band states in compounds with 3*d* transition metals has for a long time been a subject of intense investigation [1]. These aspects grew in significance in connection with the discovery of high-temperature superconductivity in $Cu^{2+}(3d^9)$ compounds and of giant magnetoresistance in $Mn^{3+}(3d^4)$ materials. Experimental studies have been conducted using diverse linear optical methods (absorption, reflection, electroabsorption). The absorption spectrum of these compounds has been established to be due to local optical transitions in the 3*d* transition ions, which are superposed on the band-to-band absorption above 3 eV. Unambiguous separation of these kinds of absorption meets, however, with difficulties, because the absorption spectra cannot be measured in the interband transition region and reflection spectra are not capable of providing much information in the transparency region and near the fundamental absorption edge. In many cases, neither the exact magnitude of the band gap E_g nor the character of the edge optical transitions is currently known. A better understanding of this problem may be gained using nonlinear two-photon spectroscopy, an efficient tool for studying electronic structure [2]. This method studies the spectrum of additional absorption of probe light $\hbar\omega_1$ of intensity I_1 created in a crystal traversed by a high-power laser pulse $\hbar\omega_2$ of intensity I_2. Both pulses suffer only weak absorption in the crystal, because the probe light energy $\hbar\omega_1 < E_g$ and the pump energy $\hbar\omega_2 < (1/2)E_g$. Under these conditions, one can study nonlinear absorption at the fundamental absorption edge in the region from $2\hbar\omega_2$ to $E_g + \hbar\omega_2$, where one-photon spectroscopy can no longer be applied because of strong absorption and due to reflection still being weak. The more complex selection rules governing two-photon absorption (TPA) [3] are capable of providing, in many cases, new information on the electronic states of crystals as compared to spectra of linear absorption. Nonlinear absorption in compounds with 3*d* transition metals is specific in that, first, two-photon transitions connecting *d* states of the metal ion are allowed and, hence, are more intense (unlike those involved in one-photon absorption) and, second, nonlinear absorption may be accompanied by resonance absorption involving intermediate levels, where the photon energy of one or both light sources employed becomes equal to the energy difference between the local *d* transitions in the metal ions. Such resonance effects may enhance the total nonlinear absorption and make it possible to study the local transitions of interest in more detail. This may prove to be of considerable interest in conjunction with the current intense search for nonlinear optical materials with a high third-order nonlinear susceptibility $\chi^{(3)}$, which can be employed to advantage in devices intended for controlling light fluxes [4].

We chose NiO nickel oxide for the present study of nonlinear absorption. The electronic level diagram of the Ni^{2+} ion in an octahedral crystal field is shown in Fig. 1. This antiferromagnet has been well studied by linear optical methods and is of particular interest in nonlinear absorption in that its first optical transition $^3\Gamma_2^+ \longrightarrow {}^3\Gamma_5^+$ lying in the energy interval 0.97–1.3 eV falls in resonance with the pump energy of our laser $E_2 = 1.17$ eV.

The NiO nickel oxide crystallizes in a centrosymmetric cubic structure (point group $m3m$) of the NaCl type. Below the Néel temperature $T_N = 523$ K, NiO is an antiferromagnet, in which the Ni^{2+} spins are ferromagnetically ordered in the {111} planes and are oppositely directed in adjacent sheets [5, 6]. Spin ordering gives rise to a small distortion of the cubic cell along the ⟨111⟩ axes [7] (perpendicular to the ferromagnetic planes), which lowers the crystallographic symmetry to $3m$. The electronic structure of NiO has been studied both theoretically [8, 9] and experimentally [1, 10, 11].

Fundamental absorption follows an exponential course [12] in the region extending from about 3.1 eV to the first peak at ~4.3 eV [13]. Therefore, the exact position of E_g and the character of the edge transitions had not been established up to now.

2. EXPERIMENTAL TECHNIQUE

Nonlinear absorption spectra of the NiO crystal were obtained on two samples, one of which was a plane-parallel plate 70 μm thick and the other, a ~7-μm-thick film on an MgO substrate. The sample faces were {100} oriented.

A neodymium (Nd-YAG) laser pulse (I_2) 10 ns long with a photon energy $\hbar\omega_2 = 1.17$ eV and a probe light pulse I_1 (of a xenon flash lamp) 1.5 μs long with a photon of energy $1.29 < \hbar\omega_1 < 3.4$ eV crossed the sample simultaneously in opposite directions [14]. As the laser pulse crossed the crystal, a modulation signal in the form of a dip appeared in the probe pulse. The probe light pulse I_1 passed through a monochromator to fall on the PM tube cathode. The laser pulse amplitude I_2 was monitored with a coaxial photocell. The signals from the PM tube and the photocell were fed through delay lines to the inputs of a three-channel gated detector, which measured the pulse amplitude of the laser, I_2, and of the lamp, I_1, during the 4.5-ns time gate in each cycle (cycle frequency 12.5 Hz). The probe pulse amplitude I_1 was measured twice: directly before the dip, the value of I_1 was measured, and at the dip, the value of $I_1 - \Delta I$ was measured. After this, the signals thus obtained were expanded to 7 ms and sent to the computer unit, where the ΔI signal was isolated and the TPA coefficient β was calculated from the relation $\beta = \Delta I/(I_1 I_2 d)$, where d is the length of the beam interaction region in the crystal. The values of β thus obtained were averaged over 10^4 pulses.

3. EXPERIMENTAL RESULTS

Figure 2 displays a spectrum of NiO nonlinear absorption. In the energy interval from 2.46 to 3.7 eV, the spectrum was measured on an NiO plate 70 μm thick, and in the interval from 3.6 to 4.575 eV, on a film ~7 μm thick.

A TPA spectrum can be conventionally divided into two parts. In the first part of the spectrum, in the 2.46- to 2.9-eV interval, one clearly sees two peaks of complex shape, which originate from transitions from the ground state $^3\Gamma_2^+$ through an intermediate state $^3\Gamma_5^+$ to the final states $^1\Gamma_5$ and $^3\Gamma_4$. The next interval, extending from 2.9 to 3.465 eV, exhibits insignificant nonlinear absorption (about ~0.02 cm/MW) and contains a small peak C connected with the excitation of two $^3\Gamma_2^+ \longrightarrow {}^3\Gamma_5^+$ transitions (excitation energy of about 1 eV) by a probe light pulse of energy ~2 eV. The second part of the spectrum starts after 3.465 eV and terminates at 4.575 eV. This region exhibits three very strong maxima (X_1, X_2, X_3) peaking at 3.768, 4.075, and 4.33 eV, respectively. Figure 1 shows the electronic level dia-

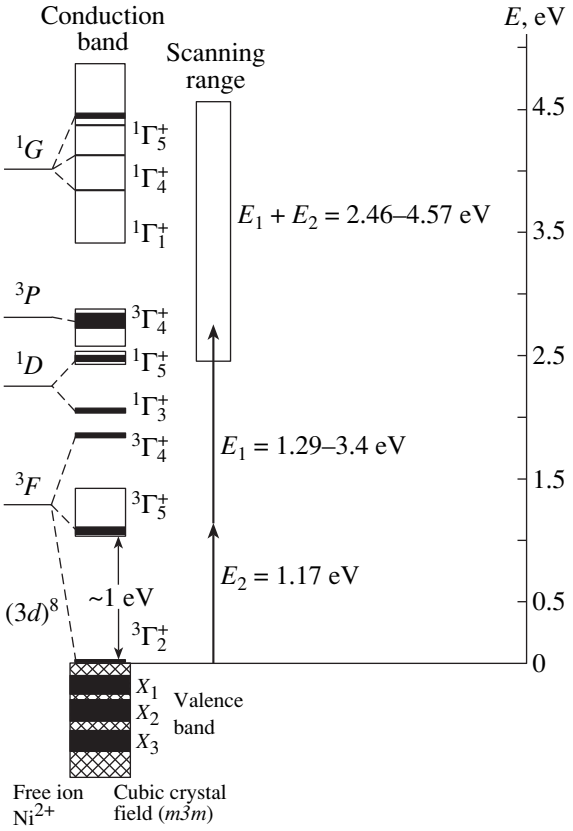

Fig. 1. Electronic level diagram of $(3d)^8$ states and NiO edge bands.

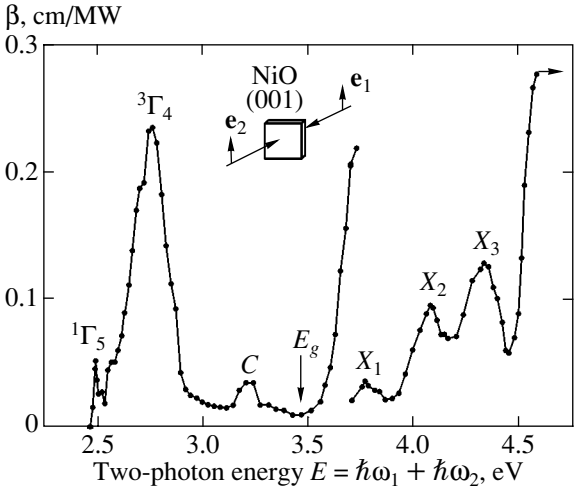

Fig. 2. Nonlinear absorption spectrum of NiO single crystals.

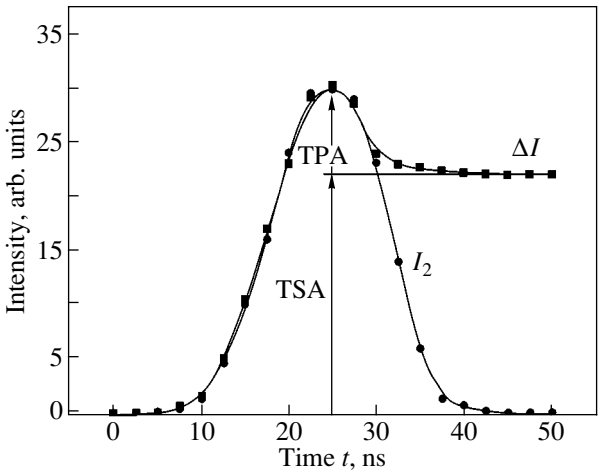

Fig. 3. Profile of the laser (I_2) and modulation (ΔI) light pulses. TPA stands for two-photon absorption, and TSA, for two-step absorption.

gram of the $(3d)^8$ Ni^{2+} ion and of the edge bands (the valence and conduction bands); the diagram specifies the observed transitions and the photon energies of the pump laser E_2 and the probe light pulse E_1.

Study of the ΔI signal showed it to differ strongly in shape from the laser pump pulse I_2 (Fig. 3). The width of the laser light pulse I_2 at half maximum is 10 ns. The leading and trailing pulse edges are about 5 ns long. The leading edge of the modulation signal ΔI is equal to that of the laser pulse, while the trailing edge is so long that it could not be measured in our experiment, because it was in excess not only of the probe light pulse I_1 itself (1.5 μs) but of the laser pulse off-duty time (80 ms) as well. One can tentatively set the trailing edge ΔI to be greater than 160 ms in length long, i.e., practically 10^6 times the laser pulse length. This unusually long trailing edge of the modulation pulse is a result of the nonlinear absorption in NiO being not purely a two-photon but largely a two-step absorption process. As seen from Fig. 1, the first optical transition in NiO is the ${}^3\Gamma_2^+ \longrightarrow {}^3\Gamma_5^+$ transition in the Ni^{2+} ion and lies in the interval 0.97–1.3 eV. The laser pump pulse I_2 with a photon energy of 1.17 eV falls on the trailing edge of this transition. Electrons absorb the laser photon energy to transfer from the ${}^3\Gamma_2^+$ ground state to the excited ${}^3\Gamma_5^+$ level. The electron lifetime in this level is inversely proportional to the level width and can be on the order of a few femtoseconds. Hence, in order to account for the long trailing edge of the modulation signal observed by us, one has to assume that electrons transfer from the ${}^3\Gamma_5^+$ level to some trapping level of an impurity or crystal defect which has an extremely long lifetime. This lifetime of the excited electrons is determined by the length of the trailing edge of the modulation pulse ΔI, which, as already mentioned, is about 160 ms long. These excited electrons can subsequently transfer to higher lying levels by absorbing probe light photons I_1.

The long electron lifetime in the intermediate trapping level results, of course, in an enhanced probability of two-step transitions, but it also results in an increase in the probability of resonance two-photon transitions because of the decrease in the energy denominator $E_m - E_i - \hbar\omega_2$ in the expression for the TPA coefficient

$$\beta = A\sum_{f,i}\left|\sum_m\left[\frac{\langle f|\mathbf{e}_2 p|m\rangle\langle m|\mathbf{e}_1 p|i\rangle}{E_m - E_i - \hbar\omega_1} + \frac{\langle f|\mathbf{e}_1 p|m\rangle\langle m|\mathbf{e}_2 p|i\rangle}{E_m - E_i - \hbar\omega_2}\right]\right|^2,$$

where $\sum_{f,i}$ is the sum over all initial (i) and final (f) states and $\sum_m$ is the sum over all intermediate states, both initial and final.

This apparently can account for the unusually large nonlinear absorption coefficients observed experimentally. The values of β here are three times larger, at the equivalent spectral points, than those in the chromium oxide Cr_2O_3 [15] (which also exhibits resonance TPA, but with only the probe light pulse I_1 falling in resonance) and two orders of magnitude larger than those observed in such model semiconductors as ZnSe and CdS, whose spectra were measured for the purpose of comparison under the same conditions.

As seen from Fig. 2, the spectrum consists of several peaks (${}^1\Gamma_5^3$, ${}^3\Gamma_4$, C, X_1, X_2, X_3) of complex shape that differ in intensity. The first two of them are obviously due to absorption in the Ni^{2+} d shell in the transitions ${}^3\Gamma_2^+ \longrightarrow {}^3\Gamma_5^+ \longrightarrow {}^1\Gamma_5^+ \longrightarrow {}^3\Gamma_4^+$. As for X_1, X_2, and X_3, they are, in our opinion, interband transitions between the three subbands of the valence band and the bottom of the conduction band. The edge of interband NiO intrinsic absorption is known to behave exponentially above 3.1 eV [12]. Near 4 eV, the one-photon absorption coefficient α reaches a value $\sim 0.5 \times 10^5$ cm^{-1}, and after this, a peak at 4.3 eV is observed [13]. This peak can apparently be identified with the two-photon X_3 feature (4.325 eV). The X_1 and X_2 peaks at 3.768 and 4.075 eV are not seen in reflection, because they fall into the region of the exponential edge.

The fundamental absorption edge in NiO should be identified with the energy of the beginning of the high-temperature region in the TPA spectrum, which is E_g = 3.465 eV at 290 K.

ACKNOWLEDGMENTS

This study was supported by the Russian Foundation for Basic Research.

REFERENCES

1. B. Fromme, in *d–d Excitations in Transition-Metal Oxides* (Springer, Berlin, 2001), p. 145.
2. H. Mahr, in *Quantum Electronics*, Ed. by H. Rabin and C. L. Tang (Academic, New York, 1975), Vol. 1, p. 285.
3. T. R. Bader and A. Gold, Phys. Rev. **171**, 997 (1968).
4. H. Kishida, H. Matsuzaki, H. Okamoto, *et al.*, Nature **405**, 929 (2000).
5. M. T. Hutching and E. D. Samuelsen, Phys. Rev. B **6**, 3447 (1972).
6. F. U. Hillebrecht, H. Ohldag, N. B. Weber, *et al.*, Phys. Rev. Lett. **86**, 3419 (2001).
7. K. Nakahigashi, N. Fukuoka, and Y. Shimomura, J. Phys. Soc. Jpn. **38**, 1634 (1975).
8. M. Takahashi and J. Igarashi, Phys. Rev. B **54**, 13566 (1996).
9. T. Bredov and A. R. Gerson, Phys. Rev. B **61**, 5194 (2000).
10. Landolt–Börnstein, *Numerical Data and Functional Relationships*, New Ser., Group III (Springer, Berlin, 1984), Vol. 17g, Comprehensive Index.
11. S. Hüfner, in *Photoelectron Spectroscopy*, Ed. by M. Cordona (Springer, Berlin, 1996).
12. J. Pattanayak and K. D. Becker, Phys. Status Solidi B **188**, 833 (1995).
13. R. T. Powell and W. E. Spiser, Phys. Rev. B **2**, 2185 (1970).
14. S. I. Shablaev, A. M. Danishevskiĭ, V. K. Subashiev, and A. A. Babashkin, Fiz. Tverd. Tela (Leningrad) **21**, 1140 (1979) [Sov. Phys. Solid State **21**, 662 (1979)].
15. S. I. Shablaev, I. P. Areshev, and R. V. Pisarev, Fiz. Tverd. Tela (St. Petersburg) **42**, 1821 (2000) [Phys. Solid State **42**, 1868 (2000)].

Translated by G. Skrebtsov

Physics of the Solid State, Vol. 45, No. 9, 2003, pp. 1746–1749. Translated from Fizika Tverdogo Tela, Vol. 45, No. 9, 2003, pp. 1664–1666.

MAGNETISM AND FERROELECTRICITY

Numerical Simulation of the Fine Structure of Domain Walls in Rare-Earth Orthoferrites

E. G. Ekomasov and M. A. Shabalin

Bashkortostan State University, ul. Frunze 32, Ufa, Bashkortostan, 450074 Russia

Received November 15, 2002; in final form, January 31, 2003

Abstract—The structure of a solitary domain wall (DW) with a Bloch line in rare-earth orthoferrites is determined using numerical methods for the values of the material parameters lying beyond the range in which the can be found analytically solution. The law of rotation of the DW magnetization vector, the effective DW width, and the energy per unit length of the Bloch line are determined. It is shown that a more accurate treatment of the two-dimensional DW using numerical methods makes it possible to reveal essential distinctions in the fine structure of the DW in comparison to the approximate analytical solutions. *© 2003 MAIK "Nauka/Interperiodica".*

Rare-earth orthoferrites (REOs) with the chemical formula $R\mathrm{FeO}_3$ (R is a rare-earth element) are canted antiferromagnets with weak ferromagnetism. Uniform domain walls (DWs) in REOs have been thoroughly studied to date (see, e.g., [1–8]). On the other hand, in contrast to garnet ferrites, no reliable methods have been found for the nucleation, observation, and investigation of the fine structure of a DW in REOs. This is possibly connected with a large in-plane anisotropy in REOs, which hinders the ferromagnetism **m** and antiferromagnetism **l** vectors deflecting out of the plane of their rotation in the DW. It was theoretically predicted in [9] that the fine structure most likely arises inside a DW or near the sample surface in the vicinity of phase transition, where one can expect a change in the ratio of anisotropy constants. Recently, several experimental results have been obtained that can be interpreted as the observation of dynamic lines on the Néel DW moving in an REO at supersonic velocity [10–14]. However, those experiments do not give clear evidence of what type of fine structure actually exists in the DW.

It is well-known [3] that, in order to describe the fine structure of the DW in REOs theoretically one needs to solve a system of coupled nonlinear differential second-order equations (which reduce to the sine-Gordon equation in a limiting case). No analytical methods have been proposed for solving these equations in the general case. For the case of $Q = |(K_{ab} - K_{cb})/K_{cb}| \gg 1$ (K_{ab}, K_{cb} are the effective anisotropy constants in the ab, cb planes, respectively), by using approximate analytical methods, it was found that the DW consists of alternating sequence of segments with and without rotation of m in this case and that the characteristics of such a DW should essentially differ from the characteristics of the DW with Bloch lines in ferromagnets [15–17]. On the other hand, there are also a large number of publications where the two-dimensional structure of the DW in magnets is studied by numerical methods. For example, considerable advances have been made in studies of thin magnetic films (see review [18]). This communication is devoted to studying the structure of a static DW with a Bloch line by numerical methods for REOs with positive values of the parameter Q.

We consider an infinite REO plate in the high-temperature magnetic phase G_xF_z in the context of a two-sublattice model described by two sublattice magnetization vectors $\mathbf{M}_1$ and $\mathbf{M}_2$ that are equal in magnitude ($|\mathbf{M}_1| = |\mathbf{M}_2| = M_0$). The vectors **m** and **l** can be represented as $\mathbf{m} = (\mathbf{M}_1 + \mathbf{M}_2)/2M_0$ and $\mathbf{l} = (\mathbf{M}_1 - \mathbf{M}_2)/2M_0$. These two vectors are assumed to satisfy the relations $m^2 + l^2 = 1$ and $(\mathbf{ml}) = 0$. The x, y, and z axes of the Cartesian coordinate system are oriented along the crystallographic axes a, b, and c, respectively. The energy density of the magnetic subsystem of an REO can be represented as [3]

$$\omega = \frac{a}{2}\mathbf{m}^2 + \frac{a_1}{2}l_x^2 + \frac{a_3}{2}l_z^2 + d_1 m_x l_z - d_3 m_z l_x + \frac{A}{2}\left(\frac{\partial \mathbf{l}}{\partial x_\delta}\right)^2, \quad (1)$$

where a and A are the uniform- and nonuniform-exchange constants, respectively; d_i is the Dzyaloshinskiĭ interaction constant; a_i are the anisotropy constants; and $\{x_\delta\} = x, y, z$. If $|\mathbf{m}|^2 \ll |\mathbf{l}|^2 \approx 1$, the vector **m** can be expressed in terms of **l** as [4]

$$\mathbf{m} = \frac{1}{a}[\mathbf{ld}], \quad (2)$$

where $\mathbf{d} = d\mathbf{e}_y$ and $d_1 = d_3 = d$. In angular variables, we have $\mathbf{l} = l(\cos\theta, \sin\theta\sin\varphi, \sin\theta\cos\varphi)$ and the equa-

tions describing the steady-state DW structure have the form [9]

$$A\Delta\theta - (K_{ab} - K_{cb}\cos^2\varphi + A(\nabla\varphi)^2)\sin\theta\cos\theta = 0, \quad (3)$$

$$\begin{aligned} A\sin^2\theta\Delta\varphi - K_{cb}\sin^2\theta\sin\varphi\cos\varphi \\ + 2A\sin\theta\cos\theta\nabla\theta\nabla\varphi = 0, \end{aligned} \quad (4)$$

where $K_{ab} = \frac{d^2}{a} - a_1$ and $K_{cb} = \frac{d^2}{a} - a_3$.

By using numerical methods, we find two-dimensional solutions of the set of equations (3) and (4) for the Néel DW with rotating **m** (such DWs were studied experimentally in [10–14]). The DW plane is parallel to the *yz* plane, and the vectors **m** and **l** in the adjacent domains are directed along the *z* and *x* axes, respectively. A well-known approximate analytical solution of the set of equations (3) and (4) has the form [9]

$$\theta_0(x) = \arctan(\exp(x/\delta)), \quad (5)$$

$$\varphi_0(y) = \arctan(\exp(y/Q^{1/2}\delta_0)), \quad (6)$$

where $\delta = \delta_0(1 + 2Q^{-1}\sin^2\varphi_0)^{-1/2}$ is the DW width, $\delta_0 = \sqrt{A/(K_{ab} - K_{cb})}$,

$$\theta_0(\pm\infty) = 0, \pi; \quad \varphi_0(\pm\infty) = 0, \pi. \quad (7)$$

Equation (5) describes the basic domain structure, and Eq. (6) describes the fine DW structure with a 180° vertical Bloch line.

Now, we assume that $\theta = \theta(x, y)$ and $\varphi = \varphi(x, y)$. Our algorithm for numerical integration of Eqs. (3) and (4) works in the following way. In the first stage, Eqs. (5) and (6) are taken as a zeroth approximation. The first approximation $\theta_1(x, y)$ is found from Eq. (3) and substituted into Eq. (4) to find $\varphi_1(x, y)$. At the next stage, the procedure is repeated with the use of $\theta_1(x, y)$ and $\varphi_1(x, y)$ as the initial functions. The calculations proceeded until the following conditions were satisfied: $|\theta_n - \theta_{n-1}| < \varepsilon$ and $|\varphi_n - \varphi_{n-1}| < \varepsilon$, where $\varepsilon = 0.0001$ rad. To solve the initial equations numerically, the relaxation method, similar to that used in [19], was applied. Numerical calculations were performed using a net consisting of 100×100 cells. We note that a solution obtained with this algorithm corresponds to the minimum of the Bloch line energy per unit length along the axis *z*

$$\begin{aligned} W_L = \frac{1}{2}\iint_S [(\nabla\theta)^2 + \sin^2\theta(\nabla\varphi)^2 \\ + \sin^2\theta(1 + Q^{-1}\sin^2\varphi)]dxdy - W_0\lambda, \end{aligned} \quad (8)$$

where W_0 is the energy of the uniform DW; *S* is the integration area, usually chosen in the form of a square with dimensions $10\delta_0 \times 10\delta_0$; and λ is the length of the range of integration along the *y* axis.

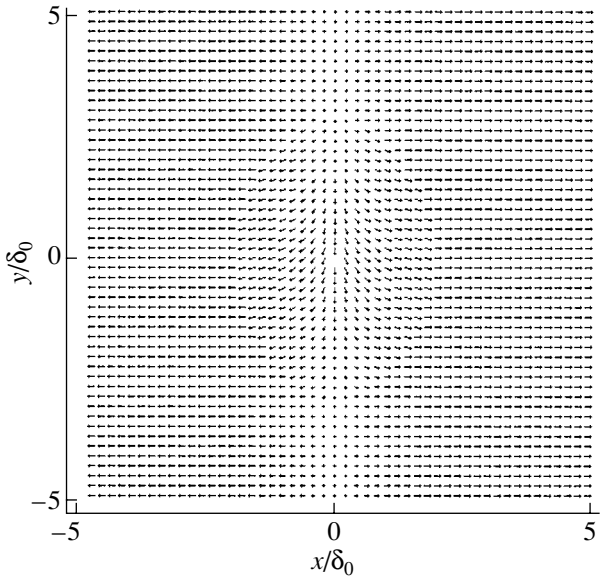

Fig. 1. Distribution of the antiferromagnetism vector in a 180° Néel DW with rotating **m** and with a vertical Bloch line at point (0, 0) for $Q = 1$.

Numerical calculations yielded the sought-for $\theta(x, y)$ and $\varphi(x, y)$ dependences, which were used to determine the "classical" DW parameters (the law of magnetization rotation, the DW width, the Bloch line width, the energy of the obtained structure, etc.) determining the type of DW structure with a Bloch line for various values of *Q*. Figure 1 shows the calculated distribution of the antiferromagnetism vector in the 180° Néel DW with rotating **m** and with a vertical Bloch line localized at point (0, 0) for the case $Q = 1$. Schematically, the rotation of **l** in such a DW can be described in the following way. The vector **l** turns out of the *ac* plane (in which this vector rotates in uniform DW), with its maximum deflection being in the DW center; this deflection φ also increases with approaching the center of the Bloch line, where DW with the rotating **m** transforms into a DW without rotation of **m**. The dependence of the maximum angle φ_{max} of deflection of the vector **l** out of the *ac* plane on the coordinate *y* for several values of *Q* is shown in Fig. 2.

The dependence of the effective DW width (which is defined according to Lilley) on the coordinate *y* along the DW is shown in Fig. 3 for various values of *Q*. It is seen that this dependence is strongly affected by *Q* and essentially differs from the analytical expression $\delta = \delta_0[1 + Q^{-1}\sin^2\varphi_0(y)]^{-1/2}$ for low values of *Q*. It should also be noted that a decrease in *Q* appreciably diminishes the region of the DW where it differs from a uniform DW, which is in accordance with the dependence of the effective width Λ of the Bloch line in the center of the DW on the parameter *Q* (Fig. 4). The analytical solution gives $\Lambda/\delta_0 = Q^{1/2}$, whereas, in our case, this dependence is virtually linear beginning from $Q = 2$.

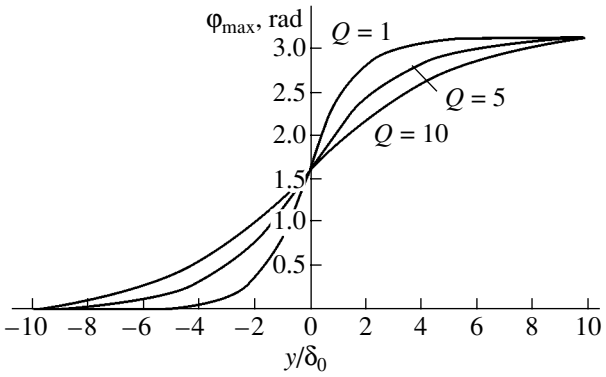

Fig. 2. Maximum angle φ_{max} of deflection of the antiferromagnetism vector out of the *ac* plane as a function of the coordinate *y*.

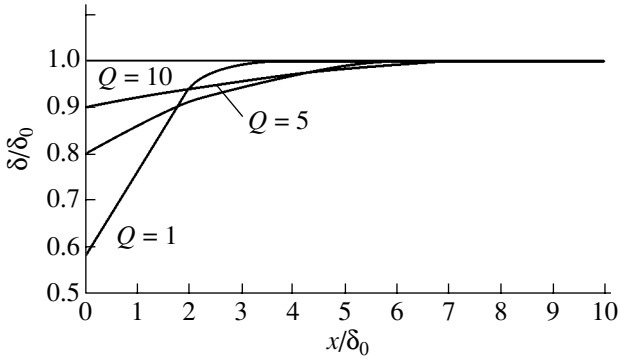

Fig. 3. Dependence of effective DW width Λ on the coordinate *y* along the DW.

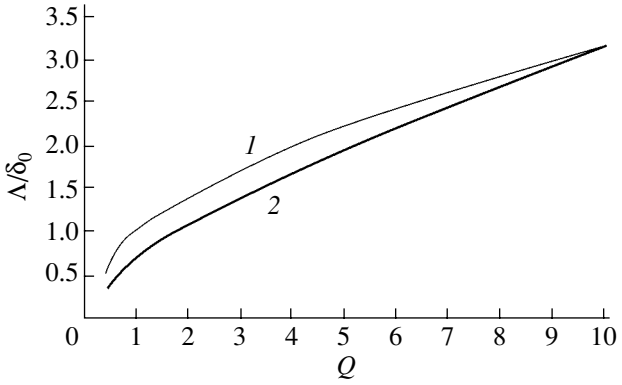

Fig. 4. Dependence of the effective width Λ of the Bloch line in the DW center on the parameter *Q*: (*1*) analytical solution and (*2*) numerical solution.

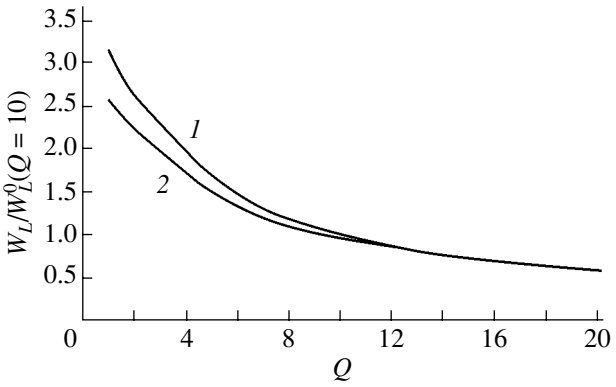

Fig. 5. Energy W_L per unit length of the Bloch line, normalized to its analytically calculated value W_L^0, as a function of parameter *Q*: (*1*) analytical solution and (*2*) numerical solution.

The energy W_L (per unit length of the Bloch line), normalized to its analytical value $W_L^0 = 4AQ^{-1/2}$ at $Q = 10$, is shown in Fig. 5 as a function of *Q*. For $Q \geq 10$, the numerically calculated energy is virtually coincident with the result obtained analytically, while at $Q = 1$, the energy is 19% lower.

An analysis shows that the result of numerical calculations for $Q \geq 10$ ($Q \gg 1$ is the range of applicability of analytical methods) coincides with the analytical solution with a high precision, but the distinctions between them essentially increase with decreasing *Q*. It should also be noted that the calculated $\theta(x, y)$ and $\varphi(x, y)$ dependences are essentially two-dimensional in the region of localization of the Bloch line. The two-dimensional character of the DW becomes progressively more pronounced with decreasing *Q*, so that the structure of the DW with the Bloch line becomes substantially different from the analytical solution given by Eqs. (5) and (6). This fact may be the reason why no success has been made so far in adequate description of the results of several experiments (e.g., the dependence of the velocity of the Bloch line on the DW velocity [14]) performed at room temperature, where the values of *Q* in $YFeO_3$ can be even less than unity [20]. It therefore becomes clear that, in order to adequately describe the Bloch line dynamics in REOs, one needs to more correctly take into account the two-dimensional variations of the angles θ and φ.

REFERENCES

1. K. P. Belov, A. K. Zvezdin, A. M. Kadomtseva, and R. Z. Levitin, *Orientational Transitions in Rare-Earth Magnets* (Nauka, Moscow, 1980).
2. A. F. Andreev and V. I. Marchenko, Usp. Fiz. Nauk **130** (1), 39 (1980) [Sov. Phys. Usp. **23**, 21 (1980)].
3. M. M. Farztdinov, *Physics of Magnetic Domains in Antiferromagnets and Ferrites* (Nauka, Moscow, 1981).
4. V. G. Barjaktar, M. V. Chetkin, B. A. Ivanov, and S. N. Gadetskiy, *Dynamics of Topological Magnetic*

Solitons. Experiment and Theory (Springer, Berlin, 1994), Tracts in Modern Physics, Vol. 129.

5. A. K. Zvezdin and A. A. Mukhin, Zh. Éksp. Teor. Fiz. **102** (2), 577 (1992) [Sov. Phys. JETP **75**, 306 (1992)].
6. N. Papanicolaou, Phys. Rev. B **55** (18), 12290 (1997).
7. M. A. Shamsutdinov and S. A. Niyazgulov, Fiz. Met. Metalloved. **85** (6), 23 (1998).
8. V. S. Gerusimchuk and A. L. Sukstanskij, Phys. Rev. B **59** (10), 6966 (1999).
9. M. M. Farztdinov, M. A. Shamsutdinov, and A. A. Khalfina, Fiz. Tverd. Tela (Leningrad) **21**, 1522 (1979) [Sov. Phys. Solid State **21**, 878 (1979)].
10. M. V. Chetkin, Yu. N. Kurbatova, and A. I. Akhutkina, J. Appl. Phys. **79** (8), 6132 (1996).
11. M. V. Chetkin, Yu. N. Kurbatova, A. I. Akhutkina, and T. B. Shapaeva, Zh. Éksp. Teor. Fiz. **115**, 2160 (1999) [JETP **88**, 1179 (1999)].
12. M. V. Chetkin and Yu. N. Kurbatova, Phys. Lett. A **260** (108), 127 (1999).
13. M. V. Chetkin and Yu. N. Kurbatova, Fiz. Tverd. Tela (St. Petersburg) **43**, 1503 (2001) [Phys. Solid State **43**, 1563 (2001)].
14. M. V. Chetkin, Yu. N. Kurbatova, and T. B. Shapaeva, Pis'ma Zh. Éksp. Teor. Fiz. **73** (6), 334 (2001) [JETP Lett. **73**, 294 (2001)].
15. Yu. V. Melikhov and O. A. Perekhod, Usp. Fiz. Nauk **28** (5), 713 (1983).
16. M. M. Farztdinov, M. A. Shamsutdinov, and E. G. Ekomasov, Fiz. Tverd. Tela (Leningrad) **30** (6), 1866 (1988) [Sov. Phys. Solid State **30**, 1076 (1988)].
17. E. G. Ekomasov and M. A. Shabalin, Fiz. Tverd. Tela (St. Petersburg) **43** (7), 1211 (2001) [Phys. Solid State **43**, 1257 (2001)].
18. B. N. Filippov, Fiz. Nizk. Temp. **28** (10), 991 (2002) [Low Temp. Phys. **28**, 707 (2002)].
19. A. B. Borisov, A. P. Tankeev, and A. G. Shagalov, Fiz. Tverd. Tela (Leningrad) **31** (5), 140 (1989) [Sov. Phys. Solid State **31**, 798 (1989)].
20. A. É. Egoyan and A. A. Mukhin, Kratk. Soobshch. Fiz. **9–10**, 55 (1993).

Translated by A. Zalesskiĭ

Physics of the Solid State, Vol. 45, No. 9, 2003, pp. 1750–1753. Translated from Fizika Tverdogo Tela, Vol. 45, No. 9, 2003, pp. 1667–1670.

MAGNETISM AND FERROELECTRICITY

Magnetic Properties of Nickel Clusters in Nanoporous Carbon

V. M. Fedosyuk*, A. M. Danishevskiĭ, D. A. Kurdyukov**, V. B. Shuman**, and S. K. Gordeev*****

**Institute of Solid-State and Semiconductor Physics, Academy of Sciences of Belarus, ul. P. Brovki 17, Minsk, 220018 Belarus*
e-mail: Fedosyuk@ifttp.bas-net.by
***Ioffe Physicotechnical Institute, Russian Academy of Sciences, Politekhnicheskaya ul. 26, St. Petersburg, 194021 Russia*
****Central Research Institute of Materials, ul. Paradnaya 8, St. Petersburg, 191014 Russia*

Received February 4, 2003

Abstract—The magnetic properties of nanoporous carbon samples whose pores were loaded by nickel are described. It is shown that a sample becomes superparamagnetic for temperatures $T < T_C$(Ni) only in the case where a noticeable fraction of Ni is contained in the nanopores. The nanopore size estimated from magnetic measurements coincides with the estimates derived earlier from small-angle x-ray scattering studies. © *2003 MAIK "Nauka/Interperiodica".*

1. INTRODUCTION

Activated or porous carbon materials enjoy numerous applications, including for adsorbents, electrodes of electrolytic supercapacitors and rechargeable lithium batteries, hydrogen and lithium containers [1], various low-friction coatings [2], and so on. The actual area of application of such materials is determined by their structure. The structure depends, in turn, on the starting material and the method used to prepare the nanoporous carbon (NPC). One method consists in obtaining a carbon material from carbide compounds by removing the carbide-forming non-carbon atoms chemically [3, 4]. This procedure leaves a nanoporous carbon system with a high (about 50% and more) porosity level. The nanopore size may vary depending on the type of the starting carbide within the interval ~1–2.5 nm, with their distribution being highly uniform. These materials can be prepared both in the form of powders and in mechanically strong bulk pieces [5, 6], whose structural properties practically do not change up to fairly high temperatures. Their thermal and chemical stability suggest the attractive idea of loading various chemical elements in the form of clusters into the nanopores and studying their properties. The characteristics of nanocomposites fabricated in this way may be affected, on the one hand, by size constraints within the cluster and, on the other, by collective interactions of the elements incorporated into the carbon matrix. The latter factor should manifest itself most vividly in the case of magnetic metals.

The present paper reports on a study of the magnetic properties of NPC-based nanocomposites with nanopores loaded by nickel. It was assumed that if we could succeed in incorporating nickel in NPC in the form of nanoclusters a few nanometers in size, they would exhibit superparamagnetic properties similar to granular alloys [7, 8]. Moreover, such structures could demonstrate isotropic giant magnetoresistance as well [9, 10].

2. EXPERIMENTAL TECHNIQUES

We studied NPC samples obtained from polycrystalline powders of molybdenum carbide (Mo_2C). Two methods were employed to prepare the NPC. In the first of them, which was used to fabricate bulk samples, Mo_2C powders were pressed into pellets that were subsequently annealed at a high temperature in a methane environment. In the macropores of the samples, decomposition of methane produced inclusions of pyrocarbon, which acted as a binder. The samples thus prepared were exposed to an atmosphere of chlorine at 600°C. The molybdenum carbide reacted chemically with chlorine to produce gaseous molybdenum chlorides, which were removed from the samples both in the course of the reaction and when placed in an argon flow. In the end, we obtained bulk carbon samples with a high total porosity, up to ~76%, and a nanoporosity of up to ~48%. Their pyrocarbon fraction did not exceed 8 vol %. The bulk nanoporous carbon materials thus prepared were circular plates measuring 20 mm in diameter and about 1 mm in thickness. From them, we cut samples of a desired shape and size to conduct specific studies.

The molybdenum carbide powders were used to prepare not only bulk but also powdered NPC samples. In this case, the nanoporosity was 71% and the macroporosity was about 5%.

In order to load foreign chemical elements into the nanopores, one has to overcome surface tension forces. Nickel was introduced in two ways. In the first of them, the pores in bulk samples were filled by a nickel nitrate solution in ethanol at its boiling temperature. Next, the samples were annealed at 250°C; during this procedure, the nickel salt decomposed in the pores to produce nickel oxide. After this, the samples were annealed in a hydrogen flow at a temperature 500°C for a long time

to reduce the oxide in the pores to metallic nickel. The other method, intended for loading nickel into NPC samples, made use of $NiCl_2$, which is a salt with a not too high sublimation temperature. Because this salt is practically always hydrated ($NiCl_2 \cdot 6H_2O$), it was preliminarily annealed at a temperature of 230°C in vacuum under continuous pumping for 7–10 h. Next, the ampoule with the salt and NPC samples was sealed and the contents were calcined at a temperature about 1000°C for 20 h. $NiCl_2$ was loaded into the NPC pores using the two-zone method with a temperature gradient. The temperature of the NPC samples was 60–100°C higher in order to avoid deposition of $NiCl_2$ on the surface and in macropores as much as possible. The $NiCl_2$ vapor pressure in the ampoule reached 1 atm. The samples were subsequently rinsed in ethanol to remove the precipitate from the surface and annealed in hydrogen to reduce the nickel salt to metal.

The magnetic properties of the carbon nanocomposites with nickel clusters were studied with a SQUID magnetometer, calibrated in magnetic-moment units, at temperatures ranging from 5 to 300 K and in fields of up to 55 kOe. The field was adjusted to within ~10 G, and the temperatures, to within $\pm 10^{-2}$ K. The conventional hysteresis loop studies were complemented by magnetic-moment measurements after sample cooling in zero (ZFC) and low (FC) magnetic fields [11, 12]. These measurements provide the possibility of estimating the size and distribution pattern of magnetic clusters in a nonmagnetic host [13].

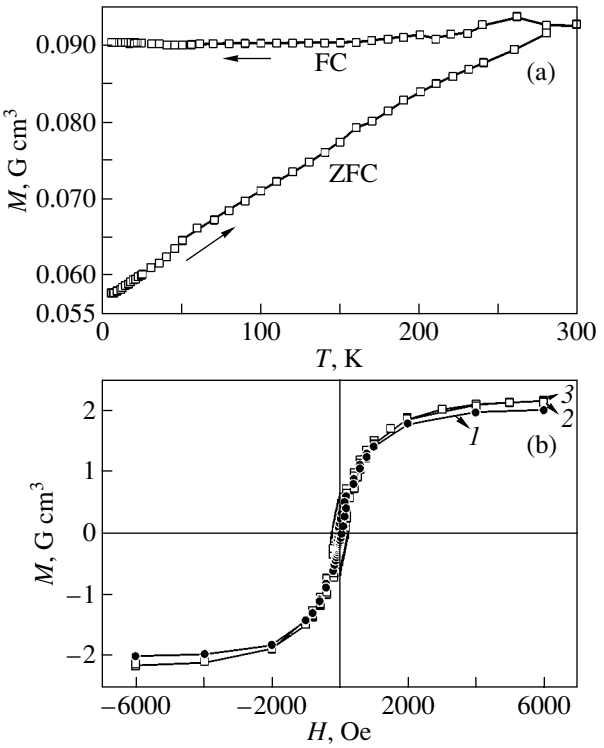

Fig. 1. Magnetic properties of an NPC–Ni sample (prepared by loading NPC with a nickel nitrate solution in ethanol followed by reduction to metallic nickel in a hydrogen flow). (a) Temperature behavior of the magnetic moment of the bulk NPC–Ni nanocomposite cooled in zero (ZFC) or weak (50 Oe) (FC) fields. (b) Remagnetization curves for the bulk NPC–Ni nanocomposite measured at temperatures of (*1*) 50, (*2*) 150, and (*3*) 300 K.

3. RESULTS AND DISCUSSION

In bulk NPC samples, a certain amount of macropores, i.e., voids between powder grains, remained. We could not fill them completely with pyrocarbon, because the reaction gases must be allowed to evolve freely. Loading bulk nanoporous carbon materials with magnetic metals could result in the formation, in these macropores 1–3 μm in size (depending on the actual powder grain dimensions), of sufficiently massive metallic crystallites with magnetic properties of conventional bulk nickel. Their presence substantially complicates investigation of the magnetic properties of small nickel nanoclusters. For this reason, we also used nanoporous carbon powders for Ni loading.

Each stage of the technological procedures described above included accurate weighing of the samples, which permitted us to estimate the final weight of the nickel introduced into the pores and, knowing the porosity and density of the starting samples, to quantify the relative volume of the NPC filled by nickel.

Figure 1 presents temperature dependences of the magnetic moment of a bulk NPC sample (Fig. 1a) with its pores loaded by nickel (from a nickel nitrate solution in ethanol) and remagnetization curves obtained at three temperatures (Fig. 1b). The samples prepared by the first method are seen to produce ZFC and FC curves of a pattern typical for conventional ferromagnets, in which the magnetic moment of the sample with nickel cooled in a zero external magnetic field increases with temperature, to remain practically constant under subsequent cooling. Moreover, the saturated magnetic moment (Fig. 1b), determined with due account of the sample weight, is close to the specific magnetic moment of pure bulk nickel, ~55.37 G cm^3/g (magnetization ~484.1 G). We thus see that, with the NPC with Ni nanoclusters prepared by the first method, a substantial part of the nickel is contained in macropores, which accounts for the typical ferromagnetic properties of the NPC.

Magnetic studies conducted on NPC–Ni powder samples (Ni loading by the second method; Fig. 2) suggest a sizable fraction of Ni is contained in the nanopores of this material. The ZFC and FC curves of the sample are typical of a superparamagnet–ferromagnet mixture, with a fairly large fraction of the superparamagnet in the sample. This is indicated by the pattern of the ZFC curve; indeed, this curve tends to a maximum in the ~300- to 350-K interval. By using the Bean–Livingstone formula [14], relating the average size of ferromagnetic inclusions in dia- or paramag-

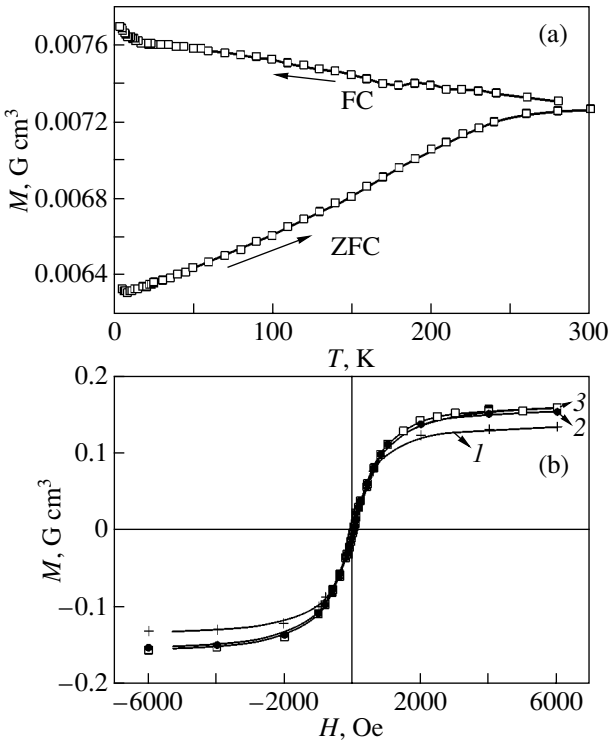

Fig. 2. Magnetic properties of an NPC–Ni powder sample (prepared by loading $NiCl_2$ into NPC by sublimation with subsequent reduction to metallic Ni in hydrogen). (a) Temperature dependence of the magnetic moment of the NPC–Ni powder nanocomposite measured after cooling in zero (ZFC) and weak (50 Oe) (FC) fields. (b) Remagnetization curves of the NPC–Ni powder nanocomposite obtained at temperatures of (*1*) 50, (*2*) 150, and (*3*) 300 K.

netic hosts to the anisotropy constant and critical temperature

$$K_A V = kT_B,$$

where K_A is the anisotropy constant of a magnetic cluster, V is its average volume, k_B is the Boltzmann constant, and T_B is the average blocking temperature (corresponding to the maximum in the ZFC curve), we can estimate the average size of nickel nanoclusters in the NPC host. Assuming nickel to reside in NPC in the form of microcrystals with an fcc lattice and the anisotropy constant $K_A \sim 5 \times 10^5$ erg/cm^3, estimation of the average nickel cluster size yields 2–3 nm. This figure is close to the nanopore size in the NPC prepared from Mo_2C [15]. This supports the starting assumption that magnetic metals loaded successfully into NPC nanopores should transfer to the superparamagnetic state at certain temperatures $T < T_C$(Ni) [T_C(Ni) is the Curie temperature of bulk nickel] provided the nanopores are small enough.

The magnetic measurements (Fig. 2) also show that the samples prepared from NPC–Ni powders behave like a mixture of superparamagnetic and ferromagnetic states. The latter is an unavoidable consequence of the presence of macropores left for the reaction products to evolve and, possibly, of the presence of Ni grains on the surface of powder grains. A certain amount of mesopores, which might form, for instance, from adjacent nanopores being joined by the mechanical stresses arising in the chlorination of the starting carbides, should give rise to an increase in the cluster volume, to enhancement of the exchange interaction between atoms in Ni clusters, and, accordingly, to displacement of the ferromagnet–superparamagnet transition point toward higher temperatures. Another interesting feature in Fig. 2a is the marked increase in the magnetic moment in both ZFC and FC curves occurring at low temperatures (about 15–5 K). This feature implies the existence of nickel nanoclusters of extremely small size, down to small groups of Ni atoms, in the NPC host. The specifics of the technology used to prepare NPC with Ni suggest that this may be due to the presence of very small pores, less than 1 nm in size.

As seen from Fig. 2b, the remagnetization curves of carbon nanocomposites with Ni also consist of an irreversible and a reversible branch. This observation, as well as the fact that the magnetization does not reach saturation even in fairly strong fields (~6000 Oe), supports the conclusion that Ni resides in both the superparamagnetic and the ferromagnetic state, in an approximate proportion of 30 to 70%. Correlation of the weight of the sample with its magnetic moment permits refinement of the content of Ni in the nanopores to yield about 17–20%. The magnetization of pure nickel of a weight equal to that of the starting sample should be ~0.94 G, while we obtain 0.162 G only, which is in agreement with the above figures.

4. CONCLUSIONS

Thus, we have presented the results of magnetic studies of NPC loaded by nickel clusters and obtained supportive evidence for the assumption that Ni inclusions in nanopores should be superparamagnetic. Incorporation of Ni into NPC materials prepared from other carbides (for instance, SiC, TiC, B_4C), which have larger or smaller nanopores than those in the NPC fabricated from Mo_2C [15] and studied here, offers the possibility of varying the value of T_B within a broad range, which may be of interest for applications involving these materials. We may thus conclude that Ni-loaded NPCs are a new class of the so-called granular alloys [16]. These nanocomposites may be expected to exhibit giant magnetoresistance. Studies of the transport properties of the nanocomposites are presently under way, and the results obtained will be published in a separate communication.

ACKNOWLEDGMENTS

This study was supported by INTAS, grant no. 00-761.

REFERENCES

1. I. M. Kotina, V. M. Lebedev, G. V. Pasekina, *et al.*, J. Non-Cryst. Solids **299–302** (2), 820 (2002).
2. Y. Gogotsi, in *Nanostructured Films and Coatings*, Ed. by Gan-Moon Chow, I. A. Ovid'ko, and T. Tsalalakos (Academic, Dordrecht, 1999), p. 25.
3. U.S. Patent No. 3066099 (1962); FRG Patent No. 1185163 (1966).
4. N. F. Fedorov, G. K. Ivakhnyuk, and D. N. Gavrilov, Zh. Prikl. Khim. (Leningrad) **55** (1), 272 (1982).
5. S. K. Gordeev and A. V. Vartanova, Zh. Prikl. Khim. (Leningrad) **64**, 1178 (1991); Zh. Prikl. Khim. (St. Petersburg) **67**, 1080 (1994); Zh. Prikl. Khim. (St. Petersburg) **67**, 1375 (1994).
6. S. K. Gordeev, A. V. Vartanova, S. G. Zhukov, *et al.*, RF Patent No. 2026735 (1995).
7. R. G. Avarbé, S. K. Gordeev, A. V. Vartanova, *et al.*, RF Patent No. 2084036 (1997).
8. V. M. Fedosyuk and T. A. Tochitskiĭ, *Electrolytically Precipitated Nanostructures* (Belorus. Gos. Univ., Minsk, 2002).
9. V. M. Fedosyuk, T. A. Tochitskii, and H. J. Blyhte, J. Magn. Magn. Mater. **224**, 221 (2002).
10. V. M. Fedosyuk, NATO ASI Ser., Ser. Math. Phys. Chem. **65**, 535 (2002).
11. V. M. Fedosyuk, Zarubezh. Radioélektron. Usp. Sovrem. Radiotekh. **5** (3) (2002).
12. K. O'Grady, M. El-Hilo, and R. W. Chantrel, J. Magn. Magn. Mater. **138**, 123 (1994).
13. R. W. Chantrel, M. El-Hilo, and K. O'Grady, IEEE Trans. Magn. **124**, 3570 (1991).
14. C. P. Bean and J. D. Livingstone, Appl. Phys. **30**, S120 (1959).
15. R. N. Kyutt, É. A. Smorgonskaya, S. K. Gordeev, *et al.*, Fiz. Tverd. Tela (St. Petersburg) **41** (5), 891 (1999) [Phys. Solid State **41**, 808 (1999)]; Fiz. Tverd. Tela (St. Petersburg) **41** (8), 1484 (1999) [Phys. Solid. State **41**, 1359 (1999)].
16. V. M. Fedosyuk, in *Encyclopedia of Nanoscience and Nanotechnology*, Ed. by Hari Singh Nalwa (Am. Sci., Los Angeles, CA, 2003), Vol. 10, pp. 1–24.

Translated by G. Skrebtsov

Physics of the Solid State, Vol. 45, No. 9, 2003, pp. 1754–1758. Translated from Fizika Tverdogo Tela, Vol. 45, No. 9, 2003, pp. 1671–1675.

MAGNETISM AND FERROELECTRICITY

Elastic and Kinetic Properties of Single-Crystal $La_{0.75}Ba_{0.25}MnO_3$

R. I. Zaĭnullina*, N. G. Bebenin*, V. V. Mashkautsan*, V. V. Ustinov*, Ya. M. Mukovskiĭ, and A. A. Arsenov****

**Institute of Metal Physics, Ural Division, Russian Academy of Sciences, ul. S. Kovalevskoĭ 18, Yekaterinburg, 620219 Russia*
e-mail: bebenin@imp.uran.ru
***Moscow Institute of Steel and Alloys, Leninskiĭ pr. 4, Moscow, 117936 Russia*
Received February 11, 2003

Abstract—An experimental study of the temperature behavior of longitudinal sound velocity, internal friction, electrical resistivity, and thermopower of single-crystal $La_{0.75}Ba_{0.25}MnO_3$ is reported. A structural transition accompanied by a large jump (18%) in the sound velocity was found to occur at $T_S \approx 170$ K. Within the interval 156–350 K, the temperature dependences of the sound velocity and internal friction reveal a temperature hysteresis. An internal-friction peak due to relaxation processes was detected. The metallic and semiconducting regions are separated by a transition domain about 80 K wide lying below the Curie temperature $T_C = 300$ K.

1. INTRODUCTION

The strong coupling between the magnetic, electronic, and lattice subsystems in lanthanum manganites $La_{1-x}D_xMnO_3$ (D = Ca, Sr, Ba) accounts for the rich diversity of their physical properties. These compounds reveal structural transformations, magnetic transitions, concentration- and temperature-driven metal–insulator transitions, etc. Phase diagrams of rare-earth manganites can be found in [1]. The $La_{1-x}Ca_xMnO_3$ crystals have orthorhombic structure for $T < 700$ K, with a transition to a rhombohedral phase occurring at higher temperatures. The phase diagram of $La_{1-x}Sr_xMnO_3$ is more complex; in particular, the transition between the orthorhombic and rhombohedral phases can take place at close-to-room temperatures when either the concentration or temperature are varied, while for $0.2 < x < 0.7$, the lattice remains rhombohedral for all values of T.

To the best of our knowledge, the literature contains information on the properties of the $La_{1-x}Ba_xMnO_3$ system for a few compositions only. For instance, the lattice parameters for $x \le 0.24$ are presented in [2] only for room temperature. The temperature behavior of the lattice parameters is known only for single-crystal $La_{0.80}Ba_{0.20}MnO_3$, which undergoes a transition between the orthorhombic (*Pnma*) and rhombohedral ($R\bar{3}c$) phases at $T_S \approx 190$ K [3]. Kinetic effects have been studied primarily on polycrystalline samples and thin films with $x \approx 1/3$ (see, e.g., [4, 5]) and on the above-mentioned single-crystal $La_{0.80}Ba_{0.20}MnO_3$ [6].

No studies of the elastic properties of the lanthanum–barium manganites have apparently been conducted at all, although such studies would be capable of producing a wealth of information. For instance, measurements of the sound velocity and internal friction in $La_{1-x}Sr_xMnO_3$ single crystals provided detailed data on the structural transitions occurring both between the *Pnma* and $R\bar{3}c$ phases and between the various modifications (*O*', *O**) of the orthorhombic phase and the observation of a giant temperature hysteresis of the sound velocity suggested the coexistence of orthorhombic and rhombohedral phases in $La_{1-x}Sr_xMnO_3$ over a broad temperature interval [7].

The present communication reports on a continuation of the investigation of the $La_{1-x}Ba_xMnO_3$ system started in our earlier publications [3, 6]. Measurements of the temperature behavior of the longitudinal sound velocity V, internal friction Q^{-1}, electrical resistivity ρ, and the Seebeck coefficient S were conducted on a $La_{0.75}Ba_{0.25}MnO_3$ single crystal grown for the first time.

2. SAMPLES AND MEASUREMENT TECHNIQUE

Polycrystalline $(La_{0.75}Ba_{0.25})_{0.95}MnO_3$ was prepared by sintering a mixture of $BaCO_3$, La_2O_3, and Mn_3O_4 at 1100°C for 24 h. After grinding and repeated pressing, the bar obtained was calcined for 24 h at 1350°C. The density of the synthesized polycrystal was about 80% of the theoretical value. The single crystal was grown from the polycrystalline stock by the floating-zone technique under radiation heating at a rate of 5 mm/h in an Ar environment. The final product represented single-crystal cylindrical rods, 4 mm in diameter and 30–40 mm long, without inclusions of other phases. The growth axis of the crystals was close to [110]. Study using a Super-Probe 733 SEM-microprobe analyzer (JEOL) showed that the composition in the central part of the ingot was close to $La_{0.75}Ba_{0.25}MnO_3$, while at the ends of the ingot the composition could differ by 1–2%.

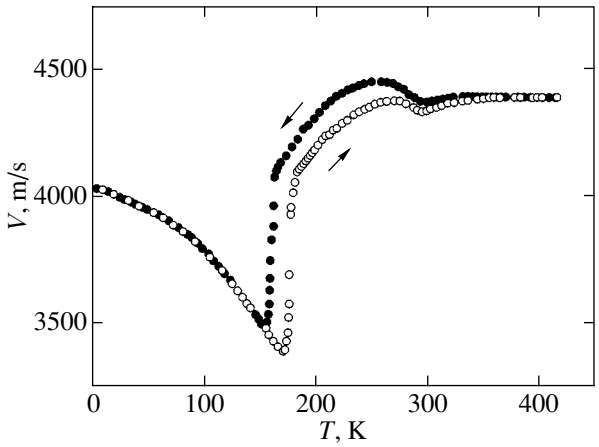

Fig. 1. Plots of the temperature behavior of longitudinal sound velocity in an $La_{0.75}Ba_{0.25}MnO_3$ single crystal measured under heating and cooling.

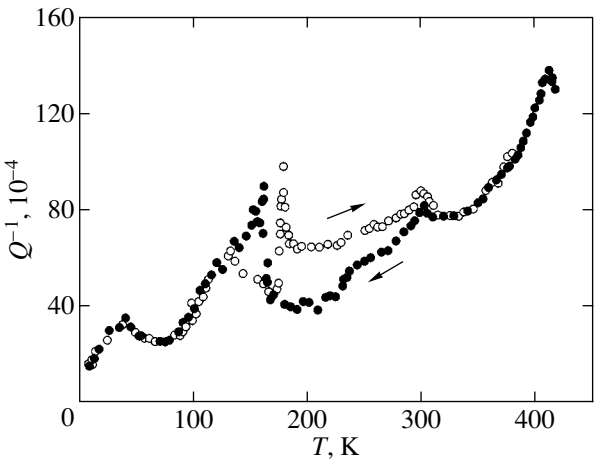

Fig. 2. Plots of the temperature behavior of internal friction Q^{-1} in an $La_{0.75}Ba_{0.25}MnO_3$ single crystal measured under heating and cooling.

The rods used to measure the sound velocity and internal friction were 20 mm long. The sound velocity and the internal friction were studied in the range 5–420 K by the composite oscillator method at frequencies on the order of 100 kHz. This method is based on measuring the resonance frequency and Q factor of a mechanical system consisting of the sample to be studied and a piezoelectric transducer attached to it [8]. The piezoelectric sensor was an X-cut quartz oscillator exciting longitudinal vibrations. The elastic properties were investigated in a helium environment at an average temperature variation rate of 20 K/h.

The samples intended for use in studying the electrical resistivity and thermopower were cut from the central part of the starting single crystal and were shaped in the form of plates with $7 \times 2.6 \times 1.4$ mm in size. The electrical resistivity was measured by the usual four-probe technique. The thermopower was studied at a temperature difference ≈2 K, which was produced by a heater placed near one end of the sample. A magnetic field of up to 15 kOe was applied perpendicular to the plate.

3. RESULTS OF MEASUREMENTS

Figure 1 presents plots of the temperature behavior of sound velocity, $V(T)$, obtained under cooling and heating. For $T > 300$ K, the sound velocity is practically independent of T. At $T = 297$ K, a weak minimum appears. As the temperature decreases, the sound velocity grows up to 250 K, after which it begins to fall off. Upon reaching $T = 165$ K, $V(T)$ begins a steep descent down to $T = 165$ K, a further decrease in temperature bringing about an increase in V. The values of $V(T)$ measured in cooling and heating runs coincide within the interval from the liquid-helium temperature to 156 K. In a heating run, the increase in the sound velocity starts at 173 K and ends at 180 K. In view of the results obtained for $La_{0.80}Ba_{0.20}MnO_3$ [3] and $La_{0.80}Sr_{0.20}MnO_3$ [7], it may be conjectured that a structural transition from the low-temperature orthorhombic *Pnma* to the high-temperature rhombohedral $R\bar{3}c$ structure takes place in the interval 156–180 K. A temperature hysteresis is observed to persist from 156 to 350 K.

Besides the main resonance, an additional resonance was observed at a lower frequency for $T < T_C$. The $V(T)$ curves derived from the characteristics of the main and additional signals are similar. One more resonance was observed in the region of the structural transition. The additional signal in the ferromagnetic region is apparently due to magnetoelastic interaction. The third resonance at the structural transition is evidently initiated by the coexistence of the orthorhombic and rhombohedral phases.

Figure 2 shows plots of the temperature dependence of internal friction Q^{-1} measured on a sample about 20 mm long. One clearly sees that Q^{-1} tends to decrease with decreasing temperature. The curve obtained under cooling exhibits internal-friction peaks at 412, 302, 162, and 40 K. The positions of these peaks do not depend on whether the measurements were conducted in heating or cooling runs, except for the peak associated with the structural transition (positioned at 162 K under cooling and at 172 K under heating). The curves obtained in heating and cooling runs coincide for $T <$ 156 K and $T > 350$ K.

The temperature dependences of the electrical resistivity $\rho(T)$ obtained under cooling at $H = 0$ and 10 kOe and of the magnetoresistance $\Delta\rho/\rho = [\rho(H) - \rho(0)]/\rho(0)$ are plotted in Fig. 3. Within the temperature interval 80–300 K, the derivative $d\rho/dT > 0$. For $T > 250$ K, the resistivity grows steeply with temperature to reach a maximum at $T = 320$ K, after which it takes on a semiconducting pattern ($d\rho/dT < 0$). The derivative $d\rho/dT$

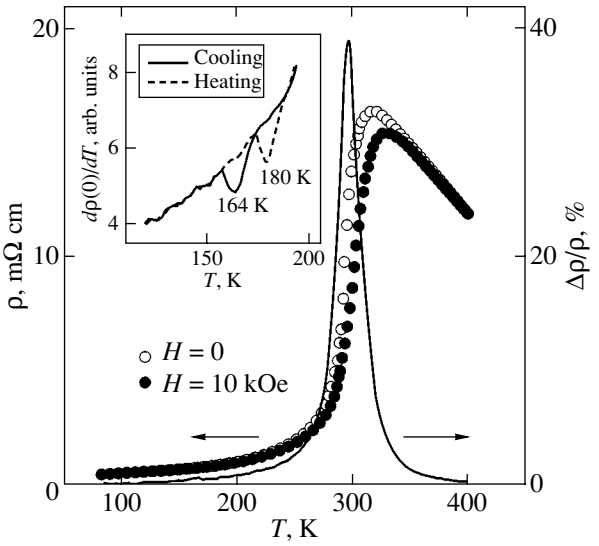

Fig. 3. Temperature dependences of the electrical resistivity ρ(*T*) measured at *H* = 0 and 10 kOe and of magnetoresistance Δρ/ρ of an $La_{0.75}Ba_{0.25}MnO_3$ single crystal. Inset shows the temperature dependences of *d*ρ(0)/*dT* measured in heating and cooling runs.

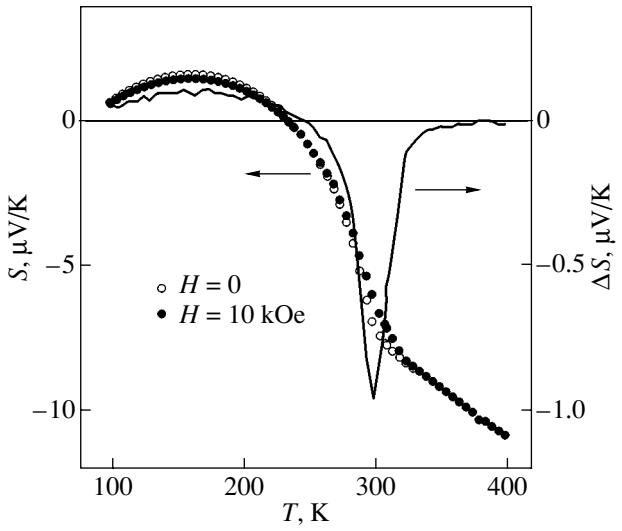

Fig. 4. Temperature behavior of the Seebeck coefficient *S* of a $La_{0.75}Ba_{0.25}MnO_3$ single crystal measured at *H* = 0 and 10 kOe and of $\Delta S = S(0) - S(H = 10\ \text{kOe})$.

passes through a maximum at *T* = 294 K. A magnetic field reduces the resistivity and shifts its maximum toward higher temperatures. The magnetoresistance attains a maximum value of 40% at *T* = 297 K. The structural transition and the associated hysteresis become manifest only in the temperature dependence of *d*ρ/*dT* (see inset to Fig. 3).

The pattern of the field dependences of the magnetoresistance of $La_{0.75}Ba_{0.25}MnO_3$ is characteristic of single crystals, namely, $\Delta\rho/\rho \sim H$ for $T \ll T_C$ and $\Delta\rho/\rho \sim H^2$ for $T \gg T_C$.

Figure 4 displays temperature dependences of the thermopower measured at *H* = 0 and 10 kOe. At low temperatures, *S*(0) and *S*(*H* = 10 kOe) are positive, reach a maximum at *T* = 160 K, and reverse sign at *T* = 234 K. The difference $\Delta S = S(0) - S(H = 10\ \text{kOe})$ passes through an extremum at *T* = 299 K.

4. DISCUSSION OF RESULTS

It is well known that the transition from the paramagnetic to ferromagnetic state is accompanied by the appearance of features in the temperature dependences *V*(*T*), $Q^{-1}(T)$, *d*ρ/*dT*, Δρ/ρ(*T*), and Δ*S*(*T*). The data presented above suggest that the Curie temperature T_C of our $La_{0.75}Ba_{0.25}MnO_3$ sample is approximately 300 K.

Consider the features associated with the *Pnma*–$R\bar{3}c$ structural transformation. Note first of all the large, about 200 K, extent of the temperature hysteresis. Such a giant temperature hysteresis was observed by us earlier in single-crystal $La_{0.80}Sr_{0.20}MnO_3$ [7]. The jump in the sound velocity is 18%, whereas, in $La_{0.80}Sr_{0.20}MnO_3$, the jump occurring at a similar structural transition does not exceed 5%. This indicates that the crystal lattice undergoes a more profound rearrangement in the *Pnma*–$R\bar{3}c$ transformation in the La–Ba manganites than that in the $La_{1-x}Sr_xMnO_3$ crystals, which may be due to the Ba^{2+} ion having a larger radius.

The peak in the $Q^{-1}(T)$ curve at 412 K is apparently due to relaxation processes. Similar maxima were observed by us earlier in $La_{0.75}Sr_{0.25}MnO_3$ [7] and $La_{0.60}Eu_{0.07}Sr_{0.33}MnO_3$ [9].

The origin of the internal friction peak at 40 K remains unclear.

Let us turn now to a discussion of the temperature behavior of the resistivity and thermopower. It is known that at *T* = 0 a material possesses a finite conductivity, i.e., is a metal, if the Fermi level E_F lies in the region of delocalized states [10]. Variation in the concentration of impurities or other defects may result in E_F coinciding with the mobility edge E_C, which separates the regions of localized and delocalized states, and this drives the metal–insulator transition. Magnetic disorder plays an important part in manganites, and its significance grows as one approaches the Curie temperature. As a consequence, there may occur a transition from metallic conduction, taking place for $T < T_C$, to conduction of the semiconducting type in the paramagnetic region. Generally speaking, the mobility edge is not sharp, since its broadening is due, first, to the inelastic carrier interaction with phonons and, second, to electron–electron interaction [11]. In view of the fact that both the interaction with phonons and the broadening of the electron distribution function grow with increasing *T*, it

may be concluded that the temperature-driven metal–insulator transition cannot be sharp and that there should exist a more or less wide transition region (the metal–insulator transition region) from a purely metallic to semiconducting type of conduction.

In the metallic region, the electrical resistivity of manganites scales quadratically with temperature; $\rho(T) = \rho_0 + AT^2$. In the transition region, as T increases, the contribution of localized carriers to the kinetic coefficients grows gradually, while on the insulator side of the transition, conduction occurs by carrier activation into the region of delocalized states (to the mobility edge) and by hopping between localized states. The conductivity can be written as $\sigma = \sigma_{deloc} + \sigma_{hop}$, where σ_{deloc} is the contribution due to delocalized states and σ_{hop} is the hopping conductivity. For the thermopower, one can write $S = S_{deloc}\frac{\sigma_{deloc}}{\sigma} + S_{hop}\frac{\sigma_{hop}}{\sigma}$. Because the Seebeck coefficient of delocalized carriers S_{deloc} can be substantially smaller than S_{hop} (in metals, S is of the order of 1 μV/K, whereas in semiconductors, the thermopower is of the order of 10^2–10^3 μV/K), the contribution of localized carriers to the thermopower can be markedly larger than that to the conductivity.

Consider now the experimental $\rho(T)$ relation. For $T < 320$ K, the derivative $d\rho/dT > 0$, which is interpreted by many researchers as indicating metallic conduction. As pointed out in review [12], however, in the free-electron model, the mean free path becomes equal to the lattice constant and the resistivity reaches 10^{-3} Ω cm for the parameters typical of manganites. This resistivity value is close to the resistivity of single-crystal $La_{0.83}Sr_{0.17}MnO_3$ at $T = 4$ K [13] (in the $La_{1-x}Sr_xMnO_3$ system with $x = 0.17$, the concentration-driven metal–insulator transition takes place). We do not attach particular significance to estimates of this kind, but they do show that the immediate neighborhood of T_C, where ρ is on the order of 10 mΩ cm and higher in our $La_{0.75}Ba_{0.25}MnO_3$ single crystal, does not belong to the region of existence of the metallic phase. To determine the temperature region within which the manganite under study is in the metallic state, we plotted the dependence of ρ on T^2 (see inset to Fig. 5). We readily see that for $T < 180$ K the electrical resistivity follows the T^2 law with the parameters $\rho_0 = 3.4 \times 10^{-4}$ Ω cm and $A = 1.7 \times 10^{-8}$ Ω cm/K^2. The magnitude of A is close to the value obtained for single-crystal $La_{0.75}Sr_{0.25}MnO_3$ [14]. The value of ρ_0 found for $La_{0.75}Ba_{0.25}MnO_3$ is about fourfold the resistivity of $La_{0.75}Sr_{0.25}MnO_3$ at $T = 4$ K, which should possibly be attributed to the larger radius of the barium ion and the corresponding strong nonmagnetic disorder in $La_{1-x}Ba_xMnO_3$ as compared to $La_{1-x}Sr_xMnO_3$ for the same contents of the divalent ions [15].

For $T > 180$ K, the temperature dependence of the electrical resistivity becomes stronger, with no features

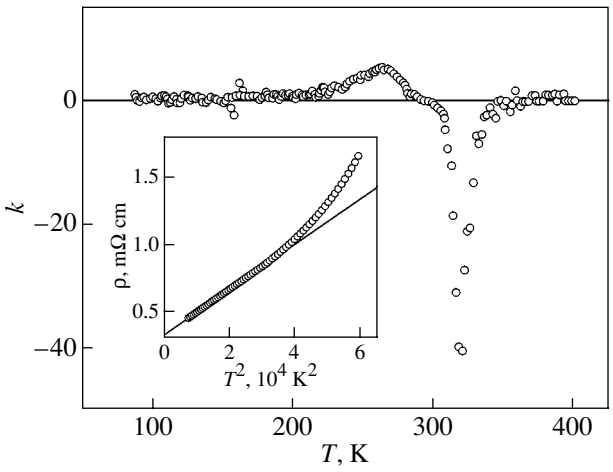

Fig. 5. Curvature k plotted vs. temperature T. Inset shows the dependence of ρ on T^2.

seemingly present up to the neighborhood of T_C. Consider, however, the geometric properties of the $\rho(T)$ curve. We set $\tau = T/T_C$ and $\tilde{\rho} = \rho(T)/\rho(T_C)$ and calculate the curvature k from the relation $k = \tilde{\rho}''/[1 + (\tilde{\rho}')^2]^{3/2}$, where the prime denotes differentiation with respect to τ; the result obtained is shown graphically in Fig. 5. For $T \ll T_C$, the curvature is small and the feature at $T \approx 160$ K can probably be assigned to the $Pnma$–$R\bar{3}c$ structural transformation. A noticeable growth in k starts near 200 K, and at $T \approx 260$ K the curvature reaches a clearly pronounced maximum, to vanish at the inflection point (the maximum in $d\rho/dT$). At 320 K, the curvature passes through a deep minimum corresponding to the maximum in ρ. Thus, the origin of the features in the $k(T)$ curve is clear, except for the maximum in the curvature occurring at 260 K. In view of the above reasoning and of the fact that $\rho(T = 260\ \text{K}) = 2.2 \times 10^{-3}$ Ω cm, we can assume this temperature to be the upper bound of the metal–insulator transition region lying between the regions of existence of the metallic and semiconducting states. For the lower boundary of the transition region, one can take $T = 180$ K.

In the paramagnetic region, for $T > 320$ K, the derivative $d\rho/dT$ is negative, but the actual pattern of the temperature dependence of the resistivity, i.e., whether it scales as $\exp(E_{activ}/T)$ or otherwise, cannot be extracted from our data.

While the temperature dependence $S(T)$ (Fig. 4) for the $La_{0.75}Ba_{0.25}MnO_3$ compound studied by us follows the same pattern as that for $La_{0.75}Sr_{0.25}MnO_3$ [16], the maximum value of S (1.6 μV/K) is about three times smaller. Below 160 K, the thermopower is small in magnitude, positive, and grows with increasing T, which suggests that the hole contribution to metallic conductivity is predominant. The decrease in S for $T >$ 160 K indicates the presence of a negative contribution due to carriers with energies $E > E_F$. Because the tem-

perature of the maximum in thermopower (160 K) is only 20 K lower than that at which the transition from the metal to semiconductor occurs (180 K), one may conclude that the negative contribution to S originates from localized carriers. For $T > 234$ K, the contribution of such carriers to thermopower dominates, which, however, does not mean that $\sigma_{hop} \gg \sigma_{deloc}$. The absolute value of S does not exceed 12 μV/K up to 400 K, which indicates that competition persists between the contributions due to the delocalized ($S_{deloc} > 0$) and localized ($S_{hop} < 0$) carriers. Unfortunately, separation of these contributions by using the available experimental data does not appear possible.

4. CONCLUSIONS

Thus, we have carried out the first studies of single-crystal $La_{0.75}Ba_{0.25}MnO_3$. A structural transition between the low-temperature orthorhombic and high-temperature rhombohedral phases was found to occur at $T_S \approx 170$ K. The jump in the sound velocity at this transition is 18%. The temperature dependences of the sound velocity and internal friction exhibit a grant temperature hysteresis (about 200 K).

At low temperatures, the conductivity is metallic, while in the vicinity of the Curie temperature $T_C = 300$ K and in the paramagnetic region, the crystal resides in the insulator state. The metal–insulator transition in temperature is not sharp, as the transition region lies below the Curie temperature in the interval 180–260 K.

It was shown that the temperature dependence of thermopower for $T > 160$ K is determined by the competition between the contributions due to the delocalized and localized carriers.

ACKNOWLEDGMENTS

This study was supported by the Russian Foundation for Basic Research (project nos. 00-02-17544, 00-15-96745) and Urals Division, Russian Academy of Sciences (young scientists' project competition, 2002).

REFERENCES

1. V. E. Naĭsh, Fiz. Met. Metalloved. **92** (5), 16 (2001).
2. B. Dabrowski, K. Rogacki, X. Xiong, *et al.*, Phys. Rev. B **58** (5), 2716 (1998).
3. V. E. Arkhipov, N. G. Bebenin, V. P. Dyakina, *et al.*, Phys. Rev. B **61** (17), 11229 (2000).
4. N. G. Bebenin, R. I. Zaĭnullina, V. V. Mashkautsan, *et al.*, Zh. Éksp. Teor. Fiz. **113** (2), 981 (1998) [JETP **86**, 534 (1998)].
5. R. von Helmolt, J. Wecker, B. Holzapfel, *et al.*, Phys. Rev. Lett. **71** (14), 2331 (1993).
6. N. G. Bebenin, R. I. Zaĭnullina, V. V. Mashkautsan, *et al.*, Zh. Éksp. Teor. Fiz. **117** (6), 1181 (2000) [JETP **90**, 1027 (2000)].
7. R. I. Zainullina, N. G. Bebenin, A. M. Burkhanov, *et al.*, Phys. Rev. B **66**, 064421 (2002).
8. H. J. McSkimin, in *Physical Acoustics. Principle and Methods*, Ed. by W. P. Mason (Academic, New York, 1964; Mir, Moscow, 1966), Vol. 1, Part A, p. 272.
9. R. I. Zaĭnullina, N. G. Bebenin, V. V. Mashkautsan, *et al.*, Fiz. Tverd. Tela (St. Petersburg) **42** (2), 284 (2000) [Phys. Solid State **42**, 292 (2000)].
10. N. F. Mott and E. A. Davis, *Electronic Processes in Non-Crystalline Materials*, 2nd ed. (Clarendon, Oxford, 1979; Mir, Moscow, 1982).
11. N. Mott, J. Phys. C: Solid State Phys. **20**, 3075 (1987).
12. M. B. Salamon and M. Jaime, Rev. Mod. Phys. **73** (3), 583 (2001).
13. T. Okuda, A. Asamitsu, Y. Tomioka, *et al.*, Phys. Rev. Lett. **81** (15), 3203 (1998).
14. A. Urushibara, Y. Moritomo, T. Arima, *et al.*, Phys. Rev. B **51** (20), 14103 (1995).
15. M. M. Savosta, A. N. Ulyanov, N. Yu. Starostyuk, *et al.*, Eur. Phys. J. B **12**, 393 (1999).
16. A. Asamitsu, Y. Moritomo, and Y. Tokura, Phys. Rev. B **53** (6), R2952 (1996).

Translated by G. Skrebtsov

Physics of the Solid State, Vol. 45, No. 9, 2003, pp. 1759–1762. Translated from Fizika Tverdogo Tela, Vol. 45, No. 9, 2003, pp. 1676–1679.

MAGNETISM AND FERROELECTRICITY

Giant Piezoelectric Effect in Layered Ferroelectric–Polymer Composites

G. S. Radchenko and A. V. Turik

Rostov State University, ul. Zorge 5, Rostov-on-Don, 344007 Russia

e-mail: turik@phys.rsu.ru

Received January 10, 2003

Abstract—The giant piezoelectric effect and giant piezoelectric relaxation are revealed for the first time in structures consisting of ferroelectric and polymer layers connected in series. Under these effects, the composites exhibit giant static permittivities. The physical mechanisms responsible for the unusual behavior of the piezoelectric coefficients and permittivities are considered. *© 2003 MAIK "Nauka/Interperiodica".*

1. INTRODUCTION

For some technical purposes (design and fabrication of actuators, sensors, etc.), it is very important to use materials with extremely large piezoelectric coefficients. To date, the largest piezoelectric coefficients ($d_{33} \geq 2500$ pC N^{-1}) have been obtained for single crystals of the ferroelectric solid solutions $Pb(Zn_{1/3}Nb_{2/3})O_3$–$PbTiO_3$ (PZN–PT) and $Pb(Mg_{1/3}Nb_{2/3})O_3$–$PbTiO_3$ (PMN–PT) [1–3]. In this paper, we will consider a new mechanism responsible for a giant increase in the piezoelectric coefficients and giant piezoelectric relaxation in composites consisting of layers of components connected in series. The components of the composite possess significantly different permittivities ε, piezoelectric coefficients d, elastic compliances, and electrical conductivities γ and exhibit a giant static permittivity. The results obtained are of interest for the design and testing of piezoelectric devices intended for low-frequency applications (sensors, actuators).

2. THE MODEL AND BASIC FORMULAS

The theoretical treatment is based on the model proposed in our recent work [4]. Within this model, it is possible to obtain exact solutions for piezoelectric coefficients and permittivities of a multilayer (or bilayer) composite with a connectivity of the *2–2* type [5], which consists of two components with numbers $n = 1, 2$ and volume concentrations θ_1 and θ_2. It is assumed that the composite layers have an infinite length along the OX_1 and OX_2 directions of a rectangular coordinate system ($X_1X_2X_3$). The vectors of the normal to the interface between the layers are parallel to the OX_3 axis. In the composite, either the first (ferroelectric) component or both components are polarized along the OX_3 axis. Moreover, both components individually and the composite as a whole are transversely isotropic (∞mm symmetry) in the X_1OX_2 plane perpendicular to the polar axis. The charges induced at the interfaces between the layers by remanent polarization of the ferroelectric are considered to be completely screened [6].

If the external uniform electric field E_3^* with a circular frequency ω (quantities averaged over the composite layers are denoted by asterisks) is applied along the polar axis OX_3 in the absence of other components of the external electric fields and mechanical stresses σ_j (specifically, $\sigma_3^* = \sigma_3^{(1)} = \sigma_3^{(2)} = 0$), the internal electric fields $E_3^{(n)}$ ($E_3^* = \theta_1 E_3^{(1)} + \theta_2 E_3^{(2)}$) and internal mechanical stresses $\sigma_1^{(n)} = \sigma_2^{(n)}$ ($\sigma_1^* = \theta_1\sigma_1^{(1)} + \theta_2\sigma_1^{(2)} = 0$) are induced in both layers. The piezoelectric equations relating the components of the electric induction $D_3^{(n)}$ and strains $\xi_i^{(n)}$ ($i = 1, 2, 3$) inside each layer with an internal electric field $E_3^{(n)}$ and internal mechanical stress $\sigma_j^{(n)}$,

$$\begin{aligned} D_3^{(n)} &= 2d_{31}^{(n)}\sigma_1^{(n)} + \varepsilon_{33}^{(n)}E_3^{(n)}, \\ \xi_1^{(n)} = \xi_2^{(n)} &= (s_{11}^{E(n)} + s_{12}^{E(n)})\sigma_1^{(n)} + d_{31}^{(n)}E_3^{(n)}, \\ \xi_3^{(n)} &= 2s_{13}^{E(n)}\sigma_1^{(n)} + d_{33}^{(n)}E_3^{(n)}, \end{aligned} \qquad (1)$$

are treated jointly with the boundary conditions

$$D_3^{(1)} = D_3^{(2)}, \quad \xi_1^{(1)} = \xi_1^{(2)}, \quad \xi_2^{(1)} = \xi_2^{(2)}. \qquad (2)$$

Here, $s_{ij}^{E(n)}$ are the elastic compliances (for $E = 0$) and $\varepsilon_{33}^n = \varepsilon^{(n)} - i\gamma_n/\omega$ (γ_n are the electrical conductivities) are the complex permittivities of the mechanically free ($\sigma = 0$) sample of the nth component of the composite.

Elastic compliances s_{ij}^F (10^{-12} Pa^{-1}), piezoelectric coefficients d_{ki} (pC N^{-1}), and permittivities $\varepsilon_{33}^\sigma/\varepsilon_0$ for the PKR-73 ferroelectric ceramics [8], PMN–PT single crystal [3], and polyethylene [9] at 25°C

Constants	s_{11}^E	s_{12}^E	s_{13}^E	s_{33}^E	d_{31}	d_{33}	$\varepsilon_{33}^\sigma/\varepsilon_0$
PKR-73	17.9	–6.8	–9.6	23.5	–380	860	6000
PMN–PT	69.0	–11.1	–55.7	119.6	–1330	2820	8200
Polyethylene	1370	–630	–630	1370	0	0	0.5

The piezoelectric coefficients d_{31}^* and d_{33}^* and the permittivity ε_{33}^*, which are obtained by averaging the components $D^{(n)}$ and $\xi^{(n)}$ in relationships (1) according to the expressions

$$\begin{aligned} D_3^* &= \theta_1 D_3^{(1)} + \theta_2 D_3^{(2)} = \varepsilon_{33}^* E_3^*, \\ \xi_i^* &= \theta_1 \xi_i^{(1)} + \theta_2 \xi_i^{(2)} = d_3^* E_3^*, \end{aligned} \tag{3}$$

can be represented by the general formulas through the permittivity of the composite $\varepsilon_{33d}^* = \varepsilon_{33}^{(1)}\varepsilon_{33}^{(2)}/(\theta_1\varepsilon_{33}^{(2)} + \theta_2\varepsilon_{33}^{(1)})$ in the absence of the transverse piezoelectric effect ($d_{31}^{(n)} = 0$) and through the piezoelectric constants of the layers $g_{31}^{(n)} = d_{31}^{(n)}/\varepsilon_{33}^{(n)}$ and $g_{33}^{(n)} = d_{33}^{(n)}/\varepsilon_{33}^{(n)}$ as follows:

$$d_{31}^* = \varepsilon_{33d}^* \left[\theta_1 g_{31}^{(1)} + \theta_2 g_{31}^{(2)} - \theta_1\theta_2 \frac{(g_{31}^{(2)} - g_{31}^{(1)})(s_{11}^{(2)} + s_{12}^{(2)} - s_{11}^{(1)} - s_{12}^{(1)})}{\theta_1(s_{11}^{(2)} + s_{12}^{(2)}) + \theta_2(s_{11}^{(1)} + s_{12}^{(1)})} \right],$$

$$d_{33}^* = \varepsilon_{33d}^* \left[\theta_1 g_{33}^{(1)} + \theta_2 g_{33}^{(2)} - 2\theta_1\theta_2 \frac{(g_{31}^{(2)} - g_{31}^{(1)})(s_{13}^{(2)} - s_{13}^{(1)})}{\theta_1(s_{11}^{(2)} + s_{12}^{(2)}) + \theta_2(s_{11}^{(1)} + s_{12}^{(1)})} \right], \tag{4}$$

$$\varepsilon_{33}^* = \varepsilon_{33d}^* \left[1 - 2\theta_1\theta_2 \frac{(g_{31}^{(2)} - g_{31}^{(1)})(d_{13}^{(2)} - d_{13}^{(1)})}{\theta_1(s_{11}^{(2)} + s_{12}^{(2)}) + \theta_2(s_{11}^{(1)} + s_{12}^{(1)})} \right].$$

In the further analysis, we will be interested primarily in the static piezoelectric coefficients d_{31}^* and d_{33}^* and the static permittivity ε_{33}^* (at $\omega \longrightarrow 0$) [4]:

$$\begin{aligned} d_{310}^* &= \frac{\theta_1\theta_2(s_{11}^{E(1)} + s_{12}^{E(1)} - s_{11}^{E(2)} - s_{12}^{E(2)})(\gamma_1 d_{31}^{(2)} - \gamma_2 d_{31}^{(1)})}{(\theta_2(s_{11}^{E(1)} + s_{12}^{E(1)}) + \theta_1(s_{11}^{E(2)} + s_{12}^{E(2)}))(\theta_1\gamma_2 + \theta_2\gamma_1)} + \frac{\theta_1 d_{31}^{(1)}\gamma_2 + \theta_2 d_{31}^2\gamma_1}{\theta_1\gamma_2 + \theta_2\gamma_1}, \\ d_{330}^* &= \frac{2\theta_1\theta_2(s_{13}^{E(1)} - s_{13}^{E(2)})(\gamma_1 d_{31}^{(2)} - \gamma_2 d_{31}^{(1)})}{(\theta_2(s_{11}^{E(1)} + s_{12}^{E(1)}) + \theta_1(s_{11}^{E(2)} + s_{12}^{E(2)}))(\theta_1\gamma_2 + \theta_2\gamma_1)} + \frac{\theta_1 d_{33}^{(1)}\gamma_2 + \theta_2 d_{33}^2\gamma_1}{\theta_1\gamma_2 + \theta_2\gamma_1}, \\ \varepsilon_{330}^* &= \frac{2\theta_1\theta_2(d_{31}^{(1)} - d_{31}^{(2)})(\gamma_1 d_{31}^{(2)} - \gamma_2 d_{31}^{(1)})}{(\theta_2(s_{11}^{E(1)} + s_{12}^{E(1)}) + \theta_1(s_{11}^{E(2)} + s_{12}^{E(2)}))(\theta_1\gamma_2 + \theta_2\gamma_1)} + A, \end{aligned} \tag{5}$$

where $A = \dfrac{\theta_1\varepsilon^{(1)}\gamma_2^2 + \theta_2\varepsilon^{(2)}\gamma_1^2}{(\theta_1\gamma_2 + \theta_2\gamma_1)^2}$ is the strictly dielectric term treated in the classical theory of the Maxwell–Wagner relaxation for piezoelectric inactive media [7].[1]

3. RESULTS AND DISCUSSION

As an example, we consider a composite consisting of either the PKR-73 ferropiezoelectric ceramics [8] (layer with $n = 1$) or the $0.67Pb(Mg_{1/3}Nb_{2/3})O_3$–$0.33PbTiO_3$ (PMN–PT [3]) single crystal, which polarized in the [001] direction coinciding with the OX_3 axis in the chosen coordinate system, and polyethylene [9] (layer with $n = 2$). The physical constants of the components are given in the table. The results of the computations performed are presented in Figs. 1 and 2.

[1] Since the general formulas are very cumbersome, they are given in shortened form. In expressions (4), the terms introducing a very small (less than 0.1%) contribution to the piezoelectric coefficients are omitted. Formulas (5) are exact.

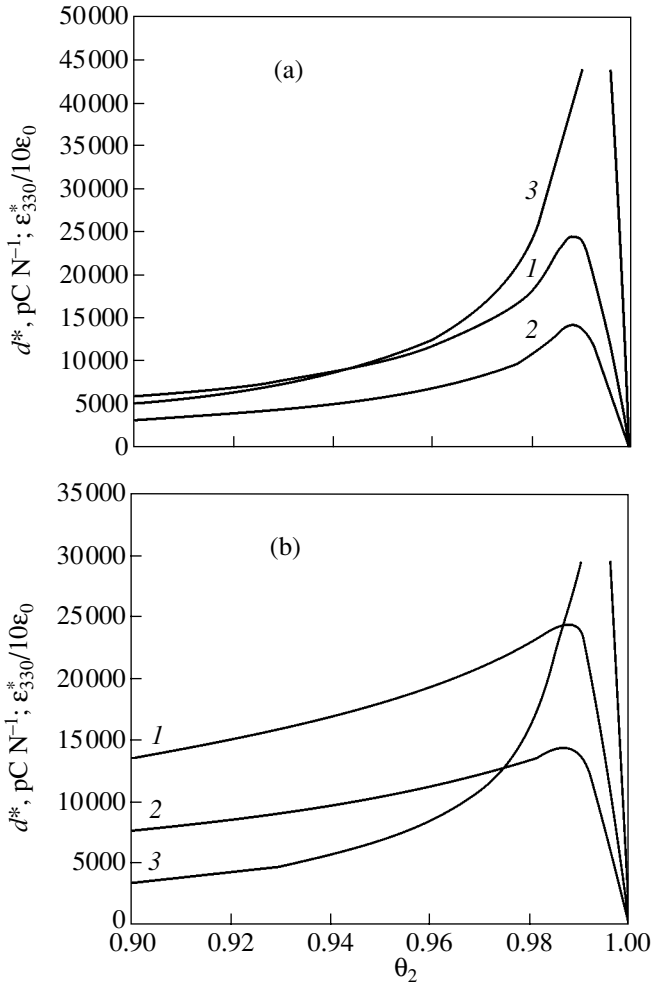

Fig. 1. Concentration dependences of the static piezoelectric coefficients (*1*) d^*_{330} and (*2*) $-d^*_{310}$ pC N^{-1} and (*3*) the static permittivity $\varepsilon^*_{330}/\varepsilon_0$ for composites consisting of layers of (a) PKR-73 piezoelectric ceramics [8] and polyethylene [9] and (b) the PMN–PT single crystal [3] and polyethylene [9]. Conditions: $\gamma_1 = 10^{-13}\ \Omega^{-1}\ m^{-1}$ and $\gamma_2 = 10^{-10}\ \Omega^{-1}\ m^{-1}$.

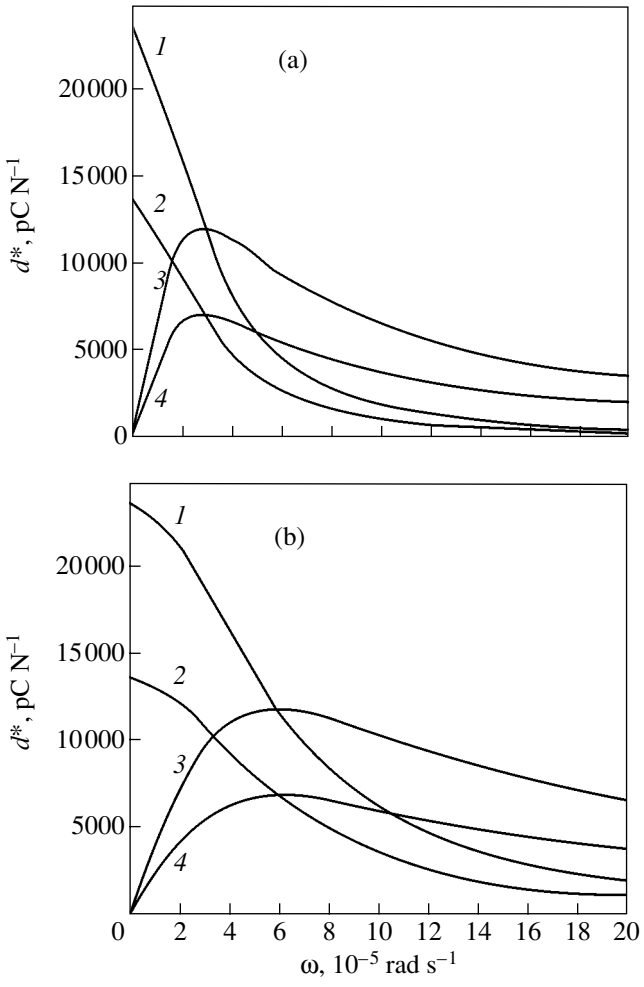

Fig. 2. Giant piezoelectric relaxation in bilayer composites consisting of layers of (a) PKR-73 piezoelectric ceramics [8] and polyethylene [9] and (b) the PMN–PT single crystal [3] and polyethylene [9]: (*1*) d'^*_{33}, (*2*) $-d'^*_{31}$, (*3*) d''^*_{33}, and (*4*) $-d''^*_{31}$. Conditions: $\gamma_1 = 10^{-13}\ \Omega^{-1}\ m^{-1}$ and $\gamma_2 = 10^{-10}\ \Omega^{-1}\ m^{-1}$.

Under the conditions $\gamma_1/\gamma_2 \ll 1$, $\varepsilon^{(1)}/\varepsilon^{(2)} \gg 1$, and $\theta_1/\theta_2 \longrightarrow 0$, the composites exhibit a giant static permittivity: $\varepsilon^*_{330} \longrightarrow \varepsilon^1/\theta_1 \longrightarrow \infty$ [4] (Fig. 1). This is attended by giant dielectric relaxation [4, 10, 11] due to a very high strength of the electric field ($E^{(1)}_3 \approx E^*_3/\theta_1 \longrightarrow \infty$) inside the very thin layer with a high permittivity $\varepsilon^{(1)}$ and a low electrical conductivity γ_1. The maximum increase in the static permittivity is observed under the condition $\gamma_1 \longrightarrow 0$. In this case, the permittivity obeys the law $\varepsilon^*_{330} \cong \text{const}/(\theta_1 - \theta_{1c})$, which is similar to the Curie–Weiss law. Here, θ_{1c} is the critical concentration of a purely dielectric component ($n = 1$). For $\gamma_1 \longrightarrow 0$, we have $\theta_{1c} \longrightarrow 0$, whereas the permittivity $\varepsilon^*_{330} \longrightarrow \infty$ due to an infinite increase in the absolute values of the complex permittivities of the layers $\varepsilon^{(n)}_{33}$ at $\omega \longrightarrow 0$. The dominant contribution to the permittivity ε^*_{330} is made by the classical dielectric term A in expression (5). The behavior of the permittivity $\varepsilon^*_{330} \longrightarrow \infty$ is actually similar to that observed in the case when the percolation threshold is approached upon the dielectric–metal phase transition [12, 13].

The physical mechanism responsible for a giant increase in the piezoelectric coefficients (Fig. 1) differs from that described above and has never been considered in the literature. It follows from expressions (4) and (5) that the main contribution to the giant piezoelectric coefficients is made by the terms proportional to $\theta_1\theta_2$, i.e., the giant transverse piezoelectric response. For this reason, Damjanovic *et al.* [6] did not reveal

giant piezoelectric coefficients in the framework of a simplified model in which the transverse piezoelectric response can be ignored. In order to obtain giant piezoelectric coefficients, a ferroelectric with large piezoelectric coefficients should be used as a component with a low electrical conductivity γ, whereas a polymer material with high elastic compliances $|s_{ij}^E|$ should be used as a component with a higher electrical conductivity γ. The giant transverse piezoelectric response is caused by high internal mechanical stresses $\sigma_1^{(1)} = \sigma_2^{(1)}$ [14] in addition to the electric field $E_3^{(1)} \longrightarrow \infty$. High internal mechanical stresses are induced by the external electric field E_3^* and reach especially high values for a large difference between the electrical conductivities ($\gamma_1/\gamma_2 \ll 1$) of the composite components and a small thickness $\theta_1 \longrightarrow 0$ of the piezoelectric active layer. The Curie–Weiss law is invalid for the static piezoelectric coefficients, and the piezoelectric coefficients d_{330}^* and $|d_{310}^*|$ at $\gamma_1 = 0$ and $\theta_1 = 0$ are very large but not infinite. It can also be seen from Fig. 1 that the effective piezoelectric coefficients of the composites under investigation are one order of magnitude greater than the maximum piezoelectric coefficients of ferropiezoelectric ceramics [8] and single-crystal PZN–PT and PMN–PT [1–3].

The giant dielectric relaxation based on the Maxwell–Wagner mechanism was described in detail in [4, 10, 11]. Consequently, we do not discuss this type of relaxation. The giant piezoelectric relaxation is illustrated in Fig. 2. The frequency dependences of the piezoelectric coefficients d_{33}^* and d_{31}^* exhibit a Debye behavior. The very large values ($d_{330}^* - d_{33\infty}^*$) and ($d_{310}^* - d_{31\infty}^*$) of the piezoelectric relaxation are characteristic of a combination of components, one of which has large piezoelectric coefficients and the other possesses high elastic compliances. For $\gamma_1/\gamma_2 \ll 1$, the relaxation frequency $\omega_r \approx (R_2C_1)^{-1} \approx \theta_1\gamma_2/\varepsilon_1$ is determined primarily by both the capacity C_1 of the weakly conducting (dielectric) component and the electrical resistance R_2 of the strongly conducting (semiconductor) component. The inclusion of the elastic and piezoelectric properties of the components leads to a slight increase in the relaxation frequency ω_r [4]. As the conductivity γ_2 increases significantly, the relaxation frequency increases by many orders of magnitude [11]. However, in all cases, the static piezoelectric coefficients d_{330}^* and $|d_{310}^*|$ at $\omega \ll \omega_r$ considerably exceed their dynamic values at $\omega \gg \omega_r$. This circumstance should be taken into account when designing piezoelectric elements and devices intended for low-frequency (static) applications.

REFERENCES

1. S.-F. Liu, S.-E. Park, T. R. Shrout, and L. E. Cross, J. Appl. Phys. **85**, 2810 (1990).
2. M. K. Durbin, E. W. Jacobs, J. C. Hicks, and S.-E. Park, Appl. Phys. Lett. **74**, 2848 (1999).
3. R. Zhang, B. Jiang, and W. Cao, J. Appl. Phys. **90**, 3471 (2001).
4. A. V. Turik and G. S. Radchenko, J. Phys. D: Appl. Phys. **35**, 1188 (2002).
5. R. E. Newnham, D. P. Skinner, and L. E. Cross, Mater. Res. Bull. **13**, 525 (1978).
6. D. Damjanovic, M. Demartin Maeder, P. Duran Martin, *et al.*, J. Appl. Phys. **90**, 5708 (2001).
7. A. R. von Hippel, *Dielectrics and Waves* (Wiley, New York, 1954; Inostrannaya Literatura, Moscow, 1960).
8. A. Ya. Dantsiger, O. N. Razumovskaya, L. A. Reznichenko, and S. I. Dudkina, *Highly Efficient Piezoceramic Materials: Optimization of Searching* (Paĭk, Rostov-on-Don, 1995).
9. F. Levassort, M. Lethiecq, C. Millar, and L. Pourcelot, IEEE Trans. Ultrason. Ferroelectr. Freq. Control **45**, 1497 (1998).
10. M. Shen, S. Ge, and W. Cao, J. Phys. D: Appl. Phys. **34**, 2935 (2001).
11. V. V. Lemanov, A. V. Sotnikov, E. P. Smirnova, and M. Weihnacht, Fiz. Tverd. Tela (St. Petersburg) **44** (11), 1948 (2002) [Phys. Solid State **44**, 2039 (2002)].
12. S. Kirkpatrick, Rev. Mod. Phys. **45**, 574 (1973).
13. A. L. Efros and B. I. Shklovskii, Phys. Status Solidi B **76**, 475 (1976).
14. A. V. Turik, Ferroelectrics **222**, 33 (1999).

Translated by N. Korovin

Physics of the Solid State, Vol. 45, No. 9, 2003, pp. 1763–1767. Translated from Fizika Tverdogo Tela, Vol. 45, No. 9, 2003, pp. 1680–1684.

MAGNETISM AND FERROELECTRICITY

Selective Effect of a Weak DC Magnetic Field on Triglycine Sulfate Crystals

M. N. Levin*, V. V. Postnikov*, and M. Yu. Palagin**

** Voronezh State University, Universitetskaya pl. 1, Voronezh, 394693 Russia*

e-mail: levin@lev.vsu.ru

*** Voronezh State Technical University, Moskovskiĭ pr. 14, Voronezh, 394026 Russia*

Received November 26, 2002; in final form, February 10, 2003

Abstract—The effect of the selective influence of a dc magnetic field on the characteristics of nominally pure triglycine sulfate crystals was detected for the first time. A short (minutes) exposure to a weak magnetic field $B_0 = 0.08 \pm 0.01$ T caused long-term (hundreds of hours) changes in the spontaneous polarization, coercive field, Curie temperature, and permittivity of the crystal at the Curie point. The effect is selective in nature presumably because of the participation of hydrogen bond protons in the spin-dependent processes of the transformation of defect complexes in real crystals. © *2003 MAIK "Nauka/Interperiodica".*

1. INTRODUCTION

Recently, long-term changes in the ferroelectric and dielectric characteristics of nominally pure triglycine sulfate (TGS) crystals caused by short-term exposures to weak pulsed magnetic fields (PMFs) have been detected [1]. In terms of classical thermodynamics, this effect is paradoxical, because the energy of PMFs with an amplitude $B \sim 0.02$ T is negligible in comparison with the thermal energy ($\mu_B B \sim 10^{-4} kT$ at $T = 300$ K, where μ_B is the Bohr magneton) and cannot cause the effect in question. Furthermore, the PMF-induced effects detected in TGS crystals were observed in fields lower than the typical threshold field (~0.1 T) for magnetoplastic effects in nonmagnetic dielectric crystals caused by changes in the spin states of structural defects [2, 3]. In particular, the magnetoplastic effect in ferroelectric $NaNO_2$ crystals manifests itself at $B = 0.2$ T [4], the influence of a magnetic field on the starting chaos-inducing fields was observed in TGS crystals at $B = 0.3$ T [5], and changes in the Curie temperature of the ferroelectric transitions in $BaTiO_3$ crystals took place in magnetic fields with $B > 0.5$ T [6]. To our knowledge, there are no papers the influence of magnetic fields with $B < 0.2$ T on the characteristics of ferroelectric crystals has been reported.

The PMF-induced effects detected in TGS crystals [1] lent impetus to studies of ferroelectrics in such weak magnetic fields. At the same time, the question of whether magnetic fields must necessary be pulsed to initiate such effects remains unanswered. According to the estimation made in [7], the electric fields induced by the PMFs used cannot be responsible for the effects observed.

The aim of this work is to study the influence of weak dc magnetic fields on the ferroelectric and dielectric characteristics of nominally pure TGS crystals.

2. EXPERIMENTAL

A TGS single crystal was grown by temperature-controlled cooling of a supersaturated aqueous solution. Samples were cut out as rectangular plane-parallel plates $7 \times 7 \times 0.5$ mm in size. The polar Y axis was normal to the large faces, onto which silver electrodes were deposited through thermal evaporation in vacuum. Then, the samples were annealed in air at $T = 350$ K for 10 h.

A crystal sample was exposed to a dc magnetic field in the gap between magnetized ferrite plates. The magnetic induction was dictated by the gap width and varied within the range 0.02–0.2 T. The magnetic field was measured using a magnetometer with a Hall probe with an error $\delta_B \le 5 \times 10^{-3}$ T. Within the accuracy of measurements, the magnetic field was uniform over the sample area. The samples were subjected to a magnetic field in the ferro- and paraelectric phases at $T = 293$ and 328 K, respectively, for time $t = 1$–40 min. The polar Y axis was normal to or along the applied magnetic field. Before the magnetic processing, some of the samples were transferred to a quasi-single-domain state at $T = 293$ K by a ten-minute exposure to a dc electric field ten times the coercive field and directed along the ferroelectric Y axis.

To determine the spontaneous polarization P_s and the coercive field E_k, ferroelectric hysteresis loops were measured at $T = 310$ K using the conventional Sawyer–Tower technique at a frequency $f = 50$ Hz. The temperature dependence of the permittivity $\varepsilon'(T)$ of the samples was measured in a special thermostat using a Tesla

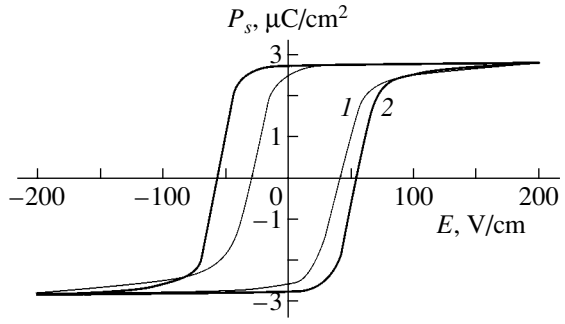

Fig. 1. Ferroelectric $P_s(E)$ hysteresis loops of the TGS crystal (*1*) before and (*2*) after 30-min exposure of a sample to a dc magnetic field $B_0 = 0.08$ T at $T = 293$ K. The measurements were carried out at $T = 310$ K at a frequency $f = 50$ Hz.

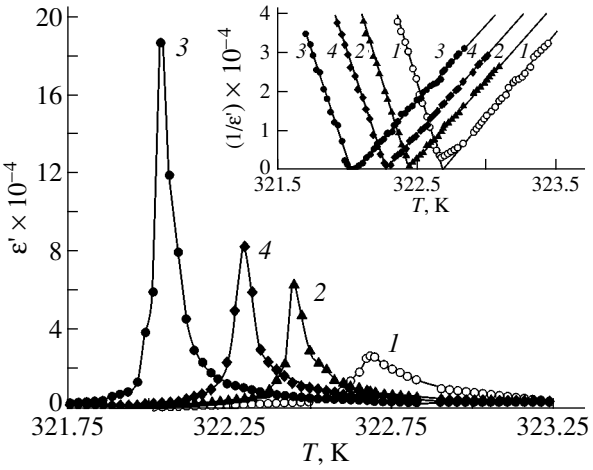

Fig. 2. Temperature dependences of the TGS crystal permittivity (*1*) before and (*2–4*) after 30-min exposure of samples to a magnetic field (*2*) $B = 0.06$, (*3*) 0.08, and (*4*) 0.1 T at $T = 293$ K. The inset shows the corresponding temperature dependences of the inverse permittivities $1/\varepsilon = c(T - T_C)$.

BM 484 bridge at a frequency $\omega = 10^4$ Hz, with the amplitude of the sinusoidal test signal being 0.5 V. The sample temperature was measured using a platinum resistance thermometer with an error $\delta_T \le 2.5 \times 10^{-3}$ K. The rate of temperature variation was controlled upon heating and was $\beta = 1.2$ K/h near the ferroelectric phase transition temperature T_C.

After the measurements of the initial values of $\varepsilon'(T)$, the sample was taken out of the thermostat and placed into the gap between the ferrite plates, where it was exposed to the magnetic field at $T = 293$ K. After the magnetic processing, the sample was again connected to the measuring circuit in the thermostat, whose temperature was maintained 1.5 K lower than the initial value of T_C.

Figure 1 shows typical ferroelectric hysteresis loops of the TGS crystal measured before and after exposure to a dc magnetic field in the ferroelectric phase. As in [1], the initial loop is shifted along the electric field (E) axis. We note that Fig. 1 shows $P_s(E)$ hysteresis loops with an extremely high value of the spontaneous polarization P_s and an extremely low value of the coercive field E_k attained after the above-mentioned long-term heating of samples. This heating seems to decrease the defect concentration in the samples. The values of P_s and E_k of TGS crystals can vary within ±80% depending on their actual structure [8], and the coercive field sharply decreases at $T > 310$ K [9]. Therefore, the measured values of P_s and E_k do not contradict the relevant data [8, 9] and demonstrate the high quality of the crystal under study.

After the exposure of a sample to the dc magnetic field, the ferroelectric hysteresis loop widened; i.e., the coercive field E_k increased. The loop asymmetry disappeared, as was the case after the exposure to PMFs [1]. The initial loop profile was totally restored in ten days after the magnetic-field exposure; the samples were stored at room temperature in an exsiccator with a silica gel.

Figure 2 shows the temperature dependence of the permittivity $\varepsilon'(T)$ near the ferroelectric phase transition point for TGS samples exposed at room temperature to various dc magnetic fields in the range from 0.02 to 0.2 T over the same time $t = 30$ min. The magnetic processing causes a long-term (tens of hours at $T = 293$ K) decrease in the ferroelectric transition temperature T_C and a manyfold increase in the permittivity in the vicinity of the Curie point. The temperature dependences of the inverse permittivity shown in the inset in Fig. 2 follow the Curie–Weiss law $1/\varepsilon = C(T - T_C)$, and the magnitude of the slope of the descending branch of the curve is two times that of the ascending branch with an accuracy of 20%. This relation is typical of second-order phase transitions, to which the ferroelectric transition in TGS belongs. The ratio of the corresponding slopes before and after the exposure to a magnetic-field is

$$|k| = \frac{d}{dT}\left(\frac{1}{\varepsilon}\right)_{T<T_C} \Big/ \frac{d}{dT}\left(\frac{1}{\varepsilon}\right)_{T>T_C} = 2.5 \pm 0.5.$$

This result agrees well with the well-known theoretical value $|k| = 2.4$, which was obtained with allowance for the fact that the permittivity measured at high (10^4 Hz) frequencies is adiabatic [9]. The Curie–Weiss constants are $C = 2408$ and 2587 K before and after magnetic processing (curves *1*, *3*), respectively.

The distinctive feature of the Curie point shift ΔT_C and of the increase in the TGS crystal permittivity due to magnetic processing is the fact that the dependence of this effect on the magnetic field strength has a pronounced peak. In other words, the effect is selective with respect to the magnetic-field value. The maximum shift $\Delta T_C = 0.67$ K of the Curie point is observed for a magnetic field $B_0 = 0.08 \pm 0.01$ T. The T_C shift is accompanied by an increase in the permittivity $\varepsilon'(T_C)$ at the Curie point; this increase also selectively depends

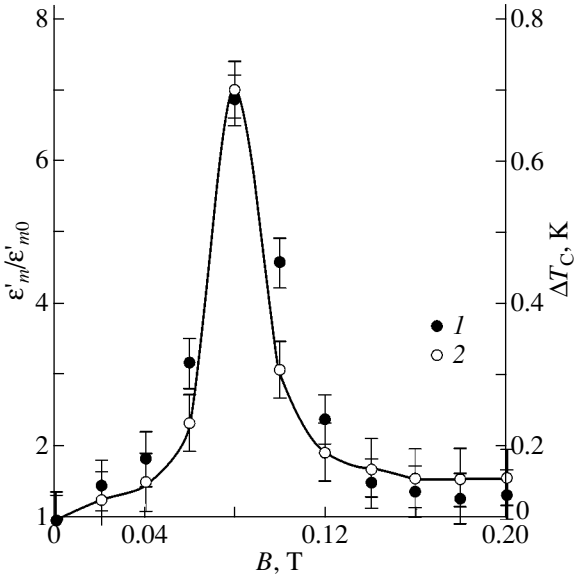

Fig. 3. Dependences (*1*) of the Curie temperature change ΔT_C and (*2*) of the relative change $\varepsilon'_m/\varepsilon'_{m0}$ of the maximum permittivity of TGS crystals on the magnetic field to which the samples were exposed at $T = 293$ K for $t = 30$ min. Each point was obtained by averaging the measurement results for seven samples.

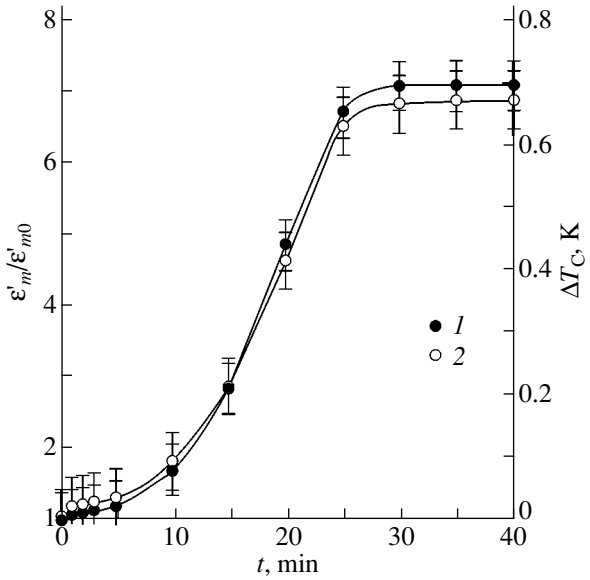

Fig. 4. Dependences (*1*) of the Curie temperature change ΔT_C and (*2*) of the relative change $\varepsilon'_m/\varepsilon'_{m0}$ of the maximum permittivity of TGS crystals on the time of exposure to a magnetic field $B_0 = 0.08$ T at $T = 293$ K.

on the magnetic field strength. The dependences of the change in the Curie temperature ΔT_C and of the relative change $\varepsilon'_m/\varepsilon'_{m0}$ on the magnetic field have a narrow peak at $B_0 = 0.08$ T, as seen from Fig. 3. Here, ε'_{m0} and ε'_m are the permittivities of the samples at the Curie point before and after the magnetic processing, respectively.

Figure 4 displays the dependences of ΔT_C and $\varepsilon'_m/\varepsilon'_{m0}$ on the duration of sample exposure to a magnetic field $B_0 = 0.08$ T. These dependences exhibit three characteristic regions: an initial portion, in which the magnetic field has no influence; a portion of a quasi-linear variation of the parameters; and a portion of flattening. It is noteworthy that the most efficient exposure effect is achieved at the processing duration $t \sim 30$ min.

An analysis of the effect of the storage time of exposed samples on the temperature dependences of the permittivity $\varepsilon'(T)$ showed that the parameters T_C and ε'_{max} relax to their initial values. The corresponding temporal dependences of $\varepsilon'_m/\varepsilon'_{m0}$ and of ΔT_C for the samples exposed to the magnetic field $B_0 = 0.08$ T for $t = 30$ min and stored at $T = 293$ K are shown in Fig. 5.

Magnetic processing in the most efficient regime ($B_0 = 0.08$ T, $t = 30$ min) of TGS crystals in the paraelectric phase (at $T = 328$ K) and in the quasi-single-domain state (at $T = 293$ K) caused no appreciable changes in their characteristics. In both cases, only an insignificant (<10%) increase in $\varepsilon'_{max}(T_C)$ was observed, which can be a consequence of a spontaneous change in this parameter near the phase transition.

The effects described above were observed for crystals exposed to a magnetic field normal to the ferroelectric *Y* axis and were absent when the field was directed along the *Y* axis.

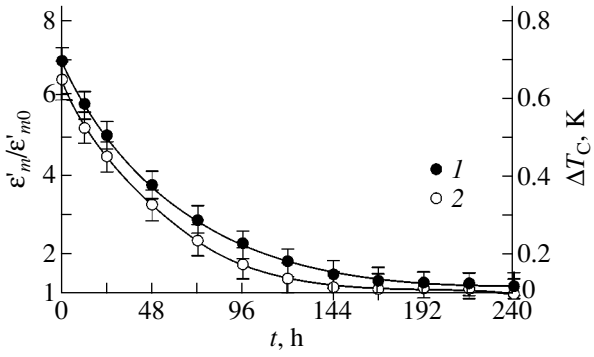

Fig. 5. Dependences (*1*) of the Curie temperature change ΔT_C and (*2*) of the relative change $\varepsilon'_m/\varepsilon'_{m0}$ of the maximum permittivity of TGS crystal samples on the time after magnetic processing with $B_0 = 0.08$ T at $T = 293$ K over the time $t = 30$ min.

3. DISCUSSION

The main result of the studies described above is the detection of the effect of a weak dc magnetic field on the properties of nominally pure ferroelectric TGS crystals.

A characteristic feature of this effect is that it has an extremum at a certain value B_0 of the dc magnetic field.

This value B_0 can be associated with the frequency ν, which satisfies the well-known condition of the electron spin resonance

$$\nu = \frac{g\mu_B B_0}{h}, \quad (1)$$

where g is the spectroscopic splitting factor.

For a free electron, we have $g \approx 2$; however, for electrons incorporated into crystal defect complexes, this value can be several times larger [10]. For example, when interpreting the effects of ionic-crystal softening caused by a change in the spin states of defects, the value $g \approx 6$ was assigned to one of the lines of the electron spin resonance spectrum [11]. For such a value of g, the resonant frequency corresponding to the magnetic field $B_0 = 0.08 \pm 0.01$ T, where the effect in question is observed in the TGS crystal, is $\nu \approx 7$ GHz; i.e., this frequency lies in the microwave range.

The effects of the resonant interaction of microwaves with nominally pure TGS crystals have also been observed previously. In [12], resonant absorption of microwave radiation by TGS crystals was detected at frequencies of 27, 28, and 33 GHz, depending on the crystallographic orientation of the samples during exposure. In [13], a dielectric-anomaly suppression by weak microwave radiation (with a peak at ~40 GHz) was detected during the ferroelectric phase transition in a TGS crystal.

We note that the above-mentioned frequencies are of the same order of magnitude, which counts in favor of the similarity of the mechanisms of the observed phenomena if we take into account the uncertainty in the factor g.

Moreover, the effect detected by us can be considered the inverse of the effect described in [13].

Indeed, the exposure of TGS crystals to a dc magnetic field decreases the ferroelectric transition temperature by ~1 K and significantly increases the permittivity near the Curie point. On the contrary, the exposure of TGS crystals to low-power microwave radiation results in an increase in the ferroelectric transition temperature of the TGS crystals by ~1 K and significantly decreases the permittivity near the Curie point [13]. In both cases, the TGS crystal characteristics relaxed to their initial values in several days after sample exposure and storage at room temperature.

The authors of [13] indicated that the regularities detected by them are typical of the case where defects are introduced into a highly perfect sample; the changes in the sample parameters described in this paper can be explained by a decrease in the number of initial defects in the crystal.

As the most weakly linked structural elements of a defect-free TGS crystal, the NH_3^+ groups of glycine bound by hydrogen bonds to other elements of the system were indicated in [13]. It was assumed that microwave radiation affects the interaction between the proton system of hydrogen bonds and the basic lattice. We note that a possible consequence of the change in this interaction can be defect generation in the TGS crystal.

At the same time, the magnetic processing can cause decay of defect complexes originally existing in a real TGS crystal. The changes in the characteristics of nominally pure TGS crystals caused by PMFs were explained in [1] by the decay of the defect and domain structures in real TGS crystals. A decrease in the number of defects that are pinning centers for domain walls in a real TGS crystal increases the permittivity, while a decrease in the concentration of ordered polar defects weakens the internal field and decreases the Curie temperature.

The changes in the characteristics of TGS crystals observed in this study, are basically similar to PMF-induced changes [1]; therefore, the same interpretation of the results remains valid in the case of exposure to a dc magnetic field. The fact that a dc magnetic field produces no effect on TGS crystals in the paraelectric phase or in the quasi-single-domain state suggests that magnetically induced processes take place in the defects–domain walls system.

The difference between the effects caused by PMFs and by dc magnetic fields (observed at various magnetic-field orientations with respect to the ferroelectric axis of the crystal) can be explained by the fact that different types of defects are sensitive to these fields.

Unfortunately, it seems to be impossible to identify the magnetosensitive defects at this stage of study of the real TGS crystal structure. While the defects pinning the domain structure of a ferroelectric TGS crystal are systematized phenomenologically in [14], their microscopic nature remains undetermined.

At the same time, it is known that the field dependence of the recombination probability of radicals in weak magnetic fields can feature a pronounced extremum in the presence of several channels of intercombination transitions [15]. Such extrema (resonances) arise in weak magnetic fields, comparable to the hyperfine interaction fields, in the case of crossing of energy levels that are separated in energy by the exchange interaction in the absence of a magnetic field or when some of the energy levels do not participate in intercombination transitions due to their Zeeman shift. In the simplest case of singlet–triplet transitions, such resonances can arise in weak magnetic fields if the transitions from the singlet state to all three sublevels of the triplet state are allowed. In dc magnetic fields, this situation is possible only when a radical pair contains at least one

nucleus with a nonzero spin involved in transitions through the hyperfine interaction.

It is reasonable to assume that the distinctive feature of the effect detected in the hydrogen-containing TGS molecular crystal, namely, its selective dependence on the magnetic field, is associated with the participation of hydrogen bond protons in spin-dependent transformations of defect complexes in real crystals.

The effect detected in this study suggests that, in complexes with hydrogen bonds, there are short-lived radicals that make these complexes sensitive to magnetic fields.

The lower resonant frequency obtained in this study for a real TGS crystal (~7 GHz), in comparison with the frequency determined in [13] for a highly perfect crystal (~40 GHz), can be explained by the fact that hydrogen bonds in defect complexes are weaker than in the lattice of the defect-free crystal.

The assumption that the selective nature of the effect in question is associated with the participation of hydrogen bond protons in spin-dependent transformations of defect complexes of real TGS crystal would be experimentally confirmed by the detection of similar effects in other molecular crystals with hydrogen bonds, in particular, in ferroelectric crystals of potassium dihydrophosphate (KDP).

REFERENCES

1. M. N. Levin, V. V. Postnikov, M. Yu. Palagin, and A. M. Kostsov, Fiz. Tverd. Tela (St. Petersburg) **45** (3), 513 (2003) [Phys. Solid State **45**, 542 (2003)].
2. M. Molotskii and V. Fleurov, Phys. Rev. B **56** (17), 10809 (1997).
3. M. Molotskii, Mater. Sci. Eng. A **287**, 248 (2000).
4. B. I. Smirnov, N. N. Peschanskaya, and V. I. Nikolaev, Fiz. Tverd. Tela (St. Petersburg) **43** (12), 2154 (2001) [Phys. Solid State **43**, 2250 (2001)].
5. S. A. Gridnev, K. S. Drozhdin, and V. V. Shmykov, Fiz. Tverd. Tela (St. Petersburg) **42** (2), 318 (2000) [Phys. Solid State **42**, 326 (2000)].
6. S. A. Flerova, N. N. Kraĭnik, N. P. Bots'va, and S. A. Popov, Pis'ma Zh. Tekh. Fiz. **29** (2), 45 (2003) [Tech. Phys. Lett. **29**, 62 (2003)].
7. M. N. Levin and B. A. Zon, Zh. Éksp. Teor. Fiz. **111** (4), 1373 (1997) [JETP **84**, 760 (1997)].
8. M. S. Tsedrik, *Physical Properties of Crystals of the Triglycinesulfate Family* (Nauka i Tekhnika, Minsk, 1986).
9. F. Jona and G. Shirane, *Ferroelectric Crystals* (Pergamon, Oxford, 1962; Mir, Moscow, 1965).
10. V. Fleurov and M. Molotskii, Ceram. Trans. **3**, 57 (2001).
11. Yu. I. Golovin, R. B. Morgunov, V. E. Ivanov, and A. A. Dmitrievskiĭ, Zh. Éksp. Teor. Fiz. **117** (6), 1080 (2000) [JETP **90**, 939 (2000)].
12. A. M. Kostsov, Izv. Ross. Akad. Nauk, Ser. Fiz. **64** (9), 1712 (2000).
13. V. K. Novik, G. I. Ovchinnikova, Yu. A. Pirogov, and A. N. Soloshenko, Izv. Ross. Akad. Nauk, Ser. Fiz. **64** (12), 2452 (2000).
14. A. N. Shil'nikov, A. P. Pozdnyakov, V. N. Nesterov, *et al.*, Fiz. Tverd. Tela (St. Petersburg) **43** (8), 1516 (2001) [Phys. Solid State **43**, 1576 (2001)].
15. A. L. Buchachenko, R. Z. Sagdeev, and K. M. Salikhov, *Magnetic and Spin Effects in Chemical Reactions* (Nauka, Novosibirsk, 1978).

Translated by A. Kazantsev

Physics of the Solid State, Vol. 45, No. 9, 2003, pp. 1768–1773. Translated from Fizika Tverdogo Tela, Vol. 45, No. 9, 2003, pp. 1685–1690.

MAGNETISM AND FERROELECTRICITY

The Effect of Stresses on Self-Polarization of Thin Ferroelectric Films

I. P. Pronin*, E. Yu. Kaptelov*, A. V. Gol'tsev*, and V. P. Afanas'ev**

** Ioffe Physicotechnical Institute, Russian Academy of Sciences, Politekhnicheskaya ul. 26, St. Petersburg, 194021 Russia*

*** St. Petersburg State Electrotechnical University, ul. Prof. Popova 5, St. Petersburg, 197376 Russia*

Received February 14, 2003

Abstract—The effect of stresses, appearing due to a difference between the temperature coefficients of linear expansion of a substrate and ferroelectric film, on the self-polarization is discussed using thin films of lead zirconate–titanate $PbZr_xTi_{1-x}O_3$ (PZT) of different compositions as an example. It is assumed that the nature of self-polarization is connected with internal polarizing electric fields caused by the different density of charged surface states at the ferroelectric-layer interfaces, while tensile or compressive stresses are able only to change the polarization orientation, which causes the self-polarization to increase or decrease in magnitude. The problem of improving the efficiency of PZT films in infrared radiation detectors and memory devices is considered.

1. INTRODUCTION

The polar state that is established in a thin-film ferroelectric capacitor without application of an external polarizing electric field is due to self-polarization [1–6]. As a rule, such a state originates in a ferroelectric film during its transition to the ferroelectric phase in the process of cooling after the formation of its crystalline structure at a high temperature. Investigations have shown that the magnitude of self-polarization depends on the structure [7–13], composition [7, 9, 14–16], and thickness of the ferroelectric film [7], as well as on the material of the electrodes [7, 17–19], electric fields [4, 6, 9, 20–22], mechanical stresses [2, 5, 14], optical radiation [20], the temperature of heat treatment [4, 6, 7, 11, 12, 23, 24], the composition of the atmosphere [8, 16] in which the multilayer structure is formed, etc.

Self-polarized films are of interest for two reasons. On the one hand, such films can be used in the production of integrated infrared radiation detectors with high spatial resolution if their pyroelectric parameters are comparable to the parameters of films polarized by an external electric field [7, 14, 15, 25, 26]. In this case, there is no need for a polarization procedure, which is usually carried out with the application of strong electric fields at elevated temperatures.

On the other hand, self-polarization turns out to be an undesirable phenomenon when films are used in devices based on the polarization switching, for example, in memory devices (FRAM) that conserve information when the energy supply is disconnected. In such devices, the asymmetry of the dielectric hysteresis makes reliable readout of information impossible, because the two logical states cannot be differentiated [3, 8, 16, 20, 21, 27].

The reasons for the origination of a self-polarized state in thin ferroelectric films are considered to be connected with the action of both electric fields [4, 6–28] and stresses [2, 3, 14, 29, 30]. Asymmetry of dielectric hysteresis loops and of *C–V* characteristics, the size effect, a change in polarity or a complete disappearance of self-polarization at high-temperature annealing, etc., are evidence in favor of the electric nature of self-polarization. Earlier, the authors suggested an electric model which explains the properties of self-polarized $PbZr_xTi_{1-x}O_3$ (PZT) films. According to this model, the necessary conditions for the origination of a self-polarized state are the presence of free charge carriers and a different density of localized charges on the interfaces of a ferroelectric film [10–12].

The properties of self-polarized films can be explained by the action of mechanical forces as well [2, 3, 14, 29, 30]. In particular, the authors of [2, 3, 14] believe that compressive stresses in films can change the polarization direction (from its orientation in the substrate plane to the orientation parallel to the normal to this plane). However, the effect of stresses on the self-polarization has not yet been evaluated in the literature. The present work offers such evaluations for thin PZT films.

2. MODEL OF THE EFFECT OF STRESSES ON SELF-POLARIZATION

A self-polarized state in a ferroelectric film can be influenced by at least two kinds of stresses of different nature. The first one is connected with a mismatch of the lattice parameters of the lower electrode and the substrate with those of the ferroelectric film. The second one is connected with different temperature coefficients of linear expansion of the substrate and the ferro-

1063-7834/03/4509-1768$24.00 © 2003 MAIK "Nauka/Interperiodica"

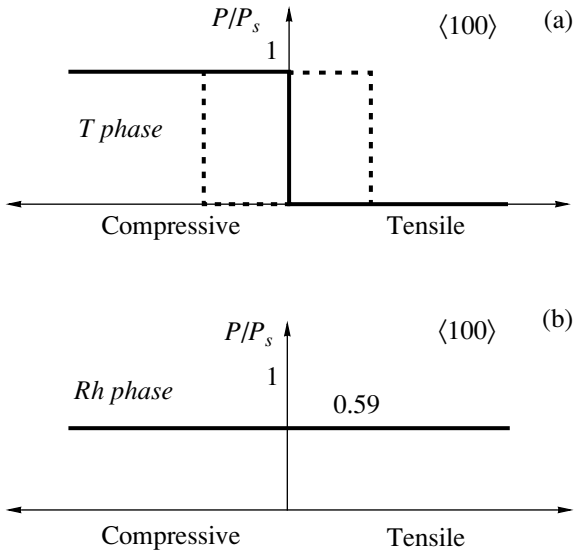

Fig. 1. Calculated diagrams showing the change in the self-polarized state (in relative units) under the influence of compressive and tensile stresses for ⟨100⟩-oriented PZT films whose compositions correspond to (a) tetragonal and (b) rhombohedral phases.

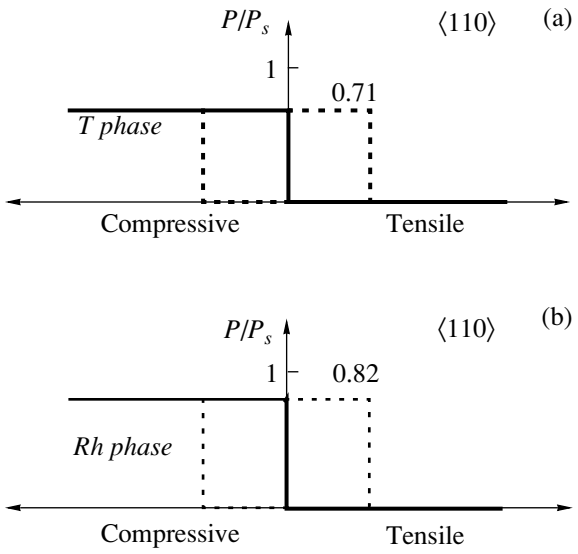

Fig. 2. Calculated diagrams showing the change in the self-polarized state (in relative units) under the influence of compressive and tensile stresses for ⟨110⟩-oriented PZT films whose compositions correspond to (a) tetragonal and (b) rhombohedral phases.

electric layer. The model under consideration is based on the fact that a polycrystalline PZT film is characterized by a columnar structure with a grain cross section of no more than 100 nm, which allows one to ignore the stresses connected with the lattice mismatch [12].

The model suggests that, in the process of deposition, a ferroelectric film crystallizes in the perovskite structure. Thus, it is natural to suppose that the forming film is in a stress-free state. During cooling, the film is subjected to mechanical compression or tension produced by the substrate (depending on the relationship between the temperature coefficients of linear expansion of the film and the substrate). By analogy with [3], we assume that the ferroelectric film is rigidly connected with the substrate and that the strains and stresses in it are homogeneous. The model does not take into account the mechanical influence of the lower electrode on the formation of a self-polarizing state, because, in the case of ferroelectric films 1 μm or greater in thickness, the lower electrode (the thickness of which is less than 100 nm) practically does not influence the magnitude of stresses produced in a PZT film by the substrate.

Due to stresses, the domain structure of a ferroelectric film is rearranged so as to minimize the free energy of the system. Therefore, in the case of compressive stresses, the orientation of the polar axis (depending on the allowed crystallographic directions) will be maximally close to the normal to the substrate. On the contrary, in the case of tensile stresses, the polar axis will be oriented maximally close to the substrate plane. It can also be supposed that the polarization of the crystalline lattice is parallel to the direction along which the unit cell is elongated. At the same time, stresses are able to orient the polarization vector only to within 180° domains. Therefore, the formation of a macroscopic polarization is possible only under the influence of an electric field. The strength of the polarizing field can be relatively low, because this field must be capable of switching 180° rather than 90° domains. Thus, when considering the effect of stresses on the self-polarization, we assume that the formation of a macroscopic polar state takes place in an electric field that switches all 180° domains along the field direction. It should be noted that a self-polarized state is mainly formed during the transition through the Curie temperature to the ferroelectric phase, where polarization switching can take place in relatively weak electric and stress fields.

The diagrams in Figs. 1–3 show the influence of compression or tension on the orientation of the spontaneous polarization P_s in a ferroelectric layer depending on the texture of the layer growth and on the symmetry of the ferroelectric phase for PZT films with different compositions. It is seen that, in ⟨100⟩-textured films of tetragonal symmetry, the polarization switching can take place when tensile stresses are changed to compressive ones (Fig. 1a). In this case, the self-polarization changes from zero to its maximum possible value, which is equal to the spontaneous polarization. In rhombohedral films, stresses do not cause polarization switching (Fig. 1b).

A somewhat different situation occurs in ⟨110⟩-oriented films (Fig. 2), in which the polarization changes in a jump, as in Fig. 1a, in both the tetragonal and rhombohedral phases. However, in ⟨110⟩-textured films, the

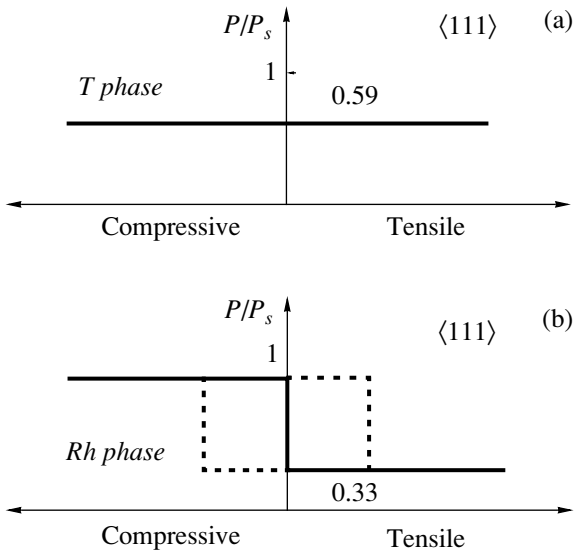

Fig. 3. Calculated diagrams showing the change in the self-polarized state (in relative units) under the influence of compressive and tensile stresses for ⟨111⟩-oriented PZT films whose compositions correspond to (a) tetragonal and (b) rhombohedral phases.

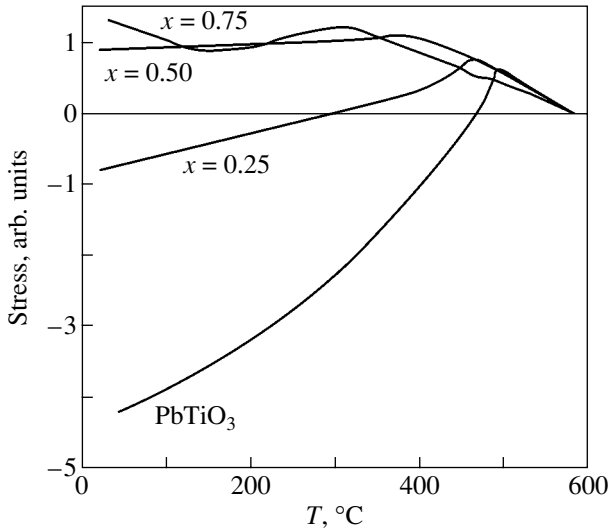

Fig. 4. Calculated temperature dependences of the stresses (in relative units) in PZT films with a different ratio x = Zr/(Zr + Ti) in the silicon substrate–PZT film system. Negative stresses correspond to compression of the films.

self-polarization produced by a compressive stress is smaller in magnitude.

Finally, in ⟨111⟩-oriented tetragonal films, stresses do not influence the magnitude of the polarization (Fig. 3a), which can be as large as $P = 0.59P_s$. In passing from compressive to tensile stresses in rhombohedral films, the polarization ($P = P_s$) undergoes a jump to the value $P = 0.33P_s$ rather than to zero, as in the two previous cases.

To determine the sign and magnitude of the change in stresses originating in thin PZT films of the perovskite structure during cooling, we used data on the linear expansion of solid solutions at different values of the ratio Zr/Ti [31]. Calculations were performed for single-crystal silicon substrates with a temperature coefficient of linear expansion $\alpha_l = 2.8 \times 10^{-6}$ K^{-1}. The results of calculations of stresses arising in a thin PZT film on a silicon substrate are presented in Fig. 4. The calculations were carried out under the assumption that the ferroelectric layer was deposited at a substrate temperature of 580°C.

As follows from Figs. 1–4, the self-polarized state in PZT films strongly depends on their texture of growth. It is seen that, as the composition of the tetragonal solid solution becomes progressively closer to that of lead titanate, compressive stresses grow. This is due to the strong positive electrostriction effect and the negative value of α_l in lead titanate and solid solutions close to lead titanate in composition below the Curie temperature. However, as the Zr concentration is increased, compressive stresses are replaced by tensile ones, because α_l becomes positive and increases. From the stress diagram (Fig. 4), it follows that, as the Zr content increases in films of tetragonal symmetry, the changes in the self-polarized state presented in Figs. 1a, 2a, and 3a should take place, because compression is replaced by tension. For rhombohedral films subjected to tensile stresses, the self-polarization is described by the right-hand parts of the diagrams in Figs. 1b, 2b, and 3b.

It is of special interest to analyze the influence of stresses on the self-polarization of PZT films whose composition corresponds to the region of the morphotropic phase boundary (MPB) dividing the tetragonal and rhombohedral phases [31, 32]. Figure 5 displays diagrams of the changes in the self-polarized state in the MPB region for films with different growth structure; these diagrams are constructed on the basis of the stress diagrams (Figs. 1–3) and Fig. 4. It is clearly seen that the behavior of self-polarization is significantly different in films with different crystallographic orientations. In particular, in ⟨111⟩-oriented films, the self-polarization decreases by a factor of approximately 1.8 with increasing Zr content (Fig. 5c).

3. COMPARISON OF THE MODEL WITH THE EXPERIMENTAL DATA

At the present time, two experimental papers are available in which the concentration dependence of the self-polarized state in thin PZT films was investigated [7, 14]. In [7], films were produced using a two-stage technology, which significantly impedes the analysis of the effect of stresses on the self-polarization. However, the results obtained in [14] on ⟨111⟩-oriented films (Fig. 6) satisfy all the requirements of our model.

According to Figs. 3 and 5c, the model describing the mechanical contribution to the polarization of such films suggests that the value of self-polarization is constant over the entire range of existence of the tetragonal phase and sharply decreases by a factor of approximately 1.8 at the transition to the region of existence of the rhombohedral phase. The experimental concentration dependence of self-polarization (curve *1* in Fig. 6) also exhibits an analogous drop in self-polarization in the MPB region; the value of the drop is close to the calculated value. Unlike the model curve, the experimental self-polarization decreases monotonically in the tetragonal phase with increasing Zr content and continues to fall after the transition to the rhombohedral phase. To explain this curve, it is necessary to take into account the electric contribution to the self-polarization. According to [7, 9–13], the self-polarized state appears in a thin film under the influence of an electric field, which produces a volume charge localized on the lower electrode–ferroelectric interface. The influence of the field during cooling of the film to below the Curie temperature leads to the formation of a polar state near the boundary of the film. If the electric field is strong enough and the film is thin, then the whole volume of the film can be polarized.

The penetration depth of the electric field into a ferroelectric can be evaluated using the method for evaluating the size of the depletion region in an extrinsic semiconductor near the metal–semiconductor junction [33]:

$$\varphi(y) = \varphi_0 \exp(-y/l_D), \quad (1)$$

where $l_D = (\varepsilon k_B T/4\pi n e^2)^{1/2}$ is the Debye screening length, ε is the dielectric constant of the ferroelectric layer, T is temperature, n is the concentration of charge carriers in the ferroelectric, k_B is Boltzmann's constant, φ_0 is the potential at the interface ($y = 0$), and $\varphi(y)$ is the distribution of the potential. By differentiating Eq. (1) with respect to the coordinate y, we obtain

$$E(y) = (\varphi_0/l_D)\exp(-y/l_D) = (A/\varepsilon^{1/2})\exp(-y/l_D), \quad (2)$$

where $E(y)$ is the distribution of the electric field in the ferroelectric and $E_0 = A/\varepsilon^{1/2}$ is the electric field at the interface. Evaluation of the screening length at a temperature close to the ferroelectric phase transition point ($T = 600$ K, $\varepsilon = 1000$, $n = 10^{17}$ cm^{-3}) gives $l_D = 0.17$ μm. If the surface potential is 0.01 V, then the electric field at the interface will be approximately 0.6 kV/cm. Such a field generated by the charges at the interface suffices to polarize the film at a temperature close to the Curie point.

As can be seen from formula (2), the value of the polarizing electric field E_0 is inversely proportional to the square root of the dielectric constant of the ferroelectric. As the dielectric constant $\varepsilon(x)$ in PZT films changes nonmonotonically and has a maximum in the MPB region [14] (curve *3* in Fig. 6), the concentration dependence of the relative self-polarization can be written as

$$P(x)/P_{max} = [\varepsilon_{th}/\varepsilon(x)]^{1/2},$$

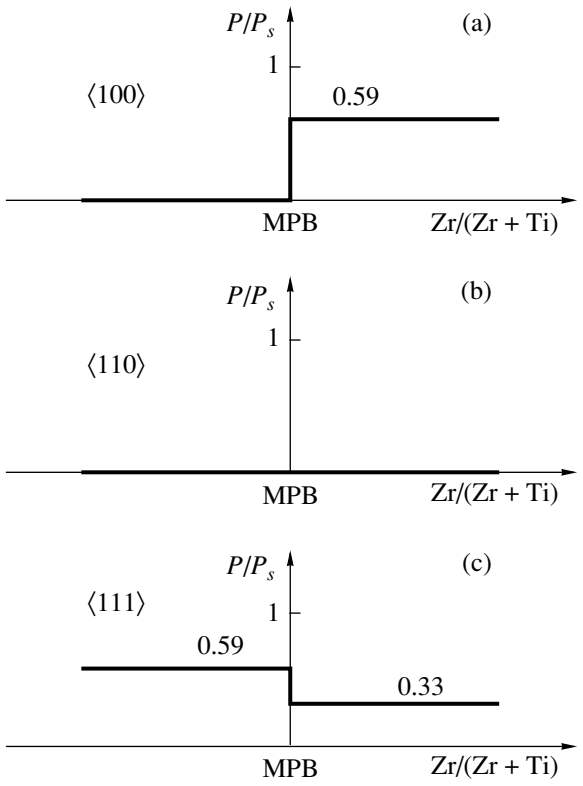

Fig. 5. Calculated diagrams showing the change in the self-polarized state (in relative units) in the region of the morphotropic phase boundary for (a) ⟨100⟩-, (b) ⟨110⟩-, and (c) ⟨111⟩-oriented thin PZT films under the conditions of tension in the silicon substrate–PZT film system.

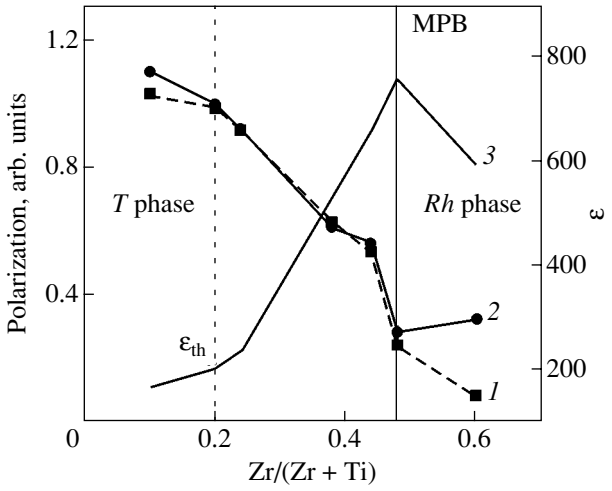

Fig. 6. Concentration dependences of the self-polarization [(*1*) experimental [14] and (*2*) calculated] and (*3*) of the dielectric constant [14] for thin films of PZT solid solutions.

where ε_{th} is the threshold dielectric constant at which the self-polarization reaches its maximal value P_{max} ($\varepsilon_{th} = 209$ for the composition Zr/(Zr + Ti) = $x = 0.20$). This dependence (with allowance for the jump in self-polarization at the MPB) is presented by curve *2* in Fig. 6. A comparison of curves *1* and *2* shows that our model adequately describes the experimental behavior of self-polarization both in the tetragonal phase and at the MPB. The model description of the influence of stresses on the behavior of the self-polarization (Fig. 5c) near the transition across the MPB in ⟨111⟩-oriented films is supported by the experimental data from [14].

4. DISCUSSION OF THE RESULTS

The above analysis shows that the self-polarization in thin ferroelectric films is of an electromechanical nature. An important feature of the model is the connection of the polarizing electric field at the interface between the lower electrode and the ferroelectric film with the dielectric constant. According to formula (2), for polarization of a ferroelectric, it is more important to have a lower dielectric constant (and, consequently, a stronger field at the interface) than larger values of the dielectric constant and Debye screening length. This fact evidently follows from the need for a higher energy for nucleation of a domain on the interface than for its growth deep into the film.

The stresses due to the difference between the α_l values of the ferroelectric layer and the substrate are not the reason for the appearance of self-polarization, but they influence the magnitude of the self-polarization during compression or tension of the ferroelectric film and a change in its structure and orientation, in the thickness ratio of the substrate and the film, and in the technology of formation of the ferroelectric layer. In the silicon substrate–PZT film system, the compressive stresses acting in PZT film close to lead titanate in composition determine the magnitude of the self-polarization. These stresses lead to the destruction of 90° domains and are favorable for the formation of a 180° domain structure, which decreases the coercive field. Unfortunately, the absence of experimental data on the concentration dependences of the self-polarized state does not allow one to test the validity of the models under consideration completely (for films of different compositions and orientations). Investigations of ⟨100⟩-oriented PZT films grown on silicon substrates are of particular interest. In this case, a distinctly expressed concentration dependence of self-polarization should be expected (Figs. 1a, 5a).

The results obtained in this work reveal the role of stresses in the origination of self-polarization and allow one to formulate criteria for choosing PZT films compositions for different applications.

(1) For pyroelectric detectors based on silicon substrates, ⟨100⟩-textured PZT films with compositions close to that of lead titanate are preferable. In these films, the self-polarization is high, because the stresses orient the polarization vector along the normal to the substrate plane. Technological difficulties in producing such structures are connected with the fact that the traditionally used platinum electrodes are characterized by ⟨111⟩ growth texture, which dictates the ⟨111⟩ orientation of PZT films. Nevertheless, there are processing techniques that allow one to obtain ⟨100⟩-oriented PZT films of good quality [34]. When using substrates with α_l equal to $(6–8) \times 10^{-6}$ K^{-1} and more, ⟨111⟩-oriented PZT films of the rhombohedral modification, which is sufficiently far from the MPB, are of great interest. The pyroelectric coefficient of such compositions is considerably higher than that for the compositions close to lead titanate, as follows from the results presented in [1].

(2) For memory devices (FRAM), it is important to decrease the concentrations of defects and charge carriers, which allows one to obtain thin stoichiometric PZT films with symmetrical hysteresis loops and *C–V* characteristics. For stable operation of the devices, it is reasonable to use PZT films without 90° domains. This situation is realized in ⟨100⟩-oriented PZT films of tetragonal modification (on silicon substrates) with compositions close to lead titanate (Figs. 1a, 4). The absence of 90° domains decreases the switched electric fields and increases the switched charge. The efficiency of memory devices can be improved by using ⟨111⟩-oriented PZT films of the rhombohedral modification formed on substrates with high values of α_l. In this case, ferroelectric films are also in a state of compression and their domain structure contains only 180° domains. The fatigue, which is one of the main reasons for premature breakdown of FRAM devices, will be connected only with the formation of head-to-head domains.

Nevertheless, the majority of investigators focus mainly on the influence of electric defects and fields on the degradation of the film parameters [35] in analyzing fatigue and do not take into account the contribution of stresses to the fatigue. Thus, it is interesting to carry out additional investigations of the role of stresses in the effect of fatigue.

ACKNOWLEDGMENTS

This work was supported by the Russian Foundation for Basic Research (project no. 01-02-17-799) and the Ministry of Education of the Russian Federation (project no. E02-3.4-89).

REFERENCES

1. M. Adachi, T. Matsuzaki, N. Yamada, *et al.*, Jpn. J. Appl. Phys. **26** (4), 550 (1987).
2. E. Sviridov, I. Sem, V. Alyoshin, *et al.*, Mater. Res. Soc. Symp. Proc. **361**, 141 (1995).
3. A. V. Gorish, V. P. Dudkevich, M. F. Kupriyanov, A. E. Panich, and A. V. Turik, *Piezoelectric Device*

Building, Vol. 1: *Physics of Ferroelectric Ceramics* (Radiotekhnika, Moscow, 1999).
4. R. Dat, D. J. Lichtenwalner, O. Auciello, and A. I. Kingon, Integr. Ferroelectr. **5**, 275 (1994).
5. G. A. C. M. Spierings, G. J. M. Dormans, W. G. J. Moors, *et al.*, J. Appl. Phys. **78**, 1926 (1995).
6. H. Maiwa, N. Ishinose, and K. Okazaki, Jpn. J. Appl. Phys., Part 1 **33** (9B), 5240 (1994).
7. A. L. Kholkin, K. G. Brooks, D. V. Taylor, *et al.*, Integr. Ferroelectr. **22**, 525 (1998).
8. J. Lee and R. Ramesh, Appl. Phys. Lett. **68** (4), 484 (1996).
9. S. Okamura, S. Miyata, Y. Mizutani, *et al.*, Jpn. J. Appl. Phys., Part 1 **38** (9B), 5364 (1999).
10. V. P. Afanasjev, A. A. Petrov, I. P. Pronin, *et al.*, J. Phys.: Condens. Matter **13** (39), 8755 (2001).
11. I. P. Pronin, E. Yu. Kaptelov, E. A. Tarakanov, and V. P. Afanas'ev, Fiz. Tverd. Tela (St. Petersburg) **44** (9), 1659 (2002) [Phys. Solid State **44**, 1736 (2002)].
12. I. P. Pronin, E. Yu. Kaptelov, E. A. Tarakanov, *et al.*, Integr. Ferroelectr. **49**, 285 (2002).
13. J. Frey, F. Schlenkrich, and A. Schonecker, Integr. Ferroelectr. **35**, 195 (2001).
14. R. Bruchhaus, D. Pitzer, M. Schreiter, and W. Wersing, J. Electroceram. **3** (2), 151 (1999).
15. M. Kobune, H. Ishito, A. Mineshige, *et al.*, Jpn. J. Appl. Phys., Part 1 **37** (9B), 5154 (1998).
16. S. Hiboux and P. Muralt, Integr. Ferroelectr. **36**, 83 (2001).
17. R. Jiménez, C. Alemany, and J. Mendiola, Ferroelectrics **268**, 131 (2002).
18. C. H. Choi, J. Lee, B. H. Park, and T. W. Noh, Integr. Ferroelectr. **18** (39) (1997).
19. K. W. Kwok, B. Wang, H. L. W. Chan, and C. L. Chov, Ferroelectrics **271**, 69 (2002).
20. G. E. Pike, W. L. Warren, D. Dimos, *et al.*, Appl. Phys. Lett. **66** (4), 484 (1995).
21. W. L. Warren, B. A. Tuttle, D. Dimos, *et al.*, Jpn. J. Appl. Phys., Part 1 **35** (2B), 1521 (1996).
22. R. Poyato, M. L. Calzada, J. Ricote, *et al.*, Integr. Ferroelectr. **35**, 77 (2001).
23. E. G. Lee, J. S. Park, J. K. Lee, and J. G. Lee, Thin Solid Films **310**, 327 (1997).
24. E. G. Lee, J. K. Lee, J.-Y. Kim, *et al.*, J. Mater. Sci. Lett. **18**, 2025 (1999).
25. R. Kohler, N. Neumann, N. Heß, *et al.*, Ferroelectrics **201**, 83 (1997).
26. R. Kohler, G. Suchaneck, P. Padmini, *et al.*, Ferroelectrics **225**, 57 (1999).
27. M. Grossmann, O. Lohse, T. Scheller, *et al.*, Integr. Ferroelectr. **37**, 205 (2001).
28. Yu. A. Boikov and T. Claeson, Physica B (Amsterdam) **311**, 250 (2002).
29. K. Abe, S. Komatsu, N. Yanase, *et al.*, Jpn. J. Appl. Phys., Part 1 **36** (9B), 5846 (1997).
30. T. Yasumoto, N. Yanase, K. Abe, and T. Kawakubo, Jpn. J. Appl. Phys., Part 1 **39** (9B), 5369 (2000).
31. B. G. Shirane, K. Suzuki, and A. Takeda, J. Phys. Soc. Jpn. **7** (1), 12 (1952).
32. B. Jaffe, W. R. Cook, and H. Jaffe, *Piezoelectric Ceramics* (Academic, New York, 1971; Mir, Moscow, 1974).
33. A. I. Ansel'm, *Introduction to the Theory of Semiconductors* (Nauka, Moscow, 1978).
34. K. A. Vorotilov, M. I. Yanovskaya, and O. A. Dorokhova, Integr. Ferroelectr. **3**, 33 (1993).
35. A. K. Tagantsev, I. Stolichnov, E. L. Colla, and N. Setter, J. Appl. Phys. **90** (3), 1387 (2001).

Translated by A. Titov

Physics of the Solid State, Vol. 45, No. 9, 2003, pp. 1774–1779. Translated from Fizika Tverdogo Tela, Vol. 45, No. 9, 2003, pp. 1691–1695.

MAGNETISM AND FERROELECTRICITY

Orientational and Fluctuation Polarizations of Langevin Dipoles in a Random Electric Field

S. A. Prosandeev

Rostov State University, ul. Zorge 5, Rostov-on-Don, 344007 Russia

Received March 3, 2003

Abstract—The polarization and dielectric susceptibility of polar regions composed of Langevin microdipoles in a random electric field are considered. It is shown that the polarization of this system has orientational and fluctuation components in addition to the conventional phonon contribution. Both components diverge when the amplitude of the random field tends to zero but can be stabilized in finite internal fields. The orientational susceptibility does not depend on the external field if its amplitude is smaller than the amplitude of the random field and rapidly decreases in the opposite case. The field dependence of the fluctuation susceptibility exhibits a maximum. With an increase in the field, the fluctuation susceptibility quadratically increases as const + AE^2 in weak fields and decreases as $E^{-1/2}$ in strong fields. The equation of state takes the form $P^2 \sim E$ in relatively strong fields (as compared to the internal field) and $P \sim E$ in weak fields. © *2003 MAIK "Nauka/Interperiodica"*.

1. INTRODUCTION

This paper is concerned with the specific features of the polarization of inhomogeneous ferroelectrics composed of isolated polar regions in random fields. The importance of this problem stems from both the unique dielectric properties of disordered ferroelectrics that are widely used in practice and the necessity of elaborating a consistent theory of these properties [1–4]. Polar regions are formed in disordered ferroelectric crystals owing to local chemical inhomogeneities and disordering of the system. As a result, the crystal contains finite ferroelectric nanoregions. Local phase transformations in ferroelectric nanoregions give rise to very large local dipole moments [2, 3]. Blinc *et al.* [2] revealed that the interaction between these dipoles can initiate either a glass phase transition or a ferroelectric phase transition, depending on whether or not the dispersion of dipole–dipole interaction forces exceeds the mean interaction force. On this basis, each dipole was described as a quasi-spin in a multidimensional vector space. In the present work, this approach was extended to the case where dipoles in the polar regions are considered in the hydrodynamic approximation [5]. Within this approximation, microdipoles in a polar region change their positions in such a way that the square of the magnitude of the total dipole moment vector remains constant but the vector direction can fluctuate. The applicability of this approximation is particularly justified in the vicinity of the morphotropic boundary, i.e., in the region where the local polarization rather readily frustrates.

2. THEORY

It is known that the average magnitude of the dipole moment oriented in an external field $\mathbf{E}_0$ is defined by the Langevin formula $\mu = \mu_0 \tanh(E_0\mu_0/3k_BT)$, where μ_0 is the dipole moment at $T \longrightarrow 0$. For this system, the longitudinal linear susceptibility is finite ($\chi_\parallel = n\mu_0^2/3k_BT$, where n is the dipole concentration) but the transverse linear susceptibility diverges, because the energy of the system is degenerate with respect to the rotation of the dipole around the longitudinal field [5]. Therefore, this idealized system is characterized by an instability (Goldstone instability) and tends to remove the energy degeneracy.

In actual fact, microdipoles in crystals reside in extra internal fields **e**, which are induced by surrounding atoms and structural defects. These fields are particularly strong in solid solutions of ferroelectrics [3, 4]. Consequently, the microdipoles in crystals are aligned not with the external field but with the local field $\mathbf{E}_l = \mathbf{e} + \mathbf{E}$, where $\mathbf{E} = \mathbf{E}_0 + \gamma\mathbf{P}$, $\mathbf{P}$ is the polarization, and γ is the Lorentz constant. As a result, there arises an intricate situation where the microdipoles deviate only slightly from the directions of random internal fields in response to an external field. It can easily be shown that, in this case, the sum of the squares of dipole moments of individual polar regions remains unchanged. Indeed, if the ith dipole moment is designated by μ_i and its small change upon dipole rotation is denoted by $\Delta\mu_i$, we can write the relationship $\langle(\mu_i + \Delta\mu_i)^2\rangle \approx \langle\mu_i^2 + 2\mu_i\Delta\mu_i\rangle \approx \langle\mu_i^2\rangle$. The latter approximate inequality was obtained under the condition that, in the course of hydrodynamic motion, the square of the magnitude of the total dipole moment of the polar region remains constant, because the rigid dipole can only execute rotational motion. Thus, the hydrodynamic approximation allows the use of the

1063-7834/03/4509-1774$24.00 © 2003 MAIK "Nauka/Interperiodica"

spherical model for describing a system of interacting polar regions. In recent years, this model has received wide acceptance, because it offers a satisfactory explanation of a number of relaxor properties [2]. It is worth noting that the classical spherical model [6] leads to the unusual critical exponent $\gamma = 2$, which is inconsistent with the Curie–Weiss law and corresponds to a quadratic temperature dependence of the square of the frequency of the soft polar mode (the reciprocal of the permittivity).

First, we investigate the usual orientational longitudinal polarization of polar regions and then analyze the effects associated with the instability of the transverse susceptibility. Instead of microdipoles, we consider the polarization field $\mathbf{P}(\mathbf{r}) = n\mu\mathbf{E}_l(\mathbf{r})/E_l$, which is directed along the local field at any point of space. (Hereafter, the italicized letters P, E, e, E_l, and μ stand for the magnitudes of the corresponding vectors.) The amplitude of the local field can be written in the form $E_l = \sqrt{E^2 + e^2 + 2Ee\cos\theta}$, where θ is the angle between the directions of the external and random fields. Under the assumption that the distribution function of random fields over the angle θ is isotropic, we take into account the temperatures obeying the inequality $k_BT \gg \mu_0E_l$. In this case, we obtain the standard expression $P = \mu_0^2nE/3k_BT$ for longitudinal polarization of Langevin dipoles. In the opposite limiting case ($k_BT \ll \mu_0E_l$), we have

$$P = \frac{\mu n}{2}\int_0^\pi p(\theta, E)\sin\theta d\theta = n\mu\begin{cases}1 - e^2/3E^2, & E > e\\ 2E/3e, & E < e,\end{cases} \quad (1)$$

$$p(\theta, E) = \frac{E + e\cos\theta}{\sqrt{E^2 + e^2 + 2eE\cos\theta}}.$$

The dependence thus obtained (Fig. 1) differs significantly from the Langevin curve. For $E < e$, the polarization linearly increases with an increase in the field. However, at $E = e$, the polarization changes drastically and rapidly reaches saturation with a further increase in the field. The singularity at $E = e$ is observed only for the second-order derivative of the polarization with respect to the field or (what is the same) for the first-order derivative of the nonlinear susceptibility. This behavior can be interpreted as follows. Dipoles are predominantly aligned with the random internal fields in weak external fields and with the external field when it becomes sufficiently strong. The crossover between these orientations occurs in the case when the amplitudes of the external and internal fields coincide with each other. Thus, the orientational polarization under the given conditions substantially depends on the random fields in the system.

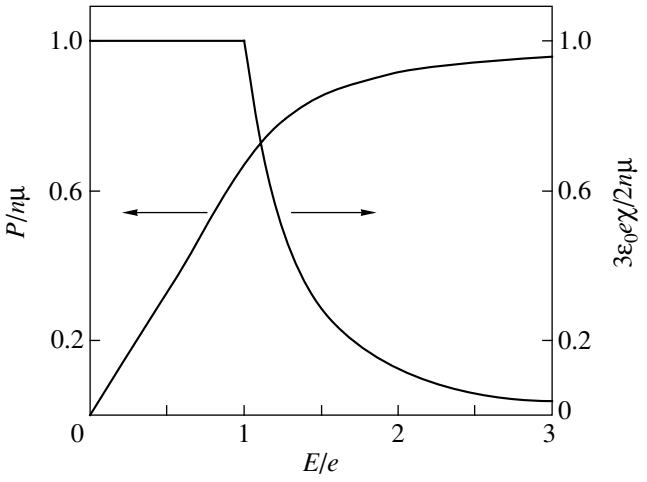

Fig. 1. Field dependences of the orientational contributions to the dielectric susceptibility and the polarization.

The inferences drawn above are also valid under the condition $\mu_0E_l \gg k_BT$. In the theory of defects, the product of the dipole moment of an individual microdipole by the electric field amplitude in dielectrics, as a rule, is assumed to be appreciably less than the thermal energy, because, otherwise, the electric fields would be very strong and lead to electrical breakdown [7]. However, in our case, we consider polar regions that involve a large number of microdipoles and change their own orientation in a cooperative manner (see below). Furthermore, each microdipole of a given polar region experiences a microscopic field that, at particular sites in ferroelectrics, can be stronger than the macroscopic field by several orders of magnitude. The microscopic fields are unrelated to the breakdown, because their averaging over a unit cell gives a usual macroscopic field. In this work, we examine a disordered crystal in which dipoles at temperatures close to a critical point execute hydrodynamic motions in regions with sizes of the order of the inhomogeneity size [5], i.e., in nanoregions. Under these conditions, the dipole moment is particularly large. It is reasonable that the large product of the dipole moment by the field amplitude can be obtained not only in strong fields (even though the local fields are very strong in ferroelectrics) but also at large dipole moments, which is assumed to be true in analyzing nanoregions. It should be emphasized that the above inequality is not necessary for hydrodynamic fluctuations to occur (for which only the local polarization need be aligned with the local field). This inequality only allows us to obtain results in an analytical form. If the given inequality is not satisfied, the required data can be calculated numerically; however, in the present work, we consider only the limiting cases for which it is possible to derived exact relationships.

Now, we analyze the behavior of the dielectric susceptibility within the same approximations. For $\mu_0 E_l \gg k_B T$, we can write the expressions

$$\chi_p = \frac{\chi_{p0}}{1-\gamma\chi_{p0}},$$
$$\chi_0 = \frac{1}{\varepsilon_0}\frac{dP}{dE_0} = \frac{2n\mu}{3\varepsilon_0}\begin{cases}1/e, & E<e\\ e^2/E^3, & E>e.\end{cases} \quad (2)$$

A specific feature of this relationship is that the dielectric susceptibility in weak fields is inversely proportional to the amplitude of the random field. Consequently, in weak random fields, the susceptibility in polar regions is very large and can even diverge when the amplitude of the random field tends to zero (provided that the temperature also approaches zero and the inequality $\mu_0 E_l \gg k_B T$ is satisfied). The results obtained suggest that the random internal fields stabilize the strongly polarized state of polar regions and contribute significantly to the permittivity due to their orientation in the field when the dipole moments in superparaelectrics are large in magnitude.

The same results can be obtained in the case when a multiwell symmetric potential rather than a continuous potential is used for an impurity. The population of each well can be determined from the Boltzmann formula, and the integrals are replaced by the sums over wells. The barriers between the wells affect only the kinetics. It can be shown that the final relationships coincide with those derived above if there exists a thermodynamic equilibrium for each field amplitude. This can be achieved by cooling the system for each field amplitude from temperatures at which the system is at thermodynamic equilibrium in the external field.

Another feature of the derived relationship is that the susceptibility does not depend on the temperature. The Langevin longitudinal susceptibility is inversely proportional to the temperature. The orientational susceptibility obtained for polar regions in the limiting case $\mu_0 E_l \gg k_B T$ does not depend on the temperature (or is only weakly dependent through the change in the dipole moment μ with temperature). This permits us to offer a new explanation for the properties of the so-called "high-k materials" [8, 9] in terms of the cooperative orientational polarization of polar regions. Actually, the specific feature of these materials is that they are characterized by the Debye susceptibility, which, as is known, is described by the expression not involving the factor $1/k_B T$ [9]. However, as was shown by Lemanov *et al.* [8], there exist a number of materials of this type for which the formula describing the susceptibility contains the factor $1/k_B T$. This implies that the size of polar regions is not large enough to satisfy the inequality $\mu_0 E_l \gg k_B T$. It should be noted that, in the majority of high-k materials, the high electrical conductivity and the formation of polar regions can be primarily associated with electrons [9].

It is also of interest to analyze the mean-square polarization. It can be assumed that, in each polar region, the mean-square polarization along the local field is finite (for example, due to a local tetragonal deformation). In this case, we have

$$\langle P^2\rangle = n\mu^2\int_{-\pi}^{\pi} p^2(\theta, E)\sin\theta d\theta$$
$$= \frac{n\mu^2}{16eE^3}\left[12eE^3 - 4e^3E + (E^2-e^2)\ln\frac{(e+E)^2}{(e-E)^2}\right]. \quad (3)$$

In weak fields E (as compared to e), we obtain

$$\langle P^2\rangle = \frac{n\mu^2}{3}\left(1 + \frac{E^2}{10e^2} + \ldots\right). \quad (4)$$

As follows from these expressions, the orientational polarization in paraelectric crystals makes a contribution to the voltage that is proportional to the field amplitude squared. For a polarized crystal, the quantity E should be replaced by $E + E_p$, where E_p is the amplitude of the internal field. As a result, the expression for the polarization takes the form

$$\langle P^2\rangle = \frac{n\mu^2}{3}\left(1 + \frac{EE_p}{5e^2} + \ldots\right). \quad (5)$$

Here, the additional voltage is linearly proportional to the field amplitude. From this analysis it is evident that polar regions can substantially contribute to the electrostriction and piezoelectric effects at small values of e (however, it should be remembered that, in the derived relationships, the amplitude e is limited from below: $\mu_0 E_l \gg k_B T$).

In the above discussion, we dealt only with quenched random fields. However, in fact, the random field has a reorientational component. In particular, the emergence of the macroscopic polarization in a sample is accompanied by alignment of the reorientational component along the polarization. This component can be described by the distribution function [10]

$$f(e) = \frac{1}{(\sqrt{\pi}d^3)}e^{-|\mathbf{e}-\eta\mathbf{P}|^2/d^2}, \quad (6)$$

where d is the distribution width and η is the coefficient relating the random field to the macroscopic polarization (as a rule, the coefficient η coincides with the Lorentz constant, which determines the difference between the local and mean fields). After averaging of the dielectric susceptibility with the given distribution function, we obtain the expression

$$\chi_0 = \frac{4n\mu}{3\varepsilon_0\eta P}\mathrm{erf}(\eta P/d),$$
$$\frac{4n\mu}{3\sqrt{\pi}\varepsilon_0 d}\left[1 - \frac{\eta^2P^2}{3d^3} + \ldots\right]. \quad (7)$$

According to relationship (7), the susceptibility increases with a decrease in the distribution width and diverges when this quantity tends to zero (provided that the temperature also approaches zero and the inequality determining saturation of the average dipole moment in the field is satisfied).

The key condition for the effects under investigation is that the system is close to an energy degeneracy. Apart from the system of oriented dipoles, one more example of such systems is provided by domains with a small elastic constant k corresponding to the restoring force acting on a domain wall. In this situation, if the field makes a random angle θ with the domain wall, the mean polarization can be represented as

$$P = \frac{2EZ^{*2}}{kv}\int_0^{\pi}\cos^2\theta\sin\theta d\theta = \frac{2EZ^{*2}}{3kv}, \qquad (8)$$

where $Z^* = P_0S$, P_0 is the domain polarization, S is the area of the domain wall, and v is the volume of one domain. As follows from relationship (8), the susceptibility (the derivative of the polarization with respect to E) is fairly high at small elastic constants k, which corresponds to a quasi-degeneracy of the system with respect to different positions of the domain walls. In order to elucidate the mechanism of the process in a particular situation, it is necessary to investigate how the orientation of microdipoles changes in the field. Rotations of the microdipoles through an angle of π correspond to motion of a domain wall. At the same time, rotations through small angles are associated with ordering of polar regions. Let us derive separating relationships for the orientational and translational polarizations. The polarization can be represented in the form $\mathbf{P} = [\boldsymbol{\mu}\varphi] + \alpha\mathbf{E}$, where φ is the rotation angle of the local microdipole under the condition $(\boldsymbol{\mu}\varphi) = 0$. Hence, we have $\alpha = (\mathbf{P}\boldsymbol{\mu})/(\boldsymbol{\mu}\mathbf{E})$ and $\varphi = \{\alpha[\boldsymbol{\mu}\mathbf{E}] - [\boldsymbol{\mu}\mathbf{P}]\}/\mu^2$. The rotational component of the polarization can be calculated from the formula $\mathbf{P}_{\text{rot}} = \mathbf{P} - (\mathbf{P}\boldsymbol{\mu})\mathbf{E}/(\boldsymbol{\mu}\mathbf{E})$. If the distribution of the angles φ is characterized by a maximum at an angle of π, the polarization occurs through the domain mechanism. It should be noted that, when the restoring force is not strong enough to return the wall to its initial position, there arises universal relaxation [11], which was recently revealed by Bokov and Ye [12] in relaxors.

Let us now analyze the transverse and longitudinal polarization fluctuations. We will follow the general approach proposed by Patashinskiĭ and Pokrovskiĭ [5], who developed a thermodynamic theory of hydrodynamic fluctuations within the continuum approximation for homogeneous isotropic media in the absence of random fields. Next, we will demonstrate how the inclusion of random fields affects the final results.

We consider a polarization field $\mathbf{P}(\mathbf{r})$ in the correlation volume of dipoles. It is assumed that a weak transverse electric field $\delta E_{l\perp}$ is applied to the system. Consequently, the transverse polarization appearing in the transverse field takes the form $\delta P_\perp = P_0\delta E_{l\perp}/E_l$, where P_0 is the polarization in the polar region. As a result, the transverse susceptibility can be written as $\chi_{l\perp} = P_0/\varepsilon_0E_l$ (for simplicity, we disregard the influence of local effects, even though it is clear that, as before, they bring about an increase in the susceptibility).

The transverse polarization at any point in space inside the polar region induces the transverse polarization at the nearest points. In order to describe this change in the polarization, the free energy of the system inside the polar region with due regard for the gradient term can be written in the following form [5]:

$$F_\perp = \int(\chi_{l\perp}^{-1}P_\perp^2 + c(\nabla P_\perp)^2 - E_{l\perp}P_\perp)dV. \qquad (9)$$

It is important to note that we consider the system in a finite longitudinal field under the assumption of an infinitesimal transverse field; i.e., we investigate the linear transverse susceptibility in the finite longitudinal field. The free energy (9) is consistent with the theory of free fluctuations, and their correlation function can be represented as

$$\langle\delta P_\perp(0)\delta P_\perp(\mathbf{r})\rangle = \frac{k_BT}{4\pi cr}\exp(-\kappa r), \qquad (10)$$

where $\kappa^2 = (c\chi_{l\perp})^{-1} = \varepsilon_0E_l/cP_0$.

With the aim of determining the longitudinal susceptibility, we use the condition for the conservation of the polarization magnitude $\delta P_P = (\delta P_\perp)^2/2P_0$ and the following mathematical operation [5]:

$$\begin{aligned}\chi_{lP} &= \frac{d}{dE_l}P_P = \frac{1}{2P}\frac{d}{dE_l}P_\perp^2 \\ &= \frac{1}{2P}\frac{d}{dE_l}\langle P_\perp(0)P_\perp(\mathbf{r})\rangle\Big|_{\mathbf{r}=0}.\end{aligned} \qquad (11)$$

As a result, we obtain

$$\delta P_P = \frac{k_BT}{8\pi(cP_0)^{3/2}(\varepsilon_0E_l)^{1/2}}\delta E_l = \frac{a}{\sqrt{E_l}}\delta E_l. \qquad (12)$$

Consequently, the local longitudinal fluctuation susceptibility $\chi_{l\parallel} = \delta P_\parallel/\varepsilon_0\delta E_l$ decreases as $E_l^{-1/2}$ in strong fields E_l.

Now, we average the polarization and the susceptibility over directions of the random field and change over to the mean susceptibility in the external field; that is,

$$\delta P_E = \delta P_\perp\frac{e\sin\theta}{E_l} + \delta P_P\frac{E + e\cos\theta}{E_l}, \qquad (13)$$

where

$$\delta P_\perp = \frac{e\sin\theta}{E_l}\frac{P_0}{\varepsilon_0E_l}\delta E, \quad \delta P_P = a\frac{E + e\cos\theta}{E_l^{3/2}}\delta E. \qquad (14)$$

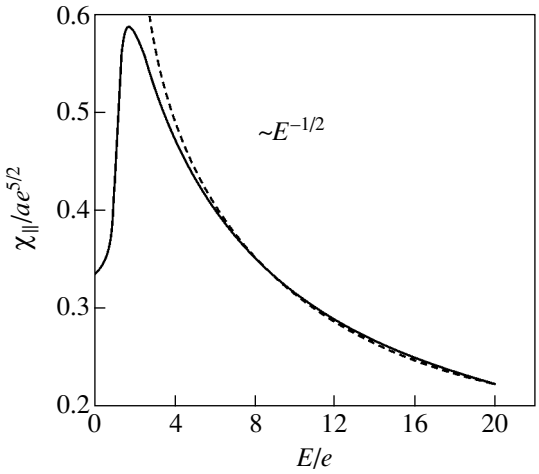

Fig. 2. Field dependence of the fluctuation contribution to the dielectric susceptibility.

Correspondingly, the dielectric susceptibility involves the transverse and longitudinal components ($\langle P_\perp \rangle = \langle \chi_\perp \rangle \delta E$ and $\langle P_\| \rangle = \langle \chi_\| \rangle \delta E$

$$\begin{aligned}\langle \chi_\perp \rangle &= \frac{1}{2}\int_0^\pi \frac{P_0 e^2 \sin^3\theta}{\varepsilon_0 E_l^3} d\theta = \frac{2P_0 e^2}{3\varepsilon_0}\begin{cases} e^{-3}, & E < e \\ E^{-3}, & E > e, \end{cases} \\ \langle \chi_\| \rangle &= \frac{a}{2}\int_0^\pi \frac{(E + e\cos\theta)^2}{E_l^{5/2}} \sin\theta d\theta \\ &= \frac{2a}{7eE^3}\{|E+e|^{7/2} - |E-e|^{7/2} \\ &\quad - \frac{7}{6}(E^2 + 2e^2)[|E+e|^{3/2} - |E-e|^{3/2}]\Big\}. \end{aligned} \quad (15)$$

The transverse component coincides with the orientational component obtained within the simpler approach. At $\mu_0 e \gg k_B T$, the transverse component is constant at field amplitudes smaller than the amplitude of the random field and rapidly decreases at $E > e$. With an increase in the amplitude of the external field, the longitudinal component increases quadratically as const + AE^2 in weak fields, passes through a maximum, and then decreases as $E^{-1/2}$ (Fig. 2). This behavior of the dielectric susceptibility is typical of antiferroelectrics and systems characterized by first-order phase transitions. However, in our case, the observed behavior is associated with the longitudinal hydrodynamic fluctuations.

It should be noted that the fluctuation contribution to the susceptibility is proportional to the temperature. However, a stronger temperature dependence arises, because the denominator of the factor a contains the term $P_0^{3/2}$. This results in the divergence (or a jump) of the fluctuation component at a temperature corresponding to the onset of polarization. Subsequently, this singularity should be smeared by the disorder occurring in the system.

3. CONCLUSIONS

Thus, it was shown that microdipoles of polar regions in disordered ferroelectrics can execute hydrodynamic cooperative motions (motions during which the magnitude of the total dipole moment of the polar region remains unchanged). This is characteristic of systems in which the amplitude of typical ferroelectric fluctuations is comparable to the radius of polar regions. The hydrodynamic motions are due to the fact that the polar region is in the state of indifferent equilibrium with respect to the direction of the total dipole moment of the region. In this case, the transverse susceptibility diverges [5] and the system turns out to be unstable. The local internal fields stabilize the system and, at not very large amplitudes, provide its high polarizability. In random fields, the transverse hydrodynamic fluctuations lead to additional orientational and fluctuation contributions to the permittivity of the system of oriented dipoles. The orientational contribution is constant in weak fields (with amplitudes smaller than the amplitude of the random field) and rapidly decreases with an increase in the field. The transverse contribution to the susceptibility first quadratically increases with an increase in the field and then decreases as $E^{-1/2}$. As a result, the equation of state takes the form $P^2 \sim E$, which was earlier experimentally observed in magnetic systems [13] and was recently revealed in dipole systems [14]. It is obvious that, as for the equation of state $P \sim E$, the polarization $P^2 \sim E$ cannot increase infinitely with an increase in the field and reaches saturation in fields E_s due to the alignment of all dipole moments with the external field. The interaction between polar regions also brings about the spontaneous alignment of dipoles in at least the nearest regions. This behavior was previously described within the models proposed in [2, 3]; however, the hydrodynamic nature of fluctuations was disregarded in these models. The present work filled this gap and generalized the theory of hydrodynamic fluctuations to systems with random fields.

The results of the investigation performed can be extended to a large number of Langevin systems. In particular, they make it possible to derive the equation of state from the data obtained in experiments on dielectric spectroscopy, second harmonic generation, etc. The proposed theory can be used for describing both the nanodipoles in relaxors, which are characterized by internal random orienting fields in addition to the frustration of the dipole moment, and dipole clusters in solid solutions of ferroelectrics, provided the procedure of freezing the system in the field is applied for each field amplitude.

ACKNOWLEDGMENTS

I am grateful to V.S. Vikhnin for his participation in discussions of the results and general support of this work.

This work was supported by the Russian Foundation for Basic Research, project no. 01-02-16029.

REFERENCES

1. A. Smolenskiĭ, V. A. Bokov, V. A. Isupov, N. N. Kraĭnik, R. E. Pasynkov, and M. S. Shur, *Ferroelectrics and Antiferroelectrics* (Nauka, Moscow, 1971).
2. R. Blinc, J. Dolinšek, A. Gregorovič, *et al.*, Phys. Rev. Lett. **83** (2), 424 (1999).
3. V. S. Vikhnin, R. Blinc, and R. Pirc, Ferroelectrics **240**, 355 (2000).
4. M. D. Glinchuk, V. A. Stephanovich, B. Hilczer, *et al.*, J. Phys.: Condens. Matter **11**, 6263 (1999).
5. A. Z. Patashinskiĭ and V. L. Pokrovskiĭ, Zh. Éksp. Teor. Fiz. **64**, 1445 (1973) [Sov. Phys. JETP **37**, 733 (1973)].
6. R. J. Baxter, *Exactly Solved Models in Statistical Mechanics* (Academic, London, 1982).
7. G. I. Skanavi, *Physics of Dielectrics* (GITTL, Leningrad, 1949).
8. V. V. Lemanov, A. V. Sotnikov, E. P. Smirnova, and M. Weilhnacht, Fiz. Tverd. Tela (St. Petersburg) **44**, 1948 (2002) [Phys. Solid State **44**, 2039 (2002)].
9. I. P. Raevski and S. A. Prosandeev, J. Appl. Phys. **93**, 4310 (2003).
10. B. E. Vugmeister and M. D. Glinchuk, Rev. Mod. Phys. **62**, 993 (1990).
11. W. Kleemann, J. Dec, S. Miga, *et al.*, Phys. Rev. B **65**, 220101-1 (2002).
12. A. A. Bokov and Z.-G. Ye, Phys. Rev. B **66** (4), 064103 (2002).
13. V. G. Vaks, A. I. Larkin, and S. A. Pikin, Zh. Éksp. Teor. Fiz. **53**, 1083 (1967) [Sov. Phys. JETP **26**, 647 (1968)].
14. S. Eden, C. Auf der Horst, and S. Kapphan, J. Korean Phys. Soc. **32**, 411 (1998).

Translated by O. Borovik-Romanova

Physics of the Solid State, Vol. 45, No. 9, 2003, pp. 1780–1783. Translated from Fizika Tverdogo Tela, Vol. 45, No. 9, 2003, pp. 1696–1699.

LATTICE DYNAMICS AND PHASE TRANSITIONS

Lattice Dynamics of Corundum Crystals with Vacancies in Various Charge States

A. N. Kislov, V. G. Mazurenko, K. N. Korzov, and V. S. Kortov

Ural State Technical University, ul. Mira 19, Yekaterinburg, 620002 Russia

e-mail: ank@dpt.ustu.ru

Received November 20, 2002

Abstract—The lattice dynamics of an α-Al_2O_3 crystal with vacancies in various charge states is simulated using the recursive method in the shell model. The frequencies of resonant vibrations induced by defects in various directions are calculated. Characteristic features in vibrational spectra of anion-nonstoichiometric α-Al_2O_3 crystals, mostly associated with changes in the effective interaction between vacancies and the nearest neighbor atoms, are analyzed and explained. *© 2003 MAIK "Nauka/Interperiodica".*

1. INTRODUCTION

Many physical properties of anion-nonstoichiometric crystals of corundum (sapphire) α-Al_2O_3 are significantly affected by oxygen sublattice defects. Therefore, it is urgent to study the features of the vibrational spectra of atoms near anion vacancies, which can be in various charge states: a vacancy with a trapped electron (F^+ center) and a vacancy with two trapped electrons (F center). The lattice dynamics of corundum crystals with vacancies has not yet been studied. There are publications devoted to experimental and theoretical study of the lattice dynamics of perfect corundum crystals [1–3]. Model and *ab initio* calculations of the energy of formation and the electronic structure of anion vacancies in various charge states in α-Al_2O_3 crystals were carried out in [4–7].

This study is aimed at numerical simulation of the lattice dynamics of α-Al_2O_3 crystals with anion vacancies in various charge states.

2. STRUCTURE, INTERATOMIC POTENTIALS, AND CALCULATION PROCEDURE

The α-Al_2O_3 crystal belongs to the rhombohedral system with space symmetry group $R\bar{3}c$ (D_{3d}^6); the primitive cell contains two formula units (ten atoms). The lattice parameters and the structure of α-Al_2O_3 are given in [2, 4]. Each oxygen O^{2-} ion is surrounded by a distorted tetrahedron of four nearest neighbor Al^{3+} ions, two of which, are Al(1), at a distance of 1.86 Å from the O^{2-} ion and the other two, Al(2), are at a distance of 1.97 Å. The nearest octahedral neighborhood of an Al^{3+} ion is formed by oxygen O^{2-} ions, three of which are at a distance of 1.86 Å from the Al^{3+} ion and the other three are at a distance of 1.97 Å.

The local atomic structure and the lattice dynamics of an α-Al_2O_3 crystal were simulated using the shell model, in which the short-range shell–shell interaction is given by

$$V(r_{ij}) = A_{ij}\exp(-r_{ij}/\rho_{ij}) - C_i/r_{ij}^6, \quad (1)$$

where A_{ij}, ρ_{ij}, and C_i are constants dependent on the ion type. The parameters of the interatomic potential taken from [5, 8] were used as the starting parameters when simulating the local atomic structure and the lattice dynamics of α-Al_2O_3 crystals.

The influence of a vacancy on the vibrational spectra of α-Al_2O_3 crystals was studied by calculating the local phonon density of states (DOS) in perfect and defect crystals by using the recursive method [9]. In this case, the local phonon DOS $g_\alpha^k(\omega)$ at the kth ion site along the Cartesian α axis is calculated as

$$g_\alpha^{lk}(\omega) = -\frac{2\omega}{\pi}\mathrm{Im}\,G_\alpha(lk, \omega), \quad (2)$$

where $G_\alpha(k, \omega)$ are the diagonal elements of the Fourier transform of the retarded Green's function,

$$G_\alpha(k, \omega) = \left\langle k\alpha\left|\frac{I}{I(\omega^2 + i\times 0) - D}\right|k\alpha\right\rangle, \quad (3)$$

I is the unit matrix and D is the dynamic matrix of the ion cluster used in the calculations.

The local-DOS calculation algorithm and the technique for separating the localized vibrations induced by defects are described in [10, 11] in more detail.

1063-7834/03/4509-1780$24.00

3. CALCULATION OF THE DISPERSION CURVES AND THE TOTAL DENSITY OF PHONON STATES OF THE PERFECT α-Al_2O_3 CRYSTAL

To check the correctness of the interatomic potential and of the cluster sizes used in modeling the crystal, we calculated the dispersion curves and the total phonon DOS of a perfect α-Al_2O_3 crystal.

The dispersion curve calculation using the starting parameters of the interatomic interaction potential from [5, 8] showed that the vibration frequencies of the first optical branch in three high-symmetry directions (Δ, Λ, Σ) in the Brillouin zone were underestimated in comparison with the experimental data [1, 2]. To improve the agreement between the calculated and experimental data by fitting the interatomic potential parameters from [5], we varied the ion charges and bond constants at fixed parameters A_{ij}, ρ_{ij}, and C_i involved in Eq. (1). The final values of the parameters are $Z_O = -1.98|e|$, $k_O = 73.07$ eV/Å^2, $Z_{Al} = 2.97|e|$, and $k_{Al} = 192.49$ eV/Å^2. The dispersion curves calculated with these parameters are shown in Fig. 1. These curves describe the experimental data much better. We note that that these parameters also adequately describe other characteristics (elastic constants and permittivities) of the perfect α-Al_2O_3 crystal.

With the parameters obtained for the interatomic potential, we calculated the total phonon DOS in perfect corundum crystals using a cluster consisting of 1000 atoms (Fig. 2). The calculated and experimental total DOS curves exhibit approximately the same number of peaks. A small-scale shift (on average by 2 THz) of the entire spectrum to lower frequencies is observed. The cutoff of the total phonon DOS in the low-frequency region is caused by the limited size of the cluster.

Thus, the satisfactory agreement between the calculated and experimental dispersion curves and total phonon DOS curves for the perfect α-Al_2O_3 crystal makes it possible to use the interatomic interaction parameters obtained and the cluster size (1000 atoms) to simulate the lattice dynamics of defect α-Al_2O_3 crystals.

4. CALCULATION OF THE LOCAL PHONON DENSITY OF STATES AND DISCUSSION

The technique described above was applied to calculate the local phonon DOS curves for perfect and defect α-Al_2O_3 crystals. The models of the F and F^+ centers (the coordinates of atoms in the defect region, the effective charge of the vacancy) are described in [6, 7]. According to those studies, the electron density localization at the vacancy center is approximately 90 and 80% for the F^+ and F centers, respectively, in the ground state. The remaining charge is spread over the nearest neighbors. The change in the charge of the vacancy and of its nearest neighbor aluminum atoms was taken into account in calculating the Coulomb component of the dynamic matrix of the cluster. The

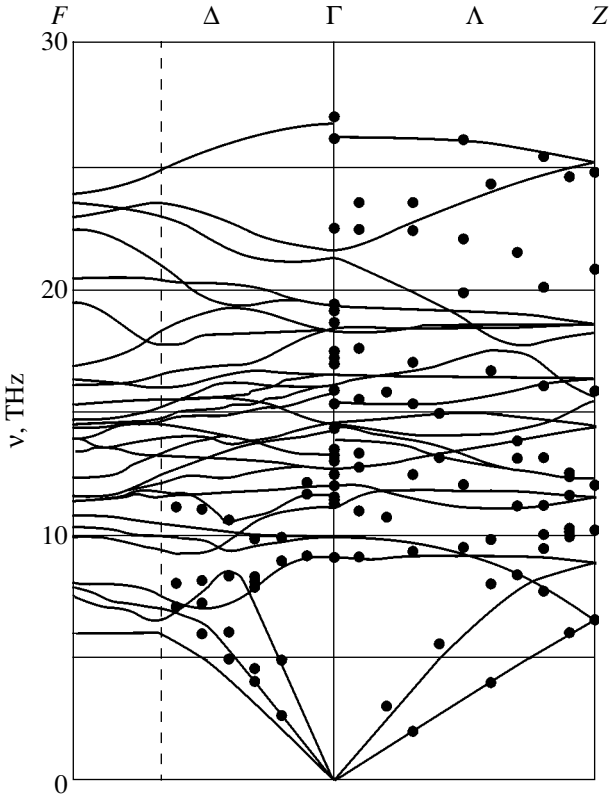

Fig. 1. Calculated dispersion curves of the α-Al_2O_3 crystal. Points are the experimental phonon frequencies [1, 2].

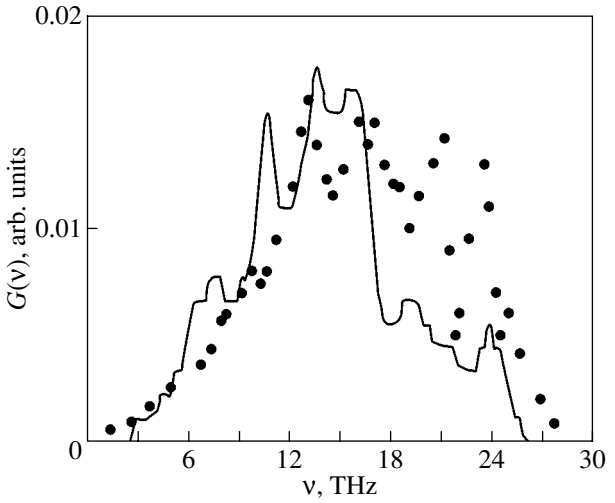

Fig. 2. Calculated total phonon density of states for the perfect α-Al_2O_3 crystal. Points are experimental data from [3].

features of the local phonon DOS of a defect crystal that are absent in the local DOS of the perfect crystal correspond to localized (resonant) vibrations induced by defects.

As an example, Fig. 3 shows the local phonon DOS at the Al(1) atom site along the Z direction in the perfect corundum (curve *1*), as well as the local phonon DOS for

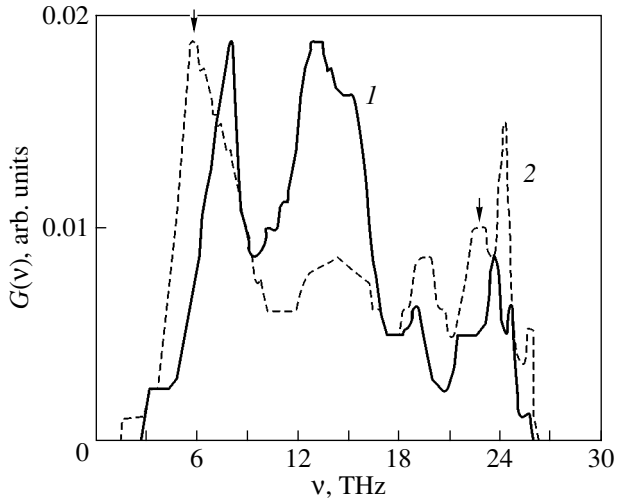

Fig. 3. Local phonon density of states along the *Z* direction at an Al^{3+} ion site (*1*) nearest to an oxygen O^{2-} ion in the perfect α-Al_2O_3 crystal and (*2*) nearest to the anion vacancy.

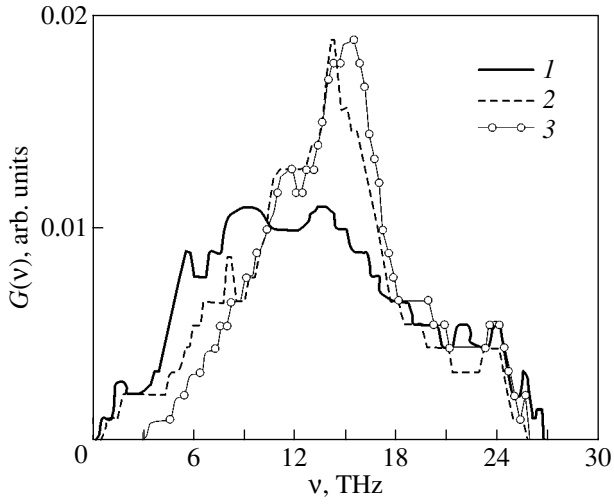

Fig. 4. Combined phonon density of states for atoms located within a sphere of radius 2.7 Å surrounding (*1*) the anion vacancy, (*2*) F^+ center, and (*3*) *F*-center.

the same atom near the anion vacancy in the defect corundum crystal (curve *2*). We can see that the introduction of the vacancy into the α-Al_2O_3 crystal gives rise to resonant vibrations at frequencies of 5.7 and 22.5 THz.

The table lists the frequencies of localized vibrations induced in the α-Al_2O_3 crystal by vacancy in various charge states along various directions at the Al ion sites from the vacancy nearest neighborhood. We can see differences in the numbers and values of the frequencies of the resonant vibration modes induced by the vacancy, F^+ center, and *F* center.

Figure 4 shows the calculated combined phonon DOS curves for all the atoms located within a sphere of radius 2.7 Å (including four Al^{3+} ions and four O^{2-} ions) near the oxygen vacancy in the crystal with a vacancy (curve *1*), an F^+ center (curve *2*), and an *F* center (curve *3*). We note that the similar combined phonon DOS for the perfect crystal coincides (except for normalization) with the total phonon DOS of the perfect crystal (Fig. 2).

Let us enumerate the basic regularities following from an analysis of Figs. 2 and 4.

(i) The combined phonon DOS curves for the perfect α-Al_2O_3 crystal and for the crystal with the F^+ center are the closest to each other.

(ii) The phonon DOS states is redistributed in the region below 19 THz when passing from the *F* center to the vacancy.

(iii) In going from the *F* center to the vacancy, the phonon DOS increases in the region below 10 THz; in the range from 10 to 19 THz, the combined phonon DOS curves for the *F* and F^+ centers are close to each other, while the combined phonon DOS for the vacancy significantly decreases.

These changes in the vibrational spectra can be explained using the concept of effective interaction between the vacancy and its nearest neighbor atoms, including the short-range and Coulomb components.

In the case of the vacancy, the effective interaction weakens, which significantly increases the combined

Frequencies of localized vibrations induced by a defect in its nearest neighbor environment

Defect	Ion	Distance to defect, Å	Frequency, THz		
			X	*Y*	*Z*
Anion vacancy	Al(1)	2.12	5.7, 22.5	6.0, 22.5	5.7, 22.0
	Al(2)	2.24	5.4	8.4	6.6
F^+ center	Al(1)	1.97		3.0, 9.6	8.2
	Al(2)	2.07		2.0, 7.8, 14.0	3.3, 11.7
F center	Al(1)	1.89		8.2, 12.0	14.7
	Al(2)	2.02	16.0	14.0	13.0

phonon DOS in the low-frequency spectral region. In the case of the F^+ center, the Coulomb interaction is partially compensated, which causes an enhancement of the effective interaction in comparison with the case of the neutral vacancy and a redistribution of the phonon DOS in the region up to 19 THz. If the vacancy center traps two electrons (with the formation of the F center), the Coulomb component of the interaction is fully restored, which further enhances the effective interaction and results in a shift of the phonon DOS in the region below 10 THz toward the high-frequency spectral region.

These data on defect vibrations will be applied to the interpretation of electron delocalization from the F and F^+ centers in α-Al_2O_3 crystals.

ACKNOWLEDGMENTS

This study was supported by INTAS, grant no. 01-0458.

REFERENCES

1. H. Bialas and H. J. Stolz, Z. Phys. B **21** (4), 319 (1975).
2. W. Kappus, Z. Phys. B **21** (4), 325 (1975).
3. C.-K. Loong, J. Eur. Ceram. Soc. **19** (13–14), 2241 (1999).
4. G. J. Dienes and D. O. Welch, Phys. Rev. B **11** (8), 3060 (1975).
5. C. R. A. Catlow, R. James, W. C. Mackrodt, and R. F. Stewart, Phys. Rev. B **25** (2), 1006 (1982).
6. A. Stashans, E. K. Kotomin, and J. L. Calais, Phys. Rev. B **49** (21), 14854 (1994).
7. Xu Yong-Nain, Gu Zhong-Quan, Zhong Xue-Fu, and W. Y. Ching, Phys. Rev. B **56** (12), 7277 (1997).
8. G. V. Lewis and C. R. A. Catlow, J. Phys. C **18** (6), 1149 (1985).
9. C. Herscovici and M. Fibish, J. Phys. C **13** (9), 1635 (1980).
10. V. G. Mazurenko and A. N. Kislov, Fiz. Tverd. Tela (Leningrad) **33** (11), 3443 (1991) [Sov. Phys. Solid State **33**, 1937 (1991)].
11. V. G. Mazurenko and A. N. Kislov, Fiz. Tverd. Tela (St. Petersburg) **34** (11), 3403 (1992) [Sov. Phys. Solid State **34**, 1822 (1992)].

Translated by A. Kazantsev

Physics of the Solid State, Vol. 45, No. 9, 2003, pp. 1784–1789. Translated from Fizika Tverdogo Tela, Vol. 45, No. 9, 2003, pp. 1700–1705.

LATTICE DYNAMICS AND PHASE TRANSITIONS

Mechanism for the Bidirectional Shape Memory Effect in Titanium Nickelide Crystals

G. A. Malygin

Ioffe Physicotechnical Institute, Russian Academy of Sciences, Politekhnicheskaya ul. 26, St. Petersburg, 194021 Russia
e-mail: malygin.ga@mail.ioffe.ru

Received February 25, 2003

Abstract—A mechanism for the bidirectional and all-round shape memory effects observed in titanium nickelide crystals is discussed quantitatively by using the theory of diffuse martensitic transformations (DMTs). These effects are associated with an anisotropic distribution of Ti_3Ni_4 particles, which arises in bent crystals subjected to annealing followed by relaxation of coherent microstresses produced by the particles. Using the DMT theory, the influence of the stepwise $B2 \longrightarrow R \longrightarrow B19'$ phase transition on the magnitude and sign of the radius of curvature of a thin strip of titanium nickelide is calculated and the conditions are determined under which the bidirectional and all-round shape memory effects occur depending on structural factors and the geometrical parameters of the strip. © *2003 MAIK "Nauka/Interperiodica".*

1. INTRODUCTION

The shape memory effect (SME) observed in crystals undergoing a martensitic transformation (MT) is usually unidirectional; that is, a crystal is deformed in the direction opposite to the direction of its preliminary deformation. However, it was established in [1–3] that titanium nickelide (TiNi) crystals subjected to special thermal treatment exhibit a bidirectional SME; that is, as the temperature is decreased, a TiNi crystal not only recovers its original shape but deforms in the opposite direction. This bidirectional SME is observed after high-temperature annealing of bent strips [1–4] and plates [5] of titanium nickelide with an Ni content of 50.5 at. % or greater.

Electron-microscopic studies of TiNi samples with such Ni contents annealed at temperatures from 600 to 800 K show [1, 6, 7] that, in addition to the solid solution, an alloy contains disk-(lens-)shaped precipitates of intermetallic Ti_3Ni_4 with a radius of 10 to 100 nm depending on the temperature and annealing time. There are four equivalent orientations of Ti_3Ni_4 particles in accordance with the number of (111)-type habit planes of the *B*2 phase [6, 7]. However, if a strip is subject to bending during annealing (and, hence, is in a strained state), only one orientation of martensite particles becomes dominant [1, 6]. In this case, disk-shaped precipitates are oriented perpendicular to the compressive-stress direction in compressed layers and are parallel to the tensile-stress direction in stretched layers. Since precipitates are coherently joined with the matrix and since the internal stresses that are associated with precipitates are anisotropic (directed) [8], plates and strips bend elastically under these stresses [1, 4, 5].

Another feature of TiNi alloys enriched in nickel is that, because of the presence of Ti_3Ni_4 particles in an alloy, the MT proceeds in two steps, with the formation of the intermediate rhombohedral (*R*) phase, as the temperature is decreased. If an alloy is not enriched, the initial bcc *B*2 phase transforms directly into the orthorhombic *B*19 or monoclinic *B*19' phase, whereas a nickel-rich alloy containing Ti_3Ni_4 precipitates undergoes the two-step transformation $B2 \longrightarrow R \longrightarrow B19'$. In the second stage of this transformation, the SME reverses sign and the bidirectional SME is observed [1, 2].

Based on the above observations, the following qualitative mechanism was proposed in [3] for the bidirectional SME. As the temperature is decreased in the temperature range of the *R*-phase formation, *R*-martensite nuclei arise near Ti_3Ni_4 precipitates, which brings about partial relaxation of the internal stresses and straightening of the strip. Due to the subsequent $R \longrightarrow B19'$ transformation, the internal stresses relax further and change sign. As a result, under tensile stresses, the strip (plate) bends backwards with respect to its initial bending.

In the present paper, this qualitative mechanism for the bidirectional SME is analyzed quantitatively in terms of the theory of diffuse martensitic transformations (DMTs) [9, 10]. The development of quantitative theory for the bidirectional SME is of great importance, because this effect extends the functional capabilities of titanium nickelide as a promising material for sensing elements in micro- and nanocomposite sensors and actuators [12–14]. The potential of microdevices with sensing units based on titanium nickelide for use in microelectromechanical systems is currently being discussed in the literature [11].

1063-7834/03/4509-1784$24.00

This paper is organized as follows. In Section 2, the two-step martensitic transformation $B2 \longrightarrow R \longrightarrow B19'$ is considered using the DMT theory. In Section 3, we consider a mechanism for the elastic and martensitic relaxation of directed microstresses associated with Ti_3Ni_4 particles. The bidirectional and all-round SMEs occurring in a thin strip of titanium nickelide are discussed in Sections 4 and 5, respectively.

2. TWO-STEP MARTENSITIC TRANSFORMATION

According to the DMT theory [15], when two types of martensite (*R*, *M*) coexist, their volume fractions φ_R and φ_M in a crystal subject to a stress σ at temperature *T* are equal to

$$\varphi_R = \frac{\exp(-\Delta U_R/kT)}{1 + \exp(-\Delta U_R/kT) + \exp(-\Delta U_M/kT)}, \quad (1a)$$

$$\varphi_M = \frac{\exp(-\Delta U_M/kT)}{1 + \exp(-\Delta U_R/kT) + \exp(-\Delta U_M/kT)}. \quad (1b)$$

Here, $\Delta U_{R,M} = \omega_{R,M}\Delta u_{R,M}$ is the change in the internal energy of the crystal caused by the transformation of an elementary volume ω into a new structural state and $\Delta u_{R,M}$ is the change in the internal-energy density due to this transformation,

$$\Delta u_{R,M} = q_{R,M}\frac{T - T_{R,M}}{T_{R,M}} - \xi_{R,M}(m_{R,M}\sigma \mp \tau_{fR,fM}), \quad (2)$$

where q is the specific heat of the transformation; T_R and T_M are the critical (characteristic) transformation temperatures; $\xi_{R,M}$ are the shear strains of the lattice caused by the respective structural transformations; τ_{fR} and τ_{fM} are the friction stresses for forward and reverse *R* and *M* martensitic transformations, which cause transformation hysteresis to occur; and $m_{R,M}$ are the orientation factors (with reference to the direction of the unidirectional mechanical stress σ applied to the crystal) of the habit planes and of the directions of the atomic displacements associated with the structural rearrangement of the lattice.

For computational convenience, we write the arguments of the exponential functions in Eqs. (1) in the form

$$\frac{\Delta U_R}{kT} = B_R(T/T_R - 1 - m_R\sigma/\tau_R \pm \tau_{fR}/\tau_R), \quad (3a)$$

$$\frac{\Delta U_M}{kT} = B_M(T/T_M - 1 - m_M\sigma/\tau_M \pm \tau_{fM}/\tau_M), \quad (3b)$$

where

$$B_{R,M} = \omega_{R,M}q_{R,M}/kT \approx \omega_{R,M}q_{R,M}/kT_{R,M}, \quad \tau_{R,M} = q_{R,M}/\xi_{R,M}. \quad (3c)$$

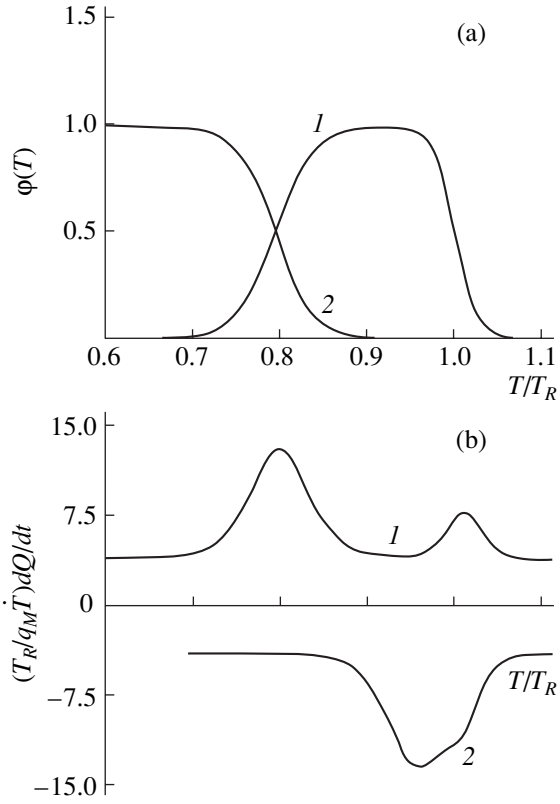

Fig. 1. Temperature dependences (a) of the volume fractions of (*1*) the *R* and (2) *M* martensites in titanium nickelide and (b) of the corresponding heat liberation rates upon (*1*) cooling and (*2*) heating.

Figure 1a shows the variations of the volume fractions of the martensite phases *R* and *M* with decreasing temperature (in the absence of external stresses, $\sigma = 0$) calculated from Eqs. (3) for the following values of the parameters: $B_R = 80$, $B_M = 120$, $T_R = 1.05T_M$, $\tau_{fR}/\tau_R = 10^{-3}$, and $\tau_{fM}/\tau_M = 3 \times 10^{-2}$. It can be seen that, for these parameters, the *R* martensite dominates in the temperature range $0.8T_R < T < T_R$, while the *M* martensite is dominant at temperatures $T < 0.8T_R$.

The temperatures at which the forward MT in TiNi begins and the reverse MT terminates are usually determined from calorimetric measurements [12] or from experimental electric-resistivity temperature dependences [2]. During the two-step forward and reverse MTs, in the case where the temperature is varied at a constant rate $\dot{T}$, the specific heat $Q(T)$ and the heat liberation rate dQ/dt are equal to

$$Q = q_R\varphi_R + q_M\varphi_M, \quad \frac{dQ}{\dot{T}dt} = q_R\frac{d\varphi_R}{dT} + q_M\frac{d\varphi_M}{dT}, \quad (4)$$

where the volume fractions of the *R* and *M* martensites are given by Eqs. (1)–(3). Figure 1b shows calorimetric curves for the forward and reverse MTs calculated from these equations for the parameters indicated above and

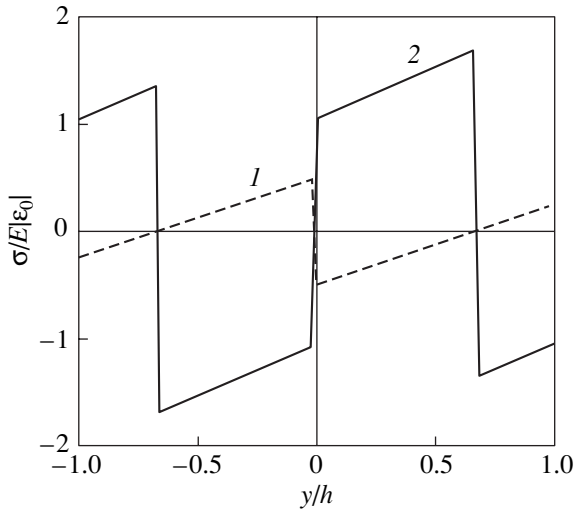

Fig. 2. Stress variations through the strip thickness after (*1*) elastic and (*2*) martensitic stress relaxation.

$q_R = 0.2q_M$. It can be seen that, when the reverse MTs proceed (curve *2*), the $B19' \longrightarrow R$ transformation occurs (because of its strong temperature hysteresis) at temperatures very close to the temperatures of the $R \longrightarrow B2$ transformation, which is in agreement with a large body of experimental data. Based on this two-step MT, we will treat the bidirectional SME occurring in titanium nickelide.

3. ELASTIC AND MARTENSITIC STRESS RELAXATION IN A STRIP

Let us consider a bent thin strip of length $2l$, width $b \ll 2l$, thickness $2h \ll b$, and radius of curvature $R_0 > 2l$. As indicated above, annealing of a bent strip brings about the formation of disk-shaped Ti_3Ni_4 particles, with the disk planes being perpendicular to the compressive stress direction in compressed layers. These precipitates are coherently joined with the matrix and, therefore, produce an (average) elastic strain $\varepsilon_0 = f\delta_0$ along the layers [8, 16], where f is the volume concentration of the precipitates and $\delta_0 < 0$ is the free-precipitate strain. After cooling and removing the external bending stress, the strip will be subjected to internal elastic stresses and strains $\varepsilon_e(y)$ or (at MT temperatures) plastic strains $\varepsilon_p(y, T)$, where y is the coordinate along the direction perpendicular to the neutral (unstrained) layer of the strip. Due to these stresses and strains, the strip will additionally be bent (forward or backwards) relative to its initial bending.

Let us determine the new radius of curvature R_{ep} (curvature R_{ep}^{-1}) of the strip and the distribution of elastic stresses $\sigma(y, T)$ over the strip. The strain ε of a layer of the strip can be represented in the form

$$\varepsilon = \varepsilon_0 H(y) + \varepsilon_e(y, T) + R_{ep}^{-1} y + \varepsilon_p(y, T), \qquad (5a)$$

where $H(y)$ is a step function: $H = 1$ for $y < 0$ and $H = 0$ for $y > 0$. Using Eq. (5a), the internal elastic stresses are found to be

$$\begin{aligned}\sigma(y, T) &= E\varepsilon_e(y, T)\\ &= E[\varepsilon - \varepsilon_0 H(y) - R_{ep}^{-1} y - \varepsilon_p(y, T)].\end{aligned} \qquad (5b)$$

The unknown parameters ε and R_{ep}^{-1} are determined by the balance of the stresses and bending moments applied to the strip:

$$\int_{-h}^{h} \sigma(y, T)ds = N, \quad \int_{-h}^{h} \sigma(y, T)yds = M, \qquad (6)$$

where $ds = bdy$ is an element of the cross-sectional area of the strip. If the ends of the strip are free and there is no external load and bending moments, we have $N = M = 0$.

Integrating Eqs. (6) gives

$$\varepsilon = \frac{1}{2}\left(-\frac{1}{2}|\varepsilon_0| + \bar{\varepsilon}_p(T)\right), \quad R_{ep}^{-1}(T) = R_e^{-1} + R_p^{-1}(T),$$

$$\bar{\varepsilon}_p(T) = \frac{1}{2h}\int_{-h}^{h} \varepsilon_p(y, T)dy, \qquad (7)$$

$$\bar{\bar{\varepsilon}}_p(T) = \frac{1}{h^2}\int_{-h}^{h} \varepsilon_p(y, T)ydy.$$

Here, $R_e^{-1} = -(3/4h)|\varepsilon_0|$ and $R_p^{-1} = -(3/2h)\bar{\bar{\varepsilon}}_p(T)$ are the changes in the curvature of the strip due to elastic and martensitic stress relaxation in the strip, respectively. Substituting Eqs. (7) into Eq. (5b), we find the stress variation through the thickness of the strip:

$$\sigma(y, T) = \sigma_0(y) - \sigma_p(y, T), \qquad (8a)$$

$$\begin{aligned}\sigma_0(y) &= \frac{1}{2}E|\varepsilon_0|\left(\frac{3y}{2h} \pm 1\right),\\ \sigma_p(y, T) &= E\left(\varepsilon_p(y, T) - \frac{3}{2}\bar{\bar{\varepsilon}}_p(T)\frac{y}{h} + \frac{1}{2}\bar{\varepsilon}_p(T)\right).\end{aligned} \qquad (8b)$$

In the first of Eqs. (8b), the plus sign corresponds to the inner layer of the strip ($y < 0$) and the minus sign corresponds to the outer layer ($y > 0$). The stresses $\sigma_0(y)$ are equivalent to the stresses that arise in a bimetallic strip consisting of layers with coefficients of thermal expansion differing by $\Delta\alpha$ when the temperature of the strip is varied by ΔT [17]; in this case, we have $\varepsilon_0 = \Delta\alpha\Delta T$. Figure 2 shows variations in the stress σ_0 through the strip thickness (curve *1*). It can be seen that compressive stresses dominate near the surface of the compressed layer ($y = -h$) and tensile stresses are dominant near the surface of the stretched layer ($y = h$).

As the temperature is decreased to the temperature of the *R*- and *M*-martensitic transformations, the elastic

stresses given by Eq. (8a) relax by an amount $\sigma_p(y, T)$ and are redistributed over the strip. The local plastic strains caused by the formation of the *R* and *M* martensites depend on the magnitude and sign of the stresses $\sigma_0(y)$ and, according to the DMT theory, are given by

$$\varepsilon_p(T, y) = [n_R m_R \varepsilon_R \varphi_R(T, \sigma_0(y)) + n_M m_M \varepsilon_M \varphi_M(T, \sigma_0(y))]\,\mathrm{sgn}[\sigma_0(y)], \quad (9a)$$

where $\varepsilon_{R,M} = f\xi_{R,M}$, with ξ_R and ξ_M being the shear strains associated with the lattice transformation into the *R* and *M* modifications, respectively, and n_R and n_M are the numbers of equivalent orientations of *R*- and *M*-martensite precipitates, respectively, for which the orientation factors are equal. In order to calculate the plastic strains in Eq. (9a), we represent expressions (3), which are involved in Eqs. (1) for the volume factors of the *R* and *M* martensites, in the form

$$\frac{\Delta U_R}{kT} = B_R(t - 1 - m_R a_R|S_0(\bar{y})| \pm \tau_{fR}/\tau_R),$$
$$\frac{\Delta U_M}{kT} = B_M(bt - 1 - m_M a_M|S_0(\bar{y})| \pm \tau_{fM}/\tau_M), \quad (9b)$$

where $t = T/T_R$, $\bar{y} = y/h$, and $b = T_R/T_M$;

$$\frac{\sigma_0(y)}{E|\varepsilon_0|} = S_0(\bar{y}) = \frac{1}{2}\left(\frac{3}{2}\bar{y} \pm 1\right),$$
$$a_R = \xi_R|\varepsilon_0|(E/q_R), \quad a_M = \xi_M|\varepsilon_0|(E/q_M). \quad (9c)$$

The variations in stresses (8a) through the strip thickness are shown in Fig. 2 (curve *2*) for the temperature $0.9T_R$ and the following values of the parameters in Eqs. (9c): $b = 1.05$, $a_R = 0.12$, $a_M = 0.1$, $\xi_R = 3 \times 10^{-2}$, $\xi_M = 0.12$, $f = 0.1$, $|\varepsilon_0| = 3 \times 10^{-3}$, $q_R = 30$ MJ m^{-3}, $q_M = 150$ MJ m^{-3}, $E = 40$ GPa, $m_R = m_M = 0.5$, and $n_R = n_M = 3$. The values of the other parameters are presented above. Calculations show that $\bar{\varepsilon}_p(T) = 0$ in Eqs. (7) and (8b).

It can be seen from Fig. 2 that, due to the formation of the *R* martensite, the stresses in the near-surface layers of the strip relax and reverse sign (curve *2*). Since the formation of the *M* martensite causes large lattice strains ($\xi_M > \xi_R$), the stress relaxation becomes progressively stronger as the temperature is decreased further, with the consequence that the strip unbends.

4. BIDIRECTIONAL SHAPE MEMORY EFFECT

The strip shape is characterized by the radius of curvature *R*(*T*), which varies during the MT. The curvature of the strip can be written as

$$R^{-1}(T) = R_e^{-1} + R_p^{-1}(T) + R_0^{-1}, \quad (10)$$

where R_0 is the initial radius of curvature of the strip before stress relaxation. For computational convenience, by using the notation in Eq. (7), we represent the curvature of the strip in the reduced form

$$\frac{R_0}{R(T)} = 1 - \frac{3R_0}{2h}\left(\frac{1}{2}|\varepsilon_0| + \bar{\bar{\varepsilon}}_p(T)\right). \quad (11)$$

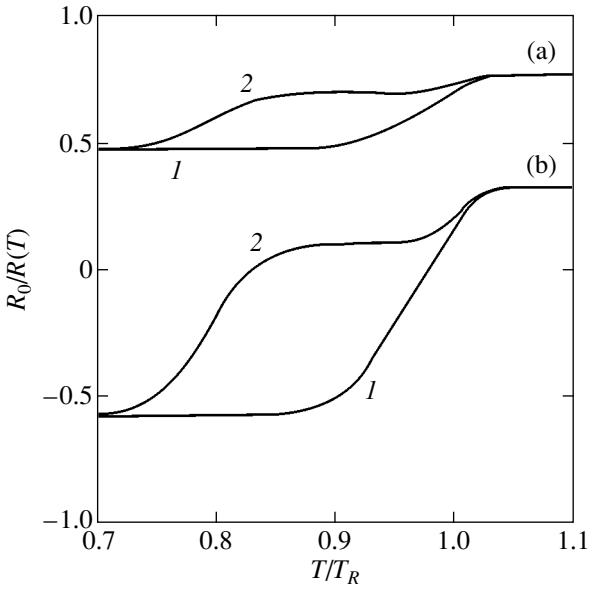

Fig. 3. Temperature dependences of the reduced strip curvature $R_0/R(T)$ under the conditions of (a) the unidirectional and (b) the bidirectional SME upon (*1*) heating and (*2*) cooling as calculated from Eq. (11).

Figure 3 shows the calculated temperature dependence of the reduced curvature for two values of the parameter R_0/h (10^2, 3×10^2) and the values of the other parameters indicated above. In the former case (Fig. 3a), the unidirectional SME takes place; that is, the curvature of the strip does not change sign as the MTs proceed. In the latter case (for a thinner strip), the bidirectional SME is observed; that is, the strip curvature reverses sign when the MT occurs (Fig. 3b). Since the strains ε_0 and $\bar{\bar{\varepsilon}}_p$ vary in proportion to the concentration *f* of Ti_3Ni_4 particles in the strip, the occurrence of the bidirectional SME is controlled by this concentration. The higher the concentration, the larger both the elastic and plastic strain in the strip and the more pronounced the bidirectional SME. These predictions agree well with the experimental data for annealed strips of titanium nickelide enriched in nickel (in comparison to the equiatomic composition) [1, 2].

The initial shape of the strip (after its high-temperature annealing) is described by the function

$$W_0(x) = R_0[\sqrt{1 - (x/R_0)^2} - \sqrt{1 - (L_0/R_0)^2}]. \quad (12)$$

In Fig. 4, the initial shape of the strip is shown in the $\overline{W}_0(x) - x/L_0$ coordinates (dashed curve), where $\overline{W}_0(x) = W_0(x)/W_0(0)$, $W_0(0)$ is the maximum deflection

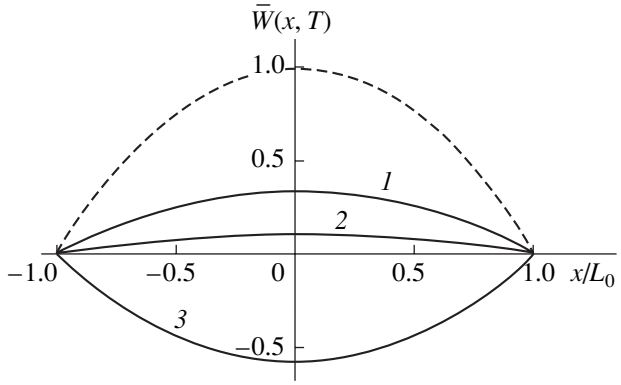

Fig. 4. Changes in the strip shape upon cooling: strip shape at temperature T equal to (*1*) $1.1T_R$, (*2*) $0.9T_R$, and (*3*) $0.7T_R$. The dashed curve is the initial strip shape before elastic and martensitic stress relaxation.

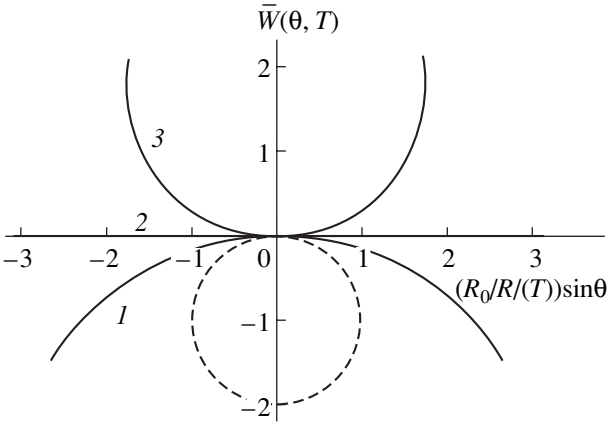

Fig. 5. Changes in the strip shape under the conditions of the all-round SME: (*1*) $T = 1.1T_R$, (*2*) $0.83T_R$, and (*3*) $0.7T_R$. The dashed curve is the initial strip shape.

of the strip, $2L_0 = 2R_0\sin\theta_0$ is the distance between the ends of the strip [the length of the chord of the arc described by Eq. (12)], and $2\theta_0 = 2l/R_0$ is the full bending angle of the strip. For Fig. 4, we have $\theta_0 = 0.5$, $2\theta_0 = 57.3°$, and $W_0(0) = R_0(1 - \cos\theta_0) \approx 0.12R_0$.

After elastic and martensitic stress relaxation, the changed strip shape is described by the expression [similar to Eq. (12)]

$$W(x, T) = R(T)\{\sqrt{1 - [x/R(T)]^2} - \sqrt{1 - [L(T)/R(T)]^2}\}, \quad (13)$$

where $R(T)$ is the temperature-dependent radius of curvature given by Eq. (10), $2L(T) = 2R(T)\sin[\theta(T)]$ is the distance between the ends of the strip, and $2\theta(T) = 2l/R(T)$ is the bending angle of the strip at a given temperature. In Fig. 4, curves *1–3* illustrate how the strip shape is changed [according to Eqs. (10), (13)] with decreasing temperature. The ordinate is the strip deflection $\bar{W}(x, T) = W(x, T)/W_0(0)$ normalized to the initial maximum deflection. At the temperature $1.1T_R$, as is seen from Fig. 3b, the change in the strip shape is caused by purely elastic relaxation of internal stresses (Fig. 4, curve *1*). At the temperature $0.9T_R$, as is also seen from Fig. 3b, the change in the strip shape is due to the formation of the *R* martensite in the strip (Fig. 4, curve *2*), and at the temperature $0.7T_R$, it is due to the formation of the *M* martensite. In the latter case, the strip curvature reverses sign (Fig. 4, curve *3*); that is, the bidirectional SME occurs. Subsequent heating causes the strip shape to vary in the reverse order. However, the temperature ranges in which the $B19' \longrightarrow R$ and $R \longrightarrow B2$ transformations occur overlap in this case (Fig. 1b, curve *2*), and, as a result, the changes in the strip shape take place in the narrow temperature range $0.9T_R$–$1.03T_R$ (Fig. 3b, curve *1*). The temperature dependence of the maximum strip deflection is given by

$$W(0, T) = R(T)\{1 - \cos[\theta(T)]\}. \quad (14)$$

For the values of the parameters indicated above, in the case of complete martensitic stress relaxation, the maximum strip deflection (at the temperature $0.7T_R$) is equal to $-7 \times 10^{-2}R_0$.

5. ALL-ROUND SHAPE MEMORY EFFECT

The value of the maximum strip deflection calculated above is much smaller than the initial radius of curvature of the strip, because the initial bending angle $2\theta_0 = 2l/R_0$ is small. If this angle is made to be as large as 2π or larger (for example, for a longer strip), the so-called all-round SME can occur [1, 2]; namely, a strip that is rolled into a ring during its annealing will straighten and then roll into a ring with a curvature of the opposite sign after cooling and undergoing the two-step MT.

In order to treat the all-round SME, we write Eqs. (12) and (13) in polar coordinates, taking the polar angle θ (measured from the vertical axis) to be zero for the fixed point of the ring (Fig. 5). In this case, Eqs. (12) and (13) take the form

$$W_0(\theta) = R_0(\cos\theta - 1), \quad (15)$$

$$W(\theta, T) = R(T)(\cos\theta - 1). \quad (16)$$

In Fig. 5, the dashed curve shows the initial shape of the strip (a ring with $2\theta = 2\pi$) in the polar coordinates $[\bar{W}_0(\theta) - \sin\theta]$, where $\bar{W}_0(\theta) = W_0(\theta)/R_0$. The strip shape calculated from Eq. (16) for the temperatures $1.1T_R$ (after elastic stress relaxation), $0.83T_R$ (the strip becomes straight), and $0.7T_R$ (after martensitic stress relaxation) is shown by curves *1–3*, respectively, constructed in the $[\bar{W}(\theta, T) - (R(T)/R_0)\sin\theta]$ coordinates, where $\bar{W}(\theta, T) = W(\theta, T)R(T)/R_0$. The opening angle of the ring is $2\theta(T) = 2l/R(T)$. It can be seen that at temperatures below $0.83T_R$ the strip curvature reverses sign and the strip rolls into a semicircle.

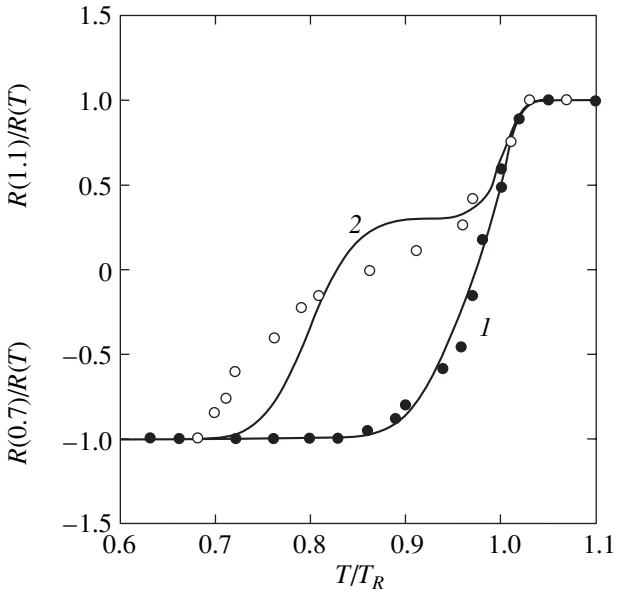

Fig. 6. Temperature dependences of the normalized curvature of a titanium nickelide strip under the conditions of the all-round SME as calculated from Eq. (11): (*1*) heating and (*2*) cooling. Dots are experimental data taken from [1].

Figure 6 compares the calculations with the experimental data [1] on the all-round SME in titanium nickelide with 51 at. % Ni (annealed at 773 K over 1 h). The experimental data represent the temperature dependence of the reduced strip curvature $R_0/R(T)$ upon heating and cooling. The curvature is normalized to its limiting values $R_0/R(1.1)$ for positive values of the curvature and $|R_0/R(0.7)|$ for negative values, where $R(1.1)$ and $R(0.7)$ are the radii of curvature at temperatures $1.1T_R$ and $0.7T_R$, respectively. According to Eq. (11), the limiting values of the reduced curvature are

$$\begin{aligned} \frac{R_0}{R(1.1)} &= 1 - \frac{3R_0}{4h}|\varepsilon_0|, \\ \frac{R_0}{R(0.7)} &= 1 - \frac{3R_0}{2h}\left(\frac{1}{2}|\varepsilon_0| + \bar{\bar{\varepsilon}}_p(0.7)\right). \end{aligned} \tag{17}$$

Using Eqs. (7) and (9), we obtain the estimate $\bar{\bar{\varepsilon}}_p(0.7) \approx (1/9)n_M m_M f \xi_M$. It is seen from Fig. 6 that the calculations agree with the experimental data.

6. CONCLUSION

Thus, by using the DMT theory, we have shown that the bidirectional and all-round shape memory effects occur in a strip (or plate) of titanium nickelide if the distribution of coherent Ti_3Ni_4 particles is anisotropic and their concentration is sufficiently high and if the ratio between the thickness of the strip and its initial bending radius (during high-temperature annealing) satisfies certain restrictions.

REFERENCES

1. N. Nishida and T. Honma, Scr. Metall. **18** (11), 1293 (1984).
2. N. Nishida and T. Honma, Scr. Metall. **18** (11), 1299 (1984).
3. T. Honma, *Shape Memory Alloy-86*, Ed. by Ch. Youyi, T. Y. Hsu, and T. Ko (China Academic, Guilin, 1986), p. 83.
4. M. A. Khusainov, Vestn. Novgorod. Gos. Univ., No. 10, 34 (1998).
5. M. A. Khusainov, Zh. Tekh. Fiz. **67** (6), 118 (1997) [Tech. Phys. **42**, 692 (1997)].
6. D. Y. Li and L. Q. Chen, Acta Mater. **45** (2), 471 (1997).
7. L. Bataillard, J. E. Bidaux, and R. Gotthardt, Philos. Mag. A **78** (2), 327 (1998).
8. G. A. Malygin, Fiz. Tverd. Tela (St. Petersburg) **45** (8), 1491 (2003) [Phys. Solid State **45**, 1566 (2003)].
9. G. A. Malygin, Fiz. Tverd. Tela (St. Petersburg) **36** (5), 1489 (1994) [Phys. Solid State **36**, 815 (1994)].
10. G. A. Malygin, Usp. Fiz. Nauk **171** (2), 187 (2001) [Phys. Usp. **44**, 173 (2001)].
11. P. Krulevitch, A. P. Lee, P. B. Ramsey, *et al.*, J. Microelectromech. Syst. **5** (4), 270 (1996).
12. J. L. Seguin, M. Bendahan, A. Isalgue, *et al.*, Sens. Actuators **74** (1/3), 65 (1999).
13. R. X. Wang, Y. Zohar, and M. Wong, J. Micromech. Microeng. **12** (3), 323 (2002).
14. G. A. Malygin, Fiz. Tverd. Tela (St. Petersburg) **43** (7), 1286 (2001) [Phys. Solid State **43**, 1339 (2001)].
15. G. A. Malygin, Fiz. Tverd. Tela (St. Petersburg) **44** (11), 2081 (2002) [Phys. Solid State **44**, 2171 (2002)].
16. J. D. Eshelby, Solid State Phys. **3**, 79 (1956) (Inostrannaya Literatura, Moscow, 1963).
17. L. E. Andreeva, *Elastic Elements of Devices* (Mashinostroenie, Moscow, 1981).

Translated by Yu. Epifanov

Physics of the Solid State, Vol. 45, No. 9, 2003, pp. 1790–1792. Translated from Fizika Tverdogo Tela, Vol. 45, No. 9, 2003, pp. 1706–1708.

LOW-DIMENSIONAL SYSTEMS AND SURFACE PHYSICS

Optical Magnetoabsorption in Quantum-Confined Systems in the Field of a Resonance Squeezed Electromagnetic Wave

É. P. Sinyavskiĭ and E. I. Brusenskaya

Institute of Applied Physics, Academy of Sciences of Moldova, Chisinau, 277028 Moldova

Received December 3, 2002

Abstract—The contribution of an intense squeezed electromagnetic wave to magnetoabsorption is analyzed. It is demonstrated that an amplitude-squeezed (or phase-squeezed) resonance electromagnetic wave more strongly affects the magnetoabsorption peaks than classical coherent radiation. © *2003 MAIK "Nauka/Interperiodica".*

1. Let us consider a quantum-confined system in a homogeneous magnetic field with a strength **H** directed along the confinement axis *OZ*. In this case, the energy of an electron ($E_\alpha^{(c)}$) or a hole ($E_\alpha^{(v)}$) for a rectangular quantum well of width a is completely quantum-confined; that is,

$$E_\alpha^{(c,v)} = \hbar\omega_{(c,v)}\left(N + \frac{1}{2}\right) + \varepsilon_{(c,v)}n^2. \quad (1)$$

Here, $\omega_{(c,v)} = \dfrac{eH}{m_{(c,v)}c}$ is the cyclotron frequency, $\varepsilon_{(c,v)} = \dfrac{\hbar^2\pi^2}{2m_{(c,v)}a}$ is the step of the spatial quantum confinement, and $m_{(c,v)}$ is the effective electron (hole) mass.

In this paper, we analyze the specific features observed in the absorption of a weak light wave of frequency Ω due to a transition of an electron from the hole state to the electron state (in the absence of a magnetic field, this is an interband optical transition) in the field of a squeezed electromagnetic wave of frequency ω in resonance with a wave of frequency ω_c. In what follows, we will consider strong quantized magnetic fields, provided the energy of the Coulomb interaction between the electron and the hole is insignificant as compared to the energy separation between the magnetically quantized levels. Under these conditions, the internal motion of the electron–hole pair is finite and, strictly speaking, free states of the electron and the hole are nonexistent [1]. Experimental photoluminescence investigations demonstrated that the binding energy of an exciton in a quantum well at $B > 10$ T in InGaAs/GaAs [2] and GaAs/AlGaAs [3] is proportional to B. Therefore, the above approximation is applicable in our case. Note that this approximation was thoroughly discussed by Edelstein *et al.* [4]. For optical excitation of an electron–hole pair, the exciton momentum is equal to the momentum of the electromagnetic wave and is very small [5]. Hence, we will ignore the exciton bands observed in quasi-two-dimensional semiconductors in a strong magnetic field [1].

The absorption coefficient $K(\Omega)$ for a weak electromagnetic wave is calculated by analogy with the calculations performed in our earlier works [6, 7]. For laser radiation incident perpendicular to the surface of the quantum-confined system, the absorption coefficient in the case of infrared magnetic resonance ($\omega = \omega_c$) can be represented by the expression

$$K(\Omega) = K_0\sum_\alpha\int_{-\infty}^{\infty}dt\exp\left\{\frac{it}{\hbar}(\hbar\Omega - E_\alpha^{(c)} - E_\alpha^{(v)} - E_g)\right\} \times \langle\exp(-Ab^+)\exp(-Db^+b)\exp(Bb)\rangle_{sq}\exp\left(-\frac{B_0t^2}{2}\right). \quad (2)$$

Here, we introduced the following designations:

$$A = \frac{a_N dt}{\hbar}, \quad B = \frac{a_N^+ dt}{\hbar}, \quad D = \frac{d^2t^2}{2\hbar},$$

$$d = e\hbar\left[\frac{\pi}{V\varepsilon_0 m_c}\right]^{1/2}, \quad K_0 = \frac{2\pi e^2|P_{cv}e_0|^2}{Vm_0^2c\sqrt{\varepsilon_0}\hbar\Omega},$$

$b^+(b)$ is the operator of production (annihilation) of photons of a resonance electromagnetic wave, $\alpha = (N, n, k_x)$ is a set of quantum numbers characterizing the carrier state in the quantum-confined system under consideration, E_g is the band gap, $\langle\ldots\rangle_{sq}$ indicates averaging with the density operator of a squeezed electromagnetic field of frequency ω [8], and B_0 is the parameter determined by the interaction of the electron with acoustic phonons and accounting for the line shape of the optical absorption in quantum-confined systems in the longitu-

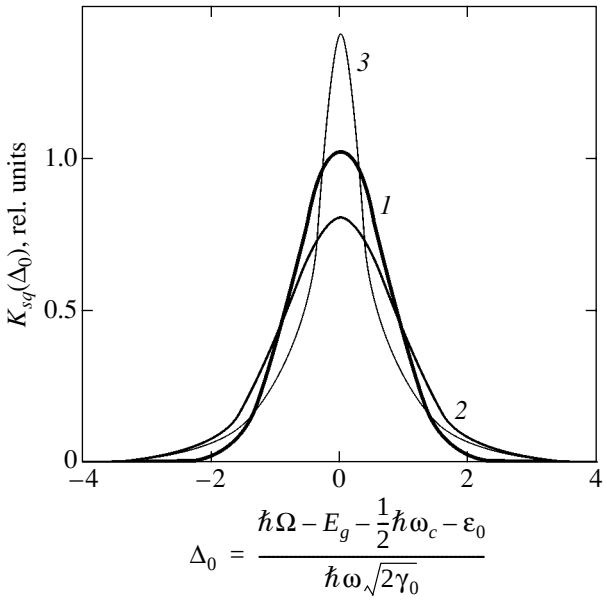

Fig. 1. Frequency dependences of the first peak of the magnetoabsorption (expressed in relative units): (*1*) coherent resonance laser radiation ($\mu = 0$, $\delta = 1$), (*2*) amplitude-squeezed resonance laser radiation ($\mu = 1$, $\delta = 1$), and (*3*) phase-squeezed resonance laser radiation ($\mu = 1$, $B^0/\gamma = 0.05$).

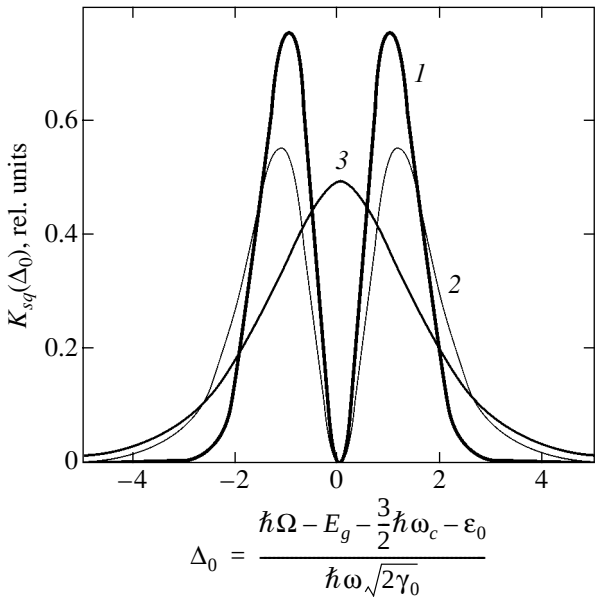

Fig. 2. Frequency dependences of the second peak of the magnetoabsorption (expressed in relative units): (*1*) coherent resonance laser radiation ($\mu = 0$, $\delta = 1$), (*2*) amplitude-squeezed resonance laser radiation ($\mu = 1$, $\delta = 1$), and (*3*) phase-squeezed resonance laser radiation ($\mu = 1$, $B^0/\gamma = 0.05$).

dinal magnetic field [9]. The operators a_N and a_N^+ are defined as

$$a_N = \sqrt{N+1}\,l_1^{(N)}, \quad a_N^+ = \sqrt{N}\,l_{-1}^{(N)},$$

where $l_m^{(N)} f(N) = f(N+m)$ and $f_m^{(N)}$ is an arbitrary function of the Landau quantum numbers N.

The above operators satisfy the standard commutation relationships $\lfloor a_{N_1} a_{N_2} \rfloor = \delta_{N_1 N_2}$ and, consequently, can be treated as Bose operators. The other designations are described in our previous paper [7].

The averaging in expression (2) can be exactly accomplished using the definition given by Loudon and Knight [10] for a squeezed state of radiation. By applying the procedure developed by Prepelitsa [11], it is a simple matter to derive the following expression for the absorption coefficient of a light wave of frequency Ω in the field of an intense resonance squeezed electromagnetic wave:

$$K(\Omega) = \frac{K_0}{\sqrt{2\pi}} \sum_{Nn} \int_{-\infty}^{\infty} dt \exp\left\{\frac{it}{\hbar}[\hbar\Omega - E_\alpha^* - E_g]\right\},$$

$$\int_{-\infty}^{\infty} dx \exp\left(-\frac{x^2}{2}\right) \exp\left(-\frac{1}{2}C(t,x)\right) L_N[C(t,x)] \qquad (3)$$

$$\times \exp\left\{-\frac{B_0 t^2}{2}\right\}.$$

Here, we used the following designations:

$$C(t,x) = \frac{d^2 t^2 |\alpha|^2}{\hbar^2}\left(\mu x^2 + 1 + 2x\sqrt{\mu}\sin\left(\varphi_\alpha - \frac{\varphi}{2}\right)\right),$$

$$E_\alpha^* = \hbar\omega_c^*\left(N + \frac{1}{2}\right) + \varepsilon^* n^2, \quad \hbar\omega_c^* = \frac{\hbar e H}{\mu_0 c},$$

$$\varepsilon^* = \frac{\hbar^2\pi^2}{2\mu_0 a^2}, \quad \mu_0^{-1} = \mu_c^{-1} + \mu_v^{-1}, \quad \mu = \frac{sh^2 r}{|\alpha|^2}.$$

In these expressions, $L_N(z)$ stands for the Laguerre polynomials; $\alpha = \sqrt{N_0}\exp(i\varphi_\alpha)$; N_0 is the mean number of photons in the mode of squeezed light; r is the squeezing parameter; φ_α and φ are arbitrary phases related to the shift and squeezing operators, respectively [10]; and μ characterizes the quantum fluctuations of the strength of the squeezed electromagnetic field and can be considered a measure of its deviation from the classical case ($\mu = 1/2$ in the case when the fluctuations of the laser radiation intensity are of the same order of magnitude as the mean strength of the field of the resonance electromagnetic wave).

It should be noted that relationship (3) at $r = 0$ ($\mu = 0$) leads to the results obtained for coherent classical laser radiation in our previous paper [7].

2. Let us now examine the specific features observed in the absorption of a weak light wave in the field of a resonance electromagnetic wave upon the amplitude

squeezing ($2\varphi_\alpha - \varphi = 0$). In this situation, according to relationship (3) at $N = 0$ and $n = 1$, we have

$$K_{(am)}(\Omega) = \frac{2K_0}{\sqrt{\gamma\omega^2}}\int_0^\infty \frac{dx}{\sqrt{\delta + x^2\mu}}\exp\left(-\frac{x}{2}\right)\exp\left\{\frac{-\Delta_0^2}{\delta + x^2\mu}\right\},$$

$$\gamma = \frac{|\alpha|^2 d^2}{\hbar^2\omega^2}, \quad \delta = \frac{B^0}{\gamma} + 1, \quad \Delta_0 = \frac{\hbar\Omega - E_0^* - E_g}{\hbar\omega\sqrt{2\gamma}}, \quad (4)$$

$$B^0 = \frac{B_0}{\omega^2}, \quad E_0^* = \frac{\hbar\omega_c^*}{2} + \varepsilon^*.$$

As follows from expressions (4), the frequency dependence of the optical absorption coefficient can be represented by a nearly Gaussian curve (Fig. 1). For $B^0/\gamma \ll 1$, the absorption curve is completely determined by an intense electromagnetic wave [7] (curve *1* in Fig. 1 is obtained for $\delta = 1$ and $\mu = 0$). It can be seen from Fig. 1 that an increase in the quantity μ at $\delta = 1$ leads to a decrease in the maximum and an increase in the half-width of the absorption curve (curve *2* is obtained for $\delta = 1$, $\mu = 1$). Therefore, the amplitude-squeezed wave more strongly affects the magnetoabsorption as compared to coherent resonance laser radiation. At $N = 1$ and $n = 1$ (electrons transfer from the hole state to the first magnetically quantized level), the frequency dependence $K(\Omega)$, according to relationship (3), exhibits two peaks (Fig. 2), which is characteristic of the process under investigation [7]. In Fig. 2, curve *1* is obtained at $\delta = 1$ and $\mu = 0$, whereas curve *2* is calculated at $\delta = 1$ and $\mu = 1$. It can be seen from Fig. 2 that an increase in the quantity μ results in an increase in the splitting, which is favorable for experimental observation of the predicted effect in the case of amplitude squeezing.

Now, we consider the contributions made to the absorption of a light wave of frequency Ω by the phase-squeezed resonance electromagnetic wave ($2\varphi_\alpha - \varphi = \pi$). From expression (2) at $N = 0$ and $n = 1$, we can easily obtain the relationship

$$K_{(f)}(\Omega) = -\frac{K_0}{\sqrt{\gamma\omega^2}}\int_{-\infty}^\infty \frac{dx}{\sqrt{B_0/\gamma + (x\sqrt{\mu} + 1)^2}} \times \exp\left(-\frac{x^2}{2}\right)\exp\left\{\frac{-\Delta_0^2}{B^0/\gamma + (x\sqrt{\mu} + 1)^2}\right\}. \quad (5)$$

For the maximum absorption ($\Delta_0 = 0$) at $B^0/\gamma \ll 1$, the frequency dependence of the absorption coefficient can be represented by a narrow curve with a maximum attributed to the electron–phonon interaction (curve *3* in Fig. 1 at $B^0/\gamma = 0.05$, $\mu = 1$). An increase in the parameter B^0 (characterizing the interaction of carriers with long-wavelength acoustic phonons) leads to a decrease in the maximum; consequently, the shape of the absorption curve can depend on temperature. This is the fundamental difference between the case of a phase-squeezed electromagnetic wave and coherent resonance laser radiation.

It follows from relationship (3) that, for a phase-squeezed electromagnetic wave of resonance laser radiation, the transition of a carrier to the first Landau level ($N = 1$, $n = 1$) does not lead to splitting of the second peak of the magnetoabsorption (curve *3* in Fig. 2 is obtained for $\mu = 1$, $B^0/\gamma = 0.05$). The above effects of the coherent and squeezed light on the frequency dependence of the magnetoabsorption indicate the possibility of designing an analyzing device based on quantum-confined systems. Such a device will make it possible to examine the statistical properties of an electromagnetic wave of laser radiation and to control the absorption of a weak light wave of frequency Ω in these systems with the use of an intense resonance electromagnetic wave.

REFERENCES

1. I. V. Lerner and Yu. E. Lozovik, Zh. Éksp. Teor. Fiz. **78** (3), 1167 (1980) [Sov. Phys. JETP **51**, 588 (1980)].
2. H. Q. Hou, W. Staguhn, N. Miura, *et al.*, Solid State Commun. **74** (8), 687 (1990).
3. L. V. Butov, A. Zrenner, M. Shayegan, *et al.*, Phys. Rev. B **49** (19), 14054 (1994).
4. W. Edelstein, H. N. Spector, and R. Marasas, Phys. Rev. B **39**, 7697 (1989).
5. R. J. Elliott and R. Loudon, J. Phys. Chem. Solids **15** (2), 196 (1960).
6. É. P. Sinyavskiĭ, Fiz. Tverd. Tela (Leningrad) **16** (11), 3201 (1974) [Sov. Phys. Solid State **16**, 2083 (1974)].
7. É. P. Sinyavskiĭ and E. I. Brusenskaya, Fiz. Tverd. Tela (St. Petersburg) **44** (6), 1116 (2002) [Phys. Solid State **44**, 1166 (2002)].
8. M. S. Kim, F. A. Olivera, and P. L. Knight, Phys. Rev. A **40** (9), 2494 (1989).
9. É. P. Sinyavskiĭ and E. I. Grebenshchikova, Zh. Éksp. Teor. Fiz. **116** (6), 2069 (1999) [JETP **89**, 1120 (1999)].
10. R. Loudon and P. Knight, J. Mod. Phys. **34** (3), 709 (1987).
11. O. B. Prepelitsa, Zh. Éksp. Teor. Fiz. **112** (5), 1543 (1997) [JETP **85**, 838 (1997)].

Translated by O. Moskalev

Physics of the Solid State, Vol. 45, No. 9, 2003, pp. 1793–1797. Translated from Fizika Tverdogo Tela, Vol. 45, No. 9, 2003, pp. 1709–1712.

LOW-DIMENSIONAL SYSTEMS AND SURFACE PHYSICS

Plasmons at a Hole in a Screen

A. V. Klyuchnik, S. Yu. Kurganov, and Yu. E. Lozovik

Institute of Spectroscopy, Russian Academy of Sciences, Troitsk, Moscow oblast, 142190 Russia

e-mail: lozovik@isan.troitsk.ru

Received January 16, 2003

Abstract—The field distribution and the spectrum of plasma eigenmodes are determined for a circular hole in a screen having the form of a hyperboloid of revolution. The spectrum of plasmons is obtained for a planar screen with a circular hole. The symmetric mode with $m = 1$ can be excited in the field of a dipole oriented along the screen plane, whereas the antisymmetric mode with $m = 0$ can be excited by a dipole perpendicular to the screen plane. © *2003 MAIK "Nauka/Interperiodica".*

1. INTRODUCTION

In recent years, considerable research attention has been focused on studies in the field of the optics of nanostructures (nanooptics). For example, a number of interesting works have been performed using near-field optical microscopy [1–3]. Particular interest has been expressed by scientists in the recently discovered effects of supertransparency of periodic structures with holes whose diameter is substantially less than the optical wavelength [4, 5]. Plasma waves at interfaces and in narrow slits or channels are of considerable importance in nanooptical studies [6–8]. In particular, the plasmons localized in the vicinity of a hole, under resonance conditions (see below), can efficiently transfer the energy through a hole of small aperture (with subsequent emission of light at the opposite end of the hole). The plasmons can also transfer the energy through channels with a diameter of appreciably less than the optical wavelength, i.e., under conditions where the light transmission is insignificant from the standpoint of tunneling.

In order to understand qualitatively the phenomenon of resonant transfer through a small hole, it is expedient to use the Babinet principle of complementary screens. In particular, the diffraction field for a hole in a screen coincides with the diffraction field for a disk congruent with it. For the disk, there occur plasma resonances due to different multipole modes. Therefore, it can be expected that resonances of transfer through the hole will be observed at frequencies corresponding, for example, to the dipole plasma mode of the disk. The induced dipole moment has a maximum at the frequency of dipole resonance; consequently, the maximum should also be observed upon emission through the hole.

In this work, we obtained the spectrum of plasma modes localized near a circular hole in a metallic screen. An analytical solution to this problem was found for the first time.

The spectrum of plasma oscillations and the structure of the field were determined in the quasi-electrostatic approximation (see, for example, review [9]), in which the spectrum of plasmons was determined from the solution to the Laplace equation with the appropriate boundary conditions. In the quasi-electrostatic approximation, we ignored the delay effects but took into account the frequency dispersion of the permittivity. This approximation is justified in the case when the characteristic size of the region of localization of the field is less than the optical wavelength.

2. PLASMA MODES AT A CIRCULAR HOLE IN A SCREEN

Let us consider a metallic screen with a circular hole. It is assumed the screen has the form of a hyperboloid of revolution (Fig. 1). The Laplace equation for the electrostatic field potential $\Phi(\mathbf{r}) = \Phi(\sigma, \tau, \varphi)$ in the coordinates of the oblate ellipsoid of revolution has the form

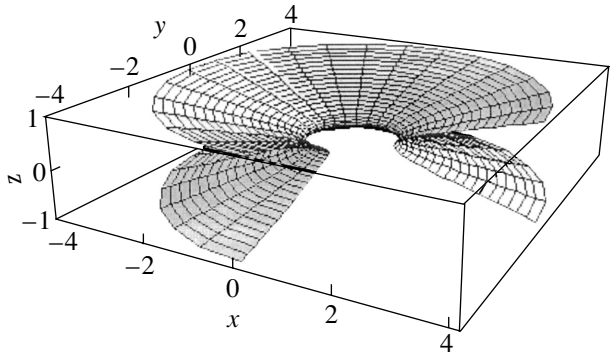

Fig. 1. Three-dimensional image of the screen with a hole (in the form of a hyperboloid of revolution with $\tau_0 = 0.25$).

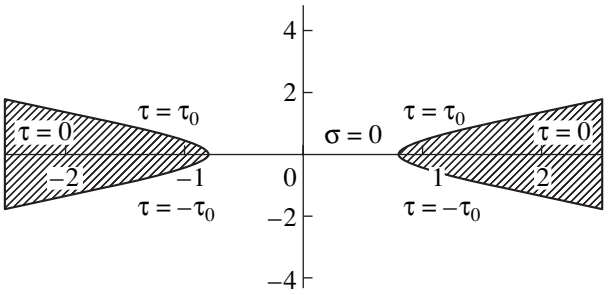

Fig. 2. Coordinate system of the hyperbolic screen with a hole.

$$\frac{\partial}{\partial\tau}\left[(1-\tau^2)\frac{\partial}{\partial\tau}\Phi^m\right] + \frac{\partial}{\partial\sigma}\left[(\sigma^2+1)\frac{\partial}{\partial\sigma}\Phi^m\right] + m^2\frac{\sigma^2+\tau^2}{(\sigma^2+1)(1-\tau^2)}\Phi^m = 0, \quad (1)$$

where

$$\Phi(\sigma, \tau, \varphi) = \sum \Phi^m(\sigma, \tau)\exp(im\varphi).$$

The coordinates σ, τ, and φ can be expressed through the Cartesian coordinates $z = a\sigma\tau$ and $x = a\cos\varphi\sqrt{(\sigma^2+1)(1-\tau^2)}$ (where a is the focal length of the ellipsoid), and the hole diameter can be determined from the focal length: $D = 2a(1-\tau_0^2)^{1/2}$. The components of the electric field can be represented in terms of the electrostatic potential Φ: $E_\sigma = [(1+\sigma^2)^{1/2}/(\sigma^2+\tau^2)^{1/2}]\partial\Phi/\partial\sigma/a$ and $E_\tau = [(1-\tau^2)^{1/2}/(\sigma^2+\tau^2)]\partial\Phi/\partial\tau/a$.

The surface of the metallic screen is determined by the equation $\tau = \pm\tau_0$ (Fig. 2). We will use the Drude model for the permittivity of the material of the screen: $\varepsilon(\omega) = 1 - \omega_p^2/[\omega(\omega + i\gamma)]$, where ω_p is the plasma frequency and γ is the collision frequency.

The symmetry of the problem is such that the solutions corresponding to the eigenmodes can be transformed through the representation of the group of rotations about the axis and the representation of the group of reflections in the plane of the screen (the *xy* plane). On this basis, the solution to the Laplace equation in three different regions of the space will be sought in the form of an expansion in Legendre functions (for brevity, the superscripts *m* on the potentials and on the associated Legendre functions are omitted):

$$\Phi(\tau, \sigma) = \int \Phi_\pm(\tau, \nu)[P_\nu(i\sigma) \mp P_\nu(-i\sigma)]d\nu. \quad (2)$$

Here, $\nu(\nu+1)$ is the constant of separation of the variables, which is taken as $\nu = -1/2 + it$, $0 < t < \infty$. For this constant of separation of the variables, the Legendre functions are real for all values of τ and are decreasing and nonsingular at $\sigma \longrightarrow \infty$. The sign "plus" in square brackets relates to the symmetric modes with respect to reflections in the *xy* plane, and the sign "minus" refers to the antisymmetric modes. The components of the electric field should be matched at the surface of the screen in the upper and lower parts, i.e., for $\tau = \pm\tau_0$, at the surface of the hole along the line $\sigma = 0$, and along the line $\tau = 0$ (Fig. 2). The specific conditions of the matching are associated with the fact that the coordinate τ exhibits a jump at $\sigma = 0$. All these conditions are satisfied for the following functions:

$$\Phi_\pm(\tau, t) = \begin{cases} A(t)P_{-1/2+it}(\tau), & 1 > \tau > \tau_0 \\ B(t)(P_{-1/2+it}(\tau) \pm P_{-1/2+it}(-\tau)), & \tau_0 > \tau > -\tau_0 \\ \pm A(t)P_{-1/2+it}(-\tau), & -\tau > \tau > -1. \end{cases} \quad (3)$$

The expansion coefficients $A(t)$, $B(t)$, … can be determined from the conditions of matching of the potential and the normal component of the induction $\varepsilon(\omega)(\partial\Phi/\partial\tau)$ at the surfaces $\tau = \pm\tau_0$. The solution to the obtained system of equations has the form

$$\varepsilon(\omega) = \frac{P'_{-1/2+it}(\tau_0)[P_{-1/2+it}(\tau_0) \pm P_{-1/2+it}(-\tau_0)]}{P_{-1/2+it}(\tau_0)[P'_{-1/2+it}(\tau_0) \mp P'_{-1/2+it}(-\tau_0)]}. \quad (4)$$

3. ANALYSIS OF THE SPECTRUM AND THE SPATIAL STRUCTURE OF NORMAL MODES

The frequencies of eigenmodes (local plasmons in the system under consideration) as functions of the continuous parameter *t* are determined from relationship (4). Let us analyze the spectrum of plasma eigenmodes in the limiting cases. First, we consider the spectrum in the limit of a thin screen ($\tau_0 \longrightarrow 0$).

In the limit of a very thin screen, the dependence of the frequency of the symmetric mode on the parameter *t* takes the form

$$\omega = \omega_{sp}(t^2/2 + 1/8)^{1/2}|\Gamma(1/4 + it/2)/\Gamma(3/4 + it/2)|, \quad \omega_{sp} = [4\pi ne^2\tau_0/m]^{1/2}. \quad (5)$$

The quantity $n\tau_0 a$ is proportional to the surface density of electrons at the screen near the focus. This quantity should be taken to be constant in the limit $\tau_0 \longrightarrow 0$. Note that, at a large distance from the edge of the screen, the above model of the screen corresponds to a screen with a hole in which the impedance is a linear function of the distance from the screen edge.

Figure 3 shows the dispersion curves for screens with different values of τ_0. The dispersion curves for different values of *m* accounting for the angular symmetry of the solutions are depicted in Fig. 4.

The spectrum is characterized by a gap in the range of small parameters *t* and approaches the frequency of a surface plasmon at large values of *t*.

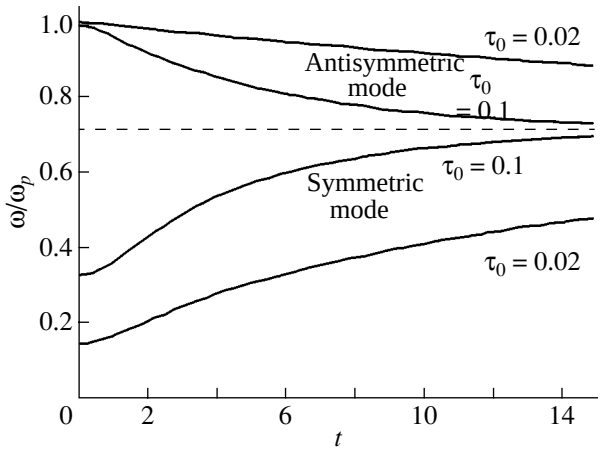

Fig. 3. Dispersion curves $\omega(t)$ for symmetric and antisymmetric modes with $m = 0$ at $\tau_0 = 0.1$ and 0.02.

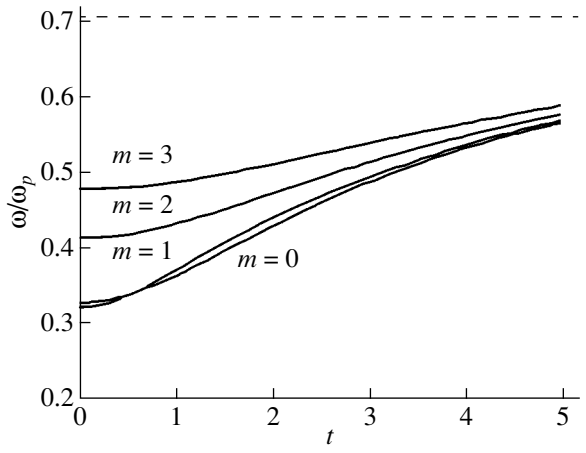

Fig. 4. Dispersion curves for symmetric modes with different values of m at $\tau_0 = 0.1$.

For symmetric modes, the spatial distributions of the fields and charges are presented in Figs. 5 and 6, respectively. In the case of a symmetric mode, the charges associated with the plasma mode have the same sign at the upper and lower parts of the screen. The charges reverse sign when the distance from the edge of the hole increases. For an antisymmetric mode, the charges at the upper and lower parts of the screen are opposite in sign (Figs. 7, 8). The spectrum of these modes is observed beginning from the plasma frequency and tends to the frequency of a surface plasmon from above at large values of t.

Judging from the spatial structure of the fields, the symmetric mode with $m = 1$ can be excited in the field of a dipole oriented along the plane of the screen, whereas the antisymmetric mode with $m = 0$ is excited by a dipole oriented along the z axis.

4. A DIPOLE AT A CIRCULAR HOLE IN A SCREEN

Let us now estimate the dipole moment induced by the plasma modes at holes in a screen:

$$\mathbf{P} = \int \mathbf{r}\sigma(\mathbf{r})dS. \qquad (6)$$

Here, $\sigma(\mathbf{r}) = \partial\varphi/4\pi\partial n$ is the charge surface density.

Upon substituting expression (2) for the potential of the plasma modes into formula (6), we obtain the following relationship for the zero ($m = 0$) symmetric mode:

$$|\mathbf{P}| = \int 2z\frac{\rho d\rho d\varphi}{\cos(\alpha(\rho))}\frac{1}{4\pi}\frac{\partial\varphi(\rho, z)}{\partial n}$$
$$\sim \int_{\rho_0}^{\rho^*} \rho d\rho (P_\nu(i\sqrt{\rho^2/\tau_1^2 - 1}) - P_\nu(-i\sqrt{\rho^2/\tau_1^2 - 1})), \qquad (7)$$

where $\alpha(\rho)$ is the slope of the tangent to the surface of the hyperboloid and $\tau_1^2 = 1 - \tau_0^2 \longrightarrow 1$ when $\tau_0 \ll 1$.

In the case when the argument is large, the Legendre functions have the asymptotics $P_\nu(x) \sim x^\nu$; hence, for $\nu = -1/2 + it$, we obtain the expression

$$|\mathbf{P}| \sim \tau_0 \frac{(t^2 + 1/4)}{|\Gamma(5/4 + it)|^2}(\rho^*)^{3/2}.$$

Here, $\rho^* = \lambda/a$ is the cutoff parameter in the quasi-electrostatic problem.

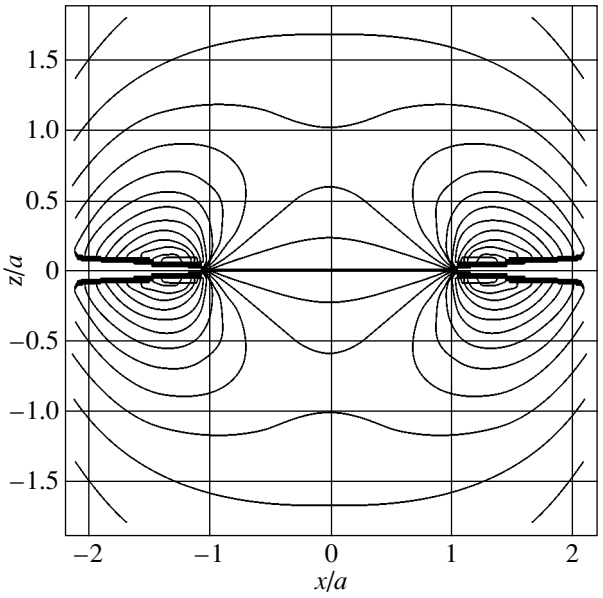

Fig. 5. The field structure of the zero ($m = 0$) symmetric mode at $t = 2$.

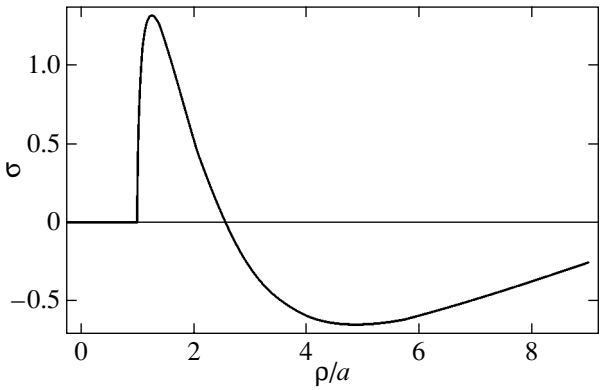

Fig. 6. Charge distribution for the zero ($m = 0$) symmetric mode at $t = 2$ and $\tau_0 = 0.05$.

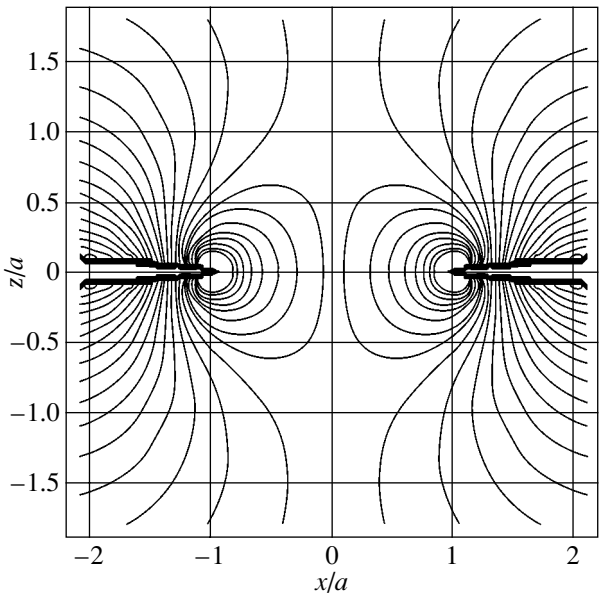

Fig. 7. The field structure of the first ($m = 1$) antisymmetric mode at $t = 2$.

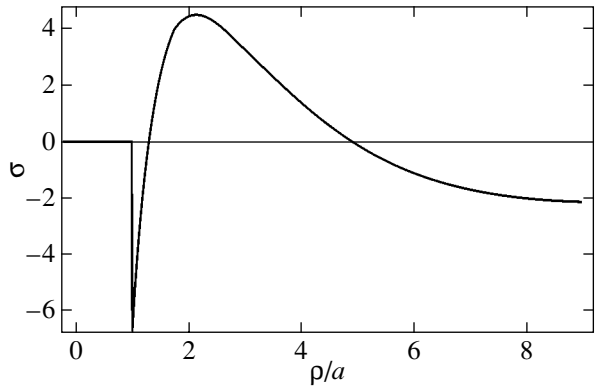

Fig. 8. Charge distribution for the first ($m = 1$) antisymmetric mode at $t = 2$ and $\tau_0 = 0.05$.

The estimation of the dipole moment induced by the first ($m = 1$) antisymmetric mode results in a similar dependence on the variables t and ρ; that is,

$$|\mathbf{P}| = \int 2\frac{\rho^2 d\rho d\varphi}{\cos(\alpha(\rho))}\cos\varphi\exp(i\varphi)\frac{1}{4\pi}\frac{\partial\varphi(\rho, z)}{\partial n} \sim \tau_0\frac{(t^2 + 1/4)}{|\Gamma(5/4 + it)|^2}(\rho^*)^{3/2}. \quad (8)$$

In this case, the dipole moment of the zero symmetric mode is perpendicular to the screen plane and the dipole moment of the first mode is aligned parallel to the screen plane.

5. THE LIMIT OF LARGE VALUES OF m

The potential of the m-mode of a plasmon localized at a circular hole in a planar screen has the following form: $\Phi^m(\sigma, \tau, \varphi) = \Phi^m(\sigma, \tau)\exp(im\varphi)$. For large values of m (and radii), we obtain the expression

$$m\varphi = \frac{2\pi R/\lambda}{R}R\varphi = k_\varphi l, \quad (9)$$

where l is the length element along the circumference of the hole in the screen.

Therefore, in the limit of large values of m, the plasma oscillations localized at a circular hole in the screen transform into edge plasmons. The amplitude of field oscillations of the edge plasmons is determined by the factor $\Phi^m(\sigma, \tau_0) = C(\tau_0)[P_\nu^m(i\sigma) \pm P_\nu^m(-i\sigma)]$. Taking into account the asymptotics of the Legendre function at large values of the argument, we can determine the field structure of the edge plasmon:

$$\Phi_R \sim \exp(ik_\varphi l)\sqrt{\rho}. \quad (10)$$

It follows from expression (10) that the plasmon is characterized by a large region of localization.

From the dispersion law for plasmons at a hole in a screen, we can obtain the dispersion relation for edge plasmons ($m \gg 1$): $\varepsilon(\omega) = -1$; i.e., the frequency of edge plasmons coincides with the frequency $\omega_p/\sqrt{2}$ of the surface plasmon.

6. CONCLUSIONS

Thus, we obtained the spectrum of plasma oscillations at a circular hole in a planar screen. The spectrum is characterized by a gap in the range of small parameters t and approaches the frequency of the surface plasmon at large values of t.

The analysis of the spatial distribution of the fields and charges associated with plasma oscillations demonstrated that the symmetric mode with $m = 1$ can be efficiently excited by a dipole oriented perpendicularly to the screen plane, whereas the antisymmetric mode with $m = 0$ is excited by a dipole aligned parallel to the

screen. At large distances, the field of the eigenmodes decrease rather slowly (as $1/\sqrt{\rho}$); i.e., the plasmons are weakly localized at the hole.

The estimates of the dipole moments for the symmetric and antisymmetric modes indicate that the dipole moment decreases linearly with a decrease in the thickness of the screen and is proportional to $(\rho^*)^{3/2}$ ($\rho^* = \lambda/a$ is the cutoff parameter in the electrostatic problem).

ACKNOWLEDGMENTS

This work was supported by the Russian Foundation for Basic Research, project nos. 01-02-18040 and 02-02-17937.

REFERENCES

1. U. Ch. Fischer and D. W. Pohl, Phys. Rev. Lett. **62**, 458 (1989).
2. W. Denk and D. W. Pohl, J. Vac. Sci. Technol. B **9**, 510 (1991).
3. M. Xiao, J. Mod. Opt. **44**, 327 (1997).
4. T. W. Ebbesen, H. J. Lezec, H. F. Ghaemi, *et al.*, Nature **391**, 667 (1998).
5. L. Martín-Moreno, F. J. García-Vidal, H. J. Lezec, *et al.*, Phys. Rev. Lett. **86** (6), 1114 (2001).
6. V. A. Kosobukin, Phys. Lett. A **160** (6), 584 (1991).
7. D. V. Khveshchenko and M. Reizer, Phys. Rev. B **57** (8), 4245 (1998).
8. J. R. Krenn, J. C. Weeber, A. Dereux, *et al.*, Phys. Rev. B **60** (7), 5029 (1999).
9. Yu. E. Lozovik and A. V. Klyuchnik, in *Modern Problems in Condensed Matter Sciences: Dielectric Susceptibility*, Ed. by L. V. Keldysh, D. A. Kirzhnitz, and A. A. Maradudin (North-Holland, Amsterdam, 1989), p. 299.

Translated by O. Moskalev

Physics of the Solid State, Vol. 45, No. 9, 2003, pp. 1798–1801. Translated from Fizika Tverdogo Tela, Vol. 45, No. 9, 2003, pp. 1713–1716.

LOW-DIMENSIONAL SYSTEMS AND SURFACE PHYSICS

Long-Wavelength IR Spectroscopy of ZnTe/CdTe Superlattices with Quantum Dots

L. K. Vodop'yanov*, S. P. Kozyrev*, and G. Karczewski**

** Lebedev Physical Institute, Russian Academy of Sciences, Leninskiĭ pr. 53, Moscow, 119991 Russia*

e-mail: vodopian@sci.lebedev.ru

*** Institute of Physics, Polish Academy of Sciences, Warsaw, 02-668 Poland*

Received January 17, 2003

Abstract—This paper reports on the results of investigations of the lattice IR reflection spectra of ZnTe/CdTe multilayer superlattices with CdTe quantum dots grown by molecular-beam epitaxy on a GaAs substrate with a CdTe buffer layer. It is found that the lattice IR reflection spectra of the studied structures exhibit three intense bands associated with vibrational excitations in the GaAs substrate, ZnTe barriers separating the layers with CdTe quantum dots, and the CdTe buffer layer. An analysis of the reflection bands and shifts in the phonon frequencies has revealed internal elastic stresses both in the surface layer of the GaAs substrate and in the ZnTe barriers. It is established that elastic stresses undergo relaxation in the separating ZnTe layers with an increase in their thickness. An additional mode observed in the reflection spectra is explained by manifestations of ZnTe-like vibrations in the ZnCdTe alloy due to interdiffusion of Cd and Zn at the interfaces. © *2003 MAIK "Nauka/Interperiodica".*

1. INTRODUCTION

In recent years, great interest has been expressed by researchers in the properties of superlattices based on semiconductor materials with a mismatch between their lattice parameters. These structures are characterized by favorable conditions for the formation of self-assembled quantum dots. Considerable attention has been given to the study of self-assembled quantum dots in structures based on Ge/Si and III–V compounds (InAs/GaAs, InSb/GaSb, etc.). However, the physical properties of quantum dots in structures based on II–VI semiconductor compounds are poorly understood. Quantum dots in II–VI structures were first found by Bagaev *et al.* [1] from analyzing the photoluminescence spectra. Multilayer structures with selenide-based quantum dots were thoroughly studied by Krestnikov *et al.* [2] and Peranio *et al.* [3], who revealed a spatial correlation between quantum dots contained in consecutive layers. Superlattices with telluride-based quantum dots were examined in [4–6]. It was found that the occurrence of correlations between self-assembled quantum dots in adjacent layers depends on the thickness of the ZnTe barriers separating the layers with quantum dots. It should be noted that all the aforementioned works dealt with the structural and electronic (photoluminescence) properties of superlattices with self-assembled quantum dots. As far as we know, the lattice dynamics of these structures, i.e., their photon properties, have not been investigated previously. However, analysis of the vibrational spectra of superlattices would provide a wealth of information on their physical properties.

This paper reports on the results of measurements and analysis of the lattice IR reflection spectra of superlattices with ZnTe/CdTe quantum dots.

2. GROWTH OF SUPERLATTICES WITH QUANTUM DOTS AND MEASUREMENTS

Superlattices were grown by molecular-beam epitaxy on a GaAs(100) substrate with a thick CdTe buffer layer. The thickness of the buffer layer was approximately equal to 4.5 μm. The structures grown involved 200 periods of CdTe layers with a thickness of 2.5 monolayers (ML). The CdTe layers were separated by ZnTe barriers with a thickness of 12 ML (structure *B*12) or 25 ML (structure *B*25). The structure with a barrier thickness of 75 ML (structure *B*75) involved 100 periods. The structures grown were examined on a JEOL 2000 transmission electron microscope (TEM) with a point resolution of 0.27 nm. An analysis of the changes in the lattice parameters in the growth direction demonstrated that the structures studied contain CdTe islands approximately 2 nm thick and 6–10 nm in diameter. These islands are identified as self-assembled quantum dots. It is of interest that the thickness of the quantum dots is considerably greater than the thickness of the CdTe layer grown (the thickness of a CdTe monolayer is equal to 0.324 nm; 2.5 ML = 0.81 nm). This can be explained by the Cd and Zn interdiffusion stimulated by elevated growth temperatures. An examination of the TEM images revealed a vertical correlation between CdTe islands. This correlation manifests itself in the fact that an island in a particular layer is located over a similar island in the lower layer, etc. The

line joining the correlated islands makes an angle of 40° with the growth direction. Moreover, the same sample contains randomly arranged CdTe islands in addition to the correlated quantum dots. The observed vertical correlation of self-assembled quantum dots is explained by the anisotropy of the elastic energy of the matrix material (ZnTe) [7].

The long-wavelength IR reflection spectra were recorded on a laboratory vacuum grating infrared spectrometer and on a Bruker Fourier-spectrometer with a spectral resolution of 1 cm^{-1}.

3. ANALYSIS OF LATTICE IR REFLECTION SPECTRA. RESULTS AND DISCUSSION

The lattice IR reflection spectra of the superlattices with CdTe quantum dots separated by ZnTe barriers with a thickness of 12 ML (structure *B*12) or 25 ML (structure *B*25) are shown in Fig. 1. In this figure, the points are the experimental data and the heavy solid lines represent the calculated spectra. For clarity, the spectrum of the *B*25 structure is shifted along the ordinate axis by 0.2. The spectral range in the vicinity of 270 cm^{-1} corresponds to lattice reflections of the GaAs substrate, and the spectral features in the vicinity of 140 and 170 cm^{-1} are attributed to the CdTe and ZnTe vibrations of the buffer layer and the superlattice. In the transparency region of the GaAs substrate, the CdTe buffer layer, and the CdTe/ZnTe superlattice, all the reflection spectra exhibit frequent oscillations associated with the interference on 400- to 500-μm-thick GaAs substrates. As can be seen from Fig. 1, these oscillations manifest themselves at frequencies below 140 cm^{-1} and, in part, in the range between the ZnTe vibrations and lattice vibrations of the GaAs substrate.

The specific features of the IR reflection spectra in the range of lattice vibrations and their interpretation for film/substrate structures with thin films (1–2 μm) were discussed in our earlier work [8] for $Zn_{1-x}Cd_xSe$/GaAs structures. In this case, the reflection spectrum has a rather simple shape. Compared to the IR reflection spectrum of the substrate in the transparency region, the main features of the reflection spectrum of the film/substrate structure resemble those observed in the spectrum of the film and can easily be mathematically treated on the basis of the dispersion analysis. However, when interpreting the lattice reflection spectra of the superlattices under investigation, it should be remembered that the structure involves a 4.5-μm-thick CdTe buffer layer. As a result, the total thickness of the structure, including the superlattice thickness (on the average, 3.5 μm), is approximately equal to 8 μm, which is comparable to the depth of penetration of exciting IR radiation into the sample. Therefore, in the strict sense, the thin-film approximation ($d_f \ll \lambda$) is inapplicable in the given case and the qualitative determination of the dispersion parameters for the CdTe layer presents considerable difficulties.

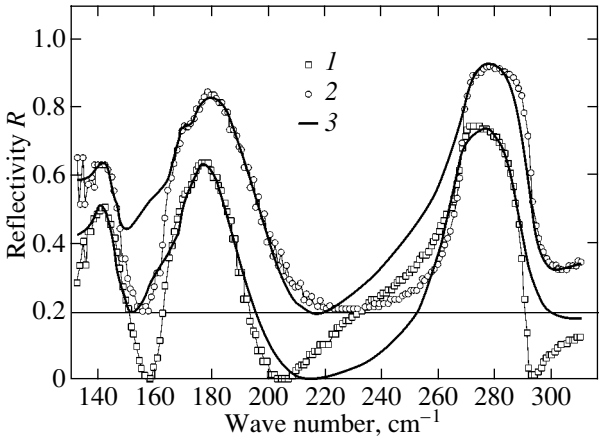

Fig. 1. (*1*, *2*) Experimental and (*3*) calculated lattice IR reflection spectra of *B*12 (open squares) and *B*25 (open circles) superlattices grown on a GaAs substrate. The thicknesses of the potential barriers in *B*12 and *B*25 superlattices are equal to 12 and 25 ML, respectively.

The dispersion analysis of the lattice IR reflection spectra of the superlattices was carried out using a model structure formed by a thin film (a superlattice and a buffer layer) on a semi-infinite substrate. In the framework of this model for a film of thickness L with a dielectric function $\varepsilon_f(\omega)$ and a substrate with a dielectric function $\varepsilon_s(\omega)$ in normally incident light, the amplitude reflectivity (without regard for the multiple reflection in the film) has the following form [9]:

$$r_{1fs}(\omega) = \frac{r_{1f}(\omega) + r_{fs}(\omega)\exp(i2\beta)}{1 + r_{1f}(\omega)r_{fs}(\omega)\exp(i2\beta)}, \qquad (1)$$

where

$$r_{1f}(\omega) = \frac{1 - \sqrt{\varepsilon_f(\omega)}}{1 + \sqrt{\varepsilon_f(\omega)}},$$

$$r_{fs}(\omega) = \frac{\sqrt{\varepsilon_f(\omega)} - \sqrt{\varepsilon_s(\omega)}}{\sqrt{\varepsilon_f(\omega)} + \sqrt{\varepsilon_s(\omega)}} \quad \text{and} \quad \beta = \frac{2\pi L\sqrt{\varepsilon_f(\omega)}}{\lambda}.$$

Here, λ is the wavelength. The reflectivity is defined by the formula $R(\omega) = |r_{1fs}(\omega)|^2$. The inclusion of the multiple reflection in the film at the film–substrate and film–vacuum interfaces leads to a very cumbersome relationship for the reflectivity, which accounts for interference effects and provides no additional information on the lattice vibrations.

The dielectric function $\varepsilon_{SL}(\omega) = \varepsilon_f(\omega)$ of the superlattice as a whole was considered in the classical additive form

$$\varepsilon_f(\omega) = \varepsilon_\infty + \sum_j \frac{S_j\omega_{ij}^2}{\omega_{ij}^2 - \omega^2 - i\omega\gamma_j}. \qquad (2)$$

In calculations of the reflectivity $R(\omega)$, we varied the following parameters in the formula for the dielectric

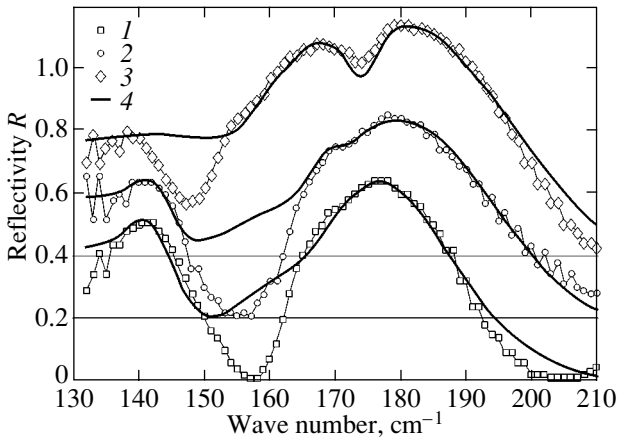

Fig. 2. (*1–3*) Experimental and (*4*) calculated lattice IR reflection spectra of *B*12 (open squares), *B*25 (open circles), and *B*75 (open rhombs) superlattices in the range of ZnTe and CdTe vibrations.

function $\varepsilon_f(\omega)$: the frequency ω_{ij} of the jth TO-phonon mode, the oscillator strength S_j of the jth TO-phonon mode, and the attenuation parameter γ_j.

First, we consider the results obtained in the analysis of the reflection band of the GaAs substrate. The calculated frequency of the GaAs lattice mode for the substrate with a 4.5-μm-thick CdTe buffer layer is equal to 267 cm^{-1}, which is 3 cm^{-1} less than that of the lattice mode for a GaAs bulk crystal. The attenuation parameter γ of the former mode is 8 cm^{-1}. For comparison, the frequency of the GaAs lattice mode for the GaAs substrate with a deposited ZnSe layer is equal to 269 cm^{-1} and the attenuation parameter γ of this mode is 2.5 cm^{-1}, which, within the limits of experimental error, coincide with the corresponding parameters for an unstrained substrate. The shift in the frequency of the lattice TO mode of the GaAs substrate by 3 cm^{-1} for the studied structures is likely caused by the elastic stresses at the interface between the GaAs substrate and the CdTe buffer layer due to a considerable difference in their lattice parameters. Actually, the difference between the lattice parameters of CdTe and GaAs is determined to be Δa = 6.48 Å – 5.65 Å = 0.83 Å, whereas this difference of ZnSe and GaAs is Δa = 0.02 Å. The large attenuation parameter γ = 8 cm^{-1} for GaAs indicates that the surface layer of the substrate is strongly strained as a result of the elastic stresses arising at the interface of the GaAs substrate with the CdTe buffer layer.

The reflection band at 140 cm^{-1} is assigned to the CdTe buffer layer. As was noted above, this mode cannot be correctly analyzed in terms of the model used in calculations due to a large thickness of the buffer layer and, therefore, is eliminated from consideration.

The most interesting effects are observed for the superstructures with CdTe quantum dots separated by ZnTe barriers when studying the ZnTe mode as a function of the barrier thickness. Figure 2 shows the lattice IR reflection spectra in the frequency range of the ZnTe mode for the *B*12 (spectrum *1*), *B*25 (spectrum *2*), and *B*75 (spectrum *3*) structures with ZnTe barrier layers of different thicknesses. The solid thick lines indicate the spectra calculated on the basis of dispersion analysis. For clarity, the spectra are shifted with respect to each other along the ordinate axis. The dispersion analysis revealed that, in the *B*12 structure with the thinnest barrier layer, the ZnTe vibrations are characterized by one dominant mode at ω_{t1} = 172 cm^{-1}. In the *B*25 structure, the frequency of the dominant mode increases to ω_{t1} = 173.5 cm^{-1} and an additional mode arises at ω_{t2} = 169 cm^{-1}. In the *B*75 structure (in which CdTe layers 2.5 ML in thickness alternate with ZnTe barrier layers 75 ML in thickness), the ZnTe vibrations involve two modes at ω_{t1} = 176 cm^{-1} and ω_{t2} = 165 cm^{-1}. As the thickness of the barrier layer changes, the frequency of the dominant mode ω_{t1} increases from 172 to 176 cm^{-1} and, within the limits of experimental error, becomes equal to the frequency of the transverse mode ω_t = 177 cm^{-1} for pure ZnTe. This implies that thin ZnTe barrier layers in the *B*12 structure are strongly stretched by the alternating CdTe layers and a thick CdTe buffer layer. The stresses in thinner CdTe layers are partially relieved through the formation of self-assembled quantum dots. In the *B*75 structure, the barrier layers are thick enough for the elastic relaxation to be completed.

We assume that the mode observed at 169 cm^{-1} for the *B*25 structure and the mode at 165 cm^{-1} for the *B*75 structure can be associated with the mode of a ZnCdTe alloy formed at the layer interfaces due to the interdiffusion of Cd and Zn. In our earlier work [10], we investigated the evolution of the phonon spectra of $Zn_{1-x}Cd_xTe$ alloys with a variation in the composition x. From analyzing of the results obtained, we determined the dependence of the frequencies of the TO modes of ZnTe- and CdTe-like vibrations on the content x. This dependence was used to evaluate the content of the formed alloy from the frequency of the additional reflection band. The alloy content was estimated to be x = 0.15–0.20.

It should be noted that, in the studied structures, we failed to observe vibrational excitations directly in the CdTe quantum dots. The point is that thin layers of quantum dots (2.5 ML = 0.81 nm) are shielded by a thick CdTe buffer layer (4.5 μm). Since the exciting IR radiation penetrates over a large depth (~10–15 μm) upon originating a reflected wave, the lattice IR reflection spectrum contains integral information on all the layers comprising the studied structure. This makes it possible to trace the appearance of elastic stresses in different structural components.

A different situation is observed in Raman spectroscopy. The Raman spectra are excited by visible light, and the penetration depth amounts to 100–200 nm. In this case, information is obtained for the upper layer of the structure, which represents the superlattice. In our

recent work [11], we observed vibrational excitations directly in CdTe quantum dots in the same samples with the use of Raman spectroscopy. It was found that the nature of these excitations differs essentially from the nature of phonons in the bulk crystal.

4. CONCLUSIONS

Thus, the above analysis of the long-wavelength lattice IR reflection spectra of ZnTe/CdTe superlattices formed by layers of self-assembled quantum dots revealed internal elastic stresses in these structures. The occurrence of these stresses was judged from the shift in the frequency of the transverse optical phonons localized in the corresponding regions of the nanostructures under investigation. It was found that elastic stresses arise in the GaAs substrate, which can be explained by the mismatch between the lattice parameters of the substrate and the CdTe buffer layer. The separating barriers are also in the strained state. It was established that elastic stresses in the ZnTe barriers undergo relaxation with an increase in the barrier thickness from 12 to 75 ML. Unfortunately, our attempts to observe vibrons in the CdTe quantum dots were unsuccessful, because the dots were shielded by a thick buffer layer. The inference was drawn that the additional band revealed in the IR reflection spectra in the frequency range of the ZnTe mode for the *B*25 and *B*75 structures is associated with the formation of a ZnCdTe solid solution during the crystal growth, which is most likely caused by the interdiffusion of zinc and cadmium at the interfaces.

ACKNOWLEDGMENTS

We are grateful to V.S. Bagaev and E. Makhov for performing the Fourier spectrometer measurements.

This work was supported by the Russian Foundation for Basic Research, project no. 03-02-7110.

REFERENCES

1. V. S. Bagaev, V. V. Zaitsev, V. V. Kalinin, *et al.*, Solid State Commun. **88**, 777 (1993).
2. L. Krestnikov, M. Strassburg, M. Caesar, *et al.*, Phys. Rev. B **60**, 8695 (1999).
3. N. Peranio, A. Rosenauer, D. Gerthsen, *et al.*, Phys. Rev. B **61**, 16015 (2000).
4. V. V. Zaĭtsev, V. S. Bagaev, and E. E. Onishchenko, Fiz. Tverd. Tela (St. Petersburg) **41** (4), 717 (1999) [Phys. Solid State **41**, 647 (1999)].
5. G. Karczewski, S. Mackowski, M. Kutrowski, *et al.*, Appl. Phys. Lett. **74**, 3011 (1999).
6. S. Mackowski, G. Karczewski, T. Wojtowicz, *et al.*, Appl. Phys. Lett. **78**, 3884 (2001).
7. V. Holy, G. Springholz, M. Pinczolits, and G. Bouer, Phys. Rev. Lett. **83**, 356 (1999).
8. L. K. Vodop'yanov, S. P. Kozyrev, and Yu. G. Sadof'ev, Fiz. Tverd. Tela (St. Petersburg) **41** (6), 982 (1999) [Phys. Solid State **41**, 893 (1999)].
9. H. W. Verleur, J. Opt. Soc. Am. **58**, 6 (1968).
10. S. P. Kozyrev, V. N. Pyrkov, and L. K. Vodop'yanov, Fiz. Tverd. Tela (St. Petersburg) **34**, 2367 (1992) [Sov. Phys. Solid State **34**, 1267 (1992)].
11. L. K. Vodop'yanov, V. S. Vinogradov, N. N. Mel'nik, and G. Karchevski, Pis'ma Zh. Éksp. Teor. Fiz. **77** (3), 171 (2003) [JETP Lett. **77**, 143 (2003)].

Translated by O. Borovik-Romanova

Physics of the Solid State, Vol. 45, No. 9, 2003, pp. 1802–1807. Translated from Fizika Tverdogo Tela, Vol. 45, No. 9, 2003, pp. 1717–1721.

LOW-DIMENSIONAL SYSTEMS AND SURFACE PHYSICS

NMR of Mercury in Porous Carbon and Silica Gel

V. S. Kasperovich*, E. V. Charnaya*, C. Tien, and C. S. Wur****

**Research Institute of Physics, St. Petersburg State University, Ul'yanovskaya ul. 1, Petrodvorets, St. Petersburg, 198504 Russia*

e-mail: charnaya@paloma.spbu.ru

***Department of Physics, National Cheng Kung University, Tainan, 10701 Taiwan*

Received February 7, 2003

Abstract—The temperature dependences of the integrated intensity and of the Knight shift of ^{199}Hg NMR signals are measured for liquid and solid mercury introduced into porous carbon and silica gel. A decrease in the temperature of completion of crystallization and a small temperature hysteresis (from 4 to 9 K) between melting and crystallization are observed. The melting temperature of mercury in pores coincides with that in the bulk. The ^{199}Hg NMR signal from crystalline mercury under the condition of restricted geometry is observed for the first time. It is established that the Knight shift for liquid and crystalline mercury in pores is smaller than in the bulk. © *2003 MAIK "Nauka/Interperiodica".*

1. INTRODUCTION

Size effects at melting–crystallization phase transitions in small particles have been studied for about a century [1, 2]. The first theoretical models describing the decrease in melting temperature with decreasing particle size were based on the assumption of the existence of a triple point corresponding to the equilibrium of solid, liquid, and gaseous phases [1]. Later, it was shown that there exists a temperature range in which the formation of a melted layer on a solid nucleus becomes energetically more favorable for nanoparticles (see [3] and references therein). The thickness of this layer grows with increasing temperature until the entire particle melts. The melting and crystallization of small isolated metallic particles have also been intensively studied experimentally [4, 5]. It was shown that if particles are isolated, the melting temperature, as a rule, decreases as compared to the melting temperature of the respective bulk metals. In several studies [2, 5], the formation of a liquid surface layer was observed in the process of melting.

Small metallic particles can also be formed by incorporating a melt into a porous matrix under pressure. In contrast to isolated particles, the phase transitions in a metal with restricted geometry are affected by the interaction with the internal surface of a porous matrix. In addition, particles in pores can interact with each other. High electrical conductivity of porous glasses filled with metals supports the idea of formation of a network of linked nanoparticles in pores [6]. X-ray diffraction studies show that the sizes of metallic crystallites in porous glasses can be much larger than the sizes of the pores [7]. These factors complicate the melting and crystallization in porous matrices. It is still unclear whether or not the melting–crystallization phase transition models developed for isolated metallic particles are applicable to the processes occurring in porous media.

Experimental studies of the melting and crystallization of metals in restricted geometry show that the melting temperatures decrease and the formation of liquid and solid phases exhibits thermal hysteresis in this case [6, 8, 9]. The results of the studies on melting–crystallization phase transitions in porous glasses conducted in [8–10] are consistent with previous results obtained for isolated mercury particles [4]. However, the existing experimental data are not sufficient for comprehensive explanation of the specific features of the melting–crystallization phase transition in porous matrices; therefore, new experiments are required.

For this purpose, one can use methods which have been successively used for studying bulk materials, e.g., nuclear magnetic resonance (NMR). The temperature variation of the NMR signal intensity from a liquid phase gives the fraction of melt in a straightforward manner. In addition, for metals in pores, the influence of the surface on the electron subsystem becomes stronger, which should specifically result in a change in the Knight shift.

In order to investigate the effect of restricted geometry on the melting– crystallization phase transition, we studied the temperature dependences of the NMR signal intensity and of the Knight shift of ^{199}Hg nuclei in mercury introduced into porous matrices.

2. EXPERIMENT

As the objects of investigation, activated porous carbon and silica gel filled with mercury were used. Two types of porous carbon were analyzed: polymeric acti-

1063-7834/03/4509-1802$24.00

vated carbon (PAC) powders with particle sizes ranging from 0.07 to 0.12 mm and spherical carbonic nitrogenated (SCN) powders of a new generation with particle sizes from 0.1 to 0.7 mm and pores approximately cylindrical in shape. The particle size of silica gel was about 3 mm, and the pores were close to spherical. The distribution function of the pore volume in radius was determined using the method of mercury porometry under pressures of up to 9 kbar. The samples obtained in the process of porometry were used in subsequent NMR measurements.

A PAC sample contains nanopores and macroscopic pores filled with bulk mercury (Fig. 1). SCN samples and silica gel, for the most part, contain nanopores. Characteristic pore sizes are listed in Table 1. NMR was observed with the aid of a Bruker AVANCE-400 pulsed spectrometer. The reference frequency with respect to which the shifts of ^{199}Hg NMR signals were measured in all samples was equal to 71.332311 MHz. A single-pulse mode was used to record NMR signals. The pulse duration was chosen so as to obtain the maximum NMR signal and was equal to 12, 14, and 18 μs for various samples. The pulse repetition period was equal to 0.5 s.

The experiments were carried out in the temperature range 190–300 K, which includes the melting point of bulk mercury (234.2 K [11]). The cooling and heating rate did not exceed 0.5 K/min. Prior to each measurement, a sample was kept at a constant temperature for a period of over 5 min. The temperature was controlled with an accuracy of 0.5 K. In order to increase the signal-to-noise ratio, accumulations of 30000 to 50000 NMR signals were used; therefore, one experiment took approximately 4–7 hours. For comparison with porous materials, NMR measurements were also made in bulk mercury prepared as a suspension of mercury drops in Vaseline, with the drop diameter being no larger than 0.1 mm.

3. RESULTS AND DISCUSSION

The NMR spectrum of liquid mercury for all samples consists of a single line. NMR spectra of ^{199}Hg in SCN powders and of the bulk mercury are shown in Fig. 2. The ^{199}Hg NMR line in all the samples studied is broadened in comparison with the signal from the bulk mercury and shifted towards lower frequencies (Table 2).

The melting–crystallization processes were studied by measuring the relative integrated intensity of ^{199}Hg NMR signals from the liquid phase. Since the integrated intensity of NMR signals is directly proportional to the amount of liquid phase in a sample, the solidification of mercury results in a decrease in the NMR signal intensity. This temperature dependence for an SCN sample is shown in Fig. 3. The amount of liquid mercury begins to decrease below 240 K, and the mercury completely freezes at 230 K for a PAC sample and at 228 K for an SCN sample. In silica gel, despite the fact that the pores in it are of the same size as in an SCN sample, the crystallization process is more extended in temperature and terminates at a temperature 11 K lower than that in the bulk mercury (Table 3). It is notable that the integrated intensity of the ^{199}Hg NMR signal in all

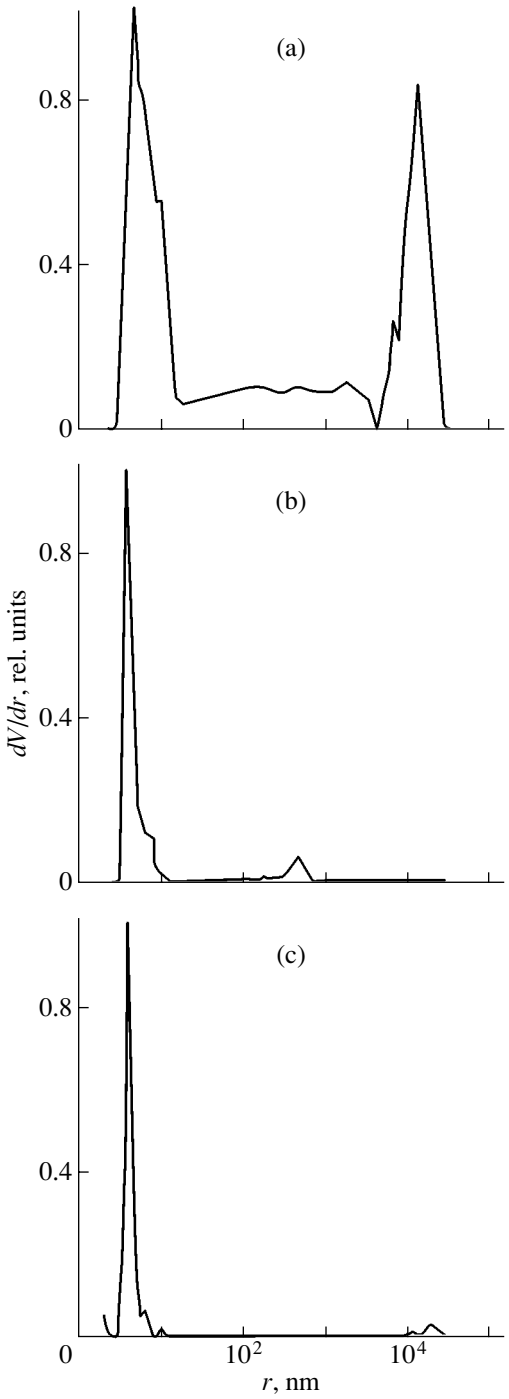

Fig. 1. Distribution of the pore volume in radius according to the mercury porometry data: (a) PAC, (b) SCN, and (c) silica gel.

Table 1. Typical pore radii (according to mercury porometry data)

Sample	*r*, nm
PAC	4.7
PAC	14000
SCN	3.8
Silica gel	3.9

Table 2. Line width δ and the Knight shifts in liquid (K_l) and crystalline mercury (K_c)

Sample	δ, ppm (T = 250 K)	K_l, ppm (T = 250 K)	K_c, ppm (T = 250 K)
PAC	81 ± 5	27438 ± 5	
SCN	110 ± 5	27385 ± 5	27910 ± 30
Silica gel	82 ± 5	27420 ± 5	27890 ± 20
Bulk Hg	78 ± 5	27452 ± 5	27990 ± 20

the samples studied steadily increases with cooling in the range from 296 to 240 K and follows the Curie law.

The melting of mercury in carbon occurs in a narrow temperature interval and becomes pronounced at 234 K for PAC and at 232 K for the SCN sample. The melting in silica gel begins at 232 K. In this case, the NMR signal from liquid mercury is observed in parallel with the signal from the solid phase and the transition is more extended than in activated carbon.

In spite of the fact that the melting and crystallization temperatures of activated-carbon samples differ from the melting temperature of the bulk mercury only slightly, the Knight shift changes noticeably both in carbon and in silica gel. This fact indicates that NMR signals come predominantly from mercury in nanopores. In previously studied samples of mercury-containing porous glasses with pore sizes of 3–4 nm [9, 10], crystallization was completed upon cooling to 165 K and melting began at 200 K. In zeolites containing mercury clusters 0.9 nm in size [12], the melting temperature decreased by 95 K in comparison to that of the bulk mercury, while in asbestos (where mercury was introduced into 10-μm-long capillaries and was kept there under a pressure of 10 kbar), the crystallization temperature decreased to 210 K in capillaries 2 nm in diameter and coincided with the crystallization temperature of the bulk mercury (260 K at a pressure of 10 kbar) in capillaries 10 nm in diameter [13]. The most pronounced hysteresis of the phase transition was observed for capillaries 5 nm in diameter.

Theoretical models of melting of small particles of any nature predict that the melting temperature decreases in comparison with bulk samples and that the decrease (ΔT) is inversely proportional to the radius of the particles ($\Delta T = C/r$) [14]. The theoretically predicted temperature change was actually observed in most melting–crystallization processes studied previously in isolated small metallic particles [2]. The dependence of the melting temperature on particle size in organic liquids in porous matrices is used in NMR cryometry [15]. A somewhat more complicated depen-

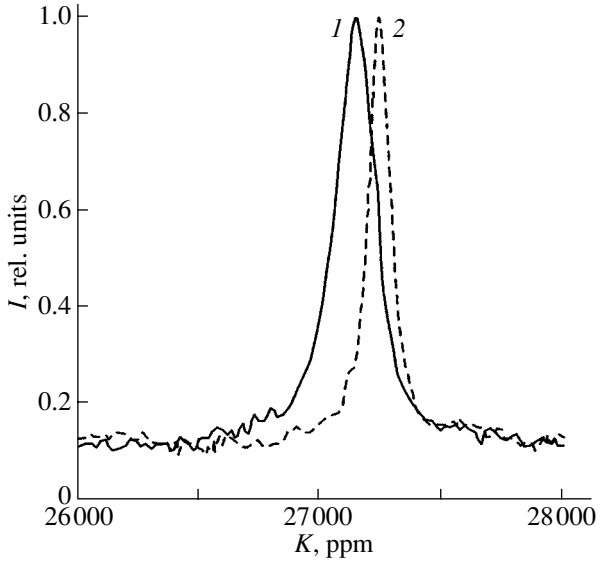

Fig. 2. ^{199}Hg NMR spectra in (*1*) activated SCN carbon and (*2*) in bulk mercury at 250 K.

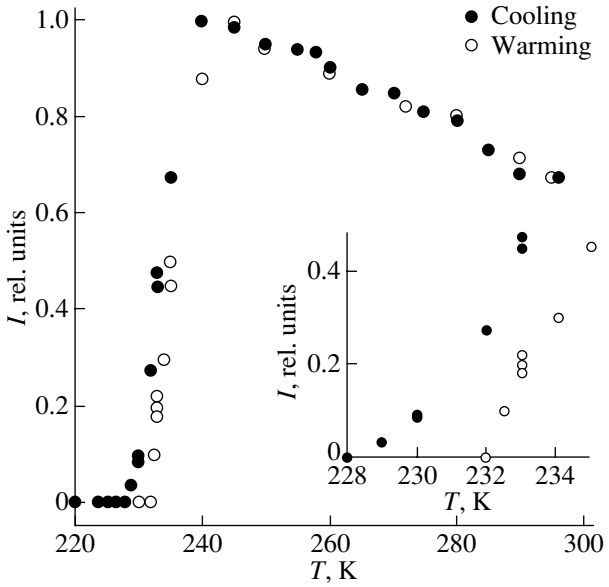

Fig. 3. Temperature dependence of the integrated intensity of ^{199}Hg NMR signals from the liquid phase in activated SCN carbon. Inset shows the same dependence in the temperature range from 228 to 235 K.

dence was observed in gallium in a restricted geometry [6]; however, in this case, the melting temperature also shifted appreciably in comparison with that of a bulk sample. The experimental results obtained for mercury in the present study show that the melting temperature of mercury in activated carbon and silica gel is virtually coincident with that of the bulk mercury. This result cannot be related to a small value of the coefficient C in the relation between ΔT and the particle size for mercury, because, e.g., in zeolites, as discussed above, an appreciable shift in the melting temperature was observed. Thus, one may assume that the decrease in the melting temperature is caused not only by the sizes of particles in pores, but also most likely by such factors as the geometry of pores, wettability, and the degree of pore filling. In addition, as discussed in [14], the existence of a bulk liquid on the sample surface or in pores of large diameter may lessen the distinction between the crystallization temperatures of a liquid in nanopores and of the bulk liquid. In actual fact, the PAC sample contained a considerable quantity of large pores and the SCN sample had drops of bulk mercury on its surface.

The temperature dependences of the Knight shift in all samples had the same character and were similar to that for bulk mercury. As an example, Fig. 4 shows the temperature dependence (upon cooling and heating) of the Knight shift for the SCN sample and compares it with the results obtained for the bulk mercury. The values of the Knight shift for liquid mercury in all samples at 250 K are listed in Table 2. The largest difference in the Knight shift between bulk mercury and mercury in a restricted geometry was observed in the SCN sample. In contrast to the data presented in [9, 10] for mercury in porous glasses, the values of the Knight shift upon heating and cooling for mercury incorporated into porous carbon and silica gel were identical to within experimental error.

Table 3. Temperature of crystallization completion T_c and the temperature hysteresis interval ΔT

Sample	T_c, K	ΔT, K
PAC	230 ± 1	4 ± 1
SCN	228 ± 1	4 ± 1
Silica gel	223 ± 1	9 ± 1
Bulk Hg	233 ± 1	2 ± 1

In the SCN samples at temperatures below 230 K and in silica gel below 225 K, ^{199}Hg NMR signals from the solid phase became observable. NMR spectra from the liquid (225 K) and solid (220 K) phases of mercury in silica gel are shown in Fig. 5. No NMR signal from the solid phase in the PAC sample was observed. Previously, the NMR signal from the solid phase of metals in a restricted geometry was not observed [9, 10], which is likely connected with an inhomogeneous distribution of the principal axes of the Knight shift tensor in various crystallites and pores. Another possible cause of the absence of an NMR signal from the solid metallic phase in pores can be the presence of mechanical stresses, which cause a large variance in the values of the Knight shift over a sample.

NMR signals from the solid phase in the SCN sample and silica gel had a small amplitude because of the large anisotropy of the Knight shift in solid mercury and, consequently, a large NMR line broadening and a

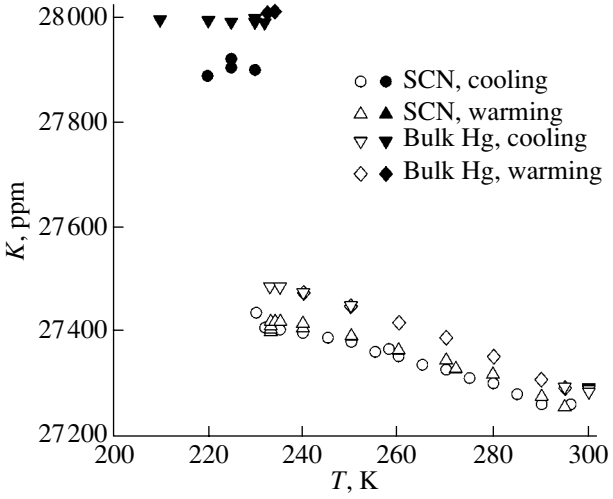

Fig. 4. Temperature dependence of the Knight shift for ^{199}Hg in activated SCN carbon and in bulk mercury. Open and bold symbols correspond to the liquid and solid phases, respectively.

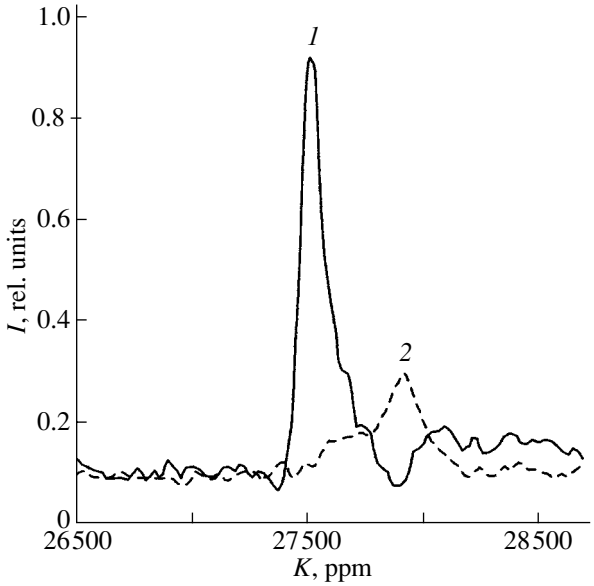

Fig. 5. NMR spectra from (*1*) the liquid and (*2*) solid phases of mercury at temperatures of 225 and 220 K, respectively.

complex line shape (Fig. 5). The positions of peaks for solid mercury in the temperature range studied (200–230 K) remained unchanged to within experimental error. It should be noted that independence of the Knight shift from temperature was also observed in bulk crystalline mercury [16]. The Knight shift values measured from the positions of the NMR peaks for the SCN samples, silica gel, and bulk mercury at 220 K are listed in Table 2. As can be seen, the values of the NMR peak shifts for solid mercury in the SCN samples and in silica gel are the same to within experimental error but are smaller than that for the bulk solid mercury.

The shift of the NMR peak from randomly oriented crystallites is determined by the isotropic ($\Delta\nu_{is}$) and anisotropic ($\Delta\nu_{an}$) parts of the Knight shift and can be estimated in the first approximation as [17]

$$\Delta\nu = \Delta\nu_{is} - \Delta\nu_{an}/2. \quad (1)$$

As is known from the literature [16], the isotropic Knight shift in bulk mercury changes insignificantly on transition from the liquid to solid phase. Assuming that this is also true for mercury in a restricted geometry, one can estimate the anisotropic component of the Knight shift from Eq. (1). The value of this component is approximately equal to –800 ppm for the SCN samples and silica gel and to –890 ppm for solid bulk mercury, which is considerably larger than for other metals [16] but smaller than the anisotropic component of the Knight shift in the superconducting phase of mercury at 1.2 K (–1400 ppm).

The observed decrease in the Knight shift for mercury in pores is related to the decrease in electronic susceptibility.The change in the electronic susceptibility near the metal surface was studied theoretically in [18]. It was shown that the effect of the surface consists in variations of the electron density in the vicinity of the Fermi level. The influence of the surface and the size effect on the Knight shift was studied by the NMR method in solid particles of platinum, vanadium, rhodium, and copper and in thin tin films [19]. The results obtained at low temperatures were interpreted in terms of the theory of quantum size effects, while the interpretation for the high-temperature region involved the dependence of the electronic susceptibility on the distance from the particle surface. For platinum and rhodium, it was experimentally found that the Knight shift for nuclei near the surface changed considerably in comparison with that in bulk samples mainly due to variations in the local density of *d* electrons at the Fermi level. A large broadening of NMR lines for such metals as Pb, Cu, and Ag was explained by the oscillations of electron density near the metal surface. Changes in the Knight shift were also observed for metals in a restricted geometry in the liquid state; e.g., for gallium and mercury, the Knight shift decreased [8, 9]. According to current theoretical ideas [18], the decrease in the Knight shift with respect to that in bulk mercury observed in the present study can be treated as a result of the decrease in electron density near the Fermi level. A characteristic feature is that the difference between the Knight shifts in liquid mercury in the SCN sample and in the bulk liquid mercury appreciably increases with decreasing temperature.

4. CONCLUSIONS

We have used the NMR method for studying the melting–crystallization processes and the Knight shift in mercury introduced into nanopores of activated carbon (PAC and SCN) and of silica gel. It has been established that the phase transitions in these samples proceed abruptly at the melting temperature coinciding with that in the bulk (in contrast to the case of melting and crystallization of mercury in zeolites, porous glasses, and asbestos). An insignificant hysteresis between melting and crystallization processes was observed. The NMR signal from solid mercury in pores was observed for the first time, and its Knight shift was measured. It was shown that the Knight shift for mercury in a restricted geometry decreases both in the liquid and in the solid phase as compared to the Knight shift in the bulk. The results obtained demonstrate a strong influence of pore geometry and of the material of porous matrices on the melting and crystallization of mercury and on its electronic susceptibility.

ACKNOWLEDGMENTS

This study was supported by the federal program "Integration" (project no. A0142) and by the National Science Council of Taiwan (grant no. 91-2112-M-006-017).

REFERENCES

1. P. Pawlov, Z. Phys. Chem. **65**, 545 (1909).
2. Yu. I. Petrov, *Clusters and Small Particles* (Nauka, Moscow, 1986).
3. R. R. Vanfleet and J. M. Mochel, Surf. Sci. **341**, 40 (1995).
4. G. S. Zhdanov, Izv. Akad. Nauk SSSR, Ser. Fiz. **41**, 1004 (1977).
5. T. Ben David, Y. Lereah, G. Deutsher, *et al.*, Phys. Mag. A **71**, 1135 (1995).
6. B. F. Borisov, E. V. Charnaya, T. Loeser, *et al.*, J. Phys.: Condens. Matter **11**, 10259 (1999).
7. K. M. Unruh, T. E. Huber, and C. A. Huber, Phys. Rev. B **48**, 9021 (1993).
8. D. Michel, B. F. Borisov, E. V. Charnaya, *et al.*, Nanostruct. Mater. **12**, 515 (1999).
9. B. F. Borisov, E. V. Charnaya, P. G. Plotnikov, *et al.*, Phys. Rev. B **58**, 5329 (1998).
10. E. V. Charnaya, P. G. Plotnikov, D. Michel, *et al.*, Physica B (Amsterdam) **299**, 56 (2001).

11. E. Méndez-Lango and J. Ancsin, Thermochim. Acta **287**, 183 (1996).
12. V. N. Bogomolov, F. I. Zadorozhnyĭ, A. A. Kapanadze, *et al.*, Fiz. Tverd. Tela (Leningrad) **18**, 3050 (1976) [Sov. Phys. Solid State **18**, 1777 (1976)].
13. V. N. Bogomolov, E. V. Kolla, and D. A. Kumzerov, Pis'ma Zh. Éksp. Teor. Fiz. **41**, 28 (1985) [JETP Lett. **41**, 34 (1985)].
14. H. K. Christenson, J. Phys.: Condens. Matter **13**, R95 (2001).
15. J. H. Strange, M. Rahan, and E. G. Smith, Phys. Rev. Lett. **71**, 3589 (1993).
16. G. C. Carter, L. H. Bennet, and D. J. Kahan, Prog. Mater. Sci. **20** (4), 2066 (1977).
17. J. Winter, *Magnetic Resonance in Metals* (Clarendon, Oxford, 1971; Mir, Moscow, 1976).
18. M. C. Desjonqueres and D. Spanjaard, *Concepts in Surface Physics* (Springer, Berlin, 1998).
19. É. L. Nagaev, Usp. Fiz. Nauk **162**, 49 (1992) [Sov. Phys. Usp. **35**, 747 (1992)].

Translated by A. Zalesskiĭ

Physics of the Solid State, Vol. 45, No. 9, 2003, pp. 1808–1813. Translated from Fizika Tverdogo Tela, Vol. 45, No. 9, 2003, pp. 1722–1726.

LOW-DIMENSIONAL SYSTEMS AND SURFACE PHYSICS

Dispersion and Attenuation of Rayleigh Waves at a One-Dimensional Random Roughness of the Free Surface of a Hexagonal Crystal

V. V. Kosachev and Yu. N. Gandurin

Moscow State Institute of Engineering Physics (Technical University), Kashirskoe sh. 31, Moscow, 115409 Russia
e-mail: kosachev@theor.mephi.ru

Received December 23, 2002; in final form, March 4, 2003

Abstract—Analytical expressions are derived for dispersion and attenuation of Rayleigh waves propagating along the statistically rough free surface of a hexagonal crystal (*Z* cut). The roughness under consideration is one-dimensional (the profile function of the roughness depends on one coordinate) and has the form of hollows of a random lattice. The results obtained earlier in the solution of an analogous problem for a two-dimensional roughness are used in the one-dimensional case. The relationships derived for the dispersion and attenuation of Rayleigh waves are treated analytically and numerically over the entire range of frequencies acceptable in the framework of the perturbation theory. It is shown that the dispersion and attenuation of Rayleigh waves are qualitatively similar to those observed in an isotropic medium. *© 2003 MAIK "Nauka/Interperiodica".*

1. INTRODUCTION

In our recent work [1], we carried out a detailed analysis of the dispersion and attenuation of Rayleigh waves at a two-dimensional random roughness of the free surface of a hexagonal crystal. In this respect, it is of interest to investigate the specific features in the behavior of the dispersion and attenuation of Rayleigh waves at a one-dimensional random roughness (hollows of a random lattice).

Wave scattering from a one-dimensional random roughness of the free interface of an isotropic solid has been studied in a number of works [2–15]. In particular, scattering of bulk waves by determinate and periodic roughnesses was examined in [2–5]. In [6–8], scattering of bulk waves by random roughnesses was considered in the scalar case (i.e., in the absence of surface and shear waves). The attenuation of Rayleigh waves was investigated experimentally by de Billy *et al.* [9] and theoretically by Maradudin and Huang [10], who derived the dispersion law for a Rayleigh wave in the framework of the mean-field (Rayleigh) method. In [11–15], the attenuation of a Rayleigh wave was considered within the scattering theory. In our previous works [11, 13], we also studied the scattering of surface Rayleigh waves and bulk acoustic waves. It should be emphasized that, in [10, 11, 13, 15], the analysis was performed for a Rayleigh wave propagating along the *x* axis, i.e., in the direction perpendicular to the hollows of the lattice.

Earlier [16], we obtained the expressions describing the dispersion and attenuation of Rayleigh waves and surface waves of shear horizontal (SH) polarization on a random rough free surface of an isotropic medium at an arbitrary angle of incidence on the lattice hollows. It should be noted that, when deriving the expressions for the dispersion and attenuation at a one-dimensional random roughness, the one-dimensional roughness was treated as a special case of the two-dimensional roughness.

In the present work, by analogy with the calculations performed in [16], the dispersion of the phase velocity and the coefficient of attenuation of Rayleigh waves at a one-dimensional random roughness with an arbitrary angle of incidence on the hollows of a random lattice were determined from the relationships obtained in [1] for a hexagonal crystal with the sixfold axis perpendicular to the surface (*Z* cut). The expressions derived were treated analytically and numerically over the entire range of frequencies acceptable in the framework of the perturbation theory.

2. FORMULATION OF THE PROBLEM

The geometry of the problem is shown in Fig. 1. A hexagonal crystal with the sixfold axis parallel to the x_3 axis is bounded by the statistically rough free surface $x_3 = \zeta(x_1)$ and occupies the half-space $x_3 \geq \zeta(x_1)$, where $\zeta(x_1)$ is the profile function of the one-dimensional roughness. The hexagonal crystal is considered in the elastic-continuum approximation and is characterized by the mass density ρ and the elastic constant tensor $C_{\alpha\beta\mu\nu}$. The one-dimensional roughness $\zeta(x_1)$ is described by the root-mean-square roughness amplitude δ and the roughness correlation length *a*. A Rayleigh wave propagates along the statistically rough surface of the hexagonal medium in the plane $x_3 = 0$

1063-7834/03/4509-1808$24.00

(*Z* cut). In order to solve the formulated problem, it is required to determine the dispersion of the phase velocity and the coefficient of attenuation of the Rayleigh wave at the surface roughness.

The solution to the problem will be sought under the assumption that the roughness is small; i.e., $\delta \ll \lambda$, where λ is the Rayleigh wavelength. Since the profile function of the roughness is unknown, the surface can be described statistically. In the case of a one-dimensional roughness, the profile function $\zeta(x_1)$ is defined as

$$\langle \zeta(x_1) \rangle = 0, \tag{1}$$

$$\langle \zeta(x_1)\zeta(x_1') \rangle = \delta^2 W(|x_1 - x_1'|), \tag{2}$$

or, in the Fourier representation,

$$\langle \zeta(k_1) \rangle = 0, \tag{3}$$

$$\langle \zeta(k_1)\zeta(q_1) \rangle = \delta^2 g(|k_1|)(2\pi)\delta(k_1 + q_1), \tag{4}$$

$$\zeta(k_1) = \int dx_1 \exp(-ik_1 x_1)\zeta(x_1). \tag{5}$$

In order to obtain the explicit analytical expressions, we will use the factor $g(|k_1|)$ in the Gaussian form

$$g(|k_1|) = a\sqrt{\pi}\exp(-k_1^2 a^2/4). \tag{6}$$

3. FORMAL PASSAGE FROM THE TWO-DIMENSIONAL CASE TO THE ONE- DIMENSIONAL CASE

For a two-dimensional roughness $x_3 = \zeta(x_1, x_2)$, the problem analogous to that formulated above was solved in our previous work [1]. The dispersion relations (see expressions (25), (26) in [1]) can be represented in the general form

$$\Delta\omega = \delta^2 \int \frac{dq_1 dq_2}{(2\pi)^2} g(|\mathbf{k}_\parallel - \mathbf{q}_\parallel|) R(q_\parallel, k_\parallel|\omega). \tag{7}$$

Here, the integral is taken over the plane $q_3 = 0$. Let us consider a one-dimensional roughness as a special case of the two-dimensional roughness. Then, we can write the equations

$$\begin{aligned}\zeta(k_1, k_2) &= \int d^2 x_\parallel \exp(-ik_\parallel x_\parallel)\zeta(x_1) \\ &= (2\pi)\delta(k_2)\zeta(k_1),\end{aligned} \tag{8}$$

$$\langle \zeta(\mathbf{k}_\parallel)\zeta(\mathbf{q}_\parallel) \rangle = \delta^2 g(|k_1|)\delta(k_2)(2\pi)^3 \delta(\mathbf{k}_\parallel + \mathbf{q}_\parallel). \tag{9}$$

For a two-dimensional roughness, expression (9) has the form

$$\langle \zeta(\mathbf{k}_\parallel)\zeta(\mathbf{q}_\parallel) \rangle = \delta^2 g(|\mathbf{k}_\parallel|)(2\pi)^2 \delta(\mathbf{k}_\parallel + \mathbf{q}_\parallel), \tag{10}$$

and relationship (6) can be written as

$$g(|\mathbf{k}_\parallel|) = \pi a^2 \exp(-k_\parallel^2 a^2/4). \tag{11}$$

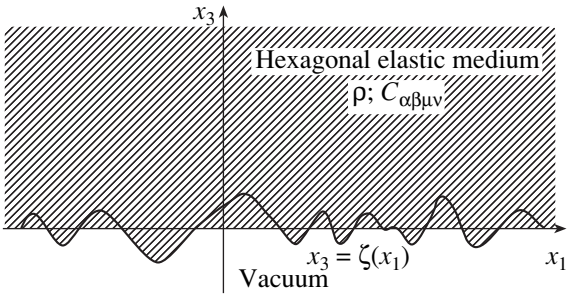

Fig. 1. Geometry of the semi-infinite homogeneous hexagonal elastic medium with a one-dimensional roughness of the free surface $x_3 = \zeta(x_1)$.

From a comparison of relationships (9) and (10), it follows that formulas describing the dispersion and attenuation of Rayleigh waves at a one-dimensional random roughness can be obtained using formal replacement in the expressions for the two-dimensional roughness; that is,

$$g(\mathbf{k}_\parallel) \longrightarrow g(\mathbf{k}_\parallel) = (2\pi)\delta(k_2)g(|k_1|). \tag{12}$$

It is assumed that the Rayleigh wave is incident on hollows of a random lattice at an arbitrary angle ψ (the ψ angle is measured from the normal to the hollows parallel to the x_2 axis). Hence, we obtain

$$\mathbf{k}_\parallel = k_\parallel(\cos\psi, \sin\psi). \tag{13}$$

By virtue of the translational invariance along the x_2 axis, the wave vector component parallel to this axis remains unchanged. As a result, according to replacement (12), we have

$$\mathbf{q}_\parallel = (q_1, k_\parallel \sin\psi) = (q_1, k_2), \tag{14}$$

$$q_\parallel = q_\parallel(q_1) = \sqrt{q_1^2 + k_\parallel^2 \sin^2\psi}. \tag{15}$$

Consequently, the ψ angle between the vectors $\mathbf{k}_\parallel$ and $\mathbf{q}_\parallel$ can be written as

$$\cos\psi = \frac{k_1 q_1 + k_2 q_2}{k_\parallel q_\parallel} = \frac{q_1 \cos\psi + k_\parallel \sin^2\psi}{\sqrt{q_1^2 + k_\parallel^2 \sin^2\psi}}, \tag{16}$$

$$\sin\psi = \frac{k_1 q_2 - k_2 q_1}{k_\parallel q_\parallel} = \frac{k_\parallel \sin\psi\cos\psi - q_1 \sin\psi}{\sqrt{q_1^2 + k_\parallel^2 \sin^2\psi}}. \tag{17}$$

Upon substituting formulas (12)–(17) into expression (7), we obtain the following relationship for the dispersion and attenuation of Rayleigh waves at the one-dimensional roughness of the surface:

$$\Delta\omega(k_\parallel, \psi) = \nu_1(k_\parallel, \psi) - i\nu_2(k_\parallel, \psi). \tag{18}$$

Here, the real part $\nu_1(k_\parallel, \psi)$ describes the dispersion of the phase velocity and the imaginary part $\nu_2(k_\parallel, \psi)$ is proportional to the inverse attenuation length.

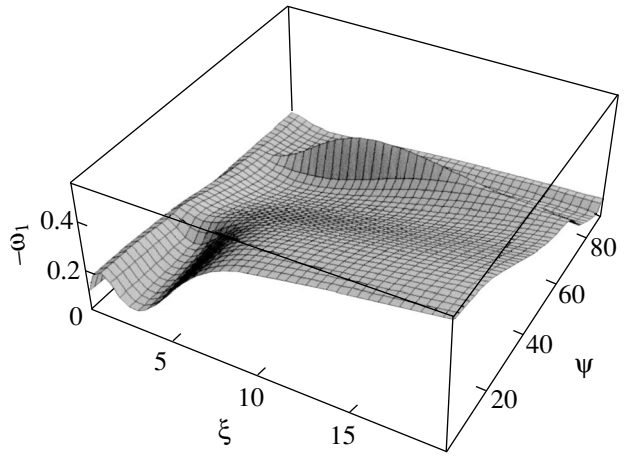

Fig. 2. Dependence of the real part of the complex frequency shift $-\omega_1$ on the dimensionless variable ξ and the angle of incidence ψ of the Rayleigh wave for a ZnO crystal.

Next, it is convenient to change over to the dimensionless function ω_{12}:

$$\frac{\Delta\omega}{\omega_R} = \frac{\delta^2}{a^2}\omega_{12}(\xi, \psi). \tag{19}$$

Here, $\xi = k_\parallel a$ is the dimensionless variable and $\omega_R = c_R k_\parallel$ (where c_R is the phase velocity of the Rayleigh wave propagating along a planar surface). Therefore, the dimensionless function $\omega_{12}(\xi, \psi)$ can be written in the form

$$\omega_{12}(\xi, \omega) = -\frac{d}{2\sqrt{\pi}}\xi^3(A(\xi, \psi) + B(\xi, \psi) + E(\xi, \psi)) + \xi^2 l. \tag{20}$$

The functions $A(\xi, \psi)$, $B(\xi, \psi)$, and $E(\xi, \psi)$ and the coefficients d and l are given in the Appendix. The dimensionless function $\omega_{12}(\xi, \psi)$ can be conveniently expressed, by analogy with formula (18), through the real and imaginary parts. We leave aside the rather cumbersome formulas describing the real and imaginary parts and write the final result

$$\omega_{12} = \omega_1 - i\omega_2. \tag{21}$$

It should be noted that the above expression for $\omega_{12}(\xi, \psi)$, which is symmetric with respect to the replacement $\psi \longrightarrow \psi + \pi$, depends on the ψ angle only as $\cos\psi$; hence, it is symmetric with respect to the replacement $\psi \longrightarrow -\psi$. Therefore, the set of ψ angles can be considered in the interval $\psi \in [0, \pi/2]$. This symmetry also follows from the statement of the problem.

4. THE LONG-WAVELENGTH LIMIT

In the long-wavelength limit ($\lambda \gg a$), we have the dimensionless variable $\xi \ll 1$. The relationship for the imaginary part $\omega_2(\xi, \psi)$ takes the form

$$\omega_2(\xi, \psi) = \frac{\Lambda(\psi)}{2}\xi^3. \tag{22}$$

Here, $\Lambda(\psi)$ depends only on the ψ angle and the coefficients of the elastic constant tensor. The expression for $\Lambda(\psi)$ is cumbersome and, hence, is not presented. Since $\nu_2(k_\parallel, \psi) = c_R/2L(k_\parallel, \psi)$ (see [17]), the inverse attenuation length $1/L$ of the Rayleigh wave can be written as

$$\frac{1}{L} = \frac{\delta^2}{a^3}\xi^4\Lambda(\psi). \tag{23}$$

For the real part of the function ω_{12}, the integral is taken at large values of the variable of integration t and the functions $D_n(t, \psi)$ with an odd subscript n are equal to zero. As a result, the expression for the real part $\omega_1(\xi, \psi)$ takes the form

$$\omega_1(\xi, \psi) = -\Phi(\psi)\xi, \tag{24}$$

where

$$\Phi(\psi) = \frac{d}{a_1\sqrt{\pi}}[a_1 h^{3/2}(1 - \cos(4\psi)) + (\sqrt{a_2 + b_2} + \sqrt{a_2 - b_2})(2(a_1 - h)^2 + h^2 + 4h(a_1 - h)\cos(2\psi) + h^2\cos(4\psi))],$$

$$a_2 = \frac{1}{2}\left(a_1 - 2\frac{c_{13}}{c_{33}}\right), \quad b_2 = \sqrt{a_2 - \frac{c_{11}}{c_{33}}}.$$

The coefficients d, a_1, and h are given in the Appendix.

Taking into account the real part of the dimensionless function (19), the relative change in the phase velocity of the Rayleigh wave can be represented in the form

$$\frac{\Delta c(\xi, \psi)}{c_R} = -\frac{\delta^2}{a^2}\Phi(\psi)\xi. \tag{25}$$

5. NUMERICAL CALCULATION

In addition to the analytical treatment, we carried out numerical calculations of the relative change in the phase velocity and the inverse attenuation length of the Rayleigh wave. As an example, let us consider the results of the numerical calculations of expressions (20), (22), and (24) for a ZnO hexagonal crystal (the coefficients of the elastic constant tensor for ZnO are taken from [18]). The real and imaginary parts of the function $\omega_{12}(\xi, \psi)$ are shown in graphic form in Figs. 2 and 3,

respectively. These figures clearly illustrate the dispersion and attenuation of the Rayleigh waves. It is evident, in particular, from Fig. 2 that the dispersion of the phase velocity of the Rayleigh wave propagating along a rough surface, as in the isotropic case, can exceed the dispersion on a planar surface for the dimensionless variable $\xi \sim 1$ and the ψ angle ranging from ~55° to 90°. The results of the numerical calculations of the coefficients $\Phi(\psi)$ and $\Lambda(\psi)$ in the long-wavelength limit ($\xi \ll 1$) are presented in Figs. 4 and 5, respectively. As can be seen from these figures, the Rayleigh waves at large angles of incidence ψ attenuate only slightly, whereas the dispersion remains nonzero. It should also be noted that, for the majority of the known hexagonal crystals, the dependences obtained from the numerical calculations of expression (20) coincide qualitatively.

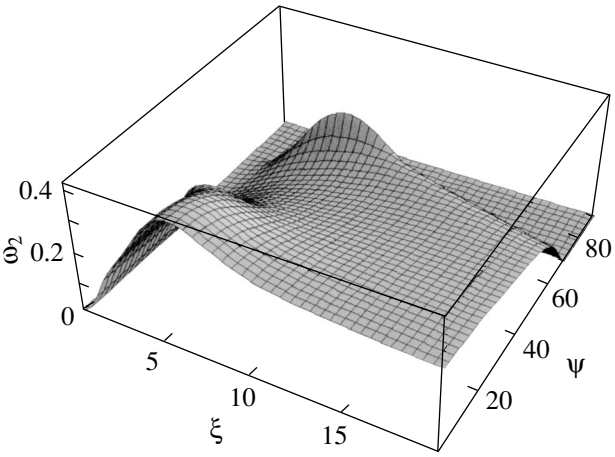

Fig. 3. Dependence of the imaginary part of the complex frequency shift ω_2 on the dimensionless variable ξ and the angle of incidence ψ of the Rayleigh wave for a ZnO crystal.

6. CONCLUSIONS

Thus, analytical expressions have been obtained for the dispersion and attenuation of Rayleigh waves propagating in an arbitrary direction along the statistically rough free surface of a hexagonal crystal with the sixfold axis perpendicular to the crystal surface (*Z* cut). The roughness under consideration is assumed to be one-dimensional and has the form of hollows of a random lattice. The expressions are deduced using the results obtained in our previous work [1] for the dispersion and attenuation of Rayleigh waves at a two-dimensional roughness within the approach described in [16]. For an isotropic medium, the derived dispersion relation (20) is transformed into expression (5.12) deduced in [16]. The relative change in the phase velocity and the inverse attenuation length of the Rayleigh wave are numerically calculated for the majority of the known hexagonal crystals at arbitrary angles of incidence on hollows of the lattice over the entire range of wavelengths acceptable in the framework of the perturbation theory. The dependences obtained for different hexagonal crystals coincide qualitatively with each other and with those for the isotropic medium [16] but differ quantitatively, which is associated with the isotropy of the *Z*-cut hexagonal crystal. It was found that, as in the isotropic case, the dispersion of the phase velocity of the Rayleigh wave propagating along a rough surface can exceed the dispersion on a planar surface. The long-wavelength limit was investigated analytically and numerically. The analytical treatment demonstrated that the inverse attenuation length of the Rayleigh wave is proportional to the fourth power of the Rayleigh wave frequency, whereas the relative change in the phase velocity is directly proportional to the Rayleigh wave frequency, which is in complete agreement with the results obtained in the isotropic case.

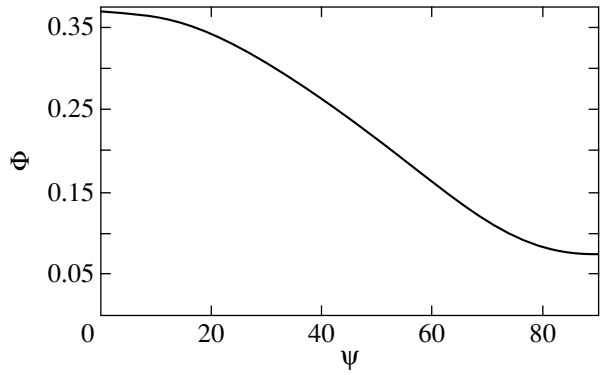

Fig. 4. Dependence of the function Φ on the angle of incidence ψ for a ZnO crystal in the long-wavelength limit ($\xi \ll 1$).

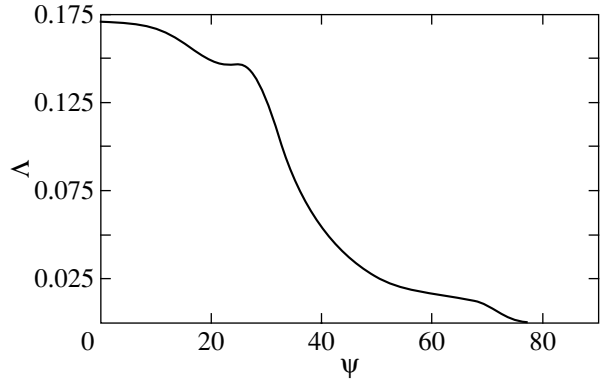

Fig. 5. Dependence of the function Λ on the angle of incidence ψ for a ZnO crystal in the long-wavelength limit ($\xi \ll 1$).

APPENDIX

$$A(\xi,\psi) = \int\limits_{\frac{\sin^2\psi}{\varepsilon}}^{\infty} \frac{\varepsilon}{2\tilde{a}_{tt}(t)}\frac{dt}{}\left\{\frac{\sqrt{\varepsilon}}{2}(\varepsilon + th^2)D_0(t,\psi)\right.$$
$$-\varepsilon\sqrt{t}hD_1(t,\psi) - \frac{\varepsilon^{3/2}}{2}D_2(t,\psi) + h\varepsilon\sqrt{t}D_3(t,\psi) \quad \text{(A.1)}$$
$$\left. - \frac{h^2\sqrt{\varepsilon}t}{2}D_4(t,\psi)\right\},$$

$$B(\xi,\psi) = -P\int\limits_{\frac{\sin^2\psi}{\varepsilon}}^{\infty} \frac{\varepsilon^{3/2}}{2}dt\frac{\tilde{\alpha}_p(t)}{\tilde{\alpha}_m(t) + (1-a_1t)\sqrt{t-1}} \quad \text{(A.2)}$$
$$\times \sum_{n=0}^{4}\Phi_n(t)D_n(t,\psi),$$

$$E(\xi,\psi) = i\pi d\frac{2\cos(\psi)}{\varepsilon}\left\{\left(a_1^2 - 2a_1h + \frac{3}{2}h^2 + \frac{\varepsilon^2}{2}\right.\right.$$
$$+ (a_1-\varepsilon)^2 - (a_1-h)\gamma\Big)D_0\Big(\frac{1}{\varepsilon},\psi\Big) + \varepsilon(\gamma + h - 2a_1) \quad \text{(A.3)}$$
$$\times D_1\Big(\frac{1}{\varepsilon},\psi\Big) + \Big(\frac{\varepsilon^2}{2} + 2h(a_1-h) - h\gamma\Big)D_2\Big(\frac{1}{\varepsilon},\psi\Big)$$
$$\left. - h\varepsilon D_3\Big(\frac{1}{\varepsilon},\psi\Big) + \frac{h^2}{2}D_4\Big(\frac{1}{\varepsilon},\psi\Big)\right\},$$

$$l = -\frac{d}{\alpha_p\varepsilon\sqrt{\varepsilon}}\Big(\varepsilon\Big(1 + \frac{c_{13}}{c_{33}}\Big) - a_1\Big)\Big(\varepsilon\Big(\frac{c_{13}}{c_{33}} - 1\Big) + a_1\Big), \quad \text{(A.4)}$$

$$d = \frac{(1-\varepsilon)\Big(\frac{c_{11}}{c_{44}} - \varepsilon\Big)\alpha_p\sqrt{\varepsilon}}{\Big(2a_1 - \frac{c_{11}}{c_{44}} + 1\Big)\varepsilon^2 - \varepsilon a_1\Big(\frac{c_{11}}{c_{44}} + 3\Big) + 2a_1\frac{c_{11}}{c_{44}}}. \quad \text{(A.5)}$$

In expressions (A.1)–(A.5), we used the following designations:

$$D_n(t,\psi) = \frac{1}{\sqrt{\varepsilon t - \sin^2\psi}}$$
$$\times\Big[\exp\Big(-\frac{\xi^2}{4}(\cos\psi - \sqrt{\varepsilon t - \sin^2\psi})^2\Big)\cos(n\Theta(\eta,\psi))$$
$$+ \exp\Big(-\frac{\xi^2}{4}(\cos\psi + \sqrt{\varepsilon t - \sin^2\psi})^2\Big)\cos(n\Theta(-\eta,\psi))\Big],$$

$$\cos(\Theta(\eta,\psi)) = \frac{\eta\cos\psi + \sin^2\psi}{\sqrt{\varepsilon t}},$$

$$\eta = \sqrt{\varepsilon t - \sin^2\psi}, \quad \psi \in [0, \pi/2],$$

$$\Phi_0(t) = t\sqrt{t-1}\frac{2(a_1-h)^2 + h^2}{2} + \frac{\varepsilon\sqrt{t-1}}{2}$$
$$+ \frac{t2(a_1-h)}{\varepsilon\alpha_p\tilde{\alpha}_p(t)}\Big(\varepsilon\frac{c_{33}+c_{13}}{c_{33}} - a_1\Big)\Big(\tilde{\alpha}_m(t) - \frac{c_{13}}{c_{33}}\sqrt{t-1}\Big)$$
$$+ \tilde{\alpha}_m(t)(a_1 - \varepsilon),$$

$$\Phi_1(t) = -\frac{2\sqrt{t}}{\sqrt{\varepsilon}\alpha_p\tilde{\alpha}_p(t)}\Big(\varepsilon\frac{c_{33}+c_{13}}{c_{33}} - a_1\Big)$$
$$\times\Big(\tilde{\alpha}_m(t) - \frac{c_{13}}{c_{33}}\sqrt{t-1}\Big) - \sqrt{\varepsilon t(t-1)}(2a_1 - h),$$

$$\Phi_2(t) = \frac{\varepsilon}{2}\sqrt{t-1} + 2h(a_1-h)t\sqrt{t-1}$$
$$+ \frac{2ht}{\varepsilon\alpha_p\tilde{\alpha}_p(t)}\Big(\varepsilon\frac{c_{33}+c_{13}}{c_{33}} - a_1\Big)\Big(\tilde{\alpha}_m(t) - \frac{c_{13}}{c_{33}}\sqrt{t-1}\Big),$$

$$\Phi_3(t) = -h\sqrt{\varepsilon t(t-1)}, \quad \Phi_4(t) = \frac{h^2}{2}t\sqrt{t-1},$$

$$\alpha_p = \tilde{\alpha}_p\Big(\frac{1}{\varepsilon}\Big), \quad \tilde{\alpha}_p(t) = \tilde{\alpha}_{t1} + \tilde{\alpha}_{t2}, \quad \tilde{\alpha}_m(t) = \frac{\tilde{\alpha}_{t1}\tilde{\alpha}_{t2}}{\sqrt{t-1}},$$

$$\tilde{\alpha}_{t1}^2 = \frac{1}{2}(z + \sqrt{z^2 - 4y_2}), \quad \tilde{\alpha}_{t2}^2 = \frac{1}{2}(z - \sqrt{z^2 - 4y_2}),$$

$$\operatorname{Re}\tilde{\alpha}_{t1,t2} > 0, \quad \operatorname{Im}\tilde{\alpha}_{t1,t2} < 0,$$

$$y_2 = \frac{c_{11}}{c_{33}}(t-1)\Big(t - \frac{c_{44}}{c_{11}}\Big),$$

$$z = \Big(a_1 - 2\frac{c_{13}}{c_{33}}\Big)t - \Big(1 + \frac{c_{44}}{c_{33}}\Big),$$

$$\tilde{\alpha}_{tt}(t) = \begin{cases}\sqrt{ht-1}, & ht - 1 \geq 0\\ -i\sqrt{1-ht}, & ht - 1 < 0,\end{cases}$$

$$a_1 = \frac{c_{11}c_{33} - c_{13}^2}{c_{33}c_{44}}, \quad h = \frac{c_{11} - c_{12}}{2c_{44}},$$

$$\gamma = \frac{2\varepsilon\Big(\varepsilon\Big(1 + \frac{c_{13}}{c_{33}}\Big) - a_1\Big)^2}{a_1^2(1-\varepsilon) - \Big(1 + \frac{2c_{13} + c_{11}}{c_{33}} - a_1\Big)\varepsilon^2},$$

$$\left(1 - \frac{c_{44}}{c_{33}}\right)\varepsilon^3 + \left(\frac{c_{11}}{c_{33}} - 1 - 2a_1\right)\varepsilon^2$$

$$+ a_1(2 + a_1)\varepsilon - a_1^2 = 0,$$

$$0 < \varepsilon < \min(1, a_1).$$

In formula (A.2), P stands for integration in the sense of the Cauchy principal value and the sign "+" corresponds to the point $t_0 = \frac{1}{\varepsilon}$.

REFERENCES

1. V. V. Kosachev and Yu. N. Gandurin, Fiz. Tverd. Tela (St. Petersburg) **45** (2), 369 (2003) [Phys. Solid State **45**, 391 (2003)].
2. V. I. Gigor'evskiĭ, Yu. V. Gulyaev, I. M. Kotelyanskiĭ, *et al.*, Akust. Zh. **31** (5), 711 (1985) [Sov. Phys. Acoust. **31**, 437 (1985)].
3. A. D. Lapin, Akust. Zh. **28** (3), 359 (1982) [Sov. Phys. Acoust. **28**, 212 (1982)].
4. R. Sato, J. Seismol. Soc. Jpn. Zisin. B **1**, 8 (1955).
5. I. I. Abubakar, Proc. Cambridge Philos. Soc. **58** (1), 136 (1962).
6. F. G. Bass and I. M. Fuks, *Wave Scattering from Statistically Rough Surfaces* (Nauka, Moscow, 1972; Pergamon Press, Oxford, 1978).
7. A. G. Voronovich, Akust. Zh. **30** (6), 747 (1984) [Sov. Phys. Acoust. **30**, 444 (1984)].
8. Yu. N. Lysanov, in *Acoustics of the Ocean*, Ed. by L. M. Brekhovskikh (Nauka, Moscow, 1974), pp. 231–330.
9. M. de Billy, G. Quentin, and E. Baron, J. Appl. Phys. **61** (6), 2140 (1987).
10. A. A. Maradudin and X. Huang, Phys. Rev. B **36** (15), 7827 (1987).
11. V. V. Kosachev, Yu. N. Lokhov, and V. N. Chukov, Preprint No. 034-88, MIFI (Moscow Inst. of Engineering Physics, 1988).
12. A. P. Mayer and M. Lehner, Waves Random Media **4** (3), 321 (1994).
13. V. V. Kosachev, Yu. N. Lokhov, and V. N. Chukov, Fiz. Tverd. Tela (Leningrad) **32** (7), 2045 (1990) [Sov. Phys. Solid State **32**, 1189 (1990)].
14. V. V. Kosachev, Yu. N. Lohov, and V. N. Chukov, Solid State Commun. **73** (8), 535 (1990).
15. S. Z. Dunin and G. A. Maksimov, Preprint No. 032-88, MIFI (Moscow Inst. of Engineering Physics, 1988).
16. V. V. Kosachev and A. V. Shchegrov, Ann. Phys. (N.Y.) **240** (2), 225 (1995).
17. A. G. Eguiluz and A. A. Maradudin, Phys. Rev. B **28** (2), 728 (1983).
18. O. L. Anderson, Phys. Acoust. B **3**, 80 (1965).

Translated by O. Borovik-Romanova